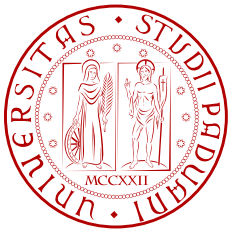

UNIVERSITÀ DEGLI STUDI DI PADOVA
Facoltà di Scienze MM.FF.NN.
Dipartimento di Fisica e Astronomia "G. Galilei"

Scuola di Dottorato di Ricerca in Fisica
Ciclo XXV

Development of New Composite Mirrors for Imaging Cherenkov Telescopes and Observations of the Two Blazar Objects 1ES 0806+524 and 1ES 1011+496 with MAGIC

Direttore della Scuola:	Prof. Andrea Vitturi
Supervisore:	Prof. Mosè Mariotti
Correlatore:	Dott. Elisa Prandini

Dottoranda: Cornelia Hanna Esther Schultz

to my parents,
Esther & Uwe,
to my twin brother,
Philipp,
and to my soulmate Mikai

Summary

This PhD thesis is addressed to the technical and scientific studies carried out in the research field of very high energy (VHE, E > 100 GeV) γ–ray astronomy, a promising discipline which is extending the frontier of our knowledge of the emission by extraterrestrial sources to the highest observable energies of the electromagnetic spectrum.

Radio–loud active galactic nuclei (AGNs) are astronomical objects whose emission along relativistic jets is powered by the accretion of matter onto the disk of a supermassive black hole. Depending on the orientation of their relativistic jets, radio–loud AGNs are divided into two categories, among them the so–called blazars. Such objects present one jet oriented at small angles with respect to the line of sight of an observer. To now, the majority of detected extragalactic VHE γ–ray emitters belongs to the class of blazars.

Most of such VHE γ–ray emitters have been discovered win the last decade thanks to the operation of the current generation of IACTs represented by the MAGIC (Major Atmospheric Imaging Cherenkov) telescopes, H.E.S.S. (High Energy Stereoscopic System) and VERITAS (Very Energetic Radiation Imaging Telescope Array System). The numerous discoveries have been possible thanks to fundamental improvements in sensitivity and the extension of the energy range of these instruments with respect to their predecessors. In addition, the cooperation with instruments observing at other energies, for example in the optical regime and in the γ–ray range below 100 GeV, has emerged to be very important.

Along the travel to Earth, the VHE γ–ray emission of distant sources is attenuated due to the interaction with the extragalactic background light (EBL). This optical to infrared radiation is composed by the star light emission which is partially reprocessed by dust and continuously redshifted by the expansion of the Universe. Due to EBL absorption of VHE γ–ray radiation, the intrinsic spectrum emitted by blazars is deformed. Such deformation scales with increasing energy of the VHE γ–ray and with the source distance. For this reason, the AGNs detected in VHE γ–rays are located at relative short distances. The most distant VHE γ–ray emitter detected so far is the blazar 3C 279 located at redshift $z = 0.536$.

This PhD thesis is focused on two research activities: a technical and a scientific part carried out within the MAGIC and CTA collaborations. The technical research is dedicated to the development of new IACT mirrors of improved optical performance and optimized price/performance ratio for future IACTs, while the scientific research concerns the detailed analysis of the VHE γ–ray emission of two distant blazars, 1ES 0806+524 and 1ES 1011+496, observed with the MAGIC telescopes.

More precisely, the first part is dedicated to the development of new mirrors for the future generation of IACTs, heralded by the CTA (Cherenkov Telescope Array) project, as well as the optical qualification of such mirrors. The challenge is to find a balanced compromise between the costs related to the realization of high reflective mirrors and the required optical quality. In particular, the focusing power and spectral reflectivity represent the most crucial optical parameters

regarding the IACT performance in terms of detection area and light detection efficiency. In addition, considering the conditions under which IACTs are operated, such mirrors should provide a high resistance against environmental impacts.

In the framework of the technical activity, first prototypes of composite mirrors have been developed based on the replica principle from a curved mold of high precision in a two step process: In a first step, a spherical mirror substrate, similar to that produced for the MAGIC telescopes, is shaped on the mold. In a second step, a reflective layer, also shaped on the mold, is deposited on the mirror substrate. Various solutions have been probed with respect to the realization of a cost efficient surface of highest reflectance achievable in the wavelength range of interest. For this purpose, different prototypes have been produced. The optical performance of these first prototypes has been studied by means of a so–called $2f$–setup that has been installed at the Legnaro National Laboratories (LNL) of INFN. Such setup is suited to measure the focusing power referred to as point spread function (PSF) and the radius of curvature of spherical mirrors. Regarding the PSF study, parametrized by the D_{80} (the diameter of 80% light containment), a software tool has been developed. The optical qualifications revealed that the PSF of these prototypes does not meet the CTA specifications demanding modifications of the replication technique to achieve a higher precision. The tuning of the replication procedure is ongoing aiming at an improvement of the PSF by a factor of three.

Beside the prototyping activity, the technical research was addressed to the coordination of a cross calibration of the optical test equipment shared in the CTA consortium. Several institutes are currently investigating the development of new IACT mirrors of adequate properties for CTA. Obviously, each of these institutes uses their own test facilities to perform optical qualifications. To evaluate the reliability of these optical qualifications, three IACT mirrors of different characteristics and dimensions were circulated among different institutes. These mirrors have been also measured with $2f$–setup installed at the LNL of INFN. The final task related to this activity regards the comparative study of the individual optical qualifications. Therefore, several testing conditions affecting the PSF determination are critically considered. Furthermore, to exclude possible discrepancies among the PSF results due to different analysis software, an additional data analysis crosscheck is performed when possible. In the context of this cross calibration, several technical and analytical aspects are spotted to have an impact on the optical qualification. In particular the PSF determination is strongly affected demanding the specification of a detailed measurement procedure and minimally standardized analysis tools.

The second part of this PhD thesis treats the scientific research activity related to the detailed analysis of the VHE γ–ray emission from two blazars of distant redshift, 1ES 0806+524 and 1ES 1011+496, observed with MAGIC.

The MAGIC system, located on the Canary island of La Palma at the Roque de Los Muchachos at 2225 m above sea level, is composed of two IACTs of 17 m diameter sensitive to VHE γ–rays of energies as low as 50 GeV. These telescopes are suited for the observation of Cherenkov radiation which is emitted by secondary particles produced by the interaction of VHE γ–rays with the atmosphere.

Both blazars have been observed in stereoscopic mode, i.e. with both MAGIC telescopes pointing simultaneously to the same source. While 1ES 0806+524 has been observed for 24 hours in 2011, 1ES 1011+496 observations have been performed in 2011 and 2012 for 13 and 23 hours respectively. The observations of 1ES 0806+524 were triggered by a high state of the source in the optical regime referred to as flare or outburst. Simultaneously, the source underwent a

short VHE γ–ray flare that has been caught by MAGIC. Thus, MAGIC observed 1ES 0806+524 in both a high and a low state. Previous observations of these objects in this energy regime lead to spectral analysis of rather low precision, motivating the observations presented in this thesis. In addition, due to the absence of simultaneous observations in other bands, in particular in HE γ–rays, the broadband spectral energy distributions (SEDs) of these two sources was only moderately constrained.

For both sources the analysis of the temporal evolution of the observed integral flux and the differential energy spectrum is presented. In the case of 1ES 0806+524, the observations indicate a short–term variability at a daily time scale, while 1ES 1011+496 seems to be a rather constant emitter in VHE γ–rays.

Typically, the observed VHE differential spectra from blazars follow a simply power law of the form $\mathrm{d}N/\mathrm{d}E = f_0 \cdot E^{-\Gamma}$, with a spectral index Γ. The differential spectra of both sources are well described by such a law. Regarding 1ES 0806+524, the spectral indeces of the low and high source state are consistent within the errors. In the case of 1ES 1011+496, the spectral index of the differential spectra observed in 2011 and 2012 is constant.

For each source, the results of this analysis have been combined with simultaneous observations carried out in other wavebands from optical to γ–rays. In the case of 1ES 1011+496, the multiwavelength (MWL) coverage in 2012 includes for the first time complementary optical polarimetry data.

Apparently, there seems to be a connection between the optical and VHE γ–ray integral flux in the case of 1ES 0806+524. By contrast, 1ES 1011+496 features only modest if any variability in VHE γ–rays, while this source shows clear variability in other energy bands. The preliminary interpretation of the polarimetric data indicates a rather low degree of polarization associated with a low ordering of the magnetic field of the source. Moreover, the data do not contain any strong signature of shocks.

Finally, the VHE γ–ray spectra are combined with simultaneous and quasi simultaneous MWL observations in order to construct the SEDs 1ES 0806+524 and 1ES 1011+496. Taking into account the VHE γ–ray flare of 1ES 0806+524 observed by MAGIC, the data set is divided into a high and low state sample. Concerning 1ES 1011+496, the observations carried out in 2011 and 2012 are treated separately.

The typical two bump structure clearly arises in both cases, in agreement with the current models of blazar emission. The SEDs are reproduced with a SSC (Synchrotron Self–Compton) model assuming one emission region in order to extract the main physical parameters that govern the emission in the blazar jet. In both cases, a first detailed coverage of the high energy peak is achieved thanks to the simultaneous data in the HE /VHE regime.

In conclusion, the status of the development of new IACT mirrors for CTA is presented together with the optical qualifications of the first prototypes. In addition, a study of the reliability of such optical qualifications is reported. The observations of the VHE γ–ray emission of 1ES 0806+524 and 1ES 1011+496 yield a detailed measure of the differential spectra which offer the possibility to probe the EBL. Finally, the MWL coverage allows a first precise SED determination.

Riassunto

Questa tesi di dottorato riguarda agli studi tecnici e scientifici svolti nell'ambito dell'astrofisica delle altissime energie (VHE; Very High Energy), promettente disciplina che sta estendendo la frontiera delle nostre conoscenze dell'emissione di sorgenti extraterrestri alle energie piú alte osservabile dello spettro elettromagnetico spettro elettromagnetico.

I nuclei galattici attivi (AGN) detti radio loud, ovvero molto brillanti nelle frequenze radio, sono degli oggetti astronomici la cui radiazione, generata tramite l'accrescimento di materia sul disco di un buco nero supermassivo, viene emessa lungo dei getti relativistiche. Sulla base dell'orientazione dei getti relativistici, AGN radio loud sono divisi in varie categorie tra le quali quella dei blazar. Tali oggetti presentano un getto orientato con degli angoli piccoli rispetto alla linea di vista dell'osservatore. Finora, blazar rappresentano la maggioranza delle sorgenti extragalattiche di emissione raggi gamma ad altissime energie osservate nell'intervallo energetico tra 100 GeV e qualche decina di TeV con i telescopi Cherenkov del tipo IACT (Imaging Atmospheric Cherenkov Telescope).

La piú parte elli sorgenti di radiazione gamma VHE è stata scoperta solo negli ultimi anni grazie ai telescopi Cherenkov di nuova generazione, MAGIC (Major Atmospheric Gamma Imaging Cherenkov), H.E.S.S. (High Energy Stereoscopic System) e VERITAS (Very Energetic Radiation Imaging Telescope Array System). Ció che ha reso possibile queste nuove scoperte sono l'alta sensitività e l'esteso intervallo energetico di questi strumenti. Inoltre, si è rivelato molto importante la cooperazione con altri strumenti che osservano a diversi intervalli di energia, tra cui l'ottico e i raggi gamma sotto i 100 GeV (HE; High Energy).

Lungo il percorso verso la terra la radiazione gamma VHE emessa da una sorgente distante viene attenuata a cause dell'interazione con la cosiddetta luce di fondo extragalattica (EBL; Extragalactic Background Light). Questa radiazione ottica ed infrarossa è composta da fotoni emessi dalle stelle e riprocessati dalle polveri, la cui energia si è diluita nel tempo a causa dell'espansione dell'Universo. A cause di questo assorbimento, lo spettro intrinsico emesso dai blazar viene deformato. Tale deformazione spettrale è una funzione crescente dell'energia del fotone γ e della distanza della sorgente. Per questo motivo, gli AGN osservati ad altissime energie hanno una distanza relativamente corta. La sorgente più lontana nota fino ad ora è il blazar 3C 279, con un redshift a $z = 0.536$.

Questa tesi di dottorato è incentrata su due attività di ricerca, una tecnica ed una scientifica, svolte in collaborazione con l'esperimento MAGIC. Mentre la ricerca tecnica è destinata allo sviluppo di nuovi specchi con elevate proprietà ottiche ed un prezzo ottimizzato per futuri telescopi Cherenkov, la ricerca scientifica riguarda le analisi dettagliate della radiazione gamma emessa da due blazar distanti 1ES 0806+524 e 1ES 1011+496 osservati da MAGIC.

La prima parte si rivolge quindi allo sviluppo di nuovi specchi per la prossima generazione di IACT, introdotta dal progetto CTA (Cherenkov Telescope Array), ed alla qualificazione ottica di tal specchi. La principale difficoltà è quella di raggiungere un equilibrato compromesso tra i costi associato alla realizzazione

di specchi con elevata riflettività e la qualità ottica richiesta. In particolare la capacità di focalizzare e la riflettivittà spettrale rappresentano i parametri ottici più cruciali per quanto riguarda la qualità di un telescopio Cherenkov in termini di area di detezione e d'efficienza di rivelazione di luce. Inoltre, considerando le condizioni con le quali vengono operati i telescopi Cherenkov, tali specchi devono presentare una elevata resistenza contro agenti atmosferici.

Nell'ambito di questo lavoro, sono stati sviluppati i primi prototipi di specchi compositi basandosi sul principio di replica da uno stampo curvato di precisione elevata in due fasi. In una prima fase, viene curvato un sostrato sferico sullo stampo simile a quelli costruiti per i telescopi di MAGIC. Nel passo successivo, uno strato riflettente egualmente curvato sullo stampo viene posto sul sostrato. Per quanto riguarda la realizzazione di un superficie di altissima riflettività raggiungibile nell'intervallo di lunghezza d'onda d'interesse a basso costo, varie soluzioni sono stati esaminate. Per questo scopo, vari prototipi sono stati costruiti. La qualità ottica di questi primi prototipi è stata studiata con un cosiddetto $2f$–setup (apparecchiatura 2f) che è istallato ai laboratori nazionali di Legnaro (LNL) di INFN. Tale apparato è adatto per la misura della capacità di focalizzare, detta Point Spread Function (PSF), e del raggio di curvatura di tali specchi sferici. Per quanto riguarda l'analisi della PSF, parametrato tramite il cosiddetto D_{80} (il diametro di 80% di contenuto di luce) è stata sviluppata un software. La qualificazione ottica ha rilevato che la PSF di questi prototipi non soddisfa le specifiche di CTA, quindi sono necessarie delle modifiche della tecnica di replica per ottenere una precisione più elevata. L'ottimizzazione/la regolazione della procedure di replicazione è attualmente in fase di sviluppo mirando ad un miglioramento della PSF per un fattore di tre.

Oltre all'attività dedicata allo sviluppo degli specchi, la parte tecnica è rivolta alla coordinazione di una calibrazione incrociata degli apparati per le misure ottiche impiegati nel consorzio di CTA. Attualmente, parecchi istituti investigano nello sviluppo di nuovi specchi di proprietà adeguate per CTA. Naturalmente, ognuno di questi istituti eseguono delle qualificazioni ottiche usando i propri sistemi di misura. Per valutare l'affidabilità di queste misuretre specchi di caratteristiche e dimensioni diverse sono stati circolati fra alcuni istituti. Questi specchi sono anche stati misurati con il $2f$–setup installato ai LNL di INFN. Il compito finale relativo a questa attività riguarda lo studio comparativo delle misure ottiche. Per questo motivo, varie condizione di misure che influenzano la determinazione della PSF sono stati considerati criticamente. In piú, per escludere discrepanze potenziali fra i risultati sulla PSF dovute a software di analisi diversi, viene effettuato un crosscheck dell'analisi dei dati quando possibile. Nel contesto della calibrazione incrociata, varie aspetti tecnici ed analitici vengono rintracciati di avere un effetto sulla qualificazione ottica. Soprattutto la determinazione della PSF dipende decisamente da questi fattori per il quale motivo bisogna specificare une procedure di misura dettagliata noncheè degli strumenti di analisi minimalmente standardizzati.

Nella seconda parte di questa tesi viene presentata la ricerca scientifica legata all'analisi dettagliata dell'emissione gamma di due blazar di intermedio redshift, 1ES 0806+524 e 1ES 1011+496, iosservati con MAGIC .

Il sistema MAGIC, situato a La Palma, nelle isole Canarie, sul Roque de los Muchachos a 2225 metri sul livello del mare, consiste di due IACT con 17 m diametro sensibili ai raggi gamma di energie basse fino a 50 GeV. Questi telescopi osservano la radiazione Cherenkov che viene emessa da particelle secondarie prodotte dall'interazione dei raggi gamma con i nuclei dell'atmosfera e dalla loro successiva propagazione in aria.

Tutti e due blazar sono stati osservati in modo stereo, ovvero con i entrambi telescopi MAGIC. Mentre 1ES 0806+524 è stato osservato per circa 24 ore nel 2011, le osservazione di 1ES 1011+496 sono state effettuate nel 2011 e 2012 per circa 13 e 23 ore rispettivamente. Le osservazioni di 1ES 0806+524 sono state innescate da un intenso brillamento, un cosiddetto flare o outburst, nell'ottico. Contemporaneamente, la sorgente ha emesso un breve outburst a frequenze VHE che MAGIC è riuscito ad osservare. Quindi, MAGIC è riuscito ad osservare 1ES 0806+524 sia in uno stato alto che basso. Le osservazioni precedenti di queste sorgenti ad altissime energie hanno condotto ad analisi spettrali poco precise il che vengono presentate in questo lavoro. Inoltre, a causa dell'assenza di osservazioni simultanee condotte a frequenze HE, le distribuzioni spettrali di energia (SED; Spectral Energy Distribution) di queste sorgenti sono state scarsamente misurate.

Sia l'analisi spettrale dell'emissione che quella temporale vengono presentate per tutte e due le sorgenti. Nel caso di 1ES 0806+524, le osservazioni indicano una rapida variabilità su scala giornaliera della componente gamma mentre 1ES 1011+496 pare essere una sorgente piuttosto constante a frequenze VHE.

Tipicamente, gli spettri VHE di blazar osservati seguono una semplice legge di potenza delle forma $\mathrm{d}N/\mathrm{d}E = f_0 \cdot E^{-\Gamma}$, con Γ indice spettrale. Anche gli spettri differenziali di entrambe le sorgenti sono compatibili con una tale legge. Per quanto riguarda 1ES 0806+524, gli indici spettrali fra gli due stati di emissione sono compatibili negli errori. Nel caso di 1ES 1011+496 , l'indice spettrale degli spettri osservati nel 2011 e 2012 è costante.

Per entrambe le sorgenti, i risultati di questi analisi sono quindi confrontati con quelli ottenuti da osservazioni effettuate da altri strumenti in diverse lunghezze d'onda, dall'ottico ai raggi gamma (MWL; multiwavelength approach). Rispetto a 1ES 0806+524, la copertura MWL nel 2012 include degli studi di polimetria ottica per la prima volta.

Apparentemente, nel caso di 1ES 0806+524 esiste una connessione tra il flusso ottico e quello TeV. Invece, la sorgente 1ES 1011+496 presenta soltanto una variabilità modesta del flusso TeV qualora variabile, mentre dimostra una chiara variabilità in qualche bande d'energia.

Infine, gli spettri osservati a frequenze VHE vengono combinati con osservazioni MWL simultanee e quasi simultanee per costruire le SED. Tenendo conto del flare ad altissima energia di 1ES 0806+524, i dati VHE sono divisi in due campiono rispetto allo stato basso ed elevata dell'emissione di raggi gamma. Nel caso di 1ES 1011+496, le osservazioni nel 2011 e 2012 sono trattati separatamente.

In entrambi i casi, si evince chiaramente la tipica struttura a due picchi nella SED, consistente con gli attuali modelli di emissione dei blazar. Tutte le due SED vengono riprodotti con un modello SSC (Synchtroton Self Compton) assumendo una zona di emissione in modo da stimare i principali parametri fisici che governano l'emissione del jet del blazar. Per la prima volta, è stato ottenuta una copertura dettagliata del picco ad alte energie, grazie ai dati simultanei nelle bande HE e VHE.

In conclusione, lo stato dello sviluppo di nuovi specchi per CTA è presentato insieme con le misure ottiche effettuate per i primi prototipi. Inoltre, viene riportato lo studio sull'affidabilità ti tale misure. Le osservazioni ad altissime energie delle sorgenti 1ES 0806+524 e 1ES 1011+496hanno portato alle misure dettagliate degli spettri differenziali il che da la possibilità di investigare/studiare/ricercare l'EBL. Infine, la copertura MWL permette per la prima volta la precisa determinazione delle SED.

Contents

Outline

One of the most active and exciting field of modern astrophysics the observation, study and interpretation of very active objects populating our Universe, generally associated with catastrophic phenomena. Cosmic rays are energetic particles from space entering the Earth atmosphere which are commonly believed to be messengers of such phenomena. The generation of cosmic rays takes place both in galactic and extragalactic objects via ejection and acceleration mechanisms. Supernova remnants and pulsars are representatives of the former category, while blazars are typical extragalactic emitters. Blazars are supermassive black holes that accrete material and feature two narrow jets of relativistic particles perpendicular to the disk plane and oriented at small angle to the observer.

Beside the predominant content of protons and other charged particles, a small fraction of cosmic rays consists of γ–rays. Due to their uncharged nature, they are not deflected by intergalactic magnetic fields and point directly to their generator. In addition, they preserve timing information. Thanks to these properties, γ–rays are ideal messengers of energetic events.

Over the last decades, the enormous effort to build new detectors, both ground based and space borne, and the development of new experimental techniques have lead to a numerous new discoveries that have populated the γ–ray sky. Among the techniques, the study of very high energy (VHE) γ–rays, i.e. photons with energy between 100 GeV to some tens TeV, from Earth via Imaging Atmospheric Imaging Cherenkov Telescopes (IACTs) turned out to be very successful. MAGIC is one of such detectors suited for ground based VHE γ–ray observations. This detector system consists of two telescopes located on the Canary island of La Palma. The first MAGIC telescope is operating since 2004 while the second has been commissioned in 2009. Currently, the next generation of IACTs, that is the Cherenkov Telescope Array (CTA), is under development aiming at an improved sensitivity and an extended energy coverage. These objectives require large surfaces of highest reflectance and good focusing power.

This PhD thesis reports the results achieved both by a technical and a scientific research activity carried to the field of VHE γ–ray astronomy. The former regards the development of new composite IACT mirror facets for the current generation of IACTs and for CTA. In addition, the qualification of the optical performance of such mirrors is treated. The scientific part concerns the detailed study of the VHE emission from two extragalactic sources, the blazars 1ES 0806+524 and 1ES 1011+496, that have been observed with MAGIC. These observations aimed at a detailed measurement of the differential spectrum over an extended energy range. Moreover, the organization of coordinated multiwavelength campaigns has been part of the scientific research activity which allowed to complement the study of the timing evolution in VHE γ–rays at other frequencies.

An important effect that needs to be considered in the study of extragalactic VHE γ–ray emitters is related to the spectral absorption by the extragalactic background light leaving an imprint on the VHE γ–ray emission.

The structure of the PhD thesis includes the following three parts:

Part I: Introduction of the physical case

Chapter 1 gives an introduction to the experimental particle astrophysics including a brief outline of the historical milestones achieved in this research field. A particular emphasis is given on recent experimental results and open questions such as the origin of cosmic rays as well as the high energy cutoff in the cosmic ray spectrum. In addition, the neutrino astronomy will be briefly introduced.

Chapter 2 is addressed to the description of the the neutral component of cosmic rays. A focus is given on γ–rays describing the fundamental properties which make them ideal messengers from the Universe. Furthermore, the production, interaction and absorption mechanisms of γ–rays are discussed. The chapter concludes with a description of the various γ–ray sources.

Part II: Technical fundamentals and research results

In the first part of Chapter 3, the detection technique of VHE γ–rays with ground based detectors is presented and compared to space born detectors used in the adjacent energy band. A special emphasis is given on the description of the current generation of IACTs as well as on the design of CTA, the future observatory for VHE γ–ray astronomy.
The second part of this chapter is focused on the description of the individual hardware components of MAGIC telescopes.

In Chapter 4 the CTA specifications in terms of mechanical, geometrical and optical properties of the IACT mirrors are introduced. A special emphasis is given to the importance of the optical specifications with respect to performances of these IACTs. Hereafter, a report on the status and outlook of the development of a new production technique of composite mirrors for IACTs is given. Beside the description of the production principle, information on the different solutions tested for the realization of high reflective surfaces at reasonable costs are discussed. In addition, the optical test bench used for the study of the optical performance of such mirrors is presented. Beside the principal description of the measurement procedure, the main analysis steps executed by a software tool developed for the calculation of the focusing power, the so–called point spread function (PSF), are described. The results of the PSF study performed on the first prototypes is reported.

Chapter 5 is focused on the cross calibration of the optical test equipment available in the CTA consortium,The cross calibration of this equipment aims at the evaluation of the reliability of the optical qualifications. For this purpose, three IACT mirrors of different characteristics and dimensions were circulated among the participating facilities. In particular, to exclude possible discrepancies among the results of the PSF calculation due to different analysis software, a crosscheck has been performed on the individual data sets obtained from the individual facilities when possible.

Part III: Scientific fundamentals and research results

The first part of Chapter 6 contains a detailed description of Active Galactic Nuclei (AGN), the main emitters of VHE γ–rays located outside our Galaxy. The physical propertied and emission mechanisms of such VHE γ–ray emitters will be presented. In particular, the physics associated to the jets in AGNs and the characteristics of the jet emission ware outlined, since they closely related to VHE

γ–ray emission. An emphasis is given on the description of the two distinct classes of AGNs, namely blazars and radio galaxies.
In the second part of this chapter, an overview of the EBL is given. The present status of EBL observations is reported and different EBL models are discussed and compared. Due to the interaction with the energetic radiation emitted by extragalactic objects, such as AGNs, the EBL is of fundamental importance for VHE γ–ray observational astronomy. Such interaction causes a deformation of the observed photon spectrum which is briefly discussed. At the end of this chapter, several methods to constrain the distance of blazars based on the EBL effects on their VHE γ–ray emission are outlined.

In Chapter 7 the results of observations of the blazar 1ES 0806+524 performed by MAGIC in 2011 are reported. In the first part, the MAGIC data analysis chain is introduced, followed by the presentation of the results on the energy spectrum and the light curve of the source. A particular emphasis is given on the variability of 1ES 0806+524. Finally, the modeling of the broadband spectral energy distribution (SED) built from simultaneous multifrequency observations is discussed.

Chapter 8 is addressed to the analysis of 2011 and 2012 MAGIC observations of 1ES 1011+496. The temporal and spectral analysis from both years is discussed. First polarimetric observations carried out in 2012 during the observation period of MAGIC are discussed and the SEDs obtained from simultaneous multiwavelength data form the respective years are modeled.

In Chapter 9 the conclusions of this PhD thesis related to the scientific and technical results are summarized and a brief outlook is given.

The Appendix A contains additional information to the MAGIC data analysis presented in Chapter 7 and 8.

1

A Brief Introduction on Cosmic Rays: From Past to Present

THIS chapter contains a brief review to the past and present status of cosmic ray observations. Recent discoveries, controversies and open questions with regards to cosmic rays will be outlined. The origin and the production mechanism of cosmic rays will be discussed as well.

1.1 Cosmic Rays

In 1912 the Austrian Viktor Franz Hess discovered Cosmic Rays (CRs), which are energetic particles from outer space, during balloon flights, see Figure 1.1, aimed at the study of atmospheric radiation [284]. For this discovery he has awarded him the Nobel Price in Physics in 1936.

As Millikan suggested an extraterrestrial origin of such particles, he denominated them *cosmic rays* first in 1926 [226]. Despite their dominant particle nature, the denomination "rays" survived since then. At that time, it was already proven that the particles detected during those balloon flights were not primary CRs, that is accelerated particles at astrophysical sources, but secondary particles initiated by the interaction of energetic CRs with atmospheric nuclei (e.g. [70]).

During the decade from 1927 to 1937, the composition of these secondary particles has been studied with ground based detectors leading to several milestone in the field of particle physics, among these the discovery of the so–called *atmospheric showers* by Bruno Rossi and Pierre Victor Auger (e.g. [279, 43]).

Subsequently, several particles such as the positron, the muon, the pion and the kaon have been discovered over the following decades [38, 235, 193, 275]. In addition, new unstable hadrons were found in CRs [241] which, after the discovery of the charm

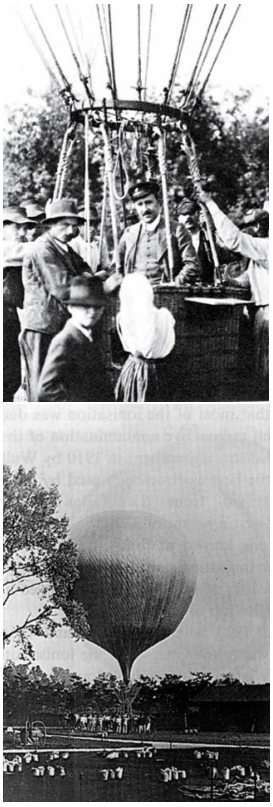

Figure 1.1: Victor Hess on a balloon flight in 1912.

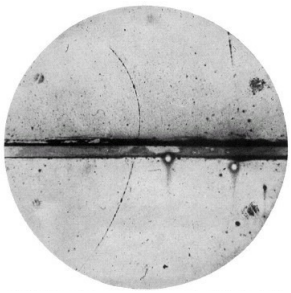

Figure 1.2: Cloud chamber picture of cosmic radiation confirming the existence of the positron by Carl Anderson.

particles, were later defined as D mesons [128]. Thus, the pioneer era of particle physics was primarily practices through the study of CRs.

Primary particles have been only directly detected in the late 1950s when CRs detectors were housed in rockets, spacecrafts and satellites (e.g. [186, 197]).

Figure 1.3: Tracks captured a streaming chamber indicating a pion (looping track to the right from a collision at the center of the image) and muon (four anticlockwise curls in the upper left corner) decay.

After this kick–off of astroparticles physics, up to now several CRs detectors have been built dedicated to study the highest energy particles of the Universe. It was found that the CR are composed of charged particles, in particular protons, and anti–particles, as well as uncharged particles such as photons, neutrinos and neutrons (see Section 1.2). As charged CRs are deflected by interstellar and intergalactic magnetic field, the direct determination of their origin has remained unclarifyed up to now. In addition, the physical processes related to the production of CRs is still under debate. For these reasons, CR are of great interest for the physics community.

Over the years up to present time, different techniques have been employed for the exploration of the various CRs components. CRs detectors can be divided into three main categories devoted to different CR components and sensitive to different energy regmies.

Balloon experiments:
These experiments are mainly dedicated to the study of the element composition of CRs in the energy range from $\sim 10^{-11}$ to 10^{15} eV. Representatives of balloon experiment are Bess, Atic, TRACER and CREAM.

Ground–based experiments:

The experiments belonging to this category can be subdivided as follows:

- Experiments like KASCADE, HiRes Fly's Eye, AGASA and the Pierre Auger Observatory study the charged component of the CR flux at energies above $10^{18}\,eV$;

- γ–ray detectors like MAGIC, H.E.S.S., Veritas and ARGO-YBJ carry out observations in the TeV energy range, whereas Milagro operates in the tens of TeV energy range studying the photon component of CRs;

- Detectors like IceCube, which is installed at the South Pole, and Antares, located in the Mediterranean sea, are addressed to the search for cosmic neutrinos with energies of 100 GeV up to 10^9 GeV.

Satellite experiments:
While satellite experiments like *Fermi*/LAT and *AGILE* are aimed at the detection of γ–rays in the MeV-GeV energy range, PAMELA and AMS-02 focus on the search of the anti–matter content of the Universe.

In the following sections an overview on the recent measurements and results in the field of charged CRs physics is given, outlining recent discoveries and unsolved problems.

1.2 The Composition

CRs are mainly composed of nuclei (98%), out of which protons represent 87% and helium 12% while 1% comprises heavier. The small fraction of the remaining consists of electrons and positrons (∼2%).

Although the CRs composition includes all elements of the periodic table [56], by far the largest fraction of *primary* CRs consists of protons (90%), while 9% are He nuclei, i.e. alpha particles and about 1% constitutes of electrons (beta particles). The remaining fraction is composed of heavier elements, such as C, O, Fe and other nuclei abundantly produced during stellar nucleosynthesis.

1.2.1 The Abundance of Elements

Beside the lighter elements Li, Be and B, which are not abundant end products of stellar nucleosynthesis, antiprotons and positrons represent a large part of *secondary* CRs, which are considered to be produced during the spallation processes between primary particles with the interstellar gas or the Earth's atmosphere. In first approximation, the chemical abundances of protons and nuclei in CRs are rather similar to those in the solar system (see Figure 1.4). However, discrepancies that have been noticed with respect to the abundance of elements in the solar system reveal information on the acceleration and propagation of CRs such as the occurrence of spallation processes for the lightest elements [64]. The overabundance found for lithium, beryllium and boron B as well as for elements below iron and lead reveal differences in the nucleosynthesis of CRs and the solar system indicating that CRs should originate from outside the solar system.

1.2.2 The Matter–Antimatter Ratio

Several space borne experiments are dedicated to the measurement of the small CR component represented by electrons and positrons (e^+; e^-) whose recent results kicked off a hot topic related to the dark matter problem[327]. While

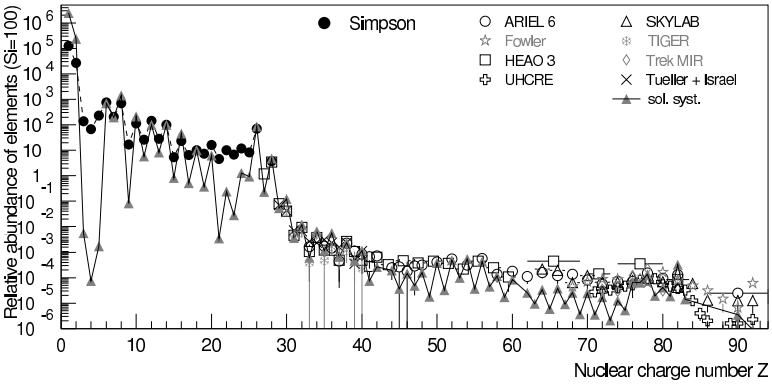

Figure 1.4: Abundance of elements in CRs as a function of their nuclear charge number Z at energies around 1 GeV [64]. The elements composition of the solar system is illustrated (gray triangles).

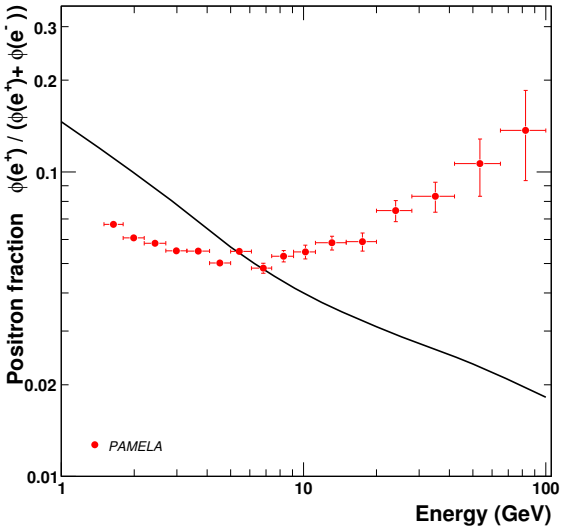

Figure 1.5: PAMELA results on the CR e^+ over e^- ratio (red circles) compared to theoretical model (continuous line) taken from [12].

the PAMELA satellite experiment reported on a e^+ excess associated to the first pssoble evidence of dark matter particle annihilation, see Figure 1.5, detailed measurements by the *Fermi*/LAT confirm the controversial peak in the e^+ e^- CR flux previously reported by the ATIC experiment [82] and seen in the H.E.S.S. and MAGIC data [19, 66] indicating the existence of local sources of high energy CR e^+ and e^- (see Figure 1.6). Beside the association with the dark matter

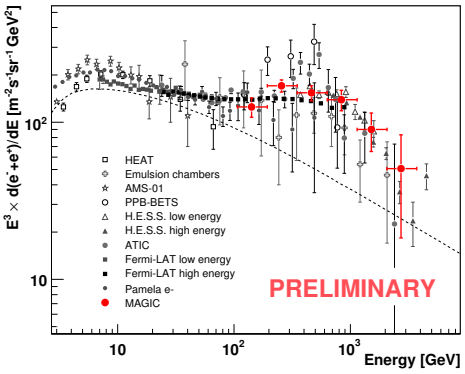

Figure 1.6: The *Fermi*/LAT CR e^++e^- spectrum (filled squares). The preliminary MAGIC spectrum (red circles) and other high-energy measurements are shown. The conventional diffusive model corresponds to the dashed line [66].

hypothesis, a pulsars could be another potential source of the e^+(e.g. [327] and references therein).

1.2.3 The Neutral Component

The smallest CR component, less than 1%, is constituted by neutral particles such as γ–rays ($\sim$0.1%), neutrons and neutrinos. Given their neutral charge, these particles are not deviated by interstellar magnetic fields. Hence, neutral CRs reveal their origin and therefore are considered to be very important messengers for the CR study.

Considering their short lifetime of the order of hundreds of seconds, neutrons typically decay before reaching the Earth which makes their detection as primary particle character difficult.

Despite their elusive nature, cosmic neutrinos are neutral particles with the potential to shed light over the CR acceleration mechanism providing a unique identification for emission models since they are associated to hadronic interactions [211].

So far, cosmic neutrinos have been only detected from two astronomical sources, the Sun (e.g. [39]) and the *supernova* SN 1987 A [248] (see Section 2.4.1).

Due to their properties as a very light weakly interacting particle, large detectors are required in order to catch the faint signal they provide. Such detector has been realized at the South Pole where the neutrino observatory IceCub has been installed (see Section 2.1).

Instead, γ–rays, i.e. photons of high energy, have been revealed to be a very powerful tool for the study of the acceleration of CRs which takes place in astrophysical objects, the origin of γ–ray radiation.

The next chapter will be focused on this fundamental neutral CR component giving a special emphasis on γ–rays.

1.3 The Energy Spectrum

The charged particle CR spectrum spans $\sim$10 energetic decades from approximately 10^8 to more than 10^{20} eV (see Figure 1.7). Within this energy range from few GeV to the ultra–high energy (UHE) regime, the particle flux decreases by roughly 30 orders of magnitude demanding the use of different detection techniques for the study of CRs (a detailed review is given in [64]). The flux is in first approximation compatible with a simple power law which is clearly related to *non–thermal* acceleration processes [64]. In addition, the CR energy scale that extends to $> 10^{20}$ eV is well beyond the capabilities of any conceivable thermal emission mechanism.

When multiplying the flux with a certain power of the particle energy, small structures appear in the steeply falling in first place rather featureless appearing spectrum (see right panel of Figure 1.7). Three main signatures referred to as *knee*, *second knee* and *ankle* represent distinct breaks in the power law where a change in the spectral index occurs. While the spectral index is -2.7 below the knee located at at energies of few PeV ($\sim 4 \cdot 10^{15}$ eV), a steepening is observed from the knee up to the second knee at $\sim 4 \cdot 10^{17}$ eV accompanied by a change in a spectral index to -3.1. Beyond the second knee the spectrum undergoes a hardening up to the ankle appearing at $\sim 4 \cdot 10^{18}$ eV, where the spectrum flattens again.

The lower edge of the CR spectrum is confined at 300 MeV as the solar wind, i.e. the expanding magnetized plasma generated by the Sun, prevents the entrance of

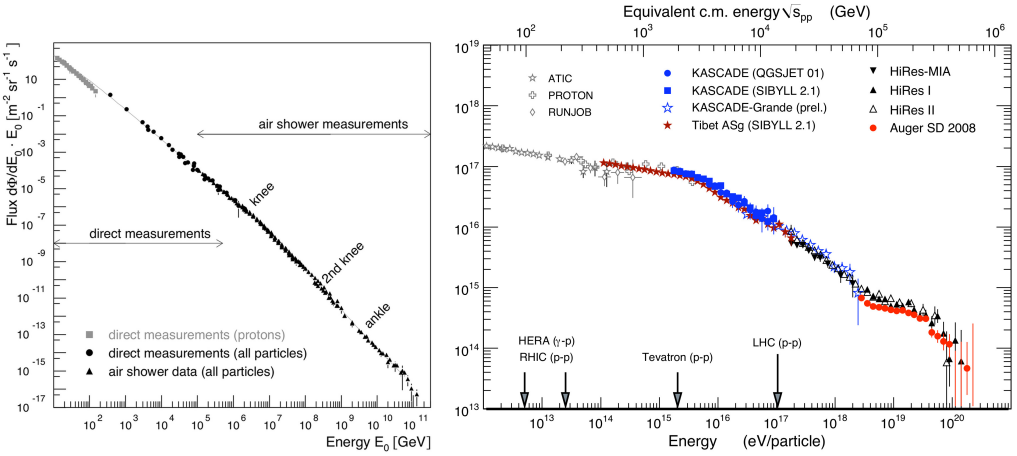

Figure 1.7: All–particle energy spectra of CRs. For a better visibility of the structures in the steeply falling spectrum, the flux is scaled by a factor $E^{2.5}$ (right). From [56].

low energy charged particles into the inner solar system due to their deceleration. In addition, a clear evidence for anti–correlation between solar activity and the CR intensity [237] below approximately 10 GeV of an alternating eleven–year–cycle has been found by the monitoring of the sunspot number and the counting rate of neutrons at sea–level (see Figure 1.8).

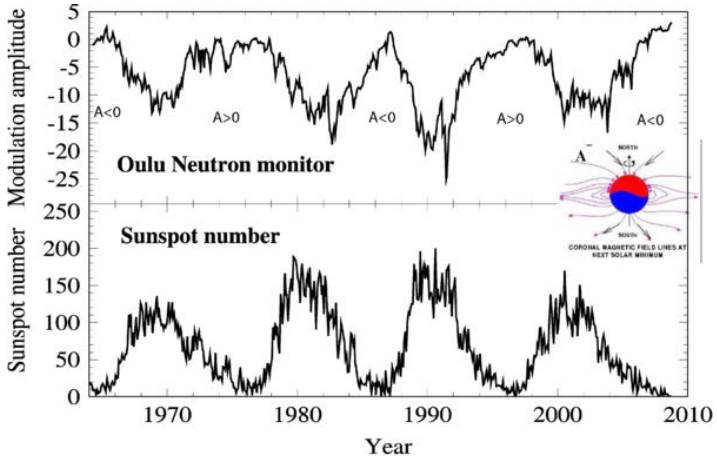

Figure 1.8: *Upper panel:*The intensity variation of galactic CR due to solar modulation as measured by the Oulu neutron monitor.*Lower panel:* Sunspot number monitoring, while the inset sketches the magnetic field configuration of the Sun during an epoch where the magnetic field is pointing inward over the northern and outward over the southern hemisphere (A < 0).The plot evidences the anti–correlation between galactic CRs and solar activity [155].

The East–West–Effect

CRs are affected by the geomagnetic field of the Earth known as the so–called *east–west–effect* which leads, especially at low geomagnetic latitudes, to an enhancement of the CRs incident on the atmosphere from the west compared to CRs arriving from the east [127] (see Figure 1.9).

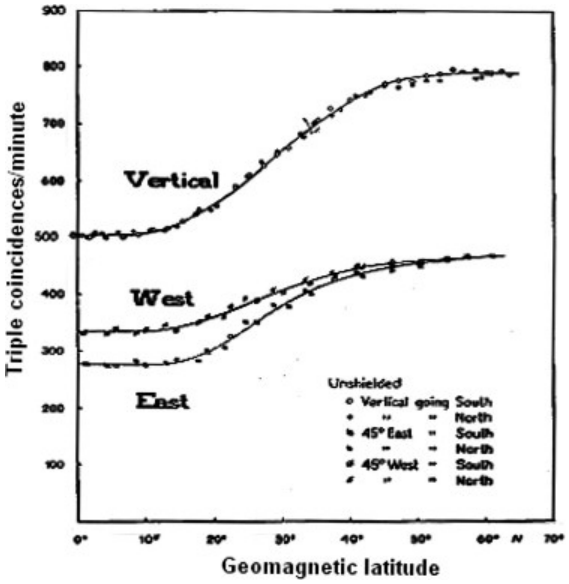

Figure 1.9: East–west–asymmetry of CRs. The CR intensity measured with three layers of Geiger counters in coincidence in vertical, 45° West and 45° East directions [236].

The GZK Cutoff

Beside the extremely low flux on the other edge of the spectrum beyond the ankle, the interaction of ultra high energy (UHE) CRs with Cosmic Microwave Background (CMB) photons, leads to a flux suppression, known as the *Greisen–Zatsepin–Kuz'min* (GZK) cutoff [150, 328], via two dominating interactions channels whereby pions are produced:

$$\gamma_{CMB} + p \rightarrow \Delta^* \rightarrow p + \pi^0 \tag{1.1}$$

and

$$\gamma_{CMB} + p \rightarrow \Delta^* \rightarrow n + \pi^+ \tag{1.2}$$

In particular the interaction of UHE protons with the low energy background photons forms a Δ^+ resonance.

While previous measurements of the GKZ cutoff carried out by the AGASA experiment lead to controversial results [13], the new generation of UHECR detectors like the Pierre Auger Observatory (PAO) and the HiRes fluorescence experiment seem to confirm the existence of such cutoff (see Figure 1.10).

Due to the extremely low flux of roughly one particle per square kilometer per century at 10^{20} eV, the measurement of the CR spectrum beyond the ankle turns out to be very challenging requiring experiments of higher sensitivity at these energies. So far, even the most powerful accelerator, the LHC, produces only particles of energies up to $\sim 10^{13}$ eV, whereas the most energetic CRs detected reach energies of seven orders of magnitude higher. To reach an improvement in sensitivity at this energy regime demands the design of experiments with extended collection area.

1.4 The Origin

CRs with energies lower than 100 MeV mainly originate from the Sun [165]. Beyond this energy, CRs are divided into two classes according to their energy and

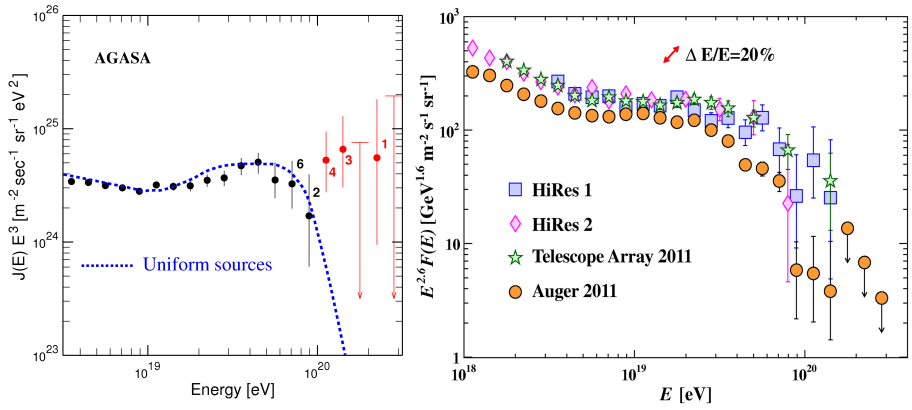

Figure 1.10: UHECR measurements beyond the ankle of the CR spectrum. *Left*: Updated AGASA results on UHECR detection beyond the GZK cut-off [154]. *Right*: The combined energy spectrum from recent UHECR experiments [56]. The flux is multiplied by $E^{2.6}$.

the possible acceleration sites. Up to energies of $\sim 10^{18}$ eV the CR origin is believed to be of *galactic* nature, whereas beyond this energy they are assumed to exhibit an *extragalactic* origin.

Such classification is motivated by considering the acceleration mechanism necessary to generate CRs at highest energies. The principal mechanism is known as *Fermi acceleration*, that has been first proposed by Enrico Fermi in [114]. This process is based on the energy gain by a particle via scattering with a moving ionized medium. In the Universe, a *plasma*, that is an ionized gas containing charged particles, is the most common state of matter. Depending on the characteristics of the moving plasma, it is distinguished between *first oder* and *second order* Fermi acceleration, denoted as Fermi–I and Fermi–II [201]. In the case of Fermi–II acceleration the scattering centers have random velocity β which provides an energy gain ΔEper collision of:

$$\frac{\Delta E}{E} \propto \beta^2 \tag{1.3}$$

Supposed that a shock is present, i.e. the motion of the scattering centers is not random, the particle interacts differently with the moving plasma. This scenario is referred to as Fermi-I acceleration, also known as *Diffuse Shock Acceleration* (DSA). While traversing the shock back and forth, it gains efficiently energy during each passage:

$$\frac{\Delta E}{E} \propto \beta \tag{1.4}$$

Therefore, shocks are of great importance in the field of astrophysics, since their presence in astrophysical objects favors these as accelerators of CR to the highest energies recorded. Common sites for strong shocks are *supernova remnants* (SNRs), see Section 2.4.1, from which the shock front propagates into the *interstellar medium* (ISM).

Based on the principle of the Fermi–I acceleration, the characteristic size of such accelerating region L_{pc} expressed in pc containing a magnetic field $B_{\mu\mathrm{G}}$ in units μG has to exceed twice the *Larmor radius* r_{L}, also known as gyroradius[1], in order to confine magnetically the CRs and thus provide an efficient acceleration of a particle with charge Z up to energies E_{15} of the order of 10^{15} [165]:

[1]The gyroradius defines the radius of the circulation motion performed by a charged particle in the presence of a uniform magnetic field

$$L_{\mathrm{pc}} B_{\mu\mathrm{G}} \geq 2 r_{\mathrm{L}} \tag{1.5}$$

$$L_{\mathrm{pc}} B_{\mu\mathrm{G}} \geq \frac{2 E_{15}}{Z \beta} \tag{1.6}$$

where β takes into account the characteristic velocity of scattering centers. With increasing energy the Larmor radius of an accelerated proton becomes comparable to and ultimately exceeds the thickness of the galactic disc which disfavors a galactic origin.

In 1984 Hillas published a diagram, shown in Figure 1.11, in which the magnetic field strength and the size of the accelerating region are related to the maximum acceleration energy [160] assuming DSA to be the propulsive mechanism. This diagram emphasis that only extragalactic objects seem to combine the physical conditions to generate UHECRs. In Chapter 6, a detailed description of *Active Galactic Nuclei* (AGN) as representatives of such extragalactic objects is given.

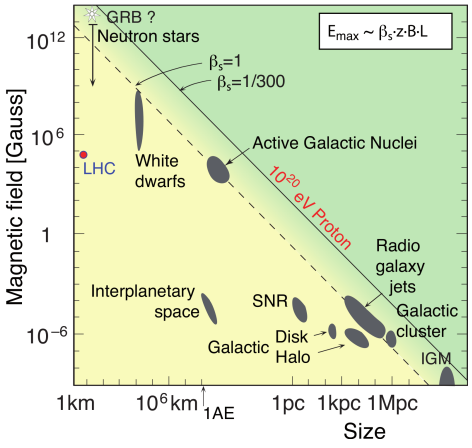

Figure 1.11: Hillas diagram of astrophysical objects capable to accelerate CRs to ultra–high energies via Fermi-I acceleration. Objects below the diagonal continuous/dashed line are ruled out to accelerate protons to 10^{20} eV from [64].

The division in galactic and extragalactic CRs is corroborated by the variation in the slope of the CR spectrum. However, after almost a century of the discovery of CRs, their origin, in particular in the case of UHECRs, and the mechanism responsible for their acceleration to such extremely high energies remains an open largely debated question within the astroparticle comunity.

1.5 The Anisotropy

Unlike their small neutral fraction, the charged component of CRs is affected by the intergalactic magnetic field by deflection resulting in completely arbitrarily arrival directions. However, such deflection is less strong at energies above $10^{19.5}$ eV. Supposed a nearby source generates UHECRs, the deflection from the direction of their emission can be neglected which offers the opportunity to study their origin. Thus, the study of the arrival direction of UHECRs represents an complementary approach to the exploration of the neutral component of CRs.

Over the last decade, a large effort has been made to search for spatial correlation between the recorded UHECRs and nearby objects of extragalactic nature, like AGNs. Recently, the studies performed by the AUGER collaboration preliminary indicated a first hint for the existence of such correlation revealed by the appearance of a small scale anisotropy of 69% probability [313]. After an update of this study by a larger data sample, the correlation probability decreased to

38% [314]. In Figure 1.12 the superimposition of the detected events with the position of 318 nearby AGNs is shown [314].

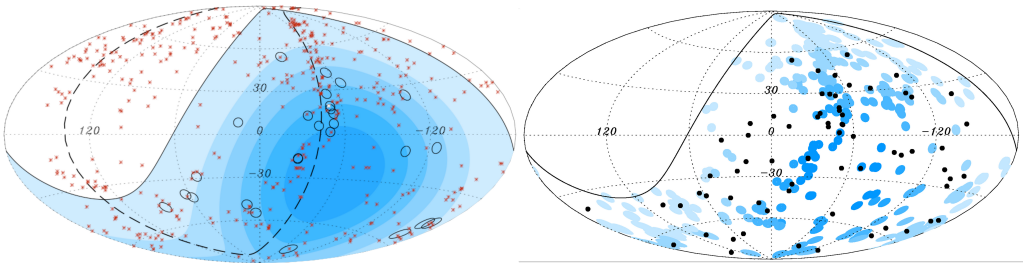

Figure 1.12: Small scale anisotropy studies of the Auger observatory. *Left*: The 27 events with energy E $\geq$ 55 EeV detected by the PAO (black circles), superimposed to the position of 442 nearby AGNs from the Véron-Cetty catalog (red dots). The position of Centaurus A is marked (white dots) [313]. *Right*: Update data sample containing 69 arrival directions events (black dots). The position of 318 AGNs from the Véron-Cetty and Véron catalog are marked as blue circles [314].

The fact, that the sky region around the position of the extra galactic object Centaurus A, a radiogalaxy (see Section 6), shows the largest event excess compared to expectations by an isotropic distribution. A plausible explanation for this excess may be the acceleration of CRs in the stellar winds that are rich in intermediate-mass nuclei [199]. Still, there are several unsettled questions regarding CRs appealing to the field of UHECR astronomy [53].

The Remaining Open Questions on Cosmic Rays

The all–particle flux of the CR is reasonably well known up to the highest energies and its charged primary particle composition is precisely determined. Nevertheless, some of the questions regarding CRs have still remained open. These questions are addressed to the features observed in the CR spectrum as well as to the origin of such particles and the physical processes involved.

The understanding of the origin of the knee in the energy spectrum is commonly thought to be a cornerstone for understanding the the origin of CRs. One popular hypothesis is that the knee is associated with the upper limit of acceleration of galactic CRs by SNRs. The ankle is usually associated with the onset of an extragalactic CR population. Despite the recent insights on the UHECR arrival direction anisotropy obtained by the Auger observatory, the origin of remains an other unsolved puzzle.
Recent measurements by HiRes and the Auger Observatory of a suppression in the spectrum are compatible with the GZK effect. However, further studies are necessary to establish this feature beyond doubt.

2

Gamma–Rays as Ideal Messengers of the Extreme Universe

γ-RAYS exhibit the virtue as ideal messengers of the violent, non–thermal Universe. An overview of astrophysical objects emitting γ–rays and the relevant production and absorption mechanism of such energetic radiation is given.

2.1 Neutral Cosmic Rays

Neutral CRs are ideal particles to study the origin of CRs. Thanks to their neutral charge, these particles do not interact with magnetic fields filling the galactic and intergalactic space. Consequently, they are not deflected from their initial travel direction. These particles preserve information on their origin, pointing back to their generators.

Due relatively short lifetime of neutrons, only a small fraction of primary particles arrives at Earth, wherefore the neutron flux observed by ground-based detectors is dominated by secondary particles whose study provides only limited insights on the distant Universe.

By contrast, neutrinos are weakly interacting light particles of much longer lifetime and thus represent potential messengers from the violent Universe. In particular, the existence of UHECRs implies the presence of other galactic and extragalactic accelerators as sources for high energy cosmic neutrinos involving hadronic interactions [**?**]. As primary candidates, AGNs and *Gamma Ray Bursts* (GRBs)(see Section 2.4.2) represent the most promising astrophysical point source candidates of high energy neutrinos. SNRs, microquasars and pulsars (see Section 2.4.1) are considered as potential galactic neutrino source candidates. In addition, cosmic neutrinos might be associated to the GZK effect as well as to dark matter annihilation [**?**] . The detection of neutrinos as a *smoking–gun* signal of CRs sources has been one of the main motivations for the development and construction of neutrino telescopes over the last decades. However, neutrino astronomy is a challenging research branch due to the low neutrino flux from astrophysical sources that requires detectors of large volumes of interacting material of the order of at least km^3 [**?**].

The IceCube observatory represents such large sized neutrino telescope of 1 km^3 detection area (see Figure 2.1). The detector is buried in the deep ice beneath the South Pole and a second detector of 1 km^2 area is put above this in–ice detector to measure CRs in the energy range from 300 TeV to 1 EeV. However, to now the detection of the faint signal from cosmic neutrinos has been unsuccessful despite the improvement in sensitivity with the IceCube detector. In particular the existence of strong backgrounds by atmospheric muons and neutrinos impede the observation of cosmic neutrinos. These particles are produced to to the interaction of CRs with the Earth's atmosphere. Atmospheric muons are commonly suppressed by observing the northern Hemisphere where they are absorbed by the Earth. Unfortunately, the Earth becomes also opaque to neutrinos above energies of ∼100 TeV. Therefore, the southern hemisphere represents the only part of the sky from which neutrinos with EeV energies and above can be observed. While, the atmospheric background at these energies is negligible, the atmospheric neutrino background is irreducible for all searches for cosmic neutrinos.

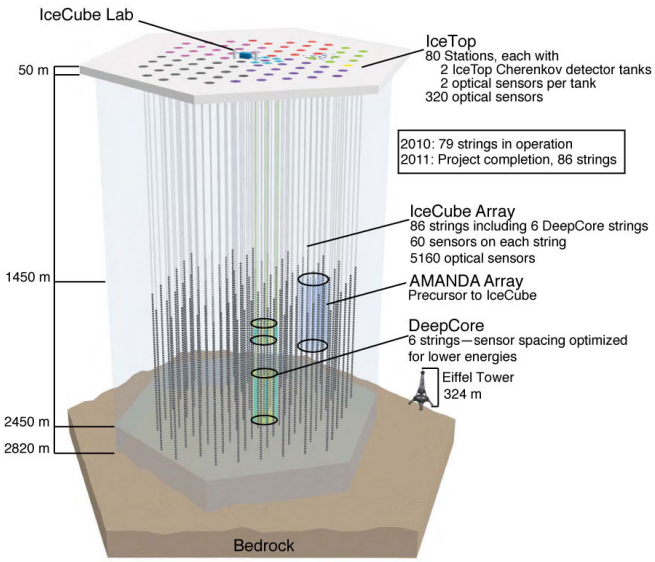

Figure 2.1: Sketch of the neutrino observatory IceCube

Beside the important aim of revealing the existence of cosmic neutrino sources, the constantly improved IceCube detector is also designed for indirect dark matter search via neutrinos from *weakly interacting massive particle* (WIMP) annihilations, and atmospheric neutrino oscillation physics [**?** **?**].

As γ–rays are more easily detectable, their study is the most successful approach to determine CR acceleration sites, allowing an insight into the deep Universe.

The very extreme objects of the Universe reveal very often their most interesting features in the γ–ray regime wherefore it is considered as the last frontier of astrophysics. The study of γ–ray emission provides conclusions on fundamental astrophysical problems. With respect to the *direct* measurement of cosmic particle, the study of γ–rays allows for an independent and complementary study of CRs as they:

- provide energetic information on the generator indicating the acceleration mechanism;
- preserve time information;
- preserve information on their origin and thus on the generating site;
- contain information on the properties of the medium crossed during their travel.

Table 2.1 gives an overview of the conventional division of γ–rays into different energy regimes.

γ–ray regime	Energy range
High Energy (HE)	1 GeV – 100 GeV
Very High Energy (VHE)	100 GeV – 100 TeV
Ultra High Energy (UHE)	$>$ 100 TeV

Table 2.1: Subdivision of the γ–ray energy band.

While HE γ–rays are observed with space born detectors (see Section 1.1), the range beyond these energies is covered by ground based detectors. In the case of VHE γ–rays Cherenkov telescopes (see Section **??**) are used, whereas large arrays of particle detectors are suited to the detection of UHE γ–rays.

2.2 The γ-Ray Production Mechanism

Usually, *thermal* radiation is associated to an emission evoked by thermal motion of charged particles in matter, e.g excitation of atoms. Such radiation takes place in a rather narrow band of the electromagnetic spectrum spanning from ultraviolet (UV) to infrared (IR) of which only a small part is visible for the human eye. In Figure 2.2, the radiation of and emitting material in thermodynamic equilibrium is plotted as a function of different temperatures assuming a black body spectrum that follows a Maxwell distribution [**?**].

This *thermal* component dominates the spectral emission of stars known to be quite stable nuclear reactors for most of their lifetime.

By contrast, γ–rays are messengers of violent events of the Universe, where *non–thermal* processes take place. Such processes dominate at higher energies and are characterized by a non–thermal equilibrium between matter and radiation. By the interaction of primary particles of even higher energy, high energetic photons are generated as secondary particles. In theory, there are five main interaction processes of such *parent particles* involving photon emission:

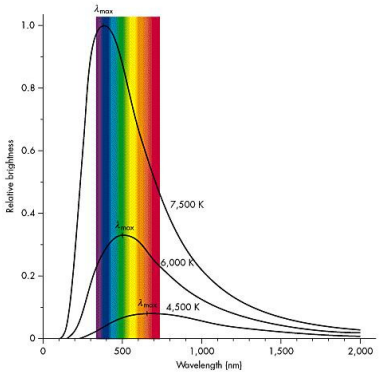

Figure 2.2: Blackbody spectra of varying peak wavelength and total radiation for different temperatures according to *Wien's displacement law*. The waveband visible for the human eye is indicated.

- **Bremsstrahlung:** This radiation mechanism is associated to the electromagnetic interaction with the electrostatic field, created by the presence of ions and atomic nuclei, by what the particle suffers centripetal acceleration (see Figure 2.3).

  The amplitude of the radiation emitted by the particle is proportional to this acceleration. Thanks to its little mass, the *Bremsstrahlung* mechanism is most efficient when electrons are involved in the interaction. Bremsstrahlung via *thermalized* electrons, known as *thermal Bremsstrahlung*, is the most important emission process in astrophysical environments, e.g. a cold ionized

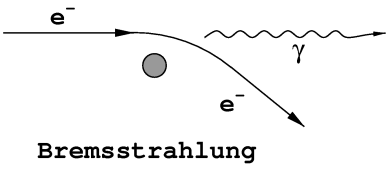

Figure 2.3: Sketch of the Bremsstrahlung mechanism.

plasma, such as the *intra–cluster medium*[2]. With a typical temperature of 10^7 to 10^8 K the emission domain by Bremsstrahlung, also called *free–free radiation* corresponds to the X-ray band [**?** **?**]. Besides, this thermal Bremsstrahlung is responsible for the X-rays emission in the accretion disk of an AGN, producing photons of energies up to ∼100 MeV. In this scenario, the electrons move with a mean velocity that is related to the plasma temperature:

$$v \simeq \frac{k_{\mathrm{B}} T}{m_e} \tag{2.1}$$

Below the spectral cut–off frequency given by

$$v = \frac{k_{\mathrm{B}} T}{\hbar} \tag{2.2}$$

the spectrum produced by this mechanism is flat while it falls rapdly off above this threshold (see Figure 2.4). At lower frequencies, the spectrum is modified by *self–absorption*.

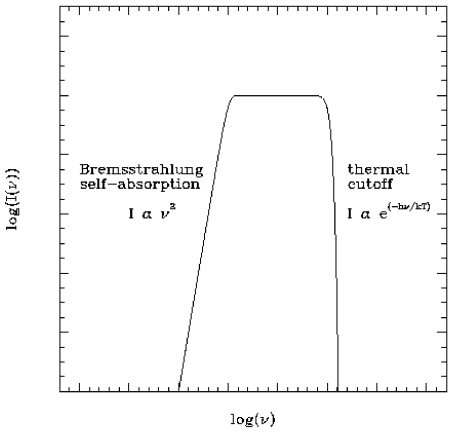

Figure 2.4: Characteristic spectrum of thermal Bremsstrahlung that is flat up to a cut–off frequency above which the spectra falls steeply. For low frequencies, self–absorption occurs.

Relativistic Bremsstrahlung[3], the energy distribution of ultra–relativistic CR electrons assumes a power law form, indicating a non–thermal interaction with the ISM that leads to γ–ray emission.

[2] Thermal Bremsstrahlung occurs when the particles populating the emitting plasma are at a uniform temperature and describe a Maxwell–Boltzmann distribution.

[3] A particle that moves with e velocity comparable to the speed of light is considered to be relativistic. In the *non–relativistic* case, the velocity of the moving particle is small with respect to the speed of light.

Depending on the density of the medium, this radiation mechanism gains importance.

- **Synchrotron radiation:** When traveling in a magnetic field, relativistic electrons undergo an acceleration associated to the Lorentz's force that induces a rotation of the particle around the magnetic field (see Figure 2.5) at an orbit given by the gyration frequency[4]:

$$\omega = \frac{eB}{\gamma m_e c} \tag{2.3}$$

The radiation associated to this relativistic scenario appears in a cone strongly beamed (see Section 6.1.4) along the direction of motion of half angle $\sim \gamma^{-1}$ emitting a power described by:

$$P = \frac{2e^2}{3c^3}\gamma^2 \frac{e^2 B^2}{m_e^2 c^2} v^2 \sin^2 \alpha \tag{2.4}$$

where

$$\gamma = \left(\frac{1}{\sqrt{1 - \frac{v^2}{c^2}}} \right) \tag{2.5}$$

and α denotes the *pitch angle* between the velocity vector and the magnetic field. The synchrotron spectrum emitted by relativistic electrons adapts the form of a continuum following an increasing power law proportional up to a characteristic frequency ω_c at which the maximum power is emitted. For higher frequencies, the spectrum features and exponential decrease [**?**]. Expressing the spectrum $P(\omega)$ as a function of ω/ω_c yields a more quantitative solution of the spectrum:

$$P(\omega/\omega_c) \propto \begin{cases} \left(\frac{\omega}{\omega_c}\right)^{1/3} & , \text{if } \omega/\omega_c \ll 1 \\ \left(\frac{\omega}{\omega_c}\right)^{1/2} e^{-\omega/\omega_c} & , \text{if } \omega/\omega_c \gg 1 \end{cases} \tag{2.6}$$

The critical frequency is marked by

$$\omega_c = \frac{3}{2}\gamma^3 \omega \sin \alpha \tag{2.7}$$

In the case of an relativistic electron involved, this frequency corresponds to approximately $0.3\,\omega_c$

To produce γ–rays, a magnetized astrophysical environment is needed. Usually, synchrotron photons are less energetic than their parent electrons, wherefore the emitted radiation typically covers the frequency range from radio to X-rays. Due to the power law distribution of energies of CR electrons of index s, the synchrotron spectrum of astrophysical sources such as AGNs is given by the integral over the electron energy distribution which is typically approximated by a power law of positive slope (see Figure 2.6):

[4] The non–relativistic case is refereed to as *cyclotron radiation* emitted at the *gyration frequency* and as described by the Larmor equations.

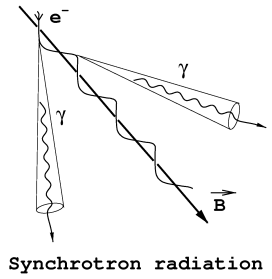

Figure 2.5: Sketch of the synchrotron radiation mechanism.

$$P(\omega) \propto \omega^{-(s-1)/2} \tag{2.8}$$

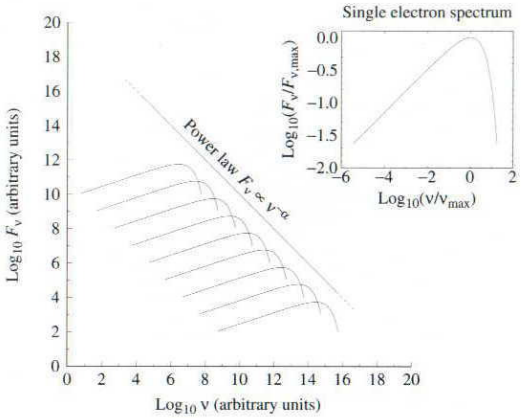

Figure 2.6: Synchrotron spectrum emitted by a typical astrophysical source as the sum of the contributions from individual electrons. The inset (upper right corner) sketches the emission of a single electron.

Due to the much higher charge–mass ratio, the synchrotron emission from electrons appears to be significantly higher which disfavors protons as efficient synchrotron radiation emitters:

$$P_e/P_p \propto (m_p/m_e)^2 \simeq 10^6 \tag{2.9}$$

- **Curvature radiation:** This mechanism occurs, when charged particles cross very strong magnetic fields ($10^8 - 10^9$ G), present in astrophysical sources like pulsars (see Section 2.4.1) eventually originating from their magnetic poles [**?**]. Instead of rotating around the magnetic field lines, the particles tend to follow theses lines [**?**]. Suppose the magnetic field lines are curved, the charged particles are accelerated, emitting radiation similar to synchrotron radiation, see Figure 2.7, with the exception that the emission takes place in the GeV regime.

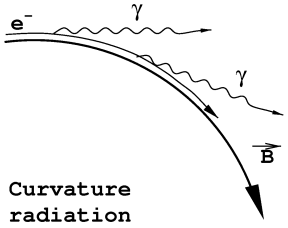

Figure 2.7: Sketch of the curvature radiation mechanism.

- **Inverse Compton scattering:** The mechanism of *Inverse Compton* (IC) scattering is the principal γ–ray production channel in astrophysics, occurring in most of the individual astrophysical object. The IC scattering

leads to the production of such VHE photons via the scattering of ultra–relativistic electrons on low energy photons during which part of the kinetic energy of the accelerated electron is transferred to these seed photons as shown in Figure 2.8).

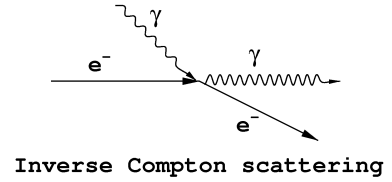

Figure 2.8: Sketch of the Inverse Compton scattering.

Based on the conservation of energy and momentum in the rest frame of an electron, the energy ϵ_s of the scattered photon is defined as:

$$\epsilon_s = \frac{\epsilon}{1 + \frac{\epsilon}{m_e c^2}(1 - \cos\theta)} \tag{2.10}$$

where ϵ is the initial energy of the seed photon before being scattered.

$$\lambda_s - \lambda = \lambda_c (1 - \cos\theta) \tag{2.11}$$

where the Compton wavelength is defined as

$$\lambda_c \equiv \frac{h}{m_e c} \tag{2.12}$$

From this expression can be deduce, that the change in wavelength is of the order of the Compton wavelength [**?**]. Depending on the scattering direction determined by θ the wavelength shift between the incident and the scattered photon amounts to:

$$\Delta\lambda = \begin{cases} 2\lambda_c & \text{, if } \theta = 180^\circ \text{ (backward scattering)} \\ 0 & \text{, if } \theta = 0^\circ \text{ (forward scattering)} \end{cases} \tag{2.13}$$

In case of photons of long wavelengths ($\lambda \gg \lambda_c$, i.e. $h\nu \ll m_e c^2$), the scattering is closely elastic so that the assumption of no change in photon energy in the electron rest frame is valid.

As a function of the energy ratio between the photon and the electron in rest ($x \equiv h\nu/m_e c^2$), two regimes that refer to the non–relativistic and extreme relativistic scenario where distinct cross sections apply:

$$\sigma \begin{cases} \simeq \sigma_T \left(1 - 2x + \frac{26x^2}{5} + \dots\right) & \text{, if } x \ll 1 \text{ (Thomson regime)} \\ = \sigma_{K--N} = \frac{3}{8}\sigma_T x^{-1}\left(\ln 2x + \frac{1}{2}\right) & \text{, if } x \gg 1 \text{ (Klein–Nishina regime)} \end{cases} \tag{2.14}$$

where

$$\sigma_T = \frac{8\pi r_0^2}{3} \tag{2.15}$$

and r_0 represents the classical radius of an electron.

Given a power law distribution of an accelerated electron population, the γ–ray spectrum assumes a power law with distinct index α depending on which regime is concerned. In the case of the Thomson regime the spectral index is defined as:

$$\alpha = (\Gamma + 1)/2 \tag{2.16}$$

, where Γ denotes the the spectral index of the power law describing the electron distribution. Compared to the Thompson regime, the Klein–Nishina regime provides a much steeper power law spectrum following:

$$\alpha = (\Gamma + 1) \tag{2.17}$$

Typically, the γ–ray emission from astrophysical objects by IC scattering peaks in the GeV-TeV range. Besides requiring the presence of radiation fields in astrophysical environments that provide seed photons, IC scattering demands a sufficient transparency of the environment, allowing the γ–rays to escape from the production site with respect to the production of high energy γ–rays in relativistic jets, such mechanism is of peculiar relevance. As the radiation emission from protons is suppressed by a factor of $(m_e/m_p)^2$, the IC scattering is apparently more efficient in the case of electrons [202].

- **Pion decay:** The inelastic scattering between protons and nuclei results in the production of charged and uncharged π mesons(π^+, π^-, π^0) each with the same probability. With regards to life-time and decay channel these particles differ among each other. Charged pions decay due to weak interaction after a typical life time of $\sim 2.6 \cdot 10^{-8}$ via a leptonic decay channel into muons and neutrinos, whereas the neutral pions decay through the electromagnetic force occurs after the much shorter life time of 8.410^{-17} s before any interaction with matter can take place. The preferred decay channel involves the creation of two photons:

$$\pi^0 \rightarrow \gamma + \gamma \qquad (\mathrm{P} = 99\%) \tag{2.18a}$$
$$\pi^0 \rightarrow e^+ + e^- + \gamma \qquad (\mathrm{P} = 1\%) \tag{2.18b}$$

Therefore, the neutral pion provides the dominant channel by what the kinetic energy of protons as primary particles is converted into high energy γ–rays. To produce γ–rays via this mechanism, the kinetic energy of the proton has to exceed the energy threshold at:

$$E_{th} = \frac{1}{2} m_\pi c^2 \left(1 + \frac{m_\pi}{4 m_p}\right) \approx 280\,\mathrm{MeV} \tag{2.19}$$

with $m_\pi = 134.97\,MeV$ corresponds to the mass of the π^0–meson.

This scenario predicts a large amount of UHE ν_e and ν_μ neutrinos as secondary particles from the leptonic decay of the charged pions (π^+ and π^-), whose spectra are quite similar to the γ–ray spectrum from the accompanying π^0–decay. Constraints on the hadronic contribution to the galactic γ–ray spectrum allow for a pionic fraction of up to 50% above 30 MeV [**?**].

Generally, the domination of one process over another is determined by the energy range and the environmental conditions. To summarize, from the five principal mechanisms that involve the generation of photons only two have the potential to generate VHE γ–rays in astrophysical environments, namely neutral pion–decay and inverse Compton scattering. Especially in extragalactic sources, the latter seems to be favored (see Section **??**).

Closely related to the γ–ray production is the *pair production* process (see next section), competing with the mechanisms depicted above.

2.3 The γ-Ray Interaction and Absorption

Even if photons are not affected by interstellar magnetic fields, they certainly suffer an attenuation along their travel from the distant Universe to Earth due to distinct absorption and interaction mechanism. Whether one mechanism is preferred over another is strongly energy dependent. Mainly three interaction mechanisms described below cause the attenuation of high energy photons.

- **Photoelectric absorption:** The interaction between photons and atoms provokes the photon absorption by an electron causing subsequently the electron ejection from the atom. The process that dominates at photon energies below $\sim$100 keV requires the presence of matter to occur at astrophysical sites.

  Usually, such *bound–free* absorption is observed in most of the spectra of X-ray sources at energies below 1 keV representing one of the principal sources of opacity in stellar interiors[202].

- **Compton scattering:** If not photoelectrically absorbed, the interaction of a high energy photon with a low energy electron via *Compton scattering* causes an energy transfer to the electron leading to a shift of the photon wavelength towards lower energies. Compton scattering occurs dominantly in the energy range from $\sim$0.1 MeV to few MeV, wherefore mainly X-rays are affected. This interaction occurs only in astrophysical environments where matter is present.

- **Pair production:** In general, *pair production* refers to the creation of a particle and its antiparticle from the interaction of a photon and matter. The production of such pair from a decaying photon can only occur if the photon exceeds the total rest mass energy of the two particles.

  A further condition is bound to the simultaneous energy and momentum conservation that is only given if matter is involved to absorb the momentum. In such a way, mainly electron positron pairs are produced from the decay of high energy photons at the presence of matter. As the space provides few matter containment to encounter, the photon absorption by *photon-matter pair production* is negligible.

  However, this interaction takes place when γ–rays penetrate the Earth atmosphere in the presence of hadronic and leptonic matter.

  The second mechanism to produce pairs is provided by the interaction of photons in case their center–of–mass energy exceeds the rest mass of the pair that is produced, e.g. $e^+ + e^-$:

$$\gamma + \gamma \rightarrow e^+ + e^- \tag{2.20}$$

In this case the energy of the photon–photon system has to exceed:

$$E_{\gamma\gamma} \geq 2 \cdot 511\,\mathrm{keV} \tag{2.21}$$

This interaction is dominant at higher energies, i.e. 100 GeV, affecting mainly VHE γ–rays. Considering the maximum pair production cross–section $\sigma_{\gamma\gamma}$ (see Figure 2.9), it is obvious that, depending on the energy of the VHE photons, the absorption will be restricted to ambient photons of a given energy range (see Table 2.2).

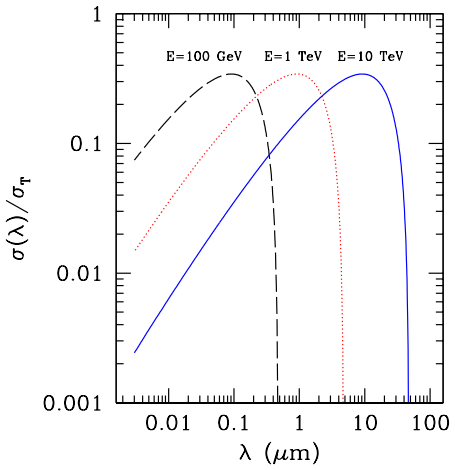

Figure 2.9: Cross section for γ–ray absorption via photon–photon pair production as a function of the background photon wavelength, integrated over the interaction angle, for three a γ–ray of 100 GeV (dashed line), 1 TeV (dotted) and 10 TeV (solid). [**?**]

The Extragalactic Background Light (EBL) which penetrates the Universe, is able to interact with the γ–rays. Consisting of the extragalactic diffuse photon emission from optical to infrared that is associated with star light emission and its reprocessing by dust filling the cosmos respectively, the EBL represents the radiation field, for which the photon–photon pair production cross section for VHE γ–rays is maximum (see Table 2.2).

γ–ray photon energy	Target photon energy range
<8 GeV	X-Rays
8 – 300 GeV	UV
300 – 600 GeV	Optical
600 GeV– ∼1 TeV	Near–Infrared
∼1– 20 TeV	Mid–Infrared
∼20–∼160 TeV	Far–Infrared
>160 TeV	Microwaves

Table 2.2: Energy range of the target photons for which the absorption of VHE photons of a given energy via pair production is maximum.

Beside the absorption by the EBL photons, VHE γ–rays can be also absorbed at the astrophysical production site provided that a dense fields of optical to ultraviolet photons are present. Such attenuation is likely to occur in some AGNs, demanding a careful consideration of the effect when modeling the final spectrum emitted by the source.

In summary, the only interaction relevant for γ–ray absorption is related to pair production. In particular the photon–photon interaction is the dominant mechanism, leading to a significant attenuation of γ–rays on their travel across

the Universe by EBL photons. The intensity of this radiation field defines the opacity of the Universe to VHE γ–rays by what the *intrinsic*[5] spectrum of distant sources is affected.

A detailed description on the EBL composition and models is given in Chapter 6. Furthermore, the interaction of the EBL photons with VHE γ–rays from extragalactic sources will be discussed.

2.4 The γ-Ray Emitter Classes

Different types of astrophysical objects are known to produce γ–rays via non–thermal processes, involving the presence of intense magnetic fields and particle acceleration. The dominating γ–ray production mechanism, is closely related to the nature and properties of the source providing the opportunity to study these astrophysical objects by means of their γ–ray emission. Figure 2.10 shows the sky map of all sources that have been detected up to know in the VHE regime.

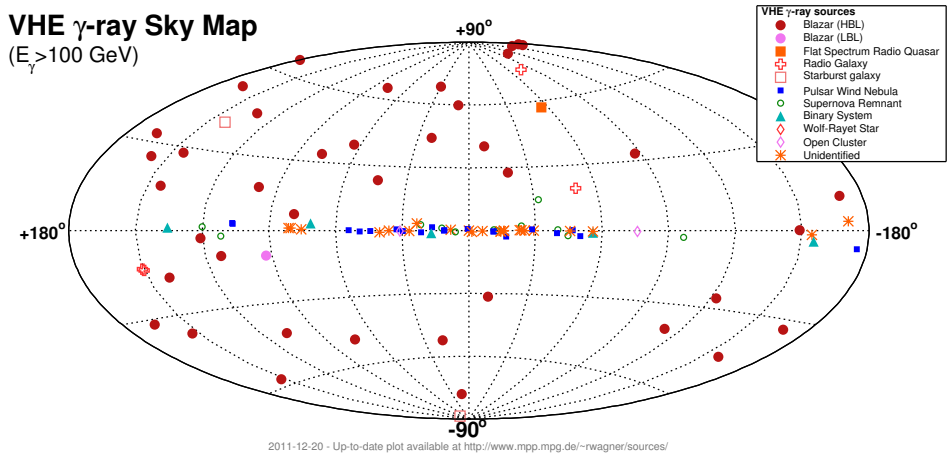

Figure 2.10: The γ–ray–sky of VHE sources discovered up to now, taken from http://magic.mppmu.mpg.de/~rwagner/sources.

Emitters of VHE γ–rays are usually divided as a function of their origin, i.e. whether they are located in our Galaxy or not, into *galactic* and *extragalactic* sources. As a consequence of their variation in size and magnetic field strength, their γ–ray radiation emission covers different energy ranges (see previous chapter, Figure 1.11).

The strong correlation of the γ–ray absorption via EBL interaction to the distance of γ–ray emitters results in a distant–dependent impact on the γ–ray emission. Consequently, the location of galactic sources their VHE γ–ray emission is negligibly affected by EBL absorption, while the radiation from extragalactic emitters is may suffer suppression on their travel through the Universe as it is opaque to γ–rays. Therefore, the γ–ray emission from galactic sources is detected up to higher energies with respect to radiation of extragalactic origin.

2.4.1 Galactic γ-Ray Emitters

To date, 61 objects of this source category have been detected. The individual source types are summarized below.

[5]Typically, the intrinsic source spectrum refers to the spectrum emitted by the source

- **Supernova Remnants (SNR):** The collapse of a super–massive star is usually associated with violent events known as supernovae in which the star as a whole explodes while its envelope violently expelled to the surrounding ISM. Ultimately, a SNR is formed by the ejection of the outer layers of the pre–supernova star (see Figure 2.11. Hence, supernovae correspond to extremely violent and luminous stellar explosion [202].

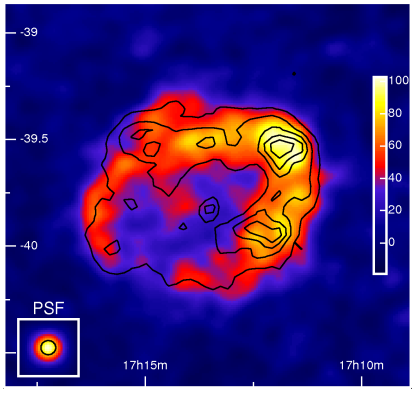

Figure 2.11: Sky map of the VHE γ–ray emission from the position of the SNR RX J1713.7-3946, superimposed to the ASCA X-ray contours (black lines). Adapted from [**?**]

Inside a SNR, particles are accelerated in non–thermal processes in virtue of the Fermi acceleration by expanding shock waves leading to the emission of VHE γ–rays. Based o morphological properties, SNRs can be classified into three broad categories: *shell-like*, *plerions* and *composite* SNR.

Both leptonic and hadronic scenarios are considered to explain the production of γ–rays [**?**]. However, hadronic models are commonly favored, interpreting such γ–ray emission by the neutral pion decay. In the case of W 51, such hadronic model fits perfectly recent VHE γ–ray observations carried out by MAGIC (see Figure 2.12).

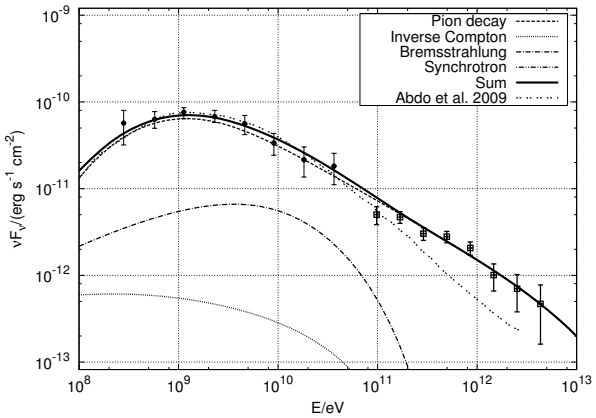

Figure 2.12: SED in from the HE to VHE γ–ray regime of the SNR W 51 from MWL observations by *Fermi* (filled circles) and MAGIC (blank squares) modeled with different scenarii. [**?**].

Due to their potential of the generation of TeV photons, young SNRs, are regarded as main producers of galactic CRs of energies at least up to the knee via DSA. In particular *Type Ia supernovae*[6] would seem to be the best candidates [**?**].

[6]Type Ia supernova is a supernova subclass that results from the violent explosion of a *white dwarf star*.

- **Pulsar Wind Nebulae (PWNs):** An object that consists of a neutron star and a nebula is referred to as *Pulsar Wind Nebula*, also known as plerion. In such system, the nebula is powered by the pulsar wind of the pulsar.

  Such objects currently represent the most populated class of galactic VHE emitters, whose origin is usually associated with IC scattering. However, also hadronic emission models have proposed for the VHE emission of plerions [**?**].

  The most important representative of PWNs is the Crab Nebula (see Figure 2.13).

Figure 2.13: Superimposition of the Crab Nebula images in X-ray (blue) and optical (red) (Credits: X-ray NASA/CXC/ASU/J. Hester et al.; Optical: NASA/HST/ASU/J. Hester et al.).

  As a bright and stable γ–ray emitter, the Crab Nebula is usually used as standard candle[7] in the field of VHE γ–ray astrophysics that has been studied intensively by both ground and space–based γ–ray detectors (see Figure 2.14).

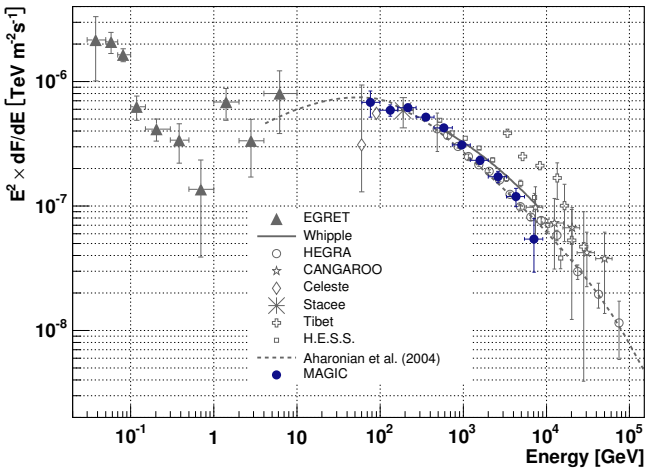

Figure 2.14: SED of the Crab Nebula [30].

  Although generally known to be of galactic origin, H.E.S.S. recently claimed the discovery of the first extragalactic PWN located in the large *Magellanic Cloud* [**?**].

- **Pulsars (PSRs):** A *pulsar* is a rotating, magnetized neutron star that originates from the collapse of a super–massive star. Due to inhomogeneities

[7] Recent variability detections of the Crab Nebula in the HE regime by various satellite borne experiments questioned its role as standard candle [**? ? ?**]. However, no associated enhanced activity in at VHE was revealed [**? ?**]

during the gravitational collapse, a net angular momentum occurs, by what the neutron star initiates a fast rotation.

Because of its intense magnetic field, the emission is collimated along the axis of the magnetic field (see Figure 2.15).

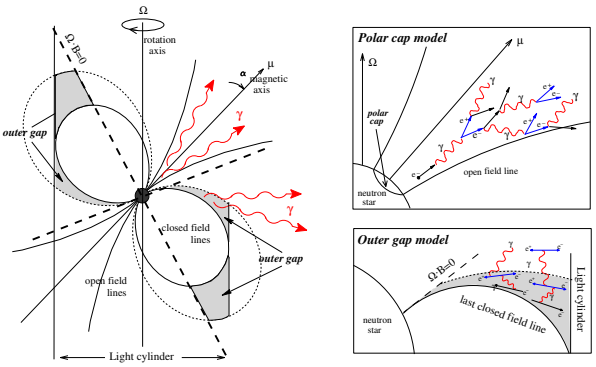

Figure 2.15: Sketch of a pulsar. *Left*: Sketch of the magnetosphere of a pulsar. *Right:* Different γ–ray emission models [**?**].

Typically, this axis differs from the rotational axis so that the emission is only observed when the magnetic field axis points towards the Earth. As this appears at the rotation frequency, typically ~ 0.1 to $\sim 10^{-9}$ Hz, the observed emission occurs as pulsed signal. Depending on the model, the predicted source spectrum follows a power law that features different cutoff location in the 10 to 100 GeV range.

The Crab Pulsar is the only object of this class detected so far, whose pulsed γ–ray emission has been discovered and subsequently studied by MAGIC [**? ? ?**]. The observations lead to the detailed measurement of the pulsar spectrum as well as to the identification of the temporal structure of the pulsed emission (see Figure 2.16).

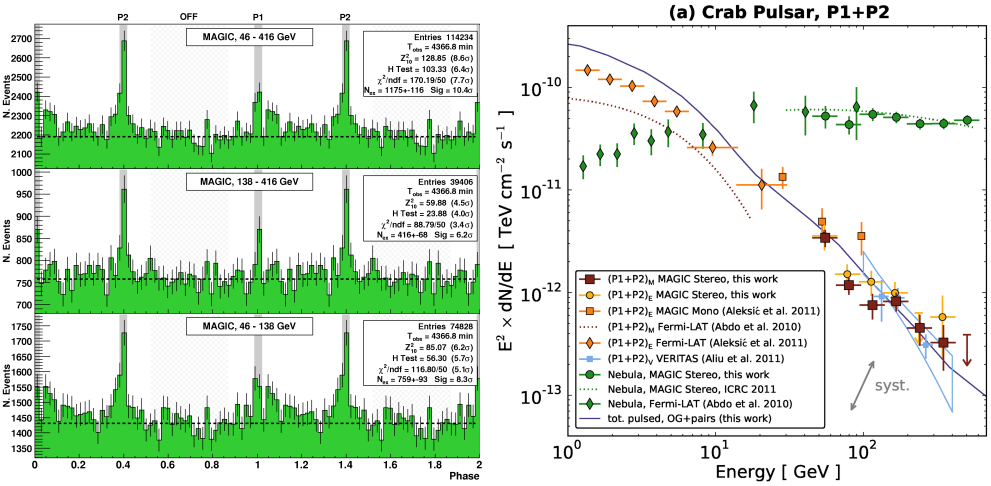

Figure 2.16: Integral and differential analysis of the pulsed γ–ray signal of the Crab Pulsar [**?**].. *Left*: MAGIC folded light curves for 3 ranges from 50 to 400 GeV in estimated energy. The on–phase regions of the main pulse P1 and the interpulse P2 are dark gray shaded, while the off-region is light shaded. *Right:* Differential energy spectrum for P1+P2.

The latest stereo observations of the Crab Pulsar by MAGIC yielded the phase–resolved energy spectrum in the range from 100 MeV to 400 GeV combining previous mono observations and HE γ–ray data from *Fermi*, by what a cut–off in the energy regime from 10 to 100 GeV can be most likely ruled out.

The VHE emission is most probably explainable with the *outer–gap* model. The model associates the VHE emission to IC scattering of secondary and tertiary electron pairs on magnetospheric IR-UV photons. Another model under debate to explain the emission of such energetic photons is proposed in the *polar gap* model associated with *curvature radiation*. However, this model has been ruled out by the MAGIC results which indicate that the emission must occur far out the Crab pulsar's magnetosphere [**?**].

- **Binary Systems (BS):** Typically, this source type consists of a compact object, either a black hole ore a neutron star, and a companion star. Depending on its type, the former either accretes or interacts with the matter ejected by the latter.

  Provided the compact object corresponds to a mass accreting black holes, the BS is considered to be a *microquasar* (MQS), showing similar emission mechanisms as an AGN (see Chapter 6) but on smaller scales. In the case that the compact object is a rotating neutron star that powers pulsar winds, the γ–rays are produced in the shock from the pulsar wind that interacts with the companion star outflow (see Figure 2.17).

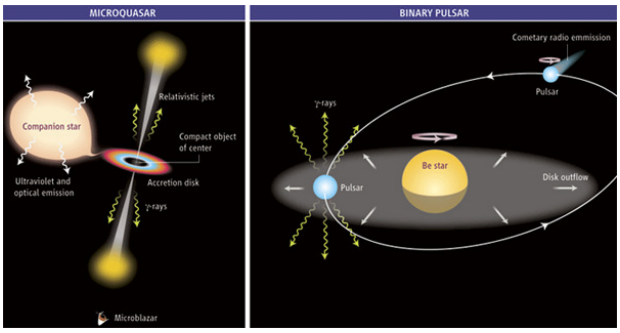

Figure 2.17: Sketches of two galactic γ–ray emitter classes. *Left:* Sketch of a microquasar, powered by a compact object via mass accretion from a companion star. *Right:* Binary system of a rotating neutron star powering pulsar winds that flows away in a comet shape tail. Their interaction with the companion star outflow initiates VHE γ–ray emission [**?**].

Such BS is known as *binary pulsar* (BP). In comparison to SNRs and PWNs, BS are much more compact objects.

Beside LS 5039 which is known to be a VHE γ–ray emitter, MAGIC detected two further galactic objects of this type in VHE γ–rays, that is LS I +61 303 and Cygnus X-1 [**?** **?**].

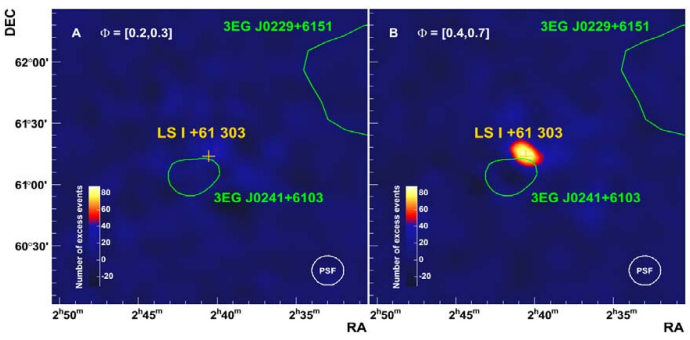

Figure 2.18: Sky map of the microquasar LS I+61 303 from two different orbital phases [**?**].

- **Galactic Center (GC):** In the past years the *galactic center* of our Galaxy has been established to be a steady γ–ray emitter. Being a densely populated sky region, there are three competing candidates to account for such VHE photon emission: beside the black hole Sgr A* that is hosted by the GC, SNRs, pulsars and massive stellar clusters are considered as potential production sites.

  However, Sgr A* is unlikely the origin of the γ–ray radiation, due to the absence of variability in the VHE regime despite its variability in IR and X-ray emission [**?**].

- **Diffuse γ–rays:** As shown in Figure 2.19, the H.E.S.S. collaboration observed an extended region of VHE γ–ray emission coming from GC, whose generation is believed to be caused by hadronic collisions of CRs with a complex of dense molecular clouds and dust located in the galactic plane.

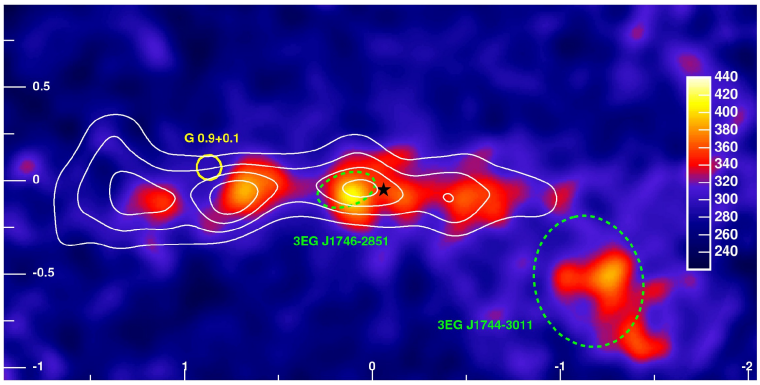

Figure 2.19: Diffuse γ–ray emission originating from the GC. The white contours indicate the molecular gas distribution, traced by its CS emission. Adapted from [**?**].

  Their collisions lead to neutral pion decay, which in turn decay into VHE γ–rays. The spatial correlation of the emission region and the distribution of the molecular gas provides strong evidence for this hypothesis.

Most of the detected VHE γ–ray emitting galactic sources, which are highly concentrated in the galactic plane (see Figure 2.20), are known to be PWNs (see Table 2.3). SNRs represents the second largest fraction of the objects, while there are only two MQSs have been detected in VHE γ–rays. During the systematic survey of the galactic plane (GP) by H.E.S.S. , a new source type of VHE γ–rays has been discovered, namely stellar clusters (OC). So far, two representatives of this source class have been found [**?** **?**]. Beside these discoveries, several other sources have been detected in the VHE regime during these survey. However, for nearly a third of them, the source type remained unidentified [**?**].

Source	Type	Discovery
Crab Nebula	PWN	1989[a]
PSR 1706-44	PWN	1995[b]
Vela x	PWN	1997[b]
RX J1713.7-3946	SNR	2000[b]
Cassiopeia A	SNR	2001[c]
TeV J2032+4130	–	2002[c]
RCW 86	SNR	2003[b]

SGR A*	–	2004[b]
SNR G0.9+0.1	PWN	2005[d]
MSH 15-52	PWN	2005[d]
RX J0852.0-4622	SNR	2005[b]
HESS J1303-631	OWN	2005[d]
PSR B1259-63	MQS	2005[d]
HESS J1614-518	–	2005[d]
HESS J1616-508	–	2005[d]
HESS J1640-465	–	2005[d]
HESS J1804-216	–	2005[d]
HESS J1813-178	SNR	2005[d]
HESS J1825-137	PWN	2005[d]
HESS J1837-087	–	2005[d]
HESS J1837-069	–	2005[d]
LS 5039	MQS	2005[d]
LSI +61 303	MQS	2006[e]
HESS J1632-478	–	2006[d]
HESS J1634-472	–	2006[d]
HESS J1702-420	–	2006[d]
HESS J1708-410	–	2006[d]
HESS J1713-281	SNR	2006[d]
HESS J1745-303	–	2006[d]
HESS J1418-606	PWN	2006[d]
HESS J1420-607	PWN	2006[d]
HESS J1718-385	PWN	2007[d]
HESS J1809-193	PWN	2007[d]
Westerlund 2	OC	2007[d]
HESS J0632+057	–	2007[d]
MGR J1908+06	–	2007[f,d]
MGR J2019+37	–	2007[f]
MGR J2031+41	–	2007[f]
MAGIC J0616+225		2007[e]
Cygnus X-1	MQS	2007[e]
Kes 75	PWN	2007[d]
SNR G21.5-0.9	PWN	2007[d]
HESS J1357-645	–	2008[d]
W28	SNR	2008[d]
HESS J1912+101	PWN	2008[d]
HESS J1427-608	–	2008[d]
HESS J1626-490	–	2008[d]
HESS J1731-346	–	2008[d]
HESS J1841-055	–	2008[d]
HESS J1857+026	–	2008[d]
HESS J1858+020	–	2008[d]
Crab Pulsar	Pulsar	2008[e]
SN 1006	SNR	2008[d]
HESS J1357-645	PWN	2008[d]
IGR J18490-0000	PWN	2008[d]
HESS J1848-018	OC	2008[d]
W51	SNR	2009[d]
G54.1+0.3	PWN	2009[g]
G106.3+2.7	PWN	2009[g]

Boomerang	PWN	2009[g]
Tycho's SNR	SNR	2010[e]

Table 2.3: List of galactic objects know to be VHE γ–ray emitters sorted by their year of discovery. The letters correspond to the the instrument by which the source has been discovered: Whipple Observatory[a]; CANGAROO[b]; HEGRA.[c]; H.E.S.S.[d]; MAGIC[e]; MILAGRO[f]; VERITAS[f]; *Fermi*-Lat[e].

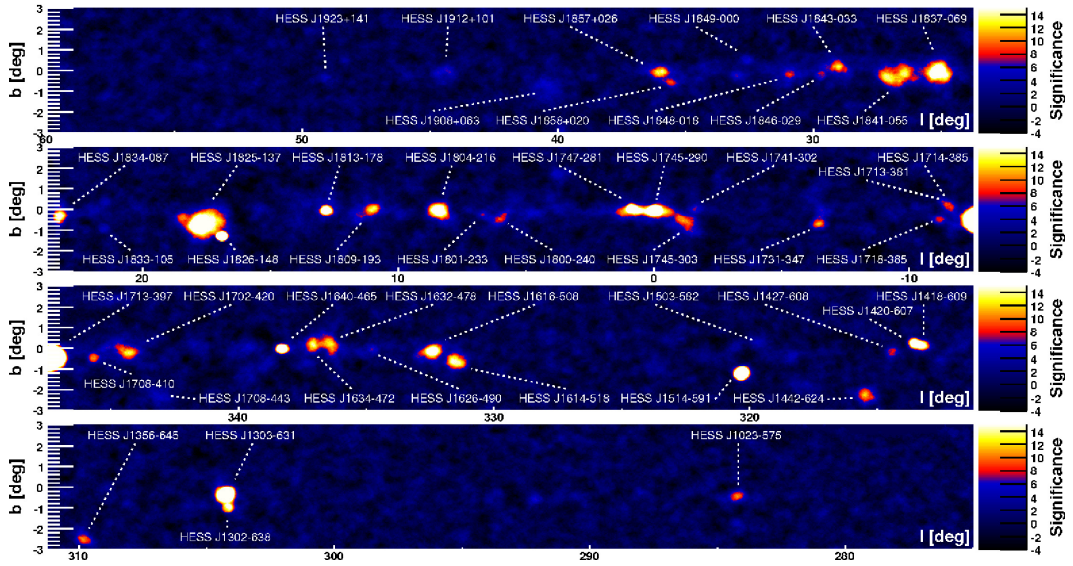

Figure 2.20: Ongoing survey of the galactic plane by H.E.S.S. adapted from [**?**].

2.4.2 Extragalactic γ-Ray Emitters

Up to now, 46 extragalactic objects have been discovered to be VHE emitters. While VHE γ–ray observations of AGNs and so–called starburst galaxies have been lead to significant detections in this energy regime, no Gamma Ray Bursts could be detected in the VHE energy. In the following, the individual objects types are briefly outlined.

- **Active Galactic Nuclei (AGNs):** An *Active Galactic nucleus* refers to a supermassive black hole located at the center of a galaxy. This compact region is characterized by its extremely high luminosity with respect to the remaining host galaxy either across some parts or potentially over the entire electromagnetic spectrum. Indeed, AGNs are known to be the most luminous and persistent emitters of electromagnetic radiation in the Universe, whose emission is believed to be powered by the supermassive black hole accreting matter.

  As this work is in parts addressed to the detailed study of AGNs, Chapter 6 is dedicated to a detailed description of such source type and its subclasses, outlining the physics involved in the observed VHE γ–ray emission.

- **Starburst Galaxies:** *Starburst Galaxies* show a high rate of supernova explosions in the central region due to an undergoing episode of intense star formation [**?**], wherefore they are preferred sites of CRs acceleration.

The radiation observed in the VHE γ–ray band is assumed to originate from decaying pions that are produced via the collision of CR protons with interstellar medium nucleons [**?**]. There are only two representatives of this extragalactic source class known to be VHE emitters, namely M 82 and NGC 253.

- **Gamma Ray Bursts (GRBs):** So–called GRBs occur very frequently isotropically distributed in the sky (see Figure 2.21).

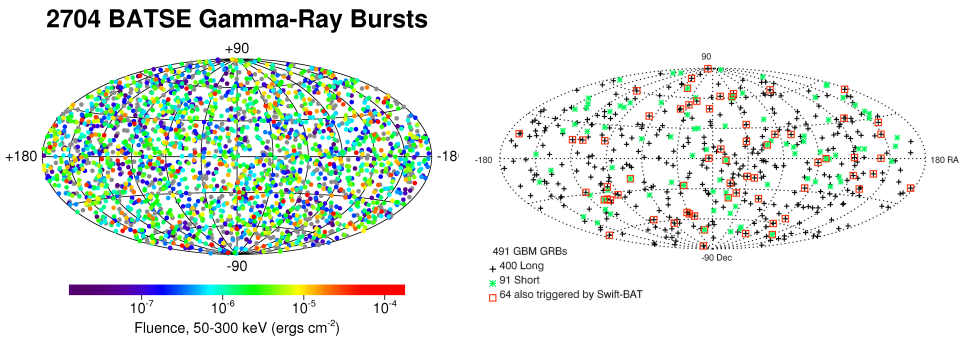

Figure 2.21: GRB detection distributions. *Left:* Distribution on the sky of the GRBs detected by the BATSE experiment from 1991 to 2000, taken from http://www.batse.msfc.nasa.gov/batse/grb/skymap/. *Right:* Sky map of GRBs detected by GBM in the first two years of operation since 2008. GRB alerts also triggered by the *Swift*-BAT are shown by open squares [**?**].

They are associated with sudden, very intense but short γ–rays emissions of extragalactic origin. Based on the main burst duration, GRBs are classified as *long* or *short* with a separating limit in time of two seconds featuring a rather hard or soft spectrum respectively. Usually, the initial VHE γ–ray emission is accompanied by a subsequent *afterglow* emission in X-rays. However, several GRB models predict an emission in the γ–ray regime also during the afterglow. The possibility to constraint theses theoretical models by TeV observations, renders GRBs interesting targets of such observations.

Although the induction mechanisms of such energetic explosions not fully understood[8], both GRB classes are associated to distinct types of progenitor systems : long GRBs are believed to be related to the core collapse of massive stars, whereas short GRBs are assumed to be associated to the merger of binary neutron stars, hosted in early and late type galaxies as sketched in Figure 2.22) (see e.g. [**? ? ?**]).

Due to the very short life time of a GRB, the observation of a GRB is a challenging issue, requiring ground based instruments with adequate properties. MAGIC is such instrument whose agility aims at a quick repositioning of the telescopes to the direction of the GRB alert [9] within some tens of seconds. Despite several successful follow–up observations of a GRB alert, no clear detection could be claimed by MAGIC [**? ? ?**] nor by other detectors sensitive to the VHE range.

[8] There are two GRB models currently under debate referred to as *Fireshell model* and *canonical GRB scenario* (for details see [**?**]).

[9] A GRB alert given by satellite experiments is distributed by the GRB Coordinates Network (GCN)

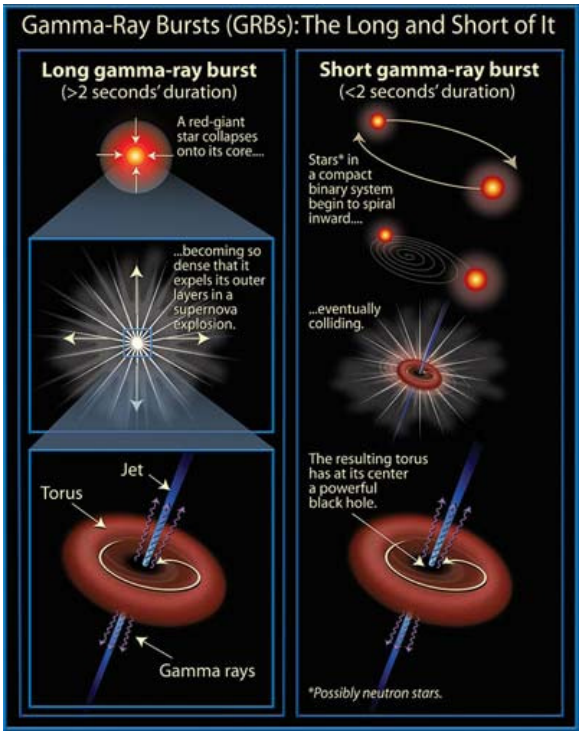

Figure 2.22: Potential scenarii for the occurrence of short and long GRBs taken from http://www.daviddarling.info/encyclopedia/G/gamma-ray_burst.html

2.4.3 Exotic γ-Ray Emitters

According to some DM models, a γ–ray emission extending up to the VHE range is evoked by **Dark Matter (DM) annihilation**. At present, one of the most promising DM particle candidates predicted by the Super–Symmetric (SUSY) theories is the neutralino (for a review see e.g. [**?**]).

Commonly, the cosmological standard model postulates the Universe to be filled with approximately one third of cold dark matter. To date, the most promising sites for indirect dark matter searches via their VHE γ–ray emissions are spheroidal dwarf galaxies, characterized by an enhanced *mass–to–luminosity* ratio inferred from their *rotation curves*, and clusters of galaxies exhibiting *gravitational lensing* (for details see [**?**]). Despite the enormous effort to catch the signature of DM annihilation made by MAGIC by means of γ–ray observations of Draco, Willman1 and Segue 1 [**?** **?** **?**] belonging to such astrophysical objects as promising dark matter sites and by other VHE γ–ray sensitive detectors like H.E.S.S. (e.g. [**?** **?**]) and VERITAS (e.e. [**?** **?**]), no VHE γ–ray emission has been detected yet from any potential DM source.

As DM candidates are assumed to be WIMPs, the absence of a detection in the VHE band is probably because of the low flux, which makes observations with the present generation of detectors almost impossible due to their lack of sensitivity. In account of this, the designs of the next generation of VHE γ–ray detectors aim at an improvement in sensitivity to suit the requirements for an efficient DM search.

3

The Detection of Very High Energy Gamma–Rays and Imaging Atmospheric Cherenkov Telescopes

After entering the Earth atmosphere, cosmic rays interact very soon with other particles creating *extensive atmospheric showers*. Via these interactions, the primary particle is continuously losing while permeating into the atmosphere to the point of its absolute absorption. Thus, a direct detection with ground–based detectors of such energetic cosmic particles is impossible. However, the study of *extensive atmospheric showers* provides a somewhat indirect access to the information on their primary particles being either VHE γ–rays or charged cosmic rays. As atmospheric showers induced by charged cosmic rays occur very predominantly with respect to γ–ray induced *cascades*, they represent the dominant source of background for ground–based γ–ray telescopes. The *imaging technique* in particular adopted by modern telescopes has been revealed to be an efficient approach for the detection and study of VHE γ–rays.
First, the physics related to atmospheric showers will be described. In addition, the differences in morphology and temporal structure of such particle cascades related to the nature of the primary particle is pointed out. The successive part of the chapter is addressed to the introduction of the imaging technique. The third part is dedicated to the description of current and future ground–based γ–ray telescopes such as MAGIC and CTA. A special emphasis will be given to the performance of theses instruments. The chapter concludes with detailed description of the MAGIC telescopes with respect to their individual hardware components.

3.1 Space–born γ–Ray Detectors

Beside radiation either emitted in the radio or in a narrow window centered in the optical band, most of the cosmic electromagnetic radiation is impeded from crossing the Earth's atmosphere by its high opacity (see Figure 3.1) which presents a disadvantage for observational astrophysics.

Consequently, many telescopes sensitive to those parts of the electromagnetic spectrum which cannot be observed from ground are nowadays housed on satellites. In fact, the first γ–ray observations have been carried out from space by the *Explorer*11 satellite in 1961 after which the *SAS*-II and *COS*-B missions took place in the 1970s. By the *Oriented Scintillation Spectrometer Experiment* (OSSE, Cameron et al. 78), the *Imaging Compton Telescope* (COMP-

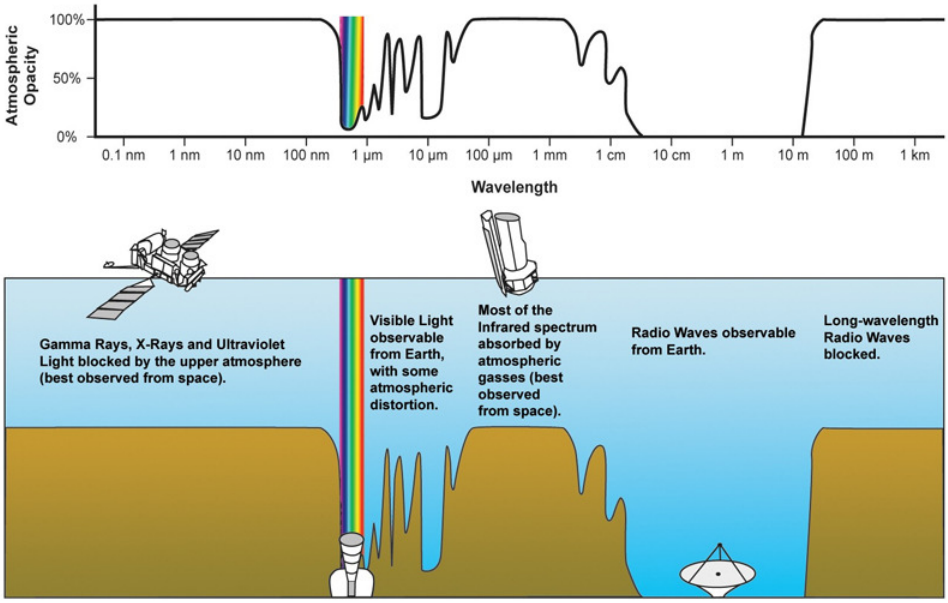

Figure 3.1: Opacity of the Earth's atmosphere. While the radio band and a narrow optical window are directly observable from ground without any transmission losses due to absorption, the atmosphere is either totally or partially opaque to most of the electromagnetic spectrum including γ–ray radiation. Therefore, direct observations of the cosmic radiation are carried out with space–born detectors. Credit: NASA

TEL, Schönfelder et al. 285) and the *Energetic Gamma Ray Experiment Telescope* (EGRET, Thompson et al. 315) all housed on the *Compton Gamma Ray Observatory* (CGRO, Gehrels et al. 133) the radiation from 0.05 MeV to 30 GeV has been explored until the CGRO mission ended in June 2000. In 2001, the *European Space Agency* observatory sent the *International Gamma–Ray Astrophysics Laboratory* (INTEGRAL) on mission [326] optimized for operations in the 15 keV to 10 MeV range, and therefore in the overlapping energy regime of soft γ–rays and hard X-rays.

After EGRET no space based experiment was suited to look at the γ–ray sky above 100 MeV until the AGILE [306] and the *Fermi* [42] satellites were launched in April 2007 and June 2008 covering the γ–ray 30 Mev to 30 GeV and $\sim$20 MeV to >300 GeV bands respectively. There are three competing processes in the γ–ray range observed by space–based telescopes that can be used for the γ–ray detection:

- Photoelectric absorption: at lower energies, i.e. in the energy range from below 100 keV, the photo–electric effect is the dominant process which can be deployed by scintillator counters or solid state detectors as used in the case of OSSE and INTEGRAL respectively;

- Compton scattering: this mechanism is known to be dominant in the energy range from $\sim$0.1 MeV to few MeV. Usually, a detector based on Compton scattering consists of two separated layers denoted as *converter* and *absorber* as art of a scintillation detector system. Such design has been used for COMPTEL;

- e^- e^+ pair production: above 30 MeV this mechanism is the dominant process that can be deployed i the γ–ray detection. In principle, the detector

system consists of a *converter* where the primary γ–ray interacts producing electron positron pairs whose direction and local energy loss is tracked by a *tracer*. In the *calorimeter* the remaining energy of the electron positron pair is determined. AGILE and *Fermi* are instruments featuring such detector systems.

The *Fermi* satellite

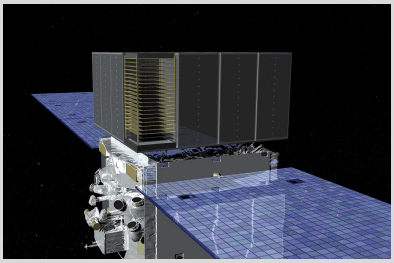

Figure 3.2: Image of the *Fermi* satellite.

The *Fermi* satellite, formerly *Gamma–ray Large Area Space Telescope* (GLAST), has been launched into the near–earth orbit on June 11^{th} 2008 with the mission to explore the Universe in the energy range from 10 keV to 300 GeV. To explore this energy band, *Fermi* employs two instruments: the LAT and the *Fermi–GLAST Burst Monitor* (GMB). While the LAT is an imaging HE γ–ray telescope sensitive to the energy range from $\sim$20 MeV to more than 300 GeV, the GMB complements the LAT observations of transient sources thanks to its sensitivity to X-rays and the coverage in γ–rays from 8 keV to 40 MeV. The *Fermi* mission has been designed for five years and the goal for mission operations is ten years.

The LAT is a pair–conversion telescope with an effective area of 9500 cm^2 providing an energy resolution of 16 to 18% in the energy range of operation. It covers a large FoV of 2.4 sr with an angular resolution from 3.5° down to less than 0.15°. The LAT has been designed for a scientific program that intends to (i) provide rapid notification of GRBs and transients as well as the monitoring of variable sources, (ii) yield an extensive catalog of several thousand of HE sources obtained from an all–sky survey, (iii) measure spectra from 20 MeV to 50 GeV for several hundred sources, (iv) localize point sources to 0.3 - 2arc minutes, (v) map and obtain spectra of extended sources, (vi) measure the diffuse isotropic γ–ray background up to TeV energies and (vii) explore the discovery for dark matter.

Beside the primary objective of the GMB, which is equipped with several scintillators of different material, and to extend the observation range of the LAT into X-rays, a secondary objective is to compute on–board the location of a GRB that triggers a reorientation of the LAT in order to perform immediate follow–up observations. In addition, the GRB sends an instant alert concerning the GRB location to the astronomic community.

Up to now, the *Fermi* mission has been very successful whose results cover all aspects of the scientific program listed above, contributing to a deeper understanding of the HE phenomena occurring in the Universe. In particular, a scientific highlights concern the measurement of the all-electron spectrum of CRs as well as the discovery of anisotropics in CR electrons. In addition, its combination with TeV observations performed by ground–based instruments played a key role in the detection method of VHE sources an in their modeling.

References: [42, 222, 46], and references therein.

Images: Artist's view of the *Fermi*/LAT satellite detector.

Considering the fact that charged nuclei represent the large majority of CRs (see Chapter 1), the space based search of γ–rays reminds of looking for a needle in a haystack. Therefore, a reliable rejection of the isotropic background of charged CRs is required. This typically realized by a so–called *anti–coincidence*.

The overall differential spectrum of the CR flux follows a steeply decreasing power law (see Chapter 1), with a spectral slope larger than two, corresponding at 100 GeV to one CR particle per m^2 per second. The differential flux of galactic and extragalactic sources shows the same spectral behavior[10]. As satellites provide a rather small effective area, the detection rate of γ–rays by satellites from cosmic sources is quite low. In the case of the *Large Area Telescope* (LAT) on–board of *Fermi*, which is the most performant space–born γ–ray detector, the effective area at 100 GeV is 1.3 m^2 [51] resulting in a maximum detectable energy of ∼300 GeV. Therefore, efficient VHE γ–rays are impossible to be carried out from space.

Based on the study of atmospheric showers a technique has been developed to perform VHE γ–ray observations with ground based instruments of large effective areas.

3.2 Extensive Atmospheric Showers

In order to allow an efficient observation of VHE γ–rays, scientists put an enormous effort into the development of a technique to measure such energetic electromagnetic radiation with ground–based detectors of large surfaces compensating the small γ–ray fluxes involved. Recalling the opacity of the atmosphere to γ–rays, the technique deploys a somewhat indirect study of such radiation via particle cascades referred to as *Extensive Air Showers* (EAS). These are produced during the interaction of either a γ–ray or a charged CR with the molecules of the Earth's atmosphere. Depending of the nature of the primary particle, the produced EAS exhibits different properties (see Figure 3.3) based on which such showers are classified as *hadronic* or *electromagnetic*.

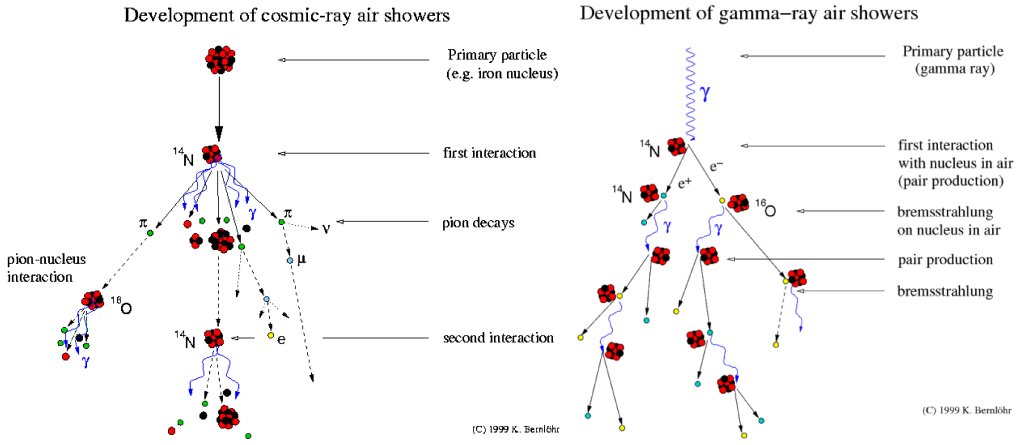

Figure 3.3: Illustration of the development of an EAS. *Left:* Hadronic shower induced by a charged CR. *Right:* Electromagnetic shower induced by a γ–ray. Credit: K. Bernlöhr

[10] For example the γ–ray flux of the Crab Nebula, the standard candle in γ–ray astronomy, at 100 GeV is ∼2 γ–rays per m^2 per year.

3.2.1 Electromagnetic Showers

When a γ–ray penetrates the Earth's atmosphere, an electromagnetic shower is initiated by its interaction with the atmospheric molecules leading to the creation of an electron positron pair[11] which in turn radiates photons via Bremsstrahlung leading to cascade sustained by these two electromagnetic processes.

During the development of the cascade the average energy of the shower particles decreases with the number of interactions until a characteristic energy of $\sim$85 MeV is reached, also defined as *critical* energy E_c. Below this energy, other processes such as the ionization of the atoms in the atmosphere, dominate over the particle production [320] by what the shower particle loose energy. Furthermore, electrons rapidly cool off through thermalization below this energy. Consequently, the shower dies out quickly so that the entire shower development lasts not longer than approximately 10^{-4} seconds.

Theoretically, other than electron positron pairs, γ–rays can also produce other particle antiparticle pairs. However, this component can be neglected in an electromagnetic shower as the cross sections of these interaction channels are much smaller with respect to those of electron positron pair production and Bremsstrahlung.

A simplified scenario of such electromagnetic showers is provided by the *Heitler model* [157] that is used to infer the essential shower properties (see Figure 3.4).

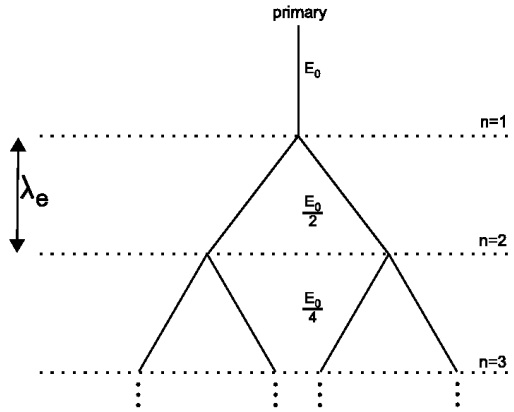

Figure 3.4: Electromagnetic shower as simplified in the Heitler model [320].

The model assumes that the primary particle with energy E interacts after one splitting length:

$$\lambda_e = 2X_0 \tag{3.1}$$

, where $X_0 \sim 37\,\mathrm{g/cm^2}$ is the electromagnetic radiation length producing two secondaries with energy $E/2$. The number of particles after each splitting length referring to the path length travelled in the atmosphere before re–interacting increases by a factor of two. Thus, the number N of particles at generation n is:

$$N_n = 2^n \tag{3.2}$$

and their energy E_n is:

$$E_n = E_0/N_n \tag{3.3}$$

where E_0 corresponds to the energy of the primary particle. Based on the

[11] Electromagnetic showers can be also induced by electrons and positrons.

critical energy E_c, two main shower observables are defined:

$$N_{\max} = E_0/E_c \sim E_0 \tag{3.4a}$$

$$\text{, and} \tag{3.4b}$$

$$X_{\max} = \lambda_e n_c \sim \lambda_e \ln E_0 \tag{3.4c}$$

with $n_c = \ln(E_0/E_c) / (\ln 2)^{-1}$. Despite the simplicity of this model, two important features of electromagnetic air showers are reproduced: while the number of particles at the shower maximum $N_{\max}$ is proportional to the energy of the primary particle E_0, the depth of the shower maximum $X_{\max}$ depends logarithmically on the primary energy.

In [280] a more precise analytical model of such showers has been proposed providing access to the *longitudinal evolution* as a function of the primary energy (see Figure 3.5). Applying the *Approximation B*, every process but pair production and Bremsstrahlung is neglected in this analytical solution for the calculation of the total number of particles, i.e. electrons and positron, N_e with atmospheric depth t also referred to as longitudinal:

$$N_e(t, E_0) = \frac{0.31}{\sqrt{\ln(E_0/E_c)}} \cdot e^{t \cdot (1 - 1.5 \ln s)} \tag{3.5}$$

, where s corresponds to the *age parameter* of the shower combining the t and the primary energy E_0:

$$s = \frac{3t}{t + 2\,\ln(E_0/E_c)} \tag{3.6}$$

Therefore, the age parameter indicates the level of the shower development. At the beginning of the shower development, this parameter is 0, while it assumes 1 at the shower maximum and 2 when the shower dies out.

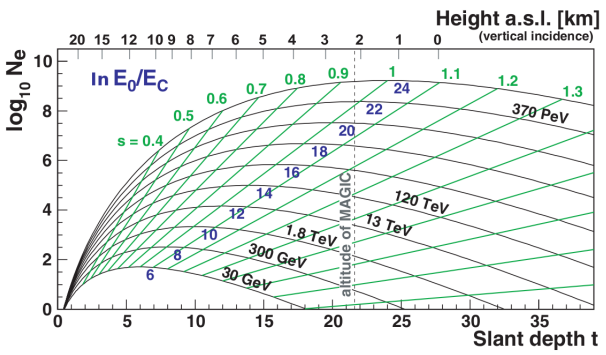

Figure 3.5: Longitudinal development of an electromagnetic shower with atmospheric depth for different values of $\ln(E_0/E_c)$. The X-axis represents the radiation length t while the Y-axis the number of electrons (and positrons) expressed in logarithmic values. The vertical dotted line indicates the altitude of the MAGIC site. Adapted from [324].

In the case of the MAGIC site, that is 2200 m above sea level (a.s.l.), an electromagnetic shower induced by a γ–ray with a primary energy of 370 PeV

reaches its maximum involving a maximum of $\sim 3 \cdot 10^8$ electrons. The critical energy corresponds to 100 MeV. Instead, electromagnetic showers created by γ–rays of 300 GeV reach their shower maximum at 9 km a.s.l. with a maximum electron number of 100 and die out at 1 km a.s.l. For primary energies lower than $\sim$200 GeV, the produced showers die out before reaching the MAGIC site.

Together with the longitudinal development, a *lateral evolution* takes place in the shower. As multiple scattering affects electrons and positrons involved in the shower development, a dispersion of the central axis of the cascade. With a typical value of $\sim 5°$, the characteristic scattering angle θ_0 is rather small [14].

The transversal evolution can be parametrized in a cylinder that contains 90% of the shower by the *Molière* radius [56]. The radius of a cylinder of 99% shower containment corresponds to 3.5 R_{M}:

$$R_{\mathrm{M}} = 21.2\,\mathrm{MeV} \cdot \frac{X_0}{E_{\mathrm{c}}} \tag{3.7}$$

The *Nishimura–Kamata–Greisen* (NKG) formula [169, 149] provides an analytic description of the lateral distribution:

$$\rho(r, t, E_0) \propto \frac{N_e(t, E_0)}{R_{\mathrm{M}}^2} \cdot \left(\frac{r}{R_{\mathrm{M}}}\right)^{s-2} \cdot \left(1 + \frac{r}{R_{\mathrm{M}}}\right)^{s-4.5} \tag{3.8}$$

where ρ and r correspond to the electron positron density function and the distance from the cascade axis respectively. It is important to mention that this formula is only valid for the range $1.0 < s < 1.4$.

In summary, electromagnetic showers show a rather regular development due to the two dominating physical mechanisms and the involvement of identical particles providing a narrow and symmetric shower structure.

3.2.2 Hadronic Showers

Most of the EASs produced in the Earth's atmosphere are initiated by cosmic protons or atomic nuclei whose first interaction generates mainly pions ($\sim$89%), two thirds being charged and one third with neutral charge, kaons ($\sim$10%) and other nuclei which form a hadronic shower *core* [64]. Based on the secondary particles created after in the subsequent cascade three components are distinguished: a hadronic, an electromagnetic and a muonic component. The latter two are also denoted as *soft* and *component*.

- **Hadronic:** this component comprises the charged fragments of the first and subsequent collisions with further atmospheric molecules. Such particle multiplication due to inelastic hadronic interactions continues until a *critical energy* corresponding to the *energy threshold* of pion production, where it begins to become most likely that a charged pion will rather decay than interact. This characteristic energy depends on the atmospheric density and is typically reached within the range from 20 to 30 GeV [216, 320].

- **Electromagnetic:** the immediate decay of neutral pions into two energetic photons (see Chapter 2) leads to an electromagnetic sub–shower that propagates via the creation of electron positron pairs. These pairs in turn produce further photons of lower energy via Bremsstrahlung. In this way, one third of the hadronic shower energy is transferred irreversibly to the electromagnetic sub–shower [216].

- **Muonic:** Once the secondary particles have reached critical energy for pion production, their decay is dominant feeding the muonic shower component. Charged pions decay into neutrinos and muons:

$$\pi^+ \rightarrow \mu^+ + \nu_\mu \tag{3.9a}$$
$$\pi^- \rightarrow \mu^- + \bar{\nu}_\mu \tag{3.9b}$$

Beside their contribution to the muon production via their decay, kaons lead to a further production of low energy charged and neutral pions:

$$\mathrm{K}^+ \rightarrow \mu^+ + \nu_\mu \tag{3.10a}$$
$$\mathrm{K}^- \rightarrow \mu^- + \bar{\nu}_\mu \tag{3.10b}$$
$$\mathrm{K}^+ \rightarrow \pi^+ + \pi^0 \tag{3.10c}$$
$$\mathrm{K}^- \rightarrow \pi^- + \pi^0 \tag{3.10d}$$

The branching ratios of the decay modes of the kaons into muons and pions are 63.5% and 21.2% respectively [269]

The weakly interaction neutrinos travel unimpeded across the atmosphere, while few of the produced muons either lose energy via ionization or undergo a decay into neutrinos and electrons:

$$\mu^+ \rightarrow e^+ + \nu_e + \bar{\nu}_\mu \tag{3.11a}$$
$$\mu^- \rightarrow e^- + \bar{\nu}_e + \nu_\mu \tag{3.11b}$$

However, due to their high initial energy, most of the muons produced in hadronic cascades remain intact until they reach the Earth's ground (see Figure 3.6).

Therefore, the shower evolution is initially powered by strong interaction whereas at the end of the cascade a dominant particle decay occurs.

Moreover, hadronic showers feature more fluctuations with respect to the shower maximum which is related to the nuclear interaction length. According to the *Superposition model* [256] a nucleus of mass A and energy E_0 can be assumed to correspond to A protons of energy $E_n{=}E_0/A$ such that the shower maximum is given by:

$$X^A_{\max} \simeq X_{\max}\left(\frac{E_0}{A}\right) \tag{3.12}$$

Therefore, the depth of the shower maximum depends on the mass of the primary particle. The heavier the shower–initiating particle the less deep is the shower maximum. In addition, the fluctuations of the position of $X_{\max}$ from one shower to another is smaller for heavy nuclei than for light ones [194].

Beside the Superposition model, the Heitler model can be extended to describe the development of hadronic showers [256, 320] so that after n generations[12] the energy in the hadronic (E_{HAD}) and electromagnetic (E_{EM}) component is given by:

[12]Simulations show that the number of interactions is typically about 5 to 6.

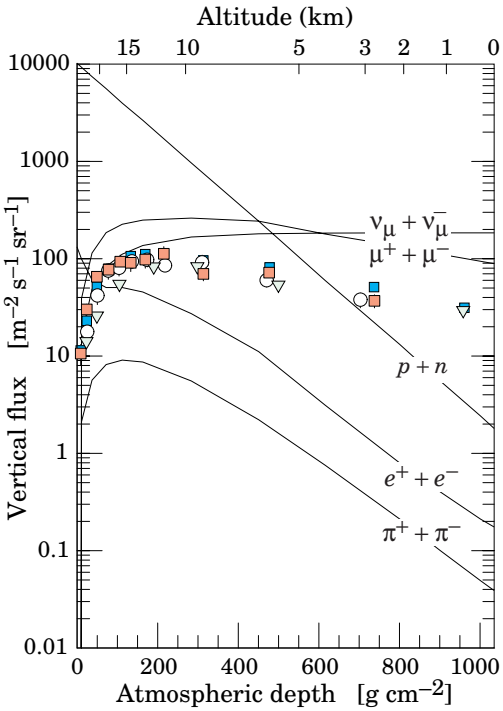

Figure 3.6: Vertical fluxes of CRs in the atmosphere with energies above 1 GeV estimated from the nucleon flux. The data present measurements on the negative muon flux above 1 GeV [56].

$$E_{\mathrm{HAD}} = \left(\frac{2}{3}\right)^n E_0 \tag{3.13}$$

$$E_{\mathrm{EM}} = \left[1 - \left(\frac{2}{3}\right)^n\right] E_0 \tag{3.14}$$

Although initiated by a hadron, most of the energy is carried by electromagnetic particles (∼90% for $n = 6$) and hence the depth of the shower maximum mostly depends on the electromagnetic shower component X^e_{max}:

$$X_{\mathrm{max}}(E_0) \propto \lambda_{\mathrm{ine}} + X^e_{\mathrm{max}} \left(\frac{E_0}{n_{\mathrm{tot}}}\right) \tag{3.15}$$

$$X_{\mathrm{max}}(E_0) \propto \lambda_{\mathrm{ine}} + \lambda^e \cdot \ln\left(\frac{E_0}{n_{\mathrm{tot}} E_{\mathrm{c}}}\right) \tag{3.16}$$

, where λ_{ine} is the hadronic interaction length and n_{tot} represents to number of newly produced particles in hadronic interaction.

Assuming that all charged hadrons decay into muons when the length for interaction and decay of charged pions are similar, the critical energy marking this transition E_{dec} after n interactions can be calculated:

$$E_{\mathrm{dec}} = \frac{E_0}{(n_{\mathrm{tot}})^n} \tag{3.17}$$

Since one muon is produced in the decay of each charged particle, the total number of such particles is given by:

$$N_\mu = n^n_{\mathrm{ch}} = \left(\frac{E_0}{E_{\mathrm{dec}}}\right)^\alpha \tag{3.18}$$

, with $\alpha = \ln n_{\mathrm{ch}}/\ln n_{\mathrm{tot}} \approx 0.82, \ldots, 0.95$ and n_{ch} representing the number of charged particles .

Due to the transverse momentum of the secondary particles produced in hadronic inelastic collisions, hadronic showers feature a wider lateral spread compared to electromagnetic scenario. Moreover, due to the different particles involved in the hadronic case, the developing shower appears more asymmetric than for electromagnetic induced particle cascades (see figures 3.7). Especially the lateral spread represents one of the most powerful discriminators between both shower types.

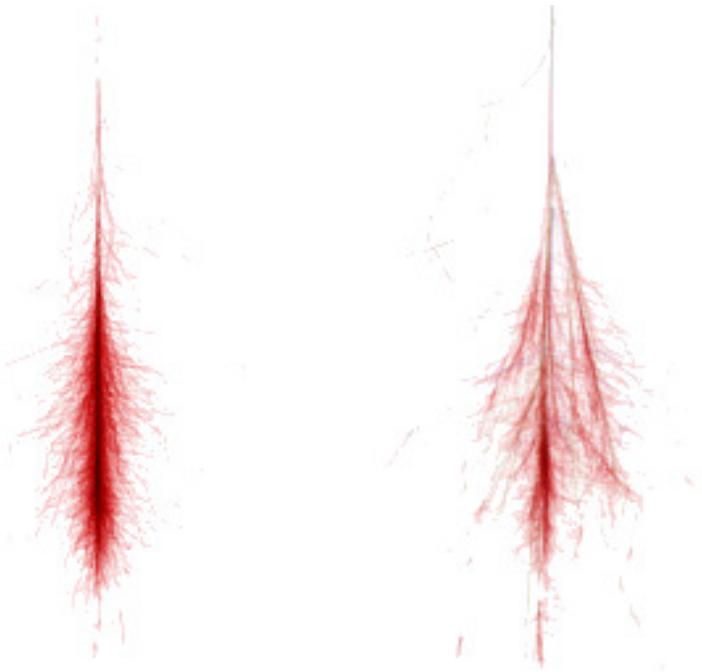

Figure 3.7: Simulation of the spatial development of an electromagnetic and hadronic shower induced by a primary particle of 100 GeV. *Left:* The electromagnetic shower evolution is narrow and concentrated along the cascade axis which coincides with the incoming direction of the primary. Right: The hadronic showers appears less concentrated due to the variety of particles and physical processes involved. Credit: F. Schmidt, "CORSIKA Shower Images", http://www.ast.leeds.ac.uk/ fs/showerimages.html

Due to their longer mean free path lengths, which depend on the density of the atmosphere, protons and pions penetrate much more the atmosphere than electrons. In addition, the interactions involved in hadronic showers last longer than those taking place in electromagnetic cascades. Thus, hadronic showers have a larger development with respect to the electromagnetic case leading to a longer temporal shower evolution.

3.2.3 The Cherenkov Light from Extensive Air Showers

Typically, the particle of showers produced by primary particles with energies below 1 TeV are too faint to be detected directly by ground–based telescopes. Therefore, a different technique has been developed to study the γ–ray energy range from tens of GeV to tens of TeV which is based on the detection of *Cherenkov light* that is emitted by CR induced atmospheric showers.

Water Cherenkov Detectors

Beside their potential of the direct detection of CRs, *imaging water Cherenkov detectors* are suited to perform γ–ray astronomy in the TeV range and are therefore complementary to atmospheric Cherenkov detectors. Typically, such detectors consist of large water tanks in which photomultiplier tubes (PMTs) are installed aiming at the detection of Cherenkov light emitted by particles on their passage through the water. From the timing information of the PMTs, the direction of the primary particle can be reconstructed. Ground–based water Cherenkov detectors offer a very wide FoV typically of $\sim$1.5 sr due to their large dimensions which allows for observations of spatially extended sources as well as for measuring the diffuse galactic γ–ray spectrum. In addition, this makes such instruments sensitive to transients and unexpected phenomena.
A disadvantage of such instruments usually consists in a moderate angular resolution, typically 0.5 to 2.5° depending on the energy regime, and a low–efficient background rejection, $\sim$90%, which results in a rather high threshold of $\sim$1 TeV. However, water Cherenkov detectors usually show best sensitivity and hadron suppression efficiency above 10 TeV wherefore they are rather designed for the study of galactic sources.
Conventionally, the hadronic shower rejection relied on the identifications of muons and hadrons which produce a distinct signal when reaching the bottom layer of the PMTs. Moreover, the spatial footprint of hadronic showers provides a good event discrimination. Due to the large fluctuation of the particle number striking the detector, the reconstruction of the primary energy is a challenging task, suffering large uncertainties and leading to a rather poor energy resolution.
Such instruments represent a low cost detector solution in terms of hardware components and provide the advantage of a high *duty cycle* of more than 95%. The *Multiple Institution Los Alamos Gamma Ray Observatory* (MILAGRO)[a] is such imaging water Cherenkov detector located at an altitude of 2530 m in the Jemez Mountains near Los Alamos, New Mexico that is composed of 723 PMTs submerged in a 24 million liter water pond of 60 x 80 m^2. MILAGRO has been operating from December 1999 to April 2008 whose scientific highlights encompass the galactic plane diffuse γ–ray emission, the Cygnus region and observations of large scale CR anisotropy.
To reduce the large uncertainties due to the distance between the detector and the shower maximum[b], the future generation of such detectors will be built at altitudes above 4000 m. For example, the *High Altitude Water Cherenkov Experiment* (HAWC) currently under construction is located at an altitude of 4100 m at Sierra Negra, Mexico. Beside this new instrument, further detectors are foreseen to be built, such as the *Large High Altitude Air Shower Observatory* (LHAASO) a future project at Tibet, China.

References: [41, 79, 37, 310], and references therein.

[a] Milagro is the Spanish word for miracle.
[b] An electromagnetic shower created by a 10 TeV γ–ray will reach its maximum at 6 to 7 km a.s.l.

The Cherenkov Effect

In 1934, Pavel Alekseyevich Čerenkov [81] discovered that charged particles emits a characteristic radiation when passing through a dielectric medium of *refractive index* n at a speed ν exceeding the phase velocity of light in this medium[13], i.e. $c_\mathrm{p} = c_0/n$, wherefore he was awarded for the Nobel Prize in 1958 together with the theorists Tamm and Frank who developed a theory to explain this phenomena in the framework of Einstein's *special relativity theory* [125].

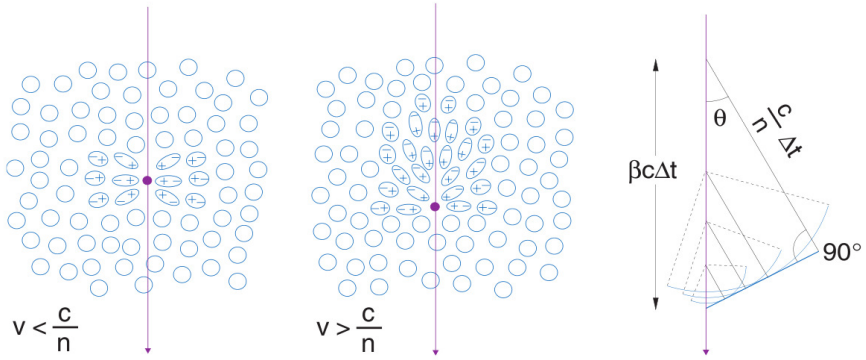

Figure 3.8: Illustration of the Cherenkov effect. *Left:* Polarization of a dielectric medium by a slowly moving charged particle. *Middle:* Polarization effect of a fast moving charged particle. *Right:* Trigonometric description of the Cherenkov angle θ.

Generally, a charged particle that moves in a dielectric medium, e.g. air, induces a local polarization of the molecules. If traveling with a velocity larger than the speed of light in such medium, the charged particle moves faster than the electromagnetic waves induced by the polarization along its path. As a consequence, a coherent wave front that is known as *Cherenkov light* is emitted into the so–called *Cherenkov cone* of angle θ (see Figure 3.8):

$$\cos\theta = \frac{c_\mathrm{p}}{\nu} \tag{3.19a}$$

$$\cos\theta = \frac{1}{\beta n} \tag{3.19b}$$

where $\beta = \nu/c_0$. Therefore, a minimal particle velocity is required in order to emit Cherenkov radiation:

$$\beta_\mathrm{min} = \frac{1}{n} \tag{3.20}$$

In the case of ultrarelativisitic particles, i.e. $\beta \approx 1$, the *Cherenkov angle* is maximum:

$$\theta_\mathrm{max} = \arccos\left(\frac{1}{n}\right) \tag{3.21}$$

Such minimum velocity can be expressed as an energy threshold for Cherenkov

[13] The speed of light in water for example is $0.75c_0$

light emission:

$$E_{\text{th}} = \frac{m_0 c_0^2}{\sqrt{1-\beta_{\text{min}}^{-2}}} \tag{3.22a}$$

$$= \frac{m_0 c_0^2}{\sqrt{1-\frac{1}{n^2}}} \tag{3.22b}$$

where m_0 refers to the rest mass of the particle. In the case of the atmosphere, the refraction index is a function of the altitude z leading to a variation of the Cherenkov angle as well as to the energy threshold. The higher the altitude, the lower the refraction index in the atmosphere and thus the lower the energy threshold. At sea level for example the energy threshold for electrons to induce Cherenkov radiation in air is 21 MeV [14]. Obviously, for heavier particles, the energy threshold increases, e.g. in the case of muons and protons the energy threshold is of 3 to 4 orders higher.

The number of Cherenkov photons emitted per path length x and wavelength λ by a particle of charge z is given by:

$$\frac{dN}{dxd\lambda} = \frac{2\pi\alpha z^2}{\lambda^2}\left(1\frac{1}{\beta^2 n^2}\right) \tag{3.23}$$

$$\frac{dN}{dEdx} \approx 370 \sin^2\theta \, e\text{V}^{-1}\,\text{cm}^{-1} \tag{3.24}$$

, where α refers to the fine structure constant [56].

The wave front features a conical shape with an opening angle θ_{p} with respect to the direction of the charged particle motion:

$$\theta_{\text{p}} = \frac{\pi}{2} - \theta \tag{3.25}$$

whereas the photon emission is perpendicular to the wave front filling rings in the plane transverse to the particle direction. As the refraction index is a function of the wavelength, Cherenkov radiation can only occur at frequencies for which n is larger than 1. Consequently, such light emission typically covers the wavelength range from UV to microwaves. In an electromagnetic shower about 500 Cherenkov photons are created per GeV of primary γ–ray energy between 300 and 600 nm for $\beta \approx 1$.

The Cherenkov radiation

Due to the low energy threshold, Cherenkov radiation is dominantly produced by electrons in atmospheric showers along their travel across the atmosphere. Thus, such emission, which is divided into *tail*, *core* and *head*, is produced at different altitudes. Due to the variation of the atmospheric conditions with altitude resulting in a variation of the refraction index, the Cherenkov angle ($\sim 0.7°$) differs [14]: the higher the altitude, the narrower the Cherenkov cone[14] (see Figure 3.9).

Therefore, the resulting emission is a superposition of the individual Cherenkov cones assuming the form of "donut rings" forming a so–called *light pool* whose properties depend on the primary particle nature and its energy. On the ground, the light pool has a typical size of around 50000 m^2. Figure 3.11 illustrates the

[14] At 10 km a.s.l. the Cherenkov angle is 0.66° whereas it increases to 0.74° at 8 km a.s.l.

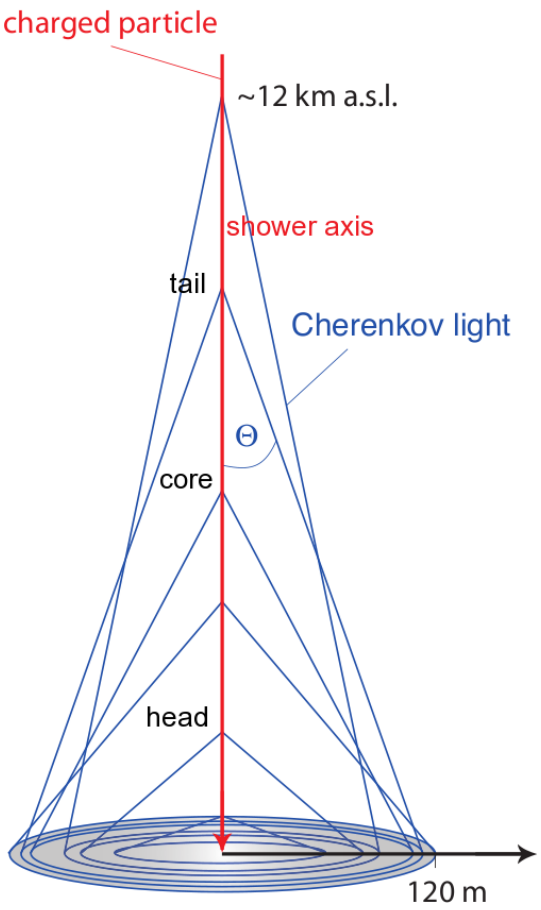

Figure 3.9: Sketch of the atmospheric Cherenkov angle variation with altitude. The atmospheric Cherenkov emission of a downward moving single particle with varying Cherenkov angle along the shower aixs. The head core and tail of the particle shower are sketched.

lateral Cherenkov photon distribution at the height of the MAGIC site. The light pool exhibits a quasi flat photon density in its *core* up to a distance of ∼120 m from the shower axis followed by a steep decrease in photon density in the *halo* region when crossing the *Cherenkov hump*. The hump is a geometrical feature associated to the change in refraction index and Cherenkov angle leading to a focusing effect [268]. Instead, the Cherenkov light pool created by a proton exhibits a photon density that peaks at the center of the core position and decreases rapidly towards the halo region.

Figure 3.10 illustrates the photon density inside the Cherenkov light pool for different types of particles. For γ–rays an almost constant fraction of the primary energy is converted to Cherenkov photons wherefore the measurement of the Cherenkov light intensity is a good measure of the primary γ–ray energy. Thus, the atmosphere behaves like a *ideal calorimeter* for γ–rays [14].

An additional effect on the Cherenkov photon density is related to the *zenith angle* of observation: at high zenith angles, i.e. the pointing position of the telescope is highly inclined with respect to a pointing vertical to the ground, the observed atmospheric shower traverses a larger atmospheric layer. Therefore, the distance between the telescope and the position of the shower maximum increases. With increasing path across the atmosphere, the total absorption or interaction of the Cherenkov radiation becomes more likely. For this reason especially the

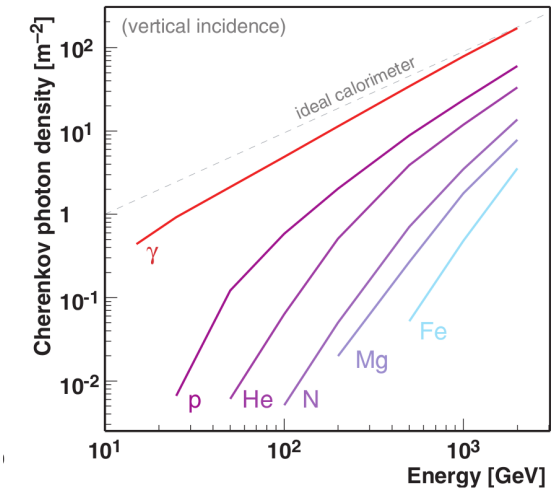

Figure 3.10: Cherenkov photon yields for different particle species. The mean Cherenkov photon density within 125 m of the shower axis for vertical incident showers are shown. For γ–ray–initiated shower the atmosphere behaves almost like an ideal calorimeter [294].

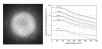

Figure 3.11: Cherenkov light pool of a γ–ray induced extensive air shower. *Left:* The light pool observed on the ground produced by a 300 GeV γ–ray featuring a rather uniform density. *Right:* Simulation of the density profile of the light pool. Starting from the core center, the density shows a quasi flat plateau up to a radial distance of ∼120 m followed by a steep decrease in the halo region. The solid and dashed lines differentiate showers developing along the Earth's magnetic field and perpendicular to it, i.e. high zenith angles [14].

Cherenkov light produced in atmospheric showers that stem from primary particles of low energy may not be detected.

Fluorescence phenomena

Beside Cherenkov radiation, a charged particle induces *fluorescence* emission when crossing the atmosphere. The emission occurs mainly due to the excitation of nitrogen molecules, being the most abundant component in the atmosphere (78%), when falling back to their ground state. The fluorescence radiation, which peaks at UV wavelengths between 300 and 450 nm, is emitted isotropically. Due to its dependence on the size of the atmospheric showers, such emission is used for the indirect observation of CRs. As the energy threshold for fluorescence emission is $\sim 10^{18}$ eV, the measurement of this radiation can only be applied for the study of UHECRs. The *Pierre Auger Observatory* (PAO), the *Akeno Giant Air Shower Array* (AGASA) and the *High Resolution Fly's Eye* (HiRes) are three large experimental facilities that perform such observations.

References: [53, 257], and references therein.

The Observed Cherenkov radiation

Equation 3.23 indicates a squared inverse dependency of the number of Cherenkov photons on the wavelength indicating a maximum emission at shorter wavelengths, that is in the UV band, whereas the Cherenkov radiation will decrease with increasing wavelengths. However, due to the interaction of the Cherenkov radiation

with the air molecules when crossing the atmosphere, the spectrum observed by the detector differs from the initially generated emission (see Figure 3.12) peaking at UV–blue wavlengths [14].

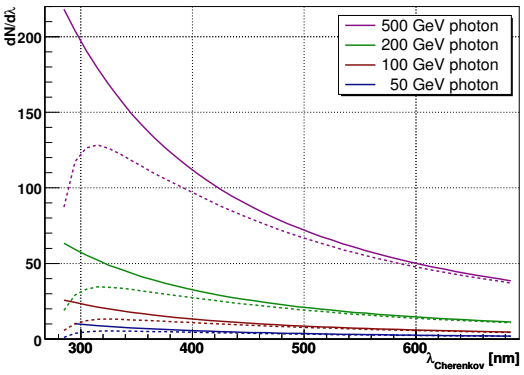

Figure 3.12: Calculation of the spectral Cherenkov radiation from a γ–ray induced air shower. The emission is computed for primary gammas of different energies created at 10 km height before (solid lines) and after (dashed lines) atmospheric extinction at 2200 m a.s.l. [324].

The following atmospheric absorption mechanisms lead to the spectral extinction of electromagnetic radiation

- **Rayleigh scattering:** due to the interaction with air molecules, photons are scattered off provided that the molecule size is of the order of the photon wavelength ($d \approx \lambda$). The cross section of *Rayleigh scattering* is proportional to λ^{-4} wherefore this process affects mainly the UV part of the Cherenkov spectrum.

- **Mie scattering:** due to the presence of *aerosols*, i.e. particles whose dimension is larger than the photon wavelength, photons undergo *Mie scattering*. This process occurs to depend only weakly on the photon wavelength ($\propto \lambda^{\alpha}$, with $\alpha = 1, \ldots, 1.5$). Variations of the aerosol content in the atmosphere make an estimation of this scattering difficult.

- **Absorption:** the presence of ozone causes a strong absorption in the UV regime ($\lambda < 280$ nm):

$$O_3 + \gamma \rightarrow O_2 + O \tag{3.26}$$

  Since ozone occurs rather in the upper part of the atmosphere, i.e. at 10 km a.s.l., a zenith angle dependence on the lower wavelength cutoff of the spectrum is introduced.

  In the lower atmosphere, the presence of water vapor and carbon dioxid lead to an absorption of photons with wavelengths longer than 800 nm.

The typical duration of Cherenkov light emission by γ–ray induced air showers is approximately 3 ns at `impact parameters`, i.e. the distance of the air–shower core to the telescope), below 120 m, whereas hadronic induced air showers exhibit a slightly wider time spread of approximately 10 ns.

3.2.4 The Imaging Technique

Hadronic–initiated air showers represent a very dominant background with respect to electromagnetic cascades. In fact the ratio of γ–rays to charged CRs is

extremely small ($\sim 10^{-4}$), demanding a very powerful tool for the discrimination of γ–rays with ground–based detectors.

Up to now, the most efficient technical solution to carry out γ–ray astronomy from the ground above $\sim$50 GeV is the *imaging technique*. A part of the atmospheric shower is sampled by an *Imaging Atmospheric Cherenkov Telescope* (IACT) placed inside the Cherenkov light pool to measure the number of Cherenkov photons and to image the shower (see Figure 3.13).

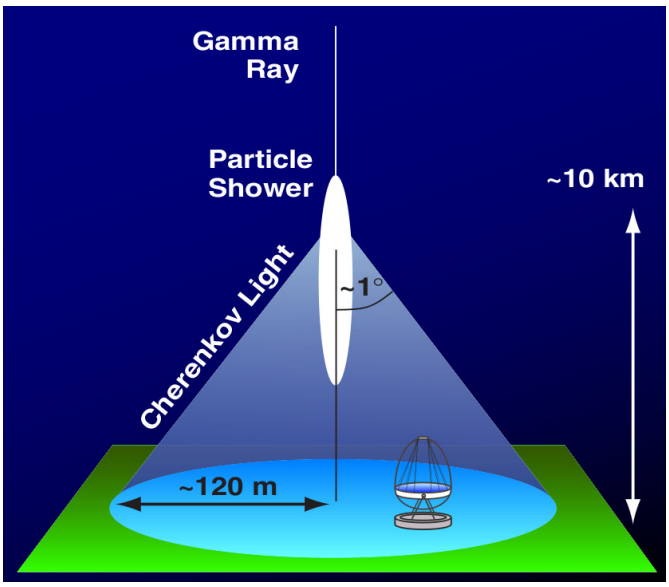

Figure 3.13: Sketch of the imaging technique. A VHE γ–ray interacts with the top atmosphere giving rise to an EAS that radiates Cherenkov light. An IACT is placed into the Cherenkov light pool.

The main conceptual with respect to optical telescope is that ground–based γ–ray telescopes do not directly measure the photon flux of interest, i.e. the γ–ray flux, but by means of secondary photons produced in the particle cascades. Therefore, contrary to standard telescopes Cherenkov telescopes are not focused to infinity but roughly at the height of the shower maximum, which in the case of primary γ–ray of tens of GeV to hundreds of GeV corresponds to a height of 10 km a.s.l.

The core of this technique is based on the study of the imaged Cherenkov radiation originating from a particle shower. Due to differences in the origin of the emission by the particle shower, the Cherenkov photons are projected on different regions of the camera depending on the angle between the telescope axis and the incoming photon direction. In general, the amount of Cherenkov photons detected provides information about the density of the shower particles at different altitudes of the atmosphere. Moreover, as the atmosphere behaves quasi like an ideal calorimeter to gammas, the Cherenkov light intensity is related to the primary energy of γ–like events. In addition, the shower image properties contain information about the incoming direction of the primary particle as well as on its nature.

Usually, the image of the Cherenkov radiation of a γ–ray induced particle cascade have a compact *elliptical* shape. whose extremities represent the head and tail of the particle shower while the central part corresponds to the core of the shower. The major axis of the ellipse indicates the projection of the shower axis onto the image plane. By contrast, compared to gamma events shower images from hadronic induced particle cascades exhibit a more complex structure.

The Image Formation

Figure 3.14 sketches in detail how the short Cherenkov light pulses are projected onto a pixelized camera consisting of sensitive photodetectors to record these emissions as *shower images*.

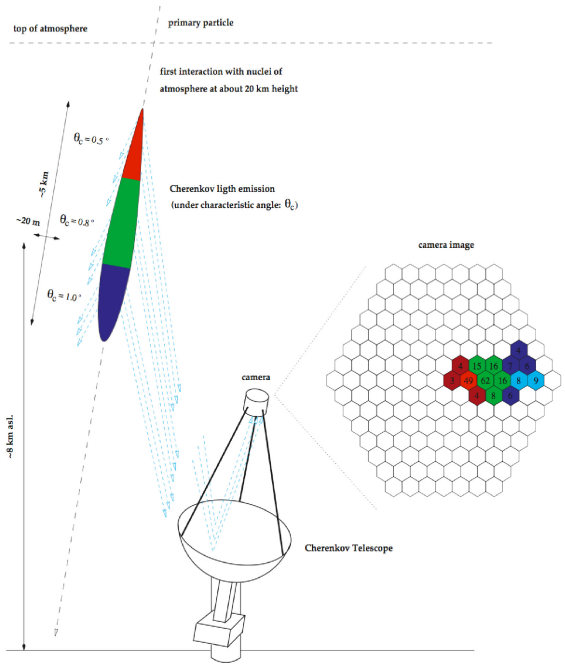

Figure 3.14: Sketch of the functionality of an IACT. A primary particle interacts with the top layers of the atmosphere initiating an extensive air shower that is characterized by a head (red), a core (green) and a tail (blue). The shower particles in return emit Cherenkov radiation (dashed lines) if exceeding the speed of light in air. under an increasing Cherenkov angles with increasing atmospheric depth creating a Cherenkov light pool. The reflector of a Cherenkov telescope placed into the light pool collects a sample of the Cherenkov light and projects its image onto a pixelized camera. The number written in the pixels indicates the number of Cherenkov photons impinging the PMTs.

Photons of parallel incidence with respect to the axis of the telescope will be concentrated into the focus of its dish, which is of concave shape, whereas photons with an incident direction inclined by the angle β with respect to the telescope axis will be concentrated into another position in the focal plane with a distance ρ to the focus (see Figure 3.15).

By fixing a polar coordinate system in the focal plane, the position of the light concentration in the camera given by the distance ρ with respect to the central camera pixel can be computed in first approximation from the incident angle β of the photon by:

$$\rho = \sin\beta \cdot f \simeq \beta \cdot f \tag{3.27}$$

where f is the focal distance of the telescope mirror. Therefore, the position of illuminated camera pixel is univocal related to the incoming direction of the Cherenkov photons with respect to the axis of the telescope: the light projected onto the central camera region refers to the shower head, while the light fraction contained in the pixel closer to the camera border is related to the shower tail. The amount of Cherenkov photons along the longitudinal extension of the

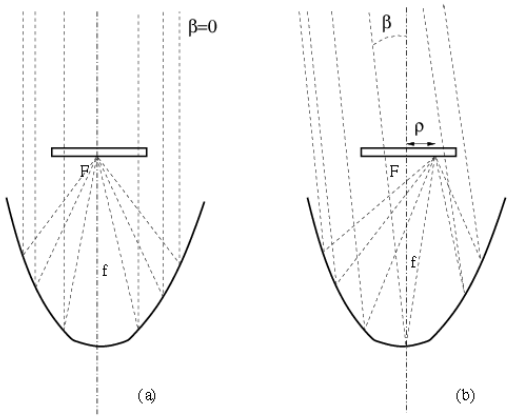

Figure 3.15: The imaging scheme of Cherenkov radiation used for IACTs. A pixelized camera is installed in the focal place of the telescope dish.

recorded shower images is connected to the number of shower particles produced at different altitudes. Instead, the lateral width of the shower image is related to the transverse elongation of the particle cascade.

The Background Radiation

Observations of Cherenkov radiation is affected by the *Nights Sky Background* (NSB) which is mainly composed by the light of bright stars, zodiacal light, diffuse light from the galactic plane, airglow, polar light, fluorescence phenomena and artificial light. Although isotropically distributed, the NSB, which peaks in the red/IR range, shows increased levels, e.g. in the galactic plane. Furthermore, it increases with increasing zenith distance. The NSB represents the main source of noise for Imaging Cherenkov telescopes.

Beside the NSB, the moon represents another important factor causing disturbing dramatically the Cherenkov light detection since its spectrum has its maximum around 500 nm. This critical issue has been considered in the design of the MAGIC telescopes so that they are adapted for data taking under moderate moon light conditions and during twilight.

As hadronic showers represent another very dominant background source for such observations, its efficient rejection is of great importance for the extraction of the γ–ray signal. Recalling the differences of the shower evolution which is reflected in the Cherenkov light emission, the hadronic background can be suppressed by studying the temporal and spatial structure of the recorded light signal.

The muonic component in hadronic showers is another not negligible background source. Typically, muons emit single Cherenkov cones whose projection forms a ring shape which can be easily distinguished. For large impact parameters, only a segment of the ring is projected on the camera since the IACT is only observing part of the Cherenkov cone. In this case, a muonic shower image may be confounded with a γ–like event. Due to their weak interaction and longer life time, muons usually travel deeper into the atmosphere than gammas wherefore a shower induced by such particle is initiated closer to the ground.

Like gammas cosmic electrons produce electromagnetic cascades representing a background whose rejection is challenging as they generate identical shower images. However, as hadronic induced particle cascades the air showers initiated by cosmic electrons exhibit an isotropic distribution.

Identical to cosmic electrons, diffuse γ–rays stemming from unresolved sources produce electromagnetic showers without any predominant direction leading in principle to an irreducible background. In Figure 3.16 different shower images

related to a gamma, a hadronic and a muonic event are presented.

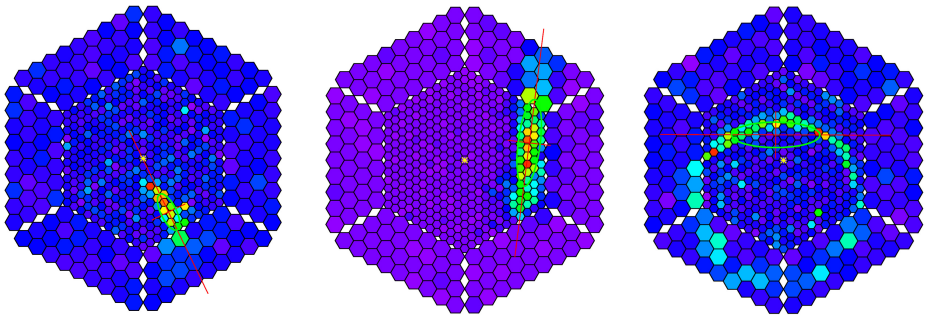

Figure 3.16: Shower images produced by different types of particle cascades. *From left to right:* A compact shower image originating of a γ–ray–induced electromagnetic particle cascade of pointing to the nominal source position in the center of camera; a widened hadronic event with random direction; a shower images with ring shape due to an isolated muon. The shower images are taken from real data.

In general, background events feature an isotropic distribution, while showers produced by gammas originating from the source under observation show a predominant arrival direction. Thus, the majority of the background events can be rejected by the selection of events whose incident direction is in agreement with the expected γ–ray source position.

The Image Parametrization

As the imaging technique relies on the analysis of the shower development information that is contained in the image formed in the camera, a very sophisticated analysis method of the shower ellipses is required. Therefore, a set of *image parameters* represent an indispensable tool of the imaging technique to characterize the primary particle by discriminating its nature and energy once the image is cleaned from the noise.

The fundamental image parameters have been proposed by [160] with the purpose to extract from the morphology and orientation of the shower image to the main physical information with regards to the primary particle (see Figure 3.17).

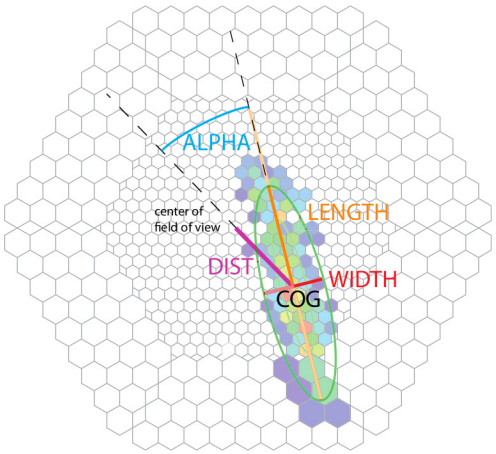

Figure 3.17: Illustration of some of the main image parameter according to [160].

In general, their computation is based on the spatial charge distribution in the camera. In the following the image parameters are listed along with other

parameters commonly used in the MAGIC standard analysis which do not belong to the original standard parameters defined by Hillas:

- `size`: The total number of phe collected in the shower image is defined as:

$$\texttt{size} = \sum_{i=1}^{k} N_i \tag{3.28}$$

  ,where N_i is the charge in a given pixel i. For fixed zenith angle of observations and impact parameter, this image parameter is in first approximation proportional to the primary particle energy.

- `length`: This parameter defined as half the length of the major image axis refers to the second moment of the light distribution along this axis. The `length` parameter is related to the longitudinal development of the shower.

- `width`: As related to the second momentum of the light distribution along the minor shower axis, the `width` parameter is defined as half the width of this axis. The parameter is correlated with the transversal shower development. Since hadronic showers feature a larger transversal momentum than γ–induced particle cascades, the image `width` provides a possible background suppression.

- `alpha`: The angle between the direction of the major axis and the line connecting the image centroid with the nominal position of the candidate γ–ray source in the camera is denoted as `aplha`. Shower images that are induced by primary gammas feature an `alpha` close to zero due to their preferential direction, while hadron–induced shower images exhibit a random distribution of this parameter since their direction is nearly isotropic. In the case of point like sources, `alpha` represents the most powerful discriminator of γ–like events.

- `dist`: The `dist` parameter defines the distance between the image centroid and the nominal source position in the camera providing information on the distance of the shower maximum and the impact parameter.

- `conc`n: The `conc` parameter is a measure of the fraction of the total photon containment in the $n = 1, \ldots, 7$ brightest pixels by what information on the shower core are obtained. In this way, the compactness of the shower image is parametrized. The `conc` parameters is expected to be higher for γ–ray induced showers. Typically, a standard value of $n = 2$ is used.

- `leakage`: The parameter indicates the light fraction of the image that is contained in the outer camera pixels and thus a useful rejection criteria of eventually cropped images due to too large impact parameters or. An image cropping might be also occur in the case of primary particles of very high energy so that the image size exceeds the camera FoV.

- `Number of islands`: This parameter accounts for the number of spatially separated clusters of pixels after the image cleaning (see Section 7.1.2). In the case of electromagnetic showers, usually one single connected image is obtained, while hadronic shower images tend to appear as several separated clusters of particles.

- `m3long`: Related to the third momentum of the charge distribution along the major axis, the `m3long` parameter is a measure for the asymmetry of the shower image along the longitudinal development. Considering a gamma event, the head of the shower, which contains a higher charge, should be closer to the nominal source position than the tail discriminated by a lower charge.

In addition to the classical Hillas parameters, the MAGIC collaboration has developed some new image parameters that are based on the timing information of the shower [36]. Their implementation lead to a significant improvement of the performance of MAGIC system.

- `time gradient`: The `time gradient` indicates how fast the arrival time changes along the major axis of the shower image. Typically, the arrival time differences increase with increasing distance from the nominal location of the source position in the camera. For simplicity purposes, the pixel coordinates are projected onto the major axis, reducing the problem to one dimension. The parameter depends strongly on the distance of the shower axis from the camera.

- `time RMS`: The parameter corresponds to width of the arrival time distribution of all pixels after the image cleaning. Usually, the arrival time distribution of a gamma event is narrower than for hadronic showers.

After their parametrization, depending on the image parameters, the shower images are either tagged as background– or γ–like events which is referred to as *γ/hadron separation* (see Section 7.1.4 for a detailed description). A powerful selection criteria is for example given by the orientation of the shower ellipse with respect to the camera center. When observing a γ–ray source, it is expected that γ–rays originating from this source will create shower images whose main axis points towards the direction of the source in the camera, whereas hadronic induced shower images show a random orientation.

Observations carried out by several IACTs in *stereoscopic* configuration, where the same shower event is seen under different angles, can achieve an improved background rejection on the *trigger* level by the selection of coincident events which in turn leads to a lower energy threshold. In addition, a stereoscopic system provides a better *angular resolution* leading to a more precise reconstruction of the direction of the primary particle and an improvement in *energy estimation* (see Section 7.1.4) [112]. Furthermore, the stereoscopic view enables the discrimination between nearby and distant events induced by primary particles of low and high energy energy respectively by the reconstruction of the shower core (see Figure 3.18).

The distance between several IACTs in a stereoscopic configuration has to be optimized such that at least two IACTs provide observations of the same Cherenkov light pool and guaranteeing at the same time different viewing angles of the same shower. In general, the larger the distance of the telescopes within the Cherenkov light the better the stereoscopic view of the event. However, with enlarging distance the effective area reduces (see Figure 3.19).

Vice-versa, the effective area increases the closer the telescopes are spaced at the cost of a less accurate reconstruction of the shower core. Therefore, a compromise between telescope spacing and effective area has to be evaluated. Beside the effect of the zenith angle on the effective area, in the stereoscopic case the azimuthal position of the telescopes has an additional effect.

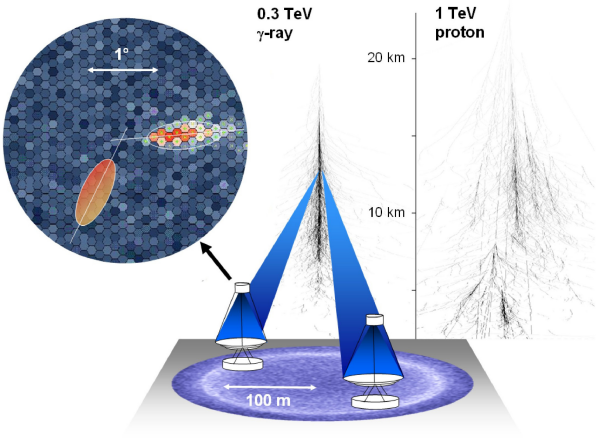

Figure 3.18: Principle of a stereoscopic IACT system. The inlet sketches the superposition of an electromagnetic shower as seen by both telescopes in order to determine the direction of the primary particle. For comparison a hadronic shower is illustrated on the right [162].

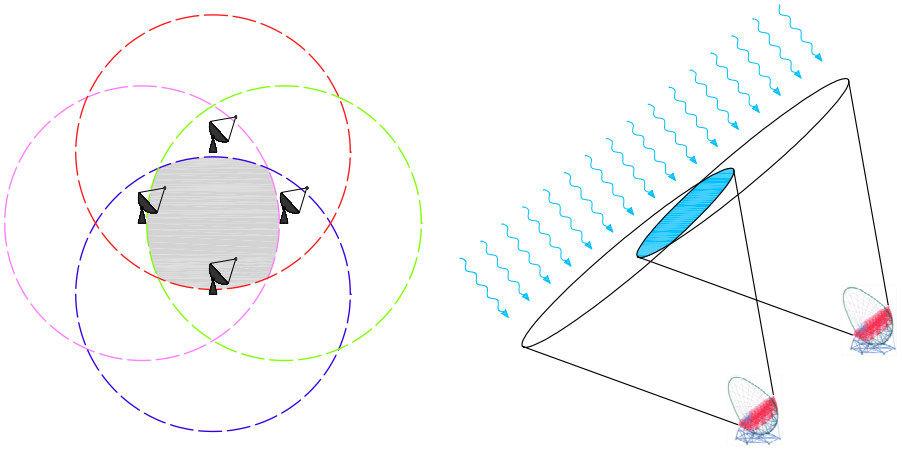

Figure 3.19: The effective area of a stereoscopic IACT system. *Left:* Sketch of the fraction of the Cherenkov light pool seen in by two IACTs. *Right:* Effective area intersection at ground level for an IACT arrays. Credit: A. Bortoluzzi & F. Dazzi

3.3 The General Design of IACTs

Although IACTs detect the radiation that comprises wavelengths in the UV band and optical frequencies, standard telescopes sensitive to the optical regime cannot be used for the imaging technique due to the rapid temporal evolution of the Cherenkov radiation. The capture of such short light pulses in a shower image requires several technical issues that need to be taken into account for the design of an IACT.

Short exposure times of less than 10 ns and a trigger concept that exploits spatial and temporal coincidences allow for the discrimination between particle shower events and statistical fluctuations of the steady NSB as a first rough background rejection on a hardware level. At the same time, this first rejection represents the most important background elimination. Such short exposure time put some constraints on the possible design of the telescope reflector. Typically, such reflector is either of spherical or parabolic shape composed of several smaller mirror facets. In particular, the latter choice provides the advantage of the preserving the timing structure of the Cherenkov light flashes due to its isochronous nature. However, a parabolic dish is characterized by larger aberrations and coma

compared to a spherical layout which in turn limits the FoV of the telescope. The FoV of the telescope is defined as the maximum angle between the telescope axis and the incident photon direction for which the photon is projected into the camera and is usually of the order of few degree. Therefore, IACTS are not suited for *sky surveys* and are usually used to perform observations of individual sources requiring a two–dimensional fast *tracking* system. In addition, the low γ–ray flux requires large collection areas in order to concentrate the maximum fraction possible of the Cherenkov light pool. Finally, a *data acquisition* (DAQ) system is needed to store the data for later analysis.

Depending on its design, an IACT will be sensitive to different types of sources and hence to different physics. In general, galactic sources except pulsars feature rather hard spectra with high γ–ray fluxes even at TeV energies, while extragalactic sources are typically characterized by softer spectra due to the flux attenuation by the EBL (see Chapter 6) and intrinsic cutoffs predicted by some emission models wherefore a lower energy threshold with respect to galactic sources is required.

The Sensitivity of an IACT

Generally, an IACT is characterized by its *sensitivity* marking the minimum detectable γ–ray flux in a given observation time. Usually, a distinction between the *integral* and differential sensitivity is made, depending whether the integral or differential photon energy flux is concerned. The sensitivity is above all related to the capability of an IACT to distinguish between shower images initiated by gammas and showers related to background events. Therefore, a significant enhancement in sensitivity can be achieved by providing an improvement in the background suppression since it reduces the time necessary to detect a statistically significant γ–ray signal. Such improvement in background rejection is obtained for example by observations performed with stereoscopic configurations of several IACTs.

The second important property of an IACT regards the energy threshold, which indicates the minimum detectable energy of the primary particle, is related to the mirror surface A, the light detection efficiency ϵ, which includes the mirror reflectivity and the light detection efficiency given by the photo sensors, the integration time Δt of the Cherenkov signals and the solid angle Ω subtended by a PMT [202]:

$$E_{\mathrm{th}} \propto \sqrt{\frac{\phi_{\mathrm{NSB}} \Delta t \Omega}{\epsilon A}} \tag{3.29}$$

, where ϕ_{NSB} is the flux of the NSB which varies among the potential IACT sites. This equation indicates that a lower energy threshold is achievable thanks to a higher light detection efficiency and a larger collection area, a small FoV and fast readout electronics to minimize the integration time of the background light.

The third parameter important for the characterization of an IACT is the angular resolution that is typically of the order of 0.1°. Similar to the sensitivity, a stereoscopic system of several IACTs leads to a significant improvement of this parameter.

3.3.1 The Current Generation of IACTs

After the *Wipple* 10 m gamma–rays telescopes and the *High Energy Gamma–Ray Astronomy* (HEGRA) telescope, the third generation of IACTs is represented by four IACTs located at different sites (see Figure 3.20): the *Major Atmospheric*

Gamma Imaging Cherenkov (MAGIC) telescopes , the *High Energy Stereoscopic System* (H.E.S.S.), the *Very Energetic Radiation Imaging Telescope Array System* (VERITAS) and *Collaboration of Australia and Nippon for a GAmma Ray Observatory* III (CANGOROO III) which are located on the Canarian Island La Palma, in Namibia, Africa, and in Arizona, United States, and Australia respectively (see Figure 3.20).

Figure 3.20: The sites of the third generation of IACTs

All four system are stereoscopic configurations of featuring different properties. MAGIC is a system of two identical 17 m diameter Cherenkov telescopes with an energy threshold of 60 GeV and a camera FoV of 3.5° [85, 88], whereas H.E.S.S. [322], and VERITAS [163] are both arrays of four 12 m diameter telescopes providing each an energy threshold of 100 GeV and a camera FoV of 5° and 3.5° respectively. Both arrays exhibit different configurations. While VERITAS CANGOROO III consists of an array of four 10 m diameter telescopes with an estimated energy threshold of ∼400 to ∼500 GeV [189] and a camera FoV of about 3°.

Recently, the H.E.S.S. experiment inaugurated the new 28 m diameter H.E.S.S. II telescope whose modified design is aiming at the detection of VHE γ–rays of energies as low as 20 GeV (see Figure 3.21).

Figure 3.21: Image of H.E.S.S. II telescope. Credit C. Medina.

While MAGIC and VERITAS are located in the northern hemisphere, the H.E.S.S., and CANGAROO III sites are located on the southern hemisphere. Therefore, in particular the H.E.S.S. telescope is well suited for observations of the galactic plane due to its large FoV, whereas MAGIC and VERITAS are more appropriate for the study of galactic and extragalactic sources situated in the northern atmosphere.

The H.E.S.S. II Telescope

On July 26th, 2012, the almost 600 tons heavy H.E.S.S II telescope started its operation. With its 28 m diameter[a] rectangular–shaped mirror dish of 596 m^2 area, composed of 875 hexagonal quartz coated mirror facets of 90 cm *flat–to–flat* (ftf) size and ∼25 kg weight, H.E.S.S. II beats the MAGIC system whose telescopes have been known to be the world's largest Cherenkov telescopes.

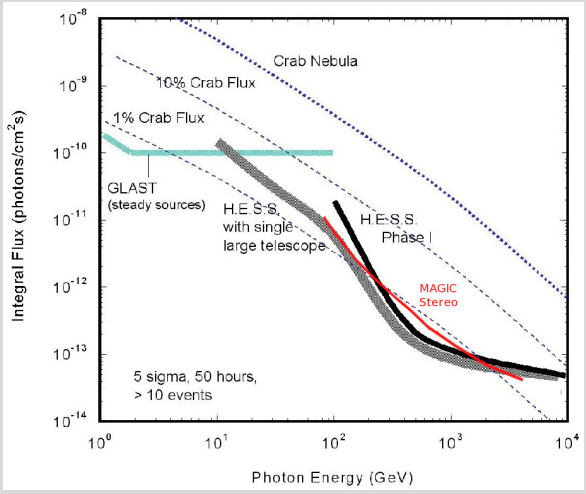

Figure 3.22: Estimated sensitivity of H.E.S.S. II.

While the telescope structure and the camera design have been kept similar to H.E.S.S. I, H.E.S.S II features a modified reflector design with respect to the the dimension of the single mirror facets whose circular shape has been replaced by a hexagonal geometry by what the reflector area has been increased. In addition, the H.E.S.S. II mirror facets exhibit improved reflectivity. To introduce a lower time–dispersion, the mirror geometry has been changed from *Davis–Cotton* to a parabolic dish structure, whose focal length f is 36 m. The defined f/d ratio of 1.2 provides a compromise between the imaging quality over the field of view and the costs of the telescope structure. The camera of 3.5° is pixelized by 2048 PMTs of hexagonal shape (42 mm ftf). Further upgrades have been performed with respect to the front–end electronics aiming at a higher acquisition rate capability and a larger dynamic range. Thanks to this modifications in the telescope design, H.E.S.S estimates to access the energy window from ∼20 GeV to few tens of TeV.

References: [323], and references therein.

Images: Sensitivity of the H.E.S.S. II telescope for standalone observations based on Monte Carlo simulations. For comparison the integral sensitivity of the MAGIC stereo system obtained with data is shown. Adapted from [35].

[a] The exact dish dimension are 32.6 m by 24.3 m.

Moreover, since fall 2011, the *First G-APD Cherenkov Telescope* (FACT) (see Figure 3.23), which is the first Cherenkov telescope whose camera consists of *Geiger–mode Avalanche Photodiodes* (G–APDs), started observations.

For the construction of FACT an old IACT with a mirror of 9.5 m^2 area has been refurbished and a fine pixelized camera consisting of G–APDs has been built with the main goal to evaluate the performance of such innovative camera with the prospective of the replacement of conventional PMTs by this novel photo sensors. Such innovative design bear the potential to significantly improve the sensitivity of IACTs thanks to their promising high *photo detection efficiency* (PDE) of such photo sensors. In addition, these devices require a much lower voltage for operation and are not damaged by the exposure to bright illumination providing the possibility to extend the operation of IACTs to observations under

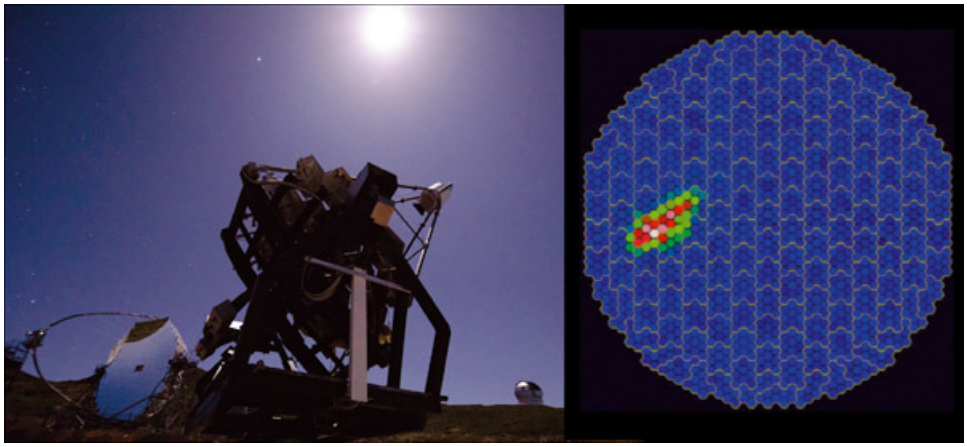

Figure 3.23: The FACT telescope. *Left:* FACT taking data first in October 11$^{\text{th}}$, 2011, during full moon. *Right:* First image shower recorded by FACT during full moon. Credit: FACT/T. Kräenbühl.

strong moon conditions. Beside serving as a test bench for this technology, FACT is aimed at monitoring bright AGNs in the TeV range.

3.3.2 The Cherenkov Telescope Array

The next generation of IACTs is herald with the future project of the *Cherenkov Telescope Array* (CTA) which will be the first open observatory for VHE γ–ray astronomy. CTA will probably consist of two arrays of IACTs located at two sites, i.e. CTA North and South providing a full sky coverage, aiming at (I) an increase in sensitivity by another order of magnitude[15] around 1 TeV (see Figure 3.25), (II) a significant boost of the collection area and hence in the detection rate, which is of particular importance for transient phenomena and at highest energies, (III) an improvement in angular resolution and thus the ability to resolve extended source morphologies, (IV) a uniform energy coverage from some tens of GeV to beyond 100 TeV [91].

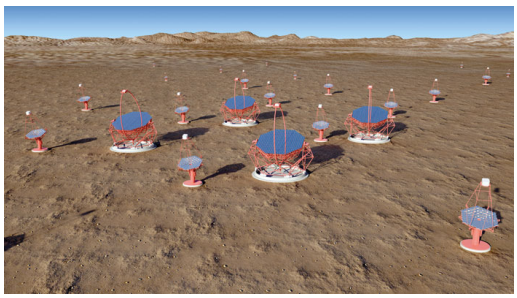

Figure 3.24: An artist's impression of CTA. Credit G. Pérez/IAC/SMM.

The main site will be located in the southern hemisphere addressed to observations of the central region of our Galaxy, while the northern array will be primarily devoted to the study of extragalactic sources (see Figure 3.26). For the northern array, Tenerife, North America, especially the south western United States like Arizona, the north west corner of Mexico and the region of northern India are considered as site candidates, while the probable southern array location are focused on South Africa and South America. In particular the H.E.S.S. location and a region near the Sutherland Observatory are considered regarding the African site candidates, while in the South America the search concentrates on two locations in Argentina [83].

In general, with its improvement in performance CTA is devoted to explore in depth our Universe in VHE γ–rays and to investigate cosmic processes leading

[15] A factor of 5 to 10 in the 100 GeV to 100 TeV range is aimed.

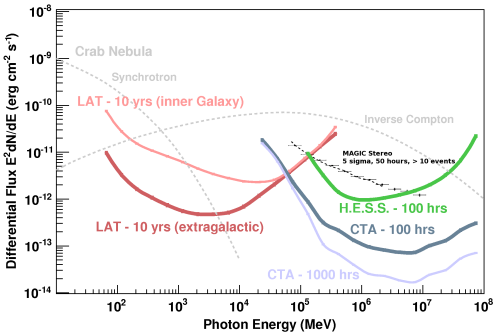

Figure 3.25: Predicted differential sensitivity and energy threshold of CTA [126].

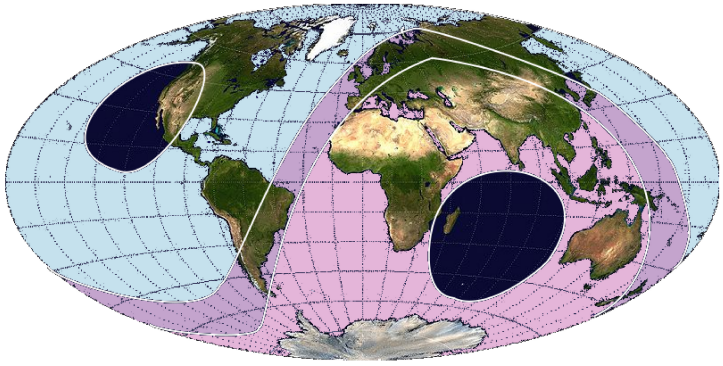

Figure 3.26: Possible CTA sites on the northern and southern hemisphere. The world map is shown in galactic coordinates. The blue shaded area indicates the sky segment visible at low zenith angle from the MAGIC and VERITAS site, located in the northern hemisphere. The pink shaded area represents the sky region visible at low zenith angle from the H.E.S.S. site situated at the southern hemisphere. The purple shaded area marks the sky fraction visible for all three IACTs. The proposed southerns sites (Argentina, Namibia) cover almost the same sky regions as H.E.S.S. The unshaded areas corresponds to blind spots of zenith angles $\geq 50°$.

to relativistic particles. Beside guaranteed astrophysics results, CTA will feature a large discovery potential in key sciences of the research fields of astronomy, astrophysics and fundamental research. Such potential aims at providing answers on some open questions like the origin of CRs, the absolute EBL, the examination of the ultimate nature of matter as well as physics beyond the *Standard Model* through searches for dark matter and the effects of quantum gravity.

The international *consortium* involves among others the collaborations of MAGIC, H.E.S.S. and VERITAS collaboration. CTA is currently in its *Preparatory Phase* involving research and development (R&D) studies on the individual hardware components, on software tools for the data analysis, on the exact position of the array sites as well as on the exact layout of the telescope arrays.

However, based on Equation 3.29 the limitation of the telescope performance has been studied in order to take these implications into account regarding the design of the individual telescopes optimized for different energy regimes (see Figure 3.27).

CTA roughly will consist of 80 telescopes of different sizes in two locations. These telescope designs are optimized for the individual energy ranges, where different parameters limit the sensitivity. To compensate these limitations, three

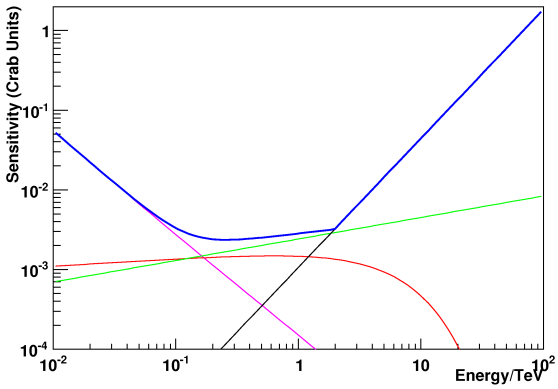

Figure 3.27: Toy model of a telescope array to illustrate the impact of different parameters on the sensitivity. The performance is limited, at high energies by the γ–ray count rate(black), at intermediate energies by electron (red) and CR background (green) and at low energies, in the area of high statistics, by systematic background uncertainties (purple) [11].

designs referred to the *Small Size Telescope* (SST), the *Medium Size Telescope* (MST) and the *Large Size Telescope* (LST) are currently under development. In Table 3.1 the principle design of the individual telescopes types, which balances costs against performance in different bands of the VHE γ–ray spectrum based on intensive MC simulations, is summarized.

Type	Number of telescopes	Dish ø[m]	Dish area[m^2]	f/d [m]	FoV [°]	Energy range	Total area
SST	~ 60	$\sim$6	–	–	9–10	$\geq$10 TeV	1–10 km^2
MST	$\sim$20	12	$\sim$100	1.35	8	100 GeV–10 TeV	1 km^2
LST	$\sim$6	23	$\sim$400	1.2	4-6–4.9	$\leq$100 GeV	10^4 m^2

Table 3.1: Principle design of the CTA telescopes [11, 121, 98, 295].

Given the steeply decreasing γ–ray flux, especially a large overall collection area in combination with a good background rekection on a hardware level is of great importance. Thus, apart from optimizing the telescope design, a careful study of the most efficient layout of the telescope array is essential. As low energy events provide a rather low photon density in the Cherenkov light pool, the CTA design foresees few LSTs with a dish of larger diameter. Instead, the MST design meets the requirement of the mid–energy range. At higher energies, the light yield is large, well beyond the Cherenkov light pool wherefore several SSTs are designed to cover a multi–km^2 areas.

In the case of the LST and MST design, a parabolic and a *Davies–Cotton* (DC) design respectively are foreseen requiring *spherical* mirror facets to tesselate the dish, while both a DC and a *Schwarzschild–Couder* are considered for the SST design, involving *secondary optics* and *aspherical* mirror facets. As part of this work is addressed to the development of mirror facets appropriate for the LST and MST dish design, their requirements will be briefly introduced in the next chapter.

3.4 The MAGIC System

The MAGIC experiment (see Figure 3.28), whose international collaboration consists a group of more than 150 members of different nationalities, among them engineers, physicists and astronomers, is located at the Roque de Los Muchachos on the Canary Islands of La Palma at an altitude of 2235 m a.s.l. (28.8° N, 17.8° W). Beside the MAGIC telescopes, which are spaced by a distance of ∼85 m, the MAGIC site hosts a *counting house*, where the electronics and the remote control are installed. In addition to the MAGIC experiment, the *Observatorio del Roque de los Muchachos* (ORM) hosts different types of telescopes belonging to international collaborations.

Figure 3.28: Image of the MAGIC stereo system. Close to the MAGIC I (left) and the MAGIC II (right) telescope, which are spaced by a distance of ∼85 m, the counting house (center). Credit R. Wagner/MPI Munich.

Before its upgrade to a stereo system by the commissioning of the second MAGIC telescope in fall 2009, the first MAGIC telescope has been successfully operated in mono mode for five years after its inauguration in 2004. Thanks to its advanced technical design featuring a large dish, a light structure and innovative electronics that allow an enhanced duty cycle, MAGIC I achieved several scientific highlighted results such as the discovery of eight AGNs as VHE γ–ray emitters, among them the most distant object detected so far, the FSRQ 3C 279, the discovery of the microquasar LSI +61 303, the giant flare of the RG M87 thanks to a MWL monitoring campaign in 2008 as well as indirect dark matter searches [203].

Since its upgrade to a stereoscopic system of two almost identical IACTs, which have been the world's largest IACTs with a 17 m diameter dish each until the construction of H.E.S.S. II this summer. This upgrade led to a further boost of the scientific outcome in terms of further detections of extragalactic sources in VHE γ–rays, among them the radio galaxies NGC 1275 the FSRQ PKS 1222+21 and several AGNs, the phase–resolved spectra of the Crab pulsar and detailed morphology studies of the SNR W51 [204, 220].

3.4.1 The Performance of the Stereo System

Usually, the sensitivity S of ground–based γ–ray telescopes is computed as the flux of a source yielding a $5\,\sigma$ detection after 50 h of effective observation time T:

$$S(50\text{hr}) = \frac{N_{\text{ex}}}{\sqrt{N_{\text{off}}}} \cdot \sqrt{\frac{50}{T}} \tag{3.30}$$

, where N_{ex} and N_{off} are the number excess and estimated background events in the signal region.

Thanks to the stereo configuration, the MAGIC system gained an important improvement in sensitivity (see Figure 3.29). Compared to expectations from MC simulations, the sensitivity yields actually an even higher sensitivity at lower energies. Above a few hundred GeV the MAGIC stereo is by a factor of 2 more sensitive than MAGIC I standalone reaching an integral sensitivity of $(0.76 \pm 0.03)\%$ of the Crab Nebula flux in 50 h of the effective time in the medium energy range (> 290 GeV). At lower energies the improvement is even higher [35] allowing ac-

cording to Equation 3.30 to reduce the needed observation time. At 100 GeV for example the observation time reduces by a factor of two, whereas at 1 TeV the reduction factor is lower less than two. This makes the MAGIC telescopes an excellent instrument for observations of gamma rays with energies around 100 GeV. In addition, the angular resolution has improved being $\sim 0.07^{\circ}$ at 300 GeV. At medium energies the energy resolution is as good as 16%.

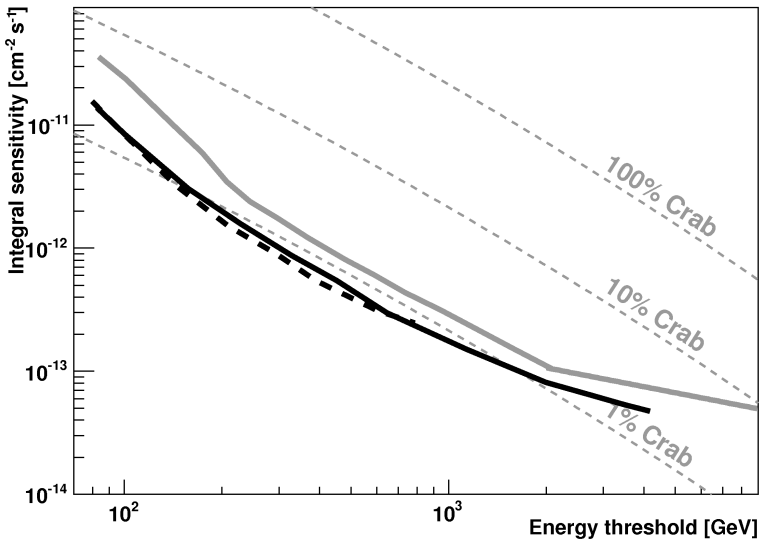

Figure 3.29: Integral sensitivity of the MAGIC stereo system. The solid black lines indicates the sensitivity achieved with MAGIC I stand alone. The black dashed and the gray solid line represent the integral sensitivity of the MAGIC stereo system expected from MC simulations and achieved with real data [35].

The stereo system conserves its capability on a fast repositioning necessary to catch transient VHE γ–ray phenomena such that both telescopes are able to point at any position in the sky within 120 s.

3.4.2 The Subsystems

The MAGIC telescopes design has been aimed at a high performance at low energies, i.e. <100 GeV, as well as at the capability to observe transient events at the γ–ray sky. Therefore, several technical innovations have been adopted for the individual hardware components providing:

- a lightweight frame structure to allow quick repositioning to any point in the sky;
- a large, parabolic mirror dish of high reflectance to provide a low energy threshold and preservation of the time structure of the Cherenkov light front;
- an *active mirror control* (AMC) for the individual mirror alignment in the reflector guaranteeing high focusing of the Cherenkov radiation;
- a fast readout aiming at precise sampling of the Cherenkov signal as well as an accurate determination of the pulse arrival time;
- photo detectors of high *quantum efficiency* (QE) to improve the PDE;

A brief description of the essential hardware components of the MAGIC telescopes is given. Most of the subsystems have been designed identically for both telescopes. However, some of the hardware components in MAGIC II have been modified exploiting improved technical designs compared to MAGIC I [88]. In particular, the mirror facets, the cameras and the readout systems have been designed differently, while the other hardware components of the second telescope have been adopted identically to the first one.

The Telescope Frame

The structure of both telescopes consist of a very lightweight space frame made of carbon fiber epoxy tubes that permits fast movements necessary for follow–up observations of GRBs. The tubes are joined by aluminum knots which results in a strong and light structure of a total weight of ∼5.5 tons for the mirror dish support, (see Figure 3.30) thats showing good resistance against environmental impact and features negligible thermal expansion as well as an excellent oscillation damping. Each camera are kept in the focus of the individual reflector by the support of an tubular arch of aluminum. The arch are stabilized by thin steel cables tied to the main frame keeping the bending of the camera at an acceptable level. In addition, counter weights are attached to the arch at the rear of the reflector frame.

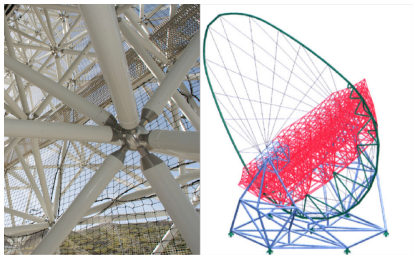

Figure 3.30: Illustration of the MAGIC frame. *Left:* Image of the MAGIC II frame showing the aluminum knot junction. Credit /ETHZ/D-PHYS/H. Hostettler. *Right:* Scheme of the MAGIC frame

The *alt–azimuth* mounting of the telescopes allows both movement in azimuth and in altitude. The reflector frame can be accessed by experts from the side via the tower of the elevation axis, while the camera is accessible through a tower installed in front of the instrument.

The Drive and Starguider System

Beside the necessity of an accurate pointing during normal tracking modeI, the *drive system* has to be powerful enough to guarantee a fast repositioning within a few tens of seconds to any position at the sky in order to allow the telescopes to follow–up the enigmatic and short lived GRBs [73]. In particular the weight of several tens of tons per telescope, 72 in the case of MAGIC I [73], represents a challenging factor regarding pointing accuracy and fast repositioning. The drive system implemented for MAGIC allows a repositioning of maximum 120 seconds in the case of a full rotation in azimuth direction, whereas the average repositioning time is around 40 seconds.

In general, the drive system implemented for the MAGIC telescopes has been kept similar to that of large, alt–azimuth–mounted optical telescopes and is based on standard industrial components to ensure robustness, reliability and proper technical support. The telescope structures are mounted on azimuth drive rings of 20 m diameter made of normal railway trails, whereas sliding bearings have been used for the elevation axis (see Figure 3.31).

Equipped with three 11 kW motors, two are mounted on small lever arms to the azimuth ring, while the third is installed on a 1 m lever arm at the elevation axis, the movements in azimuth an elevation range from $\phi = -90°$ to $\phi = +318°$

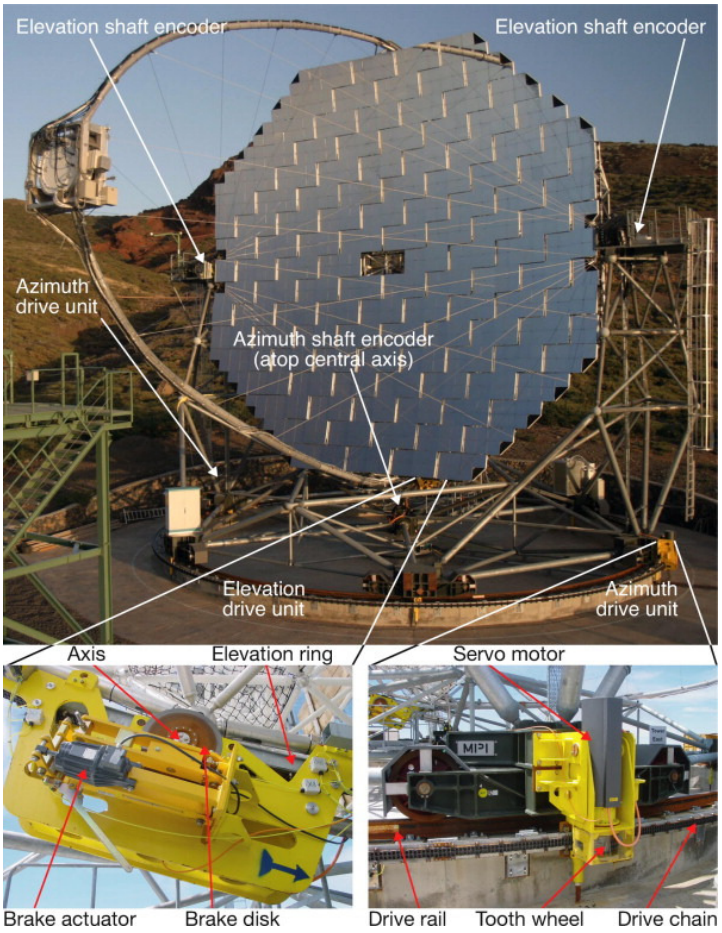

Figure 3.31: Components of the MAGIC drive system. *Top:* The major elements of the drive system installed at the MAGIC I telescope are shown. Bottom: The elevation drive (left) and the azimuth bogeys (right) are shown [73].

and $\theta = +100°$ to $\theta = -70°$ respectively, where the change of the sign implies a movement across the zenith.

The pointing and tracking accuracy of the telescope is provided by the *star-guider* system with high accuracy [72] by monitoring the exact pointing position and correcting eventual mispointings. The starguider measures by means of a sensitive *CCD* camera, which is mounted at the center of the telescope dish facing the mirror dish, the differences between stellar positions by comparing the CCD images with those recorded in standard star catalogues. Typically, in the large FoV of 5° x 3° more than 50 useful for starguiding can be found.

The Reflector

Figure 3.32: Image of the MAGIC II reflector. Credit R. Wagner/MPI Munich

Both telescope reflectors of octagonal geometry feature an overall parabolic shape of 17 m diameter by what the temporal structure the Cherenkov light pulse projected on the camera is preserved. This is of particular importance with respect to the background suppression leading to an important increase of the *signal–to–nois* ratio. In addition the minimum spread of the reflected light pulse allows the re-

duction of integration window of the signal to a very narrow width. To minimize the drawback of aberrations related to a parabolic dish, the focal distance f of the MAGIC telescopes is 17 m which leads to a large *focal–to–diameter* ratio, i.e. f/D [106].

Although the reflector shape is parabolic, the individual mirror facets which tesselate the mirror dish have a *spherical* profile. Therefore, the mirror facets have been produced with different radii of curvature varying from 33.9 to 36.4 m in order to approximate the overall parabolic shape, that is with increasing distance from the reflector center, the mirror facets have a larger radius of curvature.

In order to cover the reflector areas of $\sim$236 m^2 each, different types of mirrors have been produced. In the case of MAGIC I, the reflector is segmented with 964 squared mirrors (49.5 x 49.5 cm) of $\sim$0.25 m^2 attached in groups of 3–4 facets to 247 support *panels* (see Figure 3.33) depending on the position in the reflector frame [52].

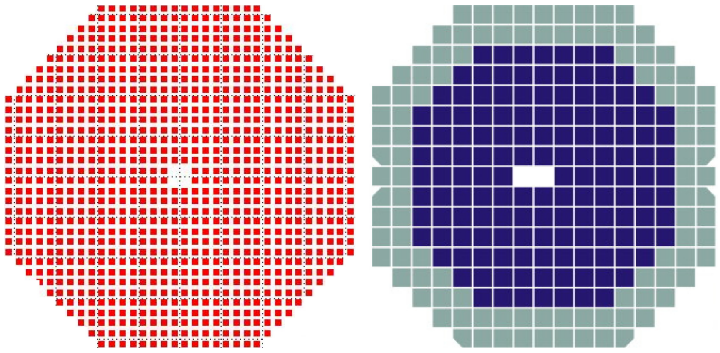

Figure 3.33: Schemes of the MAGIC telescopes reflectors. *Left:* The MAGIC I reflector consist of 964 aluminum mirror segments. Right: The MAGIC II reflector is covered by two different mirrors types. In the inner region (dark blue), 143 aluminum mirrors are installed, whereas the outer region (light blue) is covered with 104 glass mirrors. Adapted from [106].

The facets are *composite* mirrors of several *aluminum* components assembled to a *sandwich* structure. Two slightly different designs have been used for the production of this kind of mirror type [106] following a basic production scheme (see Figure 3.34).

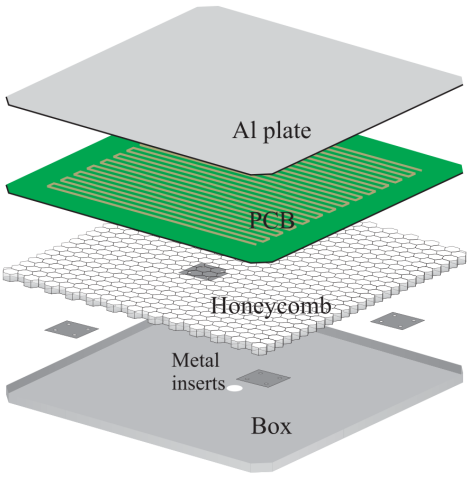

Figure 3.34: The sandwich structure of the aluminum mirrors used for MAGIC I [50].

The aluminum mirror facet is an assembly of a 1 mm Al 3003 box of 2.5 cm

height into which an Al 5052 *honeycomb* spacer of 2.5 mm thickness and a *heating printed circuit* board (PCB) are glued. Four small 5 mm thick plates are embedded into the honeycomb just in contact with the outer box to fix the mirror to a panel by four screws at each plate. On top the box is closed by another Al skin resulting in a rigid and lightweight (∼4 kg) mirror facet . For the assembly a specific adhesive films from the 3M^{TM} company was used. Studies of the mirror aging revealed that the design needed to be modified [106] so that the heating circuit has been removed to increase the compactness of the mirror and the adhesive foils have been replaced by a specific bi–component epoxy–glue from the 3M^{TM} company. To finalize the *raw* mirror, the upper Al sheet is *diamond–milled* to realize a high reflective surface. A special method, the *fly–cutter* technique as sketched in Figure 3.35, is used by the German company LT–Ultra for such polishing during which the spherical shape is introduced to the mirror surface.

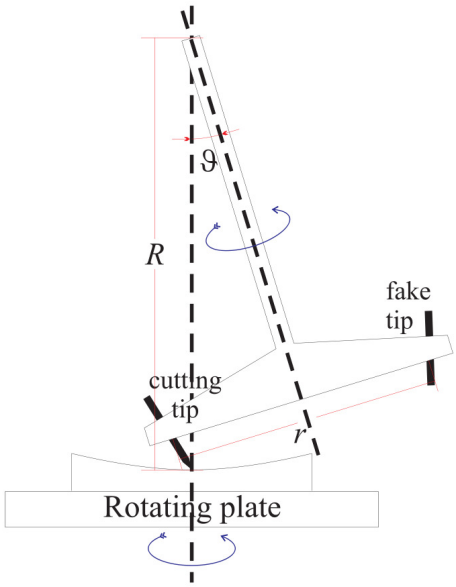

Figure 3.35: Principle of the diamond milling [52].

To protect the reflective surface against mechanical and chemical degradation, a thin quartz layer o the order of ∼100 nm is deposit via *plasma polimerization* on the mirror surface. For this purpose, the mirrors are shipped to the *Fraunhofer Institute* (IFAM) in Germany. *All-aluminum* mirrors represent a remarkable innovation with respect to the conventional *glass* mirrors historically used whose advantage consist in their lightweight but rigid structure, while maintaining a high *surface reflectance* (85 to 90%)and a small surface roughness, well below 10 RMS. Therefore, the PSF expressed as the radius of 90% light containment is less than 1 cm [49].

For the MAGIC II reflector, two different mirror types have been used: the inner part of the dish is covered with 143 1 m^2 all-aluminum mirrors [49] (see Figure 3.36), while the outer region is tessellated with 104 glass mirrors [253]. Different to MAGIC I, the MAGIC II mirrors are directly mounted on the reflector frame. The aluminum mirrors are similar in their design to the mirrors installed in MAGIC an therefore represent a scaled version whose weight is ∼18 kg. During the assembling of the raw mirror, a *mold* of spherical curvature similar is used the *pre–shape* the mirror surface. In such way, time and costs related to the diamond milling process are remarkably reduced. While the surface reflectance is on average around 85%, the major improvement has been reached in the focusing power being around 0.5 mrad for a point like source [106].

The remaining 104 consist of composite glass mirrors produced via the *cold*

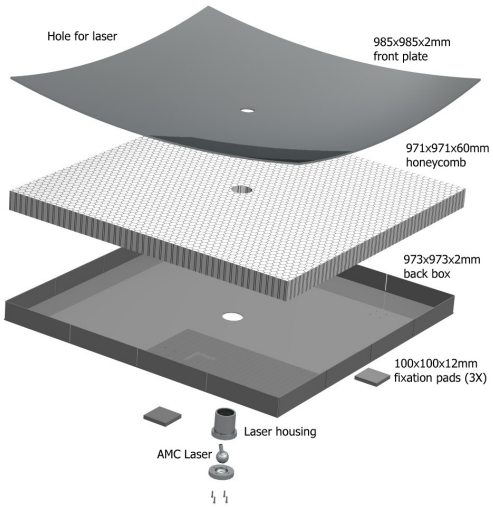

Figure 3.36: Design of the MAGIC II aluminum mirrors. Credit M. Zago.

slumping technique. This process developed by INFN in collaboration with the Media Lario Technologies company is based on the replication of the shape of a high precision mold to a thin glass sheet (1-2 mm). Using a vacuum suction, the glass sheet is elastically deformed to retain the curved shape imparted by a convex mold. A honeycomb structure of 20 mm thickness is glued under vacuum force to the deformed glass sheet providing structural rigidity. A second glass sheet (1-2 mm) is glued on top creating a sandwich structure. After releasing the vacuum, a reflecting layer of aluminum and a thin protective quartz coating are deposit on the concave side of the 14 kg mirror. The surface roughness of these mirrors is around 2 nm and the average surface reflectance is close to 90%. However, the focussing power is less pronounced for this type of mirrors, staying within 2 mrad.

When pointing the telescopes to different zenith angles, the reflectors' surfaces suffer small deformations under varying gravitation load [59]. To correct this effect, the individual mirror facets must be realigned. Such adjustment is performed by the *active mirror control* (AMC). In the case of MAGIC I, the AMC aligns the 1 m^2 panels onto which four mirror facets are mounted each, while each MAGIC II mirror is individually align by an AMC unit. The principle of the AMC is sketched in Figure 3.37.

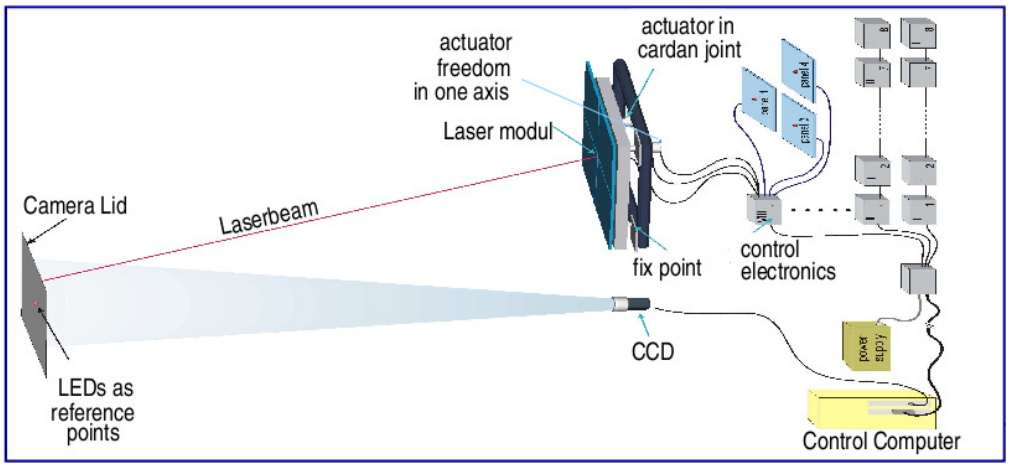

Figure 3.37: Schematic overview of the AMC [59].

The mirror facets and panels respectively are attached on three points to the

reflector frame. On of these points has a fixed distance, while the other two points are equipped with a longitudinally movable unit with a lateral freedom. Each actuator is furnished with a stepping motor and a ball–bearing–spindle allowing to displace the panels with high precision. A guidance laser module, which is pre–adjusted to point to the target of the panels, is used to monitor the orientation of the panel. Further AMC components are a CCD camera mounted on the reflector frame close to its center and four LEDs on the PMT camera frame lid used as reference points. During standard operations, the AMC is based on the laser adjustment mode, i.e. the CCD camera is used to search for the LEDs which are installed around the camera to define the camera center. Sequentially, for each mirror panel the laser is activated and the actuator moves until the laser position agrees with the previously defined individual reference point.

After eight years of operation, some of the mirror facets installed in MAGIC I show a significant degradation due to the continuous exposure to the sometimes harsh environment present on La Palma. Especially between October and March, it can rain quite frequently and often the temperature drops during night below the dew point. Although tested for water tightness, humidity may have entered the composite mirror facets. This is a crucial issue since, once permeated the cavities of the honeycomb the humidity may condensate and is trapped inside the mirror facet. In case of a temperature drops below the dew point, the water ices and may deform the mirror surface creating *bubbles* or even destroy the mirror due to its expansion. Fortunately,due to the rigidity of the mirror facets such deformations remain localized normally affecting less than 30% of the surface [106]. Another environmental condition having an impact on the mirror are the presence of aerosols leading to the coverage of the mirror surface with dust.

Both aspects lead to a decrease in the collection are of the reflector and therefore cause a correspondent loss in reflectivity. Therefore, the negative impact of the environmental conditions on the optical performance of the mirrors lead to a significant loss of Cherenkov light, which has an particular consequences at lower energies and thus leads to an increase of the energy threshold.

In order to maintain the excellent performance of the MAGIC system, a refurbishment of the MAGIC I reflector is foreseen. With the perspective of CTA and the ongoing development of a new composite mirror type, first prototypes with MAGIC I and MAGIC II dimensions are planned to be installed in the MAGIC telescopes replacing mirrors with too high degree of degradation (see Chapter 4).

The Camera

Beside the reflector, *camera* represents one of the key elements regarding the γ sensitivity of an IACT. In particular the efficiency of the γ/hadron separation strongly depends on the quality of the shower images detected by the camera. The most important parameters that define the quality of and Cherenkov camera are a high QE of the photodetectors, a fine pixelization of the camera as well as fast response. In the case of MAGIC, the light sensitive pixels consists of PMTs which convert the Cherenkov light pulses into electrical signals with a typical QE of 20 to 30% depending on the wavelength.

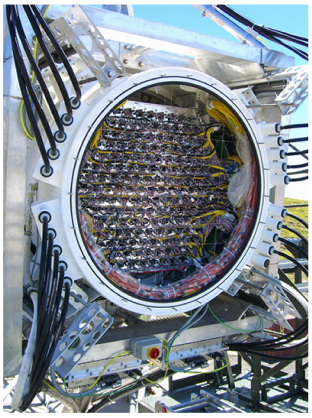

Figure 3.38: Image of the rear of the MAGIC II camera [67].

Both cameras are furnished with two *lids* with the purpose to protect the PMTs from damage due to day-

light and other strong light sources. Moreover, a water cooling system keeps the temperature in the camera stable in order to prevent an overheating are a drastic cooling down to the dew point. The whole camera structure can be moved back and forth with respect to the mirror dish so that the camera can be focused at different distances ranging from infinity to few meters. Usually, the camera is focused on a distance of 10 km where the maximum shower development takes place.

The MAGIC I camera of a hexagonal shape (114 x 104 cm) (see Figure 3.39) covering a FoV of 3.5° (4° ø) is composed of 577 pixels of different size [245].

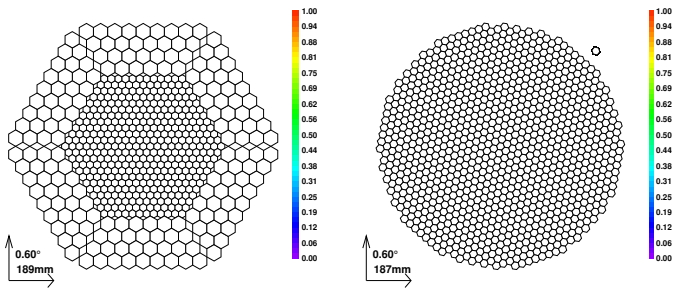

Figure 3.39: Pixel layout of the MAGIC cameras. *Left:* The pixelization of the MAGIC I camera. *Right:* The pixel layout of the MAGIC II camera.

While the central region comprises 397 1" diameter pixels of 0.1° FoV the outer camera is composed of 180 0.2° FoV pixels of 1.5" diamete. The photocathode of the PMTs is of spherical shape, wherefore hexagonal light concentrators similar to *Winston cones* have been placed in front of the photodetector matrix in order to achieve a maximum active camera area and to reject large angle background light. Due to the application of a *lacquer* to the PMTs types 9116A and 9117A from Electron Tubes used in the MAGIC I camera, an enhancement of the sensitivity by an increase from ∼20 to ∼30% at shorter wavelengths has been achieved [250].

Like MAGIC I, the MAGIC II camera exhibits a 3.5° FoV with the difference that the pixel layout features a circular shape entirely equipped with 0.1° FoV photosensors of 1" diameter [67]. Therefore, the pixelization of the MAGIC II camera is uniformer and finer. Almost twice the number of pixels with respect to the MAGIC I camera (1039) has been used which have been grouped into *clusters* of hexagonal shape consisting of seven pixels each. This modular camera design allows an easy exchange of broken clusters and, more important, eases potential upgrades. Alternatively, such modular design enables field tests of innovative photodetectors without major interference of the rest of the camera. In such way, a cluster as been installed in the outer region of the MAGIC II camera in order to test high QE *hybrid photo detectors* (HPDs).

Currently, the pixels installed in the MAGIC II camera are PMTs of the type Hamamatsu R10408 with hemispherical photocathode furnished with appropriate Winstone cones used for the *light guidance*. These PMTs typically reach a peak

QE of 34% in the UV band (see Figure 3.40 and provide a fast response of the order of ∼1 ns FWHM.

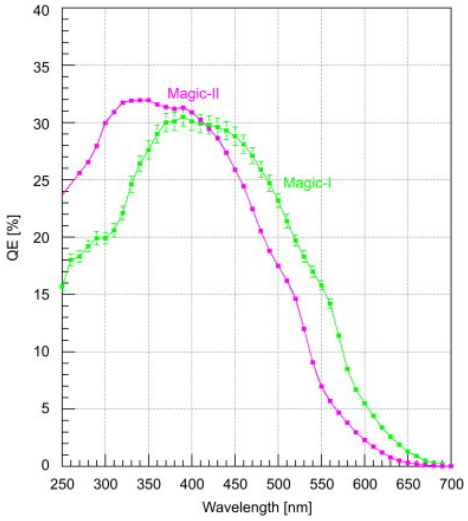

Figure 3.40: Comparison of the QE between the PMTs used for MAGIC I (green), enhance by a special lacquer, and MAGIC II (pink) [129].

The Readout Chain

The Cherenkov light signal is of very short duration which demands a vera fast *readout* system. Therefore, a fast processing of the pulses is necessary before generating a trigger signal and finally digitizing them at ultra–fast speed.

In a first step the analog signal of each PMT, whose amplitude is related to the intensity of the Cherenkov light, is amplified by an ultrafast and low–noise *pre–amplifier* located right after the cathode resulting in 2 ns pulses [207]. Subsequently, the amplified analog signal passes the *transmitter board* where it is transformed into a light pulse using *Verticle Cavity Surface Emitting Lasers* (VCSELs). Afterwards, the converted signal is coupled into optical fibers in order to transmit the signal from the camera to the counting house (see Figure 3.41).

The usage of optical fibers provides several benefits such as a low pulse dispersion and attenuation protecting the Cherenkov signal in from ambient electromagnetic noise. In the electronic room of the counting house the signal is converted are electrically multiplexed and finally sent to the *digitization* system which is also referred to as the *Flash Analog to Digital Converters* (FADCs) In virtue of its high speed. A trigger signal is generated using a fraction of the light, which is branched off by fiber optic light splitters before the delay fibers, using a 50/50 splitting ratio. On the *receiver board* the signals are converted back from optical to electrical using PIN diodes. If passing the trigger, the signals are digitized on the *receiver board* by the FADC at the speed of 2GSamples/s.

The readout systems of both MAGIC telescopes digitize at the sample sampling speed using however different electronics. In the case of MAGIC I, the digitization is based on a custom made *multiplexed* (MUX) system [207] using a commercial FADC (see Figure 3.41) that digitizes 16 read–out channels consecutively.

For the readout system of MAGIC II another digitization technique has been implemented, using the *Domino Ring Sampler* (DRS). DRS represents a low–power analog sampler. It uses a *multi–capacitor* bank, consisting of 1024 cells in DRS version 2, which is organized as *ring buffer* for the storage of the signal [254]. In this way, each single capacitor is sequentially enabled by a *shift register* driven by an internally generated 2 GHz clock. The clock is locked by a PLL to a common synchronization signal. In case of an external trigger, the signals sampled in the

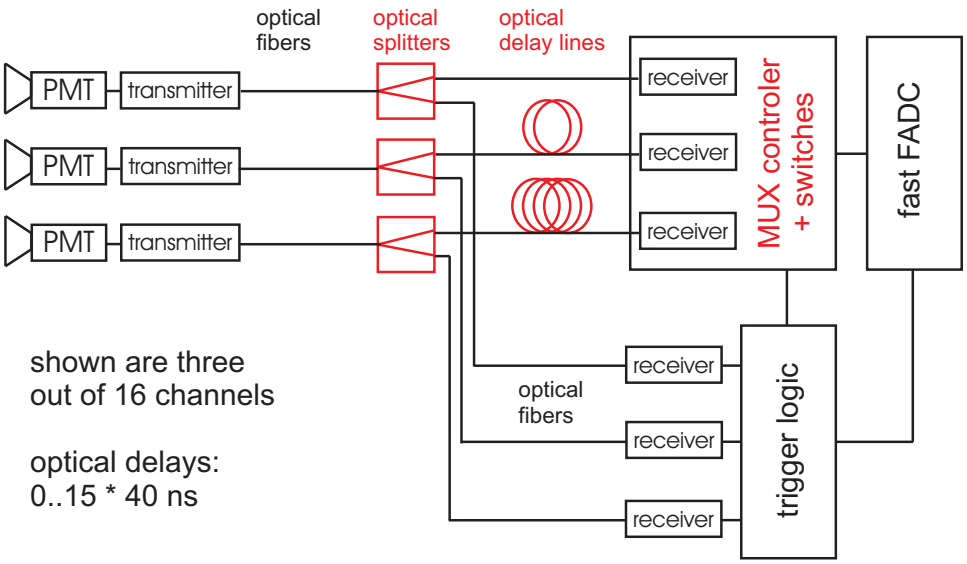

Figure 3.41: Scheme of the readout system used for MAGIC I [207].

ring buffer are read out at a rate of 40 MHz and digitized with a 12–bit resolution ADC [312].

The Trigger System

Each of the MAGIC telescope features a *trigger* system, i.e. a multiple level decisional system, which determines the rejection of the storage of background events. Typically, the PMTS are constantly hit by photons of the NSB, whereas rare events are related to the Cherenkov radiation by atmospheric showers. Compared to accidental fluctuations of the NSB, the Cherenkov light pulses are much more intense creating a compact shower image in the camera of particularly short duration.

Thus, the topological and temporal structure of the shower image enable a simple trigger programing based on the recognition of adjacent triggered pixels to can discriminate the signal originating from Cherenkov light flashes and determine its acquisition. In the case of MAGIC I, the *trigger region* has been restricted to the inner camera region covering a FoV of 2.0° [129], while for MAGIC II the trigger has bee enlarged to a FoV covering a 2.5° diameter. This enlargement provides a higher potential for the study of extended sources as well as the performance of sky scans.

Level zero (L0) trigger: The first decision level is based on a *discriminator threshold* (DT) automatically adjusted for each pixel within the *trigger region* by the *Individual Pixel Rate Control* (IPRC). Provided the signal of the pixels exceeds this threshold, the receiver board generates a digital trigger of the duration of ∼4 ns effective width for each channel that is sent to the next trigger level.

Level one (L1) trigger: Based on an n–fold ($n = 2 - 5$) *next neighbor* (NN) logic, the temporal and spatial coincidence of the signal from the individual pixels that passed the L0 trigger is determined within a tight time window generated by the L0 trigger [251]. The L1 trigger is applied to 19 overlapping trigger cells, each collecting 36 pixels (see Figure 3.42). Different topologies varying from a N *compact* next neighbors logic can be

used (typically N= 3 or N= 4). Given such cluster of pixels is determined, a *global* event trigger signal is released.

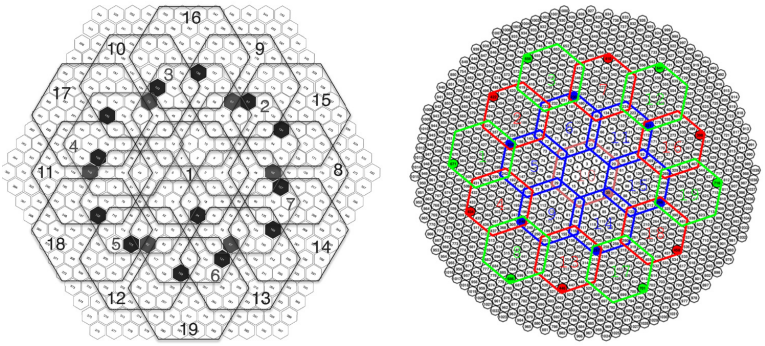

Figure 3.42: The trigger areas of the MAGIC cameras. The 19 macrocells of the L1 trigger comprising 36 pixels each are indicated.

Level one (L2) trigger: With the global trigger, the L2 trigger is accessed whose task at the moment is to measure the trigger rate and eventually to set factor,known in MAGIC as *prescaler*, that scales the rate of events which finally triggers the readout system.

Level three (L3) trigger: In case of stereoscopic observations, this coincidence trigger rejects events which have been triggered by only one of the telescopes. Depending on the pointing position, the the triggers produced by the individual telescopes are delayed so that the coincident gate in the L3 trigger is minimum, typically a narrow time window of ∼100 ns [252].

From 2007 to 2009, an additional trigger, referred to as *Sum–Trigger*, has been implemented in the MAGIC I telescope. Different to the standard trigger, this trigger is based on the analog sum of 24 *macrocells* of 18 pixels each (see Figure 3.43) which lowers the trigger threshold by a factor of two to 25 GeV [274] with relevant consequences for the scientific program of MAGIC.

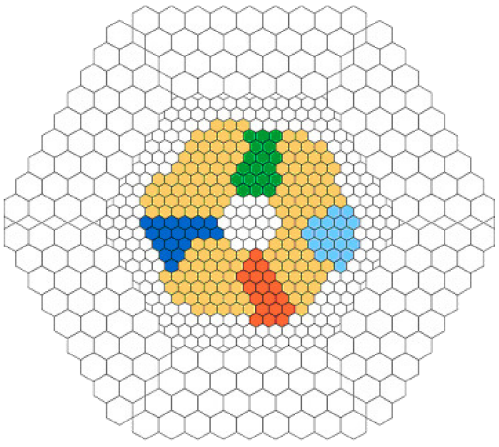

Figure 3.43: Pixel mapping of the first MAGIC Sum–Trigger . The colored regions corresponds to the 24 different patches of 18 pixels each (four different shapes repeat six times rotated in 60° angle steps) of [274].

Up to now, the Sum–Trigger has been only installed in the MAGIC I telescope. However, such trigger is currently under development whose key elements are a fully automatic calibration as well as a revised configuration of the overlapping summing patches (see Figure 3.44).

A small prototype has been installed temporarily in the MAGIC I telescope to test the functionality of the new Sum–Trigger design that will be installed in both telescopes [151]. The installation is foreseen for summer 2013.

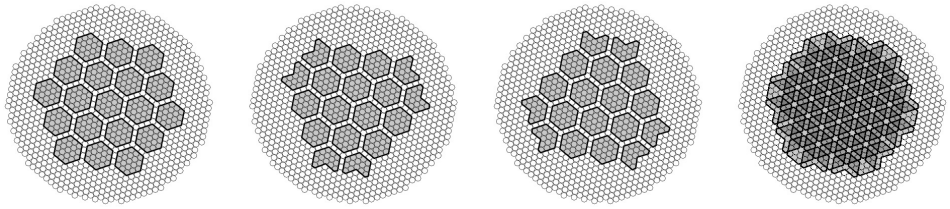

Figure 3.44: Pixel mapping of the new Sum–Trigger system. The gray shaded polygons depict the macrocells. The first three figures correspond to the first, second and third macrocell layer which are shown superimposed in the fourth figure [151].

The Calibration System

In order to translate the information recorded in FADCs from each camera channel into an incident Cherenkov light flux an *optical calibration* consisting of a number of ultrafast and powerful LED pulsers is used [132, 131]. Each camera pixel, i.e. PMT, is calibrated in three different wavelengths determining the conversion factor between the number of recorded FADC counts and the number of photoelectrons (phe) in the PMT. In addition, the QE of the individual PMTs has to be taken into account for the calibration in order to connect the conversion factor to the number of incident photons.

The system, installed in a *calibration box* that is mounted at the center of the reflector, provides fast light pulses of varying wavelengths and intensity such that the entire *dynamical range* of the PMTs is calibrated and the linearity of the entire readout chain is verified. The calibration box houses 64 LEDs comprising UV, blu and green LEDs that emit light pulses of 3–4 ns FWHM duration at 370, 460 and 520 nm respectively. The shortness of the light pulses is of high importance in order to simulate correctly Cherenkov light pulses from an atmospheric shower.

The calibration is performed in two steps, where the FADC signal is first calibrated relatively by equalizing the response of individual channels to the same light signal. In a successive step, an absolute calibration is achieved by using the *F–Factor Method* to correlate the FADCs counts recorded by each PMT to the light flux incident to the camera [131].

For MAGIC II, the calibration system has been slightly modified replacing the LEDs by an frequency tripled, passively Q-switched Nd–YAG laser that operates at its third harmonic oscillation at 355 nm providing light pulses of 700 ps. In order to provide a large dynamic range, two filter wheels are installed in from of the laser such that the camera is illuminated with intensities that vary from 1 to 10000 phes within 100 steps.

3.4.3 The Camera and Readout Upgrade

From summer 2011 to summer 2012, a further upgrade on the MAGIC hardware has been commissioned dismissing the old MAGIC I camera and MUX readout electronics aiming at a further improvement of the performance of the MAGIC stereo system that has been limited by the smaller trigger region and the somewhat lower light conversion efficiency of the MAGIC I camera. Besides the expected increase in sensitivity due to the enlarged trigger area, the main purpose of this upgrade is to assure a stable performance and operation of the telescopes for the next years as well as to ease the maintenance of the system.

In a first phase in late 2011, the readout system of the MAGIC I telescope has been upgraded to a digitizing system based on the DRS–4 instead of the DRS–2

chip previously used in MAGIC II whose dead–time has significantly been reduced to less than 1%. The MAGIC I camera has been replaced in a second step during summer 2012 by a clone of the MAGIC II camera and is now equipped with 1039 channels of 0.1° pixels and an enlarged trigger region [220].

3.4.4 The Systematic Uncertainties

Being a system of complexity, there are many factors which are only known with some uncertainties to contribute to the systematic errors of an IACT. Most important is their contribution on the systematic errors of the gamma-ray collection efficiency, i.e. on the absolute flux level, on the absolute light scale and on the reconstructed spectral slope [35]. The most crucial components contributing to the systematic errors concern the various subsystems of an IACT, as well as imperfections of MC simulations concerning the atmospheric conditions. In addition small discrepancies between real data and simulated γ–ray events may affect the precision of the energy reconstruction. An estimation is made on the main sources of uncertainties affecting the energy scale, the flux normalization and the spectral slope. The systematic uncertainties related to the individual subsystems of the MAGIC telescopes are combined to a global systematic error following the general approach of summing them up in quadrature.

Following [30] MAGIC determines the energy scale with a precision of 17% to 15% at low and medium energies respectively, while the systematic error on the spectral slope determination is $\pm$ 0.15. At medium energies the flux normalization is affected by a systematic error of 11%, whereas at lower energies the precision is 19% [35].

3.4.5 The Data–Taking Mode

As the sun represents a very strong background to the faint signal of the Cherenkov light flashes, the data taken is performed at night, and even then several dominating backgrounds, e.e. by the moon, exists. Therefore, the data ideal taking is performed during *dark night* although, in the case of MAGIC, the electronics have been conceived such that data taking under moderate light conditions, that is during twilight and at the presence of moon light, is feasible.

Beside the presence of dominating backgrounds, the data quality is considerably affected by the weather conditions under which data have been taken. In the case of the MAGIC site, especially the presence of clouds as well as high humidity, wind or *calima*, which is a a dust wind originating from the Sahara, cause a decreased data quality.

After the upgrade of MAGIC to a system of two Cherenkov telescopes, the standard data taking is performed in *stereo mode* where simultaneous observations are performed with both telescopes and the L3 trigger system is selecting events based on their coincidence. Beside stereoscopic observations, both telescopes can also be operated in *standalone* mode in order to perform *mono* observations.

Due to the small FoV of MAGIC, a typical characteristic of IACTs, observations are carried out in the *source–tracking* mode in which the telescope tracks pre–defined sky coordinates while taking data.

Basically, data can be taken in two different modes, that is the *On/Off* mode or the *wobble* mode as proposed by [122].

On/Off mode: In case of this observation mode, the On and Off data are taken separately. During the On data taking, the telescope tracks the source in the camera center, whereas Off data are taken pointing to another sky region without any known VHE γ–ray source in the FoV and with similar characteristics

with respect to NSB, zenith distance, weather conditions etc. To obtain the γ–ray signal, the normalized Off data are subtracted from the On data during the analysis.

Beside the risk, that the conditions of the Off data do not match those present during On data taking, such observation mode implies an important drawback since it requires twice observation time.

Wobble mode: In order to reduce the time of observations, the On and Off data are taken simultaneously. Therefore, both MAGIC telescopes are alternated every 20 minutes between two sky positions at a typical offset of 0.4∘ from the source [74]. The Off data are taken from the so-called *anti–source* position located opposite to the source position. Beside the benefit of the reduction in observation time, such data taking mode guarantees similar conditions for the On and Off data. Therefore, MAGIC standard observation are usually carried out in wobble mode.

When commissioning the stereo system, MAGIC data have been typically taken with two wobble positions, with an rotation angle of 180°. In practice, two more background regions are often defined at the same distance from the camera distance but ±90° displaced from the source position in order to provide a better Off computation. Since 2012 the standard data taking is carried out with four wobble position where the position of the source in camera is rotated by 90∘ around the camera center every 20 minutes in order to provide a more reliable calculation of the OFF at lower energies by further reducing eventual camera homogeneities (see Figure 3.45).

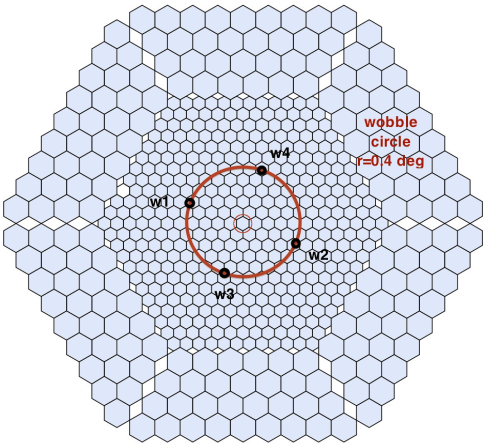

Figure 3.45: Geometry of the wobble mode. During On/Off observations, the source is centered on the camera (small red circle), while during wobble observations the source is displaced by an offset of 0.4° of the camera center rotating the source position in the camera about 90° every 20 minutes such that the source is located at W1, W2, W3, and W4 respectively. For each sour position, the remaining three positions are used for the estimation of the Off events in the signal region.

Beside advantage with respect the drastic reduction in observation time, the wobble mode has a drawback regarding the γ–ray detection efficiency, which is estimated to be reduced by 20% [74], due to the slightly smaller trigger area around the source position (see Figure 3.46).

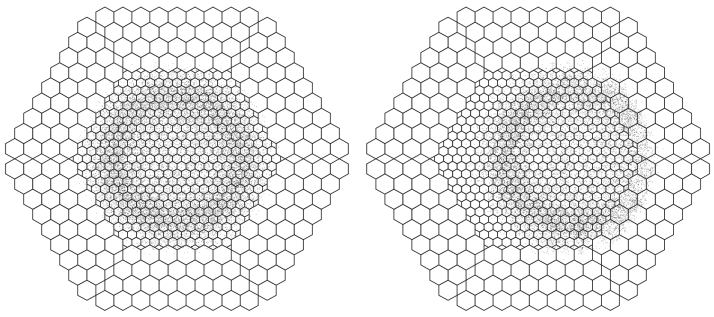

Figure 3.46: Center of gravity plots of the intensity distribution of MC simulated γ–ray events. *Left:* The source centered on the camera. *Right:* The source off–centered by 0.4° in wobble mode causing a loss in efficiency due to the limited trigger area [74].

4

Development of New Composite Mirrors for the Cherenkov Telescope Array

The Cherenkov Telescope Array marks the next generation of Imaging Atmospheric Cherenkov Telescopes for VHE γ–ray astronomy whose proposed total mirror area is approximately $10000\,\mathrm{m}^2$. The challenge is to develop light weight and cost efficient mirrors with high production rates that provide a high optical performance and good long–term durability.
The mechanical and optical properties of the all-aluminum mirrors installed in the MAGIC telescopes provide promising prospects with respect to the coverage of the CTA mirror area. However, some drawbacks are related to the cost and time efficiency of the production technique. Another crucial issue of the MAGIC mirrors regards the reflectance. Although providing a high surface reflectance, the reflectance into the focal spot is significantly lower since the diamond milling introduces a certain micro roughness to the reflective surface leading to an enhanced light scattering.
Therefore, a new mirror production technique based on the knowledges acquired during the mirror production for the MAGIC telescopes is currently under development.
This chapter addresses to the ongoing development of such mirror production technique. First, the technical specifications of the CTA project for the mirrors and the reflective surface are outlined. The second part of he chapter contains a description of the new production technique. Moreover, a report on the prototyping status will be given. To study the optical performance of the mirrors currently under development, a measurement setup has been constructed. The basic measurement principle and first results on the optical performance of the mirror prototypes will be presented in the third part. The chapter concludes with an outline of the development status and an outlook.

4.1 The Mirror Specifications for the CTA project

For the CTA project, in particular concerning the LST and MST (see Section 3.3.2), the design goal is the development of low cost, light weight, robust and reliable mirror elements of 1 to $2\,\mathrm{m}^2$ surface.

Recalling the dependence of the energy threshold of an IACT on the light detection efficiency (see Chapter 3), the optical performance of mirror facets in terms of focusing power and spectral reflectance is of great relevance. Moreover, although the requirements for the PSF are more relaxed with respect to optical

telescopes the focusing power of IACT mirror facets represents a key parameter regarding the recording of good quality shower images by an IACT. Typically, a PSF of few arcmin for a segmented reflector consisting of small mirror facets is acceptable [121]. Beside the optical performance, a high resistance against environmental impacts is another important issue associated with such mirrors since IACTs are usually not protected by domes wherefore the mirrors are permanently exposed to the environment. To summarize, considering the Cherenkov light spectrum and a PSF acceptable for an IACT, the mirror facets should provide highest reflectance possible in the spectral range of the Cherenkov light (see Figur 3.12) and focusing qualities but demanding very little maintenance.

The current generation of operating IACTs uses mostly polished glass or *diamond–milled* aluminum mirrors, which entail high costs and considerable time and labour intensive machining. In the following, the specifications are discussed in terms of geometry, mechanical properties, optical performance and durability.

As the *mechanical* specifications favor an hexagonal geometry, the principle design of LST and MST mirror facets is a hexagonal shape with a size between 1 to 2 m^2 and spherical curvature of 56 and 32 m radius respectively. Considering the handling and mounting of such large sized facets as well as the alignment during normal observation mode, a minimum *weight* of the mirror facet is an important goal. However, a reduced mirror weight should not be achieved at the expense of optical quality, stability or a significant cost increase. As a compromise, a total weight of less than 20 kg/m^2 has been considered desirable.

Another fundamental requirement of CTA specifications regards a high *rigidity* of the mirror panels. This is an important property in order to maintain the specifications for the PSF and the alignment which may be affected due to deformations of the mirror panels under gravity during movements of the telescope. Furthermore, the mirrors should neither deform during the estimated ten years of operation nor should the facets vibrate when exposed to moderate winds.

Normally, IACTs are placed at altitudes between 1000 to 3000 m a.s.l. where significant temperature changes, including dramatic temperature changes, between summer and winter. Therefore, all optical properties should met the CTA specifications between a temperature range from -10°C to +30°C. Additionally, the mirror facets should resist to temperature changes from -35°C to +60°C with all possible changes to their properties being reversible.

As mentioned before, the optical specifications are addressed to the PSF and the reflectance of the mirror facets. The final specifications on the resolution of the future CTA reflectors, i.e. the spot size of the reflected light in the focal plane, depends mainly on the pixel size of the Cherenkov camera.In general, there is no real need to produce mirrors with a PSF well below half the size of a Cherenkov camera pixel. Currently, the specifications define a PSF that corresponds to one third of the size of such Cherenkov camera pixel. In the case of the LST design, the pixel diameter is 50 mm corresponding to 0.1°. With a diameter of 90 mm corresponding to 0.18°, the pixel size of the Cherenkov camera of the MST is slightly larger. Therefore, the mirror PSF should not exceed 2 arcmin and 0.36 arcmin respectively corresponding to 0.5 mrad and 1 mrad. Usually, the exact shape of the PSF is not of critical importance as long as it is small enough. Therefore, it is typically sufficient to characterize the PSF by a diameter of a circle that contains a certain fraction of the reflected light, e.g. D_{80} for an 80% containment diameter. In the current CTA specifications the fraction of light containment is normalized on the amount of light that is reflected into 2/3 of the pixel diameter of the Cherenkov camera. In the case of the LST and MST this corresponds to a diameter of 33 mm and 60 mm respectively.

Considering the Cherenkov spectrum, the reflectance of the mirrors should exceed 80% in the focal spot for wavelengths from 300 to 600 nm[121]. Usually, the mirror facets are furnished with a protective coating of tens of nanometer thickness to assure a resistance against environmental impacts. Such coating should be optimized to achieve a maximum reflectance in the wavelength range of 300 to 450 nm where the Cherenkov light intensity peaks.

As CTA will be operated for at least ten years, the mirror facets should maintain their performance for this duration showing only few percent of degradation. Most critical is the long–term durability of the reflectance under the prevailing environmental conditions. As an example, in the case of aluminized and overcoated glass mirrors a loss in surface reflectance of up to 5% per year was found requiring a re–coating after ∼5 years. By contrast, the diamond milled aluminum mirrors mounted in the MAGIC telescope have shown a less rapid degradation of 1% of surface reflectance per year [105].

Despite their excellent durability, the diamond milled aluminum mirrors exhibit an important drawback with respect to the the total reflectance into the focal spot. As the diamond milling introduces a surface roughness of a certain periodicity, the high reflectance measured locally on the mirror surface is significantly reduced in the focal spot due to diverse scattering processes (for details see [229, 228]). Therefore, the design of the mirrors used to cover the MAGIC reflectors is not within in the CTA specifications. In addition, the production rate and the costs which depend mostly on the diamond milling are difficult to arrange with the CTA needs. Therefore, a new technique based on the existing technologies used for the mirror production for the MAGIC telescopes is currently developed aiming in particular at an increase of the production rate and a total reflectance enhancement while reducing the production costs.

4.2 Composite Mirror Replication from a Rigid Mold of High Precision

The new production technique currently under development is based on the replication of composite aluminum mirror facets from a high precision mold of convex shape. The procedure is designed as a two-step process (see Figure 4.1). First, the mirror substrate similar to the MAGIC mirror substrate is assembled using the mold to reproduce a spherical shape. The glued sandwich structure is composed of a mirror box, a honeycomb spacer providing rigidity and a thin front layer. In a second step, the reflective layer is shaped on the mold while the mirror substrate is glued on the back side. Concerning the reflective layer, several solutions are currently tested among them aluminized and quartz coated thin glass sheets. Beside this conventional approach, innovative solutions considered as discussed in the next section.

The shaping of the mirror substrate and the reflective layer is performed under low–pressure created by the attachment of a vacuum pump underneath the mold by a central hole. A good contact between the surfaces of the mold and the layer to be shaped is guaranteed by air evacuation via small channels incised on the mold surface (see Figure 4.2). The development of the production technique outlined above is carried out in close cooperation with the Compositex Srl[16], company located at Vicenza, Italy due to its successful collaboration on the production of MAGIC mirrors.

[16] http://www.compositex.com

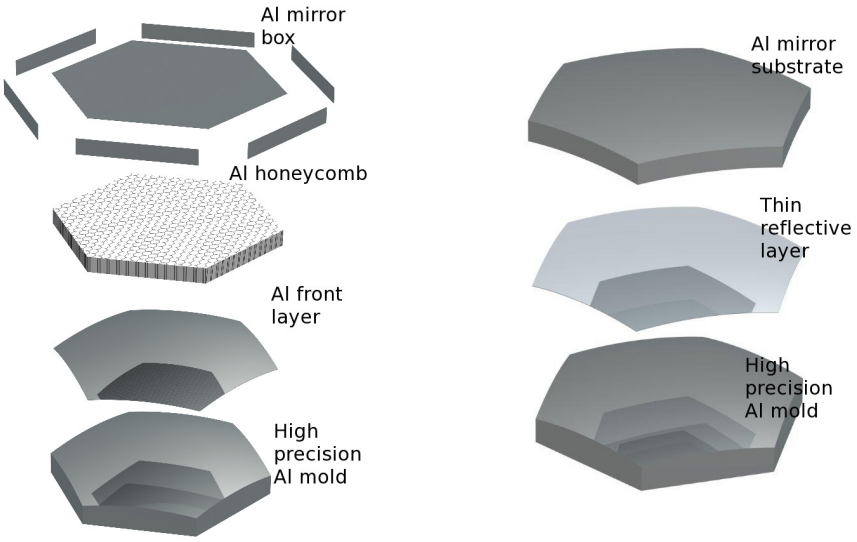

Figure 4.1: Illustration of the replication technique of an aluminum composite mirror from a high precision mold. *Left:* Sketch of the mirror substrate assembling spherically shaped by mold replication. *Right:* While the reflective layer is shaped on a mold, the raw mirror blank of spherical shape is glued to its rear.

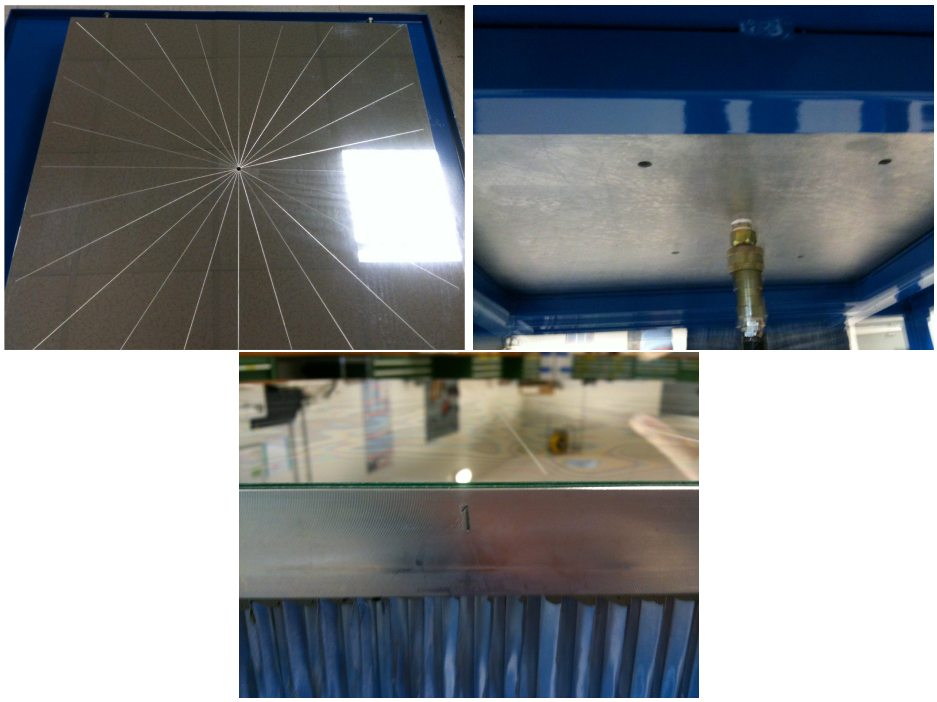

Figure 4.2: Close-up of the mold surface. *Left:* Small air channels have been incised to assure a good surface contact during the shaping. *Right:* A vacuum pump is attached underneath the mold by a central hole. *Bottom:* The reflective layer, here a thin glass sheet, is deformed on the mold.

4.2.1 Innovative Reflective Surface Solutions

Regarding the realization of the reflective layer, new solutions based on adequate industrial high reflective layers suiting the CTA specifications are currently tested in parallel. Such innovative products provide the potential to substitute the conventional design of a thin *floating* glass sheet of few millimeters thickness that is

subsequently furnished with both a reflective and a protective coating. Nevertheless, the traditional variant is also considered as potential implementation in the mirror design under development.

One alternative design involves the use of a robust dielectric multilayer reflective foil. Recent developments of reflective films used in renewable energy applications offer a suitable and cheap solution to expensive multilayer coatings usually necessary to design a conventional high reflective surface. At the moment, such product has been acquired from the 3M^{TM}[17], namely the *Solar Mirror Film 1100*[18] which is a silver metallized *weatherable* acrylic film passivated by a protective coating. Its advantages over traditional aluminized glass mirrors are mainly associated to a higher reflectance that exceeds 90% over a larger wavelength range (see Figure 4.3), less weight and improved mechanical properties. In particular, the product has been tested according to *IEC* and *ISO* standards indicating a durability of about twenty years. Unfortunately, being a silver metallized foil

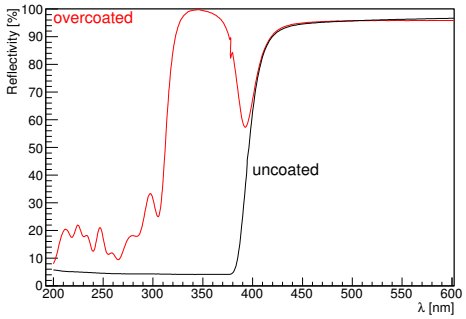

Figure 4.3: Spectral reflectance of the 3M^{TM} reflective foil. The passivated silver foil features a cutoff at ∼400 nm (black). The spectral reflectance of the foil can be extended towards shorter wavelengths by the deposition of an adequate overcoating (red).

the spectral reflectance exhibits a cutoff at wavelengths shorter than 400 nm. To overcome this drawback, in cooperation with the Italian ODL company[19] the feasibility of extending the spectral reflectance towards shorter wavelengths down to 300 nm has been tested on a small sample (see Figure 4.4). For this purpose, a dielectric coating of 1220 nm thickness formed of 23 layers has been deposited on the foil. This first attempt yielded a positive result apart from the reflectance drop located at the cutoff wavelength of the film requiring an optimization of the layer number in order to compensate this dip. Moreover, due to the interest in a large applications of their industrial product, the 3M^{TM} is currently investigating in an increase of the spectral reflectance in the wavelength range of interest for IACTs.

A second low cost solution for the implementation of a reflective layer is given by the use of industrial *front surface mirrors* deposited on thin glass substrates. As an example, the *Front surface Mirror SP94*[20] produced by the Italian EOT company[21] is certified according to *MIL* standards and provides a reflectance as high 90% at 400 nm and longer wavelengths (see Figure 4.4). Nevertheless, the reflectance of this product does not met the CTA specifications at shorter wave-

[17] http://www.3m.com
[18] http://solutions.3m.com/wps/portal/3M/e_nUS/Renewable/Energy/Product/Films/Solar_Mirror/
[19] http://www.odlcoating.com
[20] www.eot.it/pdf/fsm.pdf
[21] http://www.eotech.com

lengths. Therefore, in interaction with the EOT company it is foreseen to modify the protection layer to achieve an reflectance increase below 400 nm. Beside these

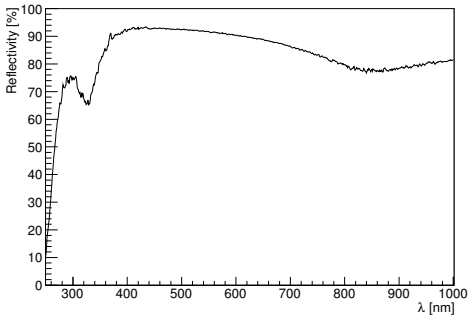

Figure 4.4: Spectral reflectance of the EOT surface front mirror SP94. The front mirror is aluminized and coated with a protective layer.

solutions, the traditional glass mirror design is investigated. In particular, the reflective coating and the surface protection are a crucial issue in terms of costs, reflectance and durability. Currently, the favored industrial partner for a eventual collaboration on the reflective surface production is the German BTE company[22] due to their experience obtained from previous collaborations with IACT experiments. At the moment, different reflective and protective coatings are under investigation among them dielectric versions and 3–layer designs of alternating layers of materials with low and high refractive index providing a reflectance greater than 95% in the wavelength regime from 300 to 600 nm (see Figure 4.5). Beside

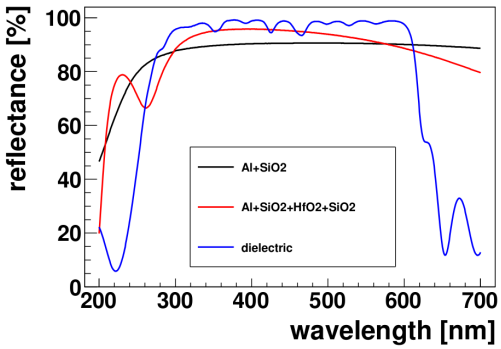

Figure 4.5: Comparison of the spectral reflectance among different coatings. The newly investigated 3–layer coating (red line) and the pure dielectric coating (blue line) show an enhanced reflectance with respect to the conventional aluminum quartz coating (black line) [120].

the BTE company, another collaboration has been recently established with the Brazilian Opto Science in Sight company[23] as industrial partner to collaborate with to realize the reflective layer.

4.2.2 The Optical Test Bench

As outlined above, the most important characteristics of IACT mirror facets concern the optical performance due to their impact on the overall performance of an IACT. In particular, the verification of the PSF and the radius of curvature for

[22] www.bte-born.dem
[23] http://www.opto.com.br

each mirror installed in an IACT reflector is of great importance. For this reason, a $2f$-setup has been installed in the Legnaro National Laboratories (LNL) of INFN being the standard procedure to determine these parameters (see fig. 4.6). The main idea of the $2f$–setup is based on the *Thin Lens Equation*:

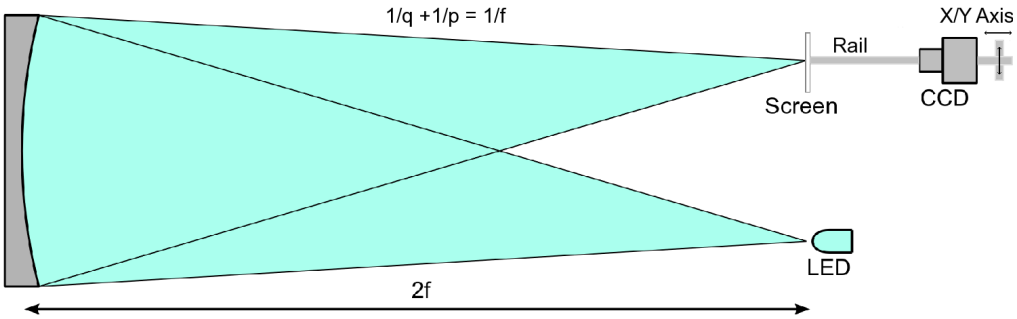

Figure 4.6: Measurement principle of an $2f$–setup for the optical characterization of IACT mirror facets.

$$\frac{1}{p} + \frac{1}{q} = \frac{1}{f} \tag{4.1}$$

where the focal length f is related to the radius of curvature R of a concave mirror of spherical shape:

$$R = 2f \tag{4.2}$$

The mirror is placed at twice its focal length f from a point like light source in order to record the return image of the mirror at twice the focal length from the mirror. In the ideal case, the light source is aligned such that the light is falling onto the mirror at an incident angle close to 0° with respect to its optical axis. Commonly, either a system composed of a CCD camera and a screen or a photodiode is used for the light detection in order to determine the PSF. To provide a reliable analysis of the PSF, the detector area should be sufficiently large, i.e. at least 2/3 of the pixel size of the Cherenkov camera since this area is used to normalize the D_{80} calculation (see Section 4.1). Considering the Cherenkov camera pixel size of the LST and MST, that the detector area should cover at least a diameter of 60 and 33 mm respectively. Typically, CCD cameras provide a very small detection area of the order of of 1 cm^2. Therefore, the FoV of such camera is usually increased to some tens of centimeters by means of an objective. In order to record the return image of the mirror at the distance where the focal spot is minimum, an imaging screen is used. The CCD is placed behind the screen on which the lens focuses.

In principle, such $2f$–setup is also suited to perform measurements of the *absolute reflectance* into the focal spot requiring an absolute determination of the light incident to the mirror. However, provided a CCD is used for the light detection, the objective and the imaging screen represent two additional optical instruments placed between the light detector and the mirror. Therefore, the measured absolute reflectance represents a convolution of these three optical instruments difficult to disentangle. For this reason, a pin diode or a is usually more adequate for this measurement. Alternatively, a CCD camera with a larger and thus much more expensive pixel matrix can be used. In such way, an adaption of the camera FoV by an objective is avoided and the imaging screen necessary for the focusing can be removed.

For the $2f$–setup used for the characterization of the prototypes the close

to point like light source is provided by a LED of ∼3 mm diameter emitting at 430 nm (see Figure 4.7). The detector system consists of an imaging screen of

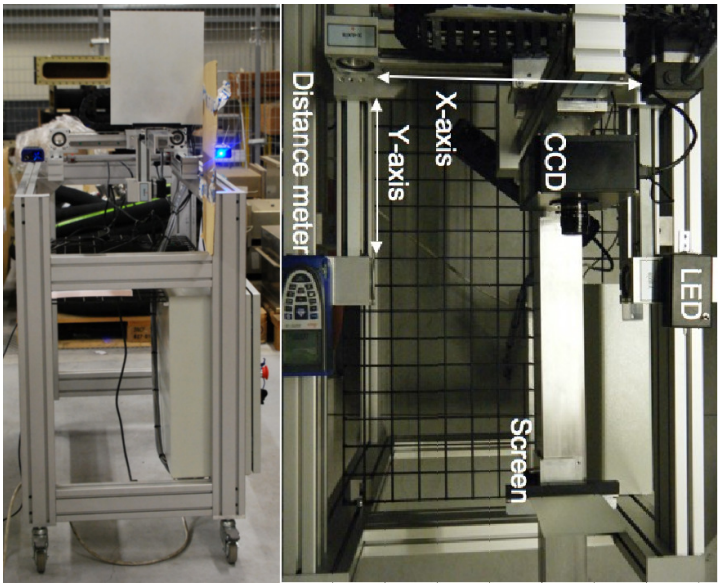

Figure 4.7: Images of the $2f$–setup installed at the LNL of INFN. *Left:* Optical test bench. *Right:* Close–up of the optical bench and the individual measurement equipment.

opaque glass and a SBIG ST–1603ME CCD camera[24] with a 1530×1020 matrix of 9×9 μm pixels and a high *dynamic range* of 10 bit. The CCD is equipped with a Tamron CCTV lens[25] of short focal length (f 25 cm) increasing the FoV of the CCD to 10×15 cm and providing a resolution of 0.15 mm. In addition, the CCD is adapted by a SBIG optical colored band pass filter to the LED emission. Thus the measurement can be performed during day time since there is generally no need for a low level of ambient light during this measurement wherefore the measurement can be performed during day time.

The detector system is mounted on the axis of an AEB RBT5 3D stepping motor that is housed on an optical bench (see Figure 4.8). This positioning unit

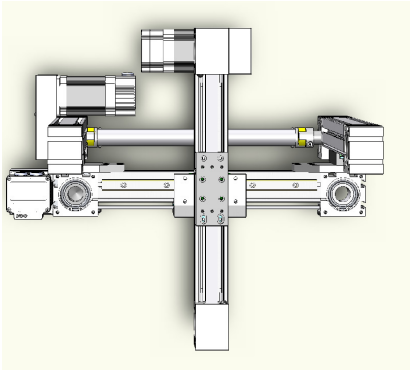

Figure 4.8: Drawing of the AEB RBT 3D stepping motor unit.

covers a range of 20 cm each axis allowing for focal distance scans. Moreover, with a minimum step size of 1 mm the detection system is aligned with high precision. Beside the detector system, the light source and a Leica DISTO^{TM} A6 distance meter are installed on the optical bench in order measure the distance determined as optimal focal length. The distance meter provides a measurement range from

[24] http://www.sbig.com/images/documents/products/42
[25] http://tamron.com

5 cm up to 200 m with an accuracy of ± 1.5 mm. Currently, the determination of the total reflectance is not feasible due to the properties of the CCD camera.

The mirror is installed on a movable unit adjustable in height (see Figure 4.9). Depending on the mirror type, different solutions are used to fix the mirror on

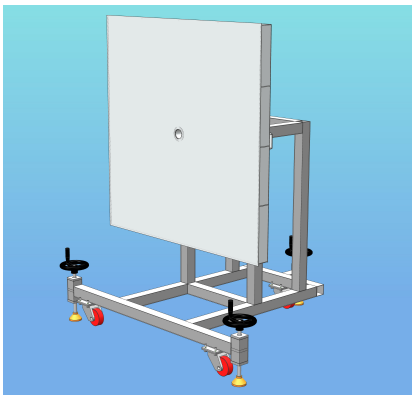

Figure 4.9: Illustration of the mirror support structure.

this support unit (see Figure 4.10). In the case of prototypes with MAGIC I dimensions, the mirror is leaned on a rigid structure. Two tips on this support panel are used to hole the lower mirror edge, while the upper edge is kept fixed by a blocker. Regarding prototypes with MST and LST dimensions, the flanges on the mirror back foreseen for the AMC (see Section 3.4.2) are used for the fixation in three points. The triangular support panel, which is attached to these flanges, can be easily adopted to the remaining support unit. For the optical qualification,

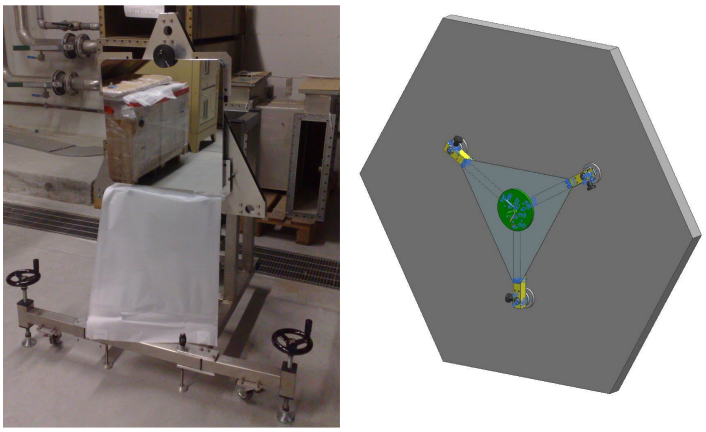

Figure 4.10: Illustration of the different mirror fixation solutions. *Left:* At the lower edge, the MAGIC I mirrors are positioned on two tips, while the upper edge is blocked. *Right:* The MST mirror fixation by means of a support structure that is attached to the flanges at the mirror back foreseen for the AMC.

the distance from the light source to the mirror is adjusted until the optimal focus is found. Generally, this is done by searching the position of the minimum focal spot size. As this adjustment is usually done "by eye", an uncertainty of the order of ± 5 cm on the determination of the focus is assumed. However, the precision of this method is sufficient considering the *focal depth* which in the case of mirror facets of small dimensions is in the range of 10 to 15 cm. Therefore, the optical depth represents a dominant limitation on the precision of the focal length determination.

Once the focal optimum is found, two images, *signal* and a *dark frame*, are acquired with the CCD. For the dark frame the light source is switched off to

measure the background illumination. During the image acquisition, an intrinsic flat fielding is performed to reduce the noise. The PSF determination is based on the analysis of the images recorded with the CCD camera. For this purpose, an executable written in C++ programming language has been developed by the author of this thesis to perform the PSF computation.

This tool relies on the AstroROOT[26] software, an extension of ROOT for astronomical data analysis whose first task is the subtraction of the dark frame from the signal frame, pixel by pixel. In a second step the center of gravity of the light spot is determined. Thereafter, the total light containment, i.e. the sum of the individual pixel counts, is calculated in a circle of pre–defined diameter centered on the focal spot. Finally, the light fraction containment is calculated by integrating over enlarging circles centered on the light spot by incrementing the radius in one pixel steps. In such way, the profile of the integrated light as well as the 80% diameter and radius, i.e. D_{80} and R_{80}, are computed.

The integrated light profile of the focal spot can be used to verify the correctness of the background subtraction. Supposing the background is correctly subtracted, the profile trends asymptotically towards the total light containment. Instead, supposed the background is underestimated, the integral will continuously increase, while in the opposite case, i.e. a background overestimation, the integral will decrease with increasing distance from center of gravity of the focal spot (see Figure 4.11).

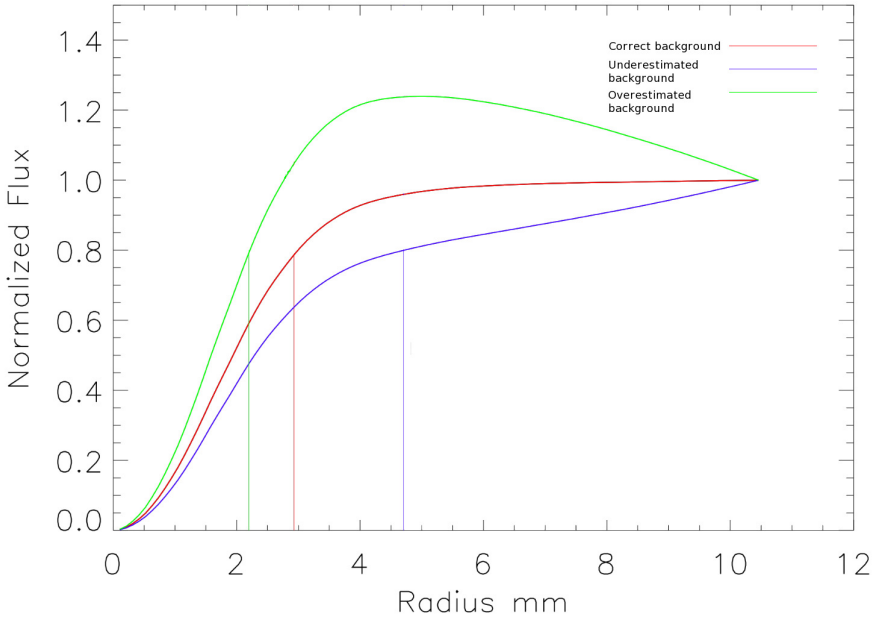

Figure 4.11: Impact of the background estimation on the PSF computation. The R_{80} strongly varies with the background estimation. In the case of a correct background subtraction (red curve), the profile of the integrated light trends asymptotically towards the total light containment. When underestimating the background (blue curve) the integral increases continuously leading to a larger R_{80} (blue vertical line). Supposed the background is overestimated (green curve), the light integral decreases shifting the R_{80} to smaller values.

[26] http://isdc.unige.ch/astroroot/index

4.2.3 First Prototyping

As the MAGIC I reflector requires a refurbishment, the first prototypes have been produced with MAGIC I dimensions to test the feasibility of the new production technique. Initial tests have been performed on discarded MAGIC I mirrors. For these tests both thin glass sheets and the reflective foil provided by the 3M^{TM} company have been used for the realization of the reflective layer. The glass sheets have been aluminized in a successive step at the facility of the Department of Physics and Astronomy of Padova in Asiago, Italy. Note that, for the time being, no protective quartz coating has been deposited on the aluminized glass sheets. As the small sized mold arrived at a later moment, the first reflective layer deposition attempts were performed without any master shape (see Figure 4.12). As the substrates of these first prototypes are actually two diamond–milled all-

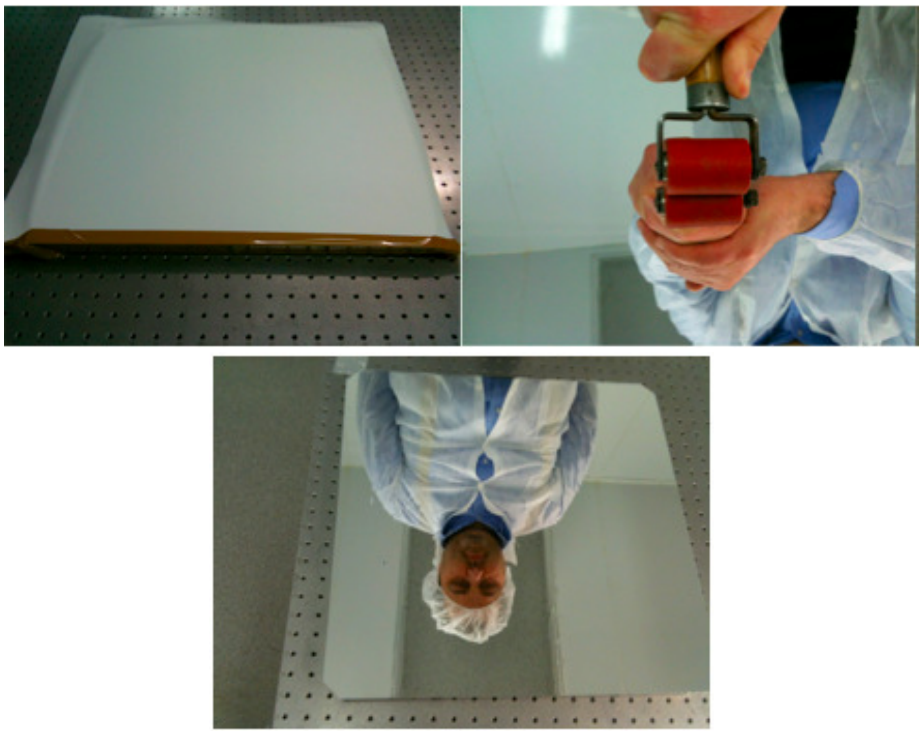

Figure 4.12: Deposition of the reflective foil on the mirror substrate. The foil is placed on the surface moistened with water and soap. Although removing trapped air while depositing, the reflective surface shows some surface irregularities.

aluminum mirrors that have been discarded from a recent production of MAGIC I mirror facets due to defects concerning the PSF and the radius of curvature, measurements of the PSF have been performed with the $2f$–setup before the reflective layer deposition (see Figure 4.13). Both substrates provide an excellent PSF, i.e. D_{80} is 0.2 and 0.4 mrad respectively, at twice their focal lengths taking into account the extension of the light source. The reliability of the measurement is confirmed by the individual integrated light profiles indicating a correct background subtraction. As reflective layer, both an aluminized but not quartz coated thin glass sheet and the 3M^{TM} foil were deposit on these first two prototypes. After the deposition, the focusing has been reanalysed (see Figure 4.14 and 4.15) indicating a clear worsening of the PSF in terms of an increased the D_{80}. In the case of the prototype on which the glass sheet has been deposited, the PSF has increased from 0.2 to 1.0 mrad while the PSF of the prototype furnished

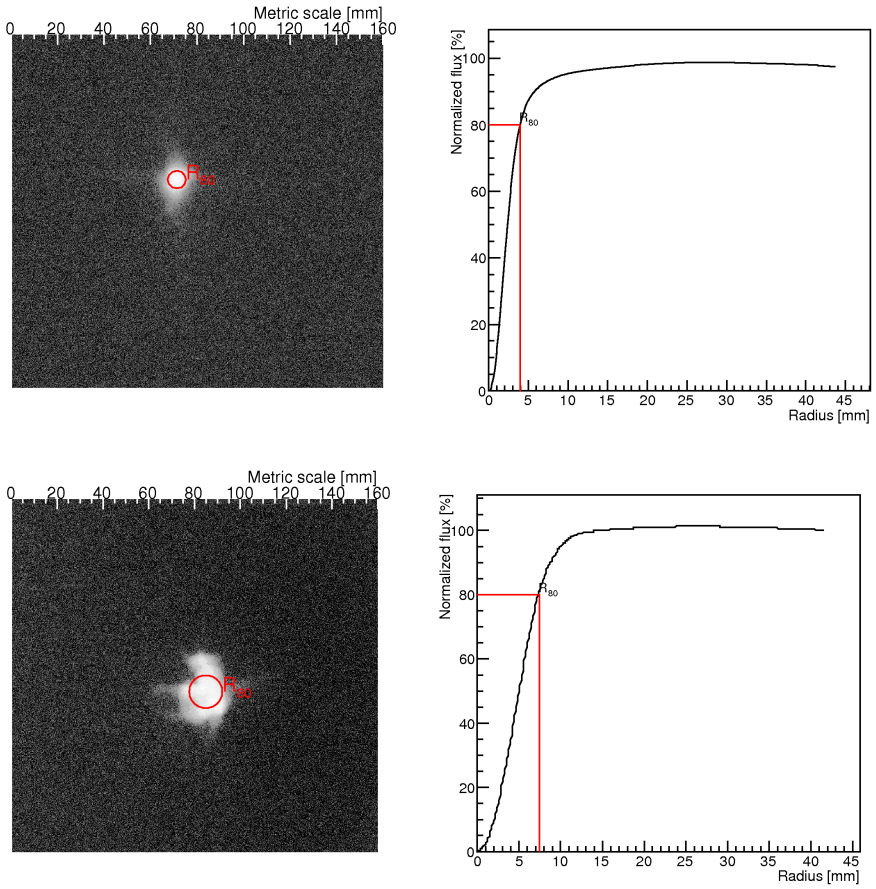

Figure 4.13: Focal spot image of the mirror substrates used for the prototyping before reflective layer deposition. *Top:* Focal spot image (left) of the mirror substrate used for the deposition of the glass sheet as reflective layer shown in logarithmic scale. A metric scale (on top) and the R_{80} (red circle) are shown. The integrated light profile of the spot (right) confirms the correctness of the background estimation. The *Bottom:* Focal spot image of the mirror substrate used for the deposition of the 3M$^{\text{TM}}$ foil reflective layer (left) and the integrated spot profile (right).

with the 3M$^{\text{TM}}$ foil provides a PSF of 1.5 mrad which is almost four times larger than before the deposition. In case of the former prototype, the PSF increase is most probably related to fact that the reproduction of the spherical shape was performed without the mold. In addition, the glue was not adequate to guarantee a smooth contact between both surfaces. Regarding the prototype on which the reflective foil was deposited, it is clearly visible how the Gaussian-like PSF of the reflective foil superimposed to the initial PSF ($D_{80} = 0.4$ mrad) of the diamond milled mirror substrate is dominating the overall PSF. In addition, the technique used for the foil production somewhat introduces a predominant direction to the foil surface causing an elliptic PSF shape.

The D_{80} for both prototypes before and after reflective layer deposition are summarized in Table 4.1. Considering the MST and LST Cherenkov cameras consisting of pixels of 90 and 50 mm diameter and the maximum PSF specified for CTA (1/3 of the pixel size), it is evident, that the focusing power provided by these first small sized prototypes is not sufficient to meet the CTA specifications. In fact, an improvement of the focusing power by a factor of almost three is

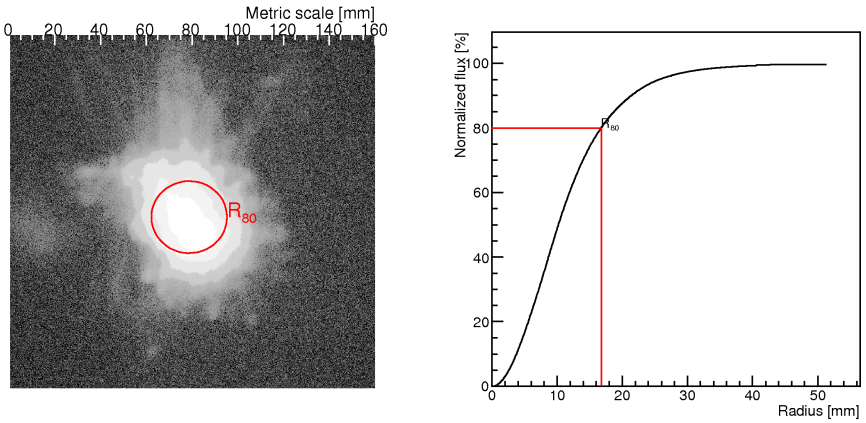

Figure 4.14: Focal spot image of one first small sized prototype. An aluminized thin glass sheet has been deposit as reflective layer. *Left:* The Focal spot image of the prototype in logarithmic scale; the red circle indicates the R_{80} determined. *Right:* The integrated light profile for the focal spot is presented and the R_{80} is marked by the vertical red line.

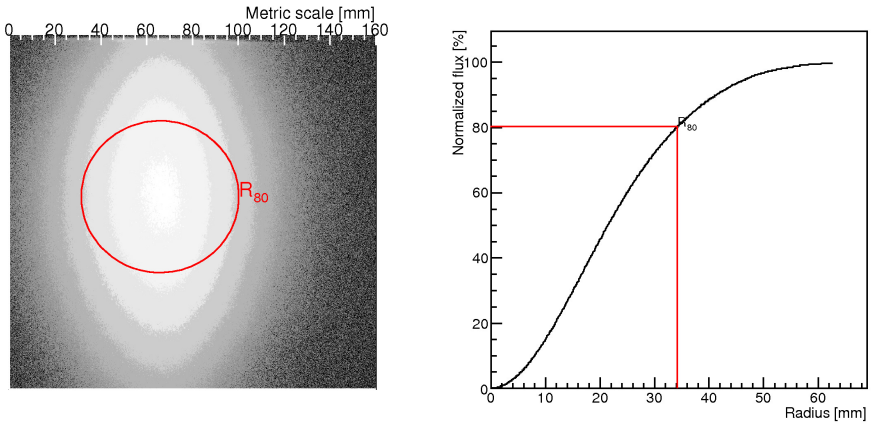

Figure 4.15: Focal spot image of the prototype for which the reflective foil provided by 3M$^{\text{TM}}$ was used. *Left:* The Focal spot image of the prototype in logarithmic scale; the red circle indicates the R_{80} determined. *Right:* The integrated light profile for the focal spot is presented and the R_{80} is marked by the vertical red line.

required.

Prototype	PSF I [mrad]	PSF II [mrad]
I	0.2[a]	1.0[b]
II	0.4[a]	1.5[c]

Table 4.1: List of the D_{80} measured for the two first small sized prototypes with different reflective layers. The PSF measured before ([a]: diamond milled surface) and after the reflective layer deposition ([b]: aluminized glass sheet; [c]: 3M$^{\text{TM}}$ foil) are reported (PSF I and PSF II) in terms of D_{80}.

4.3 The Current Status

To achieve such optical improvement, the new production technique is continuously tuned in order to optimize the deposition of the respective reflective layer in consideration of a precise surface replication. In this context, especially the absence of *stress* should be guaranteed during the curing of the mirror assembly in order to avoid posterior irregularities of the reflective layer surface. Closely related to this issue is the choice of the glue that guarantees air to evacuate as well as a good surface contact. Several glues, i.e. resin based, silicone like and bicomponent as well as epoxy films, have been tested to find an optimum in terms of curing velocity, working temperature, viscosity and elasticity. The most crucial parameter with respect to the adhesive regards probably the shrinkage behavior representing the main cause of stress. Currently, the so–called *tiler technique* is used to dispose the glue on the reflective layer, that is channels are applied to the glue to allow the air to evacuate from the contact area between the reflective layer and the mirror substrate (see Figure 4.16). The curing conditions represent

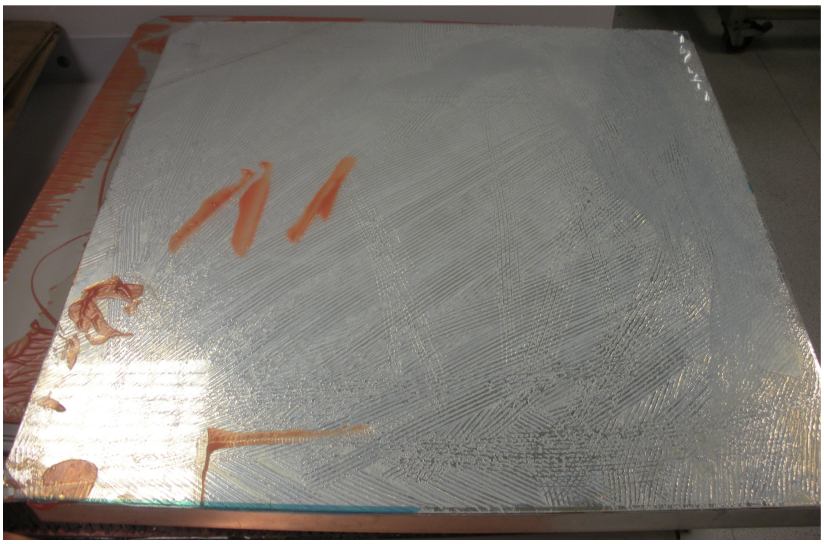

Figure 4.16: Image of a prototype for which the tiler technique was used. The channels applied to the glue are visible through the glass sheet deposit.

an important parameter on the replication quality. A crucial issue is related to the question whether the mirror assembly should be cured in an autoclave under low–pressure or not. Alternatively, is has been considered whether a force is to be applied on the backside of the mirror substrate while curing to guarantee a good surface contact between the reflectivity layer and the mirror substrate. Both curing conditions have been tested and lead to the result that the best options for an appropriate shape copying is to cure the substrate without applying any external forces since these might cause a *spring back* effect or introduce stress to the deformed surface. Clearly, the introduction of such effects affects the focusing power of the mirror due to significant local deviations from the ideal curvature.

In particular, the texture of the mirror substrate surface to which the reflective layer is glued holds a key role in guaranteeing a uniform contact between the both surfaces in terms of the absence of large *air pockets*. An alternative option to the tiler technique might be to perforate the front sheet of the mirror substrate in oder to allow air to evacuate from the contact area. Currently, tests are ongoing on small samples to investigate this modified design solution, where a thin perforated sheet is glued on top of the substrate surface before depositing the reflective layer

(see Figure 4.17). From these first tests, it seems that this interspacing layer is a possible solution to trap air enclosures and excess glue. As for the use of the 3M^{TM}

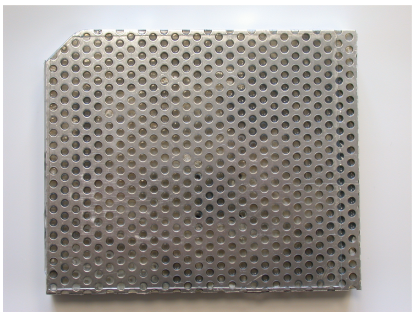

Figure 4.17: Image of a perforated substrate sample. The top layer of the substrate is perforated trapping air enclosures and excess glue. This guarantees a good surface contact between the mirror substrate

Solar Mirror Foil as reflective layer, an optimization of the foil deposition is crucial in order to improve the focusing power significantly. Regarding this solution, two parameters impede a smooth surface replication. First, the natural waviness and the predominant direction of the foil are two factors that limit the minimum achievable PSF significantly. A potential solution could be to span the foil into a frame during deposition. However, such approach will most likely only overcome the foil waviness but not the problem related to the predominant direction. To solve this second issue, most probably a modification of the production technique of the foil by the 3M^{TM} company is necessary. In addition, since this product features a low rigidity a clean environment is of high importance to avoid dust particles to form irregularities below the reflective layer.

Reflective Layers

Recently, four thin *borofloat* glass sheets coated by the Opto Science in Sight company with Cr+Al+SiO_2 of MAGIC I dimension have been produced so that further small sized prototypes will be prepared, once the deposition technique will be more advanced. In addition, thin float glass sheets of the individual dimensions have been purchased as well as EOT surface front mirrors in order to extend the technique to larger dimensions (see Figure 4.18).

Figure 4.18: Image of the glass for the production of mirror prototypes of different dimensions.

Molds & Substrates

Several molds of different dimensions have been produced to proceed with the prototyping: two squared molds of MAGIC I and MAGIC II dimension respectively,

two hexagonal MST molds and one hexagonal mold for LST mirror substrates of high precision (see Figure 4.19). The molds feature maximum roughness of 40 to

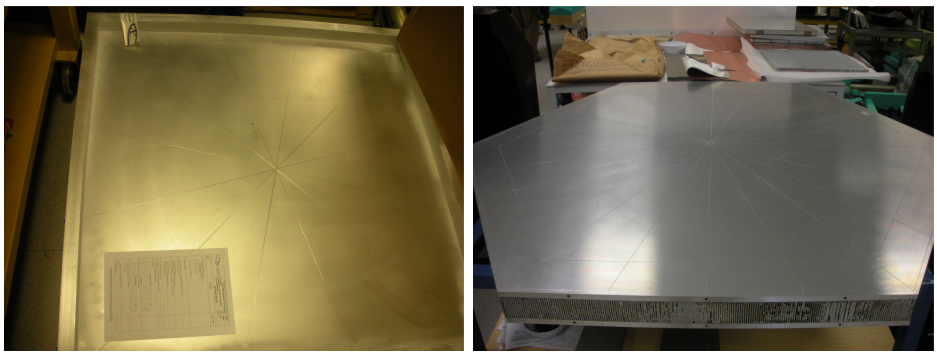

Figure 4.19: Images of two prototyping molds. *Left:* Mold with MAGIC II dimensions. *Right:* LST Mold.

80 μm RMS (see Figure 4.20). In the case that the first LST and MST prototypes

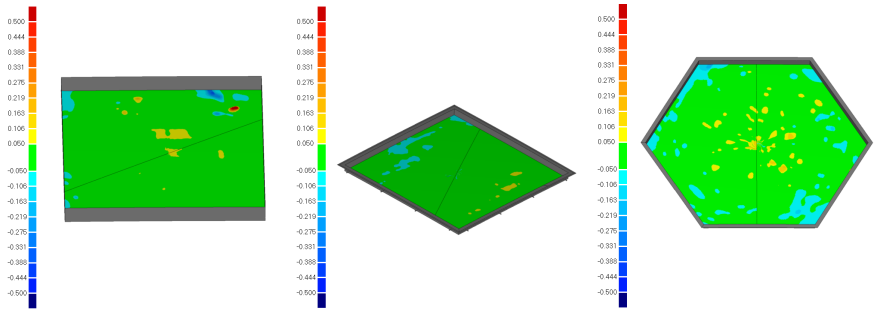

(a) 50×50 cm **(b)** 1×1 m **(c)** MST

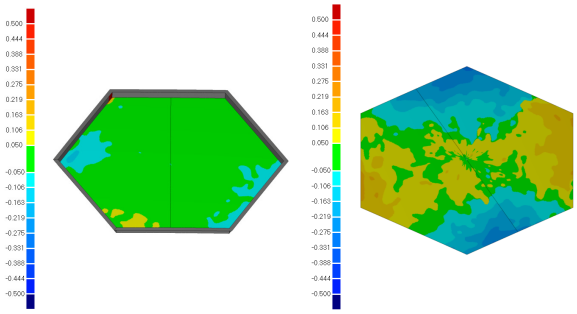

(d) MST **(e)** LST

Figure 4.20: Surface shape measurement of the individual molds. With increasing dimensions, there are slightly more deviations from the ideal surface shape which are largest for the LST sized mold. The deviation scales ranges from -0.5 to +0.5 mm.

do not provide sufficient focusing power, a repolishing of the molds is foreseen to render the mold surface preciser.

Beside several tens of small sized mirror substrates, and some substrates of MAGIC II dimensions, five substrates with hexagonal shape with a dimension of 1.2 m ftf (flat–to–flat) and three LST sized substrates of 1.5 m ftf have been produced pre–shaping them on the individual spherical molds (see Figure 4.21). The main characteristics of the MST and LST mirror substrates are summarized

Figure 4.21: Images of mirror substrates of different dimensions. *Top:* Several small substrates with MAGIC I dimensions. *Bottom:* Substrate with LST dimension.

below[27]:

MST

- panel dimension: 1.2 m ftf
- radius of curvature: spherical, 32 m
- Dimension of the single components of the all-aluminum sandwich structure:
  - rear skin: 1.2 m ftf, 2.5 mm thick
  - honeycomb spacer: 1.2 m ftf, 40 mm high
  - front skin: 1.2 m ftf, 2.5 mm thick
- panel weight: ∼20 kg
- panel height: 45 mm
- Three mounting supports installed on the back of the mirror panel: ø120 mm

LST

- panel dimension: 1.5 m ftf
- radius of curvature: spherical, 56 m
- Dimension of the single components of the all-aluminum sandwich structure:
  - rear frame: 1.5 m ftf, 2.5 mm thick

[27] Information on the reflective layer are not included.

  - honeycomb spacer: 1.5 m ftf, 60 mm high
  - front skin: 1.5 m ftf, 2.5 mm thick
- panel weight: ∼35kg
- panel height: 65 mm
- Three mounting supports installed on the back of the mirror panel: ø120 mm

4.4 Conclusion & Outlook

In this chapter, the current status of the development of new composite mirrors for the MST and LST of CTA are presented. The technique currently under investigation is based on the replica from curved mold of high precision in two steps. The design of the mirror substrate is similar to that used for the MAGIC telescopes with some modifications to the reflective layer.

Different cost efficient industrial solutions with respect to the realization of a high reflecting surface have been tested alternatively to the conventional design. Unfortunately, to now these solutions do not meet the spectral reflectance requested by CTA. Nevertheless, the industrial partners are currently investigating adaption of their products with respect to the CTA specifications.

First small size prototypes have been produced applying two different reflective layer solutions. Their optical qualification revealed that their PSF was too large with respect to the CTA requirements. The relatively low focusing power has been clearly traced to deviations from the ideal curvature of the reflective layer caused by the moderate replication precision. It has been investigated to eliminate the sources of such imperfections. Fur this purpose, different glues have been tested searching for an adhesive that provides an optimum surface contact. In addition, the conditions of the replica process have been investigated to avoid. As for the use of aluminized glass sheets as the reflective layer the curing conditions are of peculiar importance regarding the imposition of stress. Regarding the deposition of the 3M$^{\text{TM}}$ reflective foil, the waviness and the low rigidity of this product play a key role with respect to irregularities of the reflective layer. These characteristics demand an additional device to keep the foil tight during deposition. In addition, a dust free environment is probably necessary if working with this product.

A test bench based on the $2f$–setup has been set up at the LNL of INFN to perform these optical qualifications. Given the complexity of this setup and the reliability of the analysis tool developed, a very accurate study of the PSF is achieved. In addition, the motor unit of the test bench allows accurate movements of the light detecting system for all three axes which enables a precise determination of the radius of curvature.

Once the production technique is tuned with respect to the glue and the deposition of the individual reflective layer options, the next prototypes are expected to have a PSF of the order of few mrad. For economic reasons, to now the tuning is performed on small samples and small sized prototypes before deploying the technique to prototypes of larger sizes and more complex geometries.

It is important to say, that MST and LST mirror design may still be modified during the prototyping phase. Regarding the substrate dimensions a decrease of the panel thickness is possible to reduce the weight is possible unless the rigidity of the mirror is sufficient. Furthermore, a symmetric sandwich design is considered. Such design might be necessary in the case an aluminized glass sheet is used in combination with the aluminum mirror substrate. In this case, the difference in the thermal expansion coefficient between the two materials might apply stress

to the reflective surface layer. As a reaction on the insufficient water tightness due to the porosity of aluminum, there are several solutions regarding the sealing technique of the panel in which is investigated in order to render the mirror box impermeable. One solution is to apply a special paint on the borders of the honeycomb structure as well as on the rear of the mirror box.

Concerning the optical test bench installed at the LNL of INFN, a revision is foreseen in order to automate parts of the measurement procedure, such as the data acquisition and the operation of the light source. Moreover, the light source will comprise several LEDs emitting at different wavelength in order to evaluate the spectral behavior of the optical performance of the prototypes.

Currently, the mechanical and durability testing is defined according to ISO standards wherever applicable in order to study the optical quality due to the environmental exposure [121, 120]. An extensive long–term durability test equipment has been set up by the University of Durham available to the CTA consortium. Therefore, the durability of the finalized prototypes will be extensively tested with this facility. Moreover, the measurement equipment available within the CTA consortium offers the possibility to measure the optical parameters of the mirror facets in a climate chamber by means of a so–called *Phase Measuring Deflectometry* setup [288].

5 Cross Calibration of the Optical Test Equipment for CTA

Currently, several institutes are investigating the development of new IACT mirrors suited for the CTA. Naturally, each institute performs the optical qualification of the mirror prototypes on–site with its own measurement equipment and analysis tools. It is obvious, that each test facilities implies various sources of uncertainties affecting the precision of the optical mirror qualification. Therefore, a cross calibration has been organized to verify the robustness and correctness of the optical testing performed by the individual institutes. For this purpose, three IACT mirrors of different characteristics and dimensions were circulated among the individual test facilities accompanied, when possible, by two members of the cross calibration team. To exclude possible discrepancies among the testing results due to different analysis tools, a cross analysis has been performed on the individual data sets obtained from the facilities when possible. The cross calibration has been conducted and coordinated by the author of this PhD thesis.
In the first part of the chapter, the individual test facilities and the circulated IACT mirrors are briefly described. Hereafter, the commonly used test procedure and the individual measurement results are presented. Furthermore, the cross analysis of the data is presented. The chapter concludes with a brief summary on the cross calibration.

5.1 The Test Facility Description

So far, six European test facilities, located at Saclay, Erlangen, Tübingen, Olomouc, Padova[28] and Warsaw[29] have been involved in this campaign. All of these test facilities provide different realizations of a $2f$–setup (see Section 4.2.2). Furthermore, the Erlangen facility performs PMD measurements. In the following, an overview on the measurement equipment available at each facility is given.

Saclay

The facility of CEA (Commissariat à l'énergie atomique et aux énergies alternatives) Saclay is situated in a 34×5 m underground hall. The testing apparatus

[28] For a description of the Padova facility see Chapter 4.
[29] The facilities are listed in the order according to which they performed the optical testing on the circulated IACT mirrors.

consists of a rigid support holding LEDs emitting at different wavelengths, a collimator, an imaging screen where the spot image is projected on and a 16 bit Atik-4000 CCD camera[30] for the focal spot image recording (see Figure 5.1). The CCD is place at distance of about 50 cm distant from the screen covering a FOV of 14×14 cm. The resolution of the recorded images is 0.0714 mm per pixel.

Figure 5.1: Images of the test bench setup of the Saclay facility.

In order to measure the absolute reflectance into the focal spot, the imaging screen can be replaced by a photodiode. As the optical bench is installed on a rail, the optical performance can be studied at distances from 30 to 37 m from the mirror. The mirror is mounted in a fixed support attached to the wall. Two motors allow the adjustment of the mirror tip–tilt position with respect to the incident light beam in order to center the image on the imaging screen. On the same support, several photodiodes of 27.9 mm diameter are placed as close as possible to the mirror with the purpose to measure the total light flux collected by the mirror surface and to monitor the illumination uniformity and the background stability. Another identical photodiode is placed at twice the focal length to measure the light reflected into the focal spot. Figure 5.2 shows the emission spectra of the four LEDs covering emissions at different wavelengths from UV to green.

Figure 5.2: Emission spectra of the LED type light sources used for the test bench of the Saclay facility.

Erlangen

The ECAP (Erlangen Centre For Astroparticle Physics) is specialized on PMD measurements. In order to cross check the PSF results obtained with the ray–

[30] http://www.atik-cameras.com/products/info/atik-4000

tracing from such measurements [288], the test facility is equipped with a conventional $2f$–setup (see Figure 5.3) of rather low degree complexity. The optical bench consists a red LED and a detecting system composed of a ground glass as imaging screen and a Nikkon CCD camera that is installed behind the screen. With a 4608×3072 pixel matrix and pixel size is 34.5 μm the CCD covers a FoV of ∼16×10 cm.

PMD provides the spatially resolved data of the specular free form surfaces. By means of the phase shift algorithm, it is possible to encode a position on a screen which is observed by a camera via a specular object. In order to provide quantitative data, a precise calibration is needed. This consists of two major steps. First, an internal camera calibration is done to compensate the imperfections of the objective, i.e. possible distortions. Second, a relative position of the camera with respect to the screen is determined (see Figure 5.3). The calibrated setup

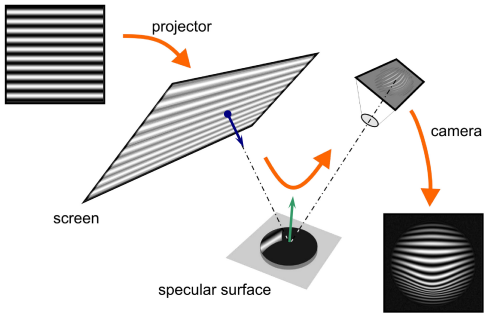

Figure 5.3: Schematic principle of the PMD measurement.

provides the coordinates of the observed position on the screen and on the camera pixel. The normal of the surface is reconstructed as a bisector of the reflected chief ray. This reconstruction is performed for every camera pixel observing the screen via the object. By an integration of the spatially resolved normals, the shape of the object is obtained. The curvature map is calculated by a numerical differentiation of the normals. These results can be used to characterize spherical and aspheric reflectors. Spatially resolved data of spherical mirrors are used to determine the PSF by means of ray–tracing (see Figure 5.4). The optical axis of

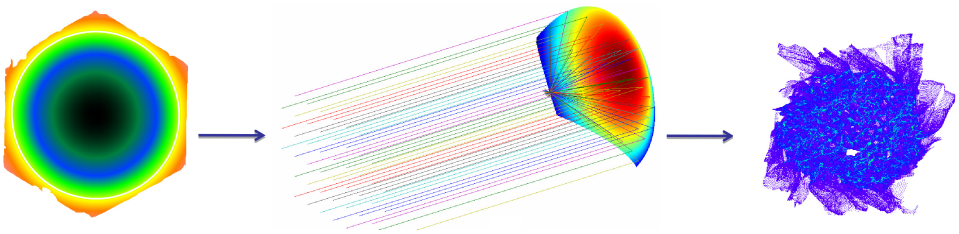

Figure 5.4: Schematic principle of reconstructing the PSF (right) from a PMD measurement (left) via ray–tracing.

the sample under test is defined as the average of all local normals. Ray–tracing permits the reconstruction of the PSF for different scenarios, i.e. light impinging the mirror from infinity or from twice the focal distance. To each single spatially resolved pixel a single ray is assigned, in order to determine the PSF in terms of the D_{80} (see Section 4.1). The D_{80} is given as the diameter of the circle containing 80% of all those rays that intersect 2/3 of the pixel diameter of the Cherenkov camera. By definition, both the Cherenkov camera pixel and the center of the integration circle are placed on the optical axis. Two assumptions are made when

performing ray-tracing: the local reflectance over the whole mirror is constant and equal to 1, and only a specular reflection on the mirror surface takes place, i.e. no light is reflected diffusely.

Tübingen

The MPIK/IAAT (Max–Planck–Institu für Kernphysik and Institut für Astronomie und Astrophysik Tübingen) implementation of the $2f$-setup is done in the following way: halogen lamp serves as light source, emitting light over a broad spectrum including the range from 300 to 600 nm. The Tübingen facility has two independent detector systems: a photodiode mounted on a precise x-y scan table to perform a scan of the reflected spot and an astronomical 16 bit Apogee Alta E9 CCD camera[31] to record the focal spot reflected on an imaging screen. With a 3073×2048 pixel matrix and a resolution of 0.089 mm per pixel, the CCD covers a FoV of 27×18 cm.

By the use of different filters, the diode scan provides the absolute reflectance into the focal spot as a function of wavelength at 310, 400, 470, and 600 nm. The light of the halogen lamp is modulated with a chopper wheel and the diode is read out with a lock in amplifier, allowing to efficiently suppress any possible remaining background light in the otherwise dark hall. Normalization measurements of the light intensity of the lamp and a carefully checked long–term stability of the lamp allow an absolute calibration to determine the reflectance into the focal spot.

It is also possible to calculate the PSF as a function of wavelength, but due to the limited resolution of 5×5 mm pixels, the results are not very precise. The PSF determined with this CCD image is of much higher resolution

The local reflectance can be measured pointwise on the surface of the mirror using an Ocean Optics JAZ Spectrometer with a custom-built measurement head. The covered wavelength range is 250 to 850 nm. This is a relative measurement, normalizing the measured reflectance to a calibrated test sample.

Olomouc

The JLO (Joint Laboratory of Optics) of UPOL (Palachý University of Olomouc) and Institute of Physics of the ASCR (Academy of Sciences of the Czech Republic) test facility at Olomouc uses a white LED equipped with a 50 μm diameter pinhole as point–like source and a 16 bit G4 -1600 CCD camera[32] as light detector covering a FoV of 36.9×36.9 cm, with a 4096×4096 pixel matrix and a resolution of 9 μm per pixel. During the measurement the temperature of mirror surface temperature is monitored by a Fluke optical non–contact thermometer. To suppress vignetting due to the large CCD chip, the effective FoV is reduced to 36.9×32.2 mm. No objective is used which means that no additional optical system is placed between the mirror and the light detector. Thus, the light impinges directly on the CCD chip set perpendicular to the optical axis. Both detector and light source are mounted on a mechanical translation stage allowing for distance scans. The Bosch DLE 50 laser distance meter[33] is used for the distance determination providing an accuracy of ± 1.5 mm.

The local surface spectral reflectance is measured using an Oriel[34] light source

[31] http://www.megapixelsystems.com/apogee/pdf/E9.pdf
[32] http://ccd.mii.cz/art?id=383&lang=409
[33] http://www.bosch-pt.com/productspecials/professional/dle50/au/en/start/index.htm
[34] http://search.newport.com/?i/1/q1/Products/q2/Oriel+Instruments/x1/pageType/x2/product_brand/nav/1/view/brand

is spanning from 320 to 700ṅm. An Avantes spectrometer[35] equipped with an Avaspec spectrophotometer and an Avantes integrating sphere of the type Avasphere 50 (see Figure 5.5). In a first step, the integrating sphere measures the total

Figure 5.5: Equipment for measuring the spectral reflectance locally on the mirror surface. The Avaspec spectrophotometer and the Orial light source are connected via optical fibers.

amount of light, that is both the diffused and the specular component, reflected from the mirror surface. In a second measurement, the diffused component is de-

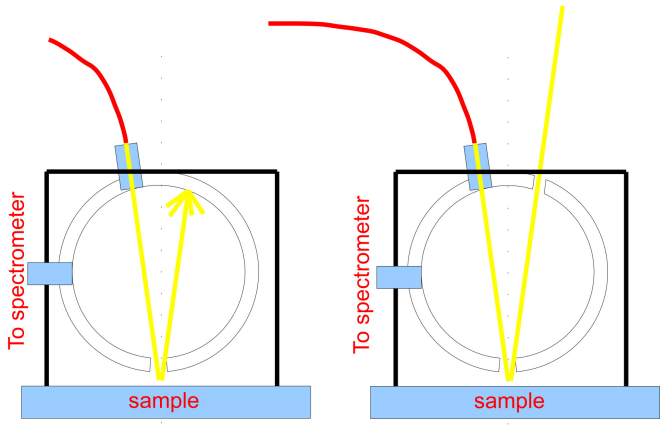

Figure 5.6: Principle of the local reflectance measurement performed with by the Olomouc facility. *Left:* Measurement of the total spectral reflectance. *Right:* Measurement of the diffuse component.

termined separately by removing a bung at the position of the specular beam so that the specular component and light within an angle of $\pm\, 6°$ exits the integrating sphere (see Figure 5.6).

By subtracting both measurements, the specular component is obtained. The measured reflectance is normalized to the reflectance measured for a calibrated reference material.

Warsaw

In Figure 5.7 the setup used at the SRC PAS (Space Research Center of Polish Academy of Sciences) Warsaw facility is sketched. With their $2f$–setup configuration it is possible to measure the PSF shape and dimension as well as the total

[35] http://www.avantes.com/

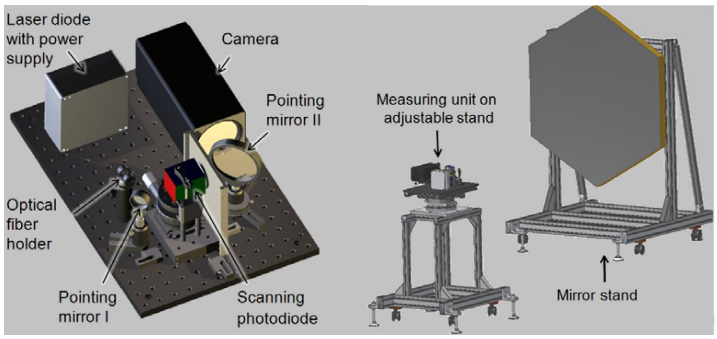

Figure 5.7: Scheme of the $2f$–setup equipment of the Warsaw facility. *Left:* Sketch of the optical bench. *Right:* Schematic view of the optical bench and the mirror support structure.

reflectance of the mirror into the focal spot. A laser diode emitting at 635 nm coupled to a fiber is used as light source. The light detection is divided into two parts: for the PSF characterization a Thorlabs DCC1545M *Complementary Metal Oxide Silicon* (CMOS) camera[36] is used, while the reflectance measurement is performed with a Hamamatsu photodiode[37]. The CMOS provides a smaller dynamic range of a 8 bit only and features a 1280×1024 pixel matrix, with a pixel size of 5.2 μm. To enlarge the FOV to ∼82×102 mm such that a detailed PSF study is possible, an objective is used reducing the resolution to 80 μm per pixel. Due to the objective with which the camera is equipped in order to record the focal spot imaged on a diffusor, the camera resolution is reduced to 80 μm per pixel. Both photodetectors are mounted on an optical bench whose distance from the mirror can be varied. In addition, the photodiode is adjustable in x and y allowing a scan of the focal spot within a diameter of 17 or 34 mm. In addition, the optical bench is equipped with a Bosch laser rangefinder DL50 providing an accurate distance measurement. The mirror is fixed on a supporting system that provides height adjustment and distance variation.

5.2 The Testing Scheme

In the subsequent sections, the main characteristics of the circulated mirrors and the testing scheme concerning the PSF study are briefly described. An emphasis is given

5.2.1 Mirror Characteristics

Three mirrors were circulating among the European test facilities. Two small mirrors from the H.E.S.S. and MAGIC experiments travelled together with a MST nominal size prototype built by the CEA Saclay. Below, the main details are listed for the individual mirrors. Furthermore, PMD measurements of the individual mirror surfaces are presented within each mirror description.

[36] http://www.thorlabs.de/newgrouppage9.cfm?objectgroup_id=4024
[37] http://sales.hamamatsu.com/en/home.php&nocache=1

H.E.S.S. A296:

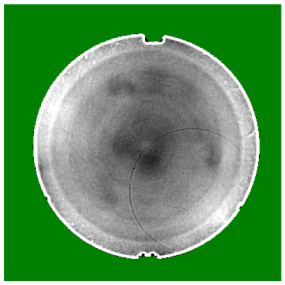

- Substrate: Solid glass.
- Circular shape. Diameter: 60 cm.
- Radius of curvature: 30 m.
- Coating: $Al + SiO_2 + HfO_2 + SiO_2$

MAGIC-1 n901:

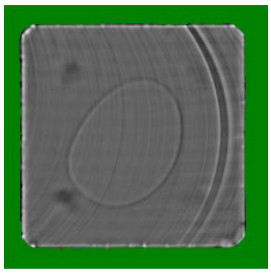

- Substrate: All-aluminum sandwich (Al-box + Al-honeycomb + Al layers diamond-milled)
- Rectangular shape. Side: 50 cm.
- Radius of curvature: 36.5 m.
- Coating: $Al + SiO_2$+ Carbon admixtures

Saclay P25:

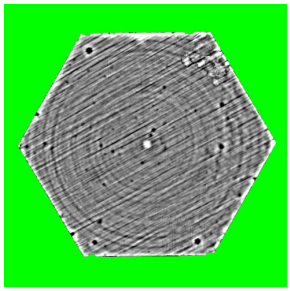

- Substrate: Sandwich of Al-honeycomb G10 sheets + glass sheets (front & back)
- Hexagonal shape. 120 cm flat to flat (FTF).
- Radius of curvature: 33.6 m.
- Coating: $Al + SiO_2 + HfO_2 + SiO_2$

Test Procedures

Following the CTA specifications regarding the PSF evaluation, the characterization was performed by the evaluation of D_{80} applying the normalization of the light flux with respect to the light containment within 2/3 of the pixel diameter of the Cherenkov camera (see Section 4.1). In the case of the H.E.S.S. (ø42 mm pixel), MAGIC (ø33 mm pixel) and CTA (CTA MST pixel of ø50 mm assumed) Cherenkov camera, the normalization area corresponds to a diameter of 28 mm, 22 mm and 33.3 mm was defined.

The PSF measurement has been performed with two different methods using the so called $2f$-setup and the PMD method. For comparison purposes the test facilities measured the PSF at the nominal distance of each mirror.

Some facilities had the adequate equipment to measure also the mirror reflectance either locally on the mirror surface or the absolute reflectance into the focal spot. An overview of the results and a comparison is given in Section 5.4 and 5.5. No common test procedure has been defined for these optical qualifications.

5.3 The PSF

In this section an overview of the measurements of the PSF performed by each test facility is given including some important information on how the test and the analysis was performed. Hereafter, the individual results are compared, followed

by the presentation of the cross check of the analysis performed by the Padova and Saclay facilities.

Saclay

The Saclay facility performed the PSF and absolute reflectance measurement. The mirrors were hold by the support structure without using the AMC (see Section 3.4.2) mounting points at the back sides of the mirrors for installation. For dark frame recording the light source was switched off. The obtained focal spot

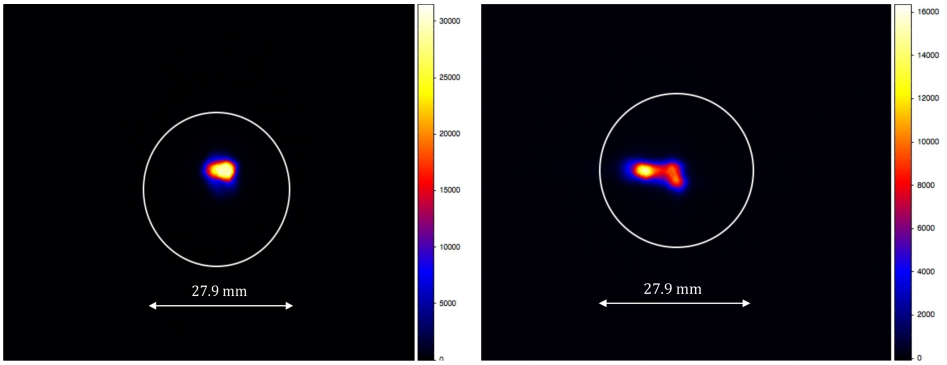

(a) A296 **(b)** n901

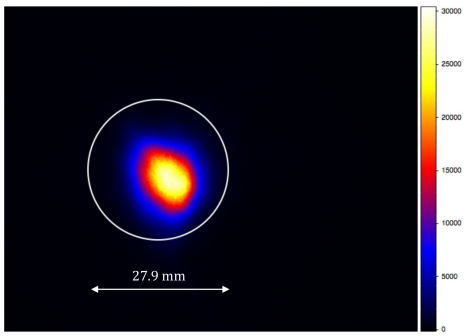

(c) P25

Figure 5.8: Returned spot images recorded the Saclay facility for the circulated mirrors at twice their nominal focal length. The white circle indicates the photodiode diameter (ø27.9 mm).

images are pre-processed using an astronomical commercial software (Prism[38]) in order to clean the images of background contamination, CCD noise and aberration from the lens. In a further step, the images are analyzed using a ROOT executable developed by the Saclay facility for the PSF determination. The focal spot images were centered on the imaging screen where the photodiode is located. This position was used as starting point for the integration procedure. The recorded spot images are shown in Figure 5.8.

Erlangen

The Erlangen facility performed the PSF measurement with both the PMD method and the $2f$–method. During both measurements the mirrors were not supported on the mounting points at the backsides foreseen for the AMC. For the dark frame acquisition the light source was switched off.

[38] http://www.prism-software.com/index.php

The data acquired with the $2f$-setup were analyzed with a ROOT routine developed by the Erlangen facility. The mean background level was calculated from the dark frame. In order reduce the camera noise, a criterion was used to set pixels with a certain variation from this mean value to zero. The barycenter of the spot was used as starting point for the D_{80} calculation. Figure 5.9, 5.10 and 5.11 show both the reconstruction of the focal spot via ray–tracing from the PMD measurement and focal spot images recorded with the $2f$-method.

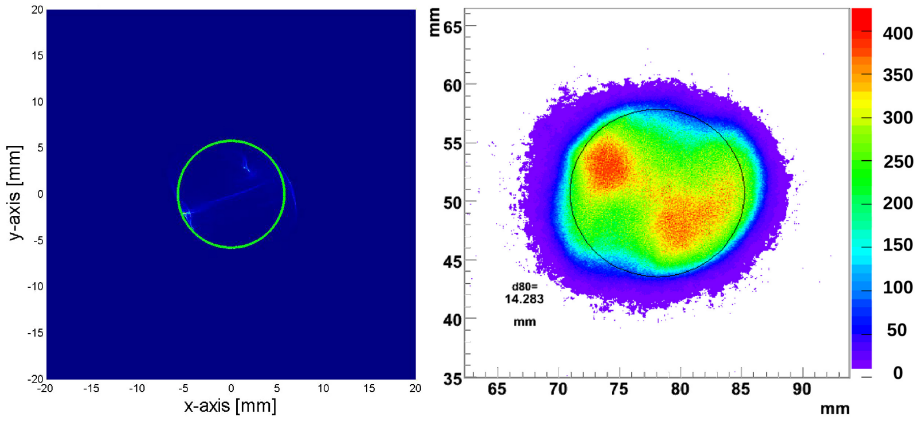

Figure 5.9: Returned spot image of A296 reconstructed by ray–tracing from the PMD measurement and recorded with the $2f$-method at twice the nominal focal length by the Erlangen facility. *Left:* Ray–traced focal spot image. *Right:*.The green and black circle indicate the D_{80}.

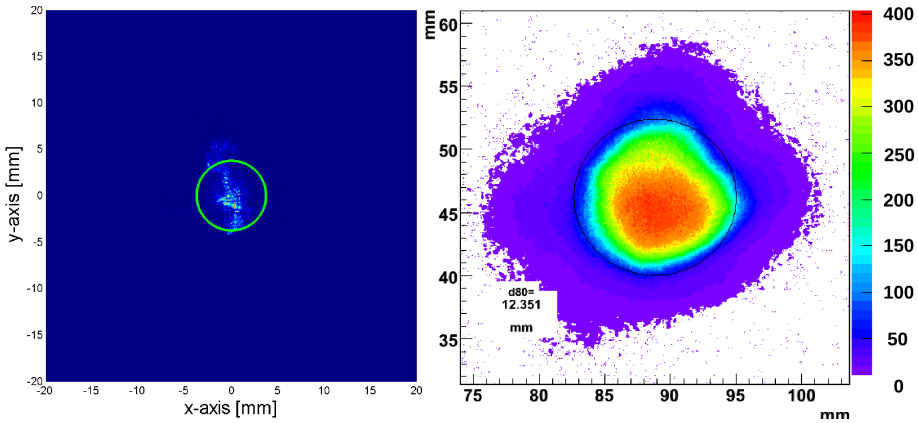

Figure 5.10: Returned spot image of n901 reconstructed by ray–tracing from the PMD measurement and recorded with the $2f$-method at twice the nominal focal length by Erlangen facility. *Left:* Ray–traced focal spot image. *Right:*.The green and black circle indicate the D_{80}.

Tübingen

Due to a loose AMC adapter flange[39], P25 was supported only on two of the three AMC mounting points while measuring. In the case of A296 and n901, the AMC mounting points were not used for fixation. Instead, the mirrors were clamped

[39] As the MST prototype P25 is also spherical at the back, the AMC flanges are not within the same plane. Thus, when attaching them to the support the flange detached. The mirror was returned to the Saclay facility to fix the AMC flange before continuing its circulation among the remaining facilities.

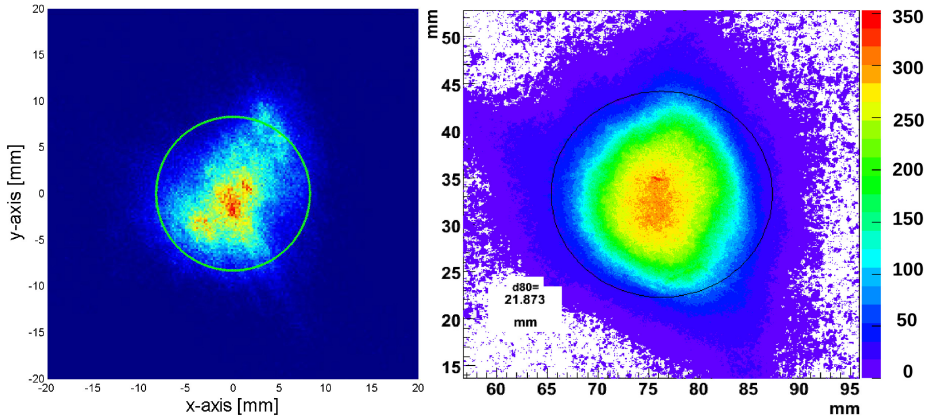

Figure 5.11: Returned spot image of P25 reconstructed by ray–tracing from the PMD measurement and recorded with the $2f$-method at twice the nominal focal length by the Erlangen facility. *Left:* Ray–traced focal spot image. *Right:*.The green and black circle indicate the D_{80}.

into the mirror support. The Tübingen facility measured the PSF using both light detecting systems (see Section 5.1). For the individual background measurements have been performed the light source was not switched off, but the mirror was covered. For the data analysis a ROOT routine developed at the Tübingen facility has been used. The barycenter of the focal spot was used as starting point for the D_{80} determination.

For the optical qualification of the H.E.S.S. and MAGIC mirror a 15 mm aperture was installed in front of the halogen lamp. Therefore, the size of the light source corresponded to the full filament of the halogen lamp (∼5 mm). For this reason, the light source can not be considered to be point–like. Consequently, the PSF might be wrongly estimated. Moreover, there have been some concerns that measurements was performed at a position significantly different from the nominal $2f$ distances of A296 and n901. For these reasons both mirrors have been remeasured by the Tübingen facility after their circulation to other laboratories with some changes to the optical test bench. It has been observed that n901 was more dirty than during the first measurements and that it featured scratches that were not present before. The changes to the test setup were the following: the aperture in front of the halogen lamp has been reduced from to 3 mm; the distance between the mirror, the plane of the halogen lamp and the imaging screen have been measured more precisely using a laser distance measurement device with a nominal accuracy 1 mm.

For the MST prototype mirror P25 the aperture of 3 mm diameter was used right away so that this mirror has not been remeasured. The focal spot images obtained are shown in Figuew 5.12, 5.13 and 5.14.

Olomouc

At the Olomouc facility all three mirrors were installed in the $2f$–setup by mounting them on their AMC supports. The dark frame was taken distance different from the nominal $2f$ while the light source was switched off. The data analysis was performed with MATLAB[40] software. The barycenter of the focal spot was used as starting point for the D_{80} calculation. The focal spot images on which the analysis was performed can be seen in Figure 5.15.

[40] http://www.mathworks.co.uk/products/matlab/

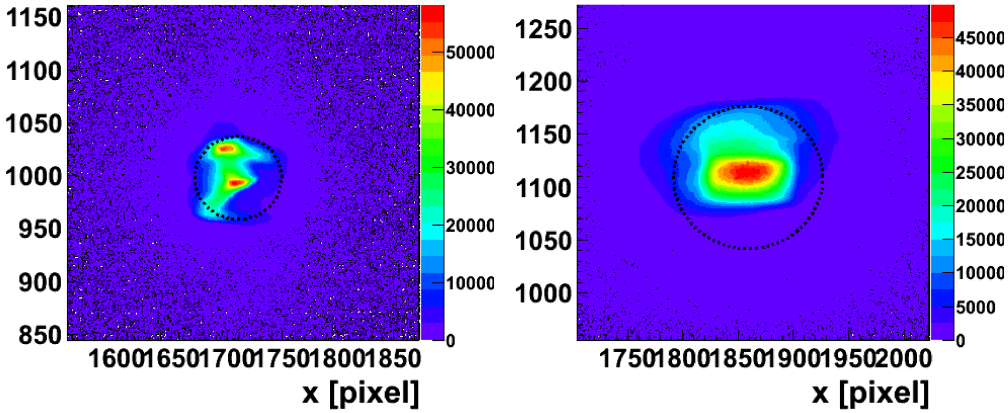

(a) March 2012 **(b)** May 2012

Figure 5.12: Returned spot images of A296 recorded at the nominal $2f$ by the Tübingen facility. The black dotted circle indicates the 80% containment diameter. The measurement has been carried out twice.

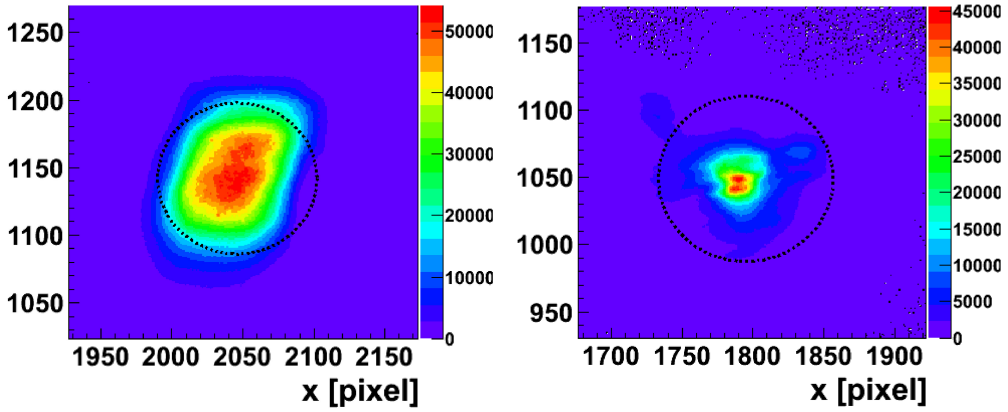

(a) March 2012 **(b)** May 2012

Figure 5.13: Returned spot images of n901 recorded at the nominal $2f$ by the Tübingen facility. The black dotted circle indicates the 80% containment diameter. The measurement has been carried out twice

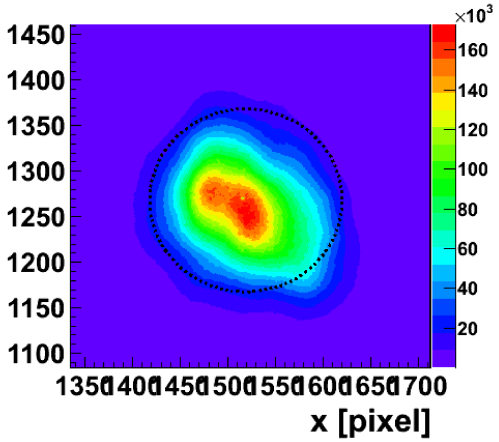

Figure 5.14: Returned spot image of P25 recorded at the nominal $2f$ by the Tübingen facility. The black dotted circle indicates the 80% containment diameter.

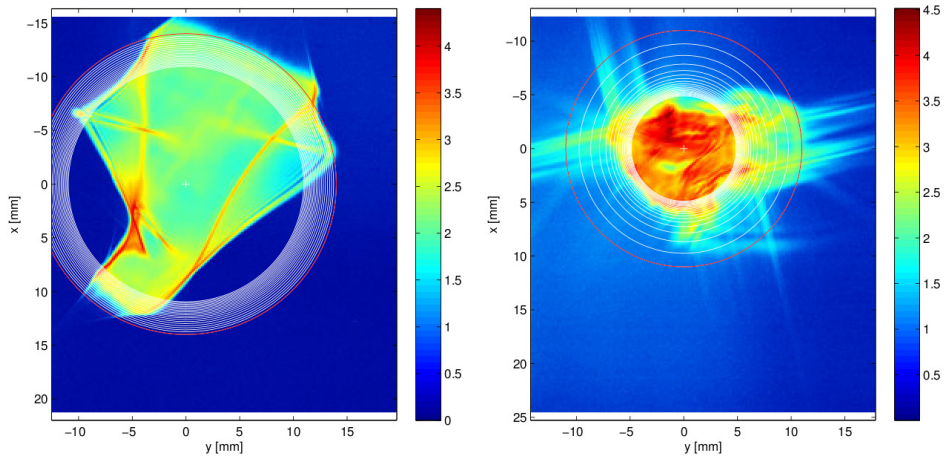

(a) A296 **(b)** n901

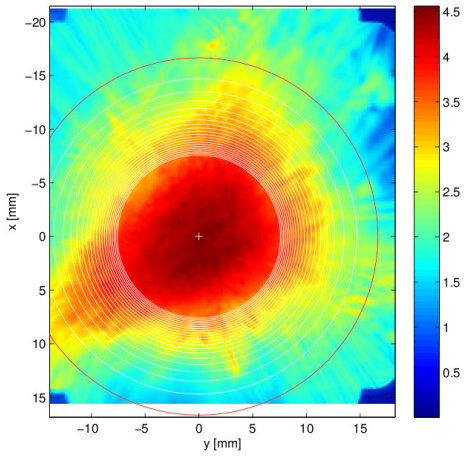

(c) P25

Figure 5.15: Returned spot images of A296, n902 and P25 recorded at nominal $2f$ by the Olomouc facility. The enlarging circles indicate the light containment increasing from 80% (red filled circle) in 1% steps to 99% (white lined circles). The red lined circle marks 100% light containment, while the white cross marks the barycenter of the focal spot. The light intensitiy scale is in Log_{10}.

Padova

As there was again a problem with a loose AMC flange, P25 was supported only on two of the three AMC flanges during the PSF measurement carried out by the Padova facility. A296 and n901 were measured without fixing them on their AMC installation positions on the backside.
For the dark frame recording the light source was switched off. The data analysis was carried out with a routine using AstroROOT developed by the Padova facility (see Section 4.2.2). As starting point of the D_{80} determination, the barycenter of the focal spot was used. The analysis results are presented in Figure 5.16.

Warsaw

During the transport from Tübingen to the Warsaw facility, the A296 broke so that this test facility could only measure n901 and P25. Both mirrors were fixed at the foreseen AMC flanges during the measurement. For the background measurement

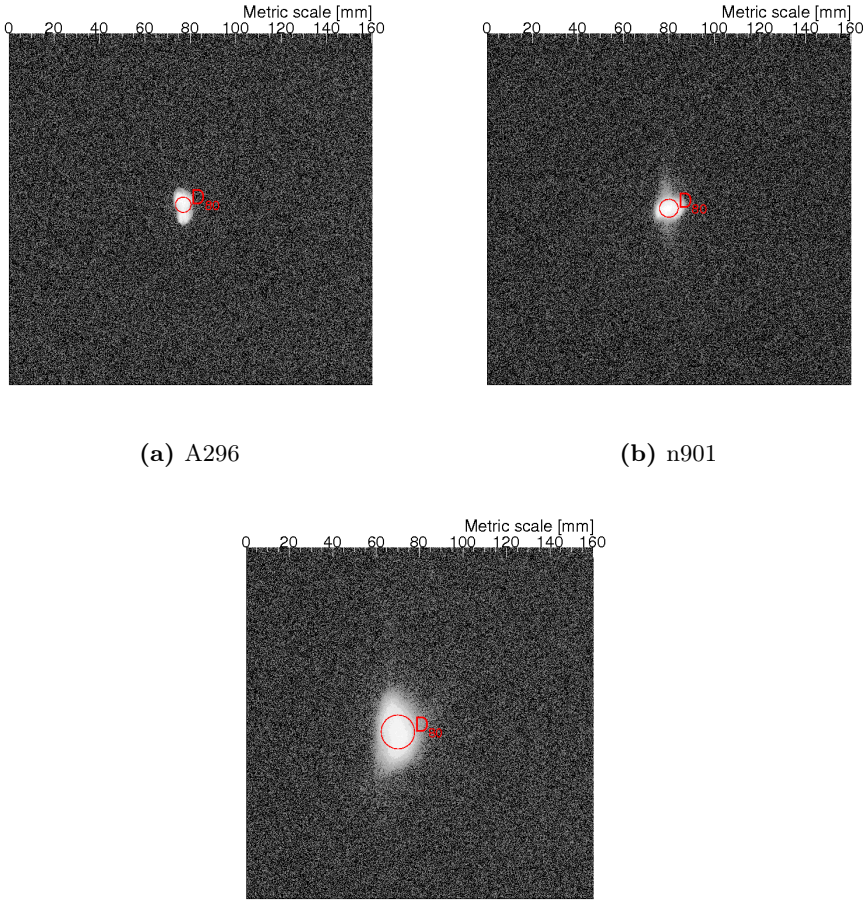

(a) A296 **(b)** n901

(c) P25

Figure 5.16: Returned spot images A296, n901 and P25 recorded at nominal $2f$ by the Padova facility. The red circles indicate the individual diameters of 80% light containment.

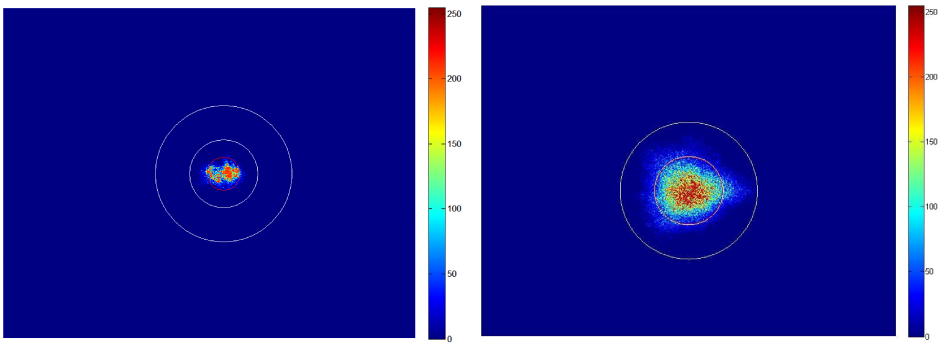

(a) n901 **(b)** P25

Figure 5.17: Returned spot images from n901 and P25 recorded at twice the nominal focal length by the Warsaw facility. The red and white circle mark 80% and 100% light containment respectively.

the laser diode was switched off. The barycenter of the focal spot was used for starting the D_{80} calculation routine for which MATLAB was used. The focal spot images are shown in Fig. 5.17.

5.3.1 Comparative Studies

In Figure 5.18, 5.19 and 5.20 the individual spot images are presented with a modified layout so that a direct comparison of the images is straightforward. As the Erlangen and Warsaw facilities could not provide their images in .fits format such modification could not be done for their data. As the Olomouc CCD is not equipped with an objective, the FoV is quite small so that it covers only a fraction of the unified image range.

The values of the D_{80} determined for the individual mirrors by each facility show a significant variation of the order of 2 mm to 10 mm for all three mirrors- In addition, there is also a discrepancy between the results obtained with the different measurement principles, even if carried out by the same facility in the case of Erlangen.

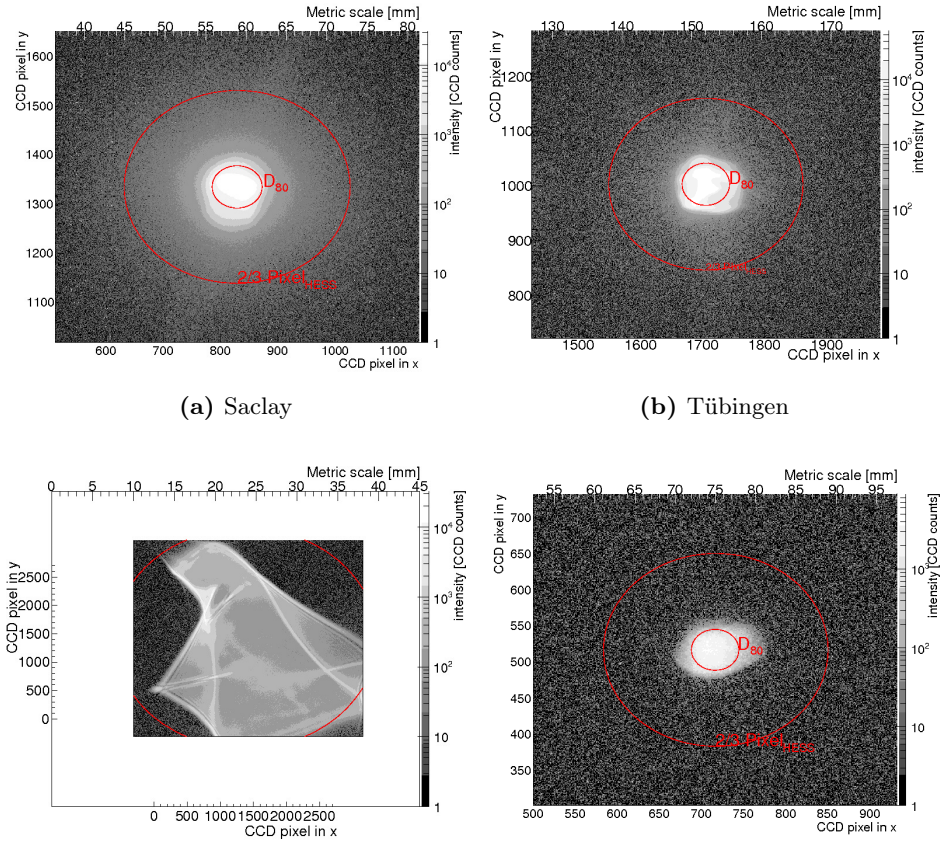

(a) Saclay **(b)** Tübingen

(c) Olomouc **(d)** Padova

Figure 5.18: Comparison of the individual spot images of A296 provided by the facilities of Tübingen, Saclay, Olomouc and Padova. The red circles mark the light containment normalization area and the D_{80}.

Looking at the individual spot images, there are clear differences in the spot size and spot shape. The reasons for such variation of the focal spot can be several. First, the measurements were not performed at the correct nominal distance. Second, the different mirror mounting during the measurement probably introduces deformations of the mirror surface wherefore focal spot shape changes. In fact, the test facilities of Olomouc and Warsaw measured the small mirrors

[40] In the case of the measurement performed by the Tübingen facility, only the second measurement is presented.

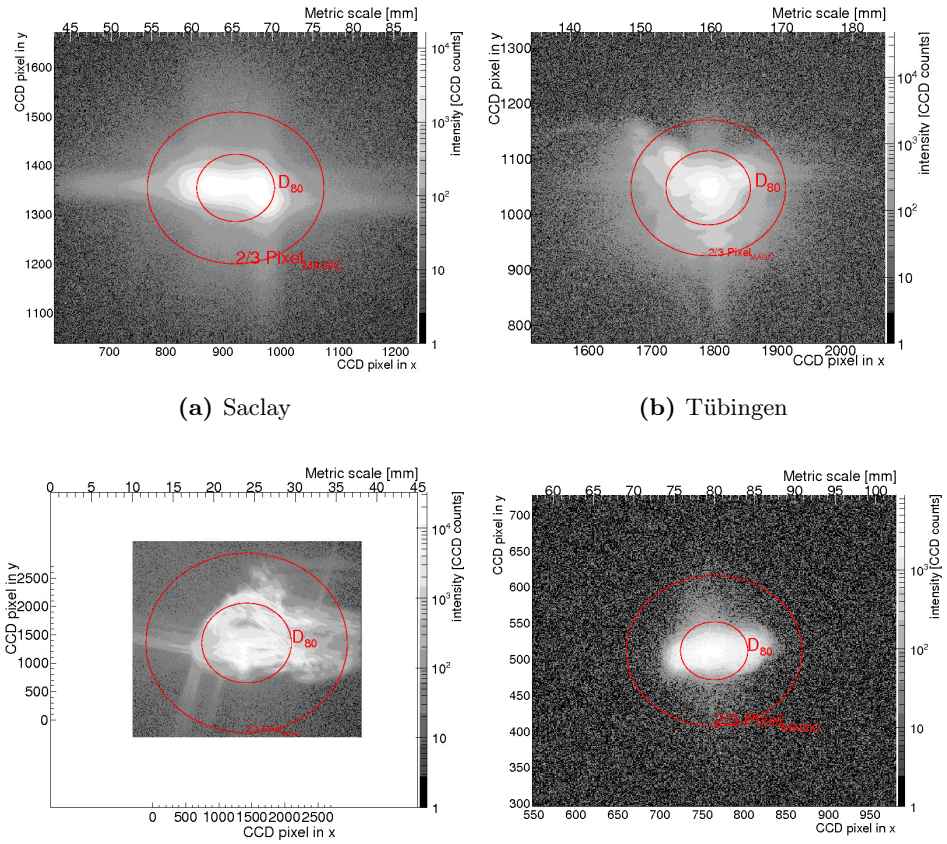

Figure 5.19: Comparison of the individual spot images of n901 provided by the facilities of Tübingen, Saclay, Olomouc and Padova.The red circles mark the light containment normalization area and the D_{80}.

holding them at the AMC mounting points, while the other test facilities measured them without any attachment to the mirror backside. Third, the variation of the FoV and the resolution provided by the individual photo detectors might also play a key role.

In the case of the Olomouc facility, the modified spot images point out, that the determined D_{80} is strongly biased. Due to the small FoV and off–center position of the focal spot with respect to the light detector, parts of the spot are cut off (see Figure 5.18c, 5.19c and 5.20c) leading to a wrong PSF calculation. In case of A296 and P25, the diameter of 100% light containment does not even fit into the FoV.

There are several caveats associated with both measurement techniques which might be responsible for the discrepancies between the two measurements carried out by the Erlangen facility. A possible reason could be that the ray–tracing neglects the micro roughness of the mirror surface which causes a spot widening. On the other hand, the $2f$–setup provides a light source of finite size whose uniformity is not guaranteed. Furthermore, the light detector for imaging the focal spot might cause a biased PSF measurement due to scattering, the detector optics and its finite resolution.

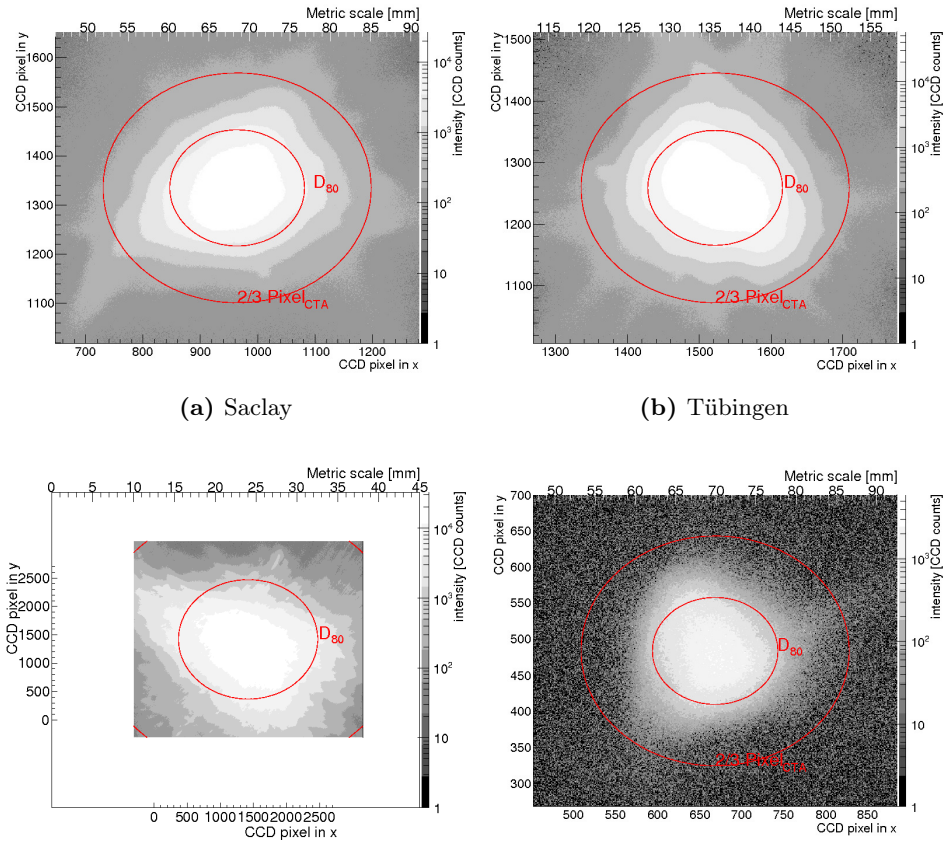

(a) Saclay **(b)** Tübingen

(c) Olomouc **(d)** Padova

Figure 5.20: Comparison of the individual spot images of P25 provided by the facilities of Tübingen, Saclay, Olomouc and Padova.The red circles mark the light containment normalization area and the D_{80}.

5.3.2 Cross Analysis

Since the PSF results, summarized in Table 5.1, showed a spread of the order of few millimeters that could not clearly be traced back to the measurement performance itself, a cross check of the D_{80} analysis has been performed by the Padova and Saclay facility using their codes. In addition, an astronomic standard analysis software has been used to check the quality of the performed analysis in terms of background definition and background subtraction correctness. As the Erlangen and Warsaw facilities could provide their data in .fits files format, those results could not be verified.

Nevertheless, there were still some discrepancies of roughly one to two millimeters between the different analysis for the same set of data. Therefore, the data were reanalyzed by the crosschecking facilities using the spot center determined by the individual facilities from which the data were obtained as starting point for the D_{80} determination. With this approach, in most cases the spread among the different analysis of the same data set could be reduced to order of less than one millimeter given the measurement had been performed correctly.

Mirror		D_{80} [mm]	Cross check I		Cross check II	
			Padova	Saclay	Padova	Saclay
A296	Saclay	9.3	6.3	–	10.6	–
	Erlangen	11.6[a], 14.3[b]	n.a.	n.a.	n.a.	n.a.
	Tübingen	7.0 (11.6[c])	7.0 (10.4[c])	9.3 (11.2[c])	7.0	7.1
	Olomouc	21.9	20.4	20.5	n.a.	20.2
	Padova	7.4	–	7.5	–	10.0
	Warsaw	n.a.	n.a.	n.a.	n.a.	n.a.
n901	Saclay	9.6	9.8	–	9.9	–
	Erlangen	7.5[a], 12.4[b]	n.a.	n.a.	n.a.	n.a.
	Tübingen	11.0 (10.0[c])	11.0 (10.0[c])	n.a. (10.3[c])	13.0	12.0
	Olomouc	9.8	10.4	9.5	9.8	9.5
	Padova	8.5	–	8.4	–	8.4
	Warsaw	7.0	n.a.	n.a.	n.a.	n.a.
P25	Saclay	17.3	16.5	–	17.4	–
	Tübingen	16.8	16.7	17.1	17.6	17.1
	Erlangen	16.6[a], 21.9[b]	n.a.	n.a.	n.a.	n.a.
	Olomouc	15.2	15.0	15.5	15.0	15.5
	Padova	15.6	–	17.0	–	15.2
	Warsaw	16.5	n.a.	n.a.	n.a.	n.a.

Table 5.1: Summary of the D_{80} evaluated by the individual facilities for the three circulating mirrors. From left to right: The first column indicates the mirror; in the second column the D_{80} determined by the individual test facilities is listed. Column three and four contains the values of the first cross check of the data analysis performed by the test facilities of Padova and Saclay. Column five and six reports the second cross check using a predefined spot center position;[a]: PMD; [b]: $2f$–setup; [c]: Data from first measurement performed at wrong nominal distance; n.a. denotes that either the data were not available or the analysis failed.

Comparison to the DAOPHOT Astronomic Standard Analysis Software

Daophot is a free software [302] largely used in astronomy to do accurate photometric analyses of variable stars, exoplanets, stellar evolutions studies and polarimetric investigations. The basic idea of the present analysis is to perform an independent estimation of the mirror PSF by Daophot software, deriving a reliable and robust result for the comparison with those retrieved by other routines (i.e. ROOT, MATLAB). Hereafter, the Daophot capabilities of PSF photometry and background removal are briefly introduced together with the results of the PSF estimation retrieved by the mirrors characterized.

The Daophot software has three main functions:

- it retrieves the image centroid;
- it performs the aperture photometry over a series of concentric apertures centered on the image centroid;
- it estimates the background residual after background–to–image frame subtraction.

The number and the radius of the circular apertures onto which Daophot executes the photometry is completely set by the user. The background estimation is a powerful and highly flexible capability of Daophot that allows the user to check eventual residuals and traces of the background contribution after its subtraction from the image frame. It can be computed automatically by the software in an annulus around the PSF or it can be set on a defined value by the user.

For each circulated mirror, there is a spread between the measurements performed in different facilities, but we are not able to disentangle if this is caused by a problem derived from the software analysis or from a real physical effect. In order to to break this degeneracy, a comparison of the difference in the D_{80} measurements retrieved by means of ROOT routines and obtained with Daophot was carried out. As illustrated in Figure 5.21, in fact there are some measurements that are in good agreement with respect to the Daophot analysis, while others attest the suspicion of a real physical difference in the D_{80} estimation.

The measurements performed in Padova and Tübingen facilities seem to be in very good agreement for all the three mirrors. The results obtained from the Saclay facility have slight deviations from the trend: As already discussed before, the results retrieved by the Olomouc facility show quite large deviations except for n901.

The differences outlined by this independent analysis tool could be originated by various environmental effects such as the system used in the individual facilities to support the mirror during the testing campaigns or sensible variations of temperature among the facilities leading to different thermal deformations of the mirror structures. In order to fix these issues and to get a complete and reliable dataset of measurements for an accurate comparison, the monitoring of the environmental conditions, in particular the temperature, seems to be an important task to be achieved by all test facilities. In addition, a complete characterization of the CCD cameras of the individual facilities should be carried out in order to determine important information for the image processing and analysis such as the gain, the read–out–noise, the dark current and the charge transfer efficiency of the detector.

5.3.3 Ray-tracing Adaptions

Due to discrepancies between the results obtained with the $2f$–setup and the ray–tracing from the PMD measurement performed by the Erlangen facility, investigations have been made to achieve a better agreement between both methods. For this reason, modifications of the ray–tracing parameters were applied, namely a distance correction for the focal length and a modification of the light source size from infinite to finit. As a result, the focal spot image measured with the $2f$–setup has been well reproduced by the adapted ray–tracing of the PMD measurement[41] (see Figure 5.22 and 5.23).

With a second H.E.S.S. mirror, that was not circulated among the other facilities, a focal spot scan has been performed with both methods. Figure 5.24 shows the results of both measurements indicating a very good agreement concerning the the focal spot shape and its dimension.

[41] This investigations have been only performed for A296 and P25.

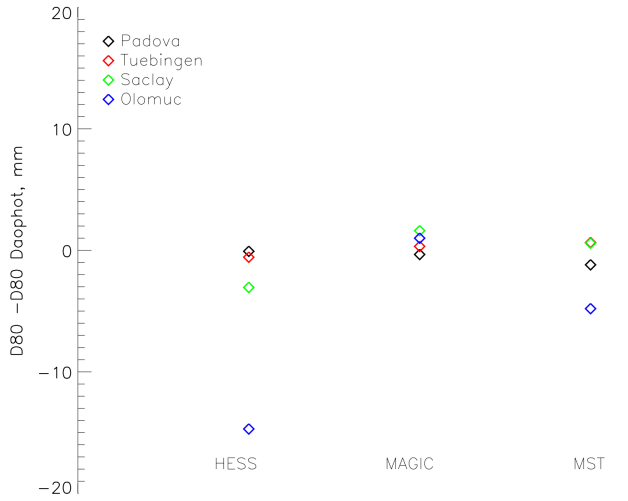

Figure 5.21: Differences among D_{80} measurements retrieved by ROOT executable and those determined by the standard analysis software. In absence of any physical difference all the measurements should lay on the zero level.

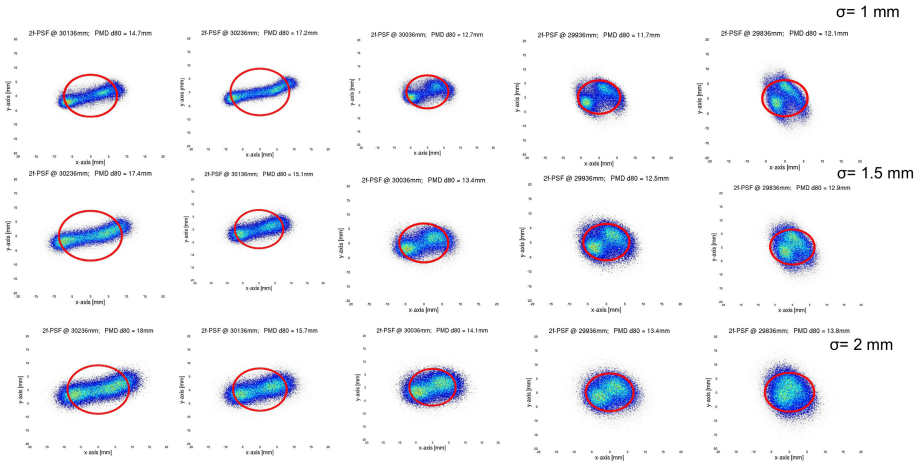

Figure 5.22: p
erformed with varying light source size σ and modification of focal length f]Ray–tracing sequence from PDM measurement of A296. The light source size σ and the focal length f are varied for the reconstruction of the focal spot. The red circle marks the D_{80}.

5.4 The Absolute Reflectance

So far, few of the participating facilities have the possibility to measure the absolute reflectance into the focal spot. The crucial component to perform this measurement is a light detector providing a sufficiently large surface so that the entire focal spot is covered. If this is not the case, a scan of the focal spot must be performed demanding a precise movement across the spot. Second, a stable light source is needed in order to normalize the measurement of the light reflected into the focal spot to that incident to the mirror. This measurement has been performed by the facilities of Saclay, Tübingen and Warsaw.

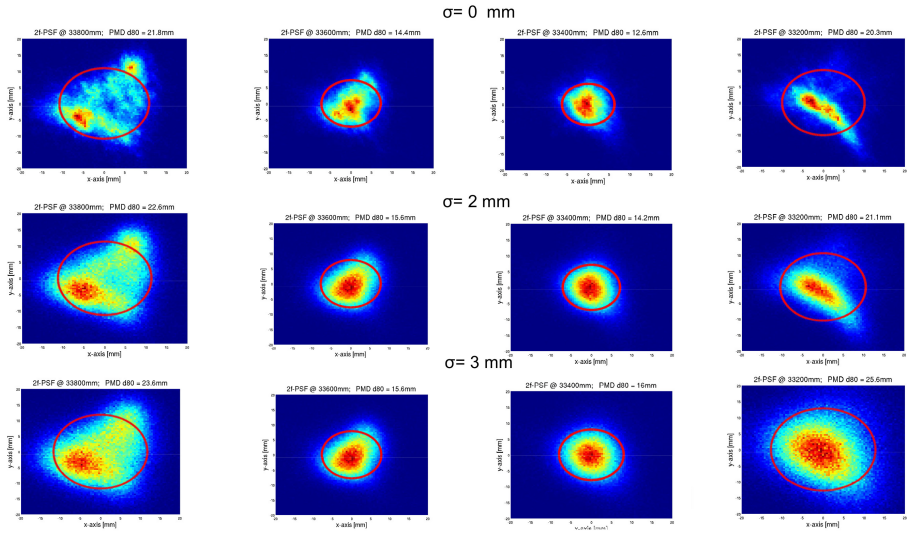

Figure 5.23: p
erformed with varying light source size σ and modification of focal length f]Ray–tracing sequence from PDM measurement of P25. The light source size σ and the focal length f are varied for the reconstruction of the focal spot. The red circle marks the D_{80}.

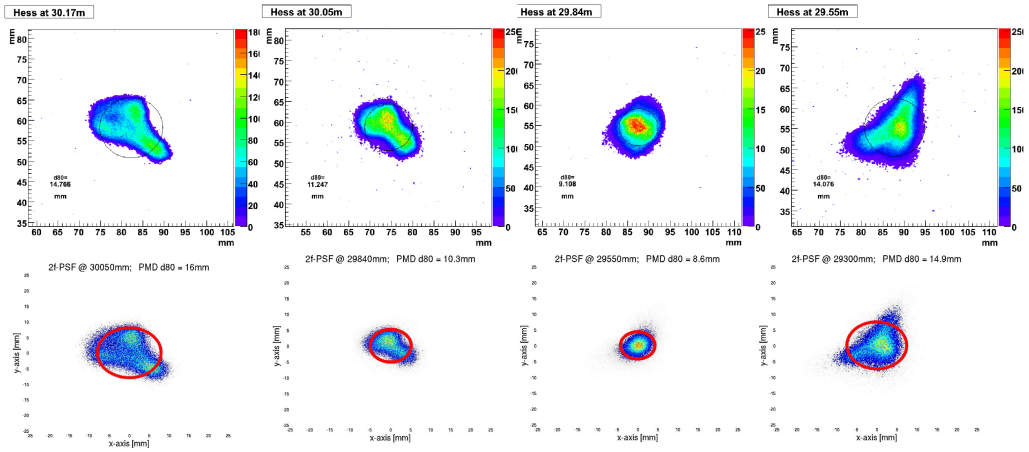

Figure 5.24: Comparison of the focal spot scan performed with the $2f$–setup and the respective reconstructed focal spot image using ray–tracing from the PMD measurement. The ray–tracing was performed with an adequate value for the light source dimension and a focal length correction of ∼20 cm. The black (upper panel) and red (lower panel) circles mark the D_{80}. The measurements have been performed for another H.E.S.S. mirror than A296.

Saclay

For each wavelength, 10 measurements have been performed out of which the average absolute reflectance and the respective statistical error have been calculated. A statistical error calculation has been performed. The normalization area corresponds to the diameter of the photodiode, that is 27.9 mm. The measurement results are shown in Tab. 5.2

Mirror	ρ [%]			
	365 nm	400 nm	460 nm	523 nm)
A296	85 ± 7	80 ± 1	84 ± 1	83 ± 1
n901	55 ± 4	53 ± 2	58 ± 1	62 ± 2
P25	80 ± 3	77 ± 1	80 ± 1	78 ± 1

Table 5.2: Results of the absolute reflectance measured at different wavelengths by the Saclay facility. The error represent the statistical uncertainty of the measurement.

Tübingen

In order to compare the same quantities, the absolute reflectance measured at the Tübingen facility is determined using a surface equal to that of the Saclay photodiode when integrating the images. The measurement results are listed in Table 5.3.

Mirror	ρ [%]			
	310 nm	400 nm	470 nm	600 nm
A296	63 ± 4 (65)	79 ± 4 (85)	84 ± 4 (90)	71 ± 4 (76)
n901	62 ± 4 (39)	54 ± 4 (57)	57± 4 (66)	60 ± 4 (60)
P25	70 ± 4	81 ± 4	87 ± 4	69 ± 4

Table 5.3: Results of the absolute reflectance measured at different wavelengths by the Tübingen facility. The error represents the systematic uncertainty of the measurement. The values indicated in brackets are obtained from the first measurement performed at a position different from the nominal $2f$ distance.

Warsaw

In Table 5.4 the results of the absolute reflectance measured for n901 and P25 are reported.

Mirror	$\rho_{635\,\mathrm{nm}}$[%]	
	ø17 mm	ø34 mm
n901	69.4	n.a.
P25	55.6	67.6

Table 5.4: Absolute reflectance measured at 635 nm by the Warsaw facility for n901 and P25. An integration area of a 17 and 34 mm diameter has been used for measuring the light intensity of the focal spot.

Comparison

In Table 5.5 the absolute reflectance measured at 400 nm with the Saclay and Tübingen test benches are presented. As the Warsaw facility did not use the same surface for integration and performed the measurement at a completely different

Mirror	Test Bench	$\rho_{400\,\mathrm{nm}}[\%]$
A296	Saclay	80 ± 3
	Tübingen	79 ± 4
n901	Saclay	53 ± 3
	Tübingen	54 ± 4
P25	Saclay	77 ± 3
	Tübingen	81 ± 4

Table 5.5: Comparison of the absolute reflectance measured at 400 nm by the Saclay and Tübingen facility. Only the second measurement performed by the Tübingen facility is considered.

wavelength, it is not included in the comparison table. Considering the errors, the measurements for all three mirrors are in agreement with each other. Considering the second measurement of the Tübingen facility, the results show a very good agreement for A296 and n901, while the discrepancy is larger for the P25. As for the remaining results of the absolute spectral reflectance, a comparison is rather difficult due to the variation in wavelength.

5.5 The Local Reflectance

The measurement of the local reflectance at different positions on the mirror surface allows for the verification of the coating homogeneity. In addition, the roughness of the surface can be evaluated by measuring the diffusely reflected component. Thus, it provides a rough estimation of the reflective losses in the focal spot.

Tübingen

The local reflectance measurement has been performed with the JAZZ spectrometer for all three mirrors on straight lines across the entire surface from one edge to the other covering five equidistant positions for the HESS and MAGIC mirror and eight equidistant positions for the MST prototype mirror (see Figure 5.25).

Olomouc

The measurement of the local reflectance was performed for all three mirror types with the Avaspec spectrophotometer. For the H.E.S.S. and the MST prototype mirror the diffuse and specular reflectance was measured at six positions, while for the MAGIC mirror n901 the measurement was performed at ten positions (see Figure 5.26).

Padova

The local reflectance was only measured for the MST prototype P25 using the Ocean Optics USB2000 spectrophotometer[42]. Although this instrument provides a spectral coverage from 350 to 650 nm, the device does not provide accurate measurements below 400 nm due to the decrease in spectral efficiency in the UV regime. The measured reflectance is normalized on a calibrated standard mirror.

[42] http://oceanoptics.com/Products/usb2000.asp

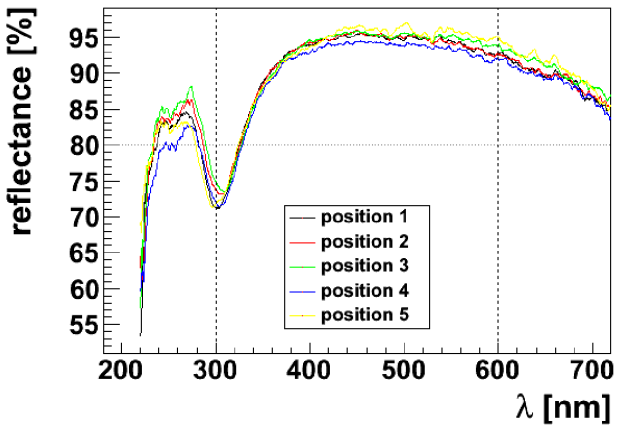

(a) A296

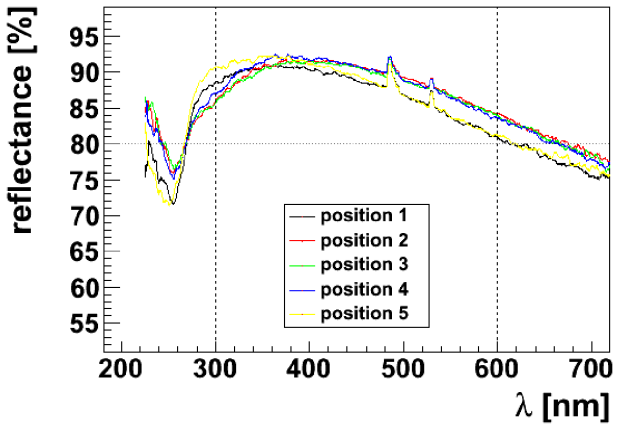

(b) n901

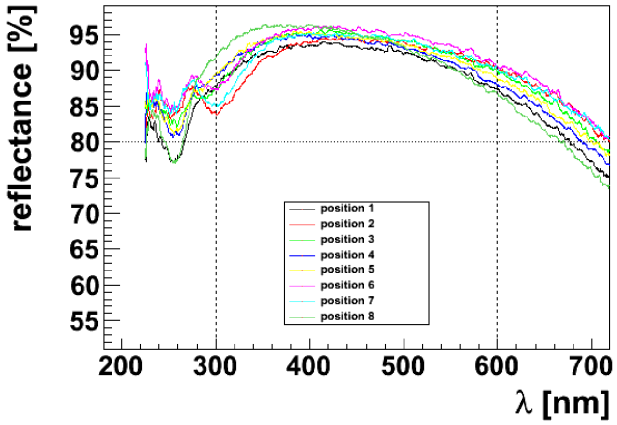

(c) MST P25

Figure 5.25: Results of the local reflectance measurement performed by the Tübingen facility.

The measurements have been performed on a straight line from one mirror edge to the other at eight equidistant positions (see Figure 5.27).

Comparison

Despite the difference of the spectral reflectance curve measured for the MAGIC mirror n901 (peaks at 480 and 520 nm, see Figure 5.27), the comparison of the spectral reflectance plots (see Figure 5.25, 5.26 and 5.27) indicates only a slight

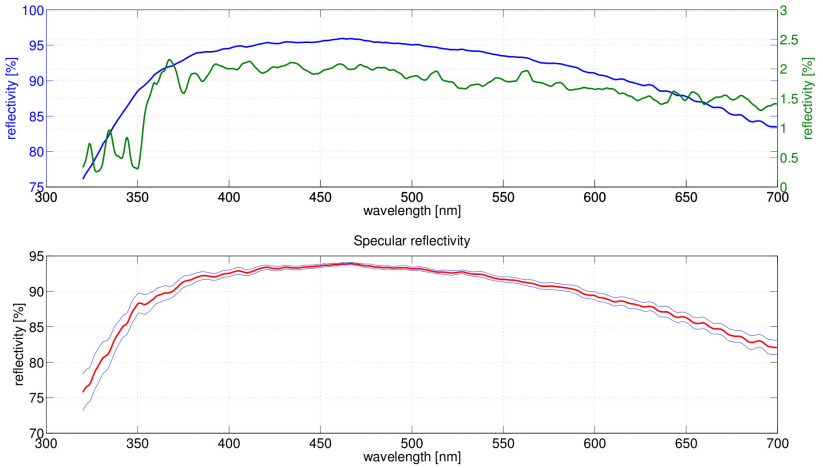

(a) A296

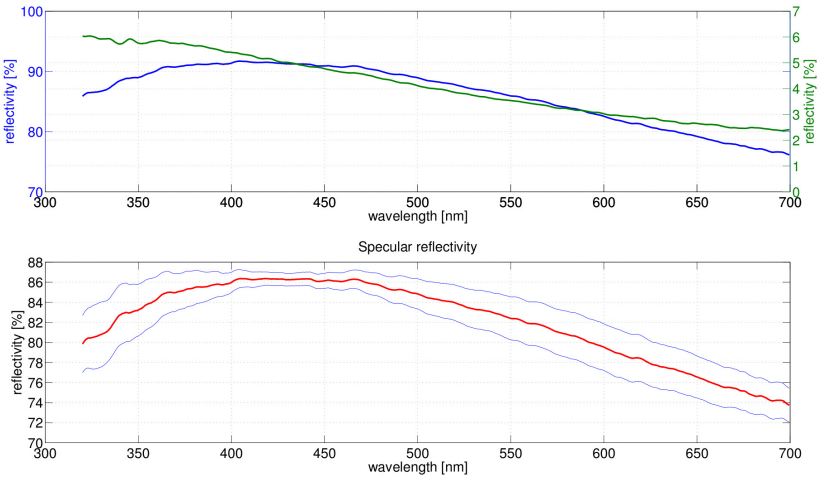

(b) n901

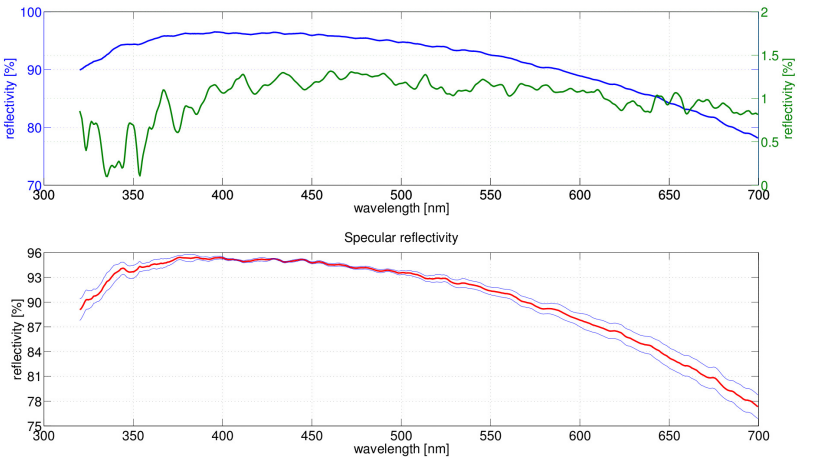

(c) MST P25

Figure 5.26: Results of the local reflectance measurement performed by the Olomouc facility.

deviation of ∼2% among the individual results.

While the spectrophotometers, used by the facilities of Tübingen and Olomouc provide a large wavelengths range, the measurement device used at the Padova facility is not optimized for measurements below 400 nm. In fact, the spec-

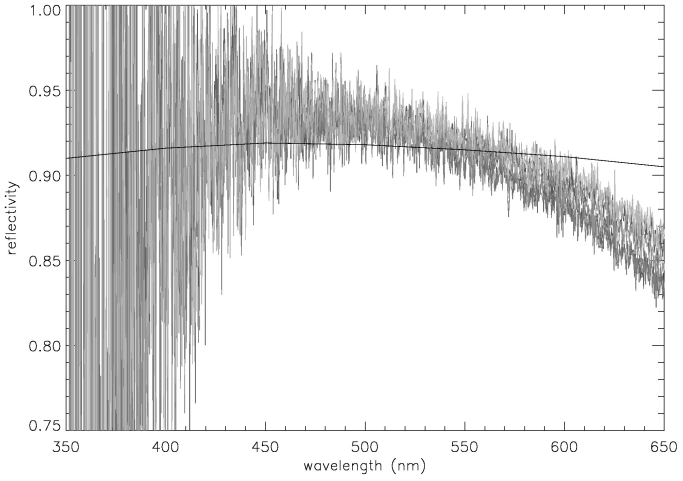

Figure 5.27: Results of the local reflectance measurement performed by the Padova facility.

trophotometer used by the Tübingen facility provides the most extended spectral coverage.

The distinct data plots provide different information. The presentation of the spectral curves measured at different positions enables the study of the coating homogeneity. Such study is not possible from the averaged spectral curve. The inclusion of the spectral curve of the diffusely reflecting component is a good estimate for the mirror roughness.

5.6 The Cross Calibration: Conclusions

It can be concluded that there are several technical and analytical reasons having a significant impact on the PSF measurement and the evaluation of the D_{80}.

First, the mirror mounting in the test setup has a significant affect: a tight fixation at the AMC mounting points might impose some deformation of the mirror surface causing a PSF enlargement. Second, the procedure to take the dark frame is another crucial issue affecting the correctness of the background subtraction and hence the PSF estimation. Third, the spot centering on the photodetector is essential to avoid the loss of information from the boundary area of the focal spot. Finally, an accurate determination of the nominal radius of curvature where the PSF is usually measured needs to be assured.

In particular, this cross calibration cycle made the necessity of a statistic and systematic error definition evident. The implementation of a temperature monitoring during the mirror testing as well as the full characterization of the light detector are recommended.

As for the data analysis, the procedure of the background subtraction is a vey crucial issue with regards to the PSF calculation. To prevent a significant over or underestimation of the PSFE, a background flatness in the Off region of the background subtracted signal frame must be guaranteed. Furthermore, the definition of the position on the focal spot image from which the signal is integrated in enlarging circles has an important impact on the D_{80} calculation. The cross check analysis of the individual data sets from the test facilities helped to point out the reasons for discrepancies between the individual results. Apparently, the discrepancy is most likely related to differences in the analysis codes. Furthermore, the comparison with the results obtained with the Daophot astronomic standard analysis software rendered the reliability of the test results from the Padova and Tübingen facilities more evident.

The discrepancy between the results obtained with PMD and the classical $2f$–method both performed by the Erlangen facility were traced back to the assumption of an ideal, point–like source used in the ray–tracing. An addition, a error in the absolute distance calibration and hence in the determination of the focal length was found. When modifying the size of the light source from infinite to the actual one used for the $2f$–method and applying an offset the focal length, the ray–tracing of the PMD results perfectly reproduces the spot image obtained with the $2f$–setup. This is an important achievement considering the compactness of the PMD setup. In addition, PMD is particularly suited to speed up mass testing.

The total reflectance has been only measured by three test facilities for slightly different wavelengths which makes a reasonable comparison at this stage rather difficult. However, the comparison of the results measured at 400 nm by the Saclay and Tübingen facilities shows a very good agreement for the H.E.S.S. and MAGIC mirror and small differences for the MST prototype.

The local reflectance measurement performed by three facilities showed good agreement, but the different data presentation disfavors a direct comparison quite difficult.

In conclusions, the definition of some guidelines on the PSF determination and data analysis are essential to assure a unified test procedure. In this way, some of the systematic errors can be ruled out. Moreover, the introduction of a standardized test log concerning including a unified result presentation as part of a detailed test report are the key element for the verification that the test was performed correctly. These guidelines are also necessary for the measurement of the absolute reflectance. In particular, the estimation of a realistic error regarding this parameter is of high importance. Recommendations for the procedure of the local reflectance testing on the mirror surface and the plots to be delivered should be also provided.

6

Active Galactic Nuclei & the Extragalactic Background Light

Active galactic Nuclei populate numerously the extragalactic sky. They are known to be the most luminous persistent objects in the Universe. Powered by the mass accretion of a *supermassive black hole*, most of their electromagnetic radiation is emitted in two narrow jets of opposite direction. In correlation with the viewing angle, the observed spectral energy distribution of the radiation varies.
The Extragalactic Background Light is an important issue with respect to the luminosity of the extragalactic VHE γ–ray sky. The term refers to the the light emission by stars that is partially reprocessed by dust. Furthermore, this emission is redshifted due to the expansion of the Universe, resulting in a background radiation in the UV, optical and IR band.
The first part of chapter is dedicated to the discussion of astrophysical mechanisms and spectral properties related to AGNs. In particular, an emphasis is given on blazars, a subclass of AGNs that is distinguished by its jet orientation at small angles with respect to the line of sight.
In the framework of the existing cosmic photon backgrounds, the Extragalactic Background Light is introduced in the second part of the chapter. A detailed report on the latest results of observational and theoretical studies on the EBL is presented. Furthermore, the impact of the EBL absorption on the VHE γ–ray emission of TeV blazars is outlined. The chapter concludes with the description of a recently derived method on constraining the distance of blazars based on the measured spectral properties by using the EBL absorption as a tracer of the distance of the TeV emitter.

6.1 Active Galactic Nuclei

It is believed that likely every galaxy hosts a nucleus at its center. Such nucleus represents a compact region, most likely a black hole (BH). In few cases, the nucleus, most likely a supermassive black holes (SMBH), exceeds the brightness of the remaining host galaxy, wherefore it is classified as active and the compact regions at is core is known as *Active Galactic Nuclei* (AGN) [55].

The radiation emitted by such luminous cores covers typically the entire electromagnetic spectrum from radio to γ–rays that cannot be clearly or directly attributed to stars. Instead, the radiation of an AGN is believed to originate from the matter accretion and ejection by the SMBH. Since such radiation is related to extreme physical processes, the study of such extragalactic objects allows for probing the Universe on large scales in terms of its formation and evolution [321].

A common belief is that AGNs are powered by the mass accreting SMBHs leading to a relativistic outflow, highly collimated into so-called *jets*. However, the accretion mechanisms are not fully understood despite their intensive study. In addition, many fundamental aspects of the jet related to its generation, its composition and the processes responsible for the particle acceleration therein are poorly determined. Therefore, the comprehension of the most relevant characteristics of an AGN and how they govern its emissivity remain a puzzle important to be solved [55].

6.1.1 Classification

It is commonly assumed that likely every galaxy hosts at its center a BH. In 99% of the cases, the BH is in a quiescent state not showing any activity. The remaining 1% of galaxies exhibit an active SMBH of the order of $\sim 10^6$ to $\sim 10^9 M_\odot$, in their center, referred to as AGN [55]. AGNs have in common to be extremely compact, massive regions, emitting radiation across the entire electromagnetic spectrum with a bolometric luminosity that ranges from $\sim 10^{42}$ to $\sim 10^{48}\,\mathrm{erg\,s{-}1}$ ($\simeq 10^{12} - 10^{15} L_\odot$. Therefore, AGNs can be up to 10^4 times brighter than an average galaxy [55, 188]. Furthermore, they are known to be variable objects, leading to a variability in their emission over the entire electromagnetic spectrum or parts of it on the time scale from minutes to days.

Despite the wide acceptance of the common SMBH scenario and the existence of a unified scheme (see Section 6.1.2), AGNs have been classified into numerous subclasses according to their observational spectral characteristics. In order to disentangle the confusing AGN zoo containing a large number of classes and subclasses appearing in AGN literature, a more simplified classification has been proposed based on the radio–loudness and the width of emission lines [321]. Table 6.1 presents the division of AGNs into the two main classes of *radio–quiet* and *radio–loud* objects depending on their radio–to–optical flux ratio, measured at 5 GHz and in the B band, with the boundary set to ∼10.

Radio Loudness	**Optical Emission Line Properties**		
	Type 2 (Narrow Line)	**Type 1** (Broad Line)	**Type 0** (Unusual)
Radio-quiet (80-90%)	Seyfert 2	Seyfert 1 QSO	
Radio-loud (10-20%)	NLRG { FR I, FR II }	BLRG SSRQ FSRQ	Blazars (<5%) { BL Lacs, (FSRQ) }
	decreasing angle to the line of sight ⟶		

Table 6.1: Scheme of a simplified AGN classification as a function of the radio-loudness and the width of emission lines in the optical and UV spectrum. Adapted from [246].

The radio–loudness distributions for AGN samples revealed a clear bimodal population (e.g. [303, 177]).

As a function of their emission line widths, radio–quiet objects are further grouped into *Seyfert 2 galaxies*, and *Seifert 1 galaxies* and *radio quiet quasars* (QSO), exhibiting narrow and broad emission lines respectively, with 1000 km be-

ing the dividing level [246]. While the majority is presented by radio–quite AGNs, radio–loud AGNs amount to not more than 10-20%.

The latter group is subdivided into the classes of *narrow–line radio galaxies* (NLRG), broad-lined objects, and objects showing weak emission lines. Based on their radio morphology, NLRGS are distinguished as *Fanaroff–Riley* I and II objects (FR I and FR II [110]), while broad–lined objects are subdivided into *broad–lined radio galaxies* (BLRG) and *radio quasars* (RQ).

According to their spectral index in radio at few GHz, RQs belong to the class of *steep–spectrum radio quasars* (SSRQs) or *flat–spectrum radio quasars* (FSRQs), with the division line set to 0.5 under the assumption of a simple power law. Such distinction reflects the size of the radio emitting region, since, if extended, a relatively steep spectrum due to synchrotron radiation is observed. In the opposite case, a compact nuclear region is associated with a flatter radio spectrum thought to result from the superposition of various self–absorbed components originating from the core. The flat spectrum indicates then a domination of the core emission over the radiation from the the extended regions, named *lobes* (see Figure 6.1).

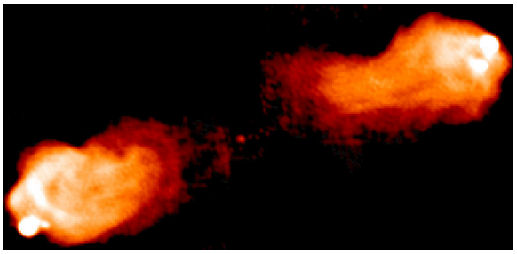

Figure 6.1: Radio image at 5 GHz of the RG Cygnus A provided by the the NRAO Very Large Array located near Socorro, New Mexico. The thin radio jets extending from the bright AGN toward the distant radio lobes are clearly visible. Thanks to their orientation to the LoS, RG allow for spatial studies of the AGN jets. Credit: VLA/J.Conway and P. Blanco.

Despite the presence of clear emission lines, FSRQs are also included in the "Type 0" class of radio–loud AGNs represented by *blazars*, characterized by weak emission lines, due to the domination of their multifrequency spectra by non–thermal emission.
The other subclass of blazars is represented by *BL Lacertae* objects (BL Lacs) that show only weak emission lines with typical equivalent widths <5 Å displaying mainly a continuum emission.

The successive descriptions will be concentrated on radio–loud types of these objects. A special emphasis is given on the BL Lacs, as this work is dedicated to the study of two such objects, namely 1ES 0806+524 and 1ES 1011+496 .

6.1.2 From the AGN Zoo to a Unified Model

The *unified model* is one of the most supported theories regarding radio–loud AGNs based on the concept that some classes of apparently different AGN might actually be intrinsically the same class of objects observed at different angles with respect to the line of sight (LoS) (e.g. [40, 321]). Thus, based on a common axissymmetric AGN structure, this theory unifies all AGN groups into one class by implying different observational properties at different aspect angles (see

Figure 6.3).

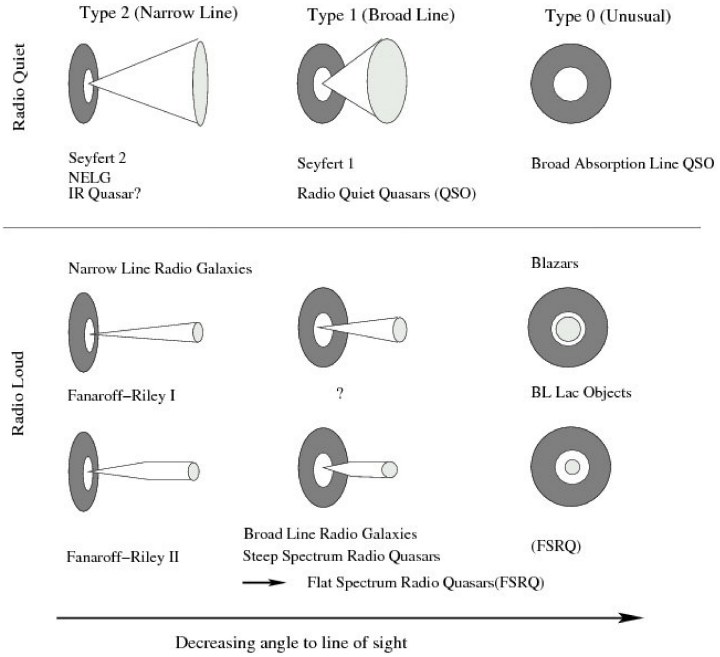

Figure 6.2: Standard classification of AGN sources based on the orientation of their jets to the LoS according to [321]. The horizontal axis indicates the inclination of the source axis with the LoS, decreasing from 90° to 0°. Adapted from [223].

The physical structure of AGNs as proposed in the unified model is illustrated in Figure 6.2. A spinning SMBH, with $M \sim 10^6 - 10^9 M_\odot$ and high gravitational potential, is considered to be the central engine of an AGN that provides an energy release through matter accretion from a surrounding, flat, rotating accretion disk. With an efficiency of the order of 10%, this process is much more efficient that nuclear fusion.

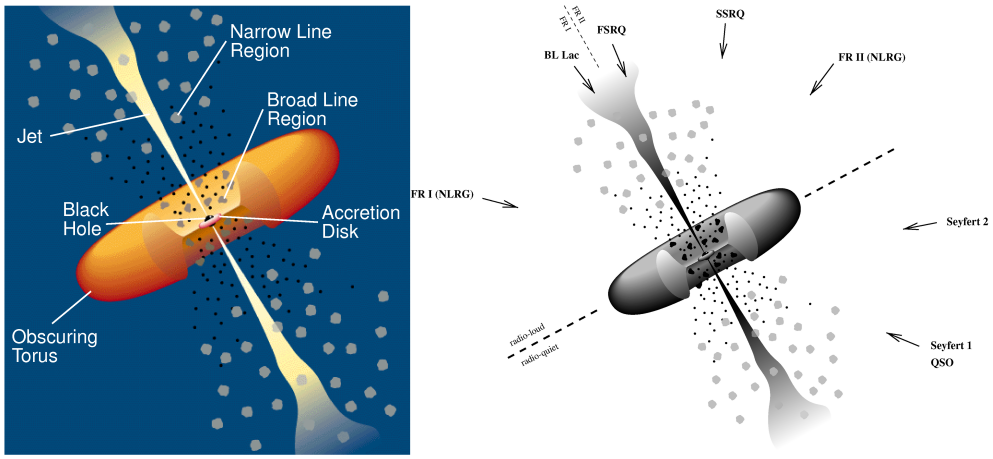

Figure 6.3: *Left:* Unified scheme of an radio–loud AGN indicating the individual components, emission regions and zones. Credit: C.M. Urry and P. Padovani. *Right:* AGN classification adapted to the viewing angle to the LoS [318].

Applying the unified model to radio–loud AGNs, these can be grouped in the following categories:

- **Radio Galaxies:** The jets of these AGNs are inclined by an angle >30° to the LoS. Due the reprocessing of the radiation from the inner disk and the BLR by the torus, the central black hole occurs obscured with respect to the galaxy, while an intense synchrotron radiation in the radio band originating from the jets and the lobes is observed.

- **Blazars:** When observing the jets face–on, i.e. 0°, the intrinsic, isotropic properties appear differently. Due to the production of GeV to TeV photons in their relativistic jets, these objects are particularly relevant in the field of γ–ray astronomy. Depending on their emission properties in the optical regime, blazars are further classified as FSRQs and BL Lacs exhibiting both a two bump continuum.
  While FSRQ spectra exhibit evidence of the BLR and the NLR added to a thermal spectrum related to the accretion disk, the optical spectra observed from BL Lacs are dominated by a continuum emission characterized by the absence of emission (see Figure 6.4).

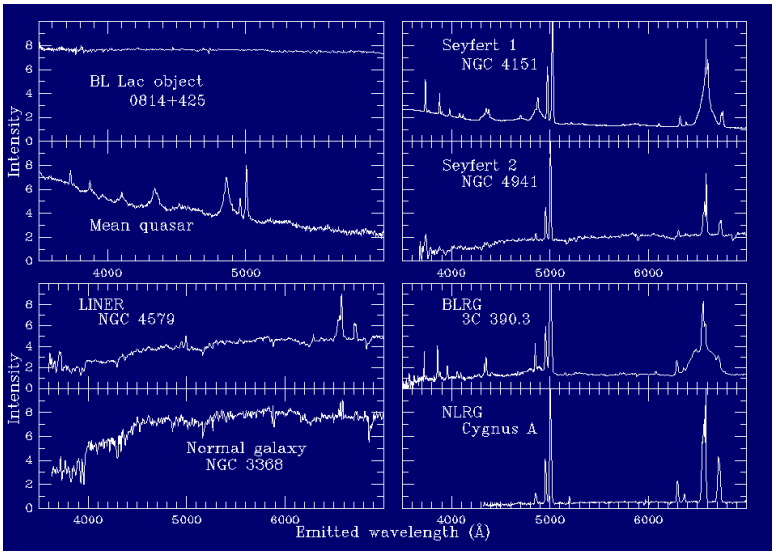

Figure 6.4: Confrontation of the optical spectra of a BL Lac object (upper left panel) with other radio–loud and radio–quite AGN objects.

Typically, the *Spectral Energy Distribution* (SED) of blazars (see Section 6.1.5) is composed of two bumps, the first occurring at low energies, that is in the radio to X-ray regime, and a second one located in the high energy range from X-ray to γ–ray that are most probably correlated. Depending on whether to the peak frequency of the bump at low energies is located in the radio, optical or X-ray band, BL Lacs are further categorized as *low*, *intermediate* and *high*–peaked objects (HBL, IBL, LBL). According to the peak position of the low energy bump, the second bump is shifted correspondingly (see Section 6.1.6). For this reason, HBLs appear to be ideal VHE photon emitters.

BL Lacs are characterized by a very fast emission variability and an unusually high and variable polarization. Such emission and polarization variability is demonstrated during a so–called *flare*, during which an AGN features a highly variable, increasing flux over a short time period.

6.1.3 The Accretion and Ejection in AGNs

Towards the SMBH, the rotation velocity of the matter, which transform their kinetic energy into thermal radiation via viscose torques acting on them, increases with temperature. Consequently, the observed radiation from the disk is a superposition of several black body spectra that appears as the so–called *big blue bump* in the the optical to UV band of the spectrum [188]. The radiation process depends strongly on the mass of the SMBH and the accretion rate so that the luminosity of the object L can be expressed by:

$$L_{\mathrm{acc}} = \epsilon \dot{M} c^2 \tag{6.1}$$

, where $\dot{M}$ and ϵ denote the mass accretion rate and accretion efficiency. In particular the properties of the accretion disk, have an impact on the efficiency of this process. In case of BL Lacs, the disk is *optically thin*, which leads to an inefficient accretion, i.e. $\epsilon \ll 0.01$, and therefore to a low luminosity. In the opposite case, an *optically thick* accretion disk, provides a relatively high accretion efficiency at the level of $\epsilon \sim 0.1$. Thus, a high luminosity is present in objects featuring such accretion disk [178]. Most likely, FSRQs provide an efficient accretion.

According to the *Eddington limit*, the disk emission is confined to an upper luminosity L_{Edd} that is reached when the outward force exerted by the pressure exceeds the inward gravitational force driven accretion:

$$L_{\mathrm{Edd}} = 1.25 \cdot 10^{38} \frac{M}{M_{\odot}} \, erg \, s^{-1} \tag{6.2}$$

,where $M_{\odot}$ refers to the mass of the Sun [188].

Potentially, a *corona* of hot electrons above the accretion disk is responsible for the emission of a hard X-ray continuum [246].

Due to the strong gravitational field, gas clouds move fast in the potential of the SMBH producing line emission that is widened by the Doppler broadening. Therefore, this very compact region formed in the central part of the AGN as region is referred to as *Broad Line Region* (BLR). Along transverse LoSs, the BRL emission is obscured by the absorption via an idealized *dust torus* located well outside the accretion disk and the BLR. The emission from the torus occurs mainly in the IR band.

Beyond this torus, gas clouds of slower motion generate narrower emission lines, wherefore this zone is denoted as *Narrow Line Region* (NLR) that consists of an extensive region. Both regions are pervaded by hot electrons on which some continuum and broad–line emission is scattered [246, 258].

6.1.4 The Relativistic Jets in AGNs

In the case of radio–loud AGNs, two relativistic jets emanate from the region near to the SMBH, extending up to large distances up to >100 kpc. Usually, they occur roughly perpendicularly to the disk, pointing to opposite directions[43]. It is commonly assumed that the jets are strictly connected to the accretion disk, as they are probably generated in the inner disk region. The jets consist of ionized matter outflow, that is most likely electrons and probably protons as well as their interaction products, moving with relativistic velocity, immersed in a strong magnetic field. Despite these commonly accepted assumptions, neither the exact

[43] In the case of head–tail RGs the jet emission is distorted

mechanism responsible for the jet formation nor the main jet properties such as their ultra relativistic nature as well as their tight collimation have been clarified.

An attempt to explain powerful jets in AGNs is based on the *Blandford–Znajek mechanism*, in which an electromagnetic extraction of energy and angular momentum from the SBMH and its surrounding disk [62] is proposed, linking the generation of the jet power closely to the accretion rate and therefore to the disk luminosity. Recently, this mechanism has been examined under varying boundary conditions, revealing its robustness upon such conditional variations [249]. Moreover, recent radio interferometry observations succeeded to spatially resolve the base of the jet of the elliptical *Radio Galaxy* (RG) M87, indicating the jet to be powered by an accretion disk in a prograde orbit around a spinning BH [99].

Beside these uncertainties regarding jet physics, it is commonly agreed that the jet emission, spanning from radio to γ–ray frequencies, is associated with blobs of charged material, which undergo acceleration in relativistic shock waves. In addition, the emitted radiation is *relativistically beamed* into the forward direction (e.g. [61, 212]) leading to a *Doppler–boosting* into the LoS (see Figure 6.5).

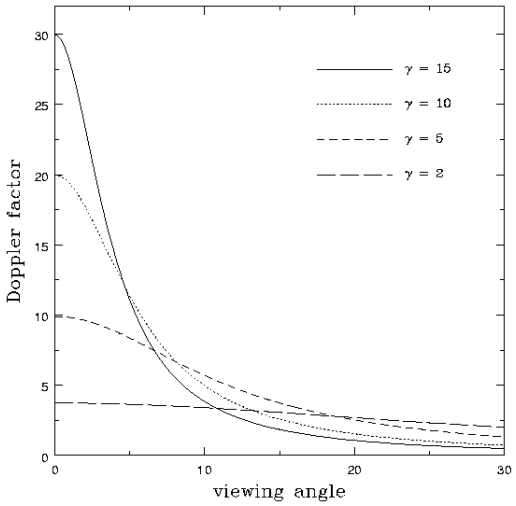

Figure 6.5: Doppler factor as a function of the angle between the velocity vector and the LoS for different Lorentz factors [247].

Relativistic Beaming

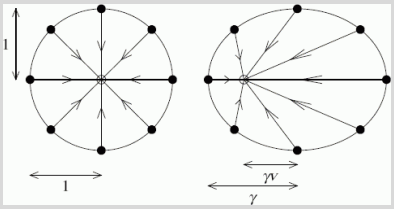

Figure 6.6: The phenomena of relativistic beaming.

Relativistic beaming, also know as Doppler beaming or headlight effect, is a process that leads due to relativistic effects to the modification of the apparent luminosity of emitting matter moving at velocities close to the speed of light. Provided a source that emits isotropically in its rest frame, is moving relativistically, its radiation appears strongly anisotropic and mainly the following effects occur in the emitted spectrum observed:

Light aberration: Depending on the relativistic velocity of the emitting particles, their radiation is collimated in a cone of an angle given by $sin\theta = 1/\gamma$. As the opening angle of the cone is strongly correlated to the relativistic velocities involved, the radiation collimation increases with higher relativistic velocities.

Arrival time contraction: The time intervals of the photon emission $\Delta t_{\rm em}$ and their arrival $\Delta t_{\rm arr}$ differ. Their relation is a function of relativistic velocity and the angle θ between the velocity vector and the LoS:

$$\Delta t_{\rm arr} = \gamma(1 - \cos\theta)\Delta t_{\rm em} \equiv \frac{\delta}{\Delta t_{\rm em}} \tag{6.3}$$

Here, the Doppler factor δ is introduced, which is of the order of tens in the case of blazars, where the orientation angle of the source to the LoS is small and high relativistic velocities are involved. The relation exceeds unity for small viewing angles so that the time intervals observed are contracted. Suppose the jet emission is variable, the variability timescale of is affected by such contraction.

Blueshift/Redshift of frequencies: As a function of the moving direction, the frequency of the emitted $\nu_{\rm em}$photons from the relativistically moving source is observed blue–shifted or red–shifted. In the case of blazars, the observer looks into the jet from which the emission is moving towards such observer, wherefore the observed spectrum is shifted to higher energies according to the relation:

$$\nu_{\rm obs} = \delta\nu_{\rm em} \tag{6.4}$$

Furthermore, it has been demonstrated that the relation between the observed and emitted luminosity are also related via the Doppler factor:

$$L_{\rm obs} = \delta^a L_{\rm em} \tag{6.5}$$

The parameter a, which assumes a value larger than one, is associated with the jet and emission properties.

References: [136] and references therein.

Images: The radiation properties as observed in the non relativistic and the relativistic case are confronted.

Observations of the jet emission confirmed the domination of non–thermal processes due to the ultra relativistic particle nature. The emission that peaks

at radio frequencies is attributed to synchrotron radiation emitted by ultra relativistic electrons interacting with the magnetic field inside the jet. In addition a high energy component probably associated with IC scattering has been observed. Further evidences of the existence of relativistically moving material have rosen from the detection of regions of *superluminal motion* observed in some *quasars* (e.g. [325]) and RGs (e.g [60]), see Figure 6.7, and from the asymmetry of the giant radio lobes [192, 130].

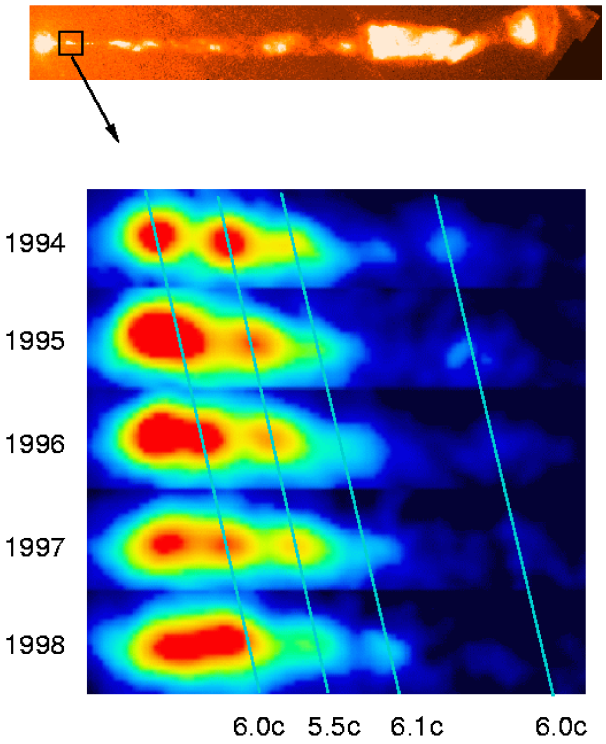

Figure 6.7: Superluminal motion as observed with the Hubble Telescope from the RG M87 seen in the black box (top panel). The sequence of Hubble images show motion at six times the speed of light (bottom panel). The slanting lines track the moving features. Credit: John Biretta, Space Telescope Science Institute.

Superluminal motion in Jets

Superluminal motion, i.e. motion at an apparent velocity that exceeds the speed of light c can be explained as a trigonometric effect. Assuming a blob of emitting material moving with a velocity close to c in a direction at a small angle θ to the LoS, that emits first a photon at position O and later at position C. An observer who sees the blob moving measures the time τ_e between both emissions and the distance l equal to $\beta c\tau_e$ the cloud has moved. The motion projected along the LoS is $\beta c\tau_e \cos\theta$ and $\beta c\tau_e \sin\theta$ respectively if projected perpendicular to it. Compared to the signal radiated when the cloud was at point O, a distant observer recognizes the emissions along the LoS delayed by an apparent time $t_{\text{app}} = \tau_e(1 - \beta\cos\theta)$. The apparent transverse velocity β_{app} of the moving blob seen by the observer is then:

$$\beta_{\text{app}} = \frac{\beta \sin\theta}{1 - \beta\cos\theta} \tag{6.6}$$

It is evident that the apparent speed exceeds the speed of light provided that small angles θ and relativistic velocities are involved. It reaches its maximum when:

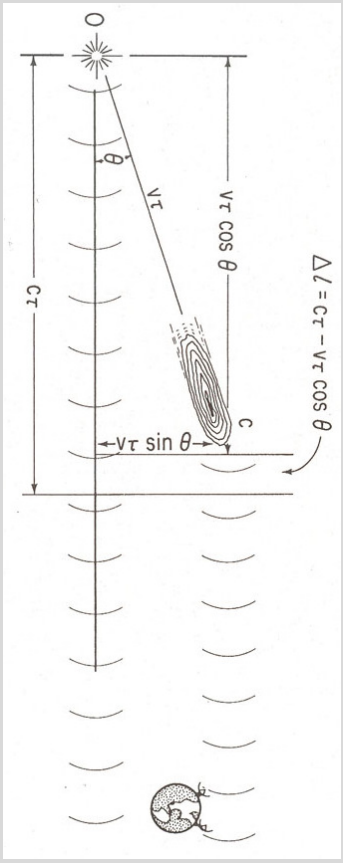

Figure 6.8: Phenomena of superluminal motion.

$$\cos\theta = \beta \tag{6.7}$$

, where $\beta_{\text{app}} = \beta\gamma$. Lorentz factor of the moving material is denoted with γ.

References: [136], and references therein.

Images: Schematic view the apparent superluminal motion [176].

6.1.5 The Spectral Energy Distribution of Blazars

The SED of blazars, i.e. radio–loud AGNs whose relativistic jets are closely aligned to the LoS, is dominated by a non–thermal, relativistic beamed continuum generated in the relativistic jets [321]. Typically, the SED shows a distinct double–peaked structure, whose broad peaks are situated at low and high energies.

The emission at low energies, usually highly polarized, is commonly interpreted as synchrotron radiation, while the emission at high energies is supposed to originate from IC scattering of photons. These are widely assumed to originate either from the same population of electrons responsible for the synchrotron radiation or due to an external photon field, referred to as *Synchrotron Self–Compton* (SSC) or *External Compton* (EC) scenario respectively (see Section 6.1.7). However, the origin of the high energy peak has been proposed to be also related to hadronic

processes, where VHE γ–rays are generated by the interaction of protons in the jets.

Depending on which blazar subclass is concerned, the SED may feature optical lines. Potentially, the SED of FSRQs exhibit further distinct features such as the so–called *big blue bump*, which refers to a component visible in the optical to UV band that is related to thermal emission from an optically thick accretion disk (see Figure 6.9).

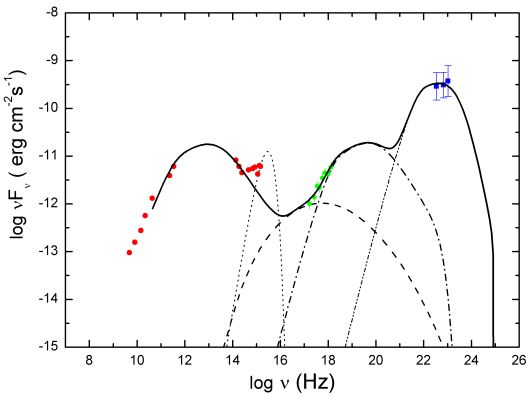

Figure 6.9: SED of the FSRQ PKS 1510-089 from quasi simultaneous multiwavelength observations of 2008. The dotted, dashed, dot–dashed and double–dot–dashed lines represent the different emissions from the accretion disk (black body), the SSC, the EC of the disk and of the BLR respectively [93].

By contrast, no or extremely weak optical lines appear in the SED of BL Lac objects, which makes the determination of their redshift difficult. Most of the extragalactic sources detected above 100 GeV are HBLs (see Section 6.1.8) whose peak of the synchrotron radiation bump is located in the UV to X-ray regime (see Figure 6.10).

The two broad bumps are mainly characterized by the flux level, the peak frequencies and the spectral slopes which typically vary in time given the fast variability of blazars exhibited at al accessible wavelengths. When undergoing a flare, the source flux can increase by several times within short time intervals. In general, the flare duration can vary in time scales from minutes to days. Such extraordinarily short flare has been observed from PKS 2155-304, where flux variations of the order of minutes occurred [17]. Also Mkn 501 is known to show such short variability [25].

The variability time scale is an important parameter by which it is possible to infer constraints on the size and location of the emission region[202]. Given a short variability for instance, the size of the emitting region can be constrained by the following causality argument:

$$R \leq ct\frac{\delta}{1+z} \tag{6.8}$$

where t denotes the characteristic variability time scale and δ and z correspond to the Doppler factor and the redshift of the source. In the case of M87, that is known to exhibit a variability of approximately one day, the 2010 TeV flare lead to an upper limit on the emission region size of $R \leq 5 \cdot 10^{15}\,\delta\,\mathrm{cm}$ [8].

Another important characteristic is the time correlation between different energy bands, which, if present, infers to a common origin inside one emission region. Such correlation has been observed in some sources between TeV and X-ray emission. However, in other cases so–called *orphan TeV flares* have been discov-

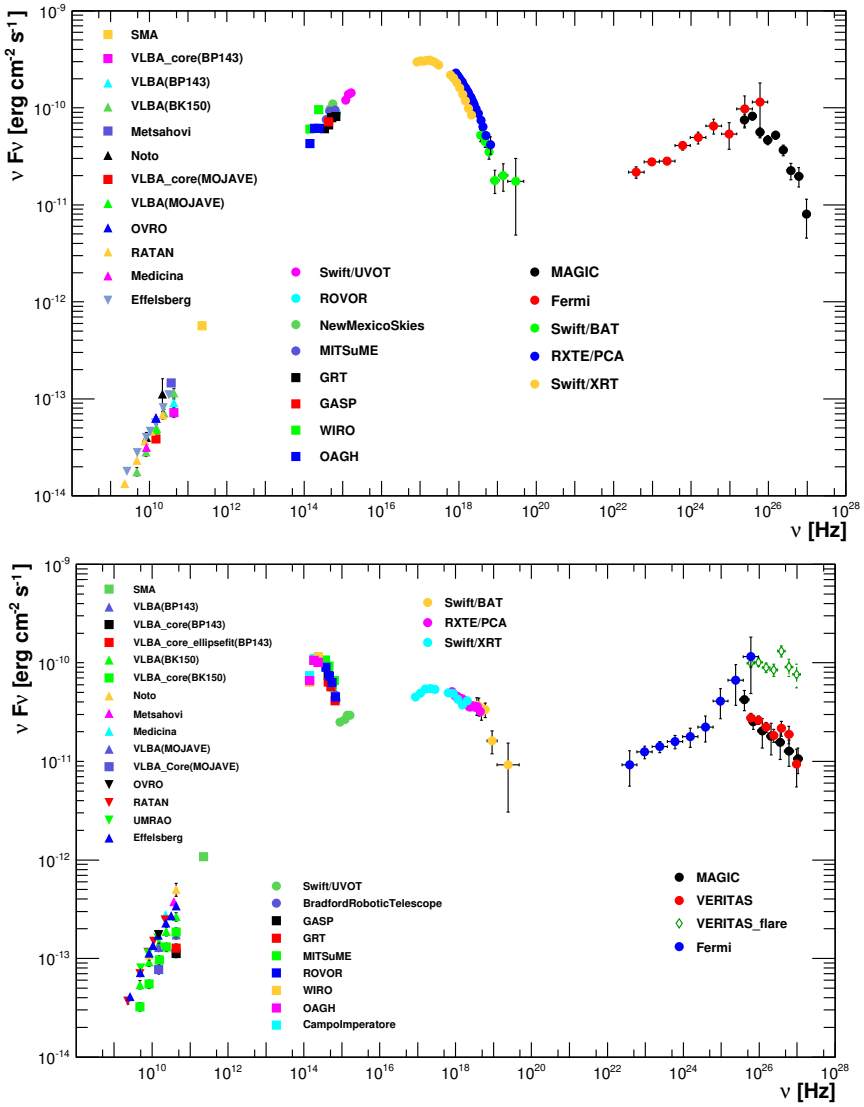

Figure 6.10: SED of the two HBLs Mkn 421 (upper panel) and Mkn 501 (lower panel) during their multiwavelengths campaigns carried out in 2009 [6, 7].

ered, missing a counterpart in X-rays. Such flares have been observed from 1ES 1959+650 [187, 94] and Mrk 421 [63] whose occurrence lead to discussion on their interpretation.

Besides the possibility to infer from short–term variability constraints on the size of the emission region, spectra variations associated to flaring states provide the opportunity to probe particle acceleration physics. Given the extreme conditions, relativistic jets are considered to be among the most powerful particle accelerators in the Universe, whose physical environment can not be reproduced on Earth. Considered as unique particle laboratories, relativistic jets allow for the study of cooling and heating processes of particles, related to a flux increase or decrease. A possible *hardening* or *softening* in the observed optical to UV spectrum respectively associated with flux variations is under debate (for details see [234]). In particular the correlation study of the fluxes observed in different wavebands is a powerful criteria to distinguish between potential emission hypothesis.

Therefore, nowadays the multiwavelength and multimessenger approach is ex-

plored to obtain a more complete picture of the physical processes powering the emission from blazars across the electromagnetic spectrum. For this reason, simultaneous observations at different frequencies as well as neutrino observations are coordinated among various instruments nowadays available. Such multi–messenger campaigns provides a detailed energy coverage allowing for the reliable study of the acting emission mechanisms (see text box) and have been established as standard approach for the study of blazars over the recent years (see Figure 6.11).

Coordinated multiwavelength observations on the Radio Galaxy M 87

Thanks to its proximity, famous jet, and very massive black hole, the giant RG M 87 provides a unique opportunity to investigate the origin of its VHE γ–ray emission, first detected in 2006, that displays strong variability on timescales as short as a day. A joint VHE monitoring campaign on M 87 by the MAGIC and VERITAS and H.E.S.S. instruments has been carried out in 2008 and 2010 during which two VHE flare detections triggered further observations at VHE. X-rays (Chandra) and radio (VLBA) were carried out to resolve the emission site in these wavebands.
Especially the detailed VHE γ–ray light curve in 2010 made the precise temporal characterization of the flare possible describing the single, isolated flare well by a two-sided exponential function with significantly different flux rise and decay times. Compared to VHE flares previously observed in 2005 and 2008, all three of them share very similar timescales of approximately on day, peak fluxes and VHE spectra.
However, the overall variability pattern of the 2010 flare appears somewhat different from these previous VHE flares. While VLBA radio observations of the inner jet regions indicate no enhanced flux in 2010 in contrast to observations in 2008, where an increase of the radio flux of the innermost core regions coincided with a VHE flare. By contrast, Chandra X-ray observations taken $\sim$3 days after the peak of the VHE gamma-ray emission in 2010 revealed an enhanced flux from the core. As the emission in VHE γ–rays is connected to radiation at longer wavelengths in a leptonic emission scenario (see Section 6.1.7), the correlation of the radio and VHE flare in 2008 enabled to constrain the VHE emission to occur well within the jet collimation region.
The long–term multiwavelength light curve of M 87 from 2001 to 2010, spanning from radio to VHE, has been used to further investigate the origin of the VHE γ–ray emission. In particular, no unique, common signature in a multiwavelength context could be identified to occur in the three detected VHE flares.

References: [8], and references therein.

Especially the correlation between the emission evolution in the X-ray and the γ–ray band allow for probing theoretical models of the VHE emission from blazars [174]. Taking into account the variability of blazars, the simultaneity of these observational campaigns is indispensable.

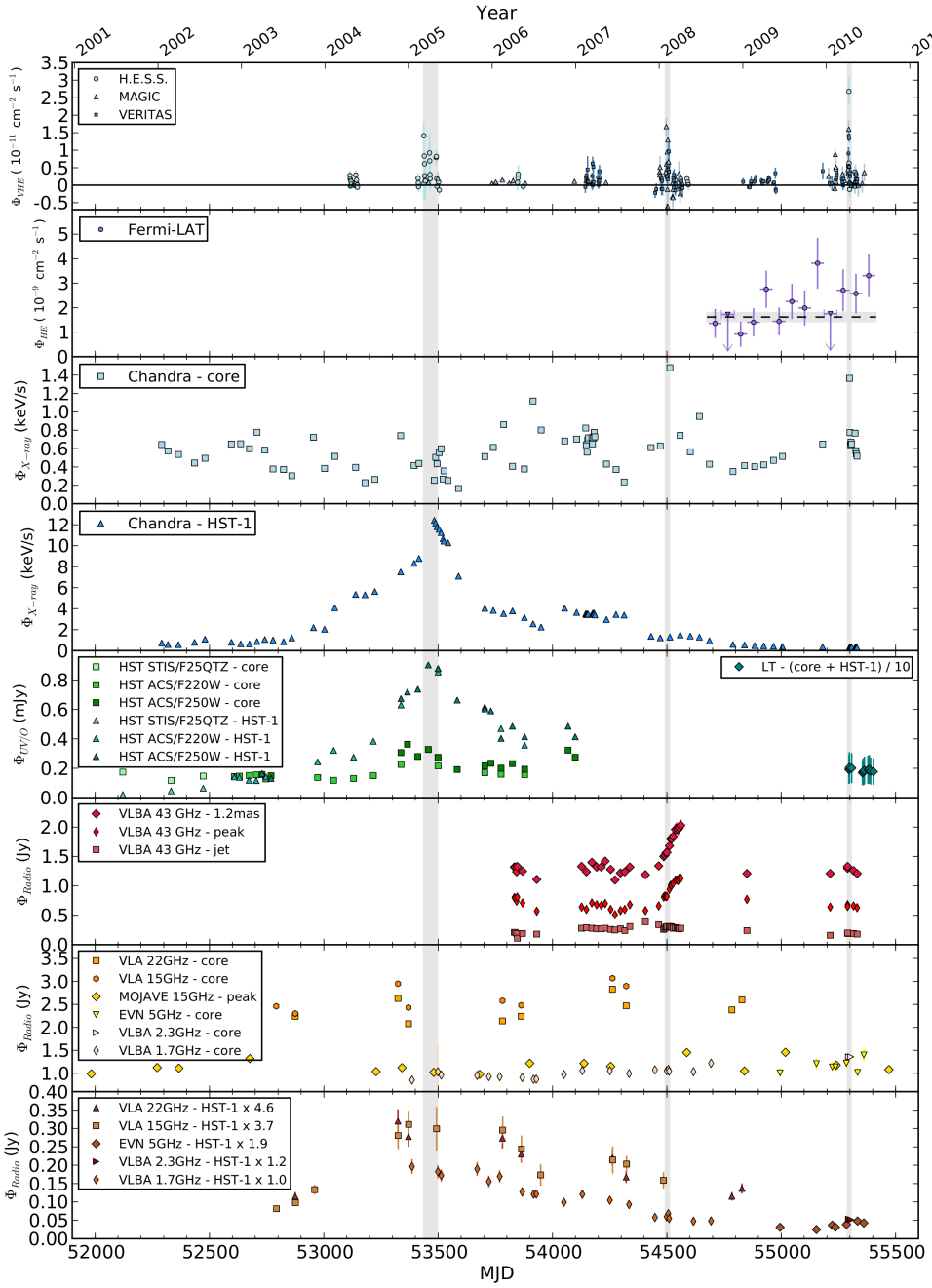

Figure 6.11: 10–years multiwavelength light curve of M 87 [8].

6.1.6 The Sequence of Blazars

The launch of the space borne *Energetic Gamma Ray Experiment Telescope* (EGRET) in 1991, gave rise to a systematic study on the various SEDs from a sample of blazars performed by [123] which resulted in a distribution named *blazar sequence* published seven years after the commissioning of EGRET (see Figure 6.12).

From this study, a blazar classification according to their radio luminosity, the position of the peak frequencies of the two emission bumps and the integral flux has been inferred. Less powerful blazars seem to present their synchrotron peak in the soft to medium X-ray band, while their high energy peak is located at the

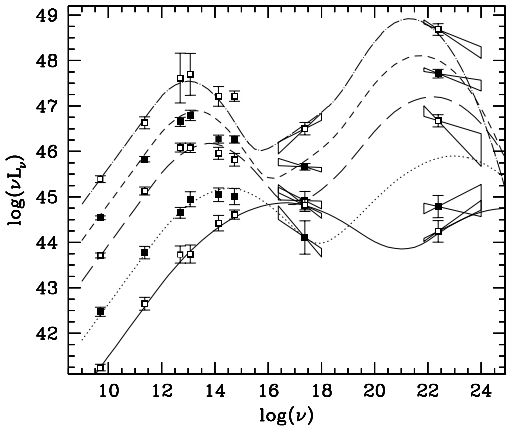

Figure 6.12: Average differential luminosity derived from a sample of 126 blazars referred to as blazar sequence. The individual markers denote different types of blazars [123].

highest γ–ray energies. With increasing power, both peaks are shifted to lower frequencies. Contemporaneously, the luminosity ratio between the high and low energy component increases with bolometric luminosity.

Based on this study and its first implications, further evidences have been proposed to apply a classification on the different blazar types. It has been proposed, that the individual blazar classes represent different sections in the blazar sequence according to their radio luminosity [141]. While FRSQs are distinguished by the most upper curve in the spectral sequence exhibiting high radio luminosity, the lower curves classify different BL Lac objects. The lowest curve in the sequence corresponds to class of HBLs featuring the high energy peak at highest γ–ray energies. The radio luminosity of HBLs is much lower with respect to FRQs. IBLs and LBLs, for which the two peak frequencies are successively shifted to lower energies, are presented by the spectral sequence region in–between the curves marking FRSQs and HBLs. The two energy bumps of FSRQS are peak at even lower energies. Thus, the blazar sequence provides two classifications, i.e from bottom to top and from left to right.

After the commissioning of the *Fermi* satellite, new insights of blazars in the HE energy range have been obtained, providing the opportunity to further investigate the blazar sequence [139, 143]. Apparently, observations in this band confirm the blazar sequencse. In addition, a connection between the spectral index and the luminosity in γ–rays could be established separating FSRQs and BL Lac objects at a γ luminosity of $\sim 10^{47}\,\mathrm{erg\,s^{-1}}$ (see Figure 6.13).

The outcome of these investigations was the suggestion that FSRQs seem to have a steeper spectral slope in γ–rays than BL Lac objects. At the same time, the data propose, that FSQRS are more luminous than BL Lac objects. Therefore, the α_γ–L_γ distribution can be considered as the γ–ray selected version of the blazar sequence which has been clearly confirmed by these data.

Recalling the previous assumptions on the accretion efficiency with respect to BL Lac objects and FSRQs, the presence of an optically thin or thick accretion disk has an impact on the jet particles. In the case of FSRQs, the power of the jet particles is strongly reduced due to the interaction with the ambient photons from the accretion disk whereas the opposite situation is present in BL Lac objects such

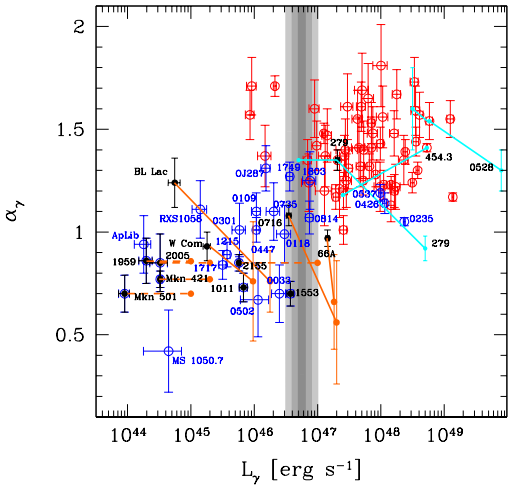

Figure 6.13: Blazar division from the first three months *Fermi* catalog. BL Lac objects and FSRQs are indicated by blue squares and red circles. The black filled circles mark the blazars already detected in the TeV band [139].

that the energy of the jet particle is preserved during their propagation. Based on these considerations physical basis was found in the framework of the blazar unification, postulating a correlation between the jet and disk luminosity. This physical concept indicates, that BL Lac objects and FSRQs might be objects of similar mass which are coupled to the radiation efficiency of the accretion disk, provided that the accretion efficiency among them differs [213].

In addition, by means of the recent blazar observations carried out by *Fermi* a study on the correlation between the jet power and the disk luminosity has been performed (see Figure 6.14). It has been found, that these parameters show a clear connection of linear scale which confirm the assumptions postulated by the Blandford–Znajek mechanism [139].

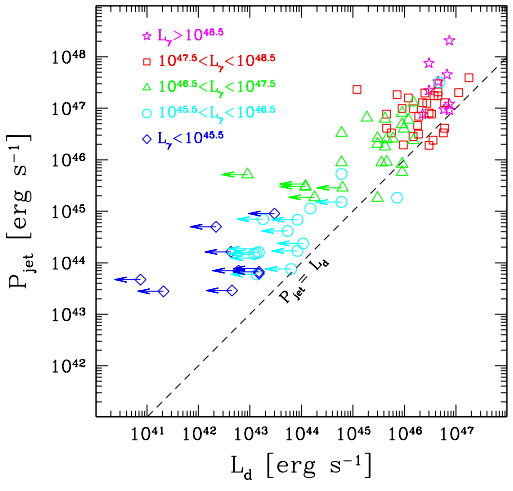

Figure 6.14: The correlation between the accretion disk luminosity and the total jet power. While the disk luminosity L_d was observed directly in FSRQs, upper limits have been derived for BL Lac objects [139].

Based on a larger data sample of *Fermi* sources, recent studies have been performed to investigate the transition between "pure" BL Lac objects and FSRQ proposing the classification of blazars based on the luminosity of the BLR measured in Eddington units [140]. This lead to a reclassification of some BL Lac objects into FSRQs (see Figure 6.15). Moreover, a trend has been found indicating that the luminosity of the BLR and the luminosity in γ–rays expressed in Eddington units $L_{\rm BLR}/L_{\rm Edd}$, $L_\gamma/L_{\rm Edd}$ as well as the SED type, i.e. LBL or HBL,

are strongly linked.

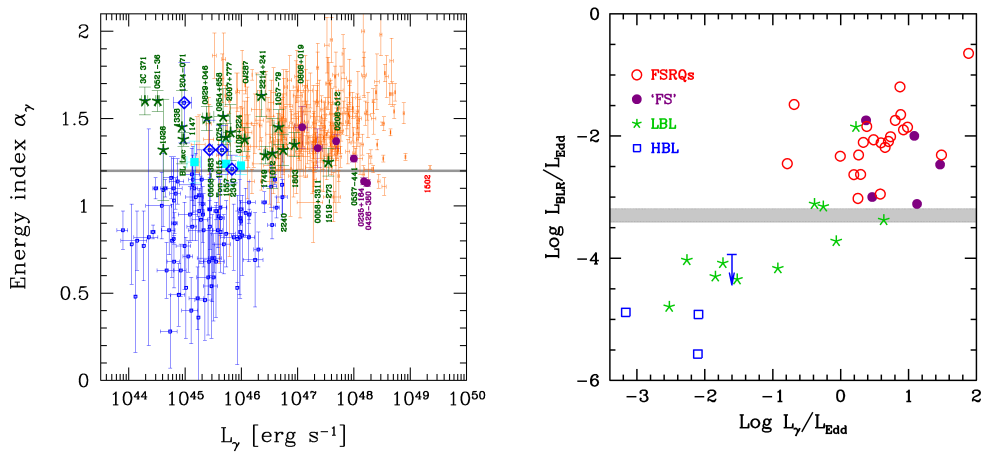

Figure 6.15: Updated blazar classification based on *Fermi* observations. *Left:*α_γ–L_γ distribution showing a reclassification of BL Lac objects (blue squares) into LBLs (green stars), IBLs (cyan squares) and HBLs (blue diamonds) and FSRQs (violet circles). The remaining FSQRs are marked in orange. *Right:* Luminosity of the BLR expressed in Eddington units [140].

Recently, the blazar sequence has been updated including the multifrequency data collected over the last decades whose classification has been based on the γ–ray luminosity (see Figure 6.16).

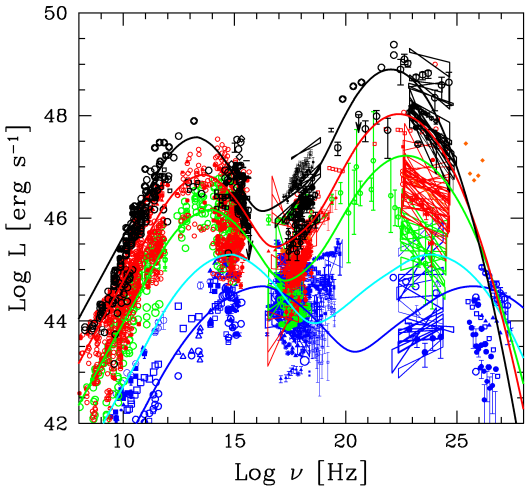

Figure 6.16: TThe updated blazar sequence binned in γ–ray luminosity [137].

6.1.7 Emission Models

In general, two different mechanisms are proposed to be the associated with the photon emission of the high energy bump observed in the SED of blazars that is related to an either leptonic or hadronic scenario. The next sections are dedicated to a brief description of both model types.

Leptonic Emission Models

Leptonic models explain the radiation in the optical to X-ray bands as synchrotron radiation from a population of non–thermal electrons, while the VHE γ–rays are proposed to originate from the upscattering of low energy photons by electrons via the IC process (see Figure 6.17).

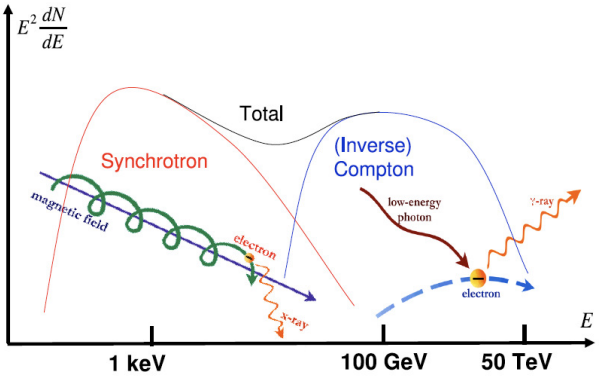

Figure 6.17: Illustration of the leptonic emission model (Courtesy A. de Angelis).

Depending on the nature of the radiation field involved, different models of varying complexity have been proposed. The simplest case is a SSC model, where the synchrotron photons act as seed photons of the VHE γ–rays produced by IC scattering assuming *one zone* as emission region limiting the involvement of electrons to one single population from one region responsible for the homogenous emission [307].

The one–zone SSC model consists of the following input parameters:

B the magnetic field intensity

R the radius of emitting region

δ the Doppler factor

n_1 the spectral index of the relativistic electron spectrum below the break energy

n_2 the spectral index of the relativistic electron spectrum above the break energy

γ_b the Lorentz factor of the electrons at the break energy

K the electron density parameter

Usually, the observed spectral shape of the SED requires a primary spectrum of the relativistic electron population to steepen with increasing energy, wherefore it is approximated with a broken power law, whose spectral index changes from $n_1 > 3$ to $n_2 < 3$, at the *break energy* at γ_b (see Figure 6.18).

In addition, the electron spectrum is characterized by a minimal, maximal Lorentz factor γ_min and γ_max and an electron density parameter K:

$$N(\gamma) = \begin{cases} K\gamma^{-n_1} & \text{if } \gamma < \gamma_b \\ K\gamma_b^{n_2-n_1}\gamma^{-n2} & \text{if } \gamma > \gamma_b \end{cases} \tag{6.9}$$

With this approximation and the inclusion of the magnetic field intensity B, the size of the emission region R and the doppler factor δ, the SSC model is completely specified by seven parameters.

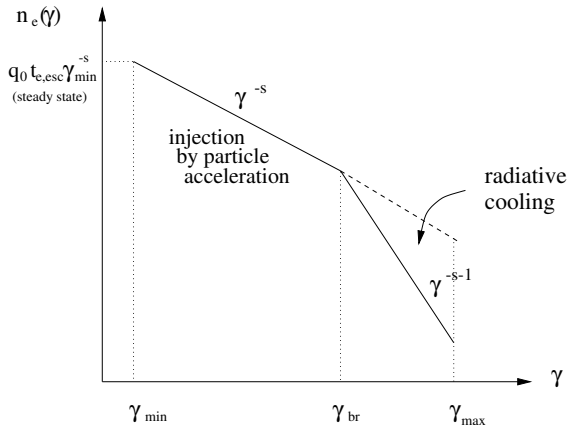

Figure 6.18: Sketch of the relativistic the relativistic electron energy spectrum assumed in the once–zone SSC model. The break in the spectrum is due to radiative cooling at high Lorentz factors [179].

When testing this model on available data of the SED, it is possible to derive six "observable" quantities as important input parameters:

- α_1 the spectral index of the rising flank of the SED bumps
- α_2 the spectral index of the falling flank of the SED bumps
- ν_s the frequency of the synchrotron peak
- ν_c the frequency of the inverse Compton peak
- L_s the luminosity of the synchrotron peak
- L_c the luminosity of the inverse Compton peak

These parameters are related to the observed SED (see Figure 6.19): the rising and falling flank of the synchrotron and the IC peak, characterized by the peak frequencies ν_s and ν_c and the luminosities L_s and L_c, can usually be well described by a power law of identical positive and negative slope α_1 and α_2.

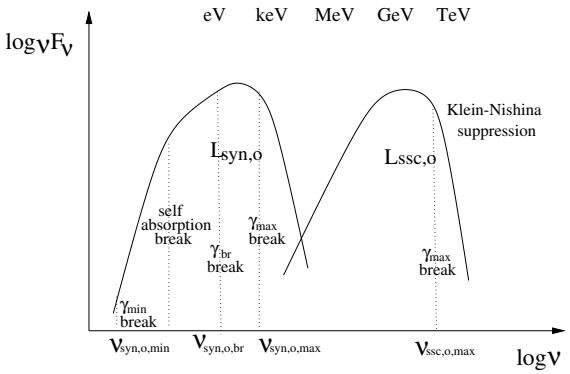

Figure 6.19: Schematic picture of the multifrequency SED of a typical TeV blazar. The break in the electron spectrum leads to a feature in the observed synchrotron spectrum [179].

Beside these quantities, the minimum time scale of variation $t_{\rm var}$ is sufficient to determine the system, as this is directly connected to the emission region R. Moreover, via the same causality argument it is possible to infer on the Doppler factor, if the transparency of the source to γ–rays is taken into account[44].

[44] High energy photons my interact with low energy photons via pair production. From observations of TeV photons, it is possible to set a limit on the optical depth of the source and therefore on the density of the soft radiation. This limit can be used to obtain a lower limit on the Doppler factor.

The typically standard parameters for HBLs during a TeV flare are listed in Table 6.2

Table 6.2: Typical one–zone SSC model parameter for the HBL Mrk 180 during a TeV flare [281].

Parameter		Value
γ_{min}	$[10^3]$	10
γ_{b}	$[10^4]$	30
γ_{max}	$[10^6]$	3.0
n_1		1.8
n_2		4.0
B	[G]	0.11
K	$[10^3\,\mathrm{cm}^{-3}]$	8.2
R	10^{15} cm]	1.0
δ	25	

As the one–zone SSC model is self–absorbed at radio frequencies, it lacks the explanation of radio emissions, implying emissions by further contributions from outer regions of the jet. Despite this defect, it is able to describe quite well a large amount of observed spectra.

In the case of external populations of low energy photons involved in the IC mechanism, the model is referred to as EC model, assuming the radiation to be associated with the accretion disk and the BLR. A more evolved model, that is the *mirror model*, assumes low energy photons that escaped from the jet to reenter the jet after their deflection on ambient dust under angles which favor their IC scattering [138]. Instead, *multiple–zone* models postulate more than one emitting region moving across the jet (see [289] and references therein for a review).

Hadronic Emission Models

According to hadronic models, the energetic photons produced in jets are the result of hadronic interactions. Different hadronic scenarii have been proposed, some of them suggesting the VHE γ–ray emission to be triggered by so–called *synchrotron pair cascades* (e.g. [210]). In this scenario, the photo–meson production, via $p\gamma$ or pp interaction leads to the generation of mesons like electrically and neutrally charged pions.

$$p + \gamma \rightarrow p + k\pi \tag{6.10}$$

$$p + p \rightarrow \pi + X \tag{6.11}$$

The neutral pions decay into photons (see Section 2.2), while charged pions generate charged muons (see Section 3.2.2). Eventually, these mesons decay further into electron–positron pairs, powering the leptonic production high energy photons.

If not escaped rom the jet, the photons can produce new electron–positron pairs that subsequently radiate a new generation of photons. Beside this mechanism, high energy radiation can also directly originate from synchrotron radiation of primary UHE protons [20, 231] and secondary muons (e.g. [267, 232]).

Although radio observations seem to confirm the presence of relativistic protons in AGN jets, hadronic models struggle to describe the luminosity observed in AGNs demanding extremely high proton velocities. In addition, the very short variability seen in some blazars is most unlikely to occur in hadronic processes which are relatively slow. For these reasons, hadronic emission mechanisms are

rather disfavored over leptonic radiation scenarios. Nevertheless, recent efforts have been made to use hadronic modeling of AGN variability (e.g. [293]).

6.1.8 The Extragalactic Sky as seen in VHE

Since the discovery of the first extragalactic VHE γ–ray emitter in 1992 by the Whipple Observatory [265], the randomly distributed population of such sources has been constantly increased (see Figure 6.20).

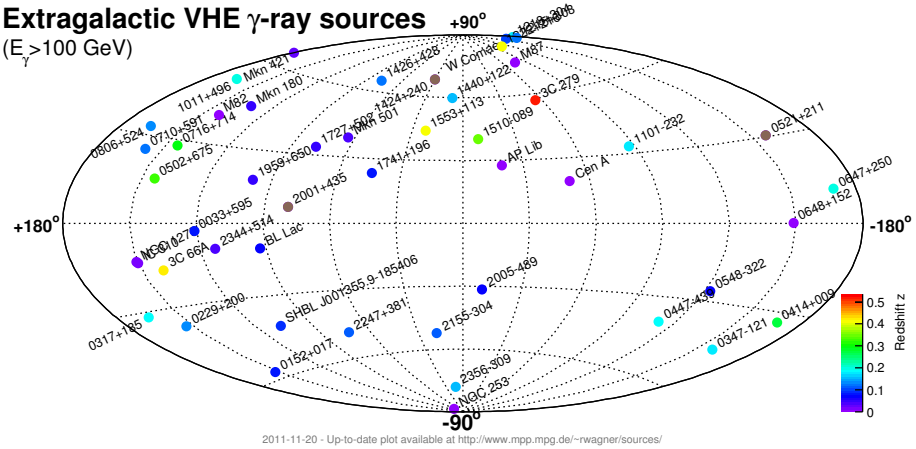

Figure 6.20: Sky map of known extragalactic VHE γ–ray emitters, taken from taken from http://magic.mppmu.mpg.de/∼rwagner/sources.

Especially the dawn of the third-generation IACT era lead to a substantial rise of VHE γ–ray source discoveries. To date, the TeV catalog, as listed in Table 6.3, accounts for 46 extragalactic objects out of which the majority constitutes of radio–loud AGNs.

Source	z	Type	Discovery
M82	0.0007	Starb.	2009^d
Centaurus A	0.0007	RG	2009^c
NGC 253	0.0008	Starb.	2009^c
M87	0.0044	RG	2004^c
NGC 1275	0.0175	Other	2010^b
IC 310	0.019	UFO	2010^e
Mkn 421	0.03	HBL	1992^a
Mkn 501	0.034	HBL	1996^a
1ES 2344+514	0.044	HBL	1998^a
Mkn 180	0.045	HBL	2006^b
1ES 1959+650	0.047	HBL	1999^f
AP Lib	0.049	LBL	2010^c
BL Lacertae	0.069	LBL	2007^b
PKS 0548-322	0.069	HBL	2007^c
PKS 2005-489	0.071	HBL	2005^c
RGB J0152+017	0.08	HBL	2008^c
SHBL J001355.9	0.0948	HBL	2010^c
W Comae	0.102	IBL	2005^d
PKS 2155-304	0.116	HBL	1999^f
B3 2247+381	0.12	HBL	2010^b
RGB J0710+591	0.125	HBL	2008^c

1H 1426+428	0.129	HBL	2002[a]
1ES 1215+303	0.13–0.237[†]	LBL	2012[b]
1ES 0806+524	0.138	HBL	2009[d]
1ES 0229+200	0.14	HBL	2007[c]
1ES 1440+122	0.162	HBL	2010[d]
H 2356-309	0.165	HBL	2006[c]
1ES 1218+304	0.182	HBL	2006[b]
1ES 0347-121	0.185	HBL	2007[c]
1ES 1101-232	0.186	HBL	2006[c]
RBS 0413	0.19	HBL	2009[c]
PKS 0447-439	0.2	HBL	2009[c]
1ES 1011+496	0.212	HBL	2007[b]
1ES 0414+009	0.287	HBL	2009[c]
S5 0716+714	0.31*	LBL	2008[b]
1ES 0502+675	0.341*	HBL	2009[d]
PKS 1510-089	0.36	FSRQ	2010[c]
PG 1553+113	0.40–0.47*	HBL	2006[c,b]
4C +21.35	0.432	FSRQ	2010[b]
3C 66A	0.444*	IBL	2009[d]
3C 279	0.536	FSRQ	2008[b]
MAGIC J2001+435	–	HBL	2010[b]
PKS 1424+240	–	IBL	2009[e]
RGB 0648+152	–	UFO	2010[d]
VER J0521+211	–	Other	2009[d]
MAGIC J0223+430	–	UFO	2009[b]

Table 6.3: List of the extragalactic objects known to be VHE γ–ray emitters sorted by redshift. Redshifts denoted with * refer to an uncertain distance, whereas † indicates the publication of two redshifts. The letters correspond to the the instrument by which the source has been discovered: Whipple Observatory[a]; MAGIC[b]; H.E.S.S.[c]; Veritas[d]; *Fermi*-LAT[e]; other[f].

While only two of the objects are known to be RGs, namely Centaurus A and M87, the major part of them belongs to the class of blazars. The three blazars PKS 1510-089, 4C +21.35 and 3C 279 are classified to be FSRQs, whereas the remaining objects are identified as BL Lacs, falling mostly into the HBL category. As the detection of LBLs and IBLs is much more difficult in the VHE band given the much lower flux at these energies (given their steeply falling spectrum), it is not surprising that only few of these objects have been discovered so far.

Beside radio–loud AGNs and the two objects that are identified as starburst galaxies, the remaining sources known to populate the VHE extragalactic sky are denoted as *other* sources and *unidentified* objects (UFOs).

The two objects labeled as "other" refer to the central radio galaxy of the Perseus galaxy cluster named NGC 1275, and to VER J0521+211, whose position is in agreement with the location of the active radio–loud galaxy RGB J0521.8+2112 within the errors.

A typical aspect of TeV emitters is their limitation in distance due to purely energetic reasons and the absorption effect of VHE photons by the interaction with the diffuse photon background during their travel (see Section 6.2). Therefore, the most distant TeV source discovered so far is 3C 279 located at redshift 0.536 [29],

neglecting the few sources of unknown distance. For some of the TeV sources the distance is determined with uncertainty.

Starburst Galaxies as VHE γ–ray emitters

Starburst galaxies feature exceptionally high star–formation rates (SFRs) in very localized regions, typically of the size of hundreds of parsecs, where the high SFR provokes an increase formation of massive stars. Hence, in these starburst regions a higher rate of supernovae explosions with respect to the remaining galaxy arises making them suitable sites for CR acceleration up to energies of $\sim 10^{15}$ eV. Both leptonic and hadronic interaction scenarii have predicted the emission of VHE γ–rays via the interaction of CRs with interstellar gas and radiation fields.

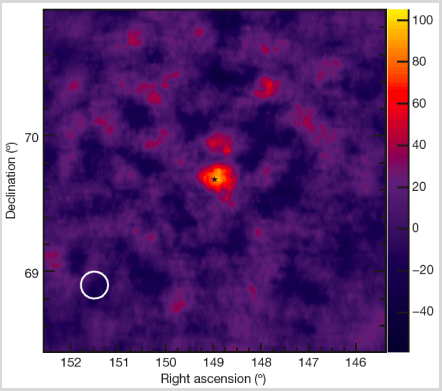

Figure 6.21: VHE γ–ray sky map of the starburst galaxy M82.

The detection of HE and VHE γ–rays from two archetypical representatives of such objects, namely M82 and NGC 253 by VERITAS and H.E.S.S triggered an enormous theoretical effort to explain the origin and properties of the γ–ray emission in different scenarios. Despite recent findings which support the theory that PWNe could significantly contribute the the observed γ–ray emission, most calculations are in favor of hadronic interaction mechanisms.

The discovery of VHE γ–ray emission of starburst galaxies strongly supports the hypothesis of the close connection between CR acceleration and massive star formation. In addition it confirms the assumption that supernovae and massive–star winds represent the dominant CR accelerators.

References: [243], and references therein.

Images: [171]

6.2 The Cosmic Background Radiation

The Universe is a huge space, whose emptiness is likely filled with some dark matter clumps located in the vicinity of galaxies and galaxy clusters as well as a diffuse radiation that covers the entire electromagnetic spectrum, also referred to as *cosmic background* (see Figure 6.22). Parts of it are believed to be a remaining from the early epochs after the *Big Bang* and therefore sometimes denoted as "primal glow" that has been redshifted over time.

The cosmic background is conventionally subdivided into several components of varying origin, which occur at different wavelength regimes. Typically, the different cosmic backgrounds are composed by diffuse radiation whose origin is both extragalactic and galactic. Obviously, the extragalactic component of these cosmic backgrounds is of higher interest since its provides deeper insights into the

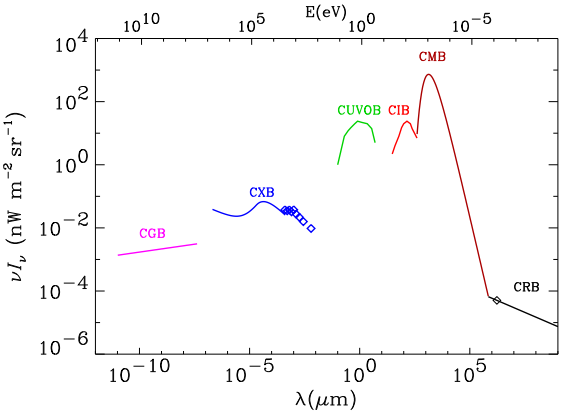

Figure 6.22: Spectrum of the cosmic background radiations permeating the Universe [153].

Universe's evolution. In most cases, the galactic component represents paradoxically a rather dominant *foreground* that often impedes the direct measurements of the extragalactic component.

- **CRB (Cosmic Radio Background):** Compared to the other backgrounds, the CRB, which consists of the diffuse extragalactic light emitted at wavelengths above 1 m, is relatively weak. Its radiation can be well described by a simple power law.

- **CMB (Cosmic Microwave Background):** The CMB, which is composed of photons that originate from the so–called *last scattering surface*, contains most of the electromagnetic energy of the cosmic background, filling the Universe almost uniformly (see Figure 6.23). As it stems from the decoupling of matter and radiation after the Big Bang, the CMB exhibits a thermal black body spectrum at a temperature of ∼2.725 K whose peak appears at a wavelengths of 1.9 mm.

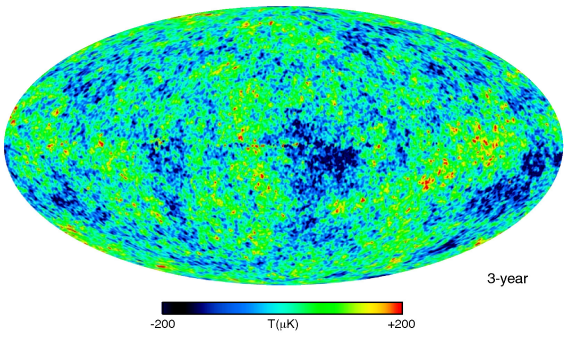

Figure 6.23: Temperature distribution of the CMB measured by the WMAP featuring few small scale anisotropy. Adapted from [161]

- **CIB (Cosmic Infrared Background):**The CIB, which covers the range from 1 to 1000 μm , arises from an extragalactic contribution and a galactic component referred to as *diffuse galactic light* (DGL). The extragalactic component accounts for the cumulative emissions of pre–galactic, protogalactic and evolved galactic systems, namely the re–emission of stellar light at longer wavelengths due to dust. Such stellar light originates from early galaxy populations spanning a large redshift range. The *zodiacal* thermal emission and further minor components as listed in Table 6.4 account for the galactic contribution to the CIB [172]. In this context, the CIB represents an integrated background of luminous events from the past to the

present time of the Universe related to the cosmic history in terms of star formation, star–burst activity and other luminous events.

Emission source	Waveband
Thermal emission from small asteroids in the Solar System	NIR–MIR
Faint galactic star	NIR
Galactic cirrus emission	FIR
Emission of intracluster dust in the Local Group	IR ($\lambda < 20\,\mu$m)
CMB emission	IR ($\lambda > 300\,\mu$m)

Table 6.4: Contributions to the diffuse galactic light in the individual infrared regime. The subranges cover the near–, mid– and far–infrared (NIR, MIR, FIR) wavebands.

- **CUVOB (Cosmic Ultraviolet and Optical Background):** Similar to the CIB, the CUVOB includes both extragalactic and galactic components. Stellar light emissions that is redshifted by the expansion of the Universe throughout the history represent the main contribution of extragalactic origin, wherefore the CUVOB is strongly correlated to the evolution of the Universe. Beside this component, the zodiacal light (ZL), produced due to the dispersion of solar radiation by the dust in the Solar System, is considered as dominant part of this background.

- **CXB (Cosmic X-ray Background):** The CXB is a combination of a galactic component, that is thought to stem from the emission of a nearby hot gas producing a *soft* spectrum below the wavelengths of ∼4 nm, and an extragalactic component responsible for the *hard* spectrum at this wavelength [144, 71]. The latter contains probably resolved and unresolved sources. Thanks to several deep surveys with X-ray telescopes such as the Chandra satellite, it has been demonstrated that up to 80% of the extragalactic X-ray background bulk is resolved into discrete sources, among them mostly dust enshrouded AGNs [319].

- **CGB (Cosmic Gamma-ray Background):** Both emission from our Galaxy and of extragalactic origin contribute to the CGB. While the former contribution is assigned to the interaction of CRs with the ISM, the origin of extragalactic γ–ray background (EGB) remains unrevealed. However, it is supposed that unresolved extragalactic sources can be mainly associated to the EGB. Figure 6.24 shows the the diffuse γ–ray emission measured by the *Fermi*-Lat in surveying mode primarily associated with the interaction of CRs and the ISM.

6.2.1 The Extragalactic Background Light

The CMB represents a frozen primordial relic radiation from the Bing Bang, whereas the other cosmic backgrounds that are strongly related to the evolution of the Universe, e.g. in terms of its expansion and structure formation processes. Clearly, the CMB represents the most energetic component of cosmic background. The CUVOB and CIB represent the second most energetic backgrounds, while the CXB, the CGB and the CRB are about two and even more orders of magnitude smaller. Keeping in mind that the maximum absorption of VHE γ–rays occurs

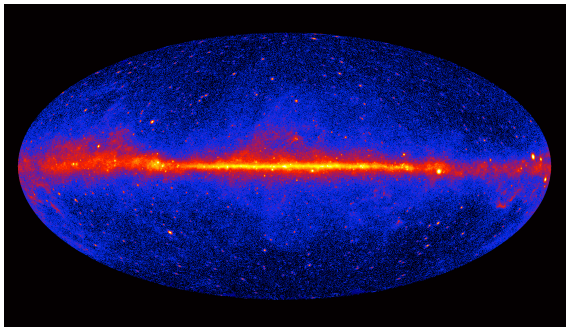

Figure 6.24: The *Fermi* LAT all–sky map of the γ–ray sky above 1 GeV after three years of operation. The diffuse emission, which appears brightest along the galactic plane, is primarily due to the interaction of CRs and the ISM. Discrete galactic and extragalactic γ–ray sources are clearly visible. Credit NASA/DOE/*Fermi* LAT Collaboration.

with target photons with energies from the UV to IR energy band (see Table 2.2), the principal contribution of the attenuation by pair production is related to the CUVOB and the CIB, whose extragalactic contributions form the so–called *Extragalactic Background Light* (EBL).
Strictly speaking, the EBL comprises the CIB and the COB, i.e. the *cosmic optical background*, spanning from 0.1to 1000 μm the ultraviolet to far–infrared (FIR) wavelength regime (see Figure 6.25). The EBL SED features two peaks of roughly equal brightness, the first located at $\sim$1 μm and the second at $\sim$100 μm, which originate from starlight emission and by dust–reprocessed starlight respectively [100].

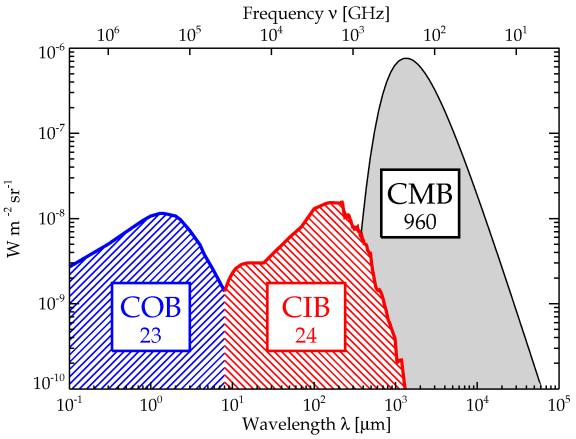

Figure 6.25: Schematic SED of the most energetic cosmic backgrounds, whose approximated brightness is indicated in the boxes. The CIB and COB constitute the EBL [100].

As the COB and the CIB are relics of structure formation processes of the Universe, the EBL represents the accumulated electromagnetic radiation from all epochs of the Universe history, which underwent a cosmological redshifting by the expanding Universe according to the emission epoch. As a consequence, emissions from objects distant in space, or in other words in time, experience a shift to lower energies, by what the radiation observed on Earth appears redshifted. Instead, in case of close–by sources the radiation remains quasi unaffected by the Universe expansion. Thus, the emission observed at a certain wavelength is equal to the sum of two emissions, one related to a nearby sources and another associated to redshifted radiation of more distant objects, e.g. distant AGNs, that has been initially emitted at even shorter wavelengths. Therefore, the study of the

EBL plays a key role in the cosmological framework, providing the possibility to shed light in the history of the Universe. The relation of observed and emitted wavelength is mathematically formulated, assuming an observer at $z = 0$, as:

$$\lambda_{\mathrm{obs}} = \lambda_{\mathrm{em}} \cdot (1 + z) \tag{6.12}$$

where z denotes the source redshift.

6.2.2 Constraining the EBL

The presence of relatively bright foregrounds, among them the ZL and the DGL, as shown in Figure 6.26, has rendered direct measurement of the EBL, which appears less bright to the foregrounds, very difficult.Beside these dominant emissions, the CMB represents a strong foreground in in the sub–millimeter wavelength range. However, at least this component can be removed thanks to the precise knowledge of its spectrum.

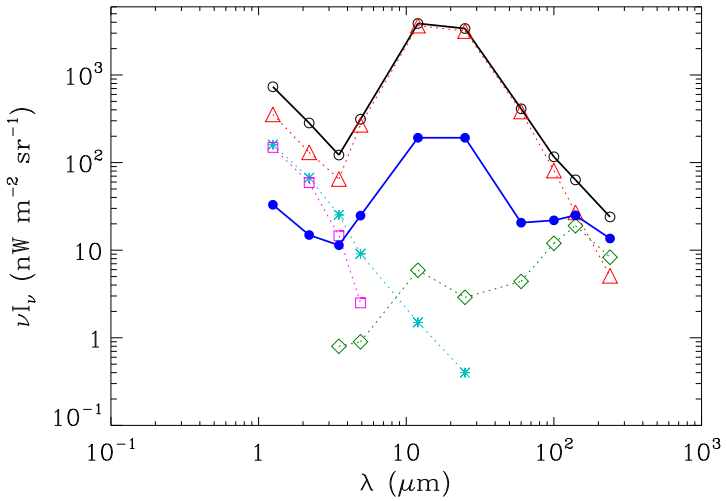

Figure 6.26: Example of foreground contribution to the DIRBE data in the Lockman Hole area: observed sky brightness (open circles), interplanetary dust (triangles),including the ZL, bright and faint galactic sources (squares and asterisks), ISM (diamonds). The residual sky brightness after subtraction of the foregrounds are marked by solid circles [153].

For this reason, different indirect approaches have been used up to now in order to set constraining limits on the EBL.

Direct measurements

Direct measurements of the EBL have been carried out by the various space–borne detectors in different wavelength ranges (see Figure 6.27).

Nevertheless, due to the existence of strong foregrounds, whose subtraction might strongly bias the faint signal of the EBL, the reliability of such measurements is often contested.

Indirect measurements

Alternatively, during the past years three methods to measure the EBL indirectly have been proposed to place constraints on this background emission:

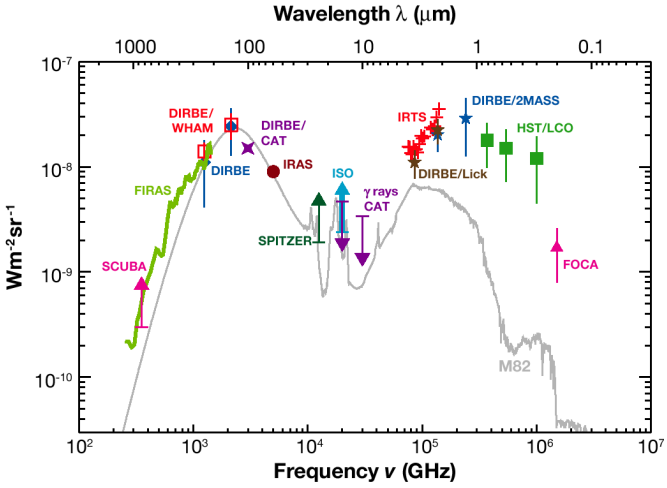

Figure 6.27: The most constraining measurements of the EBL over five frequency decades. The SED of the RG M87 is shown for comparison [191].

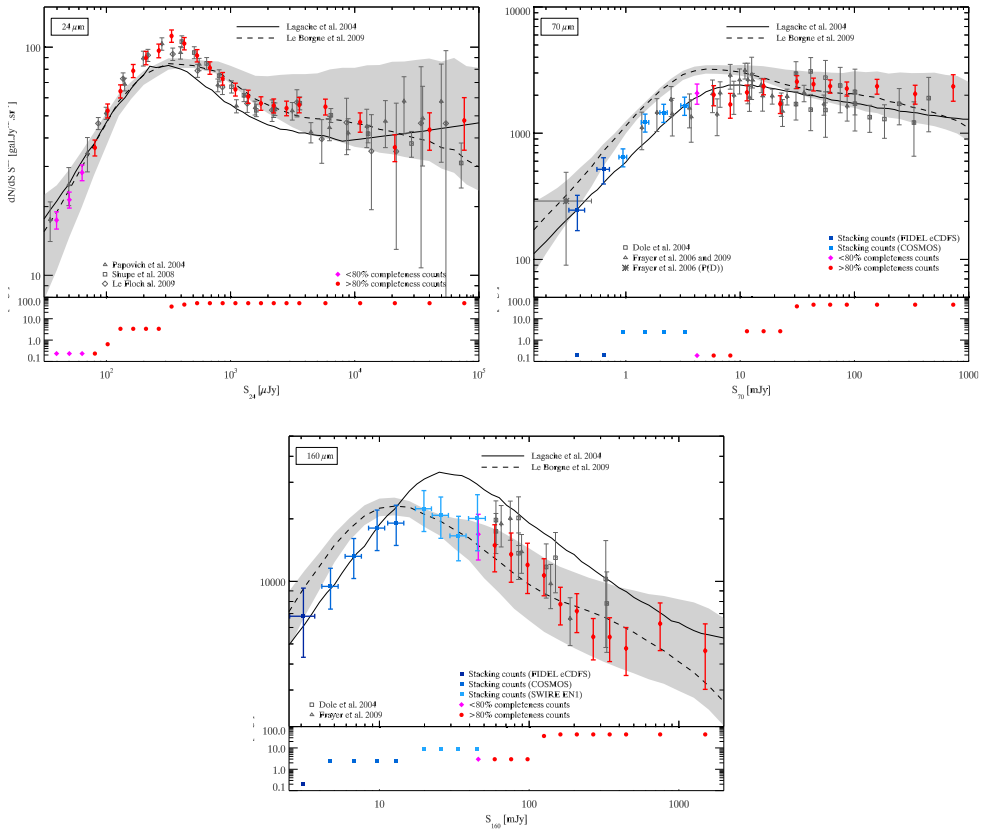

Figure 6.28: Differential number counts of sources from *Spitzer* centered at 24, 70 and 160 μm [58].

- **Source number counts:** Typically deep number counts of emitting sources provide very solid constraints of the overall light filling the Universe under the assumption, that only resolved objects, e.g. galaxies, belong to the emitters. Thus, this method has been proposed by various authors to yield lower limits on the total EBL intensity. Such measurements have been carried out by several instruments such as *Spitzer* [58] operating in the infrared regime, the *Hubble* Space Telescope (HST) sensitive in the optical band [206] and *ISO* [92, 167] observing at 170 microns. Recent results from *Spitzer* claim the resolution of the CIB at different wavelengths of up to 80% (see Figure 6.28).

Unfortunately, the depth of such surveys is limited due to unresolved galaxies depth at longer wavelengths;

- **Statistical analysis:** Based on statistical analysis, two further techniques can be used to place limits on the EBL, such as the so-called *stacking technique*, where a pile–up of infrared sky see Figure 6.29, centered at different wavelengths, is used for the detection of very faint far–infrared galaxies which are not detected individually at shorter wavelengths [100]. As unresolved galaxies are taken into account by this technique, their constraints are closer to the real EBL intensity compared to lower limits derived from source number counts.

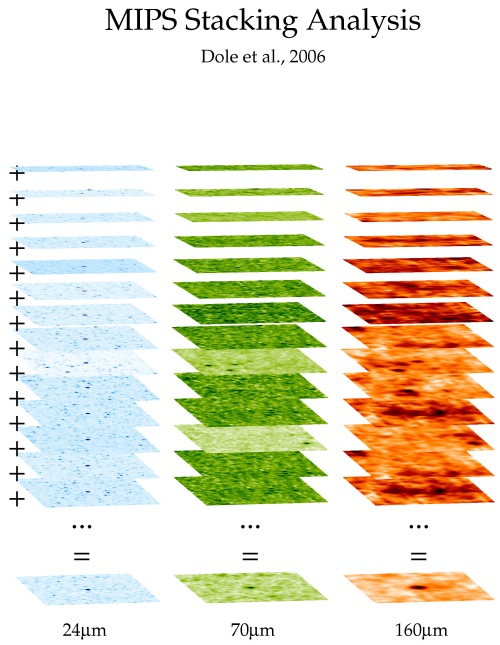

Figure 6.29: Illustration of the stacking technique of single sky maps at 24, 70 and 160 microns for the detection of a signal of all unresolved galaxies as applied in [100]. Credit: H. Dole/ IAS/ Arizona/ Nasa/ JPL-Caltech

The second method, denoted as *fluctuation technique*, allows for the derivation of upper limits on the EBL by the study of fluctuations of the background estimation from different sky regions associated to discrete sources. Thus, such spatial fluctuations reveal information on the number and distribution of sources contributing to the EBL potentially yet unknown [108, 172, 153]. Recent measurements in the *Spitzer* regime revealed an excess of fluctuations that can be attributed to known galaxy populations suggesting an origin of fait, unknown population of highly clustered sources [173, 159];

- **Studies of the opacity to TeV emitter:** The intrinsic VHE spectra of distant extragalactic sources, e.g. distant AGNs, suffer an absorption due to EBL interaction as function of the redshift, by what the spectrum is modified, leaving an imprint on the observed spectrum. By assuming some basic properties with regards to the intrinsic spectrum of the TeV photon emitter, it is possible to infer upper limits on the EBL density. Figure 6.30 presents the constraints of the EBL obtained by observations of distinct distant TeV emitters.

  The most stringent upper limits have been placed by the combination of VHE data with observations in the HE regime carried out by *Fermi*, indicating that these constraints are very close to the lower limits obtained with source number counts.

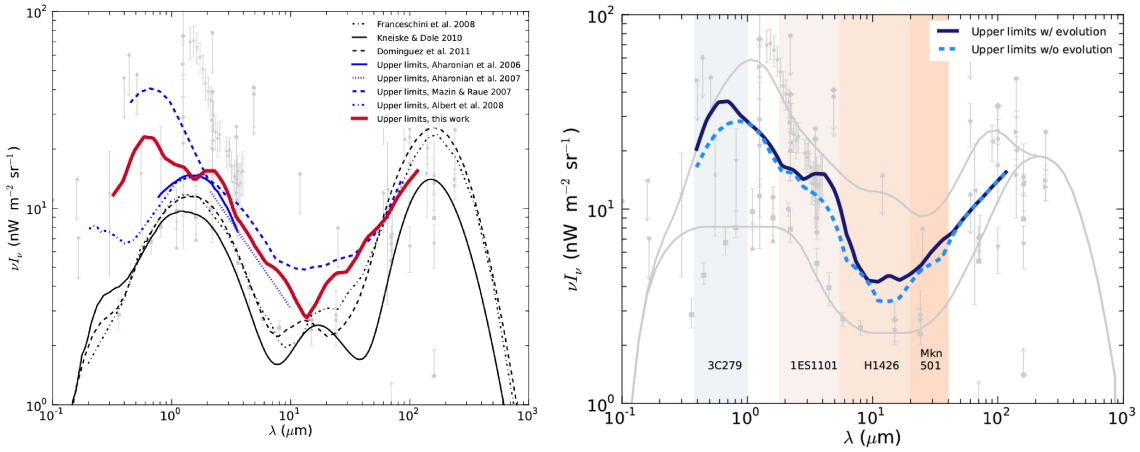

Figure 6.30: *Left:* Historical upper limits on the EBL intensity derived from the detections of distant VHE γ–ray sources (blue curves). Recent constraints obtained by the combination with HE *Fermi* data and different generic EBL models are indicated by the red and black curves respectively, superimposed to EBL measurements (gray markers). *Right:* Upper limits derived taken the evolution of four VHE spectra into account. The strongest influence on the EBL intensity by the individual spectra is marked by the correspondingly shaded regions [225].

The overall constraints on the EBL SED derived from direct and indirect measurements carried out by different instruments is presented in Figure 6.31.

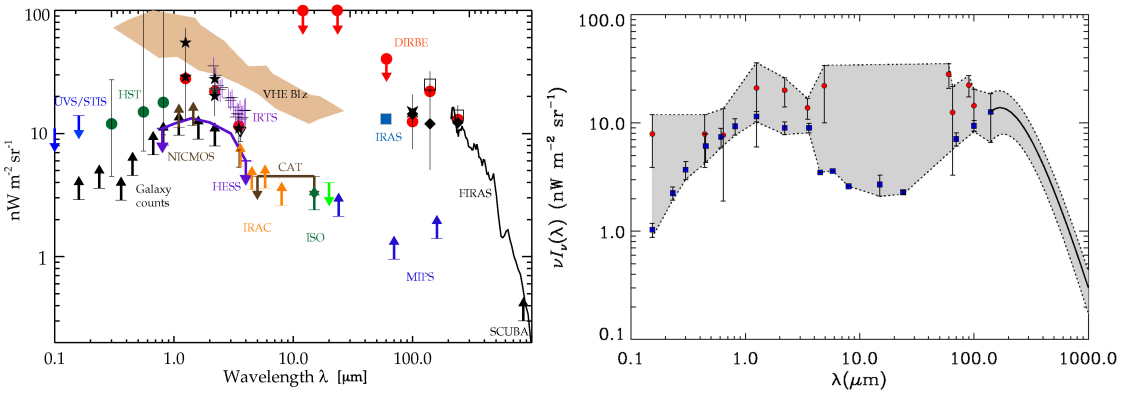

Figure 6.31: *Left:* Current direct and indirect measurements of the EBL Spectral Energy Distribution. Adapted from [87]. *Right:* Lower and upper limits on the EBL intensity determined by the intensity of the IGL and direct EBL measurements derived for the UV to sub millimeter [108].

6.2.3 Modeling the EBL

Based on the results of direct and indirect EBL measures, different models have been developed over the last decades to describe the evolving EBL with the principal objective to estimate the luminosity density evolution as a function of the redshift [103]. Depending on the modeling approach, EBL models can be grouped into four categories varying in the degree of complexity, physical realism and ability to account for observations:

- **Forward evolution:** *Forward evolution models* are based on assumption of the initial cosmological conditions, following a forward evolution of the

Universe up to present time by means of semi–analytical models (SAMs) of galaxy formation (e.g. [264, 146, 290]) and their emission (see Figure 6.32).

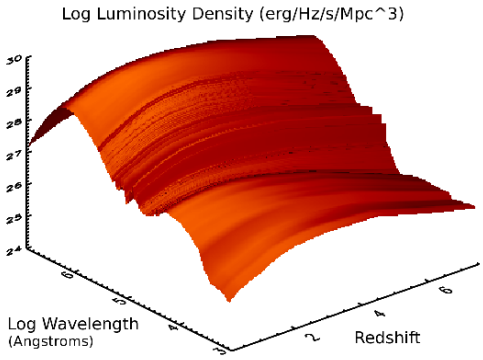

Figure 6.32: Three dimensional representation of the luminosity density evolution as a function of wavelength and redshift used in a forward evolving SAM [146].

Taking the galaxy formation and evolution into account, forward evolution models provide an interdisciplinary physical approach to the EBL evolution, where several research fields are involved requiring a relatively large amount of adjustable parameters.

- **Backward evolution:** Starting from observations of existing galaxy populations from the present local Universe, the *backward evolution* model is used to reconstruct the development of the Universe back in time by using galaxy counts at different wavelengths which are extrapolated to larger redshifts. Unlike forward evolution models, no assumptions are made on stellar physics and cosmological conditions.

  An example of such backward evolution model is proposed in [124], which is known for its robustness since it is only based on observational constraints;

- **Inferred galaxy population evolution:** These models make use of observational quantities to parametrize the SFR density of the Universe in order to derive the evolution of galaxy populations over a redshift range (e.g. [117]). In [183] such model has been proposed to reproduce a lower–limit flux for the EBL, showing a good agreement with constraints obtained from source number counts (see Figure 6.33).

  However, according to [103], this approach is less reliable, as the SDR is not directly inferred from observations but derived from several different parametrization methods, which contain varying significant uncertainties and bias;

- **Observed galaxy population evolution:** This model is only based on direct observational quantities from which the evolution of galaxy populations over the redshift range that contributes significantly to the EBL is inferred. Thus, no extrapolation on the luminosity density is required. Due to its most empirical approach, the model allows for a quantitative study of the uncertainties which originate directly from the observational data. Up to now, there is only one model proposed in [102] where this approach is applied (see Figure 6.34).

  Similar to the model based on the SDR parameterization proposed in [183], this *observational evolution* model shows an excellent agreement with lower

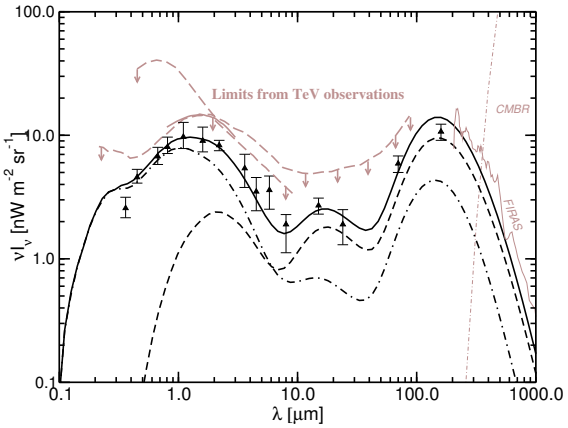

Figure 6.33: Total flux model of the EBL (black solid line), together with the contribution from dust rich (black dashed lined) and dust poor (black dot–dashed line) star forming regions. The model is superimposed to lower limits (filled triangles) and model–dependent upper limits derived from VHE observations. Detections at longer wavelengths are shown [183].

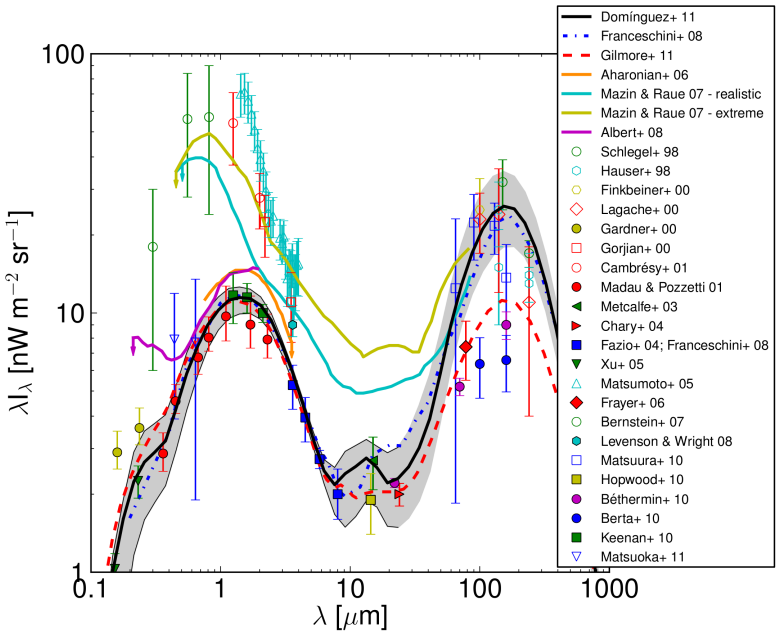

Figure 6.34: Observed evolution model (black solid line) superimposed to direct EBL data from galaxy counts, upper limits from VHE γ–ray observations and other recent EBL models [102].

limits from galaxy counts and is compatible with EBL predictions from [124] up to large redshifts.

In Figure 6.35, all four different model types are compared to the current limits from indirect and direct EBL measurements.

In general, except for the backward model from [299], all models provide adequate agreement with the EBL constraints, underlining the improvement of the EBL modeling and measuring over the recent years, providing continuously more stringent limits. Moreover, from VHE γ–ray observations it has been found that the EBL is close to the lower limits derived from source counts.

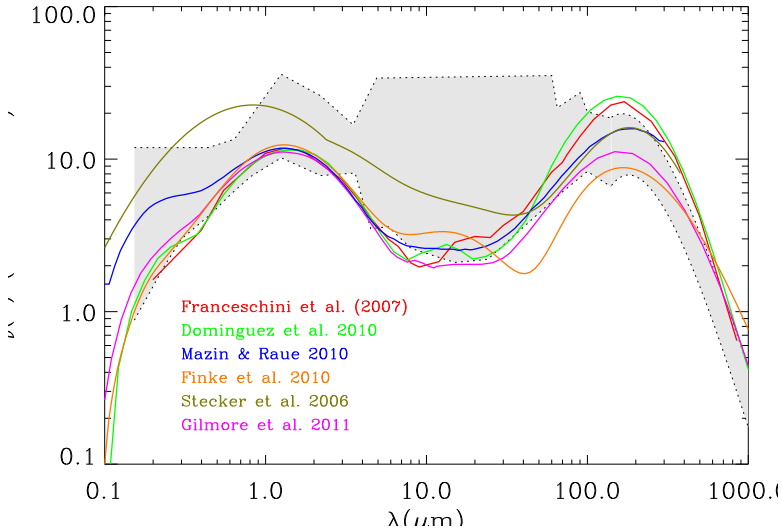

Figure 6.35: Comparison of different EBL models to the observational limits from direct and indirect EBL measures [108].

6.2.4 The EBL Imprint on Blazar Spectra

Is is commonly accepted that the Universe is partially opaque to VHE γ–rays due to the interaction with low photons and the successive pair creation [239, 148, 111]. Photons with an energy above 160 TeV interact with the CMB on their travel across the cosmos (see Table 2.2) limiting the free–path of photons with E $>$ 100 TeV to distances of $\sim$10 Mpc [298] (see Figure 6.36). As a consequence of the large CMB photon density, extragalactic sources are in principle not detectable above this energy.

In the energy range from tens of GeV to 100 TeV, the interaction of extragalactic photons takes place with the optical and NIR photons of the EBL (see Chapter 2). The strength of this photon–photon interaction scales with the energy of the VHE γ–ray emission and the distance of the extragalactic source leading to a partial or total absorption of VHE γ–rays. Therefore, so far the current generation of IACTs has been only able to detect relatively nearby objects, with a redshift smaller than 0.6, at the lower edge of this energy band, where the EBL absorption is less strong. Due to the VHE γ–ray absorption by the EBL photons, an imprint of this interaction in the case of partial attenuation is traced in the observed spectrum.

Due to the faint density of the background photons capable to interact with γ–rays of lower energies, the emission below few GeV is not affected by significant absorption, i.e. the Universe is transparent to keV–GeV photons (see Figure 6.36).

The γ–ray Horizon

The Universe features a certain *opacity* to γ–rays related to their absorption by the EBL on their travel in space via photon photon pair production. A measure of such *gamma–gamma opacity* is given by the *optical depth* $\tau_{\gamma\gamma}(E, z)$ which is a function of the photon energy E and the distance of the source z . This parameter defines the path length of a VHE γ–ray emitted by a source before suffering an attenuation by a factor e and allows to connect the observed flux $F_{\rm obs}$ from a source located at a certain redshift z to the intrinsic emission of the source $F_{\rm int}$before undergoing absorption:

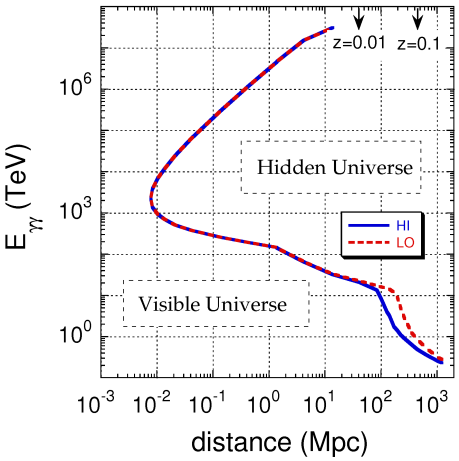

Figure 6.36: The γ–ray horizon at low redshifts as function of the photon energy and the redshift for a low and a high EBL. The γ–ray horizon is marked where $\tau_{\gamma\gamma}(E, z) = 1$ [97].

$$F_{\rm obs}(E, z) = F_{\rm int}(E) \cdot e^{-\tau(E,z)} \tag{6.13}$$

The EBL models proposed (e.g. [299, 124]) explain the opacity to TeV photons to originate dominantly from the production of electron positron pair production. Typically, the cosmic opacity for photon–photon interaction is calculated from the pair–production cross-section as proposed by [158]:

$$\sigma_{\gamma\gamma}(E_\gamma, \epsilon, \theta) = \frac{3\sigma_{\rm T}}{16} \cdot \left(1 - \beta^2\right) \left[2\beta(\beta^2 - 2)(3 - \beta^4) \ln\left(\frac{1+\beta}{1-\beta}\right)\right] \tag{6.14}$$

where ϵ and $E\gamma$ correspond to the energies of the background photon and the VHE γ–ray, $\sigma_{\rm T}$ refers to the Thomson cross section and β is related to the velocity of the created electron positron pairs as a function of the energy of the colliding photons and the collision angle θ between them:

$$\beta \equiv \left(1 - \frac{4m_e^2 c^4}{s}\right)^{1/2} \tag{6.15}$$

with

$$s \equiv 2E_\gamma \epsilon x \tag{6.16}$$

$$x \equiv (1 - \cos\theta) \tag{6.17}$$

This cross section implies a maximum absorption for background photon of the energy:

$$\epsilon_{\rm max} \simeq 2\left(m_e c^2\right)^2 / E_\gamma \tag{6.18}$$

$$\simeq 0.5 \left(\frac{1\,{\rm TeV}}{E_\gamma}\right) {\rm eV} \tag{6.19}$$

which corresponds to a maximum wavelength:

$$\lambda_{\rm max} \simeq 1.24 (E_\gamma [{\rm TeV}])\, \mu{\rm m} \tag{6.20}$$

The optical depth can then be computed as a function of the energy of the VHE γ–ray emitted by an extragalactic source located at a certain redshift z_e travelling

through a cosmic medium filled with low energy photons with density $n_\gamma(z)$ to an observer at present time:

$$\tau(E_\gamma, z_e) = c \int_0^{z_e} dz \frac{\mathrm{d}t}{\mathrm{d}z} \int_0^2 dx \frac{x}{2} \int_{\frac{2m_e c^4}{E_\gamma e x(1+z)}}^{\infty} d\epsilon \frac{\mathrm{d}n_\gamma(\epsilon, z^*)}{\mathrm{d}\epsilon} \sigma_{\gamma\gamma}(\beta) \tag{6.21}$$

where the factor s in Equation 6.16 should be replaced by:

$$s \equiv 2E_\gamma e x\,(1+z)$$

Given a flat Universe, the differential of time used in Equation6.21 is:

$$\frac{\mathrm{d}t}{\mathrm{d}z} = \frac{1}{H_0\,(1+z)} \left[(1+z)^2\,(1+\Omega_m z) - z\,(z+2)\,\Omega_\Lambda\right]^{-1/2} \tag{6.22}$$

Thus, due to the properties of the photon–photon cross section the energy of the TeV photon is linked to the wavelength of the EBL photon with maximum interaction probability as listed in Table 6.5.

E_γ	λ_{EBL}	Waveband
<8 GeV	<10 nm	X-rays
8–300 GeV	10 –390 nm	UV
300–600 GeV	390–750 nm	Optical
600 GeV–1 TeV	750 nm–1.2 μm	NIR
1–20 TeV	1.2–25 μm	MIR
20–160 TeV	25 μm–1 mm	FIR
>160 TeV	>1 mm	Microwaves

Table 6.5: Correlation of the maximal absorption of a TeV photon of distinct energy by an EBL photon of certain wavelength.

Recalling the intensity of the cosmic photon background, it is evident, that the CMB is mainly interacting with photons of energies above ∼160 TeV, while the background light from IR to UV interacts with photons of few GeV to tens of TeV. In fact, due to its high density the CMB totally absorbs the TeV photons while towards shorter wavelength the background photons interact with VHE γ–rays of lower energies where the cross section of photon–photon interaction is maximum. The density of the cosmic background light in X-rays is very low by what the interaction below few GeVs can be neglected.

Hence, studies of VHE γ–rays above 1 TeV are addressed to probe the infrared part of the EBL whereas below 600 GeV the optical to UV energy band is studied [18].

Figure 6.37 illustrates how the absorption coefficient $e^{-\tau}$ and the optical depth and scale with increasing energy of the VHE photon and with increasing redshift of the γ–ray source.

Clearly, the suppression of the differential energy flux will be less strong for a nearby source, lower curves, where the Universe is transparent to VHE γ–rays up to few tens of TeV. Therefore, the observed VHE γ–ray flux for sources located at redshifts around 0.03 will not be affected by the interaction with the EBL up to some tens of TeV while above this energy the optical depth becomes relevant. Usually, this border, that is the optical depth is equal to 1 corresponding to a flux suppression by a factor of e^{-1}, is denoted as the *γ–ray horizon*, also known as the *Fazio–Stecker relation*. Figure 6.38 illustrates which waveband of the EBL is responsible for the cut–off for a VHE γ–ray emitter located at different redshifts based on a lower EBL model proposed by [184].

By contrast, the observed VHE γ–ray flux of sources located at further dis-

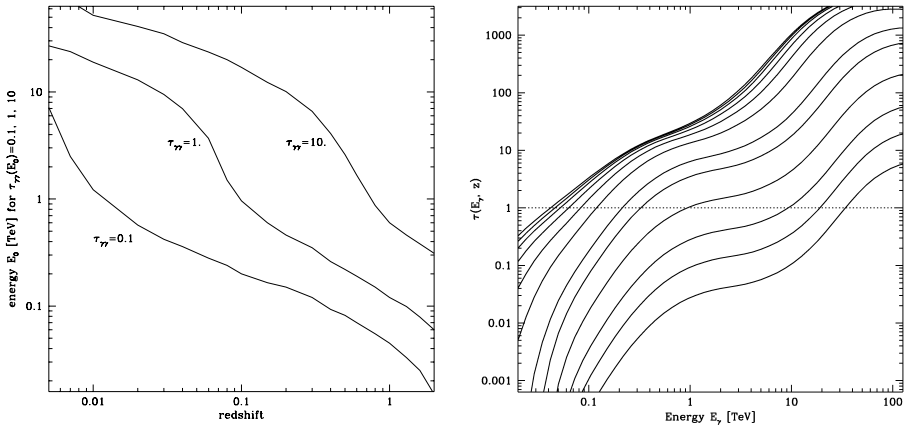

Figure 6.37: Illustration of the optical depth as a function of the energy of the VHE γ–ray and the redshift. *Left:* The energies of a VHE photon for which the optical depth corresponds to τ=0.1, 1 and 10 as a function of the redshift of the source. *Right:* The optical depth by photon–photon interaction as a function of the VHE γ–ray energy for sources located at $z = 0.003, 0.01, 0.03, 0.1, 0.3, 0.5, 1, 1.5, 2, 2.5, 3, 4$ from bottom to top [124].

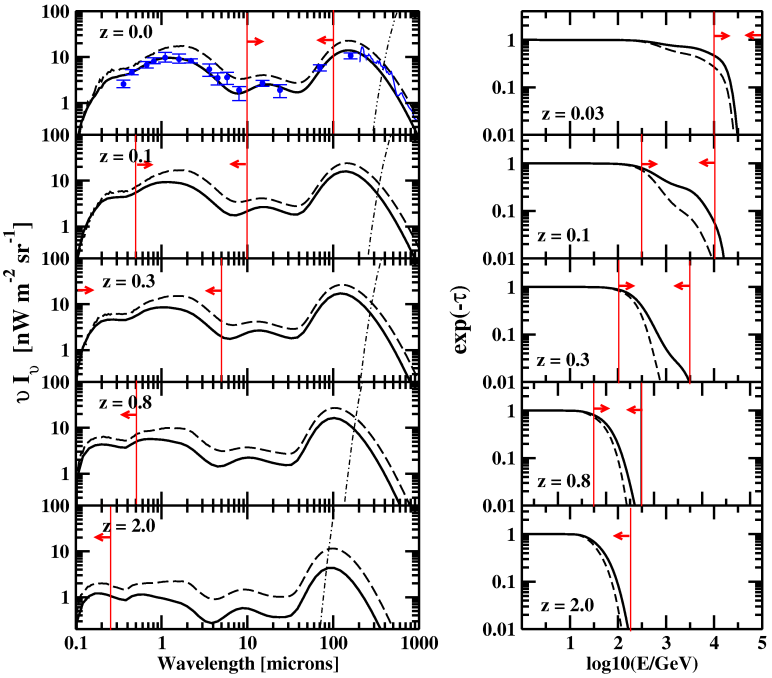

Figure 6.38: Extinction of the VHE γ–ray flux of by the EBL present at different redshifts. *Left:* Comoving EBL flux at different redshifts extrapolated from the best fit (solid line) of EBL measurements (blue points) and modeled (dashed line) according to [182] . *Right:* Extinction factor of γ–rays as a function of their energy at different redshifts. The vertical lines indicate the EBL range responsible for the γ–ray flux suppression [184].

tances will strongly be affected by EBL absorption due to the dramatic increase of the optical depth with redshift resulting in a strong flux suppression below 10 TeV. Consequently, up to now no blazar located at redshifts larger than 0.54 has been detected in the VHE regime by IACTs.

The extinction of the differential flux leads to a *spectral steeping* of the intrinsic source spectrum depending on the redshift of the source as illustrated in Figure 6.38 on the observed source spectra of Mkn 421, the nearest extragalactic source (z=0.03) known to be a VHE γ–ray emitter, 1ES 1215+303, an intermediate case (z=0.13), and 3C 66A, one of the most distance (z=0.444) extragalactic sources detected in VHE γ–rays. Knowing the source redshift and based on the observed source spectrum and τ whose function is provided by several EBL models, the Equation 6.13 can be used to estimate the deabsorbed source spectrum.

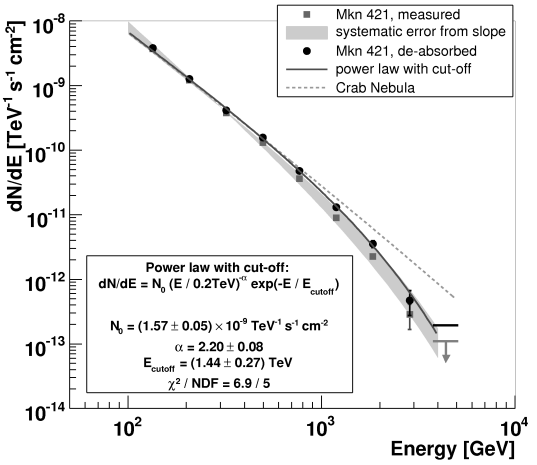

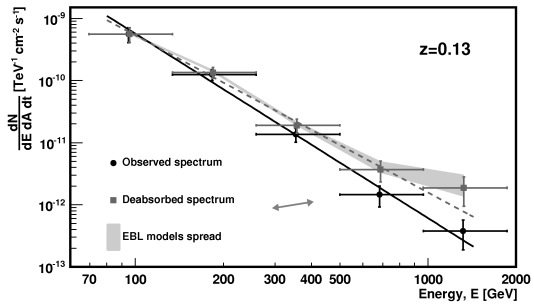

The detection of the most distant VHE γ–ray emitter the FSRQ 3C 279, located at redshift 0.536, has been a milestone in the research field of γ–ray astronomy and observational cosmology (see text box). As predicted by the EBL model of [124], VHE γ–rays emitted by such distant objects already suffer a significant EBL absorption at ∼100 GeV, and at 1 TeV the absorption coefficient is already of the order of 10 causing a total flux suppression. The detection of such distant source demonstrated that the Universe is more transparent to VHE γ–ray than previously assumed (e.g. [299]).

As outlined in the previous sections, there are several models to describe the EBL and its evolution. Being a fundamental ingredient for estimating the optical depth, differences in the models lead to very different attenuation coefficients (see Figure 6.39).

While all models show good agreement regarding the attenuation coefficient at small redshifts, the spread increases significantly with redshift. Recent investigations based on *Fermi*/LAT observations of photons of energies above 30 GeV from distant blazars and GRBs data seem to confirm the exclusion of the EBL

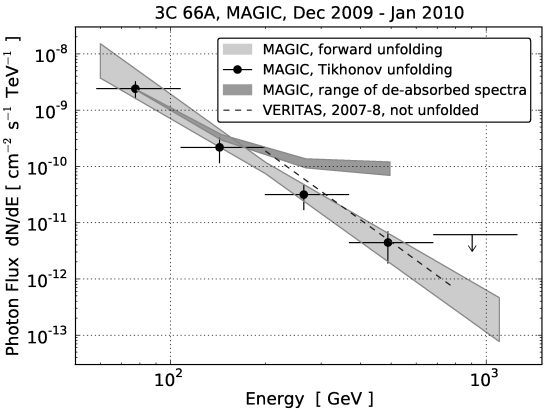

Figure 6.38: The spectral steepening of the VHE γ–ray spectrum from three blazars located at different redshifts. *Top:* Mkn 412 located at z=0.03 [23]. *Middle:* 1ES 1215+303 is located at z=0.13 [33]. *Bottom:* 3C 66A located at With a redshift of 0.444 [34].

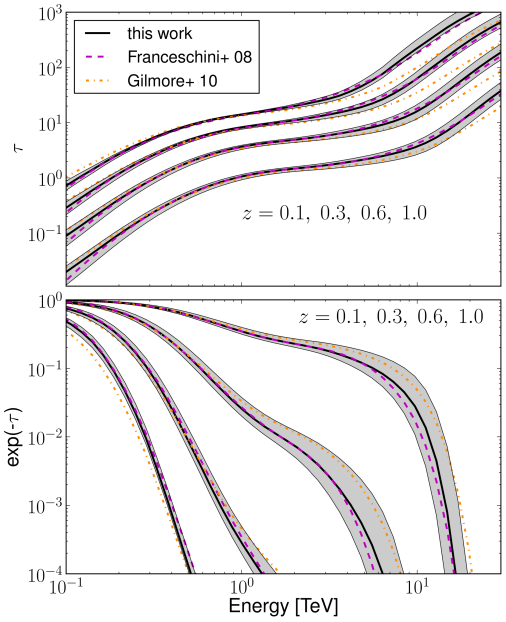

Figure 6.39: The γ–ray attenuation provided by different EBL models. Variations of the optical depth (upper panel) and the flux attenuation (lower panel) predicted by different EBL models [124, 145]at different redshifts (from bottom to top and from right to left: z= 0.1, 0.3, 0.6, 1.0) [103].

model suggested by [299]. This underlines the importance of the observation of distant VHE emitter in order to reduce the systematics introduced by the EBL models since an decrease in the uncertainties of the attenuation coefficient can be achieved.

How Transparent is the Universe?

In February 2006, the MAGIC telescope was capable to detect VHE γ–ray radiation during a giant flare from the first and unique FSQR 3C 279. Furthermore, this source is known to be the most distant VHE emitter, located at 5 billion light–years corresponding to a redshift of 0.536.

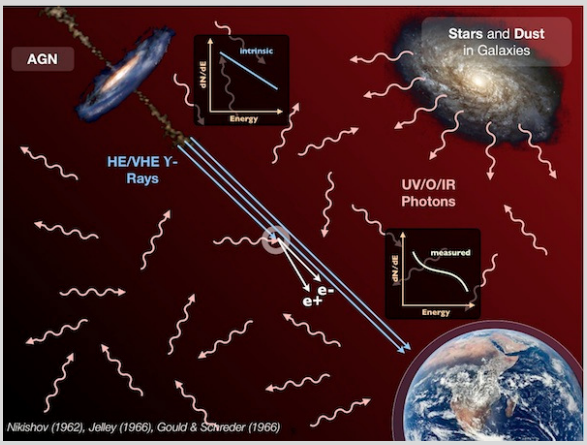

Figure 6.40: Principle of VHE γ–ray absorption via the interaction with the EBL.

Since VHE γ–rays suffer an attenuation during their travel across the opaque Universe by the interaction with the EBL, the MAGIC observations of such distant source have been an important measure that is consistent with the lower limit obtained from galaxy counts, implying a lower EBL intensity than initially believed.

The spectral measure of the FSRQ 3C 279 at energies above 80 GeV up to ∼500 GeV allowed to constrain the opacity of the Universe to VHE γ–rays by probing the γ–ray horizon.

References [29], and references therein.

Images: Credit: Martin Raue; [29].

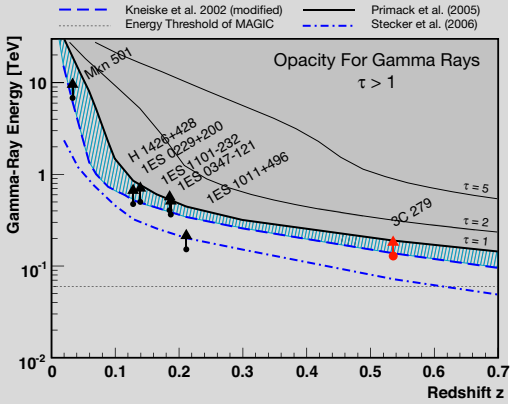

Figure 6.41: Opacity of the Universe to VHE γ–rays.

6.2.5 Probing EBL Models via Unphysical Blazar Spectra

In spite of the difficulties and the complexity associated with modeling the intrinsic spectra of blazars, a common feature predicted above some tens of GeV is a power law with an eventual curvature. Therefore, typically the overall spectrum describes a concave shape.

In case of EBL models that overestimate the optical depth, the deabsorbed γ–ray spectrum exhibits an exponential rise also referred to as *pile.–up* at highest energies [107] (see Figure 6.42). Such reconstructed emitted source spectra of TeV blazar are *unphysical* and can be used to rule out EBL. A possibility to quantify such anomaly has been proposed by [219] where a likelihood ratio test on the intrinsic spectrum is applied to probe the hypothesis of a simple power law over a *curved power law*.

In other cases, EBL models might lead to an absorption correction for which the reconstructed intrinsic spectrum follows a power law with an extremely hard

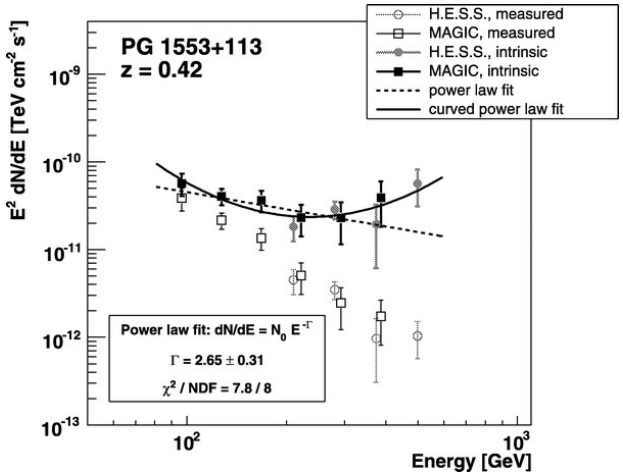

Figure 6.42: Example of an unphysical deabsorbed VHE spectrum of a distance blazar. The TeV observations of PG 1553 by MAGIC (blank squares) and H.E.S.S: (blank circles) and the respective deabsorbed source spectra (filled squares and circles) are presented. A simple power law (dashed line) and a curved power law are fitted to the reconstructed intrinsic source spectrum. The probability of the likelihood ratio test is 95.06% meaning that the fit by a curved power law is to be preferred over the fit by a power law [219].

spectral slope[45]. Therefore, additional model dependent constraints can be derived from the intrinsic spectral slope in the TeV range. In this way, EBL models leading to intrinsic slopes $\Gamma < 1.5$ have been rejected [16]. This slope is considered to be the hardest index for approximating the accelerated particle distribution with a power law predicted by shock acceleration models [209]. Despite the extensive debate on the caveats to this approach (e.g. [297, 21]) and some extreme blazars presenting hard spectrum with $\Gamma < 1.5$ [116], most GeV energy spectra of blazars obey this limit [10] confirming this general constraint on the hardness of intrinsic blazar spectra.

Finally, simultaneous HE and VHE observations of TeV blazars can be used to place upper limits on the EBL [135] based on the assumption that the intrinsic TeV SED lies below the extrapolation of the *Fermi*/LAT SED in the GeV to TeV range. However, this approach is somewhat considered to be not reliable and therefore should be considered with caution [89].

These criteria are commonly used to constrain the EBL energy density and are summarized in [225].

[45] TeV sources typically emit a spectra that can be described with a simple power law of the form $\frac{\mathrm{d}N}{\mathrm{d}E} \propto E^{\Gamma}$. Depending on whether the spectral index Γ is larger than ∼-3 or smaller than ∼-2, such spectra is considered to be *soft* or *hard* respectively.

The Gate to New Physics in the Form of Axion–like Particles

Current VHE data indicate that lower limit EBL models lead to an over–correction of observed blazar spectra for large values for the optical depth resulting in hard TeV spectra of distant blazars where a spectral softening that scales with distance is expected instead. A possible physical explanation that has been suggested is that the anomaly of the flux increase towards higher energies can be explained in terms of *VHE cascading* which leads to secondary photons via the interaction of UHECR with the EBL and the CMB.

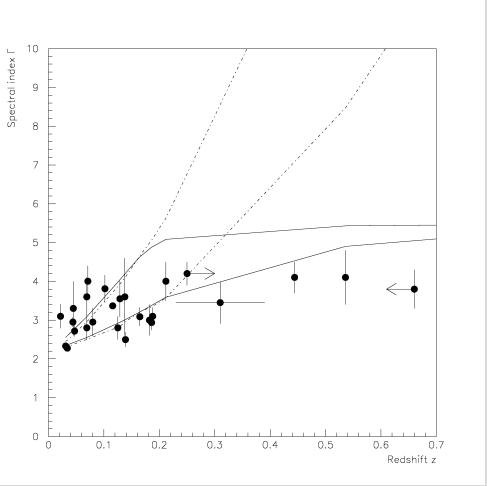

Figure 6.43: Observed spectral indices of all blazars detected so far in the VHE band.

However, under the consideration of a possible *pair production anomaly* (PPA) and the exclusion that the EBL and observational effects can entirely explain the observed spectral signature, more exotic explanation related to new physics have been approached. In general, the PPA could be explained by a suppression of the photon–photon interaction. One suggestion to lead to an effective PPA is associated to *axion*–like particles (ALPs) and its relevance and observational evidence has been extensively discussed. The scenario assumes that photons can oscillate into very light ALPs, i.e. spin–0 bosons, in the presence of cosmic magnetic fields. The ALPs travel through the Universe and convert back into photons before reaching the Earth suppressing in such way the EBL absorption.

References [95, 166, 190, 224, 308], and references therein.

Images: The spectral index is plotted versus the redshift. The area between the dotted lines corresponds to prediction of conventional physics involving conservative EBL models while the *DARMA*[a] scenario involving photon–ALP oscillation represents the region between the solid lines [278].

[a]De Angelis, Roncadelli and Mansutti

6.2.6 Constraints on the Blazar Distance from the EBL Imprint

As described in the previous section, the EBL attenuation leads to a deformation of the observed spectrum of distant VHE γ–ray emitters leading to a spectral steepening the larger the redshift and the higher energy. By inferring some fundamental assumptions on the intrinsic spectrum, limits are set on the EBL density. Based on this connection, a method has been developed to set limits on the redshift of a VHE γ–ray emitting source by using the spectral information from TeV observations.

Especially under the consideration that for some extragalactic VHE emitters the redshift is either unknown or largely uncertain, in particular for BL Lac objects (see Section 6.1.2), this method provides an approach to infer the distance from TeV observations in place of faint or absent emission or absorption lines in the

optical spectrum. The basic idea is to set an upper limit on the redshift by discriminating unphysical spectra due to the over–correction for EBL absorption. The dependence of the EBL absorption from the distance makes this principle feasible and allows to use the previously depicted artifact under the assumption of the correctness of the applied EBL model.

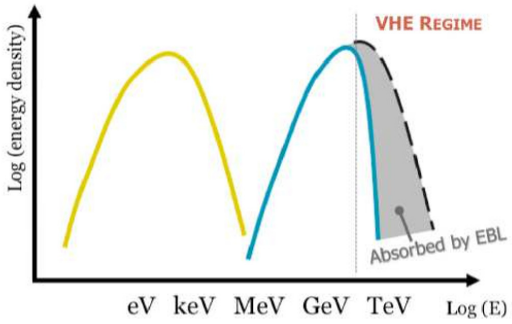

Figure 6.44: Sketch of a typical two bump blazar spectrum [262].

Recently, an empirical method has been developed by [260] to constraint the distance of blazars with combined *Fermi* and TeV data. By comparing the the GeV band observed by *Fermi* and the deabsorbed TeV spectrum provided by IACTs, the spectral slope measured by *Fermi* can be used to limit the reconstructed spectral index in the TeV band. In principle, for larger distances, the deabsorbed spectrum becomes harder. This way, a solid upper limit can be inferred on the distance by deriving the redshift at which the spectral index of the TeV spectrum coincides with the slope measured by *Fermi*, which is a complementary approach to [135, 300]and [244] (see Figure 6.45.)

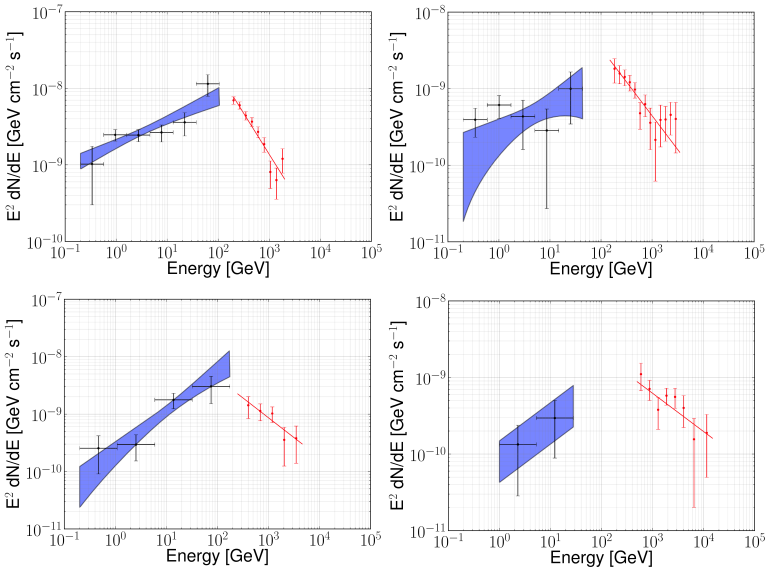

Figure 6.45: Combined *Fermi* and IACT spectra used for constraining the EBL. From top left to bottom right the data comprise 1ES 0229+200, 1ES 1218+304, 1ES 1101-232 and RGB J0710+592 [244].

Such *maximum hardness hypothesis* has been successfully tested on a sample of blazars with well known distances [261]. Moreover, a linear function law has been inferred to connect the real redshift z_{true} with its derived upper limit z^*(see Figure 6.46):

$$z^* = A + B z_{\text{true}} \tag{6.23}$$

where A is the measure of the intrinsic spectral break of the source and B quantifies the optical depth of the applied EBL model.

Assuming the standard cosmological scenario, this relation can be applied to constraint the redshift of blazars with unknown or uncertain distance under the hypothesis that the source of interest shares similar properties as the sources used for deriving the relation.

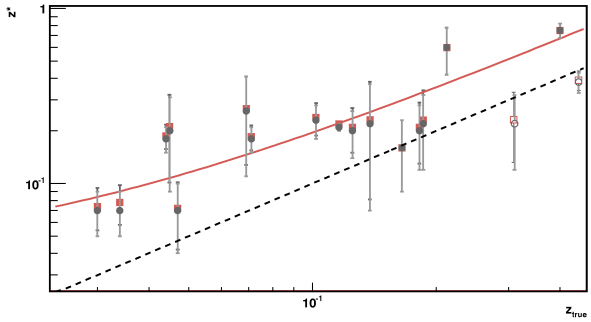

Figure 6.46: Empirically derived law to infer upper limits on the redshift of blazars of unknown or uncertain distance by combined *Fermi* and TeV data. Two different EBL models [124, 103] have been used to study the robustness of this relation (filled squares and circles). The open symbols denote two sources of uncertain redshift, namely 3C 66A and S5 076+714 wherefore they have been excluded from the linear fit [263].

To demonstrate the feasibility of the method, the procedure has been used to reconstruct the redshifts of the blazar data test sample by inverting Equation 6.23. The distribution of the differences of the reconstructed and the true redshift ($\Delta z = z_{\mathrm{true}} - z_{\mathrm{rec}}$) is presented in Figure 6.47.

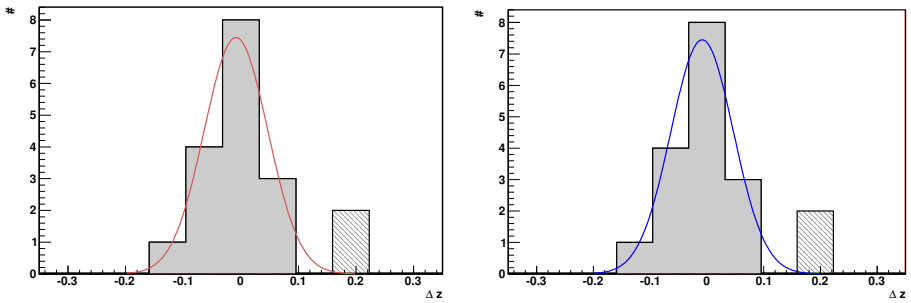

Figure 6.47: Discrepancy between the reconstructed and the true redshift obtained with the EBL model by [124] (left) and [103] (right). The shaded areas represent the two sources of uncertain redshift [263].

This method has been used to infer an upper limit on PKS 1424+240 whose redshift is unknown. From the upper limit derived on the distance, the most probable redshift corresponds to ∼0.26. In addition, this method has been applied to infer the redshift of a new TeV source, the blazar PKS 0447 [259].

Two of the sources used to derive this relation are subject of this work, namely 1ES 0806+524 and 1ES 1011+496(see Chapter 7 and 8). In the case of 1ES 0806+524 , the spectrum observed by VERITAS [9] was used for the derivation of the empirical law. As the spectrum was constrained in a rather narrow energy window, the data sample will be updated with the new TeV data from this source collected with MAGIC in 2011.

Moreover, quasi simultaneous Fermi data complement these new VHE γ–ray

observations. Usually, blazars are characterized by fast variability in all wavebands (see Section 6.1.2) wherefore simultaneous HE and VHE data are of great importance to avoid systematics of the calculation of z^*.

An important issue is the short variability of 1ES 1011+496 [287] which might represent a bias related to the calculation of the upper limit on the redshift and therefore must be considered with caution. In some cases, the variability of the VHE γ–ray emission leads to a significant change of the spectral slope. Consequently, the calculation of z^* is strongly affected.

Regarding 1ES 1011+496, the spectra has been rather poorly constrained (see [22, 272]) leading to a large uncertainty in the fit procedure and the determination of the spectral slope in the VHE regime. A more detailed spectrum has been derived from 2012 VHE data and simultaneous *Fermi* observations are available covering the high energy peak of the 1ES 1011+496 SED.

In summary, the update of the data of these sources might be very efficient to reduce the statistical error present in the derived linear correlation of the redshift. As both sources provide simultaneous observations in the HE and the VHE regime, the potential systematics due to non simultaneous data might be reduced.

In general, the extension of the number of sources included in this study provides the possibility to confirm with high confidence the potential of AGNs to be used as standard candles by ruling out the systematical and statistical errors.

7

MAGIC Observations of the High–Frequency–Peaked Blazar Object 1ES 0806+524

TRIGGERED BY AN OPTICAL ALERT, MAGIC observed the high–frequency–peaked BL Lac object 1ES 0806+524 in winter 2011 during which the source underwent a short–term flare in VHE γ–rays. In this chapter, the analysis of the 2011 MAGIC data and the results on the analysis of the source variability are presented including complementary multiwavelength data. To begin with, the analysis chain of the MAGIC data is introduced, followed by a summary on previous MWL observations of 1ES 0806+524. Hereafter, a detailed report on the signal search and the main physical results associated to the integral flux as well as to the spectral analysis is given. The analysis report concludes with the modeling of the SED 1ES 0806+524.
Parts of this analysis have been published in [287] and will published in [286](in preparation)

7.1 The MAGIC Data Analysis Chain

After its upgrade to a system of two new generation IACTs in fall 2009, MAGIC observations have been carried out in *stereoscopic* mode. From summer 2011 to summer 2012, a further upgrade on the MAGIC hardware has been commissioned on the MAGIC I camera and the readout system of both telescopes (see Section 3.4).

VHE γ–ray observations carried out by IACTs are in general aiming at measuring the cosmic γ–ray flux in this energy regime from a given sky region which is typically associated with an astrophysical object. In particular, the reconstruction of the differential flux as well as the temporal analysis of the integral VHE γ–ray flux represent two important ingredients for interpreting the physical processes present in such astrophysical sources.

In the MAGIC collaboration, a dedicated software package denoted as *MARS* (Magic Analysis and Reconstruction Software) is available to the collaboration members in order to perform the data analysis. The MARS tool is constantly evolving and represents a collection of classes and executables written in C++ programming language that is embedded in the *ROOT*[46] software framework

[46]see http://root.cern.ch

developed at CERN [230].

In a first analysis step the recorded raw data files are reduced into ROOT files including informations on the individual telescope subsystems and the weather conditions (e.g. humidity, cloudiness, etc.) under which data have been taken and merging them with the event image. This process is handled via an executable called `merpp`. The subsequent analysis pipeline of stereo data is divided into the several steps:

First, the **signal extraction and calibration** to determine the intensity of the signal as well as its arrival time and to calibrate the intensity of the signal in units of generated phe. Before the upgrade of the readout system, these analysis steps were performed with `callisto` which has now been replaced by the `sorcerer` executable.

Hereafter, an **image cleaning and parametrization** is performed via the `star` executable that cleans the shower images from the background and derives the Hillas parameters.

As the data taking conditions strongly affect the data quality, a **data quality selection** is performed on a single file basis for each telescope separately.

In case of stereo observations, the individual data sets from both telescopes are merged into one single data sample via the `superstar` executable, and the two different views of the same cleaned shower image are used for the **stereoscopic image reconstruction**.

The next analysis step is addressed to train the so–called γ/hadron separation as well as the reconstruction of the arrival direction of the atmospheric shower via the**Random Forest** method. These tasks are executed by `coach`.

The reconstruction of the energy of the shower images from stereo observations is based on so–called **energy lookup–tables** (LUTs). In order to create these LUTs, the `create_Energy_table.C` macro is used.

The γ/hadron separation, the reconstruction of the shower arrival direction and the energy reconstruction are applied by `melibea` to the output files of `superstar`.

After these applications the signal search is performed on the `melibea` files in order to determine the significance of the observed γ–ray signal. In the case of stereo observations, this task can be carried out with two different methods: either a (θ^2) plot or a *sky map* is derived.

In a final step the **differential spectrum** and the **light curve** are reconstructed by the `fluxlc` executable.In particular, the reconstruction of the differential spectrum and the light curve, are based on the comparison between real data from a γ–ray source and simulated γ–like events, i.e. *Monte Carlo Simulations* (MC) (see text box).

In the following sections, the individual steps of the analysis chain are subsequently outlined.

Monte Carlo Simulations

On particle physics experiments it is typical to calibrate the detectors by means of controlled incident light beams. Unfortunately, in the case of Cherenkov telescopes, such approach for the determination of the overall response is impossible and MC simulations are used instead.
Simulated shower images originating from γ–ray induced particle showers have to resemble the images obtained from real γ–ray events to a very high degree of precision in order to guarantee a reliable γ/h separation since this is based on the image parameters. In addition, realistic MC simulations are essential for the reconstruction of the primary energy.
The MC production of simulated γ–like events detected by MAGIC I and MAGIC II is processed or each telescope individually in three phases. Initially, the atmospheric shower is produced using the *CORSIKA* package with US standard atmospheric conditions. The output files contain the location and direction of the Cherenkov photons when reaching the altitude of the MAGIC site. Showers of varying energy and zenith angle and orientation with respect to the geomagnetic field are simulated. In a second step, absorption and scattering effects of the Cherenkov light pool due to the atmospheric conditions present at the MAGIC site are. Furthermore, the reflection of this radiation by the individual telescope reflectors is simulated taking into account the reflectance and the PSF of the telescope dishes. The output files store the directions and positions of the reflected photons in the camera plane. In a final step, a *smearing* tuned with the PSF that is evaluated from star images is applied to the simulated shower images the in order to enhance the flexibility of simulations to changes in the PSF of the reflectors due to degradation and periodical adjustment during observations. In addition, the response by the camera, the trigger system and the data acquisition electronics is simulated for both telescopes. The second and third step are carried out by the *reflector* and *camera* simulation programs as part of the MARS package.
The simulated MC files have the same format as real MAGIC raw data files and can be interpreted by MARS.

References: [156, 208, 80, 86] and references therein.

7.1.1 The Signal Extraction and Calibration

After the merging of the data, the *signal extraction* from the the recorded data is carried out. When an atmospheric shower triggers the event recorded by MAGIC, the DAQ system stores the information of each camera pixel in the raw data as FADC slices. From these slices, the signal is extracted, i.e. reconstructed. In such way, the intensity and the arrival time of the signal is recovered, associated with the peak maximum and the rising edge of the reconstructed Cherenkov light pulse at 50% of the peak value [26, 207].

In a second step, the charge of a triggered event collected by each PMT is calibrated and converted into the number of photoelectrons (phe) by means of the so–called *F–Factor* method [227]. For this purpose, special *pedestal* and *calibration* event runs are recorded during the normal data taking. The pedestal runs contains events taken with random trigger. It is is used to subtract the *baseline* of

the signal. Calibration runs are used to calibrate the pedestal subtracted charge of the signal. These runs generated by short light pulses (see Section 3.4.2) using the calibration trigger. The distribution of the calibration events is *Poisson* like and thus parametrized by the mean value of detected phe N and the root mean square (RMS) of this value $\sqrt{N}$. The pedestal subtracted charge of the signal from such calibration run is expressed in FADC counts and can be characterized by its mean charge $\langle Q \rangle$ and the RMS of this value σ. Typically, the measured charge distribution from such run is wider than the pure Poisson distributions. In order to compensate this difference in width between both distributions, the F–Factor is implemented. In this way, the broadening of the measured charge distribution of the calibration run is taken into account and the relative widths of both distributions can be expressed by:

$$F \cdot \frac{1}{\sqrt{N}} = \frac{\sigma}{\langle Q \rangle} \tag{7.1}$$

The F–factor is a PMT characteristic property, wherefore it has been previously measured in the laboratory for each PMT before installing them in the MAGIC cameras.

In general, the number of phe generated in a calibration run can be related to the mean charge measured by a *conversion factor* C:

$$C = \frac{N}{\langle Q \rangle} \tag{7.2}$$

Thus, knowing the F–Factor, C can be computed from:

$$F^2 \frac{\langle Q \rangle}{\sigma^2} \tag{7.3}$$

In this way, the calibration of number of generated phe of the signal can be inferred from its measured charge:

$$N = C \cdot \langle Q \rangle \tag{7.4}$$

Before the upgrade of the readout system, the tasks mention above were performed by `callisto` which has now been replaced by the `sorcerer` executable.

7.1.2 The Image Cleaning and Parametrization

In the third step, a cleaning and a parametrization is applied to the recorded shower images by the `star` executable as described below.

The Image Cleaning

First, the *image cleaning* is applied to the data that contain the extracted signal information in terms of number of phe and arrival time of each camera pixel in order to reject the diffuse background from each shower image. This procedure is a delicate task since the Cherenkov light fades away on the border of the shower images: depending on the signal intensity, the removal of pixels leads unavoidably to an image cropping. That means a drastic reduction of the dimension of the data files, as all the informations regarding the pixels that are not recognized to be involved in the shower image are discarded (see Figure 7.1).

The image cleaning is based on the combination of the two essential signal informations, i.e. the signal intensity and the timing information.

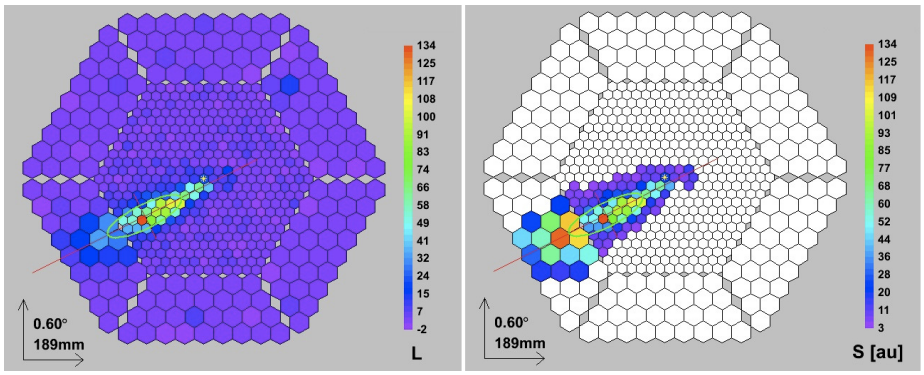

Figure 7.1: Example of γ–like event image recorded by MAGIC I. *Left:* The recorded event before the image cleaning, *Right:* The same recorded event after image cleaning. The parametrization of the event by the two shower axis and the ellipse is superimposed

The Standard Image Cleaning

The most commonly used method is the *standard–absolute* cleaning, whose application is based on a two threshold in terms of phe to determine the so–called *core* and *boundary pixels*, with a higher threshold set for the core pixel selection and the minimum criteria of two neighboring pixels exceeding this threshold. Provided the charge of the pixel exceeds the lower of the thresholds and at least one of its neighboring pixels are considered to be part of the core, then this pixel will be assigned as boundary pixel.

These thresholds are set according to an absolute number of phe recorded by each pixel. Alternatively, a *relative* cleaning is available in the MARS package that takes the noise fluctuations of the PMT by the comparison of the absolute number of phe to the characteristic pedestal RMS of the pixel. Unfortunately, this cleaning method holds some disadvantages regarding the amount of Cherenkov light that survives the cleaning in case of the presence of bright stars in the camera causing a higher pedestal RMS for those pixels to which the star light is incident and thus a higher pixel rejection.

The cleaning levels have been fixed empirically during the individual commissioning phases and first observations carried out after each upgrade and were chosen as a good compromise that produced fair results without worsen the shower image quality which would be the case of more relaxed cuts: in this case, the increased number of pixels per image would lead to a lower analysis threshold at the risk of adding noise, e.g. in terms of NSB, to the shower image. The cleaning levels used for the standard analysis before the upgrade of the MAGIC I camera were defined as follows: An absolute cleaning level of 6 phe for the core pixels and 3 phe for the boundary pixels were applied to MAGIC I data. Before the upgrade of the readout the cleaning levels for MAGIC II data were set to 9 phe and 4.5 phe for the core and boundary pixels. After this upgrade, the levels have been adjusted to 8 and 4 phe respectively.

The Time Image Cleaning

Apart from the signal intensity, the timing information assigned as number of time slices, to each extracted event is used to further constraint the core and boundary pixel assignment in the image cleaning algorithm [36].

Due to their very short lifetime of the order of few nanoseconds, the pulses of the shower images can be distinguished from the statistically asynchronous signal

produced by NBS photons. In particular the timing coincidence window between the mean arrival time and the arrival time of the individual pixels allows a reliable discrimination between the signal coming related to the NSB and tail featuring real signals.

Including the timing information in the image cleaning offers the possibility to relax the standard cleaning levels, leading to lower analysis threshold (see Figure 7.2).

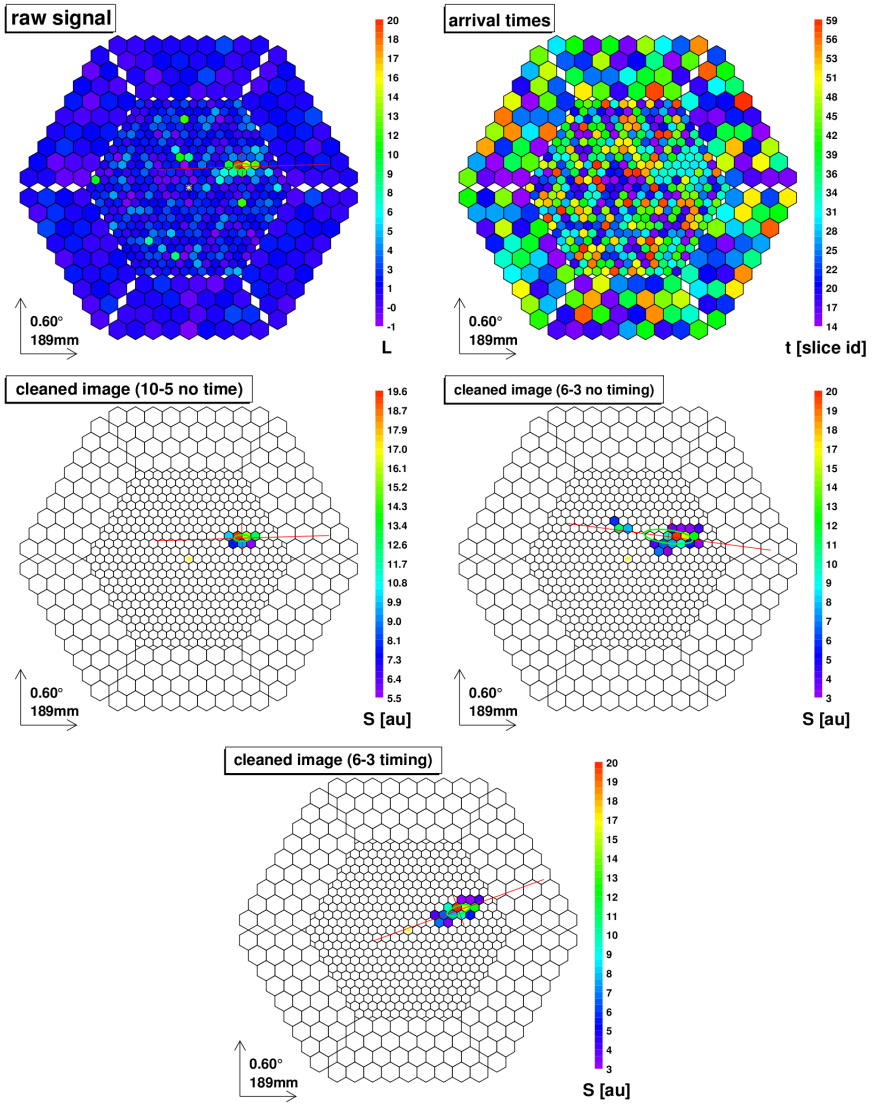

Figure 7.2: Improvement of the image cleaning by the implementation of a time cleaning. First row: Illustration of MC simulated γ–event image (left) and the arrival time informations (right). Second row: Comparison of the image cleaning with standard (left) and relaxed (right) cleaning levels. Third row: Image obtained with the time image cleaning applying relaxed cleaning levels. The simulated γ–ray source (yellow star) is located in the center of the camera [36].

This information is implemented in the image cleaning in the following way: a first cleaning step is dedicated to the identification of the core pixels which have to fulfill the condition that the difference of their arrival times with respect to the mean value does not exceed a distinct offset. During the second cleaning step, whose scope regards the determination of the boundary pixels, a second timing

condition is established setting a limit on the maximum time difference between boundary pixels and neighboring pixels.

The two maximum time differences are referred to as *TimeOffset* and *TimeDifference* and have been derived in an approach analogous to the determination of the optimal cleaning levels.

The Image Parametrization

In the successive step, the *image parametrization* with the *Hillas parameters* (see Section 3.2.4) is performed on the cleaned shower images. For the subsequent analysis, these parameters are fully sufficient, wherefore the individual pixel information are eliminated from the data files.

7.1.3 The Data and Quality Selection

Usually, a first data selection is carried out after the image cleaning by what bad quality data are rejected from the successive data analysis chain. This selection is essential to guarantee the reduction of the data to a final good quality data set. The quality of the data is mainly affected by thee factors, namely the weather, the moon light conditions and hardware problems.

The non–trivial impact of *bad* weather on the data quality is a crucial issue, whose posterior correction is unfeasible due to the lack of simulations on the shower development under different atmospheric conditions in terms of transparency. Therefore, a rejection of data collected during adverse weather conditions is unavoidable. Generally speaking, the evaluation of the weather situation is based on the sky clearness and the wind speed.

The definition of bad weather depends strongly on the source under observation. In the case of pulsars, an extremely low energy threshold for the data analysis is required wherefore the total of absence of clouds is absolutely necessary. By contrast, in case of observations of other source types like AGNs a low *cloudiness* is tolerable. If too high, clouds

In the case of the MAGIC site, a peculiar weather phenomena can affect the transparency of the atmosphere known as *calima* additional to the normal atmospheric conditions (cloudiness, wind etc.). This refers to the dust that originates from the desert. In case of its occurrence, the atmosphere shows an increase in opacity by what the energy threshold of the analysis of data taken under this circumstances increases significantly since low energy events are strongly reduced. Similar to calima, a high cloudiness renders the atmosphere less transparent leading to a partial absorption of the Cherenkov light. Consequently, the energy of the incident γ–ray might not be correctly reconstructed,

Second, observations are also affected by the presence of moon light, leading to a noise increase in the pixels by what the energy threshold of the analysis is consequently higher. In particular, the cleaning level might need an adjustment to prevent noise from background light fluctuations to not create spurious islands in the cleaned shower images. For the same reason, observations performed during twilight require a careful data treatment.

The third parameter on which the data quality depends strongly is related to potential hardware problems that might occur in the subsystems of the telescope, such as the reflector or the camera. In particular the mirror reflectivity, the pointing accuracy in terms of the point spread function (PSF) or the number of bad pixels, by what a certain inhomogeneity in the camera may occur, are some of the typical parameters affected by general hardware problems.

Usually, a selection according to the event rate after image cleaning is performed on single file basis since the rate is strongly correlated to the data taking conditions.

7.1.4 The Stereoscopic Image Reconstruction

Independently if the data were taken in single or stereoscopic mode, the previous steps of the analysis pipeline are applied to the the single data files and for each telescope separately. Therefore, in the case of stereoscopic observations two individual sets of data exists, one per telescope, that contain two different views of the same cleaned shower image.

At this point, the executable `superstar` is used to merge the essential information of the two data sets into one single file aiming at the identification of matching image pairs that belong to the same event based on the L3 Trigger numbering. In addition, the image parameters of the individual data streams are renamed including the telescope number in the conventional Hillas parameter description and further image parameters associated to the stereoscopic shower view are determined.

The stereoscopic image parameters provide information on the direction on the incoming primary particle, the impact point of the shower on the ground with respect to each telescope `impact 1` and `impact 2` as well as the height of the shower maximum `MaxHeight` [200]. These global parameters describing an air shower, are estimated using only the main axis and centroid position of both telescope images (see Figure 7.3).

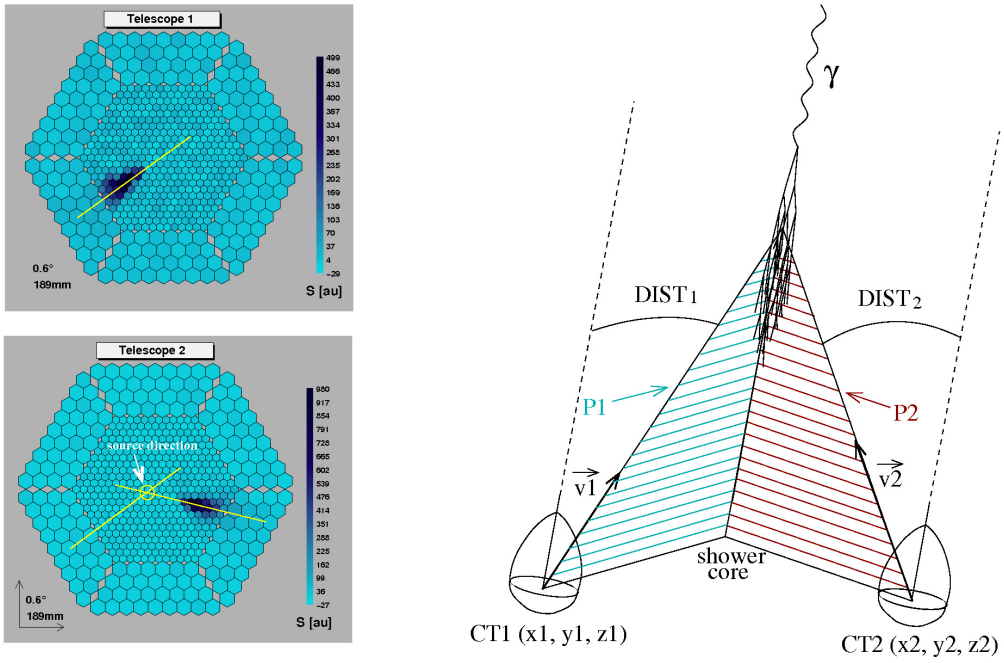

Figure 7.3: Determination of the stereoscopic image parameters. *Left:* Reconstruction ofthe shower direction through the intersection of the major axes of the images in both telescopes. *Right:* Reconstruction of the shower core position (`MaxHeight`) assuming that the shower axis is parallel to the pointing direction of the telescopes.

This geometrical reconstruction is independent of any MC simulations. The

`MaxHeight` results to be the most powerful stereoscopic shower parameter for the γ/hadron separation (see next Section).

7.1.5 The Random Forest

The *Random Forest* (RF) is a flexible multivariate classification method which is a standard tool of the MAGIC analysis package [27] since it represents an easy and effective method [65]. Based on a collection of *decision trees*, the purpose of this methods is the classification of the stored shower images by recognizing the nature of the primary particle involved in the development of the shower. In general, the decision tree represents a subsequent subdivision of the parameter space due to a cut in a parameter.The Random Forest regression method is also used to reconstruct the arrival direction of the shower using the so–called RF DISP method. These fundamental tasks of the analysis chain are carried out in the so–called *training* phase dedicated to the computation of two distinct matrices that contain information of the *hadronness*, the `DISP` parameter.

The `hadronness` represents a number between 0 and 1 indicating whether an event is γ*–like* (`hadronness` $= 0$), or *hadron–like* (`hadronness` $= 1$). To determine the `hadronness` matrix, MC simulated γ–like events and real data serving as a training sample that contains hadronic shower image parameters are required. Instead, the calculation of the `DISP` matrix is only based on sample of γ–like MC data.

The training of the RF is executed by the `coach` executable. In the successive step of the analysis, the matrices obtained from the training phase are applied by `melibea` to real data from a γ–ray source and dedicated γ–like MC simulations that have not been used for the RF training.

The γ/h Separation

In order to train the RF for the γ/h separation, a set of 11 parameters is used. This set comprises image parameters and timing information of the individual shower images from both telescopes as well as stereo parameters.

The decision tree starts with the complete sample of gammas and hadrons contained in one single *node*. This so–called root node represents the complete image parameter space. The separate the gammas from the hadrons, a subsequently *splitting* of each node into two successor nodes using one of the image parameters at a time is performed. This way, at each node two *branches* containing subsamples of mixed gammas and hadrons are created (see Figure 7.4).

The parameter cut is optimized to separate the sample into its classes, i.e. in gammas and hadrons. To measure the classification power of a given image parameter and to optimize the cut value the *Gini index* is used[47]. The choice of the image parameter taken at a node for splitting is randomized.

The splitting of the the sample stops under two conditions: Either the node size, that is the number of events per node, falls below a limit specified by the user, or there are only events of one class left on the node. That means the *leaf* of the tree is reached. Depending on the nature of the events, the leaf is labeled with 0 or 1.

In the case of mono observations carried out in wobble mode, the image parameters calculated with respect to the anti–source position can be easily used

[47] The Gini index measures the inequality of two distributions as a function of a cut in a variable. The Gini index assumes values between 0 and 1. A this coefficient is low, the distributions are more equal. By contrast, a high coefficient indicates unequal distributions.

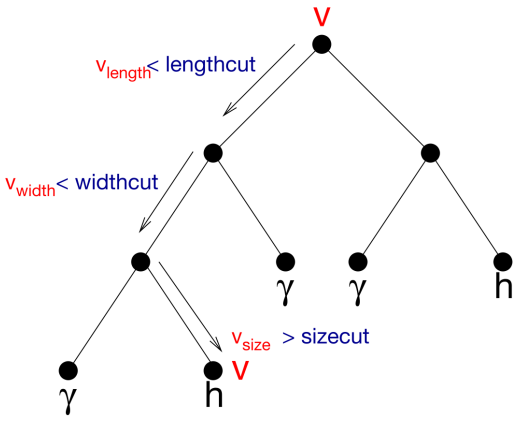

Figure 7.4: Sketch of a RF tree structure for the classification of an event. The decision path through the tree leads to the classification of the event to be hadronic [27].

for the training since the rate of the γ shower images leaking into the anti–source position is negligible. Even in the case of a strong γ–ray source, the RF method will still work despite the small contamination by γ events in the hadron sample. By contrast, stereoscopic data from observations of γ–ray sources are not the appropriate choice as hadronic sample due to the reduced background by the Level3 trigger. Thus, dedicated observations with no γ–ray source in the field of view called *dark patches* are required. Alternatively, data of γ–ray sources known to be very weak can be used, with the disadvantage that the γ/h separation might be less efficient.

For the γ/h separation the `hadronness` matrix obtained in the training phase is applied by `melibea` to real data from a γ–ray source as well as to MC simulations of γ–like events in order to assign the `hadronness` parameter. In Figure 7.5 the mean `hadronness` distributions of two tests samples of gammas and hadrons are plotted.

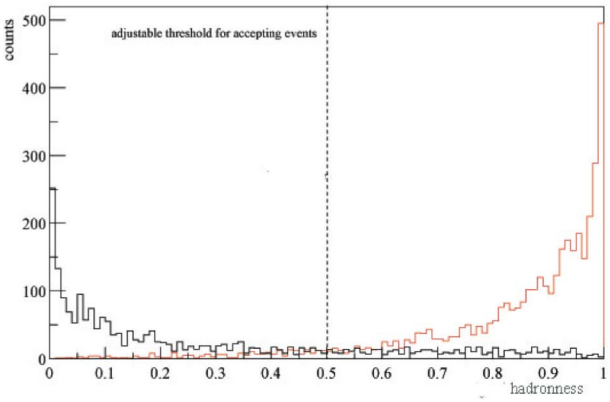

Figure 7.5: Hadronness distribution of γ (black) and hadron–like (red) events peaking at 0 and 1 [27]. From the statistics it is evident that hadron–induced showers represent the majority of the collected data.

While gamma–like events peak at `hadronness` = 0 the distribution of hadronic events peaks at `hadronness` = 1 clearly representing the majority of the collected data. Thus, an appropriate cut in `hadronness` is a powerful tool to efficiently rejected hadron–like showers and to select events that are most likely γ–induced.

The Reconstruction of the Shower Arrival Direction

The `DISP` parameter, i.e. the angular distance between the center of gravity of the image and the simulated source position(see Figure 7.6), is used to reconstruct the arrival direction of shower [31].

In principle, the `DISP` parameter is proportional to the ellipticity of the image for a given zenith angle and γ–ray energy:

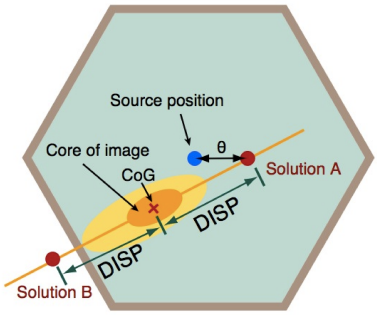

Figure 7.6: Calculation principle of the DISP parameter, providing two solutions for the source position. This method may lead to a *left–right ambiguity* of the source position with respect to the CoG of the shower image.

$$\texttt{DISP} \propto \left(1 - \frac{\texttt{Width}}{\texttt{Length}}\right) \tag{7.5}$$

By including also the dependence on possible image truncations at the camera edge and the image Size, the DISP precision can be improved [101] providing a simple function of the impact parameter. Beside the standard Hillas parameters, the modified DISP parametrization includes information on the Leakage as well as on the timing of the event.

Especially the timing information is strongly dependent on the *impact parameter*. Thus, the DISP parameter can be described as a simple function of the impact parameter that is expected to improve the estimation of the arrival direction as well as the angular resolution. To combine the information of the geometry and the timing of the shower image, the RF DISP method is a convenient solution.

The DISP matrix from the training phase is applied by melibea to data from a γ–ray source and to MC simulated γ–like events. First, the DISP parameter is calculated for the shower images in each telescope separately. In a second step, a weighted average is computed from the DISP position obtained from both telescopes.

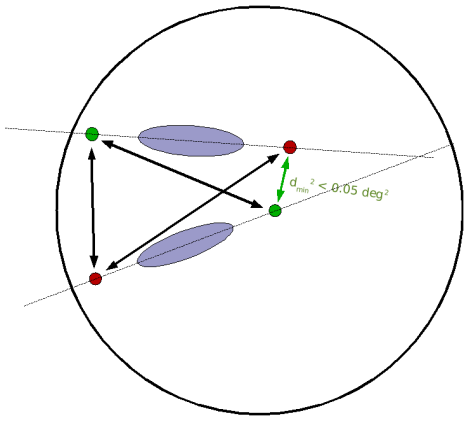

Figure 7.7: Sketch of the stereo RF Disp determination via the turbo buster method.

It may happen that the DISP direction is not correctly reconstructed such that the source position is located on the opposite site of the shower image referred to as wrong *head–tail–discrimination*. In this case, the *turbo buster method* is applied selecting the DISP solution providing the closest match out of the four possible solutions of the two DISP positions in each telescope (see Figure 7.7). Finally, this solution is used to compute the weighted average from the selected DISP solutions from both telescopes. Due to the use of the RF DISP method, the angular resolution was improved by ∼20 - 30% [31].

7.1.6 The Energy LUTs

To reconstruct the energy of the shower image, the LUTs are produced for each telescope [35]. The LUTs are based on the `Size` and the `impact` parameters of both telescopes as well as on the `MaxHeight` parameter and the zenith angle of observation. This selection of parameters provides a simple model for the light distribution of a shower. Assuming that most of the Cherenkov light produced by a γ–ray is contained in a light pool or radius, the mean photon density in the light pool from a single charged particle of the γ–ray shower can be calculated from the total power of emitted light by such particle at a given height in the atmosphere. Thus, by using a simple atmospheric model, the amount of light produced by a single particle ρ_c in the light pool of radius r_c can be computed for a given `MaxHeight` and zenith angle.

To create such LUTs, filled with information of ($E_{\text{true}} \times \rho_c$/`Size`) as a function of `impact`/r_c and `Size` to obtain the energy of an event measured by each telescope, a simple macro called `create_Energy_table.C` is applied to γ events from MC simulations. Based on the LUTs, the `melibea` executable is used to calculate the reconstructed energy for real data from a γ–ray source and to MC simulations of γ–induced events of each telescope separately, whereafter the weighted average value is computed.

The Energy Resolution

Despite the rather simple approach using LUTs with respect to the RF method, a better energy reconstruction is achieved, especially at low energies, due to the implementation three–dimensional shower parameters which are well reconstructed by stereoscopy.

The *energy resolution* is a measure for the evaluation of the energy reconstruction which refers to the standard deviation of the histogram to which a Gaussian distribution is fitted:

$$(E_{\text{rec}} - E_{\text{true}})/E_{\text{true}} \tag{7.6}$$

The bias of this method is evaluated in terms of the mean value of the distribution. In Figure 7.8, both the spectral energy resolution and the bias are plotted.

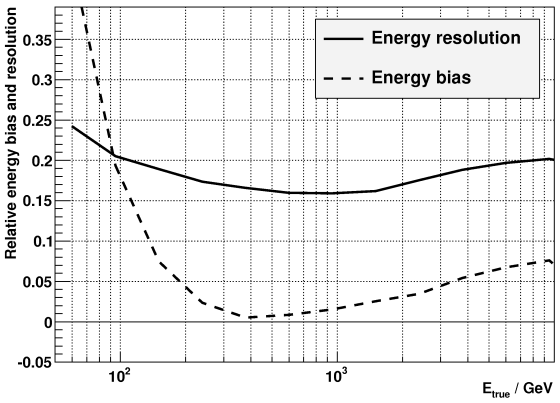

Figure 7.8: Spectral energy resolution (solid line) and the bias (dashed line) of the stereoscopic MAGIC system obtained with MC simulated γ–rays [35].

Studies of theses quantities pointed out a weak dependence on the cuts applied in `hadronness` and the squared angular distance θ^2 (see Section 7.1.7). The energy resolution is as good as 15% in the energy range of few hundred GeV, while is worsens for higher energies due to the large fraction of truncated shower images, shower events with high impact parameters and worse statistics in the training

sample. At low energies, the energy resolution is negatively affected by the higher noise with respect to a lower photon number contained in the shower images. Furthermore, the arrival direction reconstruction is less precise which spoils the impact parameter determination. This bias worsens below ∼100 GeV due to the energy threshold of MAGIC.

The Energy Threshold of the Analysis

Usually, the energy threshold of the analysis is estimated by means of studies on the reconstructed energy distribution obtained from MC simulations of γ–like data sample by using the same cuts as applied to the data set of real events. The energy threshold depends strongly on the `Size` cut applied. However, it is also related to other parameters such as the `zenith angle` and `hadronness` and θ^2 cuts. The peak of the reconstructed energy distribution surviving the cuts is usually interpreted as the energy threshold of the analysis.

7.1.7 The Signal Search

Typically, the *signal search* is based on the parameter space where a discrimination between hadronic and electromagnetic showers is possible by the application of cuts in a set of image parameters by what the hadronic background can be suppressed efficiently.

There are three different solutions how to perform a signal search on the basis of different image parameters denoted as `alpha` (α) or `theta2` (θ^2) plot and sky map.

The basic concept of these methods is the search for an *excess* in the distribution between the events stemming from *On* and *Off* data referred to as *signal region*. The On distribution consists of events stemming from the position of the observed γ–ray source in the Cherenkov camera. Contrary, the Off distribution contains events located at a certain offset with respect to the position of the observed source in the Cherenkov camera. The reconstructed direction of such excess should be consistent with the source position within a pre–defined parameter window. The significance of the excess is calculated according to the Li–Ma formula 17 from [195]. Usually, in astroparticle physics the conventional significance limit for claiming a signal detection is set to $5\,\sigma$.

The Alpha and θ^2 Plot

The `alpha` parameter, i.e. the angle between the image major axis and the line linking the image center with the pointing position (see Figure 3.17), and the squared distance between the expected and reconstructed source position in the camera θ^2 are the most powerful discriminators between hadronic and electromagnetic showers. As γ–like events are expected to be reconstructed close to the source position in the camera, their `alpha` or `theta2` distributions peak at zero given the source is not extended, i.e. point–like as it is the case e.g. for AGNs. On the other hand, sky regions without a γ–ray source exhibit a flat distribution since hadronic events exhibit an isotropic distribution.

Thus, the signal can be extracted by plotting the `alpha` or θ^2 distribution of the On and Off data after the application of selection cuts and an appropriate cut in `hadronness`. The On data should peak close to zero while the Off sample should show a flat distribution. Due to the very low signal to background ratio, the cut in `hadronness` has to be always applied, even in the case of strong γ–ray sources like the Crab Nebula or Mkn 501, in order to extract the signal.

While `alpha` is used for the signal search in mono observations, it can not be used for stereo data since the azimuth homogeneity is broken. Therefore, the $\theta 2$ plot is used for latter observations (see Figure 7.9). The signal search based on this parameter is performed by the `odie` executable.

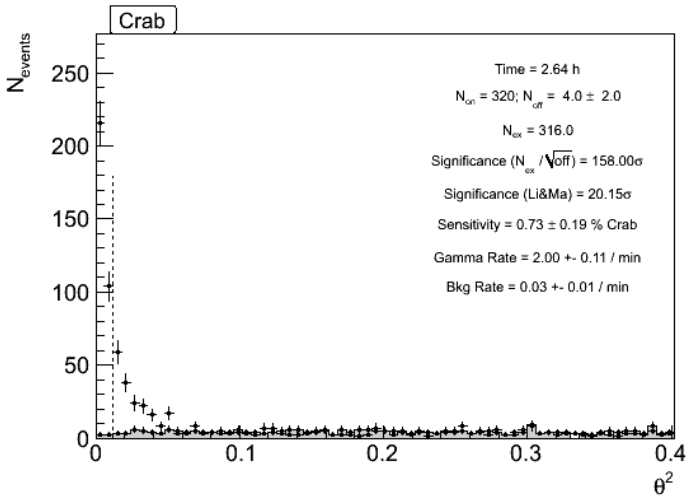

Figure 7.9: Example of a θ^2 plot. The On (black points with errors) and Off (gray shaded histogram) data distribution. The signal search is performed in the θ^2–region indicated by the vertical dashed line.

The Sky Map

A *sky map* represents another tool for the signal search, with which a bidimensional map of the reconstructed direction of each event is displayed after its transformation from camera to sky coordinates. Sky maps are very useful to check the extension of a source as well as to verify the pointing correctness of the telescopes and to estimate the analysis resolution.

In addition, sky maps provide the advantage to estimate the On/Off ratio in the entire FoV of the camera, which requires the modeling of the background. The sky maps are produced using the `caspar` executable, providing a *test statistic* (TS) based on formula 17 of [195] applied on a smoothed and modeled background estimation.

Recently, a more generalized test statistic has been developed for the significance calculation in VHE astronomy suitable for sky mapping purposes with the advantage to be unaffected by many systematic uncertainties [180]. To derive such *likelihood ratio sky map*, the `datacubes` executable is used as interface between the MAGIC data and the `skymapLRT.C` macro by what the likelihood ratio test statistic (LRT) is calculated using formula 16 of [181] providing a generalization of the likelihood ratio concept on which formula 17 of [195] is based.

In the case of a significant signal detection from VHE observations of a γ–ray emitting source, that is the signal search yields an event excess of more than $5\,\sigma$ significance, the differential and integral flux to characterize the VHE γ–ray emission is reconstrcuted via the `fluxlc` executable which will be explained in the next two sections.

7.1.8 The Differential Spectrum

The *differential spectrum* is defined as the function of excess of γ–rays N_γ estimated from the respective `alpha` or θ^2 distribution in a finite energy bin E applying bin–optimized cuts, normalized on the *effective observation time* t_{eff} and *effective collection area* A_{eff}:

$$\Phi(\mathrm{E}) = \frac{N_\gamma}{dE\, dA_{\text{eff}}\, dt_{\text{eff}}} \tag{7.7}$$

where the number of bins in a certain energy range as well as the cuts in `hadronness` and `alpha` or θ^2 are manually specified in the program.

The effective collection area defines the area in which air showers can be potentially observed by the telescope folded with the detection efficiency after all cuts applied in the analysis. The detection efficiency can be estimated from MC simulations, based on the ratio of the number of γ–like events surviving the cuts and the total number of γ–induced showers.

Usually, the effective collection area is rather constant with energy down to a certain energy below which it decreases rapidly (see Figure 7.10). This corresponds to a decrease in the statistics and hence to a less reliable flux estimation at lower energies.

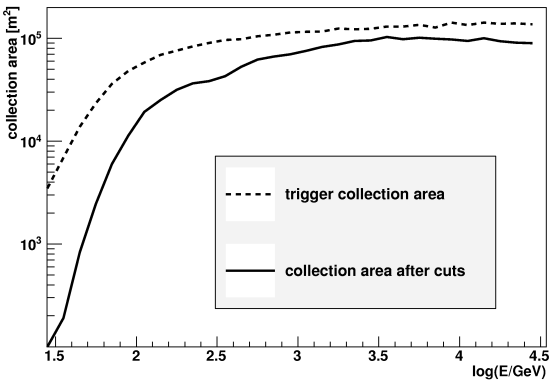

Figure 7.10: Example of the γ–ray effective collection area obtained from MC simulations before (dashed line) and after (solid) analysis cuts in `Size`, `hadronness` and θ^2 [35].

The calculation of the differential flux allows for the study of the VHE γ–ray component of the SED of the source in reconstructed energy. To correct the bias of the energy reconstruction due to the instrumental bias and finite energy resolution, an *unfolding* procedure is applied by the computation of the *migration matrix* that connects the reconstructed energy with the true energy [24].

In the macro `CombUnfold.C` different unfolding algorithm available referred to as *Tikhonov, Schmelling, Bertero* have been implemented to apply a correction to the distortion of the measured differential spectrum. Typically, the differential spectrum observed in VHE γ–rays describes a power law.

7.1.9 The Light Curve

A *light curve* represents the integral γ–ray flux above a certain energy as a function of time. Thus, an integration of the differential flux above an arbitrary energy E evaluated from MC data is performed:

$$\Phi_{\text{int}} = \int_{E}^{\infty} \frac{N_\gamma}{dE\, dA_{\text{eff}}\, dt_{\text{eff}}} \tag{7.8}$$

It is conventional to chose E such that it exceeds the energy threshold of the IACT.

Typically, VHE γ–ray observations with IACTs can not be performed evenly as they are subjected to to bad weather, moon presence or unforeseen hardware problems as well as to schedule constraints. Consequently, observations contain normally few to some tens of hours spread over the entire observation period.

Therefore, the time binning is normally a compromise between the maximum number of nights of observation and reasonably small error bars and significance of the integral fluxes.

Nevertheless, integral flux values may be below the energy threshold and therefore not significant enough. In this case, *integral upper limits* on a 95% confidence level based on [276] are computed, assuming an upper limit of possibly observed gamma events during the effective observation time.

7.2 Historical MWL Observations of 1ES 0806+524

The blazar 1ES 0806+524, located at RA 08:09:49, DEC 52:18:58, has been discovered first in the radio band [54] and was classified as BL Lac object [283] by means of X-ray data from the *Einstein* Slew Survey [109]. The comparison between X-ray data obtained from the *ROSAT* satellite All-Sky Survey (RASS) [75] and radio observations lead to the further categorization as HBL [104] (see Figure 7.12).

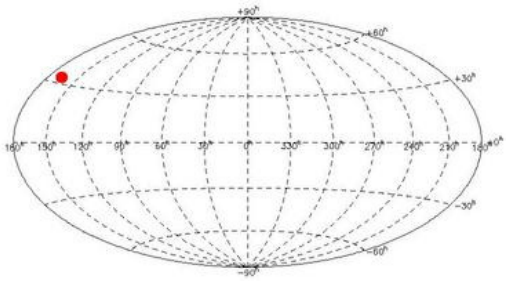

Figure 7.11: Position of the HBL 1ES 0806+524 in galactic coordinates.

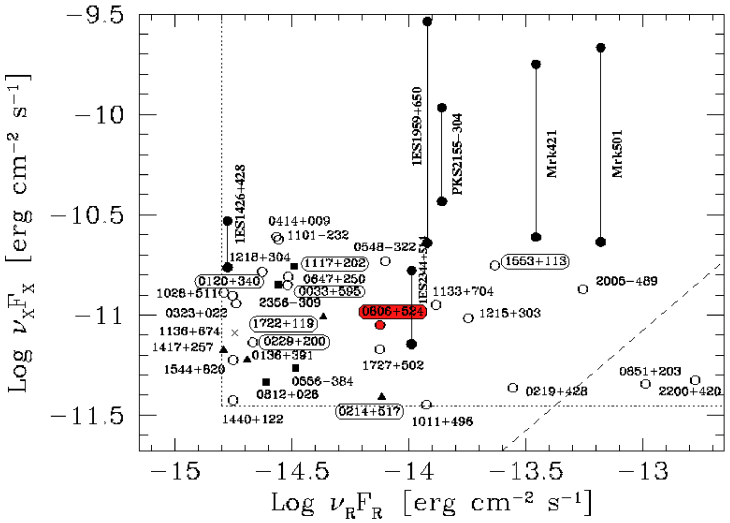

Figure 7.12: X-ray to radio flux ratio typical for HBLs, 1ES 0806+524 is marked in red. Adapted from [96].

By means of a high signal–to–noise ratio spectrum in the optical band, the redshift of the host galaxy has been inferred by [45] to be 0.138 (see Figure 7.13).

The rather stable radio flux of 1ES 0806+524 measured at different frequencies is commonly of the order of few tens to ∼170 mJy. From 2004 to present time, 1ES 0806+524 has been monitored with the *Very Long Baseline Array* (VLBA) as part of the *Monitoring of Jets in Active Galactic Nuclei with VLBA Experiments* (MOJAVE) [198]. The VLBA consists of ten radio telescopes remotely controlled from the *Array Operations Center* in Socorro, New Mexico. At 2 cm,

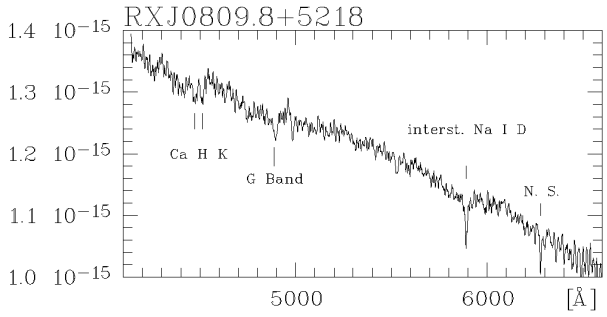

Figure 7.13: Optical spectrum of 1ES 0806+524 of high signal–to–noise ratio obtained with the Calar Alto 3.5 m telescope from which a redshift of 0.138 has been inferred [45].

the monitored flux is stable at a level of a ∼140 mJy[48]. 1ES 0806+524 has been classified as a low power radio source that is heavily core–dominated [147], see Figure 7.14.

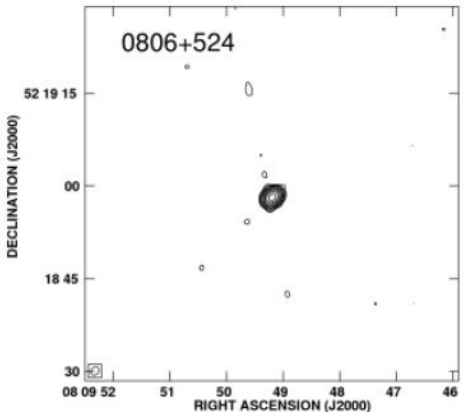

Figure 7.14: VLA image of 1ES 0806+524 taken in A configuration. The radio emission originates dominantly from the source core [147].

After its classification to be bright in X-rays and to feature a steep spectrum in this waveband [75], the source has been target of two surveys, namely *ROSAT* [76] and *Slew* [255] during which further X-ray data have been collected. In addition, 1ES 0806+524 has been constantly monitored from 1996 to present time in X-rays by the *RXTE* as part of the *All Sky Monitor* (ASM) survey[49]. These observations indicate marginal variability in 2002 [96]. Furthermore, *Swift* observations revealed a marginal flux variability on the time scale of few days in 2008 [9]. Beside *RXTE*, the *Swift* satellite is monitoring the source since 2007 as part of the program on *Fermi* LAT "sources of interest"[50].

The flux in the optical regime has been monitored in the R band by the KVA telescope as part of the *Tuorla Observatory Blazar Monitoring Program*[51] [305] since 2003, see Figure 7.15. The light curve features flux variations from ∼2 to ∼6 mJy. A non–periodical long–term variability has been found in the R band with a timescale of the order of one year showing maximum brightness of 14.72 mag and an overall variation of 0.9 mag [170].

The source has been detected in the HE regime from MeV to GeV by *EGRET* on a 50% confidence level [266]. However, due to the large error box, the γ–ray emission might be associated with another source, i.e. B 0803+5126, located at redshift 1.14 that is situated in the same sky region. Nevertheless 1ES 0806+524 is favored as origin of the revealed γ–ray radiation [291]. During its first 5.5 months of observations, the *Fermi* LAT detected a significant emission of 1ES 0806+524

[48] http://www.physics.purdue.edu/astro/MOJAVE/sourcepages/0806+524.shtml
[49] http://xte.mit.edu/asmlc/ASM.html
[50] http://www.swift.psu.edu/monitoring/source.php?source=1ES0806+524
[51] See the project webpage for details: http://users.utu.fi/kani

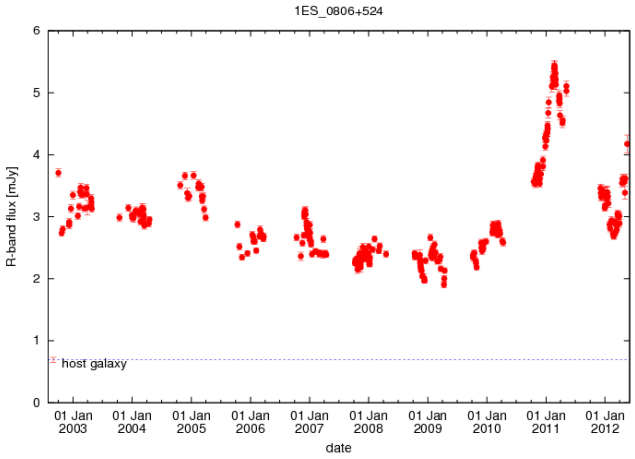

Figure 7.15: Optical light curve of 1ES 0806+524 from the Tuorla Observatory Blazar Monitoring Program from 2002 to present time, taken from http://users.utu.fi/kani/1m/1ES_0806+524_jy.html.

which is consistent with a flat spectrum that is well described by a simple power law (see Figure 7.16). The observations indicated only a marginal variability on a 28–day timescale [2]. Beside its in inclusion in the three–months catalog, the source has been also included in the first *Fermi*/LAT source catalog (1FGL) stating a high probability of a curvature in the HE spectrum [5].

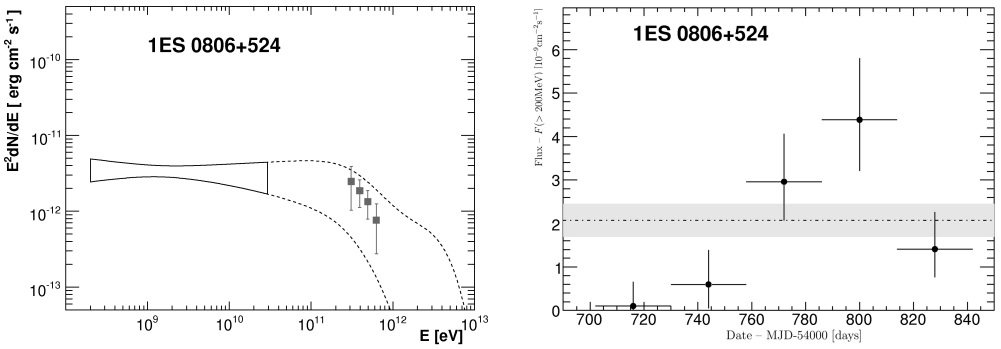

Figure 7.16: *Left:* The GeV spectrum of 1ES 0806+524 derived from *Fermi*-LAT observations indicated as "butterfly" contour. The spectral extension of the contour to TeV energies is shown as dashed line applying corrections for EBL attenuation. TeV observations from VERITAS are plotted as gray squares. *Right:* The twenty–eight day light curve above 200 MeV derived from *Fermi* observations centered on the new moon. The dashed line indicates the mean flux with an estimated systematic uncertainty of 3% (gray band. Adapted from [2].

In the second *Fermi*/LAT source catalog (2FGL) 1ES 0806+524 has been flagged to be variable[52] source [5, 242].

After first VHE γ–ray observations by the Whipple Observatory 10 m γ–ray telescope and HEGRA, the source was suggested as good candidate of VHE γ–ray emission with a predicted intrinsic flux of $F_{E>0.3\,\mathrm{Tev}} = 1.36 \times 10^{-11}\,\mathrm{cm}^{-2}\,\mathrm{s}^{-1}$ by [90], wherefore several VHE observations have been carried out leading to several upper limit of the VHE flux (see Table 7.1).

Observations by the VERITAS collaboration from late 2006 to early 2007 have

[52] Statistically, the chance to be a steady source corresponds to less than 1%.

Year	Detector	E_{th} [TeV]	U.L. [$\mathrm{cm}^{-2}\,\mathrm{s}^{-1}$]
1996[a]	Whipple	0.3	$1.4 \cdot 10^{-11}$
2000[a]	Whipple	0.3	$16.8 \cdot 10^{-11}$
2001–2002[b]	Whipple	0.39	$0.67 \cdot 10^{-11}$
1996–2002[c]	HEGRA	1.09	$4.25 \cdot 10^{-12}$
2004–2006[d]	MAGIC I	0.23	$1.01 \cdot 10^{-11}$
2004–2006[e]	MAGIC I	0.14	$2.2 \cdot 10^{-11}$

Table 7.1: Compilation of the upper limits on the integral VHE γ–ray flux obtained from various observations of 1ES 0806+524. The first and second column indicate the year of observation and the instrument; in column three and four the energy threshold and the integral upper limit are stated; [a] [164];[b] [96]; [c] [15]; [d] [28]; [e] [32]

been carried out for 35 hours during the construction phase of the VERITAS telescope array. Therefore. the data encompass the two– and three–telescope configuration (9 hours with T1/T2 and 26 hours with T1/T2/T3 configuration) [84], yielding a very weak hint of emission with a statistical significance of $2.5\,\sigma$. The data have been combined with observations performed from November 2007 to 2008 in the full four–telescope operation mode. First analysis of 46 hours yielded already a $5.8\,\sigma$ source detection due to which observations have been extended [304]. The combined data sample, which comprises 65 hours, indicates a source detection with a significance of $6.3\,\sigma$ [9]. A hint for a variability on monthly timescale was found. The differential flux of 2007/ 2008 data has been characterized by a simple power law with spectral index Γ of $3.6 \pm 1.0_{\mathrm{stat}} \pm 0.3_{\mathrm{sys}}$ between ∼300 to 700 GeV and the integral flux above 300 GeV was found to be $(2.2 \pm 0.5_{\mathrm{stat}} \pm 0.4_{\mathrm{sys}}) \cdot 10^{-12}\mathrm{cm}^{-2}\mathrm{s}^{-1}$ corresponding to 1.8% of the Crab Nebula flux (see Figure 7.17).

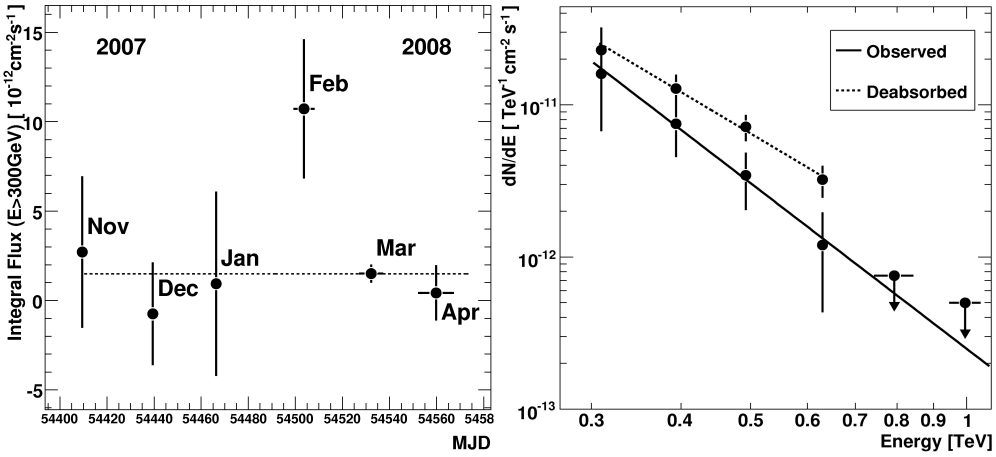

Figure 7.17: Differential and integral VHE γ–ray flux from the detection of 1ES 0806+524 by VERITAS. *Left:* The differential observed and deabsorbed VHE γ–ray spectrum of 1ES 0806+524 from ∼300 to ∼700 GeV. *Right:* The integral VHE γ–ray flux above 300 GeV indicating a hint for variability on a monthly time scale [9].

In summary, 1ES 0806+524 has been observed in all wavebands in the last decades. Since there has never been a systematic MWL study of the source, the SED of the source could not be studied in detail. Especially, because the observations were performed before *Fermi* started operations the high energy

peak has been poorly constrained so far.

As for the synchrotron emission, the peak frequency has been obtained from a parabolic fit to a collection of MWL data from different epochs. The fit indicates the peak to be located at$3.63 \cdot 10^{16}$ Hz (see Figure 7.18) corresponding to 0.15 keV [238]. As the peak is estimated to be situated in the soft X-ray regime, the classification of 1ES 0806+524 as HBL is once more confirmed.

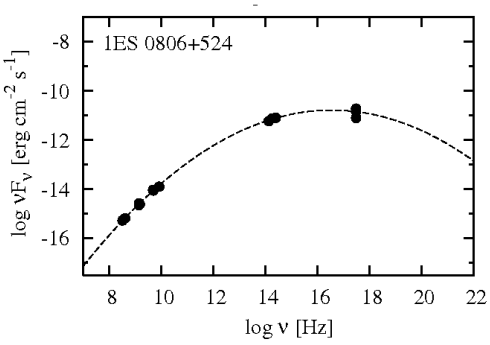

Figure 7.18: Low energy bump of the spectral energy distribution from 1ES 0806+524. The data points are fitted with a parabolic function by which a synchrotron peak frequency $log\,\nu_{\mathrm{Peak}}$ of 16.56 Hz is determined [238].

In the following, the first systematic MWL study of 1ES 0806+524 centered on the recent VHE γ–ray observations by MAGIC is presented.

7.3 The MAGIC Data Set from 2011 & Quality Selection

Due to the poor determination of the VHE spectrum by previous Cherenkov telescope observations, MAGIC reobserved 1ES 0806+524 in order to measure the VHE spectrum more detailed. Moreover, the purpose of these reobservations was to collect simultaneous data from *Fermi* to provide a good coverage of the IC peak aiming at an overlap of the data from both instruments since the SED was poorly constrained from previous MWL observations.

The observations have been performed in stereoscopic mode in winter 2011 from January to March for a total of approximately 24 hours during 13 nights. The observations were triggered by a high optical state in the R band reported by the KVA telescope. On February 24$^{\mathrm{th}}$, 1ES 0806+524 underwent a flare in VHE γ–rays which has been reported by MAGIC via an *Atel*[53] in order to alert the astronomic community [214].

Due to bad weather conditions, including high humidity, high cloudiness and strong moon, about 2.5 hours of data had to be discarded from the final data set after applying quality selection cuts based on the event rate (see Appendix A.1 for details). The reduced data set of good quality, retaining data taken under moderate moon light conditions, encompasses ∼16 hours of effective observation time, taking the dead time due to the readout system into account. Observations, which were carried out in *wobble* mode (see Section 3.4.5), cover a zenith angle range from 23° to 46°. In Table 7.2 the observational details concerning time and zenith angle coverage as well as the moon light conditions are listed for the individual nights of observation. In Figure 7.19 the stereo event rate distribution of the data surviving the quality selection cuts from 2011 observations is plotted together with the mean value. As the trigger threshold increases with the presence of ambient light, the observations carried out under moderate moon light conditions feature fall–offs in the event rate. In addition, a correlation to a decrease

[53]The *Astronomer's Telegram* (ATel) is a web based short notice publication system for reporting and commenting on new astronomical observations. It is an important media effectively distribute instantaneously time critical information for the entire professional community [282].

Night	MJD	Eff. Time [h]	Zd [°]	Moon light conditions
07/01/2011	55568	0.43	24 - 26	No Moon
08/01/2011	55569	0.76	24 - 26	No Moon
11/02/2011	55603	0.62	27 - 31	Moderate Moon
12/02/2011	55604	0.38	34 - 37	Moderate Moon
23/02/2011	55615	1.22	26 - 35	Moderate Moon
24/02/2011	55616	2.98	23 - 43	Moderate Moon
25/02/2011	55617	3.03	23- 45	No Moon
27/02/2011	55619	0.59	25 - 31	No Moon
28/02/2011	55620	2.16	26 - 43	No Moon
01/03/2011	55621	1.96	24 - 40	No Moon
02/03/2011	55622	1.98	26 - 45	No Moon

Table 7.2: Final dataset of 1ES 0806+524 observations from winter 2011 used in the analysis. From left to right: The nights of observation are indicated in dd/mm/yy (first column) and in MJD (second column); effective time of observation in hours (third column); zenith angle range in degrees (fourth column). The last column refers the moon light conditions during observations.

in rate due to observations carried out at high Zd has been inferred. Despite these effects on the rate stability, all data have been included in the subsequent analysis.

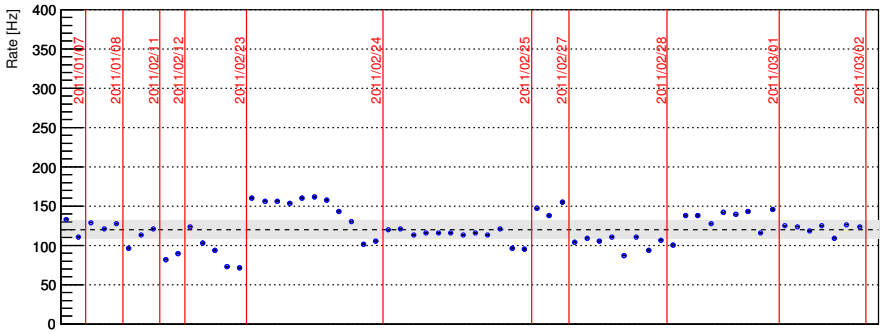

Figure 7.19: Stereo event rate distribution of 1ES 0806+524 2011 MAGIC data. The gray shaded area corresponds to the 10% variation from the mean value (dashed line).

The data analysis has been performed with the MAGIC standard analysis and reconstruction software and using dedicated MC data for the γ-like event simulation needed for the γ/h separation and the energy reconstruction.

7.4 The Signal Detection: θ^2-plot and Sky Map

The signal search is performed by means of the distribution of the squared angular distance θ^2. Two sets of cuts have been applied to the data as shown in Table 7.3.

These cuts referred to as *low energy* (LE) and *full energy* (FR) range lead to

[53]This cut is applied on the reconstructed energy.

Table 7.3: Set of event selection cuts applied to the 1ES 0806+524 data for the signal search.

Parameter	Cut	
	LE	FR
`Size`	>55 phe	>125 phe
`hadronness`	<0.28	<0.16
Energy[53]	–	>250 GeV

an energy threshold of ∼100 and ∼250 GeV[54] of the analysis (see Figure 7.20). These analysis thresholds have been determined by means of MC data using the same cuts as applied to real data and a spectral photon index Γ of -2.6.

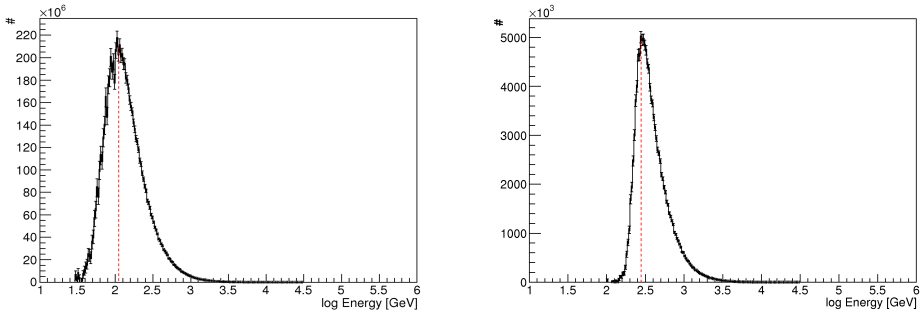

Figure 7.20: Energy thresholds for the signal detection of 1ES 0806+524, estimated from dedicated MC data to which LE (left) and FR (right) cuts have been applied as to real data from 2011 observations assuming a spectral photon index Γ= -2.6.

In the LE regime only the anti–source position located at 180° with respect to the reconstructed position of the source in the camera was used as Off region to determine the background level. In the FR range three Offs at 90°,180° and 270° with respect to the reconstructed source position in the camera were applied .

In the FR range, i.e. above 250 GeV, the 2011 data yield an excess of ∼148 γ–like events, while the background level corresponds to ∼113 events (see Figure 7.21). The significance of the event excess that has been calculated according to equation 17 from [195] is ∼9.9 σ .

With an event excess ∼484 γ–like events and a background level of ∼3009 events, the source has been also detected with a significance of ∼6 σ above 100 GeV applying LE cuts (see Figure 7.22).

In order to study an eventual short–term variability the signal search has been also performed on a daily basis. This study resulted in a strong detection of the VHE emission of 1ES 0806+524 on February 24$^{\text{th}}$, a so–called flare (see Chapter 6) wherefore an ATel was sent [214]. The ∼3 hours of effective observation during the high state in VHE γ–rays of 1ES 0806+524 yielded a signal detection of 7.6 σ significance above 250 GeV (see Figure 7.23). When excluding the flare of 1ES 0806+524 from the data set, the source is still detected with a significance of 7.3 σ during the remaining ∼13 hours of effective observation time (see Figure 7.24).

Table 7.4 summarizes the individual detection significances of the entire data set, the data from the source flare and the subsample from which the flare data have been excluded both in the LE and FR range.

[54] Note that the FR energy cut is applied to the reconstructed energy, while the threshold is reported in *true* energy. Both energies are related via *migration matrix*. Despite the linearity of this matrix, the reconstructed energy is typically overestimated at lower energies and underestimated at higher energies instead.

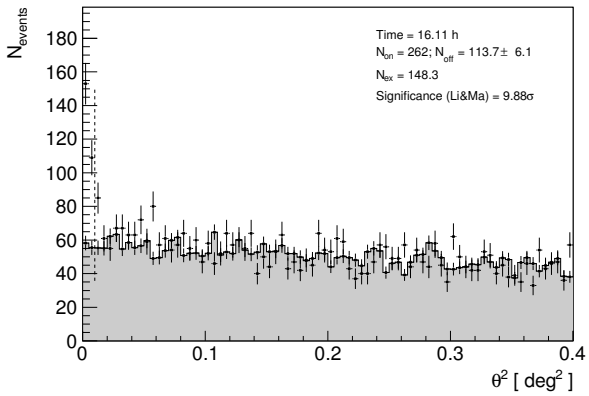

Figure 7.21: Signal detection plot of 1ES 0806+524 from MAGIC 2011 observations above 250 GeV. The distribution of the squared angular distance θ^2 for the on–source counts in the direction of 1ES 0806+524 (black points with error bars) and the normalized off–source events (gray histogram) from 2011 stereo observations after the application of FR cuts are plotted. The signal is extracted within the θ^2 region confined by the vertical dashed line. The background is calculated from three Off positions located at 90°, 180° and 270° with respect to the reconstructed source position.

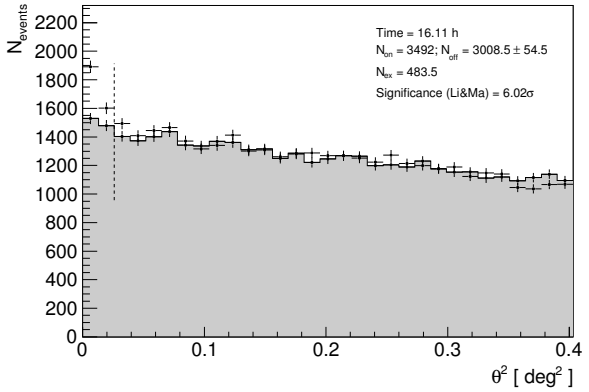

Figure 7.22: Signal detection plot of 1ES 0806+524 from MAGIC 2011 observations above 100 GeV obtained with LE cuts. The background is calculated from the anti–source position located 180° with respect to the reconstructed source position.

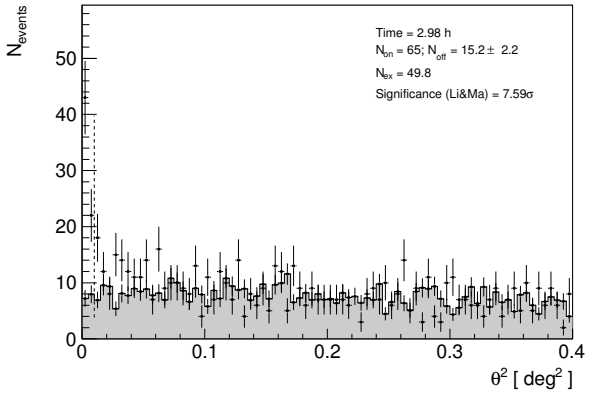

Figure 7.23: θ^2 plot of the VHE γ–ray flare of 1ES 0806+524 .

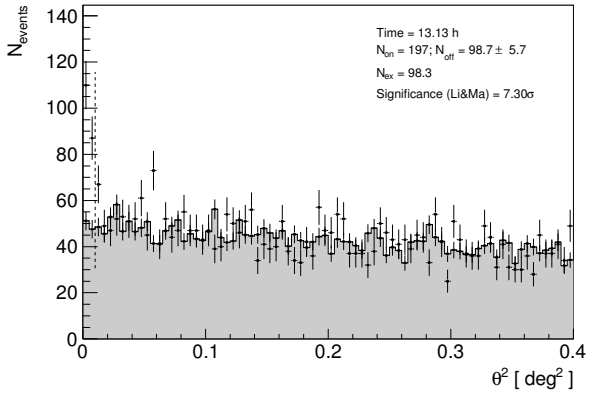

Figure 7.24: θ^2 plot of the low state data sample of 1ES 0806+524 . The source flare has been excluded from the data sample.

The entire data set shows in both energy ranges a clear detection, while when excluding the source flare from the data sample, LE range shows only a hint for detection.

Observation Period	Eff. time [h]	Significance [σ]	
		LE	FR
January - March	16.11	6.0	9.9
January - March*	13.13	4.6	7.3
February 24th	3.30	3.9	7.6

Table 7.4: Signal detection study of the 2011 data from observations of 1ES 0806+524. The * denotes the reduced data sample, from which the source flare has been excluded.

In order to determine the source extension and its position on the sky, a LRT skymap has been derived above 250 GeV applying FR cuts. The 2D Gaussian fit of the sky map yields a consistency with a point–like source located at the catalogue position of 1ES 0806+524 within a PSF of less than 1 mrad (see Figure 7.25) above 250 GeV.

7.5 1ES 0806+524: The Light Curve and Variability studies

To investigate the temporal VHE emission evolution of 1ES 0806+524, the integral flux above the energy threshold of 250 GeV has been studied as a function of time. As the source has been also detected in the LE range, the cuts reported in Table 7.5 have been applied to the data in order to derive the the light curve.

Parameter	Cut
`Size`	>50 phe
`hadronness` cut efficiency	90%
θ^2 cut efficiency	70%
minimal `hadronness`	0.07
minimal θ^2	0.02 deg^2
Energy	>250 GeV

Table 7.5: Set of cuts applied to the 1ES 0806+524 data for the temporal analysis.

The cuts in `hadronness` and θ^2 are dynamical, i.e. their definition is based on their cut efficiency as estimated from γ–like MC events, leading to energy

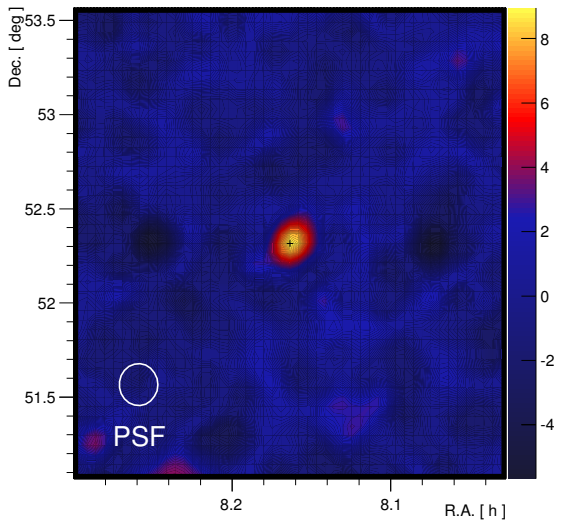

Figure 7.25: Significance of the LRT sky map of 1ES 0806+524 above 250 GeV derived from MAGIC stereo observations in 2011. A significant excess consistent with a point–like source is found at the catalogue position of 1ES 0806+524. The PSF of the MAGIC telescopes is indicated (white circle).

dependent cuts, as shown in Table 7.6. The cuts are chosen in such way that 90 and 70% of the simulated γ–like events survive respectively.

Energy bin [GeV]	θ^2 cut [deg^2]	`hadronness` cut
199<E<271	0.02	0.36
271<E<368	0.02	0.35
368<E<500	0.02	0.32
500<E<679	0.02	0.28
680<E<924	0.02	0.29
924<E<1256	0.02	0.25
1256<E<1707	0.02	0.24
1707<E<2321	0.02	0.23
2321<E<3155	0.02	0.15
3155<E<4288	0.02	0.22
4288<E<5830	0.02	0.12
5830<E<7924	0.02	0.11
7924<E<10772	0.02	0.10
10772<E<14643	0.02	0.13
14643<E<19905	0.02	0.15
19905<E<27058	0.02	0.19
27055<E<36782	0.02	0.28
36782<E<50000	0.02	0.14

Table 7.6: θ^2 and `hadronness` cuts for the study of the integral flux as a function of time. These cuts were derived for the individual energy bins by fixing the cut efficiencies at 70 and 90% respectively.

The daily–binned light curve (see Figure 7.26) of the integral flux above 250 GeV

measured during 2011 observations ranges from 0.7 to 9% Crab units (C.U.[55]), where the highest flux level appears during the source flare on February 24$^{\text{th}}$. When excluding the flare from the observation period, the mean integral flux is $(3.1 \pm 0.1_{\text{stat}} \pm 0.4_{\text{sys}}) \times 10^{-12}\,\text{cm}^{-2}\,\text{s}^{-1}$ which corresponds to (1.9 ± 0.6)% of the Crab Nebula flux. That means, that the flux during the flare of 1ES 0806+524 increased significantly (4.3σ) by a factor of four to $(14.7 \pm 0.3_{\text{stat}} \pm 0.1_{\text{sys}}) \times 10^{-12}$ $\text{cm}^{-2}\,\text{s}^{-1}$, while the flux level the night before and after February 24$^{\text{th}}$ is compatible with the mean flux of the observation period. Together with the low probability of ~0.5% (χ^2/NDF[56] = 27.28/11) for the hypothesis of a constant source emission, this is a strong argument for the presence of a short–term variability. Considering the behavior of the integral flux around the VHE flare, an upper limit of the order of one day is assumed with respect to the variability. No intra–night variability was found within the statistical and systematic uncertainties during the hight sate of 1ES 0806+524 . Beside the clear increase in emission for one night of observations, a smooth flux enhancement has been observed towards March 2$^{\text{nd}}$, reaching a level of (7.5 ± 2.6)% C.U., which agrees within the error with the previously observed high flux level. The significance of the second increase in flux with respect to the mean flux level corresponds to $2.1\,\sigma$.

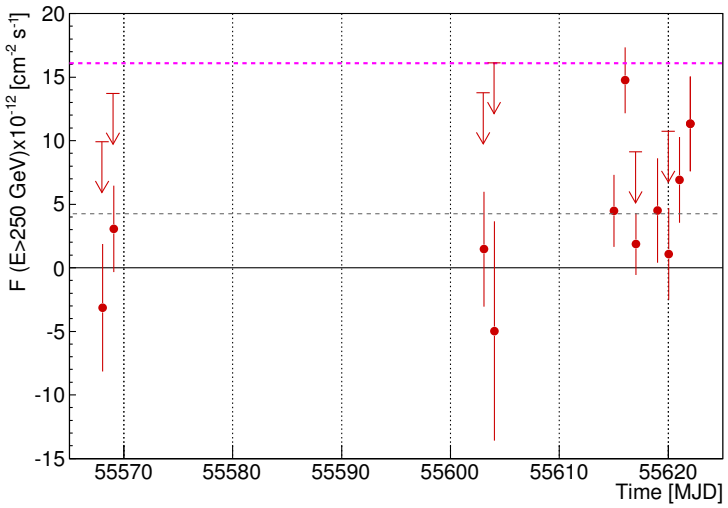

Figure 7.26: Daily–binned light curve of the integral VHE γ–ray emission from 1ES 0806+524 above 250 GeV during observations carried out by MAGIC in 2011. The arrows correspond to the 95% confidence upper limits which have been derived in case the measured integral flux was consistent with zero. The source flare (MJD = 55616) is clearly visible, while the integral flux level is significantly lower the night before and after, indicating a short–term variability. A hint for integral flux increase is observed towards the end of the observation period. The mean flux level (gray dashed line), derived from the observation period excluding the VHE γ–ray flare, and the level of 10% Crab Nebula flux are indicated (pink dashed line).

In Table 7.7, the integral flux levels for the individual nights of observation are listed. In case of consistency with a zero flux, upper limits at a 95% confidence

[55]The integrated flux level in Crab units is obtained when normalizing the integrated energy flux measured above a distinct threshold on the Crab Nebula flux, which is considered to be stable, measured above the same threshold.
[56]NDF: Number of Degrees of Freedom.

level have been derived.

Night	MJD	Eff. time [h]	Significance [σ]	$F_{>250\,\mathrm{GeV}}$ [$10^{-12}\,\mathrm{cm}^{-2}\,\mathrm{s}^{-1}$]	U.L. [f.u.]	U.L. [% C.U.]
07/01/2011	55568	0.43	-0.6	-3.2 ± 5.2	9.9	6.2
08/01/2011	55569	0.76	0.9	3.1 ± 3.4	13.7	8.5
11/02/2011	55603	0.62	0.3	1.5 ± 4.5	13.8	8.6
12/02/2011	55604	0.38	-0.6	-3.0 ± 5.3	16.1	10.0
23/02/2011	55615	1.22	1.5	4.5 ± 2.8	–	–
24/02/2011	55616	2.98	5.7	14.7± 2.6	–	–
25/02/2011	55617	3.03	0.8	1.9 ± 2.4	9.1	5.7
27/02/2011	55619	0.59	1.1	4.5 ± 4.1	–	–
28/02/2011	55620	2.16	0.3	1.1 ± 3.6	10.7	6.7
01/03/2011	55621	1.96	2.1	6.9 ± 3.4	–	–
02/03/2011	55622	1.98	3.0	11.3 ± 3.7	–	–

Table 7.7: Integral flux analysis of 1ES 0806+524. From left to right: night of observation (first and second column); exposure time (third column); significance of signal detection (fourth column); integral flux above 250 GeV (fifth column); In column six and seven, the upper limits (E > 250 GeV) calculated for those nights, where the measured integral flux was consistent with zero, are reported in flux (f.u.) and percentage Crab units (C.U.).

The flux level above 300 GeV is (2.1 ± 1.9)% C.U. and is compatible with the flux level of 1.8% C.U. observed in 2007 [9] if integrated over the entire observation period excluding the source flare.

7.6 1ES 0806+524: The Differential Flux

As discussed in the previous sections, the MAGIC observations on 1ES 0806+524 carried out in winter 2011 comprise two source states in which the source was detected, that is a high state detected at February 24$^{\mathrm{th}}$ and a low state in which the source has been for the remaining observation period (see Section 7.4). The variability in the VHE γ–ray emission of 1ES 0806+524 during this period has been confirmed by the temporal analysis of the integral flux as demonstrated in Section 7.5. Therefore, data have been split into two data sets: one encompasses the data from the source flare, whereas the other includes all data recorded during the low state of 1ES 0806+524. From the individual data sets the differential spectra expressed in estimated energy bins have been reconstructed applying the same cuts as for the light curve (see Tablen7.5).

In a successive step the effects on the spectrum determination due to the finite energy resolution introduced by the MAGIC detectors is corrected via unfolding.

The final task concerns the correction of the unfolded spectrum for the cosmological absorption of VHE γ–rays during the interaction with the EBL (see Section 6.2.4) leaving an imprint on the detected spectrum in form of an energy dependent deformation. The connection between the observed flux F_{obs} and the intrinsic flux F_{em} emitted by the source is given by an exponential function of the optical depth τ of the Universe to VHE γ–rays which is associated to the their attenuation as it refers to the interaction with the EBL:

$$F_{\mathrm{obs}} = F_{\mathrm{em}} \cdot e^{-\tau(E,z)} \tag{7.9}$$

7.6.1 The High State

For the differential flux analysis of the VHE γ–ray flare observed on February 24$^{\text{th}}$, the emission has been studied in intervals of reconstructed energy, that is in a certain range of energy bins. The number of bins used for the study of the emission in the individual energy segments is set to 32 in logarithmic scale between 5 GeV to 50 TeV, leading to a signal of 1.5 to 5.9 σ significance in the energy range from 180 to 600 GeV (see Table 7.8). The strongest signal is detected in the energy range between 300 and 450 GeV confirming the result obtained from the signal search, where a signal of high significance has been found above 250 GeV.

Mean energy [GeV]	θ^2 cut [deg^2]	`hadronness` cut	Significance [σ]	F [cm^{-2} s^{-1} TeV^{-1}]
184	0.03	0.37	2.9	$(2.9 \pm 1.1)\times10^{-10}$
246	0.02	0.36	3.6	$(1.5 \pm 0.5)\times10^{-10}$
328	0.02	0.31	3.4	$(5.9 \pm 2.0)\times10^{-11}$
437	0.02	0.32	3.7	$(3.2 \pm 1.0)\times10^{-11}$
583	0.02	0.28	4.2	$(1.7 \pm 0.5)\times10^{-11}$

Table 7.8: Differential flux of the 2011 data sample covering the flare of 1ES 0806+524. The mean energy of the bin (first column), the θ^2 and `hadronness` cuts (second and third column) are listed, derived from simulated γ–like events by applying cut efficiency of 70 and 90% respectively. Column four and five denote the significance of the signal and the differential flux before unfolding.

Table 7.9 contains the respective mean energy and differential flux computed via the application of the Tikhonov algorithm used for the unfolding [317].

The observed unfolded differential spectrum of the high state of 1ES 0806+524 presented in Figure 7.27 agrees well with a simple power law defined by:

$$\frac{dN}{dE} = f_0 \cdot \left(\frac{E}{300\,\text{GeV}}\right)^{\Gamma} \tag{7.10}$$

where f_0 and Γ denote the normalization at 300 GeV and the spectral photon index respectively. The fit of the high state differential spectrum yields a flux normalization f_0 of $(9.2 \pm 0.4_{\text{stat}} \pm 1.0_{\text{sys}})\times10^{-11}$ cm^{-2} TeV^{-1} and a photon index $\Gamma = -3.1 \pm 0.3_{\text{stat}} \pm 0.2_{\text{sys}}$ in the energy range from 150 GeV to 1 TeV. The hypothesis of a simple power law is given by probability of 69% (χ^2/NDF = 1.46/3).

The deabsorbed spectrum obtained by corrections for EBL absorption according to [103] for the given redshift of 0.138 of the source is well described by a simple power law fit parametrized by a flux normalization at 300 GeV $f_0 = (1.3 \pm 0.2_{\text{stat}})\times10^{-11}$ cm^{-2} TeV^{-1} spectral photon index Γ of -2.4 $\pm$ 0.3$_{\text{stat}}$ providing a fit probability of 72% (χ^2/NDF = 1.38/3) in the energy range between 150 GeV and 1 TeV.

Table 7.9: Differential flux of the unfolded spectrum of 1ES 0806+524 observed during the flare in VHE γ–rays.

Mean energy [GeV]	F [cm^{-2} s^{-1} TeV^{-1}]
138	$(1.9 \pm 0.7)\times10^{-10}$
230	$(2.9 \pm 1.5)\times10^{-11}$
384	$(6.1 \pm 3.5)\times10^{-12}$
641	$(1.9 \pm 1.0)\times10^{-12}$
1069	$(7.0 \pm 3.9)\times10^{-13}$

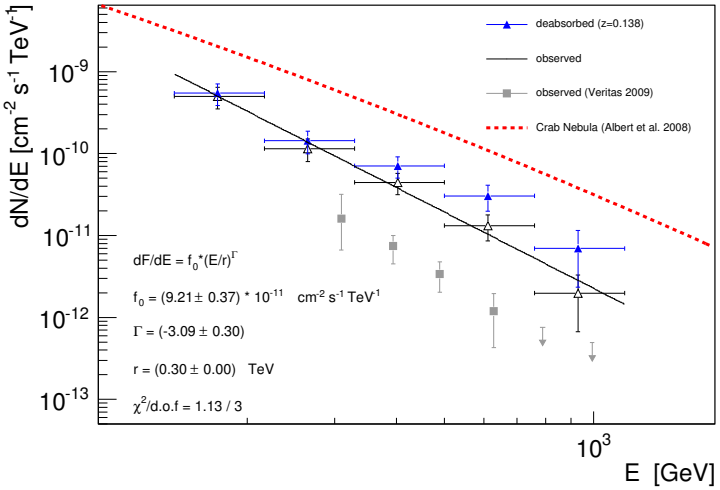

Figure 7.27: Unfolded high state differential energy spectrum of 1ES 0806+524 observed by MAGIC on February 24$^{\text{th}}$. The black triangles correspond to the measured spectra fitted by a simply power law (solid black line) whose parameters are indicated in the inlet in the bottom left corner; the blue filled triangles are corrected for EBL attenuation using the model by [103]. For comparison the observed spectrum and derived upper limits (gray filled squares and arrows respectively) published by VERITAS [9] and the Crab Nebula spectrum (red dashed line) are shown [30]. A flux increase by a more than a factor of four with respect to VERITAS observations is apparent.

Different unfolding algorithm as described in [24] were used to verify their potential effects on the spectrum determination, all agreeing within the errors except for one cases, where a particular algorithm lead to a uncertainty spread for one individual data point (see Figure 7.28).

7.6.2 The Low State

Despite the strong detection of 1ES 0806+524 during the quiescent state, the number of bins in logarithmic scale has been reduced to 24 in order to derive an unfolded spectrum sufficiently significant in the individual energy intervals (see Table 7.10). Again, the more significant signal is associated to the emission above 300 GeV.

Mean energy [GeV]	θ^2 cut [deg^2]	`hadronness` cut	Significance [σ]	F [cm^{-2} s^{-1} TeV^{-1}]
195	0.025	0.33	3.4	$(8.4 \pm 2.6)\times10^{-10}$
286	0.02	0.37	1.8	$(1.5 \pm 0.8)\times10^{-11}$
420	0.02	0.35	2.1	$(5.9 \pm 2.9)\times10^{-12}$
617	0.02	0.30	2.3	$(2.7 \pm 1.2)\times10^{-12}$
906	0.02	0.27	3.5	$(1.5 \pm 0.5)\times10^{-12}$

Table 7.10: Differential flux of the 2011 data sample covering the quiescent state of 1ES 0806+524. The mean energy of the bin (first column), the θ^2 and `hadronness` cuts (second and third column) are listed, derived from simulated γ–like events applying cut efficiency of 70 and 90% respectively. Column four and five denote the significance and the differential flux before unfolding.

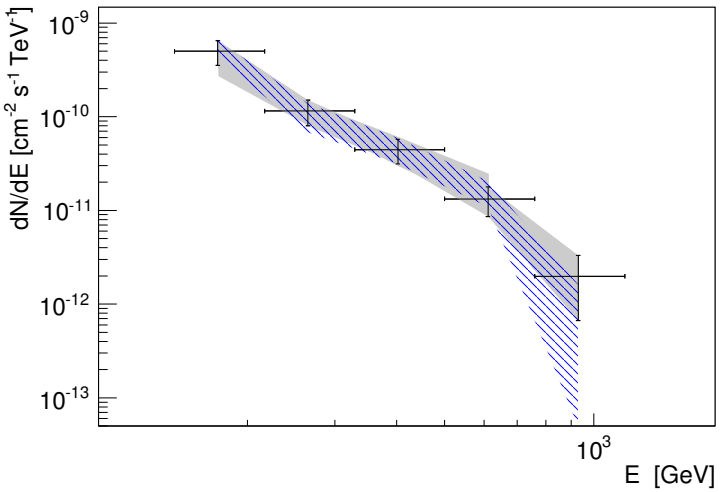

Figure 7.28: Verification of the effects on the spectrum determination of 1ES 0806+524 by different unfolding algorithms. The unfolded spectra (black points) observed during the high of 1ES 0806+524 obtained with the Tikhonov algorithm are shown. The gray–shaded band represents the spectral spread due to different unfolding algorithms to which a blue–dashed band is superimposed marking the Bertero algorithm which lead to a spread in the flux uncertainty for one individual data point.

Table 7.11: Differential flux of the unfolded spectrum of 1ES 0806+524 derived from the low state data set.

Mean energy [GeV]	F [$\mathrm{cm^{-2}\,s^{-1}\,TeV^{-1}}$]
174	$(5.0 \pm 1.5)\times10^{-10}$
264	$(1.2 \pm 0.4)\times10^{-10}$
402	$(4.4 \pm 1.3)\times10^{-11}$
612	$(1.3 \pm 0.5)\times10^{-11}$
929	$(2.0 \pm 1.3)\times10^{-12}$

The differential flux of the derived low state spectrum calculated in each energy bin between 150 GeV and 1 TeV by means of the Tikhonov unfolding algorithm is listed in Table 7.11. The unfolded spectrum is with a probability of 70% (χ^2/NDF = 1.42/3) compatible with a simple power law parametrized by a flux normalization at 300 GeV of $(1.7 \pm 0.3_{\mathrm{stat}} \pm 0.2_{\mathrm{sys}})\times10^{-11}\,\mathrm{cm^{-2}\,TeV^{-1}}$ and a photon spectral index of -2.7 $\pm$ 0.4_{stat} $\pm$ 0.2_{sys} (see Figure 7.29).

The probability of a simple power law fit application to the deabsorbed spectrum which yields an intrinsic spectral photon index of -2.3 $\pm$ 0.6_{stat} and a flux normalization at 300 GeV of $(2.3 \pm 0.5_{\mathrm{stat}})\times10^{-11}\,\mathrm{cm^{-2}\,TeV^{-1}} is 51\% (\chi^2/\mathrm{NDF} = 2.33/3)$. A possible explanation for the decrease in fit probability with respect to the simple power law fit of the observed spectrum before the correction for EBL absorption is the slight pile-up present at higher energies. This might trace an overcorrection for the VHE γ–ray attenuation by the EBL due to possible imperfections in the EBL model in terms of an overestimated optical depth τ than actually present.

Figure 7.30 shows the effects on the spectrum determination caused by different unfolding algorithms. The different unfolding algorithms provide consistent results except for one data point at medium energies where the Schmelling algorithm indicates a large statistical error.

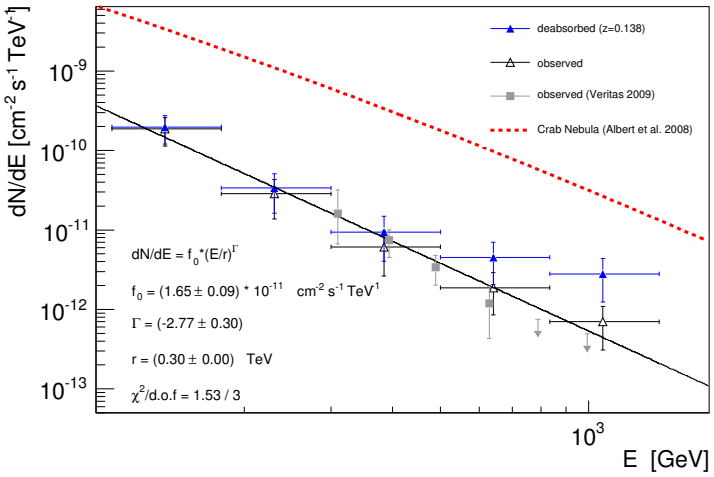

Figure 7.29: Unfolded low state differential energy spectrum of 1ES 0806+524 observed by MAGIC. The black triangles correspond to the measured spectra fitted by a simply power law (solid black line) whose parameters are indicated in the inlet in the bottom left corner; the blue filled triangles are corrected for EBL attenuation using the model by [103]. The spectrum observed by VERITAS [9] and the upper limits derived from those observations (gray filled squares and arrows respectively) are shown for comparison; the red dashed line corresponds to the Crab Nebula spectrum [30]. The spectrum agrees well within the statistical errors with previous VERITAS observations.

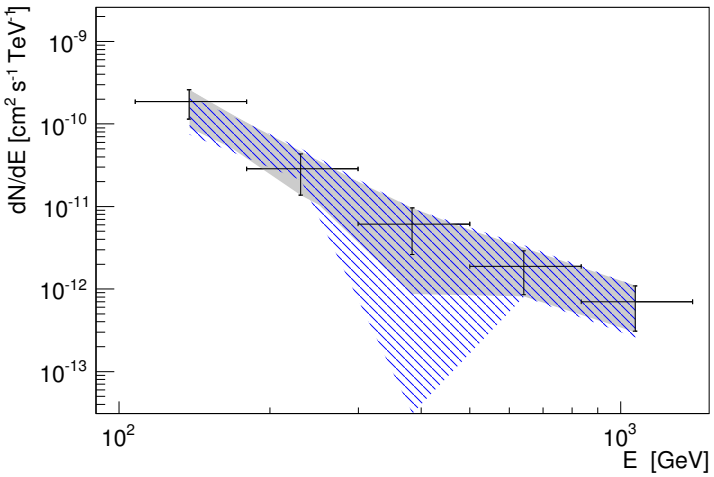

Figure 7.30: Verification of the effects on the spectrum determination of 1ES 0806+524 by different unfolding algorithms. The unfolded spectra (black points) observed during the low state of 1ES 0806+524 obtained with the Tikhonov algorithm is shown. The gray–shaded band represents the spectral spread due to different unfolding algorithms to which a blue–dashed band is superimposed marking the Schmelling algorithm which lead to a spread in the flux uncertainty for one data point.

7.6.3 Comparison with Previous VHE γ–ray Observations

The observed low state spectrum is in a good agreement within the errors with the observed spectral points published by VERITAS (see Figure7.29). However, at higher energies differential flux observed by MAGIC seems to be slightly higher

than previous differential upper limits predict. Instead, the high state spectrum observed by MAGIC exhibits a flux increase of a factor of more than four (see Figure 7.27). Visually, there seems to be a hint for a spectral hardening during the flare (see Table 7.12). However, due to the uncertainties associated to the determination of the spectral photon index, no clear conclusion can be drawn.

Source state	Fit range [TeV]	r [GeV]	f_0 [10^{-10} cm^{-2} s^{-1} TeV^{-1}]	Γ
high	0.15–1.0	300	$9.2 \pm 0.4_{\mathrm{stat}} \pm 1.0_{\mathrm{sys}}$	$-3.1 \pm 0.3_{\mathrm{stat}} \pm 0.2_{\mathrm{sys}}$
low	0.15–1.0	300	$1.7 \pm 0.3_{\mathrm{stat}} \pm 0.2_{\mathrm{sys}}$	$-2.7 \pm 0.4_{\mathrm{stat}} \pm 0.2_{\mathrm{sys}}$

Table 7.12: Parameters from a simple power law fit to the unfolded high and low stat spectra observed by MAGIC of 1ES 0806+524. The first column presents the source state, while the other columns refer to the simple power law fit in terms of fit range, level of normalization r, normalization flux $f_0$and spectral photon index Γ.

The intrinsic spectral photon indeces of the deabsorbed spectra obtained by the application of the EBL models proposed by [103] to both the high and low state spectrum of 1ES 1011+496 agree within the statistical errors (see Table 7.13)

Table 7.13: Intrinsic spectral indices obtained from a simple power law fit to deabsorbed spectra of 1ES 0806+524 after correction for EBL absorption according to [103].

Source state	Γ
high	$-2.3 \pm 0.6_{\mathrm{stat}}$
low	$-2.4 \pm 0.3_{\mathrm{stat}}$

7.7 1ES 0806+524 Multiwavelength Observations

Figure 7.31 and 7.32 show the long–term light curves which cover quasi–simultaneous observations of 1ES 0806+524 carried out from November 2010 to June 2011 as well as the multifrequency data centered on the MAGIC observation period from mid–February to beginning of March 2011. The MWL observation cover data in VHE γ–rays provided by MAGIC, in HE γ-rays from the *Fermi*-LAT, in X-rays obtained from *Swift*/XRT observations as well as in the R-band and in the radio regime from measurements performed by the KVA and OVRO telescope. Except the light curve in HE γ–rays, the integral flux data in different wavebands feature a daily time binning each.

In the following sections, details on the individual observations of 1ES 0806+524, the data analysis and the results will be presented. An emphasis is given on the discussion of the source variability examined for different wavelength ranges.

The HE γ–ray Observations by *Fermi*

Fermi-LAT is a pair conversion telescope optimized for the energy from 20 MeV up to energies beyond 300 GeV [42] (see Chapter 3). Since it is operating in all-sky survey mode, during which the entire sky is scanned every three hours, the detection of the rather weak emission of high energy photon from 1ES 0806+524

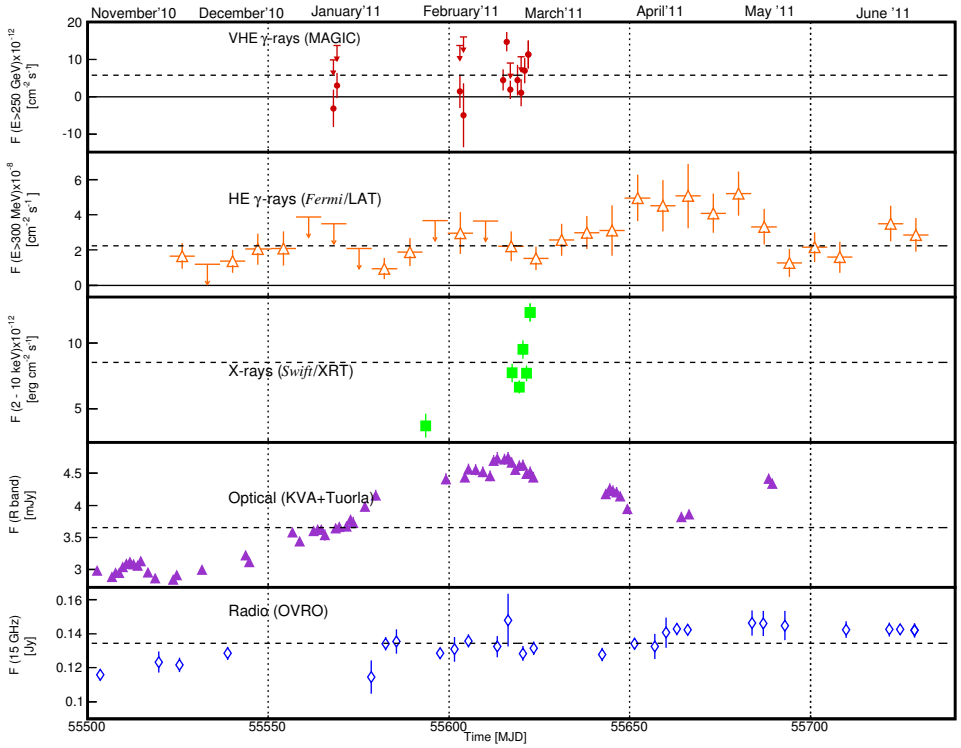

Figure 7.31: MWL light curve of 1ES 0806+524. From top to bottom: The MWL coverage from January to beginning of March 2011 is provided in VHE γ–rays by MAGIC (red circles), in HE γ–rays by *Fermi* (orange triangles), in X-rays by *Swift*/XRT, in the R band by the KVA telescope (violet triangles) and in radio by the OVRO telescope (blue diamonds). Upper limits of 95% confidence level are indicated by down–ward arrows. The individual light curves are daily binned expect in HE γ–rays, where a 7–day binning was applied. The mean fluxes (dashed lines) have been determined from the individual long–term data sets.

on a daily time scale was insignificant. Therefore, the bin size of has been enlarged to seven days for the analysis of the temporal behavior of the HE γ–ray emission above 300 MeV. The data, which are accessible to public[57], have been analyzed with the standard analysis ScienceTool software package (version 09-27-01), available from the *Fermi* Science Support Center. The analysis tools include background models, which implies a galactic diffuse component and an isotropic diffuse contribution, as well as and instrument response functions (IRF) `P7SOURCE_V6` suited for the spectral flux analysis. Based on the criteria of maximal probability for a HE γ–ray event diffusely distributed within the region of interest (ROI) of 10° from the position of 1ES 0806+524 in the radio band, the data collected during approximately eight months between November 22$^{\text{th}}$, 2010 (MJD=55522), and June 13$^{\text{th}}$, 2011 (MJD=55725), have been selected. To reduce the contamination from the Earth–limb γ-rays produced by the CRs interaction with the upper atmosphere, data were restricted to a maximum zenith angle of 100°. In addition, time period, during which the spacecraft rocking angle exceeded 52°, were excluded. In combination with the post–launch IRF, the `gtlike` tool, an unbinned maximum likelihood technique [3], has been applied to events in the energy range from 300 MeV to 300 GeV [218] to derive the spectral flux for each time bin. During the spectral point fitting, the normalizations of the com-

[57] http:/fermi.gsfc.nasa.gov

ponents of the background model were defined to vary freely. Sources from the 2FGL [242] located within 15° of 1ES 0806+524 were incorporated in the model of the region by setting the spectral models and the initial parameters for the modeling to those reported therein.

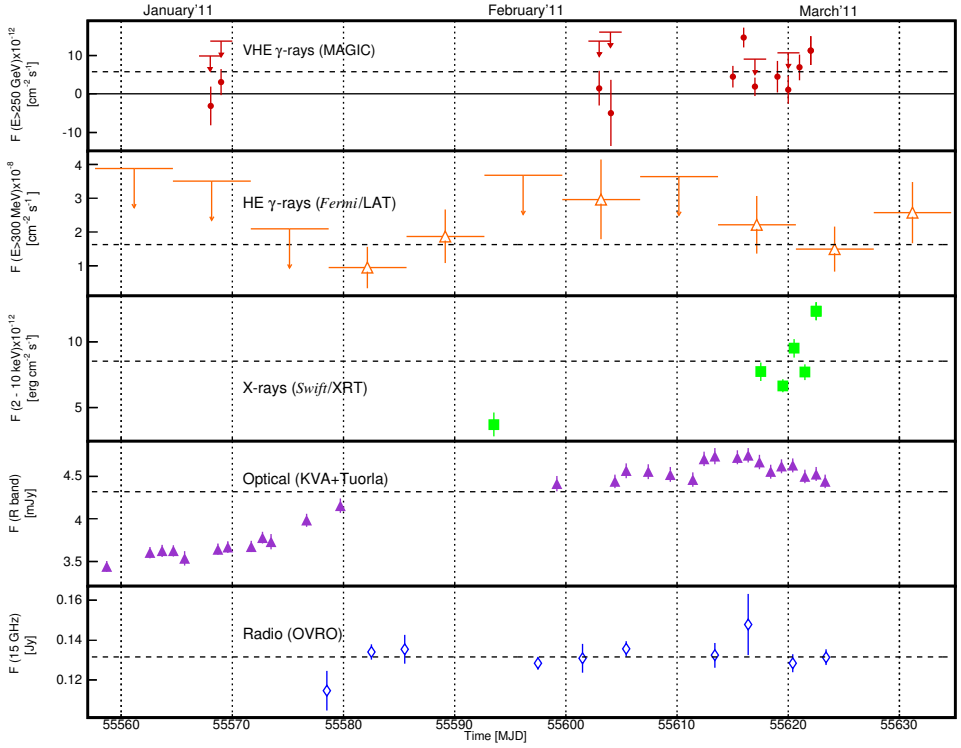

Figure 7.32: Zoom of Figure 7.31 into the period of MAGIC observations from January to the begin of March 2011. The mean flux levels, calculated from the individual data taken during this period are indicated (dashed lines).

In the fitting procedure the parameters of sources located within 10° radius centered on the source of interest were left free, while parameters of sources located within the 10°-15° annulus were fixed. A systematic uncertainty in the flux of 10% at 100 MeV, 5% at 560 MeV and 10% at 10 GeV and above is estimated. Flux upper limits at 95% confidence level were calculated for each time bin where the TS value for the source was TS<4 or the number of predicted photons $N_{\mathrm{pred}} < 3$.

During the period of MAGIC observations, i.e. from January to the beginning of March 2011, the HE data are compatible with the hypothesis of a constant flux with the probability of 54% ($\chi^2/\mathrm{NDF} = 3.14/4$) (see second upper panel of Figure 7.32), whereas a smooth flux increase from the beginning of March to the beginning of May 2011 is observed that reaches a maximum of $(5.2 \pm 1.3) \times 10^{-8}\,\mathrm{cm}^{-2}\,\mathrm{s}^{-1}$ ($E > 300\,\mathrm{MeV}$) (see second upper panel in Figure 7.31). In fact, considering the entire data set from November 2010 to May 2011, the probability of a constant flux hypothesis reduces to 7% ($\chi^2/\mathrm{NDF} = 32.68/22$).

X-ray and UVOT Observations by *Swift*

In addition to its prime objective of detecting and following up Gamma-Ray bursts, since its launch in November 2004 [134] the *Swift* Gamma-Ray Burst observatory has become an instrument suitable for various purposes due to its fast slewing response and its multiwavelength coverage. *Swift* hosts three telescopes optimized for different energy ranges: the Burst Alert Telescope (BAT; [48]) suited

for observations between 15 - 150 keV, the X-ray telescope (XRT; [77]) with a 0.3 - 10 keV coverage and the UV/Optical Telescope (UVOT; [277]) optimal for observations within the 1800–6000 Å wavelength range.

Following the VHE γ-ray flare detection by MAGIC [214], *Swift* ToO observations were requested and performed from February 26$^{\text{th}}$ to March 2$^{\text{nd}}$ for five nights. A high activity state of the source was confirmed reporting a clear variability in X-rays [296]. The source was monitored with the *Swift*/XRT in the photon counting (PC) mode with $\sim$ 2 ksec snapshots for a total exposure time of 10 ksec each night. *Swift*/UVOT data were taken in the so–called "filter of the day" mode, where different filters, either U, UVW1, UVM2, or UVW2, are chosen day by day by the Swift science planners, by what a temporal analysis in this energy regime becomes non–trivial.

Swift/XRT data were processed with the `xrtpipeline` (v0.12.6) distributed by HEASARC as part of the HEASoft package. After the selection of grades 0–12 events for the PC data, the response matrices included in the *Swift* CALDB has been applied [233]. PC source events between 0.2–10 keV within a 20 pixel radius corresponding to $\sim$47 arcsec were extracted, while the background was estimated from a circular off–source region of a 40 pixel radius. For the spectral fitting, the energy range was adopted to 0.3–10 keV, and a re–binning was applied to the data using GRPPHA with a minimum of 20 counts per energy bin to guarantee a reliable the χ^2 minimization fitting. The spectral analysis was performed with XSPEC adopting an absorbed power law model [215] in which a hydrogen–equivalent column density fixed to the Galactic value $nH = 4.1 \cdot 10^{20}\,\text{cm}^{-2}$ is included [168].

Swift/UVOT source counts were extracted from a circular region of 10 arcsec centered on the source position while the background is estimated from of a nearby source free region within circle of equal size. The data were processed with the `uvotmaghist` task provided in the HEASOFT package. A correction of the observed magnitudes for the Galactic extinction was performed [119].

The X-ray data are presented in the middle panels of Figure 7.31 and 7.32. In the range from 2 to 10 keV, the time–averaged flux during the MAGIC observations period is $(8.5 \pm 0.2) \cdot^{-12} \text{erg}\,\text{cm}^{-2}\,\text{s}^{-1}$. A flux enhancement has been observed on March 2$^{\text{nd}}$ to $(12.5 \pm 0.7) \cdot^{-12} \text{erg}\,\text{cm}^{2}\,\text{s}^{-1}$, indicating a marginal spectral hardening. In comparison to previous observations carried out on February 1$^{\text{st}}$, 2011, the mean flux is two to three times higher. Moreover, the flux level is comparable to measurements from March 2008 during the the first detection of the source in VHE γ-rays [9]. The *Swift*/XRT observations confirm the high activity state of the source exhibiting a clear variability in X-rays since the probability of a constant flux is $6.9 \cdot 10^{-21}$.

The brightness of (14.4 ± 0.03) mag in the UV-W2 and UV-M2 bands during March observations is almost unchanged with respect to the brightness of (14.5 ± 0.03) mag on February 1$^{\text{st}}$. Thus, the UV band photometry is compatible with a constant flux within the errors. However, 1ES 0806+524 appears about 1 mag brighter compared to thee UV flux observed in March 2008.

Optical Observations by the KVA Telescope

The simultaneous optical data outlined in the fourth panel from top were collected with the KVA telescope located at the Roque de los Muchachos observatory on La Palma. The Kungliga Vetenskapsakademien (KVA) telescope consists of two telescopes mounted on the same fork. The larger of the two, a 60 cm Schmidt

reflector, is used for polarimetric observations of some of the brighter sources while the smaller one, a 35 cm Celestron, is used for photometry. They are operated remotely from Finland. The photometric measurements are performed in the optical R band using differential photometry, i.e. the target and the calibrated comparison stars are recorded in the same CCD image [118]. The magnitudes of the source and comparison stars are measured by means of aperture photometry and converted to linear flux densities according to:

$$F_{\mathrm{Jy}} = F_0 \cdot 10^{mag_{\mathrm{R}}/-2.5} \tag{7.11}$$

where F_0 is a filter–dependent zero point that corresponds to $F_0 = 3080$ Jy in the R band [57]. In order to obtain the AGN core flux, contributions from the host galaxy and possible nearby stars that contribute to the observed flux have to be subtracted from the overall measured value. These contributions have been determined by [240]. In the case of 1ES 0806+524, the host galaxy contribution corresponds to (0.69 ± 0.05) mJy.

The KVA telescope is operated under the Tuorla Blazar Monitoring Program[58], which is run as a support program to the MAGIC observations. The program was started at the end of 2002 and uses the Tuorla 1 m (Finland) and the KVA telescopes to monitor candidates from the Costamante and Ghisellini catalog [90] and known TeV blazars in the optical waveband. Once a high state of these objects is observed an alerts is provided to MAGIC to trigger follow–up VHE γ–ray observations. 1ES 0806+524 was one of the objects on the original target list and has therefore been monitored regularly since the beginning of the program (see Figure 7.33). Most of the time during the monitoring, the object had been relatively dormant over the years showing some variability but no particular flaring activity until the spectacular flare began at the end of 2010, where the core flux greatly increased in the R band almost three–times over the quiescent state of 1.7 mJy [271] during the following three months. The flare reached a maximum of (4.75 ± 0.09) mJy[59] on the night of February 24$^{\mathrm{th}}$ 2011 after which the flux level began to decrease steadily until April (see Figure 7.32). This flare prompted an alert to MAGIC and a request for ToO observations of the source, which were granted on February 2011.

The hypothesis of a constant flux during observations from November 2010 to May 2011 can be rejected with high confidence since its probability corresponds to $\chi^2/\mathrm{NDF} = 647/23$.

Radio Observations by the OVRO Telescope

The Owens Valley Radio Observatory (OVRO) located in California is a 40 m radio telescope. The telescope is equipped with a cooled receiver installed at prime focus with two symmetric off–axis corrugated horn feeds providing sensitivity to left circular polarization. The telescope and receiver combination produces a pair of approximately Gaussian beams which are separated in azimuth by 12.95 arcmin referred to as "antenna" beam and "reference" beam. The center frequency of the receiver is 15.0 GHz with a 3.0 GHz bandwidth and a noise–equivalent reception bandwidth of 2.5 GHz.

1ES 0806+524 observations have been carried out in the framework of a blazar monitoring program [273] measuring the source flux density twice a week. Occasional gaps in the data sample are due to poor weather conditions or instrumental

[58] project web page: http://users.utu.fi/kani/
[59] The stated flux values are host galaxy subtracted.

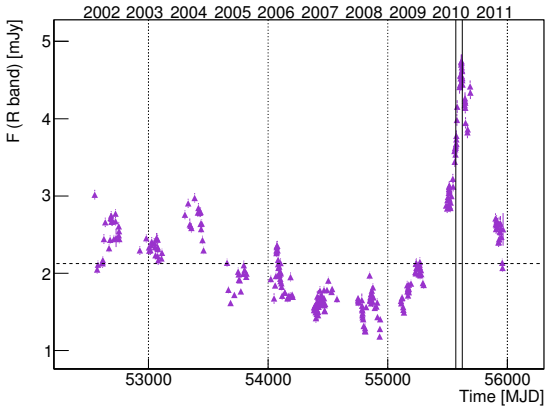

Figure 7.33: Long–term monitoring of the optical emission of 1ES 0806+524 in the R band by the KVA telescope. The black vertical lines mark the period of the MAGIC observations in 2011 while the dashed line indicates the overall mean flux level which 1ES 0806+524 started to exceed in late 2010.

problems. Observations were performed using a Dicke–switched dual–beam system, with a second level of switching in azimuth to alternate between source and sky in each of the two horns which removes much atmospheric and ground interference [270]. The calibration was referred to 3C 286 with an assumed flux density of 3.44 Jy at 15 GHz [44]. The data is analyzed using the pipeline described in [273].

The eight–months radio light curve, shown in the bottom panels of Figure 7.31 and 7.32, provides a low probability (χ^2/NDF = 61.65/25) for a non–variable source with a mean flux level of 0.14 Jy, while the data centered on the MAGIC observation period yield a constant flux level at 0.13 Jy of 59% probability (χ^2/NDF = 7.42/9). Considering the MWL light curves, presented in Figure 7.32, a correlation between the VHE γ–ray state and a flux increase in the radio band to 0.15 mJy is observable. However, due to the large error bars, the flux is with a probability of 45% (χ^2/NDF = 1.59/2) compatible with the flux level of the night before and after the flare. Compared to observations from November 2010, the radio data show a marginal flux increase from mid–January to May 2011, exceeding the mean flux level of the overall observation period.

Summary on the MWL Observations and Correlation Considerations

In summary, the MWL observations indicate a variability of 1ES 0806+524 in all observed wavelengths whose correlation is not clearly confirmed. While the optical flare clearly coincided with the outburst in VHE γ-rays accompanied by an outburst in X-rays, only a weak hint of a correlation between the VHE γ–ray flare and increasing activity in the radio flux was observed. Instead, the increase in HE γ–rays occurred with a delay of more than a month with respect to the other energy regimes. However, given the long integration time of seven days in this energy regime, no clear conclusion regarding simultaneous source variability can be drawn. Apparently, there is no short–term correlation between the VHE and optical wave band: concentrating on observations right before and after the flare, optical observations indicate a rather constant flux while the measurements performed in VHE *gamma*-rays indicates a clear flux variability on a daily basis. Instead, the flux increase in the R band proceeded rather smoothly and started

well before 1ES 0806+524 showed flaring activity in the VHE regime and in X-rays.

7.8 The Modeling of the 1ES 0806+524 SED

The SED of the source describing the high and low source state during the MAGIC observations, together with data from *Fermi*, *Swift*, the KVA and OVRO telescopes are assembled in Figure 7.34 and Figure 7.35. The simultaneous and quasi–simultaneous complementary data from other wavebands have been combined such that they match best the high and low state observed in VHE γ-rays. As observations in the optical and the radio band are carried out at one frequency, the respective mean fluxes have been computed.

Exclusively the MAGIC flare data from February 24$^{\text{th}}$ have been used to derive the VHE γ–ray high state SED component. These data have been corrected for EBL absorption according to [103].

Unfortunately, the significance of simultaneous high state SED data in HE γ–rays from *Fermi* is not sufficient. Therefore, an upper limit has been derived for February 24$^{\text{th}}$. For comparison an averaged HE γ–ray SED from eight months of observations from November 2010 to June 2011 has been derived. However, since these data are not simultaneous, the averaged HE γ–ray spectrum is not considered in the modeling of the high state SED.

The data in the X-ray regime and the U bands comprise observations on February 27$^{\text{th}}$ and March 2$^{\text{nd}}$. To the latter, corrections for galactic extinction have been applied following [119].

The data from observations performed on February 24$^{\text{th}}$ in the R band are host galaxy corrected according to [240]. In the radio band the flux was pretty constant during the observation period of MAGIC, wherefore the mean flux has been used. In addition, archival data in the radio band and in the R band taken from the NED[60], as well as in the VHE γ–ray regime published by VERITAS have been included [9].

The low state has been derived from the remaining MAGIC data. The complementary HE γ–ray data cover the MAGIC observation period from January to March 1$^{\text{st}}$, from which February 24$^{\text{th}}$ has been excluded. Data in X-rays and in the U bands encompass observations from February 1$^{\text{st}}$ to March 1$^{\text{st}}$. Measurements in the R band performed at the same nights when MAGIC observed 1ES 0806+524, excluding the night of the source flare in VHE γ–rays have been used to derive the mean low state flux in the optical regime. The same data treatment as used for the high state sample has been applied for the mean flux determination in the radio band. The archival radio and optical data provided by the NED are shown.

A comparison of the two SEDs by eye indicates a flux variability of about three orders of magnitude in VHE γ-rays between the high and low state of 1ES 0806+524. Instead, the visual comparison of the low state data from *Fermi* with the eight months averaged spectrum does not indicate any significant variation in the HE γ–ray regime. Regarding *Swift* data, no variability is observed between both activity states. However, data of the low state sample collected on February 2$^{\text{nd}}$ show a marginally lower flux in X-rays (see Figure 7.35). Observations in the U band have been carried out in "filter of the day" mode, by what no

[60] http://nedwww.ipac.caltech.edu/

[60] Green colored data correspond to observations from February 1$^{\text{st}}$, while observations from February 28$^{\text{th}}$ and March 1$^{\text{st}}$ are indicated in red and black. Due to exact superimposition of the spectra, data from February 25$^{\text{th}}$ and 27$^{\text{th}}$ are not visible.

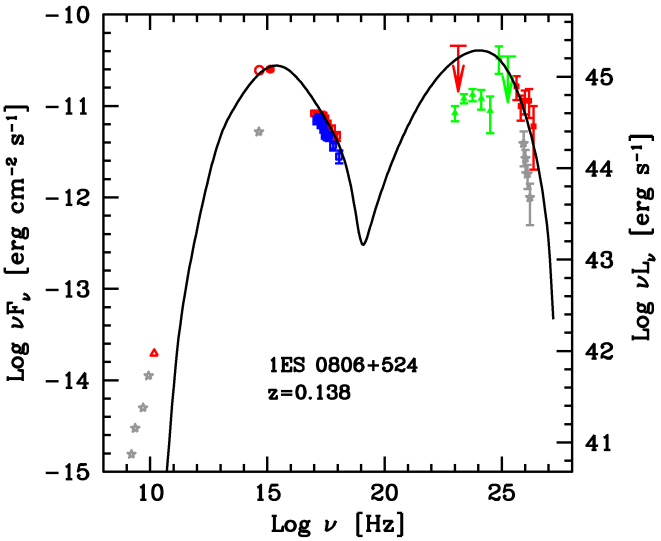

Figure 7.34: Spectral energy distributions of the high state of 1ES 0806+524. The MAGIC VHE γ–ray data (red blank squares) are corrected for EBL absorption according to [103]. Due to the limited resolution of the source in HE γ–rays, an averaged spectrum of *Fermi*-LAT data (green filled triangles and arrows) covering eight months of data taken from November 2010 to June 2011 are shown. Moreover, an upper limit of 95% confidence level (red arrow) has been derived for February 24$^{\text{th}}$. Simultaneous and quasi–simultaneous data from February 27$^{\text{th}}$ and March 1$^{\text{st}}$ are provided by *Swift*/XRT/UVOT in X-rays (blue and red filled squares) and in the U band (red filled circles) that have been taken with different filters. Optical data in the R band from KVA (red blank circle) and radio data at 15 GHz provided by the OVRO telescope (red, blank triangle) are presented. The R band and U band data have been corrected for the host galaxy contribution and galactic extinction respectively according to [240] and [119]. Archival radio and optical data accessible through the NED are also shown (gray blank stars). In addition, VHE γ–ray data (gray filled stars) from VERITAS observations are shown for comparison [9]. The solid line represents the one–zone SSC–modeling of the high state observations, for which data marked in red have been taken into account except radio data and the upper limit in HE γ–rays.

explicit comparison between the two states of 1ES 0806+524 can be made. No clear variation between the high and low state SED is seen in the optical regime. Consequently, while the inverse Compton peak indicates a clear flux variability in VHE γ–rays, the synchrotron component of both states is consistent featuring only minor changes. Unfortunately, the weak detection in the HE γ-ray band limits the determination of the inverse Compton peak.

A one–zone SSC model is applied to reproduce the SEDs of both source states (for a detailed description see [213] and Section 6.1.7), where a spherical emission region of radius R is assumed, filled with a tangled magnetic field of intensity B. A population of relativistic electrons is approximated by a smoothed broken power law that is parametrized by the minimum, break and maximum Lorentz

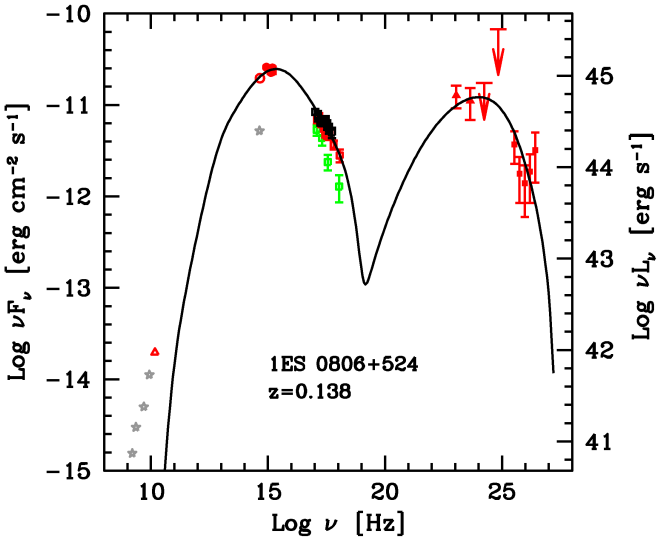

Figure 7.35: Spectral energy distributions of the low state of 1ES 0806+524. The MAGIC VHE γ–ray data (red blank squares) are corrected for EBL absorption according to [103]. Simultaneous and quasi–simultaneous *Fermi*-LAT data (filled red triangles) in HE γ–rays, data from *Swift*/XRT/UVOT in X-rays (filled squares[59]) and in the U band from February 1st to March 1st (red filled circles) are presented. Optical data in the R band from KVA (red blank circle) and radio data at 15 GHz provided by the OVRO telescope (red blank triangle) are also presented. The R band and U band data have been corrected for the host galaxy contribution and galactic extinction respectively according to [240] and [119]. Archival radio and optical data taken from the NED are also shown (gray filled stars). The solid line represents the one–zone SSC–modeling of the low state observations, considering data marked in red except radio data.

factors $\gamma_{\rm min}$, $\gamma_{\rm b}$ and $\gamma_{\rm max}$ as well as by the slopes n_1 and n_2 before and after the break respectively. By the Doppler factor δ, relativistic effects are taken into account. Moreover, the power carried by the jet through electrons ($P_{\rm e}$), magnetic field (P_B) and protons ($P_{\rm p}$), derived assuming the presence of one cold proton per emitting electrons are reported.

The physical parameters derived reproducing the SED are reported in Table 7.14. The values are similar to those typically inferred for other HBL objects (see e.g. [309]).

Examinations of the SED model indicate that the inverse Compton component slightly dominates in terms of emitted power with respect to the synchrotron bump during the high state, while the opposite case is present during the quiescent state of 1ES 0806+524. Such behavior seems to be also derivable from the SED assembled during VERITAS observations.

The magnetic field and protons appear subdominant, indicating that the electrons carry most of the jet power, whose total value $P_{\rm jet} = P_{\rm e} + P_B + P_{\rm p} \sim 10^{44}$ erg s^{-1} is typical (e.g. [142]). Based on a causality argument, the physical parameters of the SED modeling constraint a minimal variability timescale $t_{\rm var,min}$ of $\sim$0.2

SSC input & output Parameter		Source state high	low
$\gamma_{\rm min}$	$[10^3]$	1.0	1.0
$\gamma_{\rm b}$	$[10^4]$	2.0	2.0
$\gamma_{\rm max}$	$[10^5]$	7.0	7.0
n_1		2.0	2.0
n_2		3.85	3.90
B	[G]	0.05	0.05
K	$[10^3\,{\rm cm}^{-3}]$	19	4.0
R	$[10^{16}\,{\rm cm}]$	1.17	1.90
δ		28	28
$P_{\rm e}$	$[10^{43}\,{\rm erg/s}]$	44.8	22.0
P_B	$[10^{43}\,{\rm erg/s}]$	0.10	0.26
$P_{\rm p}$	$[10^{43}\,{\rm erg/s}]$	7.7	3.3

Table 7.14: Model parameters for the high and low state SEDs of 1ES 0806+524. The input and output parameters (first column) of the SSC model are reported for the high (second column) and low (third column) states SEDs presented in Figure 7.34 and 7.35.From top to bottom: the minimum, break and maximum Lorentz factors are reported in the first rows, the low and high energy slope of the electron energy distribution, the magnetic field intensity, the electron density, the radius of the emitting region and its Doppler factor are listed from row four to nine. In the last three rows, the derived power carried by electrons, magnetic field, protons are reported assuming one cold proton per emitting relativistic electron.

days which is perfectly in good agreement with the variability time scale of one day inferred from the VHE light curve:

$$t_{\rm var,min} = R/(c \cdot \delta) \tag{7.12}$$

The inverse Compton peak is more constrained by the MAGIC data comprising the high source state in comparison to archival VHE data published by VERITAS. Furthermore, the optical data in the R band presented here show a clear variation with respect to measurements performed during VERITAS observations on 1ES 0806+524. which possibly traces a quite hard spectrum.

The comparison with the SSC model used for the reproduction of the SED from VERITAS observations is challenging as the model is based on an unbroken power law distribution of the ultrarelativistic non–thermal electron population [68].

7.9 1ES 0806+524: Conclusions

In this chapter, the data analysis VHE γ–ray observations of the HBL object 1ES 0806+524 done by MAGIC during winter 2011 has been presented. Observations have been triggered by an optical high state proving the optical monitoring of candidate VHE γ–ray blazars to be a successful tool. During these observations, MAGIC caught a relatively short flare in VHE γ–rays that lasted not longer than one night, wherefore data have been subdivided into a high and a low state sample. Both data sets yielded a significant signal detection, pointing out the variable emission in VHE γ–rays by the source. From the very short high activity state, whose occurrence in weak sources like 1ES 0806+524 is rather rare, a short–term variability of one–day time scale has been inferred.

From the data comprising the high and low source state, detailed spectra in the energy range from few hundred GeV to one TeV have been produced, indicating, that the low state is compatible with previous observations performed by VERITAS, while the high state features a clear flux enhancement. A hint for a spectral hardening is observed. However, due to the overlap of the spectral photon index from the spectral fits of both source states within the errors, the change in the spectral slope can not be considered significant.

Despite the simultaneous coverage from HE γ–rays to radio during MAGIC VHE γ–ray observations, no correlation studies have been performed to probe the probability of simultaneous incidence of the high states which occurred in some of the observed wavebands due to the relatively short multifrequency campaign of 1ES 0806+524 resulting in missing statistics and due to the scarce overlap of the data. However, visual inspections of the multiwavelength light curves indicate the existence of a correlation between the optical, radio and VHE γ–ray bands, as the flux level reached its maximum in each of the energy regimes on February 24^{th}, while a flare observed in X-rays emerged only few days later on March 2^{nd}.

The larger binning applied to the light curve in HE γ–rays makes a study of the connection to the high state in other wavebands difficult. Apart from this, an increasing flux has been observed in this energy regime to take place later with respect to the high states occurred in other energies, evolving as a smooth increase starting from the end of March and resulting in a quasi–steady flux level from April to the beginning of May after which the flux started to decrease.

Due to the "filter–of–the–day" mode, in which data have been taken in the UV band, no clear conclusion of the flux development can be drawn in this energy regime.

The one–zone SSC modeling reproduced very well the spectral energy distributions obtained from the respective multifrequency data coverage of the high and the quiescent state of 1ES 0806+524 except radio data due to the lacking the explanation of the model itself with respect to the observed radio emissions (see Section 6.1.7).The physical parameters derived from the modeling are similar to those typically inferred for other HBLs. The causality argument to constraint the minimal timescale of γ–ray variability from the emission region is perfectly compatible with the upper limit inferred from the temporal analysis of the VHE γ–ray signal.

Compared to previous observations by VERITAS, the study of the differential flux levels presented here results in an energy–extended spectral description of 1ES 0806+524, whose particularity consists in the coverage of to two different source states. While comparisons of the integral and differential flux during the observed quiescent source state demonstrate a very good agreement with the results of VERITAS, the high state of 1ES 0806+524 clearly differs from those studies.

In addition, the IC peak is more constrained by the MAGIC data of the high source state, which indicate a hardening in the VHE γ–ray component. The optical data in the R band shown by VERITAS exhibit clear variation with respect to measurements performed during MAGIC observations, which possibly traces a quite hard spectrum in this energy regime.

Despite the rather low redshift of 1ES 0806+524, in particular the detailed measure of the differential spectrum up to $\sim$1 TeV during the high source state may offer the opportunity to probe the EBL

In addition, the detailed spectrum of the low source state in combination with quasi–simultaneous *Fermi* data can be used to probe the method to constrain the distance of TeV blazars from the EBL imprint (see Section 6.2.6). In particular,

the effect of the source variability on the robustness of this method can be tested.

8

Two Years of MAGIC Observations of the High–Frequency–Peaked Blazar Object 1ES 1011+496

Because of its relatively large distance, $z = 0.212$, the high–frequency–peaked blazar 1ES 1011+496 has been studied intensively by MAGIC aiming at placing more stringent constraints on the EBL. This chapter contains the analysis of the MAGIC data from stereoscopic observations carried out in winter and spring of 2011and 2012 carried out with the purpose to derive a detailed differential spectrum. The data from 2011 showed only a hint for detection, wherefore reobservations have been proposed for 2012. In addition, as the SED of 1ES 1011+496 has been poorly constrained by previous MWL observations, a coordinated MWL campaign has been carried out in 2012. The 2012 data have been taken with the hardware upgraded stereoscopic system during three different stages of the recommissioning, demanding a data stacking of the individual subsamples of these observations. While the individual subsamples showed either only a hint for a significant signal or provided a rather weak detection of 1ES 1011+496, the stacked 2012 data sample provides a clear signal detection above 100 GeV leading to a detailed differential spectrum.
After a historical review of the multifrequency observations, the results of the data analysis of both years is discussed. In addition, the results are compared to previous MAGIC observations confirming the constant VHE γ–ray emission of 1ES 1011+496. MWL observations from 2011 and 2012 provide a detailed coverage of the high energy peak of the 1ES 1011+496 SED. In particular the SED built from 2012 MWL data is well constrained.

8.1 The HBL Object 1ES 1011+496: A MWL View

1ES 1011+496 is an HBL objected, located at RA 10:15:04, DEC 49:26:01 in the northern hemisphere at high latitude (see Figure 8.1). First observed with the *Very Large Array* (VLA) radio telescope [205], the source has been classified as a flat radio spectrum core–dominated source.

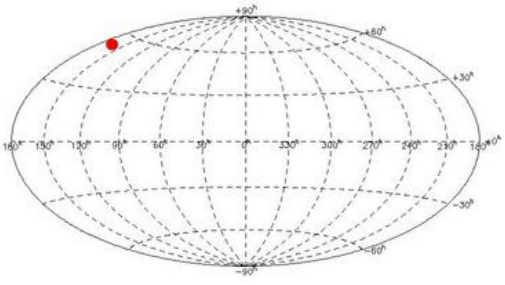

Figure 8.1: Position of the HBL 1ES 1011+496 in galactic coordinates.

1ES 1011+496 has been included in the *6C* and *7C* survey of the *Cam-*

bridge Low–Frequency Synthesis Telescope [152, 221] as well as in the *RASS–Green Bank* (RGB) catalog of radio and X-ray emitting AGNs [54]. Since 2009, the source is monitored as part of the MOJAVE program at radio wavelengths[61] (see Figure 8.2). In general, the radio flux measured between 74 MHz and 15 GHz varies from ∼250 to ∼600 mJy.After its categorization as a BL Lac object can-

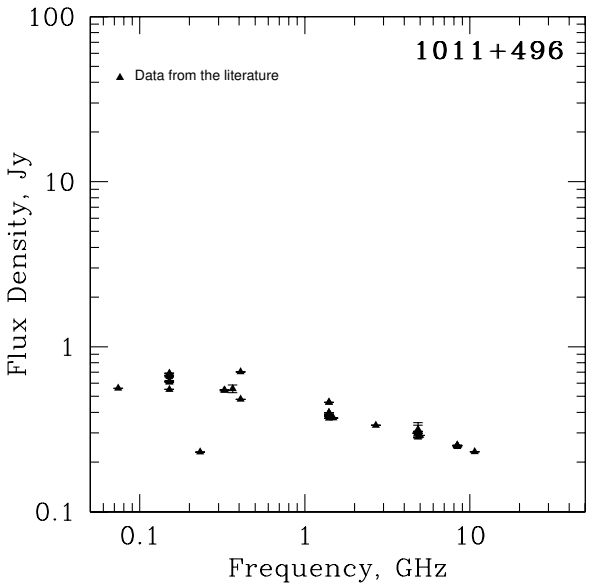

Figure 8.2: Multiepoch plot of VLBA radio data of 1ES 1011+496.

didate due to its radio and optical emission, 1ES 1011+496 has been identified as HBL object based on its radio–to–X-ray ratio by [104] (see Figure 8.3). The

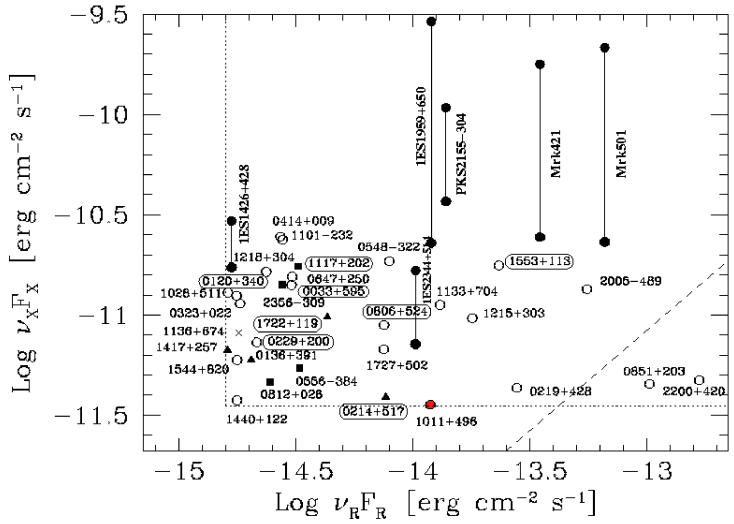

Figure 8.3: X-ray to radio flux ratio typical for HBLs, 1ES 1011+496 is marked in red. Adapted from [96].

source has been constantly monitored in the R band since 2003 showing frequent fluctuations in its optical brightness up to a factor of two to three during flares with respect to the lowest states (see Figure 8.4). An average flare duration of ∼42 days has been inferred from the long–term light curve comprising six flares with an average rise and decay time of approximately 21 days exceeding the quiescent flux level of 2.05 mJy [271].

[61] http://www.physics.purdue.edu/astro/MOJAVE/sourcepages/1011+496.shtml

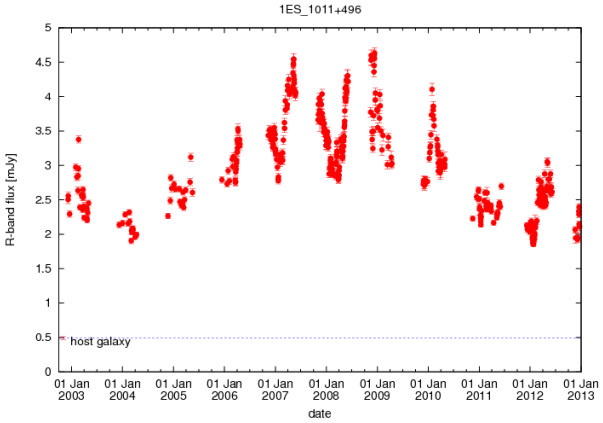

Figure 8.4: Optical light curve of 1ES 1011+496 from the Tuorla Observatory Blazar Monitoring Program from 2003 to present time, taken from http://users.utu.fi/kani/1m/1ES_1011+496_jy.html.

Five years of optical (UBRVI) observations performed with the 1.3 m McGraw–Hill Telescope yielded a moderate optical spectral variability of 1ES 1011+496 in all optical wavebands on time scales of few days [69] (see Figure 8.5).

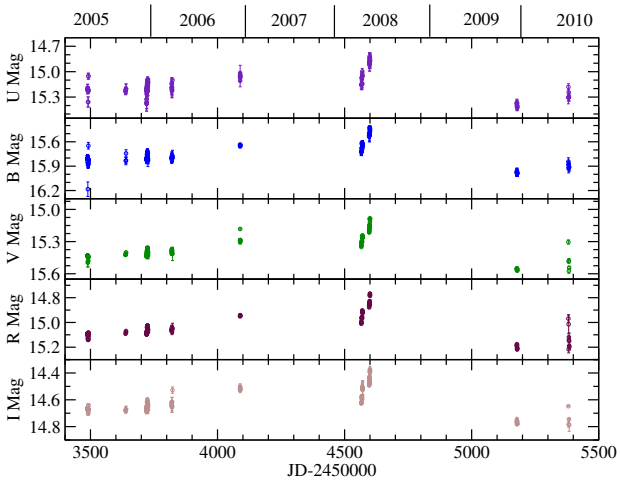

Figure 8.5: Multiband (UVRI) light curves of 1ES 1011+496 [69].

Thanks to the optical spectrum, shown in Figure 8.6, which has been obtained with the *Multi Mirror Telescope* during an optical outburst [22] the distance of 1ES 1011+496 has been accurately determined. With a distance of $z = 0.212$, 1ES 1011+496 is considered as a source of intermediate redshift.

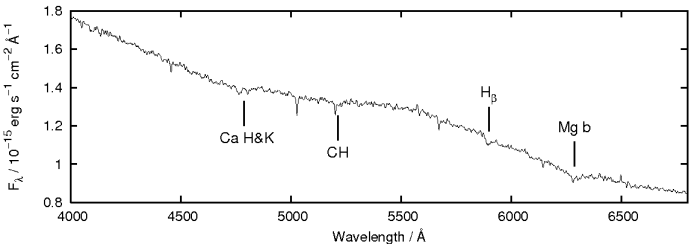

Figure 8.6: Optical spectrum of 1ES 1011+496 obtained with the Multi Mirror Telescope. The absorption lines of the host galaxy a clearly visible determining a redshift of 0.212 ± 0.002 [22].

In X-rays 1ES 1011+496 has been observed by the *Einstein Observatory* as part of the Slew Survey [109] and a survey on the broadband spectral properties [316]. Further observations in this energy regime have been carried out by *ROSAT* including the source in the RASS [76] and the Slew sample [255] respectively. From 1996 to present time 1ES 1011+496 has been constantly monitored by as part of the ASM survey by *RXTE*. In addition, since 2005 the *Swift*/XRT is monitoring the source[62]. The source features an ultra soft spectrum in this waveband consistently confirmed by individual observations. *Swift/XRT* observations carried out in the framework of a MWL campaign on 1ES 1011+496 indicated some flaring activity in 2008 [272].

The synchrotron peak frequency obtained from a parabolic fit that has been applied to a compilation of MWL data from different epochs is $5.50 \cdot 10^{16}$ Hz (see Figure 8.7) corresponding to 0.23 keV [238]. Determined peak position is situated in the energy regime typical for HBLs.

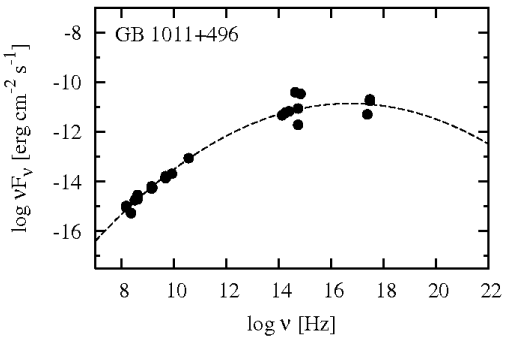

Figure 8.7: Low energy bump of the spectral energy distribution from 1ES 1011+496. The data points from a multi-epoch data sample are fitted with a parabolic function by which a synchrotron peak frequency peak frequency $log\,\nu_{\mathrm{Peak}}$ of 16.74 Hz is determined [238].

While EGRET observations of 1ES 1011+496 did not lead to a definite source detection in HE γ–rays [115, 196, 217, 292], the source has been clearly detected by *Fermi* and was included in the bright γ–ray source list of the three–months catalog [1] as well as in the LAT 1 catalog [5]. In the high energy band, i.e. E>1 GeV, the spectrum of this bright *Fermi* source is consistent with a simple power law (see Figure 8.8). No evidence of variability was seen during during the first 5.5 months of *Fermi* observations [2].

Although no initial variability in HE γ–rays was seen during the first months of observations, the source is flagged as variable in the LAT 2 catalog [242].

Before its inclusion as VHE γ–ray candidate in the Costamante & Ghisellini cataloge [90] with a predicted integral flux above 300 GeV of 0.12×10^{-11} cm^{-2} s^{-1}, HEGRA and the Whipple Observatory 10 m γ–ray telescope performed first VHE γ–ray observations on this source resulting in integral flux upper limits. From 2004 to 2006 MAGIC observations yielded further integral flux upper limits summarized in Table 8.1.

Triggered by an optical outburst, the source has been detected at TeV energies first in 2007 during mono observations carried out with the MAGIC telescope yielding a $6.2\,\sigma$ detection within 18.7 hours of effective time [22]. Quasi simultaneous multiwavelength observations did not confirm the high state of 1ES 1011+496 at other frequencies.

In spring 2008 a subsequent MWL campaign has been carried out by MAGIC confirming with a $7\,\sigma$ detection its VHE γ–ray emission within 19.8 hours of effective observation time performed in mono mode. The source was not detected in radio frequencies. In the optical R band, the source was in a relatively low state for most of the time until a major flare occurred at the end of the MWL

[62] http://www.swift.psu.edu/monitoring/source.php?source=1ES1011+496

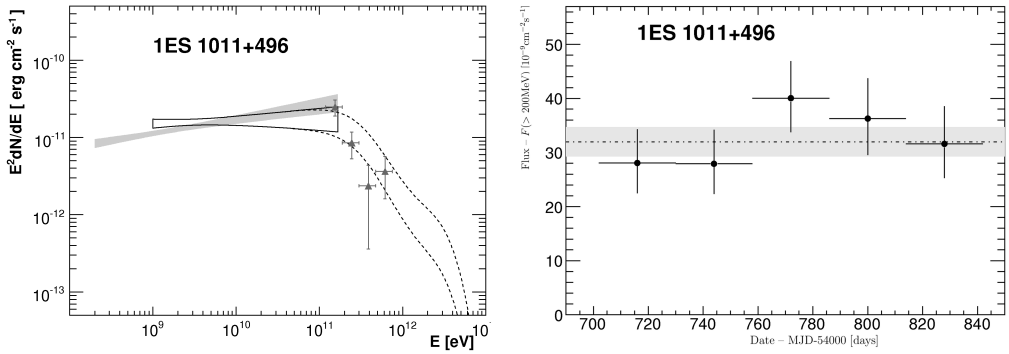

Figure 8.8: *Left:* The GeV spectrum of 1ES 1011+496 derived from *Fermi*-LAT observations indicated as "butterfly" contour. The fit over the full energy range is shown as gray band and the spectral extension of the contour to TeV energies is shown as dashed line assuming EBL absorption. Archival MAGIC TeV observations from 2007 [22] are marked as gray triangles. *Right:* The twenty–eight day light curve above 200 MeV derived from *Fermi* observations centered on the new moon. The dashed line indicates the mean flux with an estimated systematic uncertainty of 3% (gray band). Adapted from [2].

Year	Detector	$E_{\rm th}$ [TeV]	U.L. [$\rm cm^{-2}\,s^{-1}$]
1996–2002[a]	HEGRA	1.02	1.80×10^{-12}
1999–2003[b]	Whipple	0.30	3.30×10^{-11}
2004–2006[c]	MAGIC I	0.23	1.55×10^{-11}
2004–2006[d]	MAGIC I	0.14	2.10×10^{-11}

Table 8.1: Compilation of the upper limits on the integral VHE γ–ray flux obtained from various observations of 1ES 1011+496. The first and second column indicate the year of observation and the instrument; in column three and four the energy threshold and the integral upper limit are stated; [a] [15]; [b] [113]; [c] [28]; [d] [32].

campaign. While observations carried out in the V and B band indicate a trend similar to the R band, a clear flare has been observed in X-rays.

The integral flux of VHE γ–rays observed in both years, as listed in Table 8.2, did no indicate any significant flux variability.

Year	$E_{\rm th}$ [TeV]	$\rm Flux_{>Eth}$ [$\rm cm^{-2}\,s^{-1}$]$\times10^{-11}$
2007	200	1.58 ± 0.32
2008	150	see note[62]

Table 8.2: Compilation of the integral VHE γ–ray flux obtained from previous mono observations of 1ES 1011+496by MAGIC [272, 22].

The differential VHE γ–ray spectrum derived from both observation periods are well described by a power law from ∼120 GeV to ∼750 (2007) and ∼500 GeV (2008) respectively. A hint for spectral hardening in 2008 with respect to the discovery of 1ES 1011+496 as VHE source in 2007 was found (see Figure 8.9).

While the SED was poorly constrained during the source discovery in VHE γ–rays, the MWL campaign on 1ES 1011+496 provides a detailed SED of simultaneous multifrequency data that comprises the high and low state of the source

[62] The integral VHE γ–ray flux above 150 GeV is similar to the flux level similar to that measured during the source discovery in VHE γ–rays.

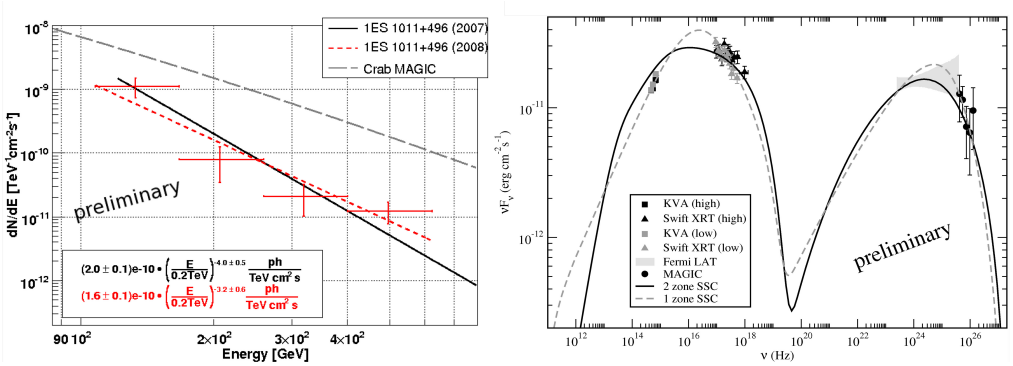

Figure 8.9: Differential VHE γ–ray flux and SED from 2007 and 2008 MAGIC mono observations of 1ES 1011+496. *Left:* The differential VHE γ–ray spectrum of 1ES 1011+496 observed in 2007 (black line) and 2008 (red line). A hint of spectral hardening is observed with respect to the discovery of 1ES 1011+496 as VHE emitter. *Right:* The simultaneous SED from the MWL campaign in 2008 on 1ES 1011+496 is divided into a high (black) and low (gray) state data set according to the activity in X-rays. Both states are reproduced with a one zone (black solid line) and a two zone (gray dashed line) SSC model. The optical and VHE data are host galaxy and EBL corrected respectively. The *Fermi* bow–tie deduced from the LAT 1 catalog is illustrated [272].

in X-rays that have been fitted by a one zone and a self–consistent two zone SSC model. While the modeling of the SED from 2007 indicated an IC dominance, simultaneous observations from 2008 corroborate the presence of a synchrotron dominance instead as observed for most HBLs.

8.2 The Data Sets & Quality Selection

After its upgrade to a stereoscopic system, MAGIC reobserved 1ES 1011+496 in 2011 during in order to derive a detailed differential spectrum with the perspective to study the IC peak of this source. A particular aim of the reobservations in VHE γ–ray was to put further constraints on the EBL by a detailed measure of the differential spectrum with extended energy coverage. Unfortunately, despite the improvement of the performance of the instrument thanks the stereo technique these observations yielded only a hint for a significant detection in VHE γ–rays.

Therefore, follow–up observations have been proposed for the subsequent observation cycle in 2012 in the framework of a MWL campaign. These data have been taken during the commissioning right after the upgrade of the readout system (see Section 3.4.3). Due to this major change in one of the hardware components of the telescopes, the data collected during the this observation periods have been analyzed separately from the 2011 data sample since they require dedicate MC simulated data. In addition, during 2012 observations two major hardware issues occurred, wherefore a subdivision of the data sample into three shorter periods was necessary.

2011 Observations

Observations of 1ES 1011+496 have been carried out on 12 individual nights in wobble mode from February to April 2011 for a total of 13 hours. Due the presence of strong moon during the beginning of the campaign, few data have

been discarded from the data sample (see Table 8.3) by applying quality cuts based on the event rate of each telescope separately.

Cycle	Night	MJD	Eff. Time [h]	Zd [°]	Moon light conditions
VI	24/02/2011	55616	1.37	27 - 40	Moderate Moon
	25/02/2011	55617	1.18	28 - 41	Moderate Moon
	28/02/2011	55620	1.06	27 - 40	No Moon
	01/03/2011	55621	0.53	24 - 41	No Moon
	02/03/2011	55621	0.72	31 - 40	No Moon
	03/03/2011	55623	0.78	30 - 37	No Moon
	27/03/2011	55647	0.80	30 - 39	No Moon
	28/03/2011	55648	0.78	30 - 41	No Moon
	30/03/2011	55650	0.56	33 - 41	No Moon
	03/04/2011	55654	0.77	31 - 40	No Moon
	09/04/2011	55660	0.72	31 - 40	No Moon

Table 8.3: Final dataset of 1ES 1011+496 observations from early 2011 used in the analysis. From left to right: The observation cycle (first column) as well as the nights of observation are indicated in dd/mm/yy (second column) and in MJD (third column); effective time of observation in hours (third column); zenith angle range in degrees (fourth column). The last column refers the moon light conditions during observations. The lower rates during the first two nights of observation reveal the presence of moderate moon[62].

In Figure 8.10 the stereo event rate of the data after the quality selection is plotted showing some lower rates during the first two nights due to the presence of moderate moon light. The data set comprises ∼9.3 hours of effective observation time covering a zenith range between 24° and 41°.

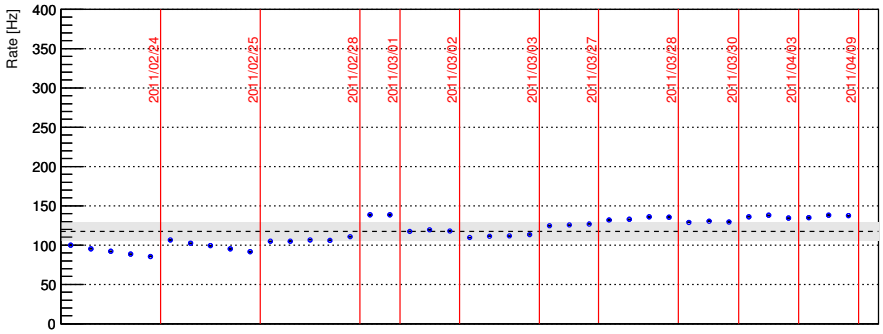

Figure 8.10: Stereo event rate distribution of 1ES 1011+496 2011 MAGIC data. The gray shaded area corresponds to the 10% variation from the mean value (dashed line). Lower rates at the beginning of the observation period can be associated to moderate moon conditions during data taking.

2012 Observations

MAGIC performed stereo observations on 1ES 1011+496 from late January to mid May 2012 during 33 nights for ∼23 hours at zenith angles from 25° to 50°. This period comprises the recommissioning of the MAGIC stereo system in January

[62] See Appendix A.2 for details on the observational conditions.

2012 after the upgrade of the readout system by the replacement of the DRS–2 chip to the latest version, i.e. DRS–4 (see Section 3.4.3). In addition, several pixels in the MAGIC I camera were dead due to several broken receiver boards including pixels that were installed in the trigger area (see Appendix A.2). Moreover, an AMC bug in MAGIC I lead to a worse PSF. This represents a serious hardware problem in terms of light sensitive area which has been taken into account by dedicated MC simulations.

During the first observation nights in January, the trigger pattern information were missing in the data files demanding a dedicate analysis on the level of `superstar`[63]. In addition, data taken in this period include the calibration pulses (see Section 7.1.1) requiring additional cuts during the analysis[64].

By the end of February, 24 dead channels in the inner camera region of MAGIC I were recovered by replacing a broken receiver board. However, the worsening of the MAGIC I PSF remained unfixed. Therefore, data taken in this period have to be treated separately requiring special MC simulations for both situations with persistent hardware problems.

In the beginning of March the problem of the MAGIC I PSF was resolved by fixing a bug in the AMC[65]. Thus, the data taken from the beginning of March until mid May represent the sample collected under best conditions from a hardware point of view, excluding problems that occurred during few observations nights. The persistent problems during 2012 observations are summarized in Table 8.4.

Observation period	Persistent hardware problem
23/01/2012 - 30/01/2012	Missing trigger pattern Inclusion of calibration pulses in data files
23/01/2012 - 25/02/2012	Holes in the MAGIC I camera
23/01/2012 - 09/03/2012	Worse PSF of MAGIC I

Table 8.4: Summary of the persistent hardware problems during 2012 observations of 1ES 1011+496.

During cycle VII 1ES 1011+496 has been observed with two wobble pairs so that the position of the source in the camera was rotated by 90° every 20 minutes so that data have been taken with four individual wobble positions. In this way, in principle the background estimation can be performed with three Off regions which is of particular importance at lower energies.

Unfortunately, 1ES 1011+496 has been scheduled for rather short time windows wherefore maximum two wobble positions during on night have been observed (see Table 8.5). In addition, initially data have been taken with the usual wobble pair (W1: rotation by 0° and 180° of the source position in the camera)[66] while in the second half of the observation period data were taken with two additional wobble positions (W2: rotation by 90° and 280° of the source position in the camera).

[63] Due to the missing information, the selection criteria of coincident events observed with both telescopes required a workaround based on the time stamp.
[64] A cut at `MNewImagePar.fConc` < 0.025 was applied to remove the calibration pulses.
[65] During the upgrade minor changes have been implemented in the AMC software of MAGIC I
[66] Note that during some nights only one of the two wobble positions was observed making the Off estimation for the daily light curve very challenging.

Cycle	Night	MJD	Eff. Time [h]	Zd [°]	Wobble pair	Moon light conditions
	23/01/2012	55949	0.70	33 - 44	W1	No Moon
	26/01/2012	55952	0.87	31 - 42	W1	No Moon
	27/01/2012	55953	1.29	30 - 46	W1	No Moon
	31/01/2012	55957	1.32	31 - 48	W1	No Moon
VII a	01/02/2012	55958	1.90	30 - 50	W1	No Moon
	02/02/2012	55959	1.63	31 - 50	W1	No Moon
	21/02/2012	55978	0.20	33 - 36	W1	No Moon
	22/02/2012	55979	0.56	30 - 35	W1/W2	No Moon
	25/02/2012	55982	0.57	30 - 35	W1	No Moon
	26/02/2012	55983	0.58	30 - 35	W1	No Moon
VII b	29/02/2012	55986	0.57	30 - 35	W1	No Moon
	01/03/2012	55987	1.18	25 - 35	W1/W2	No Moon
	18/03/2012	56004	0.58	30 - 35	W2	No Moon
	19/03/2012	56005	0.56	30 - 35	W2	No Moon
	20/03/2012	56006	0.57	30 - 35	W2	No Moon
	22/03/2012	56008	0.46	31 - 35	W2	No Moon
	23/03/2012	56009	0.13	31 - 36	W2	No Moon
	24/03/2012	56010	0.55	34 - 35	W2	No Moon
	25/03/2012	56011	0.36	30 - 35	W2	No Moon
VII c	26/03/2012	56012	0.51	32 - 35	W2	No Moon
	27/03/2012	56013	0.46	30 - 35	W2	No Moon
	28/03/2012	56014	0.48	31 - 35	W2	No Moon
	29/03/2012	56015	0.64	29 - 35	W2	No Moon
	13/04/2012	56030	0.57	30 - 35	W2	No Moon
	14/04/2012	56031	0.56	30 - 35	W2	No Moon
	15/04/2012	56032	0.58	30 - 35	W2	No Moon
	19/04/2012	56036	0.59	30 - 35	W1	No Moon
	10/05/2012	56057	1.08	33 - 44	W1/W2	No Moon
	19/05/2012	56066	0.71	33 - 44	W1/W2	No Moon

Table 8.5: Final dataset of 1ES 1011+496 observations from winter 2011 used in the analysis. From left to tight: The nights of observation are indicated in dd/mm/yy (first column) and in MJD (second column); effective time of observation in hours (third column); zenith angle range in degrees (fourth column). Column five indicates with which wobble pair (0°/180° and 90°/270°, i.e. W1 and W2 respectively). The last column refers the moon light conditions during observations.

In Figure 8.11 the stereo rate distributions of the selection from the 2012 data sets are presented. Beside few fluctuations of the individual mean rates from the three data samples, the rate distributions are quite stable on a nightly time scale.

8.3 The Signal Detection and Sky Map

Due to the steep and very soft spectrum of 1ES 1011+496, the signal search has been performed in the LE regime applying the cuts summarized in 7.3. The energy thresholds for the 2011 and 2012 data analysis has been estimated to be at

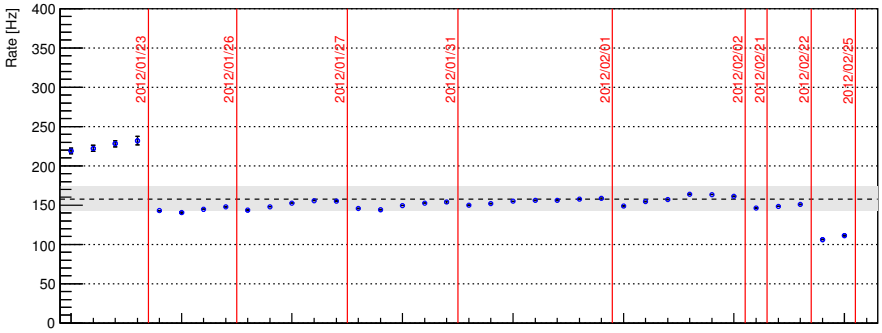

(a) VII a

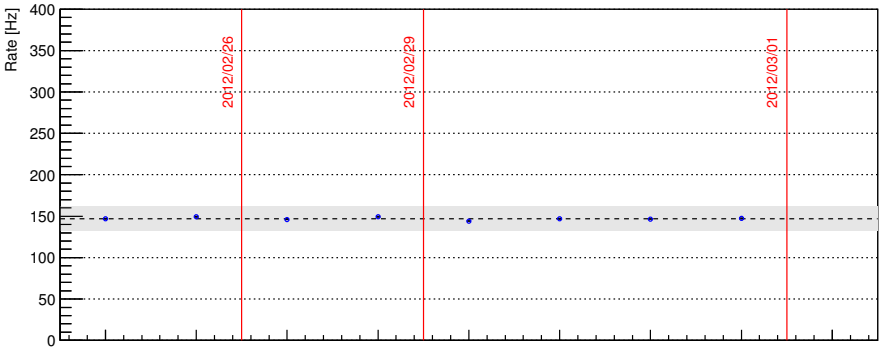

(b) VII b

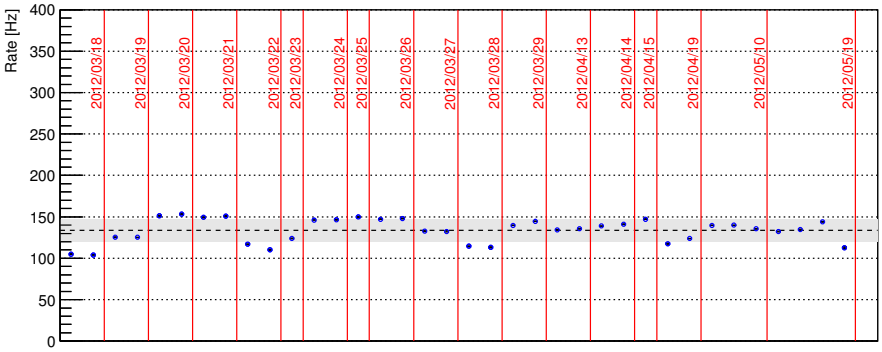

(c) VII c

Figure 8.11: Stereo event rate distribution of the three subset 1ES 1011+496 2011 MAGIC data. The gray shaded area corresponds to the 10% variation from the mean value (dashed line).

$\sim$100 GeV by means of MC simulated data to which LE standard cuts were applied assuming a spectral photon index Γ of -4.0 for 1ES 1011+496 (see Figure 8.12 and 8.12).

In the case of 2012 data, less MC events have been simulated for the periods comprising observations from January to beginning of March. Therefore, there are less statistics available for the analysis of data taken during these months.

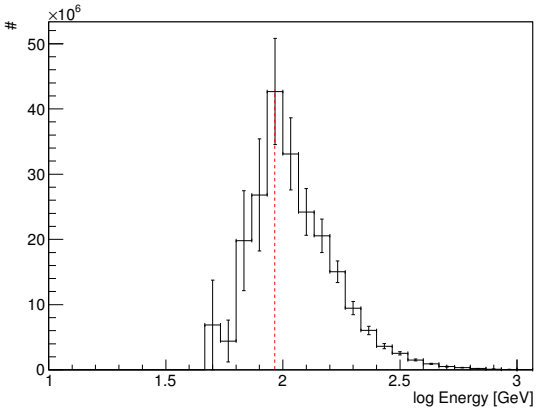

Figure 8.12: Energy threshold for the signal detection of 1ES 1011+496 from 2011 observations. The threshold has been evaluated by applying LE standard cuts to MC simulated data assuming an index of -4 for the source spectrum of 1ES 1011+496.

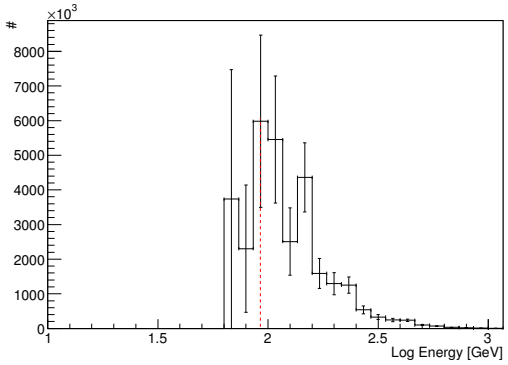

(a) VII a

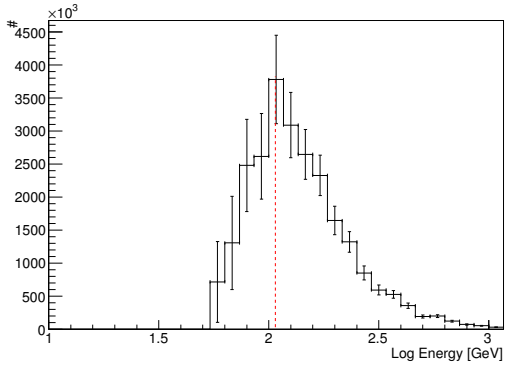

(b) VII b

2011

For the signal search, one Off region located at 180° with respect to the reconstructed source position was used determining a background level of 1514 events in the signal region (see Figure 8.13). An excess of 249 γ–like events was found above 100 GeV whose significance corresponds to $\sim$4.4 σ [195]. Thus, in astronomical terms the signal found in the VHE γ–ray data from 2011 of 1ES 1011+496 is not significant enough to claim a detection (see Section 7.1.7). However, with an significant above 4 σ the data may be considered to give a clear hint for such signal.

The sky map shown in Figure 8.14 derived above 100 GeV seems to reveal a slight misspointing of the telescopes with respect to the source position. However,

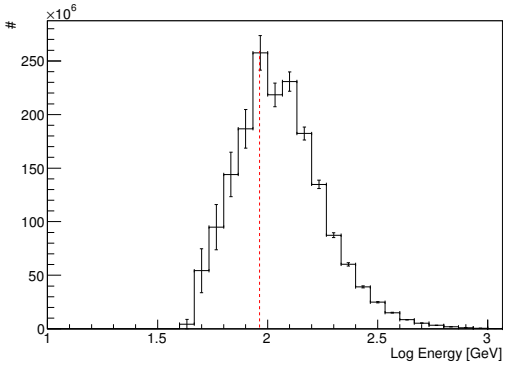

(c) VII c

Figure 8.12: Energy thresholds for the signal detection of 1ES 1011+496 from 2012 observations. The thresholds have been eveulated for the individual subsamples of the 2012 data set by applying LE standard cuts to MC simulated data assuming an index of -4 for the source spectrum of 1ES 1011+496.

Figure 8.13: Signal detection plot derived from 2011 MAGIC stereo observations of 1ES 1011+496. LE standard cuts have been applied to the data using one Off for the background level (gray histogram) calculation.

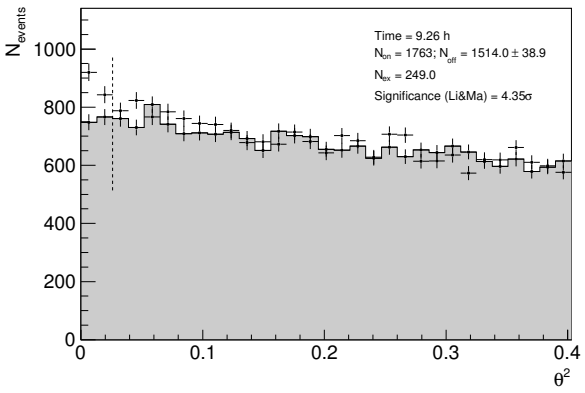

the observed signal is consistent with a point–like source located at the catalogue position of 1ES 1011+496 within the PSF of the telescopes and the significance at the source position is consistent with the results obtained from the detection plot.

2012

For the signal search of the samples comprising January to February and March to May data, 1 Off regions has been used for the background estimation since the observations performed with all four wobble positions is pretty unequal (see Table 8.6). By contrast, he rather small data set comprising February to March data allow for the application of three Off regions since these data have been collected for all four wobble positions for an acceptably equal amount of time. For the same reason three Off regions have been used when analyzing the entire data set of 2012.

The results from the signal search obtained for the subsamples of the 2012 data are summarized in Table 8.7. While 1ES 1011+496 has been detected with a significance of $6.6\,\sigma$ above 100 GeV during the first half of observations, a strong hint of signal of $4.6\,\sigma$ is found for the second half of observations. Due to the lack of observation time, the rather small data sample collected in–between yields only a faint hint of detection of $3.7\,\sigma$ significance.

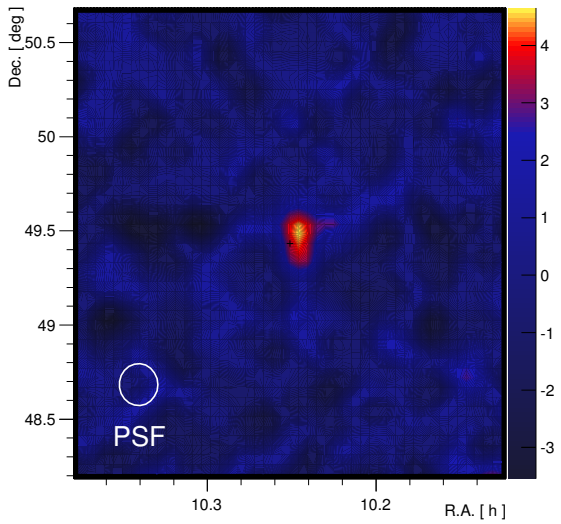

Figure 8.14: Significance of the LRT sky map of 1ES 1011+496 derived from MAGIC stereo observations in 2011 above 100 GeV. Despite the slight misspointing, the significant excess of a point–like source is consistent with the catalogue position of 1ES 1011+496 within the PSF of the MAGIC telescopes (white circle).

Observation Period	Eff. time [h]	Off regions
VII a	$W_{000^\circ} = 4.25$ $W_{180^\circ} = 4.56$ $W_{90^\circ} = 0.23$ $W_{270^\circ} = 0.00$	1
VII b	$W_{000^\circ} = 0.66$ $W_{180^\circ} = 0.91$ $W_{90^\circ} = 0.57$ $W_{270^\circ} = 0.20$	3
VII c	$W_{000^\circ} = 1.20$ $W_{180^\circ} = 0.83$ $W_{90^\circ} = 3.25$ $W_{270^\circ} = 4.66$	1
VII	$W_{000^\circ} = 6.11$ $W_{180^\circ} = 6.30$ $W_{90^\circ} = 4.04$ $W_{270^\circ} = 4.86$	3

Table 8.6: Wobble position summary from 2012 observations of 1ES 1011+496. The effective time of observations carried out with different wobble positions (0°, 90°, 180°, 270° rotation of the source position in the camera) is indicated (second column).

The overall significance of the entire 2012 data sample above 100 GeV yields a very strong detection of $\sim 12.9\,\sigma$ within ~ 21.3 hours (see Figure 8.15[67].). Prob-

[67] The individual θ^2 plots can be found in Section A.2

Period	Eff. time [h]	Significance [σ]	Off regions [#]
VII a	9.05	6.6	1
VII b	2.33	3.7	3
VII c	9.94	4.6	1
V II	21.31	12.9	3

Table 8.7: Signal detection study of the 2012 data from observations of 1ES 1011+496. LE cuts have been applied to the data individual subsamples of the 2012 data set. The signal significance (third column) is calculated according to [195]. The number of Off regions used for the background estimation is listed (fourth column).

ably, the strong signal with respect to 2011 observations is rather a merit of the longer observation time than due to the upgrade of the readyout system.

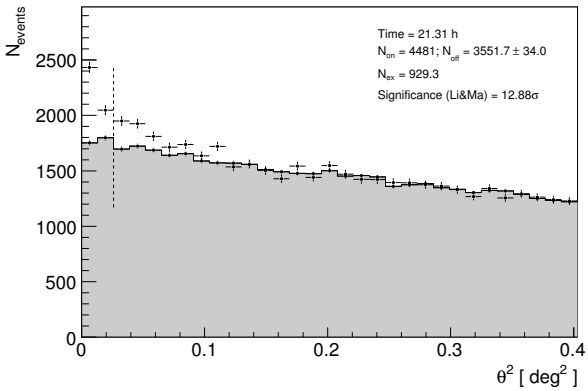

Figure 8.15: θ^2 plot of the overall 2012 data sample of 1ES 1011+496.

The comparison of the individual significances from the signal search with those from the LRT sky maps, listed in Table 8.8, points out that both analysis yield a consistent result in the case of the first two observation periods within $1\,\sigma$. By contrast, a discrepancy of more than $5\,\sigma$ is found in the analysis of the third subsample. However, as both significances are based on different calculations, such discrepancy is not that surprising. In addition, When using three Off regions for the signal search with `odie` the significance increases to $9.9\,\sigma$ providing a very good agreement between both analysis due to the better background estimation.

Table 8.8: Significances of the LRT sky maps above 100 GeV derived from 2012 1ES 1011+496 data.

Period	TS significance [σ]
VII a	7.6
VII b	4.0
VII c	9.2

The overall LRT sky map from 2012 data above 100 GeV is presented in Figure 8.16 indicating a TS significance compatible to the results from the analysis perfomed with `odie`. A consistency of the point–like signal, with the source catalog position of 1ES 1011+496 was found.

8.4 The Light Curve

In order to compare the integral flux between 2011 and 2012 observations taking into account that some data have been taken under moderate moon light conditions in 2011, the integral VHE γ–ray flux has been calculated above $\sim$150 GeV

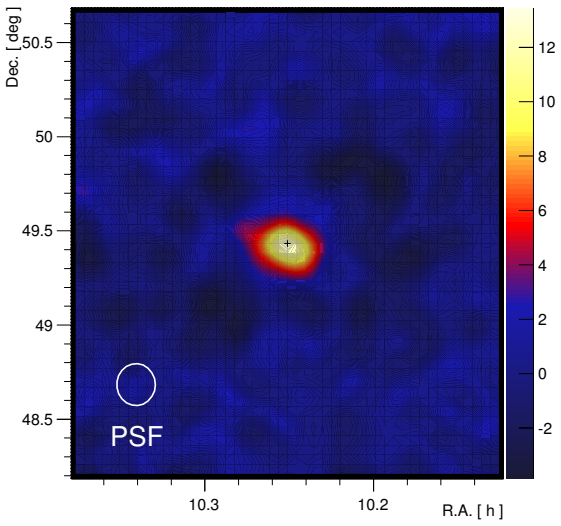

Figure 8.16: Significance of the stacked LRT sky map above 100 GeV of 1ES 1011+496 derived from MAGIC 2012 observations.

despite the lower energy threshold of 100 GeV. In Table 8.9 the cuts used for the derivation of the 2011 and 2012 integral flux above 150 GeV of 1ES 1011+496 are listed.

Parameter	Cut
`Size`	>50 phe
`hadronness` cut efficiency	90%
θ^2 cut efficiency	70%
minimal `hadronness`	0.07
minimal θ^2	0.02 deg^2

Table 8.9: Set of cuts applied to the 1ES 1011+496 data from 2011 and 2012 for the temporal analysis.

Due to their dynamical nature, the cuts in `hadronness` and θ^2 are energy dependent, as summarized in Table 8.10. Being determined based on the respective MC data samples used for the individual analysis, these cuts differ slightly in `hadronness`, whereas the cut un θ^2 is identical for the data samples of both observation cycles.

2011

The daily–binned light curve of 2011 observations of 1ES 1011+496 , reported in Table 8.11, ranges from ∼2 to 12% C.U. with a maximum flux level appearing at March 27$^{\text{th}}$ (see Figure 8.17). The mean integral flux is $(1.8 \pm 0.3_{\text{stat}} \pm 0.2_{\text{sys}}) \times 10^{-11}\,\text{cm}^{-2}\,\text{s}^{-1}$ corresponding to (5.5 ± 0.9)% of the Crab Nebula flux.

As the analysis results in a negative integral flux, which is physically meaningless, observations from March 2$^{\text{nd}}$ have been excluded from the constant flux hypothesis. The remaining data yield a probability of ∼84% ($\chi^2/\text{NDF} = 4.93/9$) for the hypothesis of a constant source emission.

2012

The daily light curve derived above 150 GeV from 2012 observations is presented in Figure 8.18 yielding a probability of 31% ($\chi^2/\text{NDF} = 27.89/25$) of a constant VHE γ–ray emission at a level of $(1.4 \pm 0.2_{\text{stat}} \pm 0.2_{\text{sys}}) \times 10^{-11}\,\text{cm}^{-2}\,\text{s}^{-1}$ equal to (4.3 ± 0.9)% C.U.

Energy bin [GeV]	θ^2 cut [deg^2]	`hadronness` cut			
		VI	VII a	VII b	VII c
126<E<199	0.02	0.33	0.41	0.42	0.32
199<E<315	0.02	0.31	0.41	0.42	0.32
315<E<500	0.02	0.35	0.41	0.45	0.28
500<E<792	0.02	0.28	0.29	0.32	0.25
792<E<1256	0.02	0.31	0.35	0.32	0.23
1256<E<1991	0.02	0.22	0.29	0.28	0.21
1991<E<3155	0.02	0.16	0.30	0.27	0.19
3155<E<5000	0.02	0.16	0.19	0.24	0.15
5000<E<7924	0.02	0.13	0.18	0.21	0.13
7924<E<12559	0.02	0.09	0.20	0.22	0.11
12550<E<19905	0.02	0.15	0.24	0.27	0.11
19905<E<31548	0.02	0.15	0.33	0.45	0.12
31548<E<50000	0.02	0.31	0.07	0.25	0.18

Table 8.10: θ^2 and `hadronness` cuts for the study of the integral flux as a function of time for observations of 1ES 1011+496 in cycle VI and VII derived for the individual energy bins by fixing the cut efficiencies at 70 and 90% respectively.

Night	MJD	Eff. time [h]	Significance [σ]	$F_{>150\,\mathrm{GeV}}$ [$10^{-11}\,\mathrm{cm}^{-2}\,\mathrm{s}^{-1}$]	U.L. [f.u.]	U.L. [% C.U.]
24/02/2011	55616	1.37	2.9	1.6 ± 0.6	–	–
25/02/2011	55617	1.18	0.8	0.8 ± 1.0	3.8	12
28/02/2011	55620	1.06	2.2	2.2 ± 1.0	–	–
01/03/2011	55621	0.53	1.5	1.8 ± 1.2	–	–
02/03/2011	55621	0.72	< 0	< 0 1.5	1.4	5
03/03/2011	55623	0.78	1.0	1.3 ± 1.3	5.3	17
27/03/2011	55647	0.80	3.2	4.0 ± 1.3	–	–
28/03/2011	55648	0.78	1.5	2.6 ± 1.7	–	–
30/03/2011	55650	0.56	0.9	2.4 ± 2.6	10.4	32
03/04/2011	55654	0.77	1.3	1.7 ± 1.4	–	–
09/04/2011	55660	0.72	0.8	1.2 ± 1.5	5.7	18

Table 8.11: Integral flux analysis of 1ES 1011+496 data taken in 2011. From left to right: night of observation (first and second column); exposure time (third column); significance of signal detection (fourth column); integral flux above 150 GeV (fifth column); In column six and seven, the upper limits (E > 150 GeV) calculated for those nights, where the measured integral flux was consistent with zero, are reported in flux (f.u.) and percentage crab units (C.U.).

Despite the rather short observation times of the individual nights (see Table 8.12) the significances of the integral fluxes derived on a nightly basis is for half of the observation period above $2\,\sigma$ and few nights yielded an integral flux consistent with zero. The flux seems to be higher at the beginning of February decreasing from 10% C.U. to a level at 3.7% of the Crab Nebula flux.

Compared to 2011, the integral VHE γ–ray flux levels observed in 2012 above 150 GeV are consistent within the errors. In addition, both measurements are compatible with the flux previously measured by MAGIC above 200 GeV within

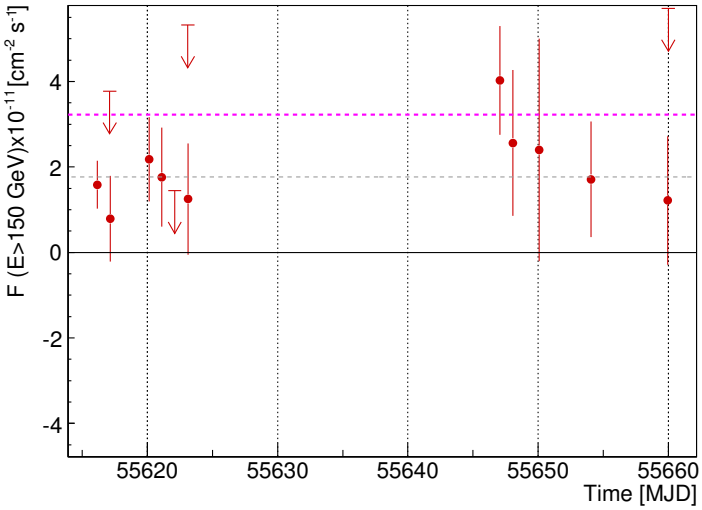

Figure 8.17: Daily–binned light curve of the integral VHE γ–ray emission from 1ES 1011+496 above 150 GeV during observations carried out in 2011. The arrows correspond to the 95% confidence level upper limits which have been derived in case the measured integral flux was consistent with zero. The mean flux level (gray dashed line) and the level of 10% Crab Nebula flux (pink dashed line) are indicated .

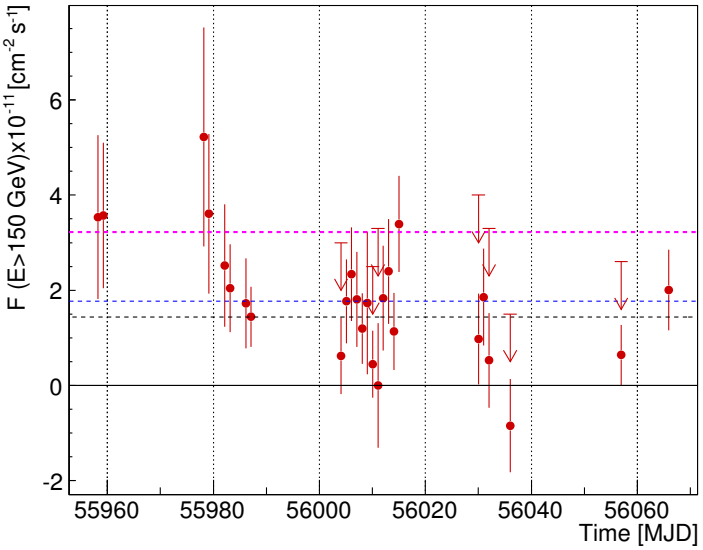

Figure 8.18: Daily–binned light curve of the integral VHE γ–ray emission from 1ES 1011+496 above 150 GeV during observations carried in 2012. The arrows correspond to the 95% confidence upper limits. The mean flux level from 2012 (gray dashed line) and 2011 (blue dashed line) are indicated. For comparison purpose, the level of 10% Crab Nebula flux (pink dashed line) is plotted.

the errors (see Table 8.2).

[67] For these observations an error occurred in the calculation of the effective time in the `fluxlc` executable necessary for the flux calculation.

Night	MJD	Eff. time [h]	Significance [σ]	$F_{>150\,\mathrm{GeV}}$ [$10^{-11}\,\mathrm{cm}^{-2}\,\mathrm{s}^{-1}$]	U.L. [f.u.]	U.L. [% c.u.]
23/01/2012	55949	n.a.[67]	1.5	n.a.		
26/01/2012	55952	n.a.	1.5	n.a.		
27/01/2012	55953	n.a.	2.1	n.a.		
31/01/2012	55957	n.a.	1.3	n.a.		
01/02/2012	55958	1.90	2.1	3.5 ± 1.7	–	–
02/02/2012	55959	1.63	2.3	3.6 ± 1.5	–	–
21/02/2012	55978	0.20	2.3	5.2 ± 2.3	–	–
22/02/2012	55979	0.56	2.2	3.6 ± 1.7	–	–
25/02/2012	55982	0.57	2.0	2.5 ± 1.3	–	–
26/02/2012	55983	0.58	2.4	2.0 ± 0.9	–	–
29/02/2012	55986	0.57	1.9	1.7 ± 0.9	–	–
01/03/2012	55987	1.18	2.4	1.4 ± 0.6	–	–
18/03/2012	56004	0.58	0.8	0.6 ± 0.8	3.0	9
19/03/2012	56005	0.56	2.0	1.8 ± 0.9	–	–
20/03/2012	56006	0.57	2.4	2.3 ± 1.0	–	–
22/03/2012	56008	0.46	1.6	1.2 ± 0.7	–	–
23/03/2012	56009	0.13	1.2	1.7 ± 1.5	–	–
24/03/2012	56010	0.55	0.6	0.4 ± 0.7	2.5	8
25/03/2012	56011	0.36	0	0.0 ± 1.3	3.3	10
26/03/2012	56012	0.51	1.7	1.8 ± 1.1	–	–
27/03/2012	56013	0.46	2.2	2.4± 1.1	–	–
28/03/2012	56014	0.48	1.4	1.1 ± 0.8	–	–
29/03/2012	56015	0.64	3.4	3.4 ± 1.0	–	–
13/04/2012	56030	0.57	1.0	1.0 ± 1.0	4.0	12
14/04/2012	56031	0.56	1.8	1.9 ± 1.0	–	–
15/04/2012	56032	0.58	0.6	0.5 ± 1.0	3.3	10
19/04/2012	56036	0.59	-0.9	-0.8 ± 1.0	1.5	5
10/05/2012	56057	1.08	1.0	0.6 ± 0.6	2.6	8
19/05/2012	56066	0.71	2.4	2.0 ± 0.8	–	–

Table 8.12: Integral flux analysis of 1ES 1011+496 observations from 2012. From left to right: night of observation (first and second column); exposure time (third column); significance of signal detection (fourth column); integral flux above 150 GeV (fifth column); In column six and seven, the upper limits (E > 150 GeV) calculated for those nights, where the measured integral flux was consistent with zero, are reported in flux (f.u.) and percentage Crab units (C.U.)

8.5 The Differential Flux

Despite the rather compatible level of the integral fluxes from 2011 and 2012 observations of 1ES 1011+496, the differential flux has been studied separately since the detection in 2012 of 1ES 1011+496 in the LE regime is stronger than in 2011 allowing a fine–binned spectral analysis. The differential spectra and the significances of the individual spectral points is presented in the following sections. The same set of cuts as used for the temporal analysis of the integral VHE γ–ray flux observed from 1ES 1011+496 (see Table 8.9) have been applied.

2011

To derive the differential spectra of 2011 observations, the energy binning in logarithmic scale between 5 GeV to 50 TeV has been set to 20. Table 8.13 summarizes the energy dependent cuts in θ^2 and `hadronness` as well as the significance and the differential flux of the individual spectral points. Clearly, the VHE γ–ray signal observed from 1ES 1011+496 is more significant at lower energies, especially above 150 GeV of where a significance of more than 2.5 σ is found.

Mean energy [GeV]	θ^2 cut [deg^2]	`hadronness` cut	Significance [σ]	N_{ex} [cm^{-2} s^{-1} TeV^{-1}]	F
102	0.03	0.39	1.9	92 ± 51	$(8.5 \pm 4.5)\times10^{-10}$
162	0.02	0.33	2.9	126 ± 43	$(2.7 \pm 1.0)\times10^{-10}$
257	0.02	0.31	2.6	56 ± 21	$(4.9 \pm 2.0)\times10^{-11}$
408	0.02	0.35	0.6	10 ± 15	$(3.2 \pm 1.0)\times10^{-11}$
646	0.02	0.28	1.4	14 ± 10	$(2.5 \pm 1.8)\times10^{-12}$

Table 8.13: Differential flux of the 2011 data sample of 1ES 1011+496. The mean energy of the bin (first column), the θ^2 and `hadronness` cuts (second and third column) are listed, derived from simulated γ–like events applying cut efficiency of 90 and 70% respectively. Column four and five denote the significance and the number of excess events. In column six the differential flux before unfolding is listed.

Due to the steep nature of the differential VHE γ–ray spectrum, the significance drops dramatically above 400 GeV leading to larger uncertainties regarding the flux calculation. The observed differential spectrum from ∼100 to 700 GeV, unfolded with the Tikhonov algorithm [24], is presented in Figure8.19 together with the deabsorbed spectrum according to Equation 7.9 using the EBL model of [103].

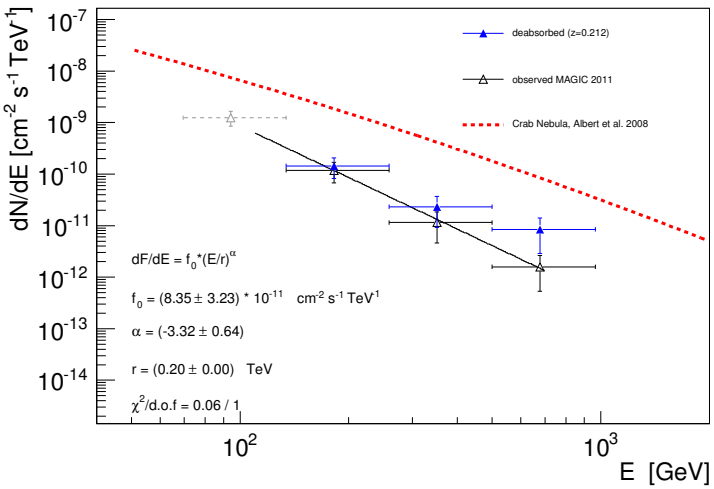

Figure 8.19: Unfolded differential energy spectrum of 1ES 1011+496 observed by MAGIC in 2011. The black triangles correspond to the measured spectra fitted by a simple power law (solid black line) whose parameters are indicated in the inlet in the bottom left corner; the gray triangle indicates the differential flux measured slightly below the energy threshold of the analysis. The blue filled triangles indicate the deabsorbed spectrum corrected for EBL attenuation using the model by [103]. The Crab Nebula spectrum (red dashed line) is shown [30].

The observed spectrum has been fitted by simple power law normalizing the flux at 200 GeV:

$$\frac{dN}{dE} = f_0 \cdot \left(\frac{E}{200\,\mathrm{GeV}}\right)^{\Gamma} \tag{8.1}$$

The hypothesis of a simple power law has a probability of 80% (χ^2/NDF = 0.06/1) yielding a flux normalization f_0 of $(8.3 \pm 3.2_{\mathrm{stat}} \pm 1.6_{\mathrm{sys}})\times10^{-11}\,\mathrm{cm}^{-2}\,\mathrm{TeV}^{-1}$ and a spectral slope Γ of -3.3 $\pm$ 0.6_{stat} $\pm$ 0.2_{sys}. Despite the slight pile–up of the deabsorbed spectrum at the highest observed energy, the probability of a simple power law defined by f_0 of $(1.1 \pm 0.4_{\mathrm{stat}})\times10^{-10}\,\mathrm{cm}^{-2}\,\mathrm{TeV}^{-1}$ and Γ = -2.3 $\pm$ 0.8_{stat} corresponds to 55% (χ^2/NDF = 0.35/1).

In Table 8.14 the differential flux obtained with the Tikhonov unfolding algorithm is reported. Due to the correction of the finite energy resolution, the first point of the unfolded spectrum is slightly below the energy threshold of the analysis (see Section 8.3). Therefore, the differential flux is probably overestimated due to a low effective collection area (see Section 7.1.8).

Table 8.14: Differential flux of the unfolded VHE γ–ray spectrum of 1ES 1011+496 observed in 2011.

Mean energy [GeV]	F [$\mathrm{cm}^{-2}\,\mathrm{s}^{-1}\,\mathrm{TeV}^{-1}$]
94	$(1.2 \pm 0.4)\times10^{-9}$
182	$(1.2 \pm 0.5)\times10^{-10}$
351	$(1.1 \pm 0.7)\times10^{-11}$
678	$(1.6 \pm 1.0)\times10^{-12}$

The study of the systematics on the differential flux determination related to different unfolding algorithm shows that at higher energies different unfolding methods indicate large discrepancies in the uncertainty of the determined flux (see Figure 8.20). This is not surprising considering the low significance of the data collected at high energies associated to a low number of excess events (see Table 8.13).

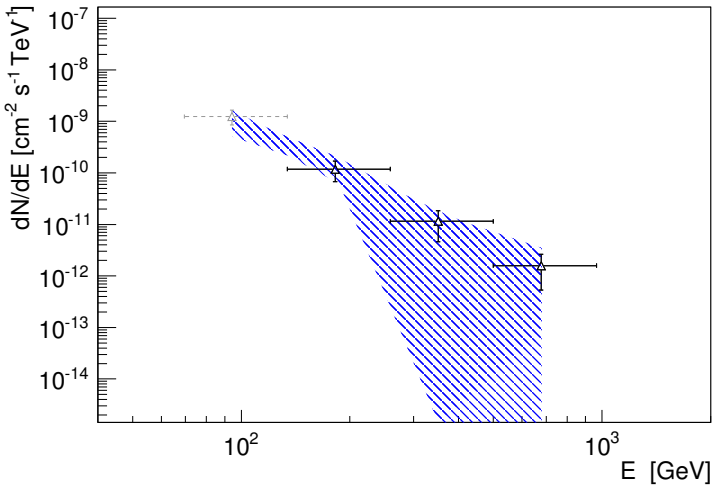

Figure 8.20: Verification of the effects on the VHE spectrum determination from 2011 observations of 1ES 0806+524 by different unfolding algorithms. The unfolded spectrum (gray and black points) obtained with the Tikhonov algorithm is illustrated. The blue–dashed band represents the spectral spread due to different unfolding algorithms leading to a spread in the flux uncertainty towards higher energies.

2012

For the study of the differential VHE γ–ray flux observed in 2012 from 1ES 1011+496 the logarithmic energy binning has been set to 28 between 5 GeV to 50 TeV. The `fluxlc` executable has been applied to the individual subsamples of the 2012 data sample and the appropriate MC data respectively. In a final step, the determined differential fluxes have been stacked to one sample for the application of the unfolding.

The energy dependent cuts in θ^2 and `hadronness` of the relevant energy bins are summarized in Table 8.15. Being derived from the different MC simulations used for the individual periods the cuts differ slightly among the individual subsamples.

Mean energy [GeV]	θ^2 cut [deg^2]			`hadronness` cut		
	VII a	VII b	VII c	VII a	VII b	VII c
115	0.02	0.035	0.045	0.43	0.43	0.42
160	0.02	0.03	0.035	0.41	0.41	0.31
223	0.02	0.03	0.025	0.42	0.41	0.32
309	0.02	0.02	0.02	0.38	0.38	0.31
430	0.02	0.02	0.02	0.40	0.46	0.27

Table 8.15: Summary of the energy dependent cuts for the reconstruction of the differential spectrum of 1ES 1011+496 from 2012 observations. The θ^2 and `hadronness` cut are reported derived from MC simulations of γ–like events. A cut efficiency of 70 and

The significance of the excess events found in the respective energy bin for each subsample are summarized in Table 8.16. During the observation periods which yield a detection of 1ES 1011+496 , namely VII a and VII c, a significant signal extends from ∼100 to 300 GeV. The data from period VII b indicate only a hint of signal due to the short time of observations which is reflected in the lower significances of the excess events found in the individual energy bins of the differential spectrum. In particular, the more significant signal is concentrated at energies between ∼150 to 250 GeV.

Mean energy [GeV]	Significance σ		
	VII a	VII b	VII c
115	2.5	1.6	4.6
160	3.0	2.3	5.0
223	3.6	3.3	4.7
309	4.1	1.8	3.8
430	2.0	1.1	1.2

Table 8.16: Compilation of the spectral significance of the differential flux observed from 1ES 1011+496 in 2012. The spectral significance is reported for the individual subsamples of the 2012 data set. The values reported correspond to the differential flux before unfolding.

A comparison of the differential fluxes derived from the data of the subsamples is listed in Table 8.17. Although agreeing within the statistical errors, the differential flux levels determined in the individual energy bins show rather large variations probably due to missing statistics.

Mean energy [GeV]	F [$\mathrm{cm^{-2}\,s^{-1}\,TeV^{-1}}$]		
	VII a	VII b	VII c
115	$(1.8 \pm 0.8)\times10^{-9}$	$(0.7 \pm 0.4)\times10^{-9}$	$(1.1 \pm 0.3)\times10^{-9}$
160	$(5.2 \pm 1.9)\times10^{-10}$	$(2.2 \pm 1.0)\times10^{-10}$	$(3.3 \pm 0.7)\times10^{-10}$
223	$(2.2 \pm 0.7)\times10^{-10}$	$(1.3 \pm 0.4)\times10^{-11}$	$(9.9 \pm 0.2)\times10^{-10}$
309	$(1.3 \pm 0.4)\times10^{-11}$	$(2.6 \pm 1.4)\times10^{-11}$	$(2.8 \pm 0.7)\times10^{-11}$
430	$(1.5 \pm 0.8)\times10^{-11}$	$(0.8 \pm 0.7)\times10^{-11}$	$(0.4 \pm 0.3)\times10^{-11}$

Table 8.17: Differential flux of 2012 data from 1ES 1011+496 observations before unfolding. The mean energy of the bin (first column) and the respective differential flux are listed for the individual subsamples (column two to four).

The stacked VHE differential spectrum unfolded with the Tikonov method is plotted together with the deabsorbed spectrum of 1ES 1011+496 in Figure 8.21. Despite the small errors of the individual differential VHE γ–ray fluxes computed between ∼100 and 400 GeV, the hypothesis of a simple power law, parametrized by a flux normalization f_0 at 200 GeV of $(1.5 \pm 0.2_{\mathrm{stat}} \pm 0.3_{\mathrm{sys}})\times10^{-11}\,\mathrm{cm^{-2}\,TeV^{-1}}$ and a spectral slope Γ of $-3.2 \pm 0.3_{\mathrm{stat}} \pm 0.2_{\mathrm{sys}}$, is given by a probability of 47% ($\chi^2/\mathrm{NDF} = 0.51/1$).

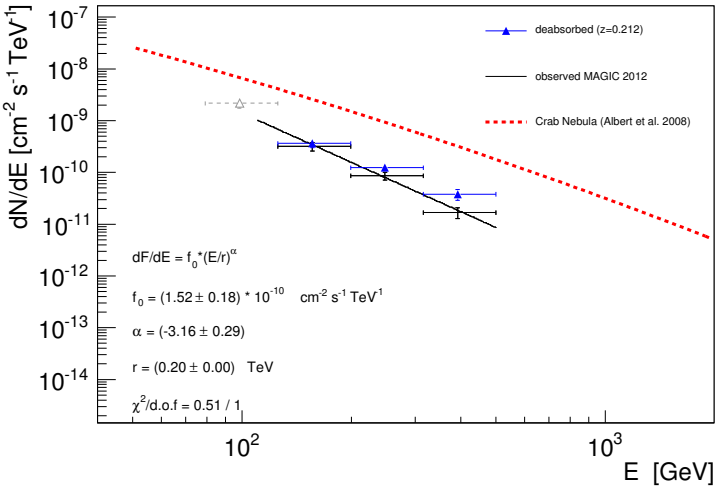

Figure 8.21: Unfolded VHE differential spectrum of 1ES 1011+496 observed in 2012. The black triangles correspond to the measured spectrum fitted by a simple power law (solid black line) whose parameters are indicated in the inlet in the bottom left corner; the gray triangle indicates the differential flux measured slightly below the energy threshold of the analysis; the blue filled triangles are corrected for EBL attenuation using the model by [103]. For comparison the Crab Nebula spectrum (red dashed line) is plotted [30].

Being too close to the analysis threshold, the first spectral point is probably overestimated, while the differential flux at highest energies is apparently underestimated. The latter case is most likely related to a rather low number of excess events. In fact, the spectral significance of the differential flux reconstructed at these energies from the individual subsamples of 2012 data is clearly lower with respect to the signal observed at lower energies (see Table 8.16)

In the case of the deabsorbed VHE source spectrum, the probability of the

Mean energy [GeV]	F [$\mathrm{cm^{-2}\,s^{-1}\,TeV^{-1}}$]
99	$(2.2 \pm 0.4)\times10^{-9}$
156	$(3.2 \pm 0.6)\times10^{-10}$
247	$(8.6 \pm 1.5)\times10^{-11}$
392	$(1.7 \pm 0.4)\times10^{-11}$

Table 8.18: Differential flux of the unfolded VHE γ–ray spectrum of 1ES 1011+496 observed in 2012.

hypothesis of a simple power law corresponds to 83% (χ^2/NDF = 0.05/1) yielding an intrinsic spectral slope of -2.4 $\pm$ 0.3_{stat} and a normalized flux f_0 of $(2.0 \pm 0.2_{\mathrm{stat}})\times10^{-10}\,\mathrm{cm^{-2}\,TeV^{-1}}$.

The study of the systematics on the differential flux determination from 2011 observations related to different unfolding algorithms indicates a very robust result as illustrated in Figure 8.22.

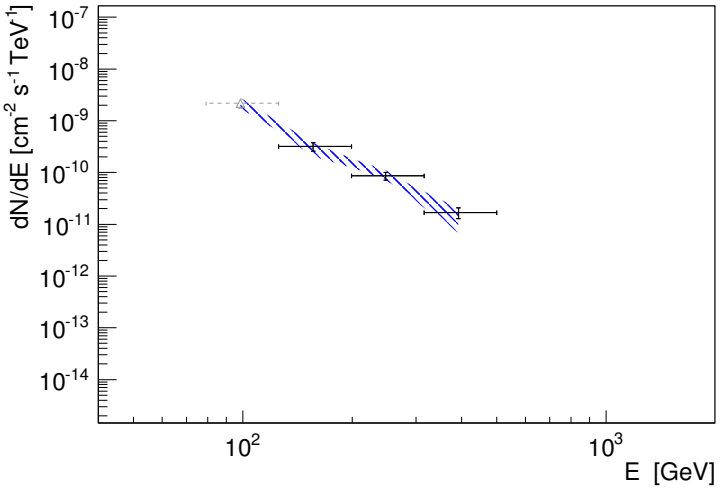

Figure 8.22: Verification of the effects on the VHE spectrum determination from 2012 observations of 1ES 0806+524 by different unfolding algorithms. The unfolded spectrum (black points) obtained with the Tikhonov algorithm is illustrated. The blue–dashed band represents the marginal spectral spread due to different unfolding algorithms.

Similar

Comparison of the Differential Flux of 1ES 1011+496 from Four Years of MAGIC Observations

In Table 8.19 the parameters of simple power law fit to the individual VHE γ–ray spectra of 1ES 1011+496, presented in Figure 8.23, that have been observed in mono and stereoscopic mode from 2007 to 2012 are listed together with the intrinsic spectral slope of the deabsorbed spectra when available. Thanks to the compatible energy range in which the power law fit has been applied as well as the common flux normalization at 200 GeV, the comparison of the fit parameters is straight forward.

Due to the rather large statistical error, the spectral slopes obtained from the fits of the different observations are compatible. Therefore, no clear conclusion on the trend of a spectral hardening [272] can be drawn although in particular the observations from 2008, 2011 and 2012 show a very consistent result with respect to the spectral index. By contrast, the normalized flux of all observations show

Year	Energy range [GeV]	$f_{0\,\mathrm{obs}}$ [$\mathrm{cm^{-2}\,s^{-1}\,TeV^{-1}}$]	Γ_{obs}
2007[a]	∼120 - 750	$(2.0 \pm 0.1_{\mathrm{stat}} \pm 1.5_{\mathrm{sys}})\times10^{-10}$	$-4.0 \pm 0.5_{\mathrm{stat}} \pm 0.2_{\mathrm{sys}}$
2008[b]	∼120 - 500	$(1.6 \pm 0.1_{\mathrm{stat}})\times10^{-10}$	$-3.2 \pm 0.6_{\mathrm{stat}}$
2011	∼100 - 700	$(0.8 \pm 0.3_{\mathrm{stat}} \pm 0.2_{\mathrm{sys}})\times10^{-10}$	$-3.3 \pm 0.6_{\mathrm{stat}} \pm 0.2_{\mathrm{sys}}$
2012	∼100 - 400	$(1.5 \pm 0.2_{\mathrm{stat}} \pm 0.3_{\mathrm{sys}})\times10^{-10}$	$-3.2 \pm 0.3_{\mathrm{stat}} \pm 0.2_{\mathrm{sys}}$

Table 8.19: Compilation of the VHE γ–ray spectrum of 1ES 1011+496 observed from 2007 to 2012 by MAGIC. The year of observation and the observed energy range are reported in the first two columns. The flux normalized at 200 GeV and the spectral slope of the simple power law fit to the observed spectra are listed in the third and fourth column.The archival data have been taken from: [a] [22] and [b] [272].

larger discrepancies. While in 2007, the flux normalization indicates a higher flux, in 2011 the flux seems to be clearly lower. However, the results on the differential flux are consistent within the systematic errors indicating a rather constant VHE γ–ray emission. The highest flux observed in 2011 is consistent with the upper limit published in [22].

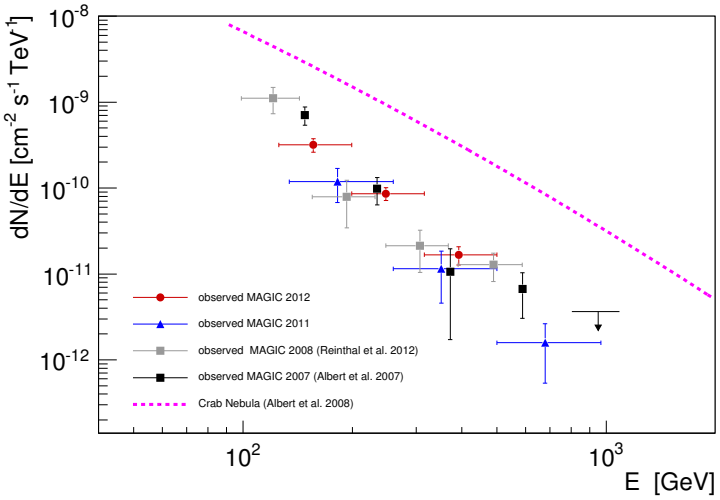

Figure 8.23: Observed differential fluxes from four years of VHE γ–ray observations of 1ES 1011+496 with MAGIC. Observations from 2011 and 2012 are marked with blue triangles and red circles respectively. The differential spectra from [22] and [272] are indicated with black and gray circles. Differential upper limits are represented as arrows. No EBL correction os applied to these data.

Despite the different EBL models [185, 103] used for the reconstruction of the deabsorbed spectrum, the individual intrinsic spectral slopes show consistency within the statistical errors (see Table 8.20).

8.6 1ES 1011+496: Complementary Multiwavelength Observations

Different MWL coverage has been provided during the VHE γ–ray observations carried out in 2011 and 2012 to provide a simultaneous mutlifrequency picture of

[67] No EBL correction has been applied to the differential spectrum observed in 2008.

Year	Γ_{intr}
2007	-3.3 $\pm$ 0.7[a]
2011	-2.3 $\pm$ 0.8$_{\mathrm{stat}}$ [b]
2012	-2.4 $\pm$ 0.3$_{\mathrm{stat}}$ [b]

Table 8.20: Comparison of the intrinsic spectral slope of 1ES 1011+496. The EBL models of [a] [185] and [b] [103] have been used for reconstruction the deabsorbed spectra[67]

1ES 1011+496. In particular, in 2012 a MWL campaign has been coordinated including additional optical polarimetry data allowing a detailed study of the SED.

2011

Simultaneous data to the MAGIC VHE γ–ray observations have been collected by *Fermi* in HE γ–rays as well as by the KVA and OVRO telescopes in the optical R band and the radio band respectively (see Figure 8.24). The individual light curves are daily binned except the HE light curve where a seven day binning has been applied. Unfortunately, no simultaneous *Swift* observation were available for a complete MWL coverage in 2011.

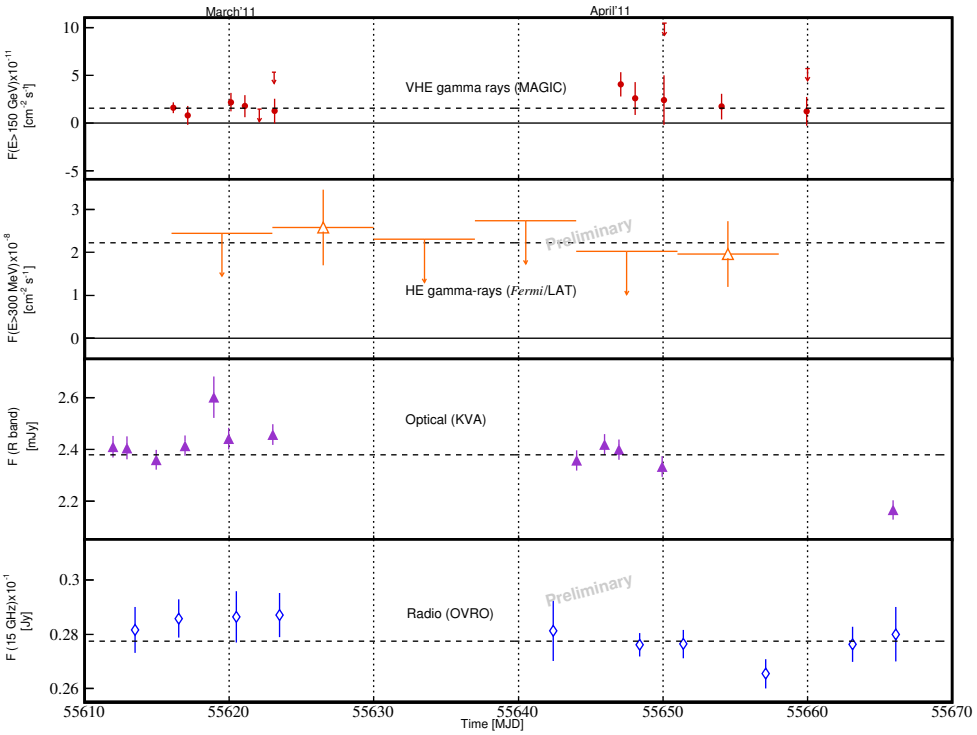

Figure 8.24: MWL light curve of 1ES 1011+496. From top to bottom: The MWL coverage from the end of February to the beginning of April 2011 in VHE γ–rays (red circles) and HE γ–rays (orange triangles) by MAGIC and by *Fermi*, in the R band (violet triangles) by the KVA telescope, and in the radio band (blue diamonds) the OVRO telescope. Upper limits of 95% confidence level are indicated by down–ward arrows. No host galaxy correction has been performed on the optical data. The individual light curves are daily binned expect in HE γ–rays, where a 7–day binning was applied.

The VHE light curve seems to indicate a rather constant emission, the hypoth-

esis of constant flux at $(1.8 \pm 0.3_{\rm stat} \pm 0.2_{\rm sys}) \times 10^{-11}\,{\rm cm}^{-2}\,{\rm s}^{-1}$ shows a rather low probability of 84% (see Section 8.4). The flux level in HE γ–rays which corresponds to $(2.2 \pm 0.6_{\rm stat}) \times 10^{-8}\,{\rm cm}^{-2}\,{\rm s}^{-1}$ yields a probability of 60% (χ^2/NDF = 0.28/1) to be constant. The optical flux features modest variability in the R band during the observation window of MAGIC. However, a clear variability with respect to the mean flux level of $(2.38 \pm 0.01_{\rm stat})$ mJy in this waveband is observed. With respect to the quiescent state as defined in [271], 1ES 1011+496 appears rather active in this energy regime. However, no clear optical flare has been observed during this period. Compared to measurements during the previous MWL observations in 2007 and 2008, the optical flux is clearly lower (see Figure 8.25).

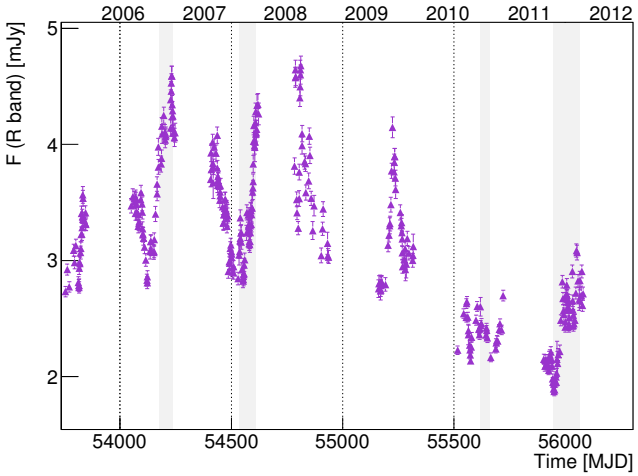

Figure 8.25: Long–term light curve of 1ES 1011+496 in the optical R band monitored by the KVA telescope centered on the individual MAGIC observations. The individual MAGIC observation windows are indicated by the gray shaded bands.

In fact, 2011 observations were not triggered by an optical flare. fFinally, the radio flux is constant with a probability of 90% (χ^2/NDF = 3.45/8) at a level of $(0.277 \pm 0.002_{\rm stat})$ Jy. The mean flux levels are summarized in Table 8.21

Waveband	Mean flux level	Constant flux probability [%]
VHE (E > 150 GeV)	$(1.8 \pm 0.3) \times 10^{-11}\,{\rm cm}^{-2}\,{\rm s}^{-1}$	84
HE (E > 300 MeV)	$(2.2 \pm 0.6) \times 10^{-8}\,{\rm cm}^{-2}\,{\rm s}^{-1}$	60
Optical (R band)	(2.38 ± 0.01) mJy	> 0.01
Radio (15 GHz)	(0.277 ± 0.002) Jy	90

Table 8.21: Compilation of the mean flux levels of 1ES 1011+496 from 2011 MWL observations. From left to right: The waveband (first two columns) and the mean flux (second column) assuming a constant emission are reported. In column three the probability of a constant flux hypothesis excluding upper limits is stated.

2012

Thanks to the coordination of multifrequency observation on 1ES 1011+496, the VHE γ–ray data collected by MAGIC in 2012 are complemented in all wavebands by simultaneous data necessary to constrain the low and high energy peak of the SED. In Figure 8.26 the individual light curves are presented. Beside X-ray data, additional data in the UV and optical V and B bands are provided by *Swift*. Additional to the OVRO data measured at 15 GHz, radio data at 37 GHz have been collected by the 14 m diameter *Metsähovi Radio Telescope* [311].

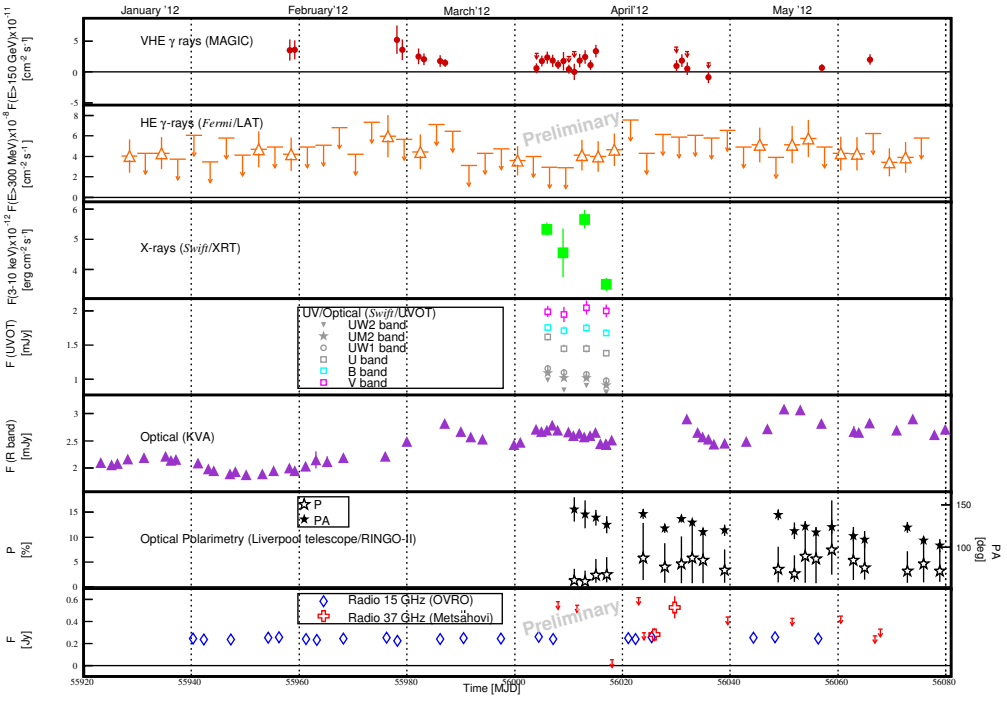

Figure 8.26: MWL light curve of 1ES 1011+496. From top to bottom: The MWL coverage from January to the end of May 2012 is provided in VHE γ–rays by MAGIC (red circles), in HE γ–rays by *Fermi* (orange triangles), in X-rays by (green squares) *Swift*/XRT, and UV (gray data points) as well as V and B band (cyan and pink squares) data provided by *Swift*/XRT. Measurements in the R band are carried out by the KVA telescope (violet triangles). No host galaxy correction has been performed on the optical data. The optical data are combined with optical polarimetry measurements of the Liverpool telescope/ Ringo II (polarization degree and position angle are marked as blank and filled stars respectively). The radio coverage is provided by the OVRO telescope (blue diamonds) and the Methsähovi Radio Observatory (red crosses). Upper limits of 95% confidence level are indicated by downward arrows. The individual light curves are daily binned expect in HE γ–rays, where a 3–day binning was applied.

Furthermore, the Liverpool Telescope has collected polarimetric data in the optical regime in order to put further constraints on the site and structure of the VHE γ–ray emission location. In particular, the study of the *polarization* (P) represent a powerful tool to distinguish between the competing physical models regarding the particle and photon populations responsible for the VHE emission from blazars [47]. Moreover, the study of the *position angle* (PA) can provide information on the intensity and orientation of the magnetic field of the emitting region. Most likely, a change in optical polarization can be associated with γ–ray flares in blazars [4]. The data were taken with the fast readout imaging

polarimeter *RINGO* 2 [301]. The polarimeter uses a rotating polaroid with a frequency of ∼1 Hz that takes eight exposures of the source during a cycle. To determine the degree and angle of polarization, these exposures are synchronized with the phase of the polaroid.

All light curves are daily binned except in HE γ–rays, where a three day binning was applied.

In Table 8.22 the individual mean fluxes as well as the probability of a constant flux hypothesis are reported. Beside the rather constant VHE γ–ray emission, the *Fermi* data yield a very constant flux level which doubled with respect to the flux level observed in 2011.

Compared to previous observations in X-rays by *Swift*/XRT [272], the mean flux level is by a factor of four to six lower. In addition, the flux observed in 2012 exhibits some variability. Nevertheless, no significant flux increase was found.

The flux measured with *Swift*/UVOT seems to be rather constant in the V and B bands whereas a slight decrease seems to be present in the UV bands towards April. The mean flux levels of $(15{,}65 \pm 0.01)$ mag, $(15{,}83 \pm 0.01)$ mag and $(14{,}98 \pm 0.04)$ mag observed in the V, B and U band respectively are compatible with previous multiband (UBVRI) observations performed by the McGraw–Hill Telescope [69]. Compared to the measurements performed in the V and B band in 2008, the mean fluxes are slightly lower [272].

In 2012, the optical flux in the R band is highly variable. A smooth increase from a flux level comparable with the quiescent state of 1ES 1011+496 is observed reaching a maximum of ∼3 mJy at the beginning of May followed by an unstable flux at a level of ∼2.5 mJy, compatible with the flux observed in 2011.

Waveband		Mean flux level	Constant flux probability [%]
VHE (E > 150 GeV)		$(1.4 \pm 0.2) \times 10^{-11}$ cm^{-2} s^{-1}	31
HE (E > 300 MeV)		$(4.5 \pm 0.5) \times 10^{-8}$ cm^{-2} s^{-1}	100
X-ray (3 - 10 keV)		$(4.7 \pm 0.1) \times 10^{-12}$ erg cm^{-2} s^{-1}	> 0.01
UV	UW2	(0.86 ± 0.01) mJy	> 0.01
	UM2	(1.07 ± 0.02) mJy	4
	UW1	(1.07 ± 0.02) mJy	> 0.01
	U	(1.47 ± 0.03) mJy	0.7
Optical	B	(1.72 ± 0.03) mJy	69
	V	(2.0 ± 0.05) mJy	93
	R	(2.533 ± 0.007) mJy	> 0.01
Radio	37 GHz	(0.35 ± 0.05) Jy	3
	15 GHz	(0.246 ± 0.001) Jy	> 0.01

Table 8.22: Compilation of the mean flux levels of 1ES 1011+496 from the 2012 MWL campaign. From left to right: The waveband (first two columns) and the mean flux (second column) assuming a constant emission are reported. In column three the probability of a constant flux hypothesis excluding upper limits is stated.

By eye, the radio flux at 15 GHz seems to be constant at a level slightly lower than in 2011. Observations at 37 GHz seem to yield a slightly higher mean flux

level.

Throughout the second half of the 2012 MWL campaign, the degree of optical polarization is very low with a mean value of (2.5 ± 0.6)%. Due to the rather larger errors, no clear conclusions can be drawn on variability of the polarization. Usually, such low degree of polarization indicates a low ordering of the magnetic field of the source. The position angle has a general trend to decrease from ∼150 to 100°. However, no strong signature of shocks was found in the data.

8.7 The SED Modeling of 1ES 1011+496

Due to variability in the R band, the missing simultaneous X-ray coverage in 2011 and the higher HE γ–ray flux in 2012, the simultaneous SEDs of 2011 and 2012 multifrequency observations are modeled separately. As no significant flares of 1ES 1011+496 in the individual wavelength regimes during 2011 and 2012 was observed, the data from both years have been separately averaged where applicable even if, in some cases, variability was found.

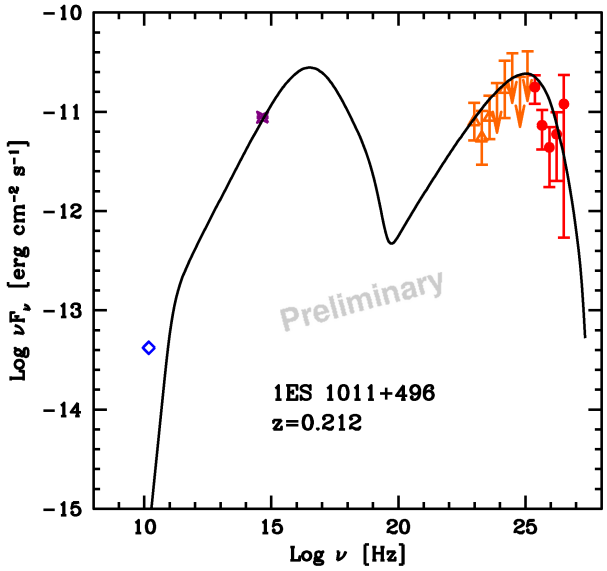

Figure 8.27: Spectral energy distributions of simultaneous MWL observations of the 1ES 1011+496 carried out in 2011. The MAGIC VHE γ–ray data (red circles) are corrected for EBL absorption according to [103]. The HE γ–rays spectrum from *Fermi*-LAT is marked with orange triangles. At higher energies upper limits (orange arrows) of 95% confidence level have been derived. Optical data in the R band from KVA (violet triangle) and radio data at 15 GHz provided by the OVRO (blue diamond) are presented. The R band are corrected for the host galaxy contribution [240].

The VHE data have been corrected for EBL absorption according to [103] and host galaxy contributions of (0.49 ± 0.02) mJy [240]) have been applied to the optical R band data respectively. The *Swift*/UVOT data from 2012 were corrected for galactic extinction [119].

Due to the missing coverage in X-rays in 2011, the synchrotron bump is rather poorly constrained (see Figure 8.27). In addition, the rather short time window for simultaneous observations leads to a rather limited determination of the HE and VHE spectra. However, the simultaneous data by MAGIC and *Fermi* data provide a good coverage of the high energy bump.

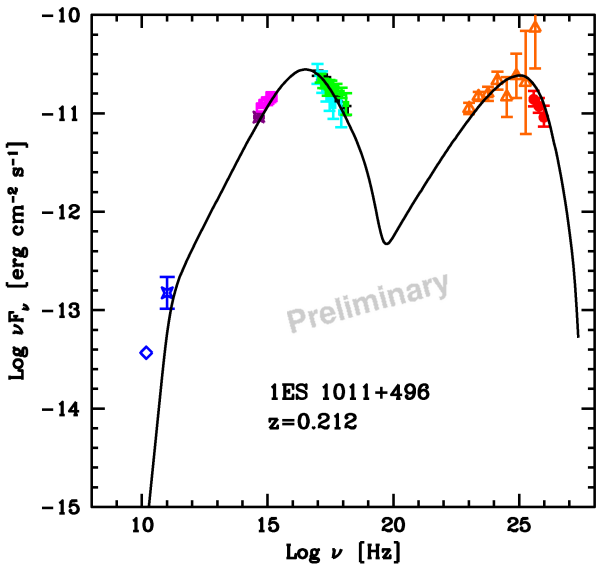

Figure 8.28: Spectral energy distributions of simultaneous MWL observations of the 1ES 1011+496 carried out in 2012. The MAGIC VHE γ–ray data (red circles) are corrected for EBL absorption according to [103]. The HE γ–rays spectrum from *Fermi*-LAT is marked with orange triangles, while *Swift*/XRT X-ray data are plotted as green, cyan and black squares. Corrections for galactic extinction [119] have been applied to the UVOT data (magenta squares) from *Swift*. Optical data in the R band from KVA (violet triangle) are corrected for the host galaxy contribution [240]. Radio data at 15 GHz (blue diamond) and 37 GHz (blue star) provided by the OVRO and Metsähovi telescopes are presented.

Compared to the SED of 2011, the extended MWL campaign in 2012 yields a very detailed coverage of the SED. Especially the high energy bump is well constrained thanks to a connection of the MAGIC and *Fermi* data for the first time for this source. This detailed coverage locates the peak frequency of the high energy bump at $\sim$40 GeV.

None of the SEDs indicate the previous hypothesis of dominance of one radiation component over the other [22, 272]. This previous assumption is likely related to the absence of complementary MWL data, wherefore both peaks were sparely constrained. Indeed, the luminosity of both the low energy bump corresponds to $\sim 2.5 \times 10^{-11}\,\mathrm{erg\,cm^{-2}\,s^{-1}}$.

A one–zone SSC model (see Section 6.1.7) has been applied to reproduce the multifrequency observations. In Table 8.23 a compilation of the model parameters used to reproduce the individual MWL observations is presented.

Except for the rather low minimum Lorentz factor, the physical parameters used in the model are similar to those typically inferred for other HBL objects (see e.g. [309]). The comparison to previous models of the 1ES 1011+496 SED indicates a good agreement for most of the parameters. Only the minimum and maximum Lorentz factor show large variations. However these parameters are usually not well constrained and thus acceptable as long as they are not too high or low respectively. In fact, a too high minimum Lorentz factor causes a narrowing of the two bumps [175]. In particular, the parameters reproduced from the 2008 modeling are in good agreement. Most likely, variations among the individual parameters are rather related to the previously poor MWL coverage than to important variations of the physical processes presented in 1ES 0806+524.

SSC input & output Parameter		Year 2007	2008	2011 & 2012
$\gamma_{\rm min}$		3.0×10^3	1.0	10
$\gamma_{\rm b}$	$[10^4]$	5.0	4.0	6.0
$\gamma_{\rm max}$	$[10^5]$	200	6.0	10
n_1		2.0	2.0	2.0
n_2		5.0	4.1	4.1
B	[G]	0.15	0.19	0.10
K	$[10^3\,{\rm cm}^{-3}]$	20	6.6	10
R	$[10^{16}\,{\rm cm}]$	1.0	1.0	0.8
δ		20	25	30

Table 8.23: Compilation of the input and output parameters of the one–zone SSC model applied to the individual SEDs from MWL observations of 1ES 1011+496 . Input model parameters (first column) for modeling the individual SEDs obtained during four years of MWL observations (column two to four[67]). From top to bottom: the minimum, break and maximum Lorentz factors are reported in the first three rows, the low and high energy slope of the electron energy distribution, the magnetic field intensity, the electron density, the radius of the emitting region and its Doppler factor are listed from row four to nine.

8.8 1ES 1011+496: Conclusions

In comparison to mono observations carried out by MAGIC, the upgraded stereoscopic system resulted in a hint of signal in almost half of observation time in 2011. Moreover, in 2012 almost the same effective time of stereo observations lead to a strong detection of 1ES 1011+496 confirming the importance of stereoscopic IACT systems.

Regarding the temporal analysis, the data samples from both years lead to the conclusion that 1ES 1011+496 seems indeed to be a rather stable VHE γ–ray emitter at a flux level of $\sim$4 to 6 % of the Crab Nebula flux above 150 GeV, which is compatible with previous measurements performed by MAGIC.

The differential spectra measured in 2011 and 2012 are in good agreement with a simple power law with a spectral index of $\sim$-3.3. These results are in good agreement with observations from 2008, while the spectrum measured during the source discovery seems to be much softer with a spectral index of $\sim$-4. However, due to the rather large statistical errors related to the spectral index, no clear conclusion can be drawn on the hypothesis of a spectral hardening. Although the extended observations from 2012 allowed for a detailed measurement of the differential flux of 1ES 1011+496 , the spectrum could not be extended towards higher energies. Therefore, the achievement of further constraints on the EBL from these observations seems to be rather unlikely.

For both years, complementary MWL observations have been collected for 1ES 1011+496. In HE γ–rays the source seems to feature a pretty stable emission. Nevertheless, a doubling of the mean flux level from 2011 to 2012 has been observed. Instead, the source seems to be confirmed to be highly variable in X-rays. In the adjacent U bands no weak for variability was found in 2012. Clearly, the emission of 1ES 1011+496 in the optical R band showed variability during both years, while observations from 2012 in the V and B bands indicate a constant

[67] For MWL observations carried out in 2007 and 2008 The model parameters have been taken from the [22] and [272].

emission. The radio emission seems to be rather constant during both years. The optical polarimetric data indicate a rather low ordering of the magnetic field of 1ES 1011+496 during 2012. To summarize, 1ES 1011+496 seems to have been in a rather quiescent state in all observed wavebands during 2011 and 2012. Given the extended time window of the MWL campaign in 2012, detailed correlation studies could be performed.

From the simultaneous MWL observations from 2011 and 2012, two individual SEDs have been derived. In particular the extended MWL campaign in 2012 yielded for the first time a detailed coverage of both the low and high energy peak. More important, a coupling of the MAGIC data with *Fermi* observations has been achieved. Apparently, this detailed SED disfavors the previously assumed scenarii of the dominance of one radiation component over the other.In addition, the rough position of the IC peak frequency seems to be located at $\sim$40 GeV.

Given the likely constant emission of 1ES 1011+496 in HE/VHE γ–rays and the detailed IC peak coverage obtained from simultaneous observations from 2012, these data can be used to probe the method to constrain the blazar distance from the EBL imprint 6.2.6.

9
Conclusions and Outlook

This PhD thesis was divided into a technical and a scientific research activity both carried out as a member of the MAGIC collaboration and the CTA consortium. While the former research was addressed to the design of a hardware component suitable for CTA, a future ground based VHE γ–ray detector, the latter was carried out in the field of extragalactic VHE γ–ray astrophysics.

In the case of the technical research activity, the aim was to develop a new cost efficient composite mirror of high optical performance suited for the MST and LST of CTA. The development and design status of such mirrors was reported. The principle of the replication of such composite mirrors from a spherical shape mold of high precision in a two step process was outlined. The mirror assembly was kept similar to that used for MAGIC applying some modifications to the reflective surface. Several solutions concerning the realization of a cost efficient and high reflective surface were outlined. Beside the conservative technique of an aluminized thin glass sheet, industrial products as alternative solutions like high reflective foils were presented. The first prototypes were produced with the dimensions of the MAGIC I mirrors, testing different glues for the assembling as well as various solutions with respect to the optimum reflective layer deposition. The optical test bench setup designed for the verification of the optical performance of such IACT mirrors was presented. A brief description of the principal measurement procedure with such $2f$–setup was given outlining the main analysis steps of the software tool developed for the D_{80} calculation. The results of the PSF study performed for the first small sized prototypes with different reflective layers were reported. The analysis revealed that the focusing power of these first prototypes is insufficient with respect to the CTA specifications, demanding an optimization of the production technique. In particular the prototype on which the reflective foil was deposited featured a rather poor focussing power. To meet the CTA specifications, an improvement of the optical performance by at least a factor of three is necessary. In order to achieve such improvement, some possibilities regarding the modification of the mirror substrate design were presented.
As member of the CTA consortium, a cross calibration campaign of the measurement equipment used by different institutes for the qualification of the optical performance of IACT mirrors has been conducted. Several European test facilities participated in this campaign for which three IACT mirrors of different characteristics and dimensions were circulated among the institutes. The optical

qualification included the PSF determination as well as the measurement of the reflectance when possible. Generally, either a $2f$–setup or the MPD method in combination with ray–tracing were used to test the PSF.
Given the importance of a reliable PSF determination, a detailed comparative study was performed inspecting carefully the testing procedure. In such way, discrepancies among the test results were traced back to some crucial testing circumstances. In particular the mirror installation in the test setup significantly affected the PSF due to distortions of the mirror surface. Another important factor was related to the the alignment of the mirror with respect to the light sensor used for the study of the PSF, parametrized by the D_{80}. Finally, the flatness of the background played a key role in the correctness of the D_{80} calculation.
After the adaption of the ray–tracing parameters, the D_{80} determined with the PMD method was consistent with the results obtained with the $2f$–setup.
The comparison of the results included a cross analysis of the data in order to trace back potential errors regarding the PSF determination related to the analysis software. It was found that the definition of the focal spot center had a major impact on the calculation of the D_{80}. The correctness of the functionality of the software tools was tested by comparing the analysis results with those retrieved with an astronomical standard analysis software. A characterization of the individual light detectors as well as the implementation of the temperature monitoring in the test setup was recommended.
The tests of the local spectral reflectance on the mirror surface showed a good agreement. Where comparable, the tests of the absolute spectral reflectance in the focal spot yielded compatible results.
In the following month, the production of further small sized is foreseen to optimize the replica technique. This tuning will be conducted for the different reflective layer solutions. Once, an acceptable optical performance is achieved, the prototyping will be extended to mirrors with MST and LST dimensions. The material and the molds for the production of such large size mirrors is already available. As for the optical test bench, some modifications and upgrades are foreseen to automate the remote control of parts of test equipment and to allow the spectral behavior of the PSF.

Regarding the scientific research activity, the detailed study of the VHE γ–ray emission of the two TeV blazars 1ES 0806+524 and 1ES 1011+496 observed with MAGIC was discussed. The observations were carried out with the upgraded stereoscopic system of MAGIC with the purpose of an accurate measure of the source spectra over a large energy range. In the case of 1ES 0806+524 , the observations carried out in 2011 were triggered by a high state of the source in the optical regime which lead to the detection of a VHE γ–ray flare. The MAGIC source 1ES 1011+496 observed in 2010 and in 2012, right after the upgrade of the MAGIC readout system.
For each source the differential energy spectrum and the temporal evolution of the integral flux detected were analyzed. 1ES 0806+524 revealed a short–term variability at a daily time scale 1ES 1011+496 exhibited a pretty constant emission in this energy band. The differential spectra of both sources were well described by a simple power law. The spectral slope of the high and low state spectrum of 1ES 0806+524 was found to be -3.1 and -2.7 respectively. Both indices were consistent within the errors. In the case of 1ES 1011+496, the spectral slope of both observed source spectra was $\sim$-3. Thus, with a spectral index larger than -2 the differential spectra of 1ES 0806+524 and 1ES 1011+496 appeared rather soft. During the outburst of 1ES 0806+524 in VHE γ–rays, a hint of a hardening of the differential spectrum was observed. For both sources the determination

of the differential spectra has been significantly improved with respect to the results derived from previous VHE γ–ray observations. Especially in the case of 1ES 0806+524 , the source spectrum has been measured up to TeV energies during the source flare with improved precision.
For each source, the results obtained have been combined with simultaneous observations carried out in other wavebands from optical to HE γ–rays. Beside the MWL coverage from radio to γ–rays, first complementary optical polarimetry data have been collected for 1ES 1011+496. Regarding 1ES 0806+524, the temporal analysis of the MWL light curve yielded a hint for correlation between the optical regime and VHE γ–rays. However, the rather short simultaneous coverage and the sparse monitoring in some wavebands prevented a more detailed study of the correlation. Beside its clear variability in the optical R band, 1ES 1011+496 showed only modest if any variability in the other energy ranges covered. In 2011, the window of simultaneous observations is too narrow and the MWL coverage too poor to carry out dedicated correlation studies. Instead, the coordinated MWL campaign in 2012 on this source would favor a study of correlations. Regarding the polarimetric data collected in the optical regime, the detailed interpretation is ongoing. The preliminary analysis indicated a very low degree of polarization associated with a low ordering of the magnetic field of the source. Moreover, the data did not contain any strong signature of shocks.
Finally, the SEDs of both sources were built by means of simultaneous and quasi simultaneous MWL data. In particular the emission in γ–rays of both sources was covered by simultaneous observations in the HE and VHE range for the first time. Both sources showed a clear two bump structure which is in agreement with current blazar emission models. In the case of 1ES 0806+524, the data set was split into a high and low state sample, while the data collected for 1ES 1011+496 during 2011 and 2012 were treated separately. A one–zone SSC model was applied to reproduce the individual SEDs and to derive the main physical parameters governing the emission in the blazar jet. A mild dominance of the radiation from the high energy bump over the synchrotron emission was found for 1ES 0806+524 during the high state, while the opposite case is present its low state. Being a rather faint source, the SED was moderately constrained, especially due to the subdivision of the data. A coordinated MWL campaign of extended time coverage would be necessary to put furthers constraints on the two emission bumps of the SED. Beside the detailed coverage of the SED of 1ES 1011+496 thanks to the coordinated MWL campaign in 2012, a connection between the HE and VHE γ–ray components was achieved providing a particularly detailed coverage of the high energy bump. This allowed the rough position of the peak frequency which is approximately at 40 GeV. These observations clearly rule out the previous hypothesis of a dominant radiation component.

As an outlook, the detailed VHE source spectra presented in this work can be used to probe the recently developed technique to set constraints on the redshift of TeV blazars from the EBL imprint on the VHE γ–ray emission. Since many new TeV sources have an unknown or uncertain redshift, this technique is of particular interest for current VHE γ–rays astrophysics. Despite the large test sample on which the technique has been already tested successfully, there are still several vaguely determined sources of uncertainties such as the impact of the variability of VHE γ–ray emitters. By increasing the test statistics to a large collection of such observations combined with HE γ–ray data, the hypothesis to use AGNs as standard candles can be probed with high certainty. In addition, as this method implies the assumption of a certain EBL model, the validity of such model can be verified.

APPENDIXES

A

MAGIC Data Analysis of 1ES 0806+524 and 1ES 1011+496: Additional Material

In this appendix, additional material to Chapter 7 and 8 is presented. In particular, the rate distributions after image cleaning of 2011 and 2012 data of the sources 1ES 0806+524 and 1ES 1011+496 before quality selection are presented, along with information on the weather conditions during data taking in terms of `humidity`, `cloudiness` and `moon light`. In the case of 1ES 1011+496 , the analysis plots of the individual subsamples of 2012 data are shown.

A.1 Details on the 1ES 0806+524 Data Analysis

1ES 1011+496 observation have been carried out in 2011 on 13 different nights from the beginning of January to the beginning of March. The rate distribution after the image cleaning, plotted in Figure A.1, shows that during several observation nights the mean rate is alternating. In particular one night shows a pretty unstable rate. Therefore, data exhibiting no stable mean rate have been excluded from the successive analysis.

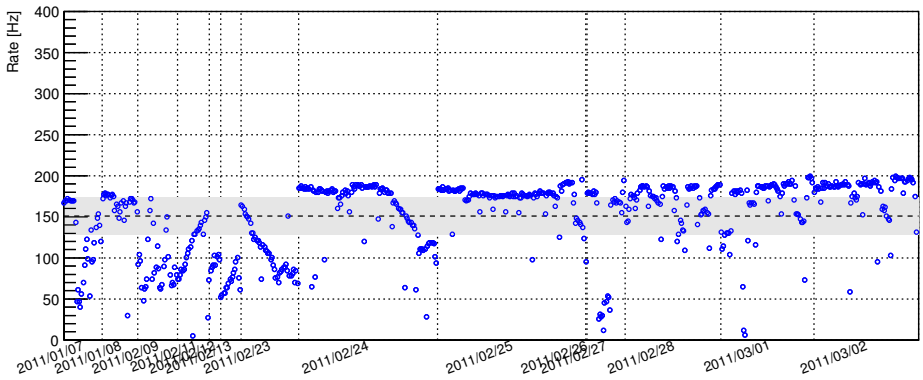

Figure A.1: Event rate distribution after image cleaning of the 2011 data of 1ES 0806+524. Discontinuous drops in the event rate are either due to alternations of the wobble position or due to unstable data taking conditions. The mean flux (dashed horizontal line) and 10% variation form this value (gray band) are indicated.

Discontinuous drops in the rate distribution can be either associated with alternations of the wobble position or with unstable data taking conditions (see Section 7.1.3). By contrast, continuous decreases are typically related to an increase by the presence of `moon light` (see Figure A.2). In addition, data taking at high zenith angle, i.e. Zd $> 40°$, typically feature a decrease in the event rate due to stronger absorption effects (see Section 3.2.3). Furthermore, instabilities in the rate can be related to hardware problems occurring during the data taking.

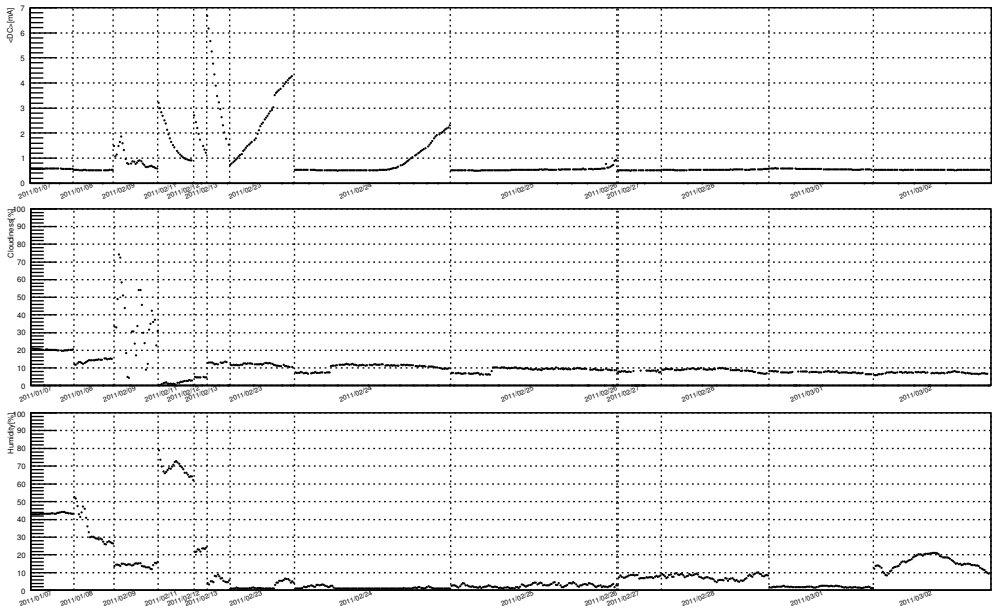

Figure A.2: Data taking conditions during 2011 data of 1ES 0806+524. From top to bottom: The mean DC current of the MAGIC I camera, the `cloudiness` and the `humidity` are plotted. The `moon light` conditions are expressed by the DC current, i.e. the higher the DC current, the stronger the `moon light`.

In Table A.1 the nightly event rates as well as the data taking conditions are reported. In general, observation carried out at mid February are strongly affected by strong Moon leading to a decreasing and increasing rates. In addition, observations from January 9$^{\text{th}}$ are affected by fluctuations in `cloudiness`[68] resulting in an unstable rate, while data from February 13$^{\text{th}}$ have been taken under very strong `moon light`. Due to strong wind on February 26$^{\text{th}}$, the data taking was suspended after few minutes.

Figure A.3 shows the remaining data rates after quality selection based on a minimal event rate of ∼100 Hz as well as its stability on a nightly basis keeping in mind the data taking conditions.

A.2 Details on the 1ES 1011+496 Data Analysis

The following sections contain details on the rate distributions and the data taking conditions of 2011 and 2012 data collected for 1ES 1011+496. In addition, the analysis plots of the signal search from the subsamples of 2012 observations are presented.

[68] The parameter `cloudiness` is a measure of the sky transparency that is related to the sky temperature. Its value spans from 0 (clear sky) to 100 (completely opaque sky)

Cycle	Night	Rate	Rate affecting data taking conditions
	07/01/2011	Decreasing ∼170 - 50 Hz	–
	08/01/2011	Stable ∼170 Hz	–
	09/01/2011	Unstable ∼50 - 170 Hz	Unstable cloudiness
	11/02/2011	Increasing ∼70 - 170 Hz	Decreasing moon light
	12/02/2011	Increasing ∼70 - 100 Hz	Decreasing moon light
	13/02/2011	Increasing ∼50 - 100 Hz	Decreasing moon light
VI	23/02/2011	Increasing ∼60 - 160 Hz	Increasing moon light
	24/02/2011	Decreasing ∼170 - 100 Hz	Increasing moon light
	25/02/2011	Stable ∼175 Hz	–
	26/02/2011	–	Strong wind
	27/02/2011	Unstable ∼170 - 30 Hz	–
	28/02/2011	Unstable ∼110 - 190 Hz	–
	01/03/2011	Unstable ∼140 - 190 Hz	–
	02/03/2011	Stable ∼160 Hz	–

Table A.1: 1ES 0806+524 2011 data collected by MAGIC. From left to right: The first column denotes the observations cycle. The nights of observation are indicated in dd/mm/yy (second column); The event rate is indicated in the third column; The last column refers the data taking conditions during observations.

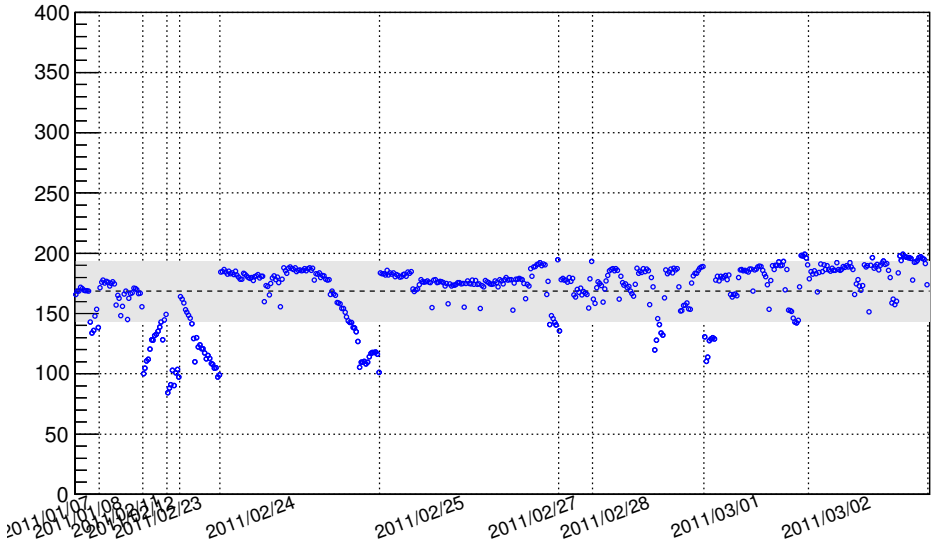

Figure A.3: Quality selection of 1ES 0806+524 data from 2011 MAGIC observations.

1ES 1011+496: Rate Distribution and Data Taking Conditions

1ES 1011+496 observations have been carried out in 2011 and 2012. The data taking conditions and the individual event rates as well as the individual data selections are shown below.

2011 sample: 1ES 1011+496 was observed in 2011 on 12 different nights from the end of February to the beginning of April plotted in Figure A.4. Apart for the first two nights, the mean rates of the individual observations are pretty stable since data have been taken under quasi perfect weather conditions (see Figure A.5).

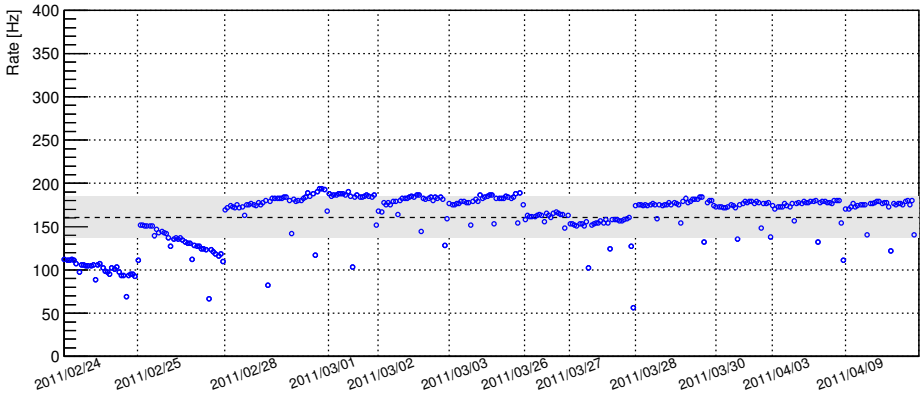

Figure A.4: Event rate distribution after image cleaning of the 2011 data of 1ES 1011+496. The mean value (dashed horizontal line) and 10% variations (gray band) from this value are indicated.

The decreasing rate during February 24$^{\text{th}}$ and 25$^{\text{th}}$ is related to the increasing `moon light`, while the remaining observations have been performed during dark night. Especially during the first night of observation, the `moon light` presence is rather strong wherefore a cut at an event rate of ∼100 Hz has been applied. Despite the high `humidity` during March 27$^{\text{th}}$, the rate distributions is quite stable but slightly lower with respect to the mean rate the other nights.

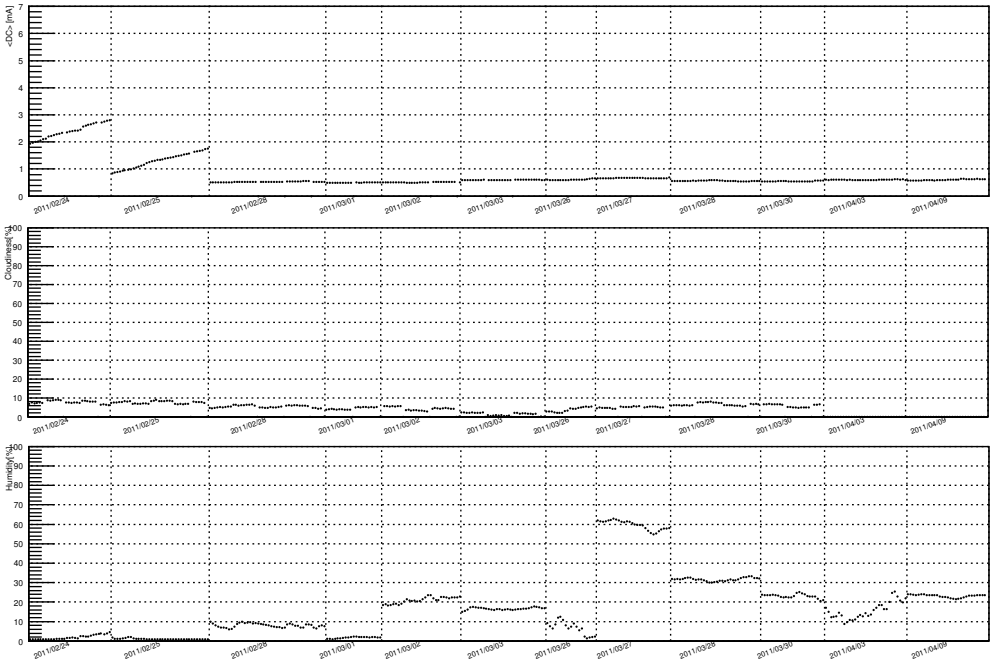

Figure A.5: Data taking conditions during 2011 data of 1ES 1011+496. From top to bottom: The mean DC current of the MAGIC I camera, the `cloudiness` and the `humidity` are plotted. The `moon light` conditions are expressed by the DC current, i.e. the higher the DC current, the stronger the `moon light`.

The rate distribution is summarized in Table A.2.

Beside this cut, individual subruns with a variation of more than 10% with

Cycle	Night	Rate	Rate affecting data taking conditions
VI	24/02/2011	Decreasing ∼110 - 90 Hz	Increasing moon light
	25/02/2011	Decreasing ∼150 - 110 Hz	Increasing moon light
	28/02/2011	Increasing ∼160 - 190 Hz	–
	01/03/2011	Stable ∼180 Hz	–
	02/03/2011	Stable ∼180 Hz	–
	03/03/2011	Stable ∼180 Hz	–
	26/03/2011	Stable ∼160 Hz	–
	27/03/2011	Stable ∼150 Hz	–
	28/03/2011	Stable ∼180 Hz	–
	30/03/2011	Stable ∼180 Hz	–
	03/04/2011	Stable ∼180 Hz	–
	09/04/2011	Stable ∼180 Hz	–

Table A.2: 1ES 1011+496 2011 data collected by MAGIC. From left to right: The nights of observation are indicated in dd/mm/yy (second column); The event rate is indicated in the third column; The last column refers the data taking conditions during observations.

respect to the mean value have been excluded from the further analysis (see Figure A.6.

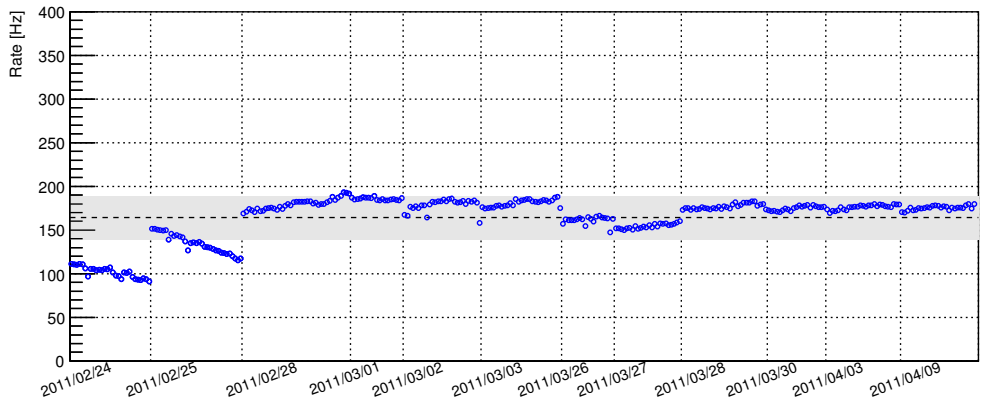

Figure A.6: Quality selection of 1ES 1011+496 data from 2011 MAGIC observations.

2012 sample: In 2012, 1ES 1011+496 has been observed during 34 individual nights from the end of January to mid May.

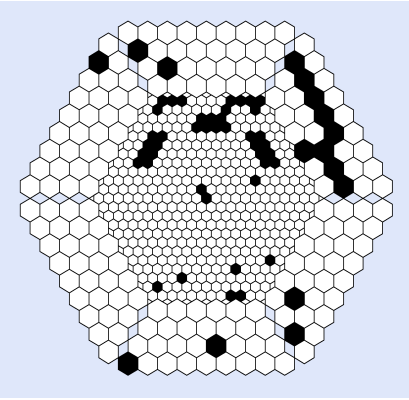

Figure A.7: MAGIC I camera display indicating the broken channels during initial 2012 observations. Dead pixels are marked with black.

During the nights January 28th and April 16th, the telescope focussing was wrong wherefore the data have been excluded from the analysis right away.

Due to important differences in the hardware components, the 2012 data sample has been subdivided into three individual data sets. Especially the first period carried out from January to end of February is affected by several holes in the MAGIC I camera due to dead pixels (see Figure A.7).

Figure A.8 shows the event rate distribution of the individual subsamples during 2012 observations. Beside the very high event rate during the first two observations at the end of January and two nights with pretty fluctuating low rates, the event rates are very quite stable during the first subsample. The second subsample, consisting of few observation nights, shows a perfectly stable event rate distribution. Except for few nights with unstable rate, also the third data sample exhibits a pretty stable event rate distribution.

Checking the data taking conditions, plotted in Figure A.9 for the respective subsample, it seems that unstable rates are dominantly affected by fluctuations in the `cloudiness` parameter, while variations in the `humidity` do not seem to lead to an unstable rate.

Beside the tow nights during which data were taking with wrong focussing, there are few nights which had to be further excluded from the subsequent analysis. In the case of data from January 22nd, the MAGIC II are somehow corrupted making an application of `superstar` impossible. In Table A.3 the rate event distribution and the rate affecting data taking condition are listed for the entire observation period during 2012 available for both telescopes.

[h!]

Cycle	Night	Rate	Rate affecting data taking conditions
VII a	22/01/2012	Stable ∼240 Hz	–
	23/01/2012	Decreasing ∼270 - 250 Hz	–
	26/01/2012	Increasing ∼185 - 200 Hz	–
	27/01/2012	Increasing ∼200 - 220 Hz	–
	30/01/2012	Unstable ∼120 - 20 Hz	Unstable cloudiness
	31/01/2012	Increasing ∼160 - 180 Hz	–
	01/02/2012	Increasing ∼160 - ∼180 Hz	–
	02/02/2012	Decreasing ∼170 - ∼50 Hz	–
	21/02/2012	Stable ∼165 Hz	–
	22/02/2012	Stable ∼165 Hz	–
	25/02/2012	Unstable ∼110 - 50 Hz	Unstable cloudiness
VII b	26/02/2012	Stable ∼160 Hz	–
	29/02/2012	Stable ∼160 Hz	–
	01/03/2012	Stable ∼160 Hz	–
VII c	18/03/2012	Stable ∼120	–
	19/03/2012	Stable ∼145 Hz	–
	20/03/2012	Stable ∼175 Hz	–
	21/03/2012	Stable ∼170 Hz	–
	22/03/2012	Unstable ∼150 - 110 Hz	Unstable cloudiness
	23/03/2012	Increasing ∼130 - 150 Hz	Unstable cloudiness
	24/03/2012	Stable ∼165 Hz	–

25/03/2012	Stable ∼170 Hz	–
26/03/2012	Stable ∼165 Hz	–
27/03/2012	Stable ∼150 Hz	–
28/03/2012	Stable ∼130 Hz	–
29/03/2012	Stable ∼165 Hz	–
13/04/2012	Stable ∼150 Hz	–
14/04/2012	Stable ∼155 Hz	–
15/04/2012	Stable ∼165 Hz	–
19/04/2012	Increasing ∼30 - 150 Hz	–
10/05/2012	Stable ∼155 Hz	–
19/05/2012	Unstable ∼150 - 50 Hz	Unstable cloudiness

Table A.3: 1ES 1011+496 2012 data collected by MAGIC. From left to right: The first column indicates the observation cycle. The nights of observation are indicated in dd/mm/yy (first column); The event rate is indicated in the second column; The last column refers the data taking conditions during observations.

For some reasons for stereo observations during i.e. 30$^{\text{th}}$ the application of `superstar` fails in such way that the stereo rate is 0 although both telescopes recorded data properly. Therefore, for the time being this nights are also excluded from the data analysis since the rate was anyway rather low.

The quality selection of these data is mainly based on a minimum event rate of ∼100 Hz leading to a pretty stable overall 2012 data sample as presented in Figure A.10.

Analysis Plots of the Subsets of 2012 1ES 1011+496 Data

The sections below contain additional information on the analysis of the individual data sets from 1ES 1011+496 2012 observation that have been stacked where applicable providing the individual analysis plots.

In Figure A.11 the plots from the performed signal search are shown.

Comparing the the LRT sky maps (see Figure A.12), the event excess observed is consistent with a point–like source located at the source catalog position of 1ES 1011+496 well within the telescopes PSF. However, during the observation period from March to May 2012 the signal located at the source position seems to be slightly extended indicating a potential misspointing.

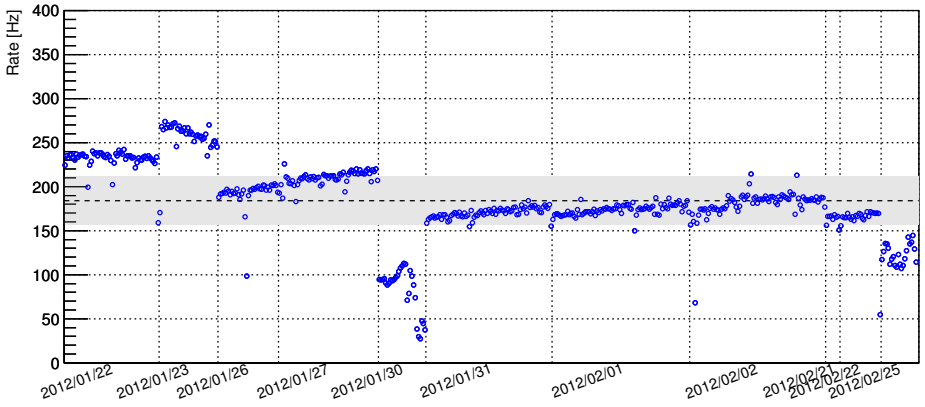

(a) VII a

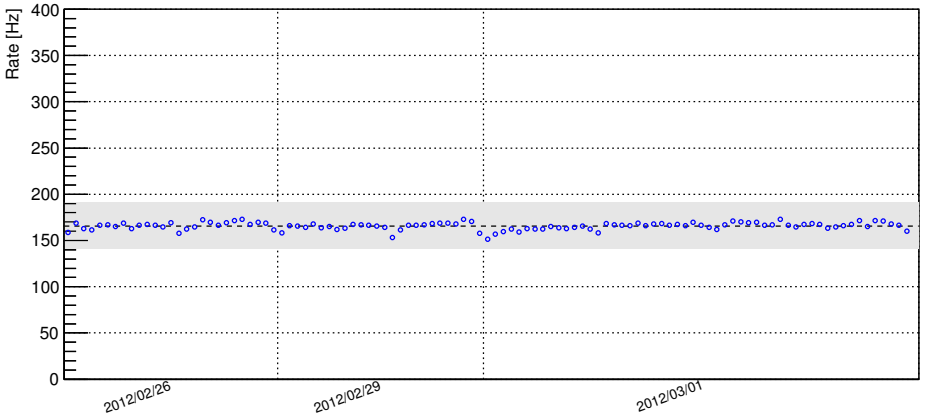

(b) VII b

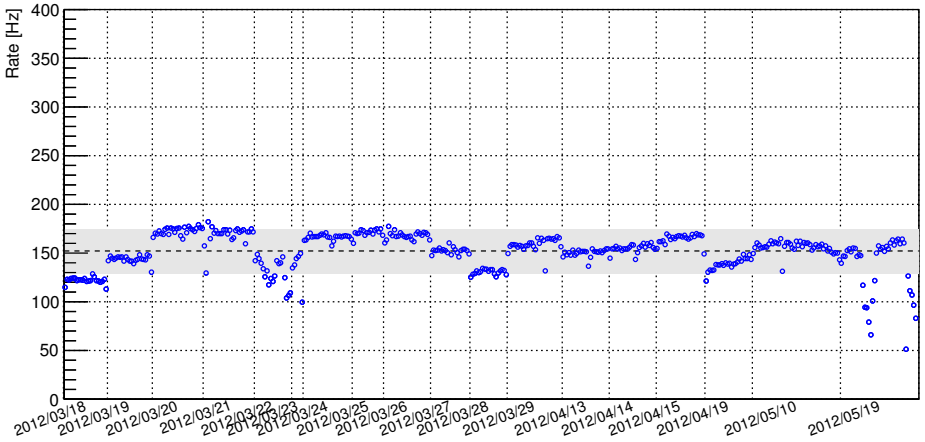

(c) VII c

Figure A.8: Event rate distribution after image cleaning of the 2012 data of 1ES 1011+496. The individual observation periods with varying hardware situations are plotted from top to bottom.

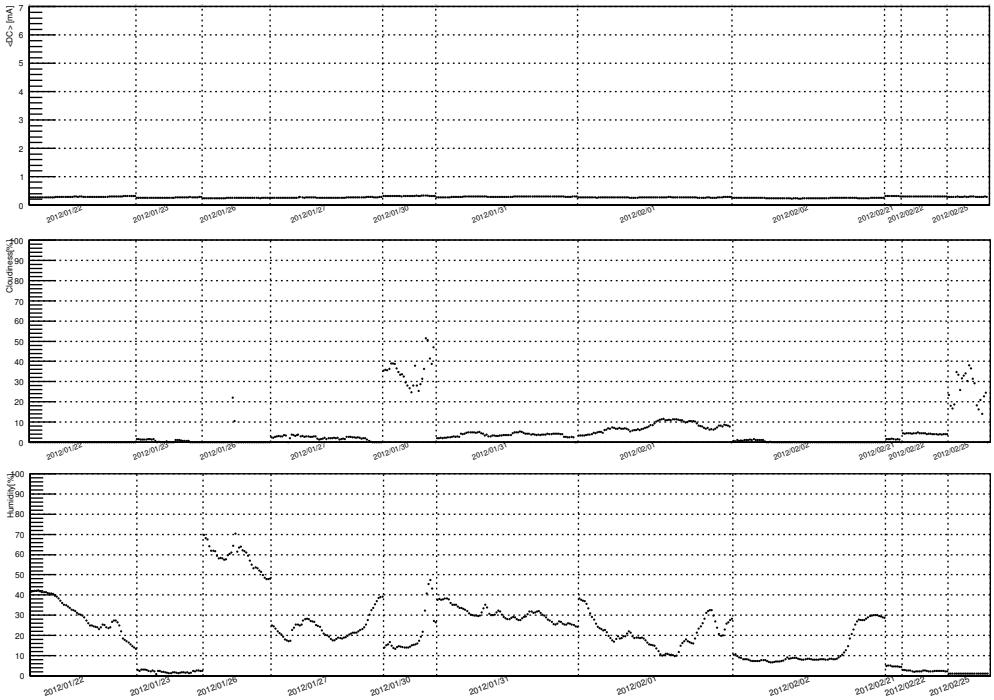
<DC> [mA]
Cloudiness[%]
Humidity[%]
2012/01/22
2012/01/23
2012/01/26
2012/01/27
2012/01/30
2012/01/31
2012/02/01
2012/02/02
2012/02/21
2012/02/22
2012/02/23

(a) VII a

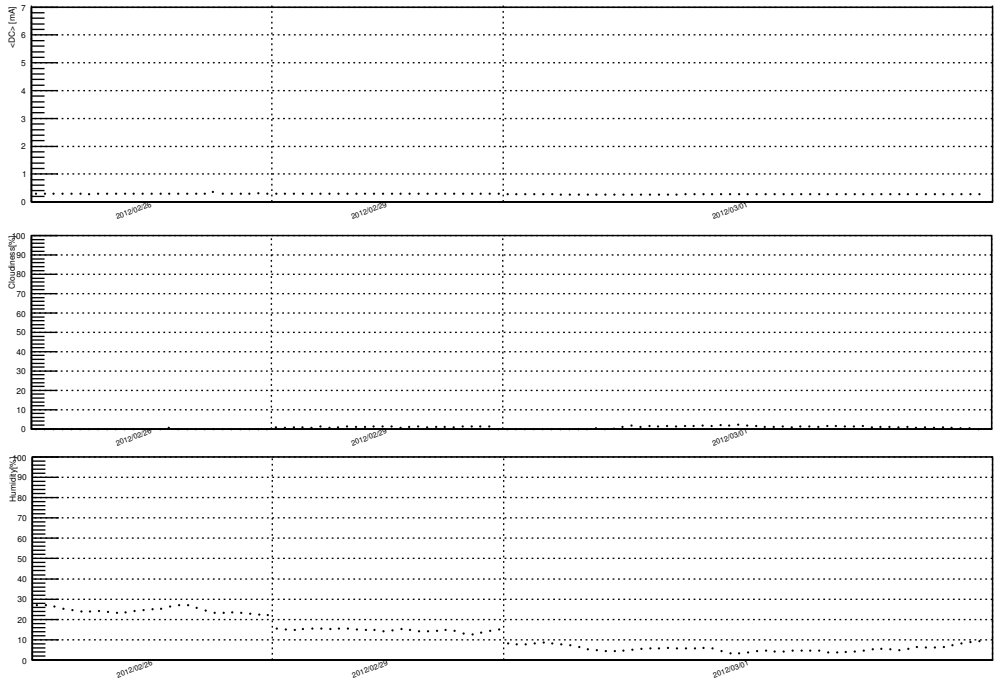

(b) VII b

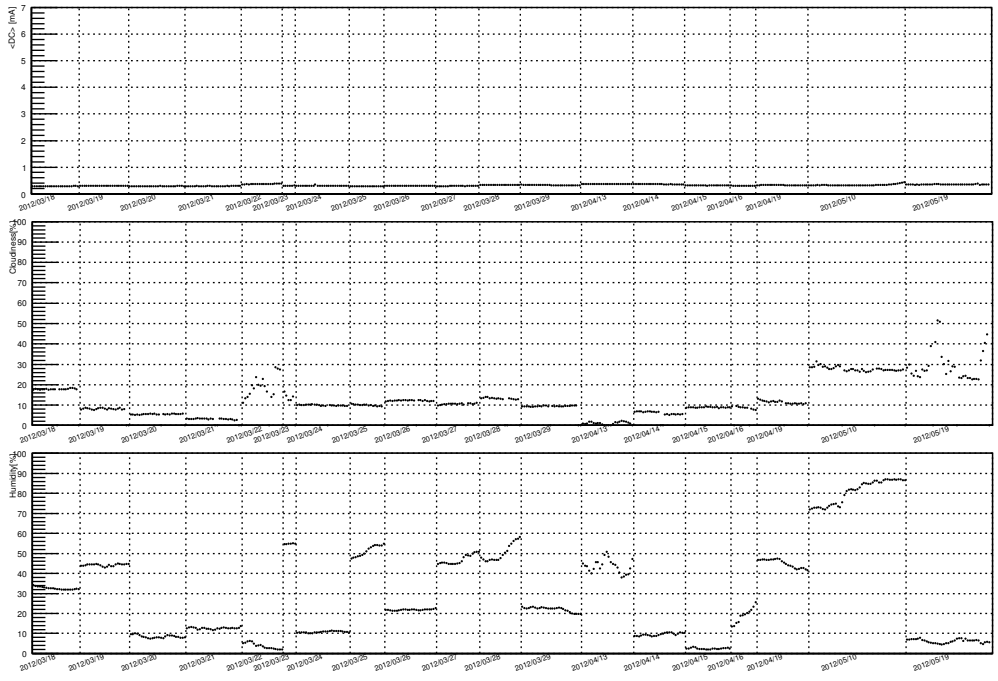

(c) VII c

Figure A.9: Data taking conditions during 2012 data of 1ES 1011+496. From top to bottom: The mean DC current of the MAGIC I camera, the `cloudiness` and the `humidity` are plotted. The `moon light` conditions are expressed by the DC current, i.e. the higher the DC current, the stronger the `moon light`.

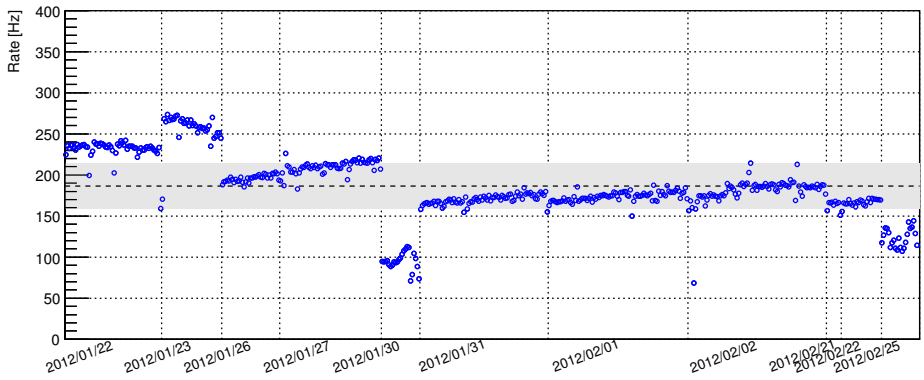

(a) VII a

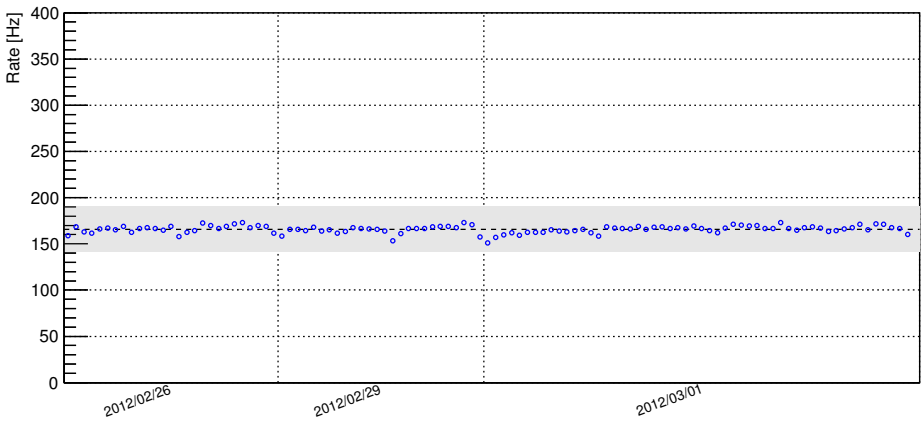

(b) VII b

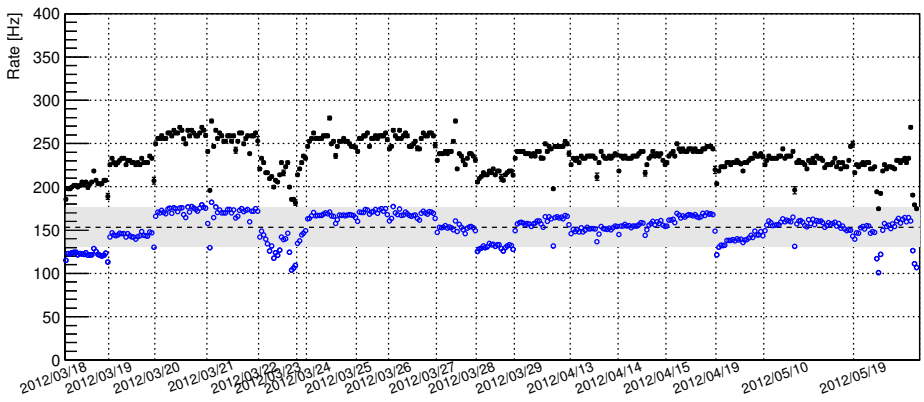

(c) VII c

Figure A.10: Quality selection of 1ES 1011+496 data from 2012 MAGIC observations. From top to bottom: The selected data based on the event rate distribution of the individual subsamples form 2012 observations are presented.

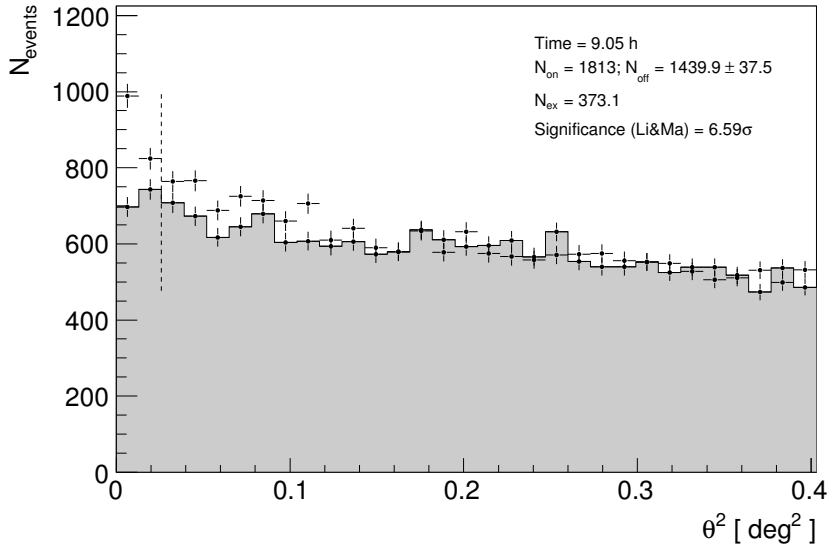

(a) VII a

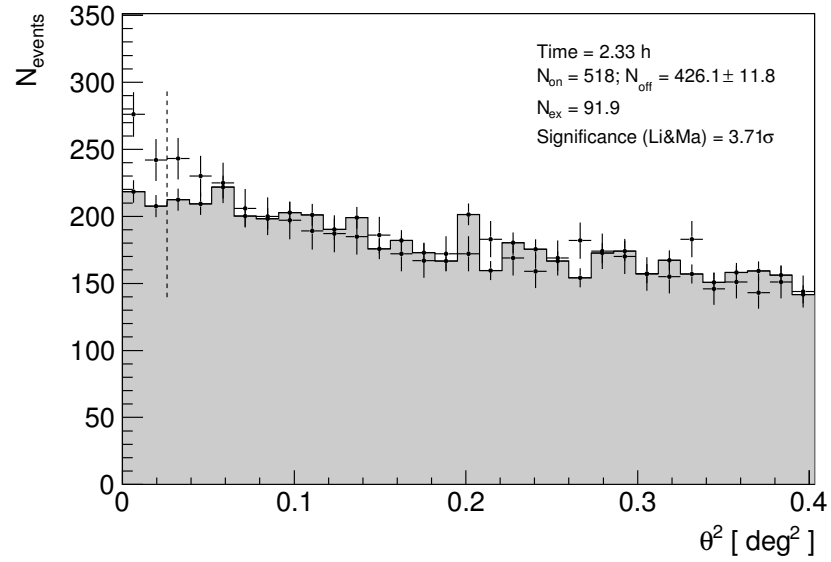

(b) VII b

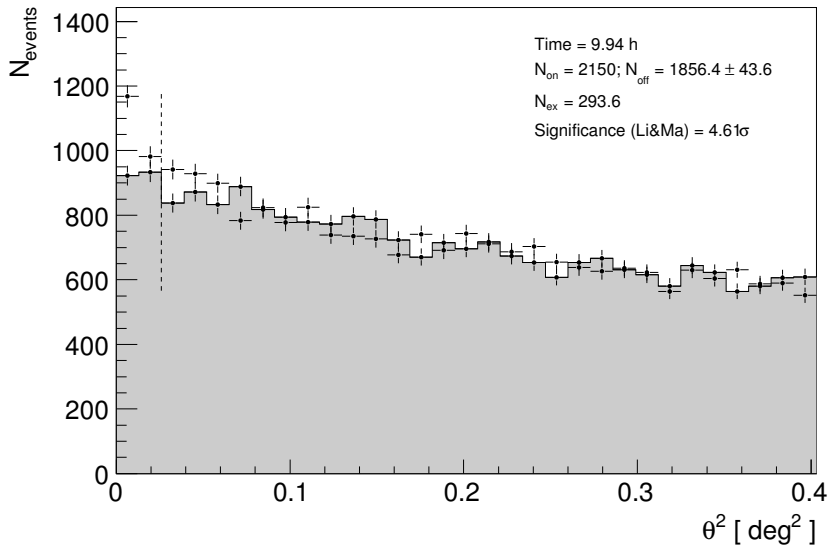

(c) VII c

Figure A.11: θ^2 Plots of the individual subsamples from 1ES 1011+496 2012 data.

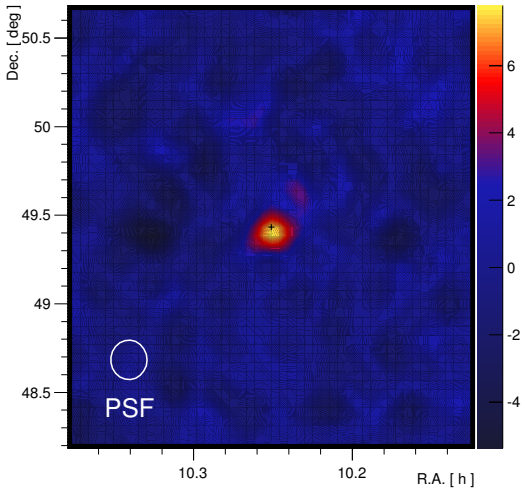

(a) VII a

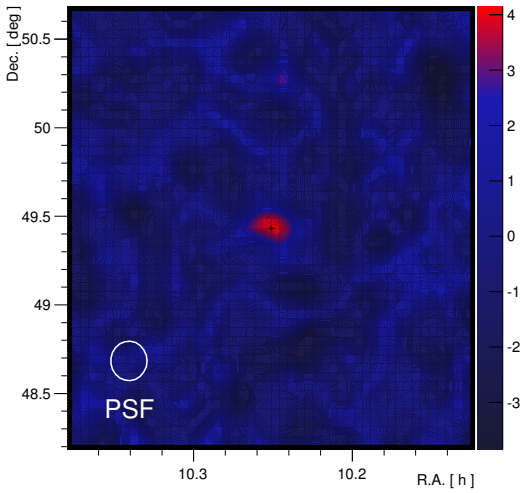

(b) VII b

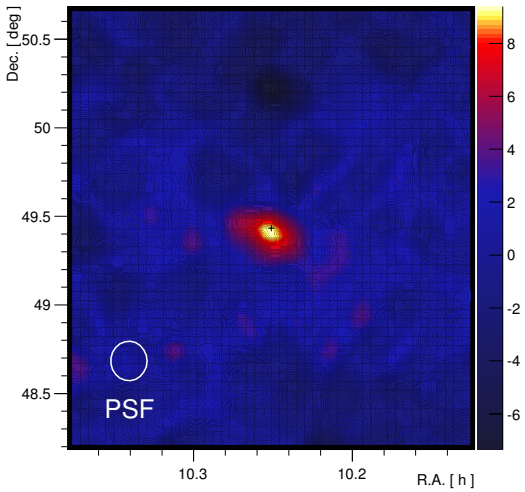

(c) VII c

Figure A.12: Significance LRT sky maps of the individual subsamples from 1ES 1011+496 2012 data.

Bibliography

[1] Abdo, A.A. et al., 2009. 'Bright Active Galactic Nuclei Source List from the First Three Months of the Fermi Large Area Telescope All-Sky Survey.' *ApJ*, **700**, 597–622. doi:10.1088/0004-637X/700/1/597.

[2] Abdo, A.A. et al., 2009. 'Fermi Observations of TeV-Selected Active Galactic Nuclei.' *ApJ*, **707**, 1310–1333. doi:10.1088/0004-637X/707/2/1310.

[3] Abdo, A.A. et al., 2009. 'Fermi/Large Area Telescope Bright Gamma-Ray Source List.' *ApJS*, **183**, 46–66. doi:10.1088/0067-0049/183/1/46.

[4] Abdo, A.A. et al., 2010. 'A change in the optical polarization associated with a γ-ray flare in the blazar 3C279.' *Nature*, **463**, 919–923. doi:10.1038/nature08841.

[5] Abdo, A.A. et al., 2010. 'Fermi Large Area Telescope First Source Catalog.' *ApJS*, **188**, 405–436.

[6] Abdo, A.A. et al., 2011. 'Fermi/lat observations of markarian 421: the missing piece of its spectral energy distribution.' *Submitted to ApJ*.

[7] Abdo, A.A. et al., 2011. 'Insights into the High-energy γ-ray Emission of Markarian 501 from Extensive Multifrequency Observations in the Fermi Era.' *ApJ*, **727**, 129. doi:10.1088/0004-637X/727/2/129.

[8] Abramowski, A. et al., 2012. 'The 2010 Very High Energy γ-Ray Flare and 10 Years of Multi-wavelength Observations of M 87.' *ApJ*, **746**, 151. doi:10.1088/0004-637X/746/2/151.

[9] Acciari, V. et al., 2009. 'Discovery of Very High Energy Gamma-ray Radiation from the BL Lac 1ES 0806+524.' *ApJ Letters*, **690**, L126–L129. doi:10.1088/0004-637X/690/2/L126.

[10] Ackermann, M. et al., 2011. 'The Second Catalog of Active Galactic Nuclei Detected by the Fermi Large Area Telescope.' *ApJ*, **743**, 171. doi:10.1088/0004-637X/743/2/171.

[11] Actis, M. et al., 2011. 'Design concepts for the Cherenkov Telescope Array CTA: an advanced facility for ground-based high-energy gamma-ray astronomy.' *Experimental Astronomy*, **32**, 193–316. doi:10.1007/s10686-011-9247-0.

[12] Adriani, O. et al., 2010. 'PAMELA Results on the Cosmic-Ray Antiproton Flux from 60 MeV to 180 GeV in Kinetic Energy.' *Physical Review Letters*, **105**, 12, 121101–+.

[13] Agasa Collaboration, 2006. 'AGASA results.' *Nuclear Physics B Proceedings Supplements*, **151**, 3–10. doi:10.1016/j.nuclphysbps.2005.07.002.

[14] Aharonian, F., Buckley, J., Kifune, T. and Sinnis, G., 2008. 'High energy astrophysics with ground-based gamma ray detectors.' *Reports on Progress in Physics*, **71**, 9, 096901. doi:10.1088/0034-4885/71/9/096901.

[15] Aharonian, F. et al., 2004. 'Observations of 54 Active Galactic Nuclei with the HEGRA system of Cherenkov telescopes.' *A&A*, **421**, 529–537. doi:10.1051/0004-6361:20035764.

[16] Aharonian, F. et al., 2006. 'A low level of extragalactic background light as revealed by γ-rays from blazars.' *Nature*, **440**, 1018–1021.

[17] Aharonian, F. et al., 2007. 'An Exceptional Very High Energy Gamma-Ray Flare of PKS 2155-304.' *ApJ Letters*, **664**, L71–L74. doi:10.1086/520635.

[18] Aharonian, F. et al., 2007. 'New constraints on the mid-IR EBL from the HESS discovery of VHE γ-rays from 1ES 0229+200.' *A&A*, **475**, L9–L13.

[19] Aharonian, F. et al., 2008. 'Energy Spectrum of Cosmic-Ray Electrons at TeV Energies.' *Physical Review Letters*, **101**, 26, 261104. doi:10.1103/PhysRevLett.101.261104.

[20] Aharonian, F.A., 2000. 'TeV gamma rays from BL Lac objects due to synchrotron radiation of extremely high energy protons.' *New Astronomer*, **5**, 377–395.

[21] Aharonian, F.A., Khangulyan, D. and Costamante, L., 2008. 'Formation of hard very high energy gamma-ray spectra of blazars due to internal photon-photon absorption.' *MNRAS*, **387**, 1206–1214.

[22] Albert, J. et al., 2007. 'Discovery of Very High Energy γ-Rays from 1ES 1011+496 at z = 0.212.' *ApJ Letters*, **667**, L21–L24.

[23] Albert, J. et al., 2007. 'Observations of Markarian 421 with the MAGIC Telescope.' *ApJ*, **663**, 125–138. doi:10.1086/518221.

[24] Albert, J. et al., 2007. 'Unfolding of differential energy spectra in the MAGIC experiment.' *Nuclear Instruments and Methods in Physics Research A*, **583**, 494–506. doi:10.1016/j.nima.2007.09.048.

[25] Albert, J. et al., 2007. 'Variable Very High Energy γ-Ray Emission from Markarian 501.' *ApJ*, **669**, 862–883.

[26] Albert, J. et al., 2008. 'FADC signal reconstruction for the MAGIC telescope.' *Nuclear Instruments and Methods in Physics Research A*, **594**, 407–419. doi:10.1016/j.nima.2008.06.043.

[27] Albert, J. et al., 2008. 'Implementation of the Random Forest method for the Imaging Atmospheric Cherenkov Telescope MAGIC.' *NIM A*, **588**, 424–432.

[28] Albert, J. et al., 2008. 'Systematic Search for VHE Gamma-Ray Emission from X-Ray-bright High-Frequency BL Lac Objects.' *ApJ*, **681**, 944–953. doi:10.1086/587499.

[29] Albert, J. et al., 2008. 'Very-High-Energy gamma rays from a Distant Quasar: How Transparent Is the Universe?' *Science*, **320**, 1752–.

[30] Albert, J. et al., 2008. 'Vhe γ-ray observation of the crab nebula and its pulsar with the magic telescope.' *ApJ*, **674**, 2, 1037.

[31] Aleksić, J. et al., 2010. 'Search for an extended VHE γ-ray emission from Mrk 421 and Mrk 501 with the MAGIC Telescope.' *A&A*, **524**, A77+.

[32] Aleksić, J. et al., 2011. 'Gamma-ray Excess from a Stacked Sample of High- and Intermediate-frequency Peaked Blazars Observed with the MAGIC Telescope.' *ApJ*, **729**, 115. doi:10.1088/0004-637X/729/2/115.

[33] Aleksić, J. et al., 2011. 'Observations of the Blazar 3C 66A with the Magic Telescopes in Stereoscopic Mode.' *ApJ*, **726**, 58. doi:10.1088/0004-637X/726/2/58.

[34] Aleksić, J. et al., 2012. 'Discovery of VHE γ-rays from the blazar 1ES 1215+303 with the MAGIC telescopes and simultaneous multi-wavelength observations.' *A&A*, **544**, A142. doi:10.1051/0004-6361/201219133.

[35] Aleksić, J. et al., 2012. 'Performance of the MAGIC stereo system obtained with Crab Nebula data.' *Astroparticle Physics*, **35**, 435–448. doi:10.1016/j.astropartphys.2011.11.007.

[36] Aliu, E. et al., 2009. 'Improving the performance of the single-dish Cherenkov telescope MAGIC through the use of signal timing.' *Astroparticle Physics*, **30**, 293–305.

[37] An, Q. et al., 2011. 'Performance of a prototype water Cherenkov detector for LHAASO project.' *Nuclear Instruments and Methods in Physics Research A*, **644**, 11–17. doi:10.1016/j.nima.2011.04.016.

[38] Anderson, C.D., 1933. 'The Positive Electron.' *Physical Review*, **43**, 491–494. doi:10.1103/PhysRev.43.491.

[39] Antonelli, V., Miramonti, L., Pena-Garay, C. and Serenelli, A., 2012. 'Solar Neutrinos.' *ArXiv e-prints*.

[40] Antonucci, R., 1993. 'Unified models for active galactic nuclei and quasars.' *ARA&A*, **31**, 473–521. doi:10.1146/annurev.aa.31.090193.002353.

[41] Atkins, R. et al., 2003. 'Observation of TeV Gamma Rays from the Crab Nebula with Milagro Using a New Background Rejection Technique.' *ApJ*, **595**, 803–811.

[42] Atwood, W.B. et al., 2009. 'The Large Area Telescope on the Fermi Gamma-Ray Space Telescope Mission.' *ApJ*, **697**, 1071–1102.

[43] Auger, P. et al., 1939. 'Extensive Cosmic-Ray Showers.' *Reviews of Modern Physics*, **11**, 288–291. doi:10.1103/RevModPhys.11.288.

[44] Baars, J.W.M., Genzel, R., Pauliny-Toth, I.I.K. and Witzel, A., 1977. 'The absolute spectrum of CAS A - an accurate flux density scale and a set of secondary calibrators.' *A&A*, **61**, 99–106.

[45] Bade, N. et al., 1998. 'On the evolutionary behaviour of BL Lac objects.' *A&A*, **334**, 459–472.

[46] Baldini, L., Tibaldo, L. and for the Fermi LAT collaboration, 2011. 'Science highlights from the Fermi Large Area Telescope.' *ArXiv e-prints*.

[47] Barres de Almeida, U. et al., 2009. 'Optical Polarimetric Observations of TeV Blazars.' In 'Proceedings of the 31st ICRC,' International Cosmic Ray Conference, page 1462.

[48] Barthelmy, S.D. et al., 2005. 'The Burst Alert Telescope (BAT) on the SWIFT Midex Mission.' *Space Sci. Rev.*, **120**, 143–164. doi:10.1007/s11214-005-5096-3.

[49] Bastieri, D., Arnold, J., Baixeras, C. and et al., 2008. 'The reflecting surface of the MAGIC-II Telescope.' In 'International Cosmic Ray Conference,' Volume 3 of *International Cosmic Ray Conference*, pages 1547–1550.

[50] Bastieri, D. et al., 2003. 'The Reflecting Surface of the MAGIC Telescope.' In 'International Cosmic Ray Conference,' Volume 5 of *International Cosmic Ray Conference*, page 2919.

[51] Bastieri, D. et al., 2005a. 'Using the photons from the Crab Nebula seen by GLAST to calibrate MAGIC and the imaging air Cherenkov telescopes.' *Astroparticle Physics*, **23**, 572–576. doi:10.1016/j.astropartphys.2005.05.002.

[52] Bastieri, D. et al., 2005b. 'The Mirrors for the MAGIC Telescopes.' In 'International Cosmic Ray Conference,' Volume 5 of *International Cosmic Ray Conference*, page 283.

[53] Bauleo, P.M. and Martino, J.R., 2009. 'The dawn of the particle astronomy era in ultra-high-energy cosmic rays.' *Nature*, **458**, 7240, 847–851.

[54] Becker, R.H., White, R.L. and Edwards, A.L., 1991. 'A new catalog of 53,522 4.85 GHz sources.' *ApJS*, **75**, 1–229. doi:10.1086/191529.

[55] Beckmann, V. and Shrader, C.R., 2012. *Active Galactic Nuclei* (Wiley-VCH Verlag GmbH).

[56] Beringer, J. et al., 2012. 'Review of Particle Physics.' *Phys. Rev. D*, **86**, 1, 010001. doi:10.1103/PhysRevD.86.010001.

[57] Bessell, M.S., 1979. 'UBVRI photometry. II - The Cousins VRI system, its temperature and absolute flux calibration, and relevance for two-dimensional photometry.' *PASP*, **91**, 589–607. doi:10.1086/130542.

[58] Béthermin, M., Dole, H., Beelen, A. and Aussel, H., 2010. 'Spitzer deep and wide legacy mid- and far-infrared number counts and lower limits of cosmic infrared background.' *A&A*, **512**, A78+.

[59] Biland, A., Garczarczyk, M., Anderhub, H. and et al., 2008. 'The Active Mirror Control of the MAGIC Telescopes.' In 'International Cosmic Ray Conference,' Volume 3 of *International Cosmic Ray Conference*, pages 1353–1356.

[60] Biretta, J.A., Sparks, W.B. and Macchetto, F., 1999. 'Hubble Space Telescope Observations of Superluminal Motion in the M87 Jet.' *ApJ*, **520**, 621–626. doi:10.1086/307499.

[61] Blandford, R.D. and Königl, A., 1979. 'Relativistic jets as compact radio sources.' *ApJ*, **232**, 34–48. doi:10.1086/157262.

[62] Blandford, R.D. and Znajek, R.L., 1977. 'Electromagnetic extraction of energy from Kerr black holes.' *MNRAS*, **179**, 433–456.

[63] Błażejowski, M. et al., 2005. 'A Multiwavelength View of the TeV Blazar Markarian 421: Correlated Variability, Flaring, and Spectral Evolution.' *ApJ*, **630**, 130–141. doi:10.1086/431925.

[64] Blümer, J., Engel, R. and Hörandel, J.R., 2009. 'Cosmic rays from the knee to the highest energies.' *Progress in Particle and Nuclear Physics*, **63**, 293–338. doi:10.1016/j.ppnp.2009.05.002.

[65] Bock, R. et al., 2004. 'Methods for multidimensional event classification: a case study using images from a cherenkov gamma-ray telescope.' *Nuclear Instruments and Methods in Physics Research Section A: Accelerators, Spectrometers, Detectors and Associated Equipment*, **516**, 511 – 528. ISSN 0168-9002. doi:10.1016/j.nima.2003.08.157.

[66] Borla Tridon, D., 2011. 'Measurement of the cosmic electron spectrum with the MAGIC telescopes.' In 'International Cosmic Ray Conference,' Volume 6 of *International Cosmic Ray Conference*, page 43.

[67] Borla Tridon, D. et al., 2009. 'Performance of the Camera of the MAGIC II Telescope.' *ArXiv e-prints*.

[68] Böttcher, M. and Chiang, J., 2002. 'X-Ray Spectral Variability Signatures of Flares in BL Lacertae Objects.' *ApJ*, **581**, 127–142. doi:10.1086/344155.

[69] Böttcher, M. et al., 2010. 'Optical Spectral Variability of the Very High Energy Gamma-ray Blazar 1ES 1011+496.' *ApJ*, **725**, 2344–2348. doi:10.1088/0004-637X/725/2/2344.

[70] Bowen, I.S., Millikan, R.A. and Neher, H.V., 1934. 'A Very High Altitude Survey of the Effect of Latitude upon Cosmic-Ray Intensities And an Attempt at a General Interpretation of Cosmic-Ray Phenomena.' *Physical Review*, **46**, 641–652. doi:10.1103/PhysRev.46.641.

[71] Brandt, W.N. and Hasinger, G., 2005. 'Deep Extragalactic X-Ray Surveys.' *ARA&A*, **43**, 827–859.

[72] Bretz, T., Dorner, D., Wagner, R. and MAGIC Collaboration, 2003. 'The Tracking System of the MAGIC Telescope.' In 'International Cosmic Ray Conference,' Volume 5 of *International Cosmic Ray Conference*, page 2943.

[73] Bretz, T., Dorner, D., Wagner, R.M. and Sawallisch, P., 2009. 'The drive system of the major atmospheric gamma-ray imaging Cherenkov telescope.' *Astroparticle Physics*, **31**, 92–101. doi:10.1016/j.astropartphys.2008.12.001.

[74] Bretz, T. et al., 2005. 'Comparison of On-Off and Wobble mode observations for MAGIC.' In 'International Cosmic Ray Conference,' Volume 4 of *International Cosmic Ray Conference*, page 311.

[75] Brinkmann, W. and Siebert, J., 1994. 'Spectral properties of X-ray loud extragalactic radio sources.' *A&A*, **285**, 812–818.

[76] Brinkmann, W. et al., 1995. 'The ROSAT AGN content of the 87GB 5 GHz survey: bulk properties of previously optically identified sources.' *A&AS*, **109**, 147–170.

[77] Burrows, D.N. et al., 2005. 'The Swift X-Ray Telescope.' *Space Sci. Rev.*, **120**, 165–195. doi:10.1007/s11214-005-5097-2.

[78] Cameron, R.A. et al., 1992. 'Operation and performance of the OSSE instrument.' In C.R. Shrader, N. Gehrels and B. Dennis, editors, 'NASA Conference Publication,' Volume 3137 of *NASA Conference Publication*, pages 3–14.

[79] Cao, Z. et al., 2010. 'A Future Project at Tibet: The Large High Altitude Air Shower Observatory (LHAASO).' In '38th COSPAR Scientific Assembly,' Volume 38 of *COSPAR Meeting*, page 2322.

[80] Carmona, E., Majumdar, P., Moralejo, A. and et al., 2008. 'Monte Carlo Simulation for the MAGIC-II System.' In 'International Cosmic Ray Conference,' Volume 3 of *International Cosmic Ray Conference*, pages 1373–1376.

[81] Čerenkov, P.A., 1934. 'Visible emission of clean liquids by action of gamma radiation.' *Doklady Akademii Nauk SSSR*, **2**, 451+.

[82] Chang, J. et al., 2008. 'An excess of cosmic ray electrons at energies of 300-800GeV.' *Nature*, **456**, 362–365. doi:10.1038/nature07477.

[83] CHEN, S., 2011. 'THE CTA site search.' In 'International Cosmic Ray Conference,' Volume 7 of *International Cosmic Ray Conference*, page 191.

[84] Cogan, P., 2008. 'Observations of 1ES 0647+250 and 1ES 0806+524 with VERITAS.' In 'International Cosmic Ray Conference,' Volume 3 of *International Cosmic Ray Conference*, pages 921–924.

[85] Colin, P. et al., 2009. 'Performance of the MAGIC telescopes in stereoscopic mode.' *ArXiv e-prints*.

[86] Commichau, S.C., Biland, A., Kranich, D. and et al., 2008. 'Geomagnetic Field Effects on the Imaging Air Shower Cherenkov Technique.' In 'International Cosmic Ray Conference,' Volume 3 of *International Cosmic Ray Conference*, pages 1357–1360.

[87] Cooray, A. et al., 2009. 'A New Era in Extragalactic Background Light Measurements: The Cosmic History of Accretion, Nucleosynthesis and Reionization.' In 'astro2010: The Astronomy and Astrophysics Decadal Survey,' Volume 2010 of *ArXiv Astrophysics e-prints*, page 54.

[88] Cortina, J., Goebel, F., Schweizer, T. and for the MAGIC Collaboration, 2009. 'Technical Performance of the MAGIC Telescopes.' *ArXiv e-prints*.

[89] Costamante, L., 2012. 'A Warning on the GeV-TeV Connection in Blazars.' *ArXiv e-prints*.

[90] Costamante, L. and Ghisellini, G., 2002. 'TeV candidate BL Lac objects.' *A&A*, **384**, 56–71. doi:10.1051/0004-6361:20011749.

[91] CTA Consortium, T., 2010. 'Design Concepts for the Cherenkov Telescope Array.' *ArXiv e-prints*.

[92] D. Elbaz et al., 2002. 'The bulk of the cosmic infrared background resolved by isocam.' *A&A*, **384**, 3, 848–865. doi:10.1051/0004-6361:20020106.

[93] D'Ammando, F. et al., 2010. 'Not Only Once: The Amazing γ-ray Activity of the Blazar PKS 1510-089.' In L. Maraschi, G. Ghisellini, R. Della Ceca and F. Tavecchio, editors, 'Accretion and Ejection in AGN: a Global View,'

Volume 427 of *Astronomical Society of the Pacific Conference Series*, page 271.

[94] Daniel, M.K. et al., 2005. 'Spectrum of Very High Energy Gamma-Rays from the blazar 1ES 1959+650 during Flaring Activity in 2002.' *ApJ*, **621**, 181–187. doi:10.1086/427406.

[95] de Angelis, A., Galanti, G. and Roncadelli, M., 2011. 'Relevance of axionlike particles for very-high-energy astrophysics.' *Phys. Rev. D*, **84**, 10, 105030. doi:10.1103/PhysRevD.84.105030.

[96] de la Calle Pérez, I. et al., 2003. 'Search for High-Energy Gamma Rays from an X-Ray-selected Blazar Sample.' *ApJ*, **599**, 909–917. doi:10.1086/379544.

[97] Dermer, C.D., 2007. 'On Gamma Ray Burst and Blazar AGN Origins of the Ultra-High Energy Cosmic Rays in Light of First Results from Auger.' *ArXiv e-prints*.

[98] di Pierro, F., 2011. 'Performance studies of the CTA observatory.' In 'International Cosmic Ray Conference,' Volume 9 of *International Cosmic Ray Conference*, page 54.

[99] Doeleman, S.S. et al., 2012. 'Jet-launching structure resolved near the supermassive black hole in m87.' *Science*, **338**, 6105, 355–358. doi:10.1126/science.1224768.

[100] Dole, H. et al., 2006. 'The cosmic infrared background resolved by Spitzer. Contributions of mid-infrared galaxies to the far-infrared background.' *A&A*, **451**, 417–429.

[101] Domingo-Santamaria, E. et al., 2005. 'The DISP analysis method for point-like or extended gamma source searches/studies with the MAGIC Telescope.' In 'International Cosmic Ray Conference,' Volume 5 of *International Cosmic Ray Conference*, page 363.

[102] Domínguez, A., 2012. 'An empirical approach to the extragalactic background light from AEGIS galaxy SED-type fractions.' In 'IAU Symposium,' Volume 284 of *IAU Symposium*, pages 442–445. doi:10.1017/S1743921312009593.

[103] Domínguez, A. et al., 2011. 'Extragalactic background light inferred from AEGIS galaxy-SED-type fractions.' *MNRAS*, **410**, 2556–2578.

[104] Donato, D., Ghisellini, G., Tagliaferri, G. and Fossati, G., 2001. 'Hard X-ray properties of blazars.' *A&A*, **375**, 739–751. doi:10.1051/0004-6361:20010675.

[105] Doro, M., 2009. 'Mirror Facet Technologies for the Telescopes of the CTA Observatory.' In 'Proceedings of the 31st ICRC,' International Cosmic Ray Conference.

[106] Doro, M. et al., 2008. 'The reflective surface of the MAGIC telescope.' *Nuclear Instruments and Methods in Physics Research A*, **595**, 200–203. doi:10.1016/j.nima.2008.07.073.

[107] Dwek, E. and Krennrich, F., 2005. 'Simultaneous Constraints on the Spectrum of the Extragalactic Background Light and the Intrinsic TeV Spectra of Markarian 421, Markarian 501, and H1426+428.' *ApJ*, **618**, 657–674. doi:10.1086/426010.

[108] Dwek, E. and Krennrich, F., 2012. 'The Extragalactic Background Light and the Gamma-ray Opacity of the Universe.' *ArXiv e-prints*.

[109] Elvis, M., Plummer, D., Schachter, J. and Fabbiano, G., 1992. 'The Einstein Slew Survey.' *ApJS*, **80**, 257–303. doi:10.1086/191665.

[110] Fanaroff, B.L. and Riley, J.M., 1974. 'The morphology of extragalactic radio sources of high and low luminosity.' *MNRAS*, **167**, 31P–36P.

[111] Fazio, G.G. and Stecker, F.W., 1970. 'Predicted High Energy Break in the Isotropic Gamma Ray Spectrum: a Test of Cosmological Origin.' *Nature*, **226**, 135–136. doi:10.1038/226135a0.

[112] Fegan, D.J., 1997. 'TOPICAL REVIEW: γ/hadron separation at TeV energies.' *Journal of Physics G Nuclear Physics*, **23**, 1013–1060. doi:10.1088/0954-3899/23/9/004.

[113] Fegan, S.J. et al., 2005. 'A Survey of Unidentified EGRET Sources at Very High Energies.' *ApJ*, **624**, 638–655. doi:10.1086/429123.

[114] Fermi, E., 1949. 'On the origin of the cosmic radiation.' *Phys. Rev.*, **75**, 1169–1174. doi:10.1103/PhysRev.75.1169.

[115] Fichtel, C.E. et al., 1994. 'The first energetic gamma-ray experiment telescope (EGRET) source catalog.' *ApJS*, **94**, 551–581. doi:10.1086/192082.

[116] Finke, J.D. and Razzaque, S., 2009. 'Constraints on the Extragalactic Background Light from very High Energy Gamma-Ray Observations of Blazars.' *ApJ*, **698**, 1761–1766.

[117] Finke, J.D., Razzaque, S. and Dermer, C.D., 2010. 'Modeling the Extragalactic Background Light from Stars and Dust.' *ApJ*, **712**, 238–249.

[118] Fiorucci, M., Tosti, G. and Rizzi, N., 1998. 'VRI Photometry of Stars in the Fields of 16 Blazars.' *PASP*, **110**, 105–110. doi:10.1086/316127.

[119] Fitzpatrick, E.L., 1999. 'Correcting for the Effects of Interstellar Extinction.' *PASP*, **111**, 63–75. doi:10.1086/316293.

[120] Foerster, A., 2011. 'High-reflectance, high-durability coatings for IACT mirrors.' In 'International Cosmic Ray Conference,' Volume 9 of *International Cosmic Ray Conference*, page 133.

[121] Foerster, A., 2011. 'Mirror development for CTA.' In 'International Cosmic Ray Conference,' Volume 9 of *International Cosmic Ray Conference*, page 129.

[122] Fomin, V.P. et al., 1994. 'New methods of atmospheric Cherenkov imaging for gamma-ray astronomy. I. The false source method.' *Astroparticle Physics*, **2**, 137–150.

[123] Fossati, G. et al., 1998. 'A unifying view of the spectral energy distributions of blazars.' *MNRAS*, **299**, 433–448.

[124] Franceschini, A., Rodighiero, G. and Vaccari, M., 2008. 'Extragalactic optical-infrared background radiation, its time evolution and the cosmic photon-photon opacity.' *A&A*, **487**, 837–852.

[125] Frank, I.M. and Tamm, I.E., 1937. 'Coherent visible radiation of fast electrons passing through matter.' *Doklady Akademii Nauk SSSR*, **14**, 109–114.

[126] Funk, S. and Hinton, J., 2012. 'Comparison of Fermi-LAT and CTA in the region between 10-100 GeV.' *ArXiv e-prints*.

[127] Gaisser, T. and Stanev, T., 2000. 'Cosmic rays.' *The European Physical Journal C - Particles and Fields*, **15**, 150–156. ISSN 1434-6044. 10.1007/BF02683416.

[128] Gaisser, T.K. and Halzen, F., 1976. 'Long-lived tracks in emulsions: New hadrons or background?' *Phys. Rev. D*, **14**, 3153–3166. doi:10.1103/PhysRevD.14.3153.

[129] Garczarczyk, M., 2011. 'The major atmospheric gamma-ray imaging cherenkov telescope.' *Nuclear Instruments and Methods in Physics Research Section A: Accelerators, Spectrometers, Detectors and Associated Equipment*, **639**, 1, 33 – 36. ISSN 0168-9002. doi:10.1016/j.nima.2010.09.020. <ce:title>Proceedings of the Seventh International Workshop on Ring Imaging Cherenkov Detectors</ce:title>.

[130] Garrington, S.T. and Conway, R.G., 1991. 'The interpretation of asymmetric depolarization in extragalactic radio sources.' *MNRAS*, **250**, 198–208.

[131] Gaug, M., Bartko, H., Cortina, J. and Rico, J., 2005. 'Calibration of the MAGIC Telescope.' In 'International Cosmic Ray Conference,' Volume 5 of *International Cosmic Ray Conference*, page 375.

[132] Gaug, M. et al., 2003. 'An Absolute Light Flux Calibration for the MAGIC Telescope.' In 'International Cosmic Ray Conference,' Volume 5 of *International Cosmic Ray Conference*, page 2923.

[133] Gehrels, N., Chipman, E. and Kniffen, D., 1994. 'The Compton Gamma Ray Observatory.' *ApJS*, **92**, 351–362. doi:10.1086/191978.

[134] Gehrels, N. et al., 2004. 'The Swift Gamma-Ray Burst Mission.' *ApJ*, **611**, 1005–1020. doi:10.1086/422091.

[135] Georganopoulos, M., Finke, J.D. and Reyes, L.C., 2010. 'A Method for Setting Upper Limits to the Extragalactic Background Light with Fermi-lat and TeV Observations of Blazars.' *ApJ Letters*, **714**, L157–L161. doi:10.1088/2041-8205/714/1/L157.

[136] Ghisellini, G., 2000. 'Special Relativity at Action in the Universe.' In B. Casciaro, D. Fortunato, M. Francaviglia and A. Masiello, editors, 'Recent Developments in General Relativity,' page 5.

[137] Ghisellini, G., 2011. 'Extragalactic relativistic jets.' In F.A. Aharonian, W. Hofmann and F.M. Rieger, editors, 'American Institute of Physics Conference Series,' Volume 1381 of *American Institute of Physics Conference Series*, pages 180–198. doi:10.1063/1.3635832.

[138] Ghisellini, G. and Madau, P., 1996. 'On the origin of the gamma-ray emission in blazars.' *MNRAS*, **280**, 67–76.

[139] Ghisellini, G., Maraschi, L. and Tavecchio, F., 2009. 'The Fermi blazars' divide.' *MNRAS*, **396**, L105–L109.

[140] Ghisellini, G., Tavecchio, F., Foschini, L. and Ghirlanda, G., 2011. 'The transition between BL Lac objects and flat spectrum radio quasars.' *MNRAS*, **414**, 2674–2689. doi:10.1111/j.1365-2966.2011.18578.x.

[141] Ghisellini, G. et al., 1998. 'A theoretical unifying scheme for gamma-ray bright blazars.' *MNRAS*, **301**, 451–468.

[142] Ghisellini, G. et al., 2010. 'General physical properties of bright Fermi blazars.' *MNRAS*, **402**, 497–518. doi:10.1111/j.1365-2966.2009.15898.x.

[143] Ghisellini, G. et al., 2010. 'High-redshift Fermi blazars.' *MNRAS*, pages 1729–+.

[144] Gilli, R., 2004. 'The X-ray background and the deep X-ray surveys.' *Advances in Space Research*, **34**, 2470–2477. doi:10.1016/j.asr.2003.03.073.

[145] Gilmore, R.C., Prada, F. and Primack, J., 2010. 'Modelling gamma-ray burst observations by Fermi and MAGIC including attenuation due to diffuse background light.' *MNRAS*, **402**, 565–574. doi:10.1111/j.1365-2966.2009.15909.x.

[146] Gilmore, R.C., Somerville, R.S., Primack, J.R. and Domínguez, A., 2012. 'Semi-analytic modelling of the extragalactic background light and consequences for extragalactic gamma-ray spectra.' *MNRAS*, **422**, 3189–3207. doi:10.1111/j.1365-2966.2012.20841.x.

[147] Giroletti, M., Giovannini, G., Taylor, G.B. and Falomo, R., 2004. 'A Sample of Low-Redshift BL Lacertae Objects. I. The Radio Data.' *ApJ*, **613**, 752–769. doi:10.1086/423231.

[148] Gould, R.J. and Schréder, G., 1966. 'Opacity of the Universe to High-Energy Photons.' *Physical Review Letters*, **16**, 252–254. doi:10.1103/PhysRevLett.16.252.

[149] Greisen, K., 1960. 'Cosmic Ray Showers.' *Annual Review of Nuclear and Particle Science*, **10**, 63–108. doi:10.1146/annurev.ns.10.120160.000431.

[150] Greisen, K., 1966. 'End to the cosmic-ray spectrum?' *Phys. Rev. Lett.*, **16**, 17, 748–750.

[151] Haefner, D., 2011. 'New improved Sum-Trigger system for the MAGIC telescopes.' In 'International Cosmic Ray Conference,' Volume 9 of *International Cosmic Ray Conference*, page 246.

[152] Hales, S.E.G., Masson, C.R., Warner, P.J. and Baldwin, J.E., 1990. 'The 6c Survey of Radio Sources - Part Three - the Zone Dec: 48DEG< 68DEG Ra: 05H25< 18H17M.' *MNRAS*, **246**, 256.

[153] Hauser, M.G. and Dwek, E., 2001. 'The Cosmic Infrared Background: Measurements and Implications.' *ARA&A*, **39**, 249–307.

[154] Hayashida, N. et al., 2000. 'Updated AGASA event list above 4x10^19eV.' *ArXiv Astrophysics e-prints*.

[155] Heber, B. et al., 2009. 'Modulation of Galactic Cosmic Ray Protons and Electrons During an Unusual Solar Minimum.' *ApJ*, **699**, 1956–1963. doi:10.1088/0004-637X/699/2/1956.

[156] Heck, D. et al., 1998. *CORSIKA: a Monte Carlo code to simulate extensive air showers.* (TIB Hannover, Hannover, Germany).

[157] Heitler, W., 1954. *The quantum theory of radiation / by W. Heitler* (Clarendon Press, Oxford :), 3rd ed. edition.

[158] Heitler, W., 1960. *The Quantum Theory of Radiation* (Oxford Press, Oxford).

[159] Helgason, K., Ricotti, M. and Kashlinsky, A., 2012. 'Reconstructing the Near-infrared Background Fluctuations from Known Galaxy Populations Using Multiband Measurements of Luminosity Functions.' *ApJ*, **752**, 113. doi:10.1088/0004-637X/752/2/113.

[160] Hillas, A.M., 1984. 'The Origin of Ultra-High-Energy Cosmic Rays.' *ARA&A*, **22**, 425–444.

[161] Hinshaw, G. et al., 2007. 'Three-Year Wilkinson Microwave Anisotropy Probe (WMAP) Observations: Temperature Analysis.' *ApJS*, **170**, 288–334. doi:10.1086/513698.

[162] Hinton, J.A. and Hofmann, W., 2009. 'Teraelectronvolt Astronomy.' *ARA&A*, **47**, 523–565.

[163] Holder, J., 2007. 'VERITAS: Status and Performance.' In M. M. Massai, N. Omodei, & G. Spandre, editor, 'Science with the New Generation of High Energy Gamma-Ray Experiments,' pages 69–+.

[164] Horan, D. et al., 2004. 'Constraints on the Very High Energy Emission from BL Lacertae Objects.' *ApJ*, **603**, 51–61. doi:10.1086/381430.

[165] Hörandel, J.R., 2010. 'Cosmic rays at the highest energies.' *Progress in Particle and Nuclear Physics*, **64**, 2, 351 – 359. ISSN 0146-6410. Neutrinos in Cosmology, in Astro, Particle and Nuclear Physics, International Workshop on Nuclear Physics, 31st course.

[166] Horns, D. and Meyer, M., 2012. 'Indications for a pair-production anomaly from the propagation of VHE gamma-rays.' *J. Cosmology Astropart. Phys.*, **2**, 033. doi:10.1088/1475-7516/2012/02/033.

[167] Juvela, M. et al., 2009. 'Determination of the cosmic far-infrared background level with the ISOPHOT instrument.' *A&A*, **500**, 763–768.

[168] Kalberla, P.M.W. et al., 2005. 'The Leiden/Argentine/Bonn (LAB) Survey of Galactic HI. Final data release of the combined LDS and IAR surveys with improved stray-radiation corrections.' *A&A*, **440**, 775–782. doi:10.1051/0004-6361:20041864.

[169] Kamata, K. and Nishimura, J., 1958. 'The Lateral and the Angular Structure Functions of Electron Showers.' *Progress of Theoretical Physics Supplement*, **6**, 93–155. doi:10.1143/PTPS.6.93.

[170] Kapanadze, B.Z., 2009. 'Optical R-band variability of seven X-ray-selected BL Lacertae objects.' *MNRAS*, **398**, 832–840. doi:10.1111/j.1365-2966.2009.14976.x.

[171] Karlsson, N.f., 2009. 'Discovery of VHE Gamma-ray Emission from the Starburst Galaxy M82.' *ArXiv e-prints*.

[172] Kashlinsky, A., 2005. 'Cosmic infrared background and early galaxy evolution.' *Physics Reports*, **409**, 361–438.

[173] Kashlinsky, A. et al., 2012. 'New Measurements of the Cosmic Infrared Background Fluctuations in Deep Spitzer/IRAC Survey Data and Their Cosmological Implications.' *ApJ*, **753**, 63. doi:10.1088/0004-637X/753/1/63.

[174] Katarzyński, K. and Walczewska, K., 2010. 'On the correlation between the X-ray and gamma-ray emission in TeV blazars.' *A&A*, **510**, A63. doi:10.1051/0004-6361/200913128.

[175] Katarzyński, K. et al., 2006. 'Hard TeV spectra of blazars and the constraints to the infrared intergalactic background.' *MNRAS*, **368**, L52–L56.

[176] Kellermann, K.I. and Owen, F.N., 1988. *Radio galaxies and quasars*, pages 563–602 (Springer-Verlag).

[177] Kellermann, K.I. et al., 1989. 'VLA observations of objects in the Palomar Bright Quasar Survey.' *AJ*, **98**, 1195–1207.

[178] King, A., 2008. 'Disc accretion in active galactic nuclei.' *New A Rev.*, **52**, 253–256. doi:10.1016/j.newar.2008.06.006.

[179] Kino, M., Takahara, F. and Kusunose, M., 2002. 'Energetics of TeV Blazars and Physical Constraints on Their Emission Regions.' *ApJ*, **564**, 97–107. doi:10.1086/323363.

[180] Klepser, S., 2012. 'A generalized likelihood ratio test statistic for Cherenkov telescope data.' *Astroparticle Physics*, **36**, 64–76. doi:10.1016/j.astropartphys.2012.04.008.

[181] Klepser, S., 2012. 'A generalized likelihood ratio test statistic for Cherenkov telescope data.' *Astroparticle Physics*, **36**, 64–76. doi:10.1016/j.astropartphys.2012.04.008.

[182] Kneiske, T.M., Bretz, T., Mannheim, K. and Hartmann, D.H., 2004. 'Implications of cosmological gamma-ray absorption. II. Modification of gamma-ray spectra.' *A&A*, **413**, 807–815.

[183] Kneiske, T.M. and Dole, H., 2010. 'A lower-limit flux for the extragalactic background light.' *A&A*, **515**, A19+.

[184] Kneiske, T.M. and Dole, H., 2010. 'A lower-limit flux for the extragalactic background light.' *A&A*, **515**, A19. doi:10.1051/0004-6361/200912000.

[185] Kneiske, T.M., Mannheim, K. and Hartmann, D.H., 2002. 'Implications of cosmological gamma-ray absorption. I. Evolution of the metagalactic radiation field.' *A&A*, **386**, 1–11. doi:10.1051/0004-6361:20020211.

[186] Kraushaar, W.L. and Clark, G.W., 1962. 'Search for Primary Cosmic Gamma Rays with the Satellite Explorer XI.' *Physical Review Letters*, **8**, 106–109. doi:10.1103/PhysRevLett.8.106.

[187] Krawczynski, H. et al., 2004. 'Multiwavelength Observations of Strong Flares from the TeV Blazar 1ES 1959+650.' *ApJ*, **601**, 151–164.

[188] Krolik, J.H., 1999. *Active galactic nuclei : from the central black hole to the galactic environment*. Princeton series in astrophysics (Princeton University Press, Princeton, NJ).

[189] Kubo, H. et al., 2004. 'Status of the CANGAROO-III project.' *New A Rev.*, **48**, 323–329. doi:10.1016/j.newar.2003.12.002.

[190] Kusenko, A., 2012. 'Cosmic connections: from cosmic rays to gamma rays, to cosmic backgrounds and magnetic fields.' *ArXiv e-prints*.

[191] Lagache, G., Puget, J. and Dole, H., 2005. 'Dusty Infrared Galaxies: Sources of the Cosmic Infrared Background.' *ARA&A*, **43**, 727–768.

[192] Laing, R.A., 1988. 'The sidedness of jets and depolarization in powerful extragalactic radio sources.' *Nature*, **331**, 149–151. doi:10.1038/331149a0.

[193] Lattes, C.M.G., Occhialini, G.P.S. and Powell, C.F., 1947. 'Observations on the Tracks of Slow Mesons in Photographic Emulsions.' *Nature*, **160**, 453–456. doi:10.1038/160453a0.

[194] Letessier-Selvon, A. and Stanev, T., 2011. 'Ultrahigh energy cosmic rays.' *Reviews of Modern Physics*, **83**, 907–942. doi:10.1103/RevModPhys.83.907.

[195] Li, T. and Ma, Y., 1983. 'Analysis methods for results in gamma-ray astronomy.' *ApJ*, **272**, 317–324.

[196] Lin, Y.C. et al., 1996. 'EGRET observations of BL Lacertae objects with redshifts below 0.2.' *A&AS*, **120**, C499.

[197] Linsley, J., 1963. 'Evidence for a Primary Cosmic-Ray Particle with Energy 10^{20} eV.' *Physical Review Letters*, **10**, 146–148. doi:10.1103/PhysRevLett.10.146.

[198] Lister, M.L. et al., 2009. 'MOJAVE: Monitoring of Jets in Active Galactic Nuclei with VLBA Experiments. VI. Kinematics Analysis of a Complete Sample of Blazar Jets.' *AJ*, **138**, 1874–1892. doi:10.1088/0004-6256/138/6/1874.

[199] Liu, R.Y., Wang, X.Y., Wang, W. and Taylor, A.M., 2012. 'On the Excess of Ultra-high Energy Cosmic Rays in the Direction of Centaurus A.' *ApJ*, **755**, 139. doi:10.1088/0004-637X/755/2/139.

[200] Lombardi, S., 2011. 'Advanced stereoscopic gamma-ray shower analysis with the MAGIC telescopes.' In 'International Cosmic Ray Conference,' Volume 3 of *International Cosmic Ray Conference*, page 262.

[201] Longair, M.S., 1994. *High energy astrophysics. Volume 2. Stars, the Galaxy and the interstellar medium.* (Cambridge University Press).

[202] Longair, M.S., 2010. *High Energy Astrophysics* (Cambridge University Press).

[203] López Moya, M., 2010. 'Scientific Highlights and Status of the MAGIC Telescope.' In C. Cecchi, S. Ciprini, P. Lubrano and G. Tosti, editors, 'American Institute of Physics Conference Series,' Volume 1223 of *American Institute of Physics Conference Series*, pages 99–108. doi:10.1063/1.3396001.

[204] López Moya, M., 2011. 'Recent highlights from the MAGIC telescopes.' In 'Extreme and Variable High Energy Sky (Extremesky 2011),' .

[205] Machalski, J. and Condon, J.J., 1983. 'A complete sample of intermediate-strength radio sources selected from the GB/GB2 1400-MHz surveys. IV. VLA Observations and Optical Identifications of a Set of Sources with 0.20 $\leq$ S $<$ 0.55 Jy.' *AJ*, **88**, 1591–1615. doi:10.1086/113450.

[206] Madau, P. and Pozzetti, L., 2000. 'Deep galaxy counts, extragalactic background light and the stellar baryon budget.' *MNRAS*, **312**, L9–L15.

[207] MAGIC Collaboration: Florian Goebel et al., 2007. 'Upgrade of the MAGIC Telescope with a Multiplexed Fiber-Optic 2 GSamples/s FADC Data Acquisition system.' *ArXiv e-prints*.

[208] Majumdar, P. et al., 2005. 'Monte Carlo simulation for the MAGIC telescope.' In 'International Cosmic Ray Conference,' Volume 5 of *International Cosmic Ray Conference*, page 203.

[209] Malkov, M.A. and O'C Drury, L., 2001. 'Nonlinear theory of diffusive acceleration of particles by shock waves.' *Reports on Progress in Physics*, **64**, 429–481.

[210] Mannheim, K., 1993. 'The proton blazar.' *A&A*, **269**, 67–76.

[211] Mannheim, K., Protheroe, R.J. and Rachen, J.P., 2001. 'Cosmic ray bound for models of extragalactic neutrino production.' *Phys. Rev. D*, **63**, 2, 023003. doi:10.1103/PhysRevD.63.023003.

[212] Maraschi, L., Ghisellini, G. and Celotti, A., 1992. 'A jet model for the gamma-ray emitting blazar 3C 279.' *ApJ Letters*, **397**, L5–L9. doi:10.1086/186531.

[213] Maraschi, L. and Tavecchio, F., 2003. 'The Jet-Disk Connection and Blazar Unification.' *ApJ*, **593**, 667–675. doi:10.1086/342118.

[214] Mariotti, M., 2011. 'MAGIC observes a very high energy gamma-ray flare from 1ES0806+524.' *The Astronomer's Telegram*, **3192**, 1.

[215] Massaro, E., Perri, M., Giommi, P. and Nesci, R., 2004. 'Log-parabolic spectra and particle acceleration in the BL Lac object Mkn 421: Spectral analysis of the complete BeppoSAX wide band X-ray data set.' *A&A*, **413**, 489–503. doi:10.1051/0004-6361:20031558.

[216] Matthews, J., 2005. 'A heitler model of extensive air showers.' *Astroparticle Physics*, **22**, 5âĂŞ6, 387 – 397. ISSN 0927-6505. doi:10.1016/j.astropartphys.2004.09.003.

[217] Mattox, J.R., Hartman, R.C. and Reimer, O., 2001. 'A quantitative evaluation of potential radio identifications for 3eg egret sources.' *The Astrophysical Journal Supplement Series*, **135**, 2, 155.

[218] Mattox, J.R. et al., 1996. 'The Likelihood Analysis of EGRET Data.' *ApJ*, **461**, 396–+.

[219] Mazin, D. and Goebel, F., 2007. 'Break in the Very High Energy Spectrum of PG 1553+113: New Upper Limit on Its Redshift?' *ApJ Letters*, **655**, L13–L16. doi:10.1086/511751.

[220] Mazin, D. and Collaboration, M., 2012. 'Highlights from the magic telescopes.' *AIP Conference Proceedings*, **1505**, 1, 186–193. doi:10.1063/1.4772232.

[221] McGilchrist, M.M. et al., 1990. 'The 7c Survey of Radio Sources at 151-MHZ - Two Regions Centred at Ra: 10H28M Dec: 41DEG and Ra: 06H28M Dec: 45DEG.' *MNRAS*, **246**, 110–122.

[222] Meegan, C. et al., 2009. 'The Fermi Gamma-ray Burst Monitor.' *ApJ*, **702**, 791–804. doi:10.1088/0004-637X/702/1/791.

[223] Meliani, Z. et al., 2010. 'Relativistic spine jets from Schwarzschild black holes. Application to AGN radio-loud sources.' *A&A*, **521**, A67. doi:10.1051/0004-6361/200912920.

[224] Meyer, M., Horns, D. and Raue, M., 2012. 'Revisiting the Indication for a low opacity Universe for very high energy gamma-rays.' *ArXiv e-prints*.

[225] Meyer, M., Raue, M., Mazin, D. and Horns, D., 2012. 'Limits on the extragalactic background light in the Fermi era.' *A&A*, **542**, A59. doi:10.1051/0004-6361/201118284.

[226] Millikan, R.A. and Cameron, G.H., 1926. 'High Frequency Rays of Cosmic Origin III. Measurements in Snow-Fed Lakes at High Altitudes.' *Physical Review*, **28**, 851–868. doi:10.1103/PhysRev.28.851.

[227] Mirzoyan, R., 1997. 'On the calibration accuracy of light sensors in atmospheric Cherenkov fluorescence and neutrino experiment.' In 'International Cosmic Ray Conference,' Volume 7 of *International Cosmic Ray Conference*, page 265.

[228] Mirzoyan, R., Garczarczyk, M., Kellermann, H. and Schultz, C., in preparation. 'Absolute reflectivity of a concave mirror.' *ApJ*.

[229] Mirzoyan, R., Garczarczyk, M., Hose, J. and Paneque, D., 2007. 'A method to measure the mirror reflectivity of a prime focus telescope.' *Astropart. Phys.*, **27**, 509–511.

[230] Moralejo, A. et al., 2009. 'MARS, the MAGIC Analysis and Reconstruction Software.' *ArXiv e-prints*.

[231] Mücke, A. and Protheroe, R.J., 2000. 'Modeling the April 1997 flare of Mkn 501.' In B.L. Dingus, M.H. Salamon and D.B. Kieda, editors, 'American Institute of Physics Conference Series,' Volume 515 of *American Institute of Physics Conference Series*, pages 149–153. doi:10.1063/1.1291360.

[232] Mücke, A. et al., 2003. 'BL Lac objects in the synchrotron proton blazar model.' *Astroparticle Physics*, **18**, 593–613. doi:10.1016/S0927-6505(02)00185-8.

[233] Mukerjee, K. et al., 2004. 'A spectroscopic performance of the Swift X-ray Telescope for gamma-ray burst afterglow studies.' In K.A. Flanagan and O.H.W. Siegmund, editors, 'Society of Photo-Optical Instrumentation Engineers (SPIE) Conference Series,' Volume 5165 of *Society of Photo-Optical Instrumentation Engineers (SPIE) Conference Series*, pages 251–261. doi:10.1117/12.507852.

[234] Nandikotkur, G. et al., 2007. 'Does the Blazar Gamma-Ray Spectrum Harden with Increasing Flux? Analysis of 9 Years of EGRET Data.' *ApJ*, **657**, 706–724. doi:10.1086/510795.

[235] Neddermeyer, S.H. and Anderson, C.D., 1937. 'Note on the Nature of Cosmic-Ray Particles.' *Physical Review*, **51**, 884–886. doi:10.1103/PhysRev.51.884.

[236] Neher, H.V. and Forbush, S.E., 1952. 'Correlation of Cosmic-Ray Ionization Measurements at High Altitudes, at Sea Level, and Neutron Intensities at Mountain Tops.' *Physical Review*, **87**, 889–890. doi:10.1103/PhysRev.87.889.

[237] Ney, E.P., 1959. 'Cosmic Radiation and the Weather.' *Nature*, **183**, 451–452. doi:10.1038/183451a0.

[238] Nieppola, E., Tornikoski, M. and Valtaoja, E., 2006. 'Spectral energy distributions of a large sample of BL Lacertae objects.' *A&A*, **445**, 441–450.

[239] Nikishov, A.I., 1962. *Sov. Phys. JETP*, **14**, 393.

[240] Nilsson, K. et al., 2007. 'Host galaxy subtraction of TeV candidate BL Lacertae objects.' *A&A*, **475**, 199–207. doi:10.1051/0004-6361:20077624.

[241] Niu, K., Mikumo, E. and Maeda, Y., 1971. 'A Possible Decay in Flight of a New Type Particle.' *Progress of Theoretical Physics*, **46**, 1644–1646. doi:10.1143/PTP.46.1644.

[242] Nolan, P.L. et al., 2012. 'Fermi Large Area Telescope Second Source Catalog.' *ApJS*, **199**, 31. doi:10.1088/0067-0049/199/2/31.

[243] Ohm, S., 2012. 'γ-rays from starburst galaxies.' *ArXiv e-prints*.

[244] Orr, M.R., Krennrich, F. and Dwek, E., 2011. 'Strong New Constraints on the Extragalactic Background Light in the Near- to Mid-infrared.' *ApJ*, **733**, 77. doi:10.1088/0004-637X/733/2/77.

[245] Ostankov, A. and MAGIC Collaboration, 2001. 'The image camera of the 17m diameter air Cherenkov telescope MAGIC.' *Nuclear Instruments and Methods in Physics Research A*, **471**, 188–191. doi:10.1016/S0168-9002(01)00961-5.

[246] Padovani, P., 1997. 'Gamma-Ray Emitting AGN and Unified Schemes.' In Y. Giraud-Heraud and J. Tran Thanh van, editors, 'Very High Energy Phenomena in the Universe; Moriond Workshop,' page 7.

[247] Padovani, P., 1999. 'High energy emission from AGN and unified schemes.' In F. Giovannelli and G. Mannocchi, editors, 'Vulcano Workshop 1998: Frontier Objects in Astrophysics and Particle Physics,' page 159.

[248] Pagliaroli, G., Vissani, F., Costantini, M.L. and Ianni, A., 2009. 'Improved analysis of SN1987A antineutrino events.' *Astroparticle Physics*, **31**, 163–176.

[249] Palenzuela, C., Bona, C., Lehner, L. and Reula, O., 2011. 'Robustness of the Blandford-Znajek mechanism.' *Classical and Quantum Gravity*, **28**, 13, 134007. doi:10.1088/0264-9381/28/13/134007.

[250] Paneque, D., Gebauer, H.J., Lorenz, E. and Mirzoyan, R., 2004. 'A method to enhance the sensitivity of photomultipliers for Air Cherenkov Telescopes by applying a lacquer that scatters light.' *Nuclear Instruments and Methods in Physics Research A*, **518**, 619–621. doi:10.1016/j.nima.2003.11.101.

[251] Paoletti, R. et al., 2007. 'The trigger system of the magic telescope.' *Nuclear Science, IEEE Transactions on*, **54**, 2, 404 –409. ISSN 0018-9499. doi:10.1109/TNS.2007.892649.

[252] Paoletti, R. et al., 2008. 'The global trigger system of the magic telescope array.' In 'Nuclear Science Symposium Conference Record, 2008. NSS '08. IEEE,' pages 2781 –2783. ISSN 1095-7863. doi:10.1109/NSSMIC.2008.4774948.

[253] Pareschi, G. et al., 2008. 'Glass mirrors by cold slumping to cover 100 m^2 of the MAGIC II Cherenkov telescope reflecting surface.' In 'Society of Photo-Optical Instrumentation Engineers (SPIE) Conference Series,' Volume 7018 of *Society of Photo-Optical Instrumentation Engineers (SPIE) Conference Series*. doi:10.1117/12.790404.

[254] Pegna, R. et al., 2006. 'Performance of the Domino Ring Sampler in the MAGIC experiment.' *Nuclear Instruments and Methods in Physics Research A*, **567**, 218–221. doi:10.1016/j.nima.2006.05.205.

[255] Perlman, E.S. et al., 1996. 'The Einstein Slew Survey Sample of BL Lacertae Objects.' *ApJS*, **104**, 251. doi:10.1086/192300.

[256] Pierog, T., Engel, R. and Heck, D., 2006. 'Impact of uncertainties in hadron production on air-shower predictions.' *Czechoslovak Journal of Physics*, **56**, 26, A260000–A172. doi:10.1007/s10582-006-0152-0.

[257] Pierre AUGER Collaboration et al., 2010. 'Measurement of the energy spectrum of cosmic rays above 10^{18} eV using the Pierre Auger Observatory.' *Physics Letters B*, **685**, 239–246.

[258] Popovic, L.C., 2006. 'The Broad Line Region of AGN: Kinematics and Physics.' *Serbian Astronomical Journal*, **173**, 1. doi:10.2298/SAJ0673001P.

[259] Prandini, E., Bonnoli, G. and Tavecchio, F., 2012. 'Estimating the redshift of PKS 0447-439 through its GeV-TeV emission.' *A&A*, **543**, A111. doi:10.1051/0004-6361/201118289.

[260] Prandini, E., Mariotti, M. and Tavecchio, F., 2011. 'Constraining blazars distances with combined GeV and TeV data.' *ArXiv e-prints*.

[261] Prandini, E. et al., 2010. 'Constraining blazar distances with combined Fermi and TeV data: an empirical approach.' *MNRAS*, **405**, L76–L80.

[262] Prandini, E. et al., 2011. 'Blazars distance indications from Fermi and TeV data.' *ArXiv e-prints*.

[263] Prandini, E. et al., 2011. 'TeV blazars and their distance.' *ArXiv e-prints*.

[264] Primack, J.R., Bullock, J.S., Somerville, R.S. and MacMinn, D., 1999. 'Probing galaxy formation with TeV gamma ray absorption.' *Astroparticle Physics*, **11**, 93–102. doi:10.1016/S0927-6505(99)00031-6.

[265] Punch, M. et al., 1992. 'Detection of TeV photons from the active galaxy Markarian 421.' *Nature*, **358**, 477–+.

[266] Punsly, B., 1999. 'Possible New X-Ray-selected EGRET Identifications.' *ApJ*, **516**, 141–144. doi:10.1086/307094.

[267] Rachen, J.P. and Mészáros, P., 1998. 'Photohadronic neutrinos from transients in astrophysical sources.' *Phys. Rev. D*, **58**, 12, 123005.

[268] Rao, M.V.S. and Sinha, S., 1988. 'The origin of the hump in the cerenkov lateral distribution in gamma-ray showers and a possible means of separating them from proton showers.' *Journal of Physics G: Nuclear Physics*, **14**, 6, 811.

[269] Rao, V. and Sreekantan, B., 1998. *Extensive Air Showers* (World Scientific). ISBN 9789810228880.

[270] Readhead, A.C.S. et al., 1989. 'A limit of the anisotropy of the microwave background radiation on arc minute scales.' *ApJ*, **346**, 566–587. doi:10.1086/168039.

[271] Reinthal, R. et al., 2012. 'Connection Between Optical and VHE Gamma-ray Emission in Blazar Jets.' *Journal of Physics Conference Series*, **355**, 1, 012013. doi:10.1088/1742-6596/355/1/012013.

[272] Reinthal, R. et al., 2012. 'Multi-wavelength Observations of the HBL 1ES 1011+496 in Spring 2008.' *Journal of Physics Conference Series*, **355**, 1, 012017. doi:10.1088/1742-6596/355/1/012017.

[273] Richards, J.L. et al., 2011. 'Observations of blazars at 15GHz (Richards+, 2011).' *VizieR Online Data Catalog*, **219**, 40029.

[274] Rissi, M., Otte, N., Schweizer, T. and Shayduk, M., 2009. 'A New Sum Trigger to Provide a Lower Energy Threshold for the MAGIC Telescope.' *IEEE Transactions on Nuclear Science*, **56**, 3840–3843. doi:10.1109/TNS.2009.2030802.

[275] Rochester, G.D. and Butler, C.C., 1947. 'Evidence for the Existence of New Unstable Elementary Particles.' *Nature*, **160**, 855–857. doi:10.1038/160855a0.

[276] Rolke, W.A., López, A.M. and Conrad, J., 2005. 'Limits and confidence intervals in the presence of nuisance parameters.' *Nuclear Instruments and Methods in Physics Research A*, **551**, 493–503. doi:10.1016/j.nima.2005.05.068.

[277] Roming, P.W.A. et al., 2005. 'The Swift Ultra-Violet/Optical Telescope.' *Space Sci. Rev.*, **120**, 95–142. doi:10.1007/s11214-005-5095-4.

[278] Roncadelli, M., De Angelis, A., Galanti, G. and Persic, M., 2011. 'Evidence for an axion-like particle from blazar spectra?' *ArXiv e-prints*.

[279] Rossi, B., 1933. 'Interaction between Cosmic Rays and Matter.' *Nature*, **132**, 173–174. doi:10.1038/132173b0.

[280] Rossi, B. and Greisen, K., 1941. 'Cosmic-ray theory.' *Rev. Mod. Phys.*, **13**, 240–309. doi:10.1103/RevModPhys.13.240.

[281] Rügamer, S. et al., 2011. 'MAGIC and Multi-Wavelength Observations of Mrk 180 and 1ES 2344+514 in 2008.' *ArXiv e-prints*.

[282] Rutledge, R.E., 1998. 'The Astronomer's Telegram: A Web-based Short-Notice Publication System for the Professional Astronomical Community.' *PASP*, **110**, 754–756. doi:10.1086/316184.

[283] Schachter, J.F. et al., 1993. 'Ten new BL Lacertae objects discovered by an efficient X-ray/radio/optical technique.' *ApJ*, **412**, 541–549. doi:10.1086/172942.

[284] Schlickeiser, R., 2002. *Cosmic Ray Astrophysics* (Springer-Verlag, Berlin, Heidelberg, New York).

[285] Schönfelder, V. et al., 1984. 'The imaging Compton telescope COMPTEL on the Gamma Ray Observatory.' *IEEE Transactions on Nuclear Science*, **31**, 766–770. doi:10.1109/TNS.1984.4333363.

[286] Schultz, C., Berger, K. and Reinthal, R., in preparation. 'MAGIC detection of short–term variability of the high–peaked BL Lac object 1ES 0806+524.' *A&A*. For the MAGIC Collaboration.

[287] Schultz, C. et al., 2012. 'Spectral variability and multiwavelength studies of the high-frequency-peaked bl lacertae object 1es 0806 + 524 with the magic telescopes.' *AIP Conference Proceedings*, **1505**, 1, 534–537. doi:10.1063/1.4772315.

[288] Schulz, A., 2011. 'Methods for the characterization of mirror facets of Imaging Atmospheric Cherenkov Telescopes.' In 'International Cosmic Ray Conference,' Volume 9 of *International Cosmic Ray Conference*, page 34.

[289] Sikora, M. et al., 2009. 'Constraining Emission Models of Luminous Blazar Sources.' *ApJ*, **704**, 38–50. doi:10.1088/0004-637X/704/1/38.

[290] Somerville, R.S., Gilmore, R.C., Primack, J.R. and Domínguez, A., 2012. 'Galaxy properties from the ultraviolet to the far-infrared: Λ cold dark matter models confront observations.' *MNRAS*, **423**, 1992–2015. doi:10.1111/j.1365-2966.2012.20490.x.

[291] Sowards-Emmerd, D., Romani, R.W. and Michelson, P.F., 2003. 'The Gamma-Ray Blazar Content of the Northern Sky.' *ApJ*, **590**, 109–122. doi:10.1086/374981.

[292] Sowards-Emmerd, D. et al., 2005. 'A Northern Survey of Gamma-Ray Blazar Candidates.' *ApJ*, **626**, 95–103. doi:10.1086/429902.

[293] Spanier, F. and Weidinger, M., 2012. 'Hadronic modeling of agn variability.' *International Journal of Modern Physics: Conference Series*, **08**, 01, 293–298. doi:10.1142/S2010194512004734.

[294] STACEE Collaboration: S. Oser et al., 2000. 'High Energy Gamma-Ray Observations of the Crab Nebula and Pulsar with the Solar Tower Atmospheric Cherenkov Effect Experiment.' *ArXiv Astrophysics e-prints*.

[295] Stamatescu, V. et al., 2012. 'Towards an optimized design for the Cherenkov Telescope Array.' In F.A. Aharonian, W. Hofmann and F.M. Rieger, editors, 'American Institute of Physics Conference Series,' Volume 1505 of *American Institute of Physics Conference Series*, pages 758–761. doi:10.1063/1.4772370.

[296] Stamerra, A. et al., 2011. 'Swift follow-up of the flaring BL Lac 1ES0806+524.' *The Astronomer's Telegram*, **3208**, 1.

[297] Stecker, F.W., Baring, M.G. and Summerlin, E.J., 2007. 'Blazar γ-Rays, Shock Acceleration, and the Extragalactic Background Light.' *ApJ Letters*, **667**, L29–L32. doi:10.1086/522005.

[298] Stecker, F.W. and de Jager, O.C., 1996. 'Absorption of high energy gamma-rays by low energy intergalactic photons.' *Space Sci. Rev.*, **75**, 401–412. doi:10.1007/BF00195048.

[299] Stecker, F.W., Malkan, M.A. and Scully, S.T., 2006. 'Intergalactic Photon Spectra from the Far-IR to the UV Lyman Limit for $0<z<6$ and the Optical Depth of the Universe to High-Energy Gamma Rays.' *ApJ*, **648**, 774–783.

[300] Stecker, F.W. and Scully, S.T., 2010. 'Derivation of a Relation for the Steepening of Tev-Selected Blazar γ-ray Spectra with Energy and Redshift.' *ApJ Letters*, **709**, L124–L126.

[301] Steele, I.A. et al., 2010. 'RINGO2: an EMCCD-based polarimeter for GRB followup.' In 'Society of Photo-Optical Instrumentation Engineers (SPIE) Conference Series,' Volume 7735 of *Society of Photo-Optical Instrumentation Engineers (SPIE) Conference Series*. doi:10.1117/12.856842.

[302] Stetson, P.B., 1987. 'DAOPHOT - A computer program for crowded-field stellar photometry.' *PASP*, **99**, 191–222. doi:10.1086/131977.

[303] Stocke, J.T., Morris, S.L., Weymann, R.J. and Foltz, C.B., 1992. 'The radio properties of the broad-absorption-line QSOs.' *ApJ*, **396**, 487–503. doi:10.1086/171735.

[304] Swordy, S., 2008. 'VERITAS discovers VHE gamma rays from BL Lac 1ES0806+524.' *The Astronomer's Telegram*, **1415**, 1.

[305] Takalo, L.O. et al., 2007. 'Optical Monitoring of Candidate TeV Blazars.' In L. C. Ho & J.-W. Wang, editor, 'The Central Engine of Active Galactic Nuclei,' Volume 373 of *Astronomical Society of the Pacific Conference Series*, pages 249–+.

[306] Tavani, M. et al., 2009. 'The AGILE Mission.' *A&A*, **502**, 995–1013. doi:10.1051/0004-6361/200810527.

[307] Tavecchio, F., Maraschi, L. and Ghisellini, G., 1998. 'Constraints on the Physical Parameters of TeV Blazars.' *ApJ*, **509**, 608–619.

[308] Tavecchio, F., Roncadelli, M., Galanti, G. and Bonnoli, G., 2012. 'Evidence for an axion-like particle from PKS 1222+216?' *Phys. Rev. D*, **86**, 8, 085036. doi:10.1103/PhysRevD.86.085036.

[309] Tavecchio, F. et al., 2010. 'TeV BL Lac objects at the dawn of the Fermi era.' *MNRAS*, **401**, 1570–1586.

[310] Tepe, A. and the Hawc Collaboration, 2012. 'HAWC - The High Altitude Water Cherenkov Detector.' *Journal of Physics Conference Series*, **375**, 5, 052026. doi:10.1088/1742-6596/375/1/052026.

[311] Teraesranta, H. et al., 1998. 'Fifteen years monitoring of extragalactic radio sources at 22, 37 and 87 GHz.' *A&AS*, **132**, 305–331. doi:10.1051/aas:1998297.

[312] Tescaro, D. et al., 2009. 'The readout system of the MAGIC-II Cherenkov Telescope.' *ArXiv e-prints*.

[313] The Pierre AUGER Collaboration et al., 2008. 'Correlation of the highest-energy cosmic rays with the positions of nearby active galactic nuclei.' *Astroparticle Physics*, **29**, 188–204.

[314] The Pierre AUGER Collaboration et al., 2010. 'Update on the correlation of the highest energy cosmic rays with nearby extragalactic matter.' *Astroparticle Physics*, **34**, 314–326.

[315] Thompson, D.J. et al., 1993. 'Calibration of the Energetic Gamma-Ray Experiment Telescope (EGRET) for the Compton Gamma-Ray Observatory.' *ApJS*, **86**, 629–656. doi:10.1086/191793.

[316] Thompson, R.J. and Cordova, F.A., 1994. 'A statistical analysis of the broadband 0.1 to 3.5 keV spectral properties of X-ray-selected active galactic nuclei.' *ApJ*, **434**, 54–66. doi:10.1086/174704.

[317] Tikhonov, A.N. and Arsenin, V.A., 1977. *Solution of iII-posed Problems* (Winston & Sons, Washington).

[318] Torres, D.F., 2003. 'Gamma-ray sources at high latitudes (Extragalactic gamma-ray sources).' *ArXiv Astrophysics e-prints*.

[319] Türler, M. et al., 2010. 'INTEGRAL hard X-ray spectra of the cosmic X-ray background and Galactic ridge emission.' *A&A*, **512**, A49. doi:10.1051/0004-6361/200913072.

[320] Ulrich, R., Engel, R. and Unger, M., 2011. 'Hadronic multiparticle production at ultrahigh energies and extensive air showers.' *Phys. Rev. D*, **83**, 5, 054026. doi:10.1103/PhysRevD.83.054026.

[321] Urry, C.M. and Padovani, P., 1995. 'Unified Schemes for Radio-Loud Active Galactic Nuclei.' *PASP*, **107**, 803–+.

[322] Vasileiadis, G. and H.E.S.S. Collaboration, 2005. 'The H.E.S.S experimental project.' *Nuclear Instruments and Methods in Physics Research A*, **553**, 268–273. doi:10.1016/j.nima.2005.08.056.

[323] Vincent, P., 2005. 'H.E.S.S. Phase II.' In 'International Cosmic Ray Conference,' Volume 5 of *International Cosmic Ray Conference*, page 163.

[324] Wagner, S.M., 2006. *Measurement of Very High Energy Gamma-Ray EMission from Four Blazars Using the MAGIC Telescope and a Comparative Blazar Study*. Ph.D. thesis, Technical University Munich, Munich.

[325] Wehrle, A.E. et al., 2001. 'Kinematics of the Parsec-Scale Relativistic Jet in Quasar 3C 279: 1991-1997.' *ApJS*, **133**, 297–320.

[326] Winkler, C. et al., 2003. 'The INTEGRAL mission.' *A&A*, **411**, L1–L6. doi:10.1051/0004-6361:20031288.

[327] Yang, R.Z., Chang, J. and Wu, J., 2010. 'A possible explanation for the electron/positron excess of ATIC/PAMELA.' *Research in Astronomy and Astrophysics*, **10**, 39–46. doi:10.1088/1674-4527/10/1/004.

[328] Zatsepin, G.T. and Kuz'min, V.A., 1966. 'Upper Limit of the Spectrum of Cosmic Rays.' *Soviet Journal of Experimental and Theoretical Physics Letters*, **4**, 78–+.

Units

Crab (Nebula) Unit is an integral flux unit. The measured or reported integral flux above a certain energy threshold is commonly expressed as the fraction of the Crab Nebula flux above this threshold. The integrated Crab Nebula flux used as reference in this work is estimated from the power law fit of its differential energy spectrum published in (Albert et al., 2008).

erg is an energy unit used in astrophysics. One erg is equal to 10^{-7} J.

eV the electron volt corresponds to an energy unit typically used in particle and astroparticle physics; it is equal to approximately 1.602×10^{19} J. This unit is commonly used with the metric prefixes kilo-, mega-, giga-, tera-, peta- or exa-, thus 1 keV (10^3 eV), 1 MeV (10^6 eV), 1 GeV (10^9 eV), 1 TeV (10^{12} eV), 1PeV (10^{15} eV) and 1EeV (10^{18} eV) respectively.

High Energy (HE) refers conventionally to the energy regime from 0.1 GeV to 100 GeV.

light year is a unit of length. One ly is defined by the International Astronomical Union as the distance that light travels in vacuum in one Julian year corresponding to approximately 9.461×10^{15} m.

Jy stands for Jansky and is an integral flux unit commonly used in optical and radio astronomy. One Jy is equivalent to 10^{26} W m^{-2}s^{-1}.

MJD stands for Modified Julian Date. The MJD is an abbreviated version of the Julian Day dating method, an unambiguous time unit based un continuing day counts. The MJD corresponds to the number of days elapsed since midnight of November 17th, 1858 representing the modification of the JD by its reduction of 2400000,5 days.

parsec is a unit of length used in astronomy equivalent to 30.857×10^{15} m.

phe stands for number of photoelectrons. It is commonly used as unit to characterize the images collected by an IACT representing the sum of the calibrated charge of a triggered event collected by each PMT of the Cherenokov camera. In other words the phe represents the `size` of a detected image.

redshift is characterized by the relative difference between the observed and emitted wavelengths of an object in Doppler motion with respect to an observer. Typically, this change in wavelength is refered to the dimensionless quantity z:

$$z = \frac{\lambda_{\text{obs}} - \lambda_{\text{em}}}{\lambda_{\text{em}}}$$

In astronomy, the z is commonly used as a unit of distance or time since it is related to the gravitational redshift experienced by the radiation traveling cosmological distances, due to the expansion of the Universe. Consequently, the redshift dependents strongly on the cosmological model assumed.

Very High Energy (VHE) to TeV energies cover conventionally the range from 100 GeV to tens of TeV.

Acronyms

AGASA Akeno Giant Air Shower Array

AGILE Astro–Rivelatore Gamma a Immagini Leggero

ALP Axion–Like Particle

AGN Active Galactic Nucleus

AMC Active Mirror Control

ASM All Sky Monitor

BS Binary System

BP Binary Pulsar

BH Black Hole

BLR Broad Line Region

CCD Charged Coupled Device

CCNN Close Compact Next Neighbors

CERN Conseil Européen pour la Recherche Nucléaire

CGB Cosmic Gamma-ray Background

CGRO Compton Gamma–Ray Observatory

CIB Cosmic Infrared Background

CMB Cosmic Microwave Background

COB Cosmic Optical Background

COBE Cosmic Background Explorer

COMPTEL Compton Telecope

CR Cosmic Ray

CRB Cosmic Radio Background

CTA Cherenkov Telescope Array

CUVOB Cosmic Ultraviolet and Optical Background

CXB Cosmic X-ray Background

DARMA De Angelis–Roncadelli–Mansutti

DAQ Data Acquisition

DGL Diffuse Galactic Light

DIRBE Diffuse Infrared Background Experiment

DM Dark Matter

DRS Domino Ring Sampler

EAS Extended Air Showers

EBL Extragalactic Background Light

EC External Compton

EGB Extragalactic Gamma-ray Background

EGRET Energetic Gamma Ray Experiment Telescope

FACT First G–APD Cherenkov Telescope

FADC Fast Analog to Digital Converter

FIR Far Infrared

FoV Field of View

FR Full Range

FSRQ Flat Spectrum Radio Quasar

fTf Flat–to–flat

G–APD Geiger–mode Avalanche Photodiode

GC Galactic Center

GBM GLAST Burst Monitor

GP Galactic Plane

GRB Gamma–Ray Burst

GZK Greisen–Zatsepin–Kuz'min

HBL High–frequency peaked BL Lac

H.E.S.S. High Energy Stereoscopic System

HAWC High Altitude Water Cherenkov Experiment

HE High Energy

HEGRA High Energy Gamma–Ray Astronomy

HiRes High Resolution

HPD Hybrid Photo Detector

HST Hubble Space Telescope

IACTs Imaging Atmospheric Cherenkov Telescopes

IBL Intermediate–frequency peaked BL Lac

IC Inverse Compton

IGM InterGalactic Medium

INTEGRAL International Gamma–Ray Astrophysics Laboratory

IR Infrared

ISM InterStellar Medium

KVA Kungliga Vetenskapsakademien

LAT Large Area Telescope

LBL Low–frequency peaked BL Lac

LE Low Energy

LED Light Emitting Diode

LHAASO Large High Altitude Air Shower Observatory

LST Large Size Telescope

LoS Line of Sight

LRT Likelihood ratio test statistics

LUT Look Up Table

MAGIC Major Atmospheric Gamma Imaging Cherenkov

MARS Magic Analysis and Reconstruction Software

MC MonteCarlo

MILAGRO Multiple Institution Los Alamos Gamma Ray Observatory

MIR Mid Infrared

MJD Modified Julian Date

MOJAVE Monitoring of Jets in Active Galactic Nuclei with VLBA Experiments

MQS Microquasar

MST Medium Size Telescope

MUX Multiplex

NIR Near Infrared

NLR Narrow Line Region

NSB Night Sky Background

OC Stellar Cluster

ORM Observatorio del Roque de los Muchachos

OSSE Oriented Scintillation Spectrometer Experiment

OVRO Owens Valley Radio Observatory

PAO Pierre Auger Observatory

PAMELA Payload for Antimatter Matter Exploration and Light-nuclei Astrophysics

PDE Photo Detection Efficiency

PMT Photomultiplier Tube

PPA Pair Production Anomaly

PSF Point Spread Function

PWD Pulsar Wind Nebula

QE Quantum Efficiency

RA Right Ascension

RASS ROSAT All Sky Survey

RG Radio Galaxy

RF Random Forest

RMS Root Mean Square

ROI Region of Interest

RQ Radio Quasar

SAM Semi–Analytical Model

SED Spectral Energy Distribution

SMBH Supermassive Black Hole

SNR SuperNova Remnant

SSC Synchrotron Self Compton

SFR Star Formation Rate

SST Small Size Telescope

SUSY Super–Symmetric

TS Test Statistic

UFU Unidentified Object

UHE Ultra High Energy

UHECR Ultra High Energy Cosmic Ray

UV Ultraviolet

VERITAS Very Energetic Radiation Imaging Telescope Array System

VCSELs Vertical Cavity Surface Emitting Laser Drivers

VHE Very High Energy ($> 100\,\mathrm{GeV}$)

VLBA Very Long Baseline Arrays

WIMP Weakly Interacting Massive Particle

WMAP Wilkinson Microwave Anisotropy Probe

ZL Zodiacal Light

Acknowledgments

There are several people which were involved in the scientific and technical work of this PhD thesis whom I would like to thank.
First, I want to thank my tutor, Prof Mosé Mariotti, for his encouragement in applying for a PhD position in Padova as a foreign student, for his trust in me, for his valuable advices and the opportunities he has given to me.
A special acknowledgement to Elisa Prandini, my "little Genius", for her general helpfulness. In particular, her advices concerning the data analysis and her suggestions on how to write proposals and other scientific documents have been priceless. I am deeply grateful for the corrections and suggestions she gave me for writing this thesis. Thank you so much for your encouragement and optimism, the phone calls and skype sessions despite your full time job as a mother!
I am much obliged to Mosé Mariotti, Michele Doro and Villi Scalzotto for their useful comments on this thesis. A special thank to Francesco Dazzi for his occasional support during the last months in decrypting the hand writing of the corrections on this manuscript.
Many thanks to the members of the MAGIC collaboration for their friendship and their enthusiasm about doing research in the field of VHE γ–ray astrophysics. A particular thank to Karsten Berger, my 1ES 0806+524 mentor, and to my other 1ES 0806+524 friend Riho Reinthal. I am very grateful to Simona Paiano and Paolo Da Vela for sharing 1ES 1011+496 with me and to all the people I collaborated with: Elina Linfdors, my 3C 279 companion Gessica De Caneva, Fabrizio Tavecchio, Ulisses Barres de Almeida and many, many more.
I will always keep my data taking shifts in good memory. The long nights of observations, the breathtaking sunrises, the long car drives up and down the Roque de los Muchachos, a day during Los Indianos remain unforgettable thanks to the colleagues of the shift crews P92 and P113: Villi Scalzotto, Valeria Scapin, Natalia Lewandowska, Karsten Berger and Riho Reinthal.
I am very thankful to Enrico Giro for his support, help and knowledge in the performance of optical measurements. Thanks for the pleasant company during numerous hours in the dim corridor of the Legnaro National Laboratories, in various occasions during CTA meetings and diverse car rides both as a colleague and a friend.
Many thanks to Luigi Lessio, the mechanic workshop and the draftsmen of the Padova University for their help in setting up the optical measurement system in the Legnaro National Laboratories.
I would like to express my thankfulness to my colleagues of the MAGIC Padova group: Elisa, Simona, my dearest "FuCo" Saverio, "TO" Villi, Francesco, Daniele, Michele, Antonio and not to forget Mosé. My work wouldn't have been them same without sharing office with some of you and the everyday laughters we had. It was a pleasure working and discussing with you and I am much obliged for your support and help.
I am grateful to Antonio Saggion and Rossella Faraldo who gave me the opportunity to carry on the activity MAGIC-D together with Villi in parallel to my

research activities.
I want to thank Mikai, my family and friends for having enriched my life so much during these years. I wouldn't be the same person without having them around and it is a great wish of mine to spend one day with all of you united.
I am especially grateful that Mikai stepped into my life right at the beginning of this exciting experience. His love, care, support, patience and sympathy in our common everyday life have been priceless, especially during the last four months. Thank you for teaching me that it takes two to Tango!
Thanks to my parents Esther and Uwe for their believe in me. Their pride and unconditional support in what I am doing is simply invaluable! A kiss to Mikai's family and a great hug to Christiane and Dimitrio, my "Leiheltern" from the Black Forest for their care about me. Many kisses to my Italian family, the Lupis: Manu, Michela and Sergio who welcomed me so warmly in Padova right after my arrival, who hosted me in their house and who are always taking care of me as being part of their family. How wonderful to be part of so many families!
Laura, Jana, Hauke and Moritz, you are the best friends someone can imagine. Thank you for the time spent together, for the laughters, discussions, and the consolation and sympathy in times of crisis.
Thanks to all my Padova friends: Sofia for sharing lunch breaks with me, you know best what it's like to do your PhD as a foreigner in Italy, Fabio and Giulia for the numerous dinners and their wonderful hospitality, the desert is waiting for us, my choir and tango companions for sharing the passion in singing and dancing.
To my Munich crew. Beside the distance between us I am very grateful to each of you for your friendship, your phone calls, your emails, your visits in Padova and the wonderful memories that helped me to move on: Caro for these crazy nights at the X bar, the laughters and tears we shared, the scientific discussion we had, the days we hang out in the English Garden, for being my ideal without probably knowing it, I fell deeply connected to you... Anna for hosting me whenever the longing for Munich was calling, I am looking forward for a last "hanging around" in MacBeth together with you, MC aka Bao, for always having a place to stay and for her open ear and heart, la piccola borghese Jenny for her unshaken and contagious cheerfulness, Florian for his unmistakable laugh and this very special friendship that connects us, Zoran for creating the most wonderful birthday buffet in my kitchen at the cost of driving everyone crazy, I adore you for this one moment in Munich in your apartment when you played the first bars of Rachmaninoff's piano concert n.2 while smoking a cigarette... my ex-neighbors, Katja, Pano, Dennis & Diego for their frankly and hearty manner, what would I have done without you when it was time to move house... Kerstin and & Lion, for these special moments in their kitchen, Hans for his geniality, his creative gift and those summer nights when we were sitting in the window ledges of our apartments chatting, I am very proud of you an it's my honor to call you a friend... Eva for her delicious tarragon chicken, her touching poems, her patience during those endless conversations in a desperate snowy winter in Munich, will we ever make it to Madagascar...
I final thought goes across the Ocean to Montreal to my dearest friend Emily and to my teachers from the McGill University Marguerite & Henriette. You were right Henriette: "La vie est belle!"... Someday I'm coming back... soon...

List of Figures

List of Tables